Copyright is owned by the Author of the thesis. Permission is given for a copy to be downloaded by an individual for the purpose of research and private study only. The thesis may not be reproduced elsewhere without the permission of the Author.

Understanding Aspects of Andesitic Dome-forming Eruptions Through the Last 1000 yrs of Volcanism at Mt. Taranaki, New Zealand

A dissertation presented in partial fulfilment of the requirements
for the degree of
Doctor of Philosophy
in
Earth Science

Thomas Platz

Massey University, Palmerston North
New Zealand

2007



The summit of Mt. Taranaki. Photographed by G. Lube.

Dedicated to my parents,
to Katrin and my son August

Abstract

Andesitic volcanoes are notorious for their rapid and unpredictable changes in eruptive style between and during volcanic events, a feature normally attributed to shallow-crustal and intra-edifice magmatic processes. Using the example of eruptions during the last 1000 yrs at Mt. Taranaki (the Maero Eruptive Period), deposit sequences were studied to (1) understand lava dome formation and destruction, (2) interpret the causes of rapid shifts from extrusive to explosive eruption styles, and (3) to build a model of crustal magmatic processes that impact on eruption style.

A new detailed reconstruction of this period identifies at least 10 eruptive episodes characterised by extrusive, lava dome- and lava flow-producing events and one sub-Plinian eruption. To achieve this, a new evaluation procedure was developed to purge glass datasets of contaminated mineral-glass analyses by using compositional diagrams of mineral incompatible-compatible elements. Along with careful examination of particle textures, this procedure can be broadly applied to build a higher degree of resolution in any tephrostratigraphic record. Geochemical contrasts show that the products of the latest Mt. Taranaki eruption, the remnant summit dome (Pyramid Dome) was not formed during the Tahurangi eruptive episode but extruded post-AD1755. Its inferred original maximum volume of 4.9×10^6 m^3 (DRE) was formed by simultaneous endogenous and exogenous dome growth within days. Magma ascent and extrusion rates are estimated at $\geq$0.012 ms^{-1} and $\geq$6 m^3s^{-1}, respectively, based on hornblende textures. Some of the Maero-Period dome effusions were preceded by a vent-clearing phase producing layers of scattered lithic lapilli around the edifice [Newall Ash (a), Mangahume Lapilli, Pyramid Lapilli]. The type of dome failure controlled successive eruptive phases in most instances. The destruction of a pressurised dome either caused instantaneous but short-lived magmatic fragmentation (Newall and Puniho episodes), or triggered a directed blast-explosion (Newall episode), or initiated sustained magmatic fragmentation (Burrell Episode). The transition from dome effusion to a sustained, sub-Plinian eruption during the Burrell Lapilli (AD1655) episode was caused by unroofing a conduit of stalled magma, vertically segregated into three layers with different degrees of vesiculation and crystallisation. The resultant ejecta range from brown, grey and black coloured vesicular clasts to dense grey lithics. Bulk compositional variation of erupted clasts can be modelled by fractionation of hornblende, plagioclase, clinopyroxene, and Fe-Ti oxides. Pre-eruption magma ascent for the Maero Period events is assumed to begin at depths of c.9.5 km.

Acknowledgements

I wish to thank every person who contributed to the outcome of this study.

I went back to New Zealand to study one of the most fascinating phenomena nature has to offer: volcanoes. Of the North Island volcanoes, Mount Taranaki stands out as being the most imposing, and to me the most striking. Despite its dormancy, it proved a real challenge, to climb, find samples and sections, and to draw out some of his secrets.

For the opportunity to work again on Mt. Taranaki I am indebted to my chief-supervisor Dr Shane J. Cronin. Through him I learnt much about how to observe volcanic deposits and to understand the various processes involved in generating them. His aid in my receiving a Massey University Doctoral scholarship is highly appreciated. In past years Dr Cronin supported numerous overseas trips, which offered me the opportunity to meet other scientists, either on conferences or at the institutions where my overseas supervisors are based. I also benefited from his extraordinary skills in writing and presenting ideas and thoughts.

I also wish to thank all my co-supervisors: Prof. Vince E. Neall and Dr Robert B. Stewart (Massey University, New Zealand), Prof. Katharine V. Cashman (University of Oregon, USA), and Prof. Stephen F. Foley (University of Mainz, Germany) for their guidance and support over the years, their fruitful discussions and criticisms. I gratefully acknowledge the skill of all my supervisors to catch my thoughts especially when articulated in a Germanic English.

During my studies a lot of people were involved that helped and supported me from different parts of the globe.

New Zealand: First of all I wish to thank Jonathan N. Procter, Michael B. Turner, Anke V. Zernack and Kat A. Holt, my fellow inhabitants in the “Magma Chamber”. Without their friendship, life at Massey would have been colourless. Sharing “ups and downs” made many situations easier to bear.

I am also grateful to the staff of the Soil and Earth Sciences Group for assisting with everyday needs: Bob Toes (for also helping to fix Emma), Ian F. Furkert, Ross W. Wallace, Mike R. Bretherton, Moira Hubbard, Glenys C. Wallace, Anne R. West, Dr R. Clel Wallace, Dr Jerome A. Lecointre, Julie A. Palmer and Dr Alan S. Palmer. Carolyn B. Hedley (Landcare Research) introduced me to the thermal analysis technique. Dr Ritchie Sims and John Wilmshurst assisted in XRF- and electron microprobe analysis at The University of Auckland. For discussions on aspects of Taranaki and access to their

geochemical data I sincerely thank Assoc. Prof. Ian E.M. Smith (The University of Auckland) and Prof. Richard C. Price (Waikato University). Garry Bastin (Taranaki Research Centre) is thanked for his assistance in looking for historic references.

Eugene: From the Department of Geological Sciences I wish to thank Dr Heather M.N. Wright for introducing and assisting in sample preparation and measurement using the He-pycnometer and porosimeter. For inspiring discussions on pumice I especially acknowledge Drs Alison C. Rust and Heather M.N. Wright. Emily Johnson, Dr Julie Roberge, and Celeste Mercer are also thanked for their help in preparing melt inclusions. For discussions and access to the FTIR- and SEM facilities, the help of Assoc. Prof. Paul J. Wallace and Dr John J. Donovan are appreciated.

Kiel: Encouraging and fruitful discussions with Dr Armin Freundt and Sebastian Münn (IfM-GEOMAR) are especially acknowledged.

Mainz: For assistance in sample preparation and measurement I wish to thank the team on the Laser-ICP-MS, Institute of Geosciences, especially Drs Franziska Nehring and Matthias Barth.

Copenhagen: For encouragement, discussion, and analysis Dr Holger B. Lindgren of the Geological Survey of Denmark and Greenland is highly appreciated.

Potsdam: My thanks go also to Dr Thomas R. Walter (GeoForschungsZentrum Potsdam) for his unreserved discussions.

Studying abroad would have been far more difficult without the support of friends and family back home. My sincere thanks go to my parents who always supported me in everything I pursued. My friends Dr Gert Lube, Sebastian Münn, Dr Franziska Nehring, Luzie Herklotz, Dr Diana Reckien, and Jonathan N. Procter were always there when I needed them.

But the most important part was contributed by Katrin Bauer, through her love, respect, and honesty.

This work was funded and supported by a Massey University Doctoral Scholarship, the George Mason Trust of Taranaki, the Helen E. Akers Scholarship, the FRST-PGST contract MAUX0401, and an Institute of Natural Resources transitional scholarship.

Table of Contents

Abstract i

Acknowledgements iii

List of Tables xi

List of Figures xiii

Chapter 1 Introduction 1

1.1 Introduction 1

1.2 Objectives and Strategy 5

1.3 Thesis Outline 6

1.4 Background Geology 7

1.4.1 Regional Geological Setting 7

1.4.2 Taranaki Basin 9

1.4.3 Taranaki Volcanic Lineament 12

1.4.4 Mount Taranaki/Egmont 12

1.4.5 Petrology of Mt. Taranaki Rocks 15

1.5 References 19

Chapter 2 Methodology 31

2.1 Brief Outline 31

2.2 Field Studies 32

2.3 Mineralogy 33

2.3.1 Sample Preparation 33

2.3.2 Microscopic Studies 34

2.4 Geochemistry 34
2.4.1 X-ray Fluorescence Spectroscopy 34
2.4.2 Electron Microprobe Analysis 35
2.4.3 Laser Inductively Coupled Plasma Mass Spectrometry 36

2.5 Porosity and Permeability 37

2.6 Scanning Electron Microscopy 41

2.7 Fourier Transform Infrared Spectroscopy 41

2.8 Thermal Analysis 43

2.9 References 46

Chapter 3 The Maero Eruptive Period 49

3.1 Introduction 49
3.1.1 Previous Studies 51
3.1.1.1 Previous Work on Lava Flow Stratigraphy 54

3.2 Results 57
3.2.1 Stratigraphic Type and Reference Sections 57
3.2.1.1 Type Section of the Maero Formation 58
3.2.1.2 Reference Sections of the Maero Formation 64
3.2.2 Block-and-Ash Flow Deposits 68
3.2.2.1 Distribution and Flow Paths 68
3.2.3 Lava Flows 71
3.2.4 Glass Chemistry 75
3.2.4.1 Special Characteristics of Some Erupted Units 76
3.2.4.2 Correlation of Tephra and Pyroclastic Flow Deposits 77

3.3 Discussion **81**
3.3.1 Eruption Frequency of the Maero Eruptive Period 81
3.3.2 Comparison to the Previously Known Stratigraphy 86
3.3.3 Tephrostratigraphy of the Maero Eruptive Period 87

3.4 References **91**

Chapter 4 Improving the Reliability of Microprobe-based Glass Analyses **95**

4.1 Abstract 97

4.2 Introduction 97

4.2.1 Andesitic Volcanism, Tephra Generation and Dispersal 100

4.2.2 Sample Sites 103

4.3 Results 103

4.3.1 Contrasts in Particle Texture 103

4.3.2 Glass Chemistry and Data Evaluation 105

4.3.3 Estimating Plagioclase Proportions in Contaminated Analyses 111

4.4 Discussion 112

4.5 Conclusions 116

4.6 References 117

Chapter 5 Non-explosive, Dome-forming Eruptions **121**

5.1 Introduction 121

5.1.1 Lava Domes 122

5.1.1.1 Lava Dome Distribution in Taranaki 124

5.2 Field Observations 124

5.2.1 Tahurangi Eruptive Deposits 124

5.2.2 The Present Summit Lava Dome 128

5.2.3 Rock-Avalanche Deposit 130

5.3 Sample Sites and Methods 131

5.4 Results 132

5.4.1 Dome Volume Calculations 132

5.4.2 Mineralogy and Mineral Chemistry 134

5.4.3 Bulk Rock Composition 139

5.4.4 Microstructure, Density and Permeabilitiy of Dome Rocks 142

5.5 Discussion 142

5.5.1 Lava Dome Emplacement and Growth 142
5.5.2 Lava Dome Collapse 145
5.5.3 Estimation of Eruption Parameters 148
5.5.3.1 Magma Source Areas 148
5.5.3.2 Magma Storage at the Level of Neutral Buoyancy 151
5.5.3.3 Inferences for Hornblende Stability 153
5.5.3.4 Magma Ascent Rate 154
5.5.4 Eruption Duration 155
5.5.5 Approximation of the Time of Eruption 158
5.5.6 Historic References to Volcanic Activity in the 19th Century 161

5.6 Conclusions 166

5.7 References 167

Chapter 6 Transition to Explosive Eruptions 175

6.1 Abstract 177

6.2 Introduction 178
6.2.1 Geological Setting 179

6.3 Methodology 180

6.4 Results 182
6.4.1 Field Observations 182
6.4.1.1 Fall Deposits 182
6.4.1.2 Pumice Pyroclastic Flow Deposits 182
6.4.1.3 Block-and-Ash Flow Deposits 185
6.4.2 Volume Estimates 185
6.4.3 Clast Types and Textures 186
6.4.4 Mineralogy and Mineral Chemistry 189
6.4.5 Bulk Rock Geochemistry 190
6.4.6 Glass Composition 194
6.4.7 Porosity and Permeability 196

6.5 Discussion 198
6.5.1 Pre-climactic Conditions 199
6.5.1.1 Grey Lithics 199
6.5.1.2 Grey Pumice (Unit 1) 201
6.5.1.3 Brown Pumice (Unit 2) 202
6.5.2 Syn-climactic Conditions 203
6.5.2.1 Black, Banded, and Unit 3 Grey Pumice Clasts 203
6.5.3 Eruption Dynamics 204

6.6 Conclusions 206

6.7 References 208

6.8 Appendix 213
6.8.1 Appendix A: Correlation of Burrell Deposits, NW Sector 213
6.8.2 Appendix B: Location of Pyroclastic Flow Deposits 214
6.8.3 Appendix C: Volatile Contents in Glass – Preliminary Results and Conclusions 215
6.8.3.1 FTIR Spectroscopy 215
6.8.3.2 Thermal Analysis 217

Chapter 7 Reconstruction of Eruption Mechanisms Using Physico-chemical Data 221

7.1 Introduction 221
7.1.1 Viscosity of Magmas 222

7.2 Methods and Approach 225

7.3 Results 225
7.3.1 Petrography 225
7.3.1.1 Pyroclastic Flow Deposits 225
7.3.1.2 Lava Flows 230
7.3.2 Bulk Rock Chemistry 230
7.3.2.1 Pyroclastic Flow Deposits 230
7.3.2.2 Lava Flows 232

7.3.3 Physical Properties 232
7.3.3.1 Water Estimates of Volcanic Glasses 233
7.3.3.2 Viscosity 234

7.4 Discussion 238
7.4.1 Comparison of Physico-chemical Properties 238
7.4.1.1 Bulk Rock Composition 238
7.4.1.2 Melt and Magma Viscosities 239
7.4.2 Course and Eruption Styles of the Maero Eruptive Period 243
7.4.2.1 Types of Lava Domes 243
7.4.2.2 Causes of Dome Collapse and Associated Deposits 244
7.4.2.3 Reconstruction of the Maero Eruptive Period 247
7.5 Conclusion 251

7.6 References 252

Chapter 8 Conclusions 259

8.1 Avenues of Future Research 263

Appendices I

List of Tables

Table 2-1……..36
Detection limit of element oxides measured at the EMP (University of Auckland) including the deviation from a reference glass composition.

Table 2-2……..43
Water and carbon dioxide peaks on the FTIR spectra including their bonds within glasses.

Table 3-1……..52
Stratigraphy of the youngest deposits of Mt. Taranaki (Druce, 1966).

Table 3-2……..53
Stratigraphy of the youngest deposits at Mt. Taranaki until 2003 (Druce, 1966; Neall, 1972; Neall, 1979; McGlone et al., 1988; Lees and Neall, 1993).

Table 3-3……..54
Stratigraphy of the last 1000 yrs of activity at Mt. Taranaki established in 2003 (modified after Cronin et al., 2003).

Table 3-4……..73
Sample list, description and stratigraphy of studied lava flows and scoria-and-ash flow deposits.

Table 3-5……..83
New tephrostratigraphy of the Maero Eruptive Period.

Table 4-1……106
Glass EMPA of Taranaki (Burrell Lapilli eruption) and Ruapehu (14. October 1995 eruption) sorted by classed uncontaminated and contaminated data points. Detection limits for Taranaki glass EMPA only. All data in wt. %.

Table 4-2……108
Plagioclase microlite rim and centre compositions (Burrell Lapilli eruption, Mt. Taranaki). All data in wt.%.

Table 4-3……112
Calculation of various plagioclase mixing proportions within Taranaki hybrid glass EMPA. EMPA data in wt.%. See text for explanation.

Table 5-1……132
Sample location and description of studied summit dome rocks.

Table 5-2……134
Comparison of the modelled summit dome to other Taranaki flank lava domes.

Table 5-3……156
Historic lava dome eruptions compiled from Newhall and Melson (1983) and the Smithsonian Institution Catalogue.

Table 5-4……158
Physical parameters and results for equations 5-4 to 5-6.

Table 5-5……160
Physical parameters used for conductive cooling and rainfall-quenching of the lava dome.

Table 5-6……163
Selected eyewitness reports of the 18th and 19th century.

Table 6-1……186
Minimum volume and mass calculations of erupted tephra.

Table 6-2……191
XRF bulk rock geochemistry of Burrell Lapilli clasts. Samples are mostly from pumice flow deposits with one BAF deposit sample (P10).

Table 6-3……193
Mass balance calculation for the inferred fractionation process for pumice-lithics.

Table 6-4……195
Representative normalised matrix glass compositions. All data in wt. %.

Table 6-5……214
Location of pyroclastic flow deposits on the NW and S sector of Mt. Taranaki.

Table 7-1……226
Sample list and description of studied pyroclastic flow deposits.

Table 7-2……228
Summary of petrographic studies of BAF samples.

List of Figures

Figure 1-1…….. 8
Tectonic setting and its relation to Holocene volcanism in the North Island, New Zealand. Area between the Hikurangi Trough and the axial ranges is the forearc. Arrow indicates Pacific Plate movement with a rate of 42 mm yr^{-1}. AVF – Auckland Volcanic Field; TgVC – Tongariro Volcanic Centre; TVL – Taranaki Volcanic Lineament; TVZ – Taupo Volcanic Zone. AD and RD refers to andesite and rhyolite dominance within TVZ, respectively. Modified after Reyners et al. (2006) and Wilson et al. (1995).

Figure 1-2…….10
Regional tectonic setting of the Taranaki peninsula. The Taranaki Volcanic Lineament comprises the Sugar Loaf Islands (SLI), Kaitake (K), Pouakai (P) and Mt. Taranaki (T). Major onshore (thick lines) and offshore (thin lines) faults are indicated: IF-Inglewood Fault, MF-Manaia Fault, NF-Norfolk Fault, OF-Oaonui Fault. Contours are at 300 m intervals for the volcanic edifices only. New Plymouth (NP) as the major settlement is identified. Modified after Sherburn and White (2005).

Figure 1-3…….14
Orthophotograph of Mt. Taranaki including the lower northwestern flanks. Inset shows upper cone area including Fanthams Peak. Major morphological features are indicated by letters: a-summit crater of Mt. Taranaki, b-Fanthams Peak, c-the Beehives (two lava domes), d-scarp of the Opua amphitheatre, e-Big Pyramid, f-The Dome, g-Skinner Hill (probably a buried dome structure), h-Pyramid Stream, i-Maero Stream, j-Waiweranui Stream, k-Hangatahua River, l-Egmont National Park boundary (forest/pasture border, here 390 m), m-Kapuni Gorge (marks the eastern border of the amphitheatre), n-Sharks Tooth (second highest peak, 2510 m), o-Fanthams Peak (comprising multiple vents), p-remnant summit dome, q-Turtle, r-Bobs Ridge (western border of the Opua amphitheatre), s-NW flank and main path for BAFs.

Figure 1-4…….16
Classification of Mt. Taranaki and Mt. Ruapehu rocks after Gill (1981). Modified after Price et al. (1999).

Figure 1-5…….17
Trace element patterns of selected Mt. Taranaki rocks. Warwicks/Staircase refers to lava flow groups of the main cone of Mt. Taranaki; Fanthams describes lava flows of the satellite vent Fanthams Peak. Data compiled from Price et al. (1992, 1999). Normalisation after Sun and McDonough (1989).

Figure 2-1…….38
The specimen illustrates how pumice cores were obtained. As in this case, six cores in three mutually perpendicular orientations were drilled.

Figure 2-2…….39
Standard deviations for diameter and length of the cores (a) and for volumes V_c and V_{He} (b). It is noted that one sample in a) is off the chart at a standard deviation of 0.1321 cm. b) Samples are differentiated into those drilled in Oregon and at Massey. Oregon samples show small variations for both V_c and V_{He}.

Figure 2-3…….40
Standard deviation for connected porosities. The limit of 0.3 cm^3 for V_c and V_{He} in Fig. 2-2b is used as maximum limit. Cores drilled in Oregon are shown for comparison.

Figure 2-4…….40
Permeability measurements of individual cores were performed three to six times, partially using multiple flow rates, in order to assess reproducibility. In this case, the red graph suggests higher flow rates compared to the other three runs and was excluded from further calculations.

Figure 2-5…….44
Separated groundmass glass fraction from a pumice clast (SD32).

Figure 2-6…….45
Thermal analysis of volcanic glass to 850 °C. The change in weight (green axis) was measured after the isothermal break at 110 °C.

Figure 3-1…….55
Distribution of lava flows on the Mt. Taranaki main cone and Fanthams Peak. Sampled lava flows and scoria-and-ash flow units are highlighted. The thick solid line represents the Opua amphitheatre scarps. The map has been modified after Neall (2003); map details were kindly provided by J.N. Procter.

Figure 3-2…….57
Location of type and reference sections around the edifice of Mt. Taranaki. TS-type section, P-Pembroke Road, W-Waingongoro Stream, M-Manaia Road. Numbered black squares refer to reference sections. Black diamonds mark distal locations of pyroclastic flow deposits in the area of Saunders Road – Wiremu Road – Waiweranui Stream.

Figure 3-3…….59
Type section of the Maero Formation located in Maero Stream, NW sector of Mt. Taranaki. Reference sections Nos. 1 and 2 are located in Pyramid Stream and Hangatahua River, respectively. The outcrops comprise deposits of BAFs, surges and pumice flows as well as co-ignimbrite ashes. Debris flow-, lahar-, and fluvial deposits are also exposed but not always differentiated. For further details see text and appendices. Labels Py7 etc refer to sample numbers. See also Fig. 3-4 for field photographs.

Figure 3-4…….62
Field photographs of deposits from the NW sector of Mt. Taranaki. a) NW sector of Mt. Taranaki as viewed from the summit. Note the depression in vegetation caused by an avalanche (see Chapter 5). H. R. - Hangatahua River . b) exposure in the upper right Pyramid fork. Cliff section is approx. 30 m high and shows mainly lahar and hyperconcentrated flow deposits. Note Shane Cronin for scale (arrow). c) outcrop on the true left side of the Maero Stream near the intersection of Puniho and Holly Hut track. The upper unit shows the Tahurangi Block-and-Ash Flow deposit (unit a) with its upper matrix-supported and lower clast-supported zones. d) reference section No.1, lower Pyramid Stream, true right side. Only major units are labelled. Discolouration of units IV-Bb and II-B is caused by a raised iron-rich water table. Note the black bar has same height as the spate (arrow). e) close-up of c); basal portion of Tahurangi BAF (unit a) which consists of fine to medium ash. Dashed line marks the boundary between main body of the BAF and its basal portion. f) close-up of d); finely laminated and cross-bedded fine to medium ash surge deposit. Some pumice clasts (arrows) are present. g) exposure on the true right side of Maero Stream. Major units are labelled. The reworked section is 2.5 m thick and represents predominantly fluvial deposits. h) close-up of g); unit IV-Bb. Noteworthy are boulder trains and weak reverse grading of the lower to middle portion. i) distal blast deposit [Newall Breccia (a)] showing its typical pocketing appearance. j) stream exposure of a BAF deposit with pervasive red coloured top portion and grey bottom portion (Waiweranui Stream). k) in situ charcolised tree at a distal BAF exposure [Burrell Breccia (A)] near Saunders Road. l) degassing pipe originating at a charred log within the BAF deposit (same unit as in k). Note that the pipe branches at the centre of the photograph. Same unit as in k). Labelled units in c, d and g refer to the lithostratigraphic code. See discussion of Chapter 3 for further details. Detailed description of reference section No.1 can be found in the appendix. Photographs of f) and i) were taken by Shane Cronin.

Figure 3-5…….64
Reference sections Nos. 3 and 4 located on the east flank of Mt. Taranaki. Reference site: No.3–Pembroke Road cutting; No.4–intersection of Wain- gongoro Stream and Round-The-Mountain-Track. E02-72 etc are sample numbers.

Figure 3-6……66
Reference sections Nos. 5 and 6 located on the south flank of Mt. Taranaki. Reference site: No.5–at the site of the Old Mangahume Hut; No.6–near the Old Mangahume Hut, upslope of No.5. Labels E03-35 etc are sample numbers.

Figure 3-7……67
Reference sections Nos. 7, 8 and 9 located on the west and north sector of Mt. Taranaki. Reference site: No.7–Ahukawakawa Swamp; No.8–Marupakoko Stream near Kahui Hut; No.9–Parihaka Road cutting. Labels E02-4 etc refer to sample numbers.

Figure 3-8……68
Crater rim stratigraphy as exposed on its SW side at the entrance of Okahu Gorge. Four lava flows are identifiable with the youngest flow (4) being known as South Flow.

Figure 3-9……69
Composite photograph of the upper NW flank of Mt. Taranaki showing named and described morphological features.

Figure 3-10..……70
Flow paths and distribution of BAF and surge deposits on the N to W sectors. Crater exit areas: 1-north sector, 2-northwest sector, 3-southwest sector.

Figure 3-11……...75
Histogram of all glass chemical analyses for SiO_2 (a) and K_2O (b).

Figure 3-12……...77
Backscatter-electron microscopy images of individual glass shards. Different glass shard shapes within individual samples are illustrated (top: vesicular, partially deformed; bottom: dense and angular). Label in images gives analysis number and approximate beam location (black dot). Grey=glass; light grey=minerals; black=epoxy. a-b) Tahurangi Ash sample (T04-98) with chemically homogenous glass shards but of different texture; a) deformed vesicles, b) dense angular. Note that the presence of large minerals (bottom) may alter vesicle distribution. c-d) Newall Ash sample (E02-75) with distinct shard textures; glass chemistry of shard (d) is similar to those of scoria-and-ash flow glass shard (c). Note regular to irregular vesicles in c). e-f) Burrell Lapilli sample (E03-35) with Taranaki glass shard (f) and Taupo volcano-derived glass shard (e), which shows a deformed vesicle.

Figure 3-13……...78
Glass chemistry of Burrell Lapilli-erupted deposits. The SiO_2 vs. K_2O diagram shows a general positive correlation. Highest mean silica and potassium contents are observed for BAF and surge deposits. The crosses represent the 95% confidence interval of the sample mean. The tephra sample E03-35 is bimodal containing glass shards with a signature similar to Taupo volcano (or atypical of Taranaki). If foreign glass shard analyses are excluded the sample mean is located within the field of BAF/surges (=E03-35'). Also included are sample means of a surge deposit pre-dating the Maero Eruptive Period showing a rhyolitic glass chemistry. It is noted that one sample (WW19) shows large variations and a bimodal sample population.

Figure 3-14……...79
Comparison of mean sample values of scoria-and-ash flow units (T04-53, T04-56) to pyroclastic pumice flow deposits of the Burrell episode (units 1-3) and Puniho Ash, and other Maero deposits (crosses). Individual glass shards (small black squares) within deposits, other than T04-53 and T04-56, that have compositions similar to scoria-and-ash flows. a) SiO_2 vs. K_2O, b) CaO vs. FeO.

Figure 3-15……...80
Correlation of individual tephra and pyroclastic flow units based on field studies and glass chemistry (SiO_2 vs. K_2O). a) Waingongoro and Waiweranui episodes, b) Newall and Puniho episodes, c) Tahurangi and Te Popo episodes.

Figure 4-1…….99
Locations of Holocene volcanic centres in the North Island of New Zealand: Auckland Volcanic Field, Taupo Volcanic Zone (TVZ), Tongariro Volcanic Centre (TgVC), Mt. Taranaki. Numbers 1-4 refer to distal andesite tephra sites: 1-Onepoto Basin/Pukaki Lagoon/Lake Pupuke (Sandiford et al., 2001; Shane and Hoverd, 2002; Shane, 2005), 2-Waikato lakes (Lowe, 1988b), 3-Kaipo Bog (Lowe et al., 1999), 4-Lake Tutira (Eden and Froggatt, 1996), 5-Lake Poukawa (Shane et al., 2002), 6-Kaimanawa Mts. and Ruahine Ranges (Froggatt and Rogers, 1990).

Figure 4-2……...104
Particle textures found in Burrell Lapilli sub-Plinian fall deposits. a) pumice clast, type 1, with clear to pale brownish glass; b) hypocrystalline groundmass texture of type 2 clast showing plagioclase, Fe-Ti oxide and minor clinopyroxene microlites; c) semi-vesicular type 3 clast with brown groundmass glass, large crystals are hornblende; d) for comparison, hypocrystalline groundmass of the present summit dome of Mt. Taranaki with abundant microlites of plagioclase, Fe-Ti oxides and minor clinopyroxene. Scale bars are in µm.

Figure 4-3……...105
Standard deviations of all major oxides are shown for the original glass EMPA dataset and the glass dataset classed as uncontaminated by plagioclase for the Taranaki (a) and Ruapehu (b) samples. A clear reduction in SiO_2, Al_2O_3 and CaO variations is observed. See text for further details. All Fe expressed as FeO.

Figure 4-4……...109
Bivariate plots of Al_2O_3 and K_2O vs. SiO_2 for Burrell Lapilli (Taranaki) and Ruapehu glass data. Data points with lowest SiO_2 show linear relationship towards mean plagioclase compositions (dashed lines).

Figure 4-5……...110
Bivariate oxide plots for Burrell Lapilli eruption, Taranaki (a-d) and 14. October 1995 eruption, Ruapehu (e-f) demonstrate how contaminated glass analyses were identified. Open symbols are classed uncontaminated, closed symbols represent hybrid glass-plagioclase analyses. Dashed lines point towards mean plagioclase compositions.

Figure 4-6……...114
The glass evaluation procedure cannot be directly applied to BAF deposits as demonstrated for the Burrell Lapilli equivalent BAF deposit. Although data points above a threshold value of 17.9 wt.% Al_2O_3 clearly embrace contaminated glass analyses, the transitional data between 17.1 and 17.9 wt.% Al_2O_3 cannot be uniquely classified. Dashed line points toward mean plagioclase composition.

Figure 4-7……...115
Glass compositions of Taranaki and TgVC tephras (Lowe 1988b; Lowe et al., 1999; Eden and Froggatt, 1996 and Shane and Hoverd, 2002) show large variations, here only shown the means and standard deviations for K_2O and Al_2O_3. Contaminated plagioclase-glass analyses and/or the analysis of two or more particle types may have caused the apparent glass compositional heterogeneity. The small variation in the unmodified Burrell Lapilli dataset (Taranaki) is shown for comparison (in grey).

Figure 5-1……...123
Lava dome types: a) spiny (Rock Mesa ENE, Oregon), b) spiny-lobate (Mt. St. Helens lava dome, Washington, July 2004), c) lobate-platy (Big Obsidian Flow, Newberry, Oregon).

Figure 5-2……...125
NW sector of Mt. Taranaki showing the main deposition area of Maero BAF deposits. The extent of the Tahurangi BAF A is outlined (light grey); unit B is only observed in the Maero Stream and is omitted for clarity. The rock-avalanche deposit (RAD) is outlined as observed on aerial photographs from 1959 (mid-grey) with an additional area based on field observations (dark grey). Contour interval is 20 m. The upper right inset shows the general slope inclinations.

Figure 5-3……...127
Correlation of Tahurangi BAF A and B units and the rock-avalanche deposit across the Pyramid-Maero-Hangatahua area. The exposures are sorted by stream and planimetric distance from source (filled squares in Fig. 5-2). See figure legend for further details (RAD – rock-avalanche deposit). Magnetism was measured by a portable fluxgate magnetometer. For clarity, older exposed units were omitted. Outcrop numbers and profiles refer to Platz (2001) except S04-133.

Figure 5-4……...129
The remnant present summit dome. a) hemispherical shape of the dome as viewed from the SE; arrow points to a person for scale. Photographed by S.J. Cronin. b) dome amphitheatre as viewed from the W; the arrow points to the summit marker (2518 m); the dashed lines mark the hydrothermally altered central dome portion. c) northern scar of the amphitheatre showing listric faults. d) the summit marker is a sub-vertical extrusion penetrating the carapace; note weak columnar jointing; summit marker is highest point of the dome. e) orthophotograph of the summit region of Mt. Taranaki; outline shows mapped deposits associated with the lava dome; note the blocky lava flow to the N; crosses mark sample locations. f) the 'Three Sisters' (background) mark the NW border of the intra-crater collapse zone with resulting deposit still preserved in the crater (foreground).

Figure 5-5……...130
Black and white photograph taken between 1898 and 1901 showing the fresh bouldery rock-avalanche deposit (centre to right). The photograph is taken from the Round-The-Mountain-Track just west of Maero Stream from the top of a buried lava ridge. The view is NNW towards Pouakai. Photographed by the surveyor H.M. Skeet.

Figure 5-6……...133
Reconstruction of the Pyramid Dome geometry. a) dashed white line illustrates the former ideal crater wall position; the solid line marks the inferred dome outline; the black dot is the assumed vent location at the break in slope. b) view of the remnant summit dome from the W. c) top view of the combined paraboloid with a composite elliptical base; dimensions of elliptical radii are given. d) side view of the inferred dome geometry; the dome remnants are in dark grey; the inferred underlying slope on the upper flank is estimated to be c.20°.

Figure 5-7……...135
Hornblende types. a) type 1 with continuous reaction rim. b) type 2 with discontinuous reaction rim; present only in sample SD1; note individual Fe-Ti oxide crystals are visible. c) type 3 partial to fully replaced hornblende crystals. d) type 1 with observed brown glass fringing the reaction rim; only observed in sample SD6. Scale bar is 100 µm in a) otherwise 25 µm.

Figure 5-8……...136
Histogram of type 1 hornblende reaction rim thicknesses averaged for crystals and entire samples.

Figure 5-9……...137
Hornblende compositions of the summit lava dome, Mt. Taranaki. a) Na+K (A-site) vs. Al^{IV}. b) Mg# vs. Si; (c.p.f.–cation per formula unit). For comparison are shown recalculated pargasitic hornblende compositions of Unzen volcano, Japan (Sato et al., 1999; Browne et al., 2006; Nakada and Motomura, 1999) [Unzen matrix refers to groundmass crystals], Soufrière Hills Volcano, Montserrat (Barclay et al., 1998; Rutherford and Devine, 2003), Mt. St. Helens, USA (Rutherford and Hill, 1993), Colima, Mexico (Luhr, 2002) and Cerro la Pilita, Mexico (Barclay and Carmichael, 2004).

Figure 5-10…….138
Compositions of Fe-Ti oxide phenocrysts and inclusions in clinopyroxene and hornblende. a) Al vs. Ti. b) Ti/Al vs. Fe^{3+}# (c.p.f.–cations per formula unit). Cations are calculated on the basis of 32 oxygens.

Figure 5-11…….139
Glass compositions of inclusions in clinopyroxene and hornblende. Silica is used as differentiation index. Note that inclusions in different host minerals form separate groups.

Figure 5-12…….140
Bulk rock compositions of the summit lava dome and the Tahurangi BAF A and B deposits. Dome compositions are distinct to Tahurangi rocks as illustrated for Al_2O_3 (a), Mg# (b, d) Fe_2O_3 (e) and Zr (f).

Figure 5-13…….141
Trace element patterns of the Pyramid Dome and Tahurangi BAF deposits normalised to N-MORB (a) and chondrite (b). Pyramid Dome rocks and Tahurangi BAF deposits show nearly identical trace element patterns. For the light rare earth elements slightly higher abundances in Tahurangi BAF deposits are noted. Normalisation after Sun and McDonough (1989).

Figure 5-14…….142
Texture of rock sample SD6. a) photograph shows sub-vertical, near parallel crack patterns and cavities. b) modified image of a) highlighting cracks and cavities in black.

Figure 5-15…….144
Lava dome growth patterns are illustrated in a-e. Exogenous and endogenous dome growth occurred simultaneously. f) demonstration of the inferred exogenously (dark grey) and endogenously (light grey) formed surfaces as observed on the dome remnants.

Figure 5-16…….147
Reconstruction of the summit dome failure. a) erosion scars on upper flank (white arrows) as well as the curvatures of the amphitheatre, and the scars to the SW and S define the geometry of individual collapse sectors. b) dome geometry with individual sectors I-IV and their flow directions. c) cross-section of the dome showing the dome remnants (grey), and the disintegration of dome rocks along listric faults.

Figure 5-17…….149
Aluminium-in-hornblende geobarometer shown as histogram for hornblende phenocrysts (core and rim) and microphenocrysts. Calculated after Johnson and Rutherford (1989) and corrected by -1.5 kbar.

Figure 5-18…….150
Comparison of calculated hornblende crystallisation pressures for various Mt. Taranaki rocks and xenoliths. Granodiorite xenoliths contain all required mineral phases for the Al-in-hornblende geobarometer (Johnson and Rutherford, 1989) and therefore were not corrected. Note that some hornblende crystals of hornblende gabbros and hornblende-pyroxene gabbros indicate crystallisation below (<1 kbar) the inferred hornblende stability limit.

Figure 6-1……...179
Mount Taranaki (lower right) has produced mainly lava dome eruptions in the past 800 years with Block-and-Ash Flow deposits making up the fan between the Maero and Pyramid Stream and in the Hangatahua River (BAF – Block-and-Ash Flow, ppf – pumice pyroclastic flow). Star (top left) indicates the most distal outcrop discussed in the text. To the NNW of Mt. Taranaki are the south flanks of Pouakai volcano. The inset shows the Taranaki peninsula with the Taranaki Volcanic Lineament (SLI-Sugar Loaf Islands, K-Kaitake, P-Pouakai, T-Taranaki). Major onshore and offshore faults: IF-Inglewood Fault, MF-Manaia Fault, NF-Norfolk Fault, OF-Oanui Fault. Contours are 300 m. Modified after Sherburn and White (2005).

Figure 6-2……...181
Variations in bulk vesicularity and connected porosity of single clasts for grey pumice (a), banded pumice (b), and black and brown pumice (c). Crosses represent the range in vesicularity per clast using minimum, mean and maximum values (see inset in a). Variations in bulk vesicularity refer to single cores cut in two (φ_{core}) and overall clast variations with multiple cores (φ_{clast}). Note different scale in b). See text for details.

Figure 6-3……...183
Field photographs of a) succession of three pumice pyroclastic flow deposits on the upper south flanks; sketch shows a general assembly of pumice types and grey dense lithics, b) grey pumice clasts of unit 3, c) eroded surface into unit 2 showing the scattered grey pumice [1] from airfall, brown pumice [2], banded pale grey to dark brown pumice [4], and the dense fractured andesite clasts [L]; d) lower contact of a distal BAF deposit, c.13.5 km from source (star in Fig. 1). See text for field description.

Figure 6-4……...184
Distribution of Burrell Lapilli deposits: a) isopachs in cm including the BAF deposit (black) to the NW for reference, black squares represent mapping locations for fall deposits only, P-Pouakai, contours 100 m; b) isopleths for pumice clasts and pumice pyroclastic flow deposits on the upper flanks (black), see inset in a) for location; c) isopleths for lithic clasts, same outline as in b). Numbers in b) and c) are clast diameters in cm.

Figure 6-5……...187
Thin-section photographs illustrating basic vesicularity differences of juvenile clasts. a) dense grey lithic, b) semi-vesicular black pumice, c) vesicular black pumice with isolated and coalesced vesicles, crosses mark plagioclase crystals; d) grey pumice with isolated large single vesicles as well as larger coalesced vesicle. Scale bar is 100 µm in a-c and 500 µm in d. See text for details.

Figure 6-6……...188
SEM images of grey (a) and brown (b) pumice (note a and b are binarised; black=vesicles, white=glass + crystals); c) shows a large coalesced vesicle; d) consists of three SEM images showing the transition from grey to brown in banded pumice. Scale bar is 10 µm in c), otherwise 100 µm.

Figure 6-7……...189
Hornblende reaction textures in different clast types: a) fresh hornblende with no reaction rims in pumice, b) single Fe-Ti oxide crystals are attached to the hornblende rims in black semi-vesicular pumice, c) hornblende in dense grey lithic clast shows resorption textures and is partially replaced by clinopyroxene, plagioclase and Fe-Ti oxide crystals or is fully replaced (lower left); note abundant plagioclase microlites in groundmass. Scale bar is 100 µm.

Figure 6-8……...190
Bulk rock geochemistry of pumice and grey andesite clasts in a multi element oxide vs. SiO_2 diagram. The calculated fractionation trend pumice – grey lithics is in good agreement for the majority of clasts (solid line) with some variation for the most evolved clast (dashed line). See Table 6-3 for details.

Fig. 6-9……...194
Groundmass glass compositions of pumice types presented in the Al_2O_3 vs. SiO_2 diagram. Modelled glass composition changes due to plagioclase and clinopyroxene crystallisation (thick solid line) and is in good agreement with linear regression line (thin solid line). The small inset shows six data points of one lapillus (SD20) demonstrating relative glass homogeneity. The dimensions of the box are 1 wt. % for Al_2O_3 and SiO_2.

Figure 6-10……196
Connected porosity vs. bulk vesicularity of all pumice types. Brackets represent 95% confidence limit for the mean of each pumice population. Solid lines represent 0% and 10% and dashed line 5% isolated pore volume.

Figure 6-11……197
Connected and bulk vesicularity vs. permeability. a) data of this study with upper and lower data limits (black lines) of $y=5\times10^{-19}\ x^{-4.5314}$ and $y=6\times10^{-21}\ x^{-4.5314}$, respectively. Note there are six specimens with three cores cut in three mutually perpendicular directions. Upper inset shows cores cut in two perpendicular directions. b) comparison of our data with published literature: Montserrat (Melnik and Sparks, 2002), Big and Little Glass Mountains (Rust and Cashman, 2004), Pichincha (Wright et al., 2007); grey lines are limits of Klug and Cashman (1996).

Figure 6-12……202
Reconstruction of eruptive events during the Burrell Lapilli eruption. Changes in bulk rock silica contents are illustrated in Stage a. Bubble nucleation levels 1-3 correspond with erupted units 1-3. See text for further details.

Figure 6-13……213
Correlation of pyroclastic flow deposits associated with the Burrell episode. Note that the major unit from medial to distal represents the Burrell Breccia (A). In section S04-133, the thin pyroclastic pumice flow deposits represent Burrell Breccia (B) units 1-3. Exposures are sorted by stream and planimetric distance from source. See figure legend for further details (RAD – rock-avalanche deposit). Magnetism was measured by a portable fluxgate magnetometer. For clarity, older exposed units were omitted. Outcrop numbers and profiles refer to Platz (2001) except S04-133. For list of samples and coordinates of outcrops see Appendix B.

Figure 6-14……215
Estimates of total water and carbon dioxide contents in melt inclusions. a) total H_2O at 3550 cm^{-1} vs. molecular H_2O at 1630 cm^{-1}, and b) molecular CO_2 at 2350 cm^{-1} vs. total H_2O at 3550 cm^{-1}.

Figure 6-15……216
Different shapes of melt inclusions in clinopyroxene. a) overview of crystal 2 (sample SD20); note the many inclusions of glass, plagioclase, apatite and Fe-Ti oxide which are mostly oriented along crystallographic planes, b) two close-ups as marked in a); I - represents common but very small melt inclusions found in clinopyroxene, which are unsuitable for FTIR analysis. Their shape is near spherical to ovate; II - the bottle-neck shape is typical for leaked melt inclusions, c) overview of crystal 11 (sample SD32) showing a large irregular shaped melt inclusion, d) close-up of c) showing the impossibility of using these inclusions for FTIR analysis; it can be assumed that the inclusion extends further into the crystals as indicated by the diffuse outline of the melt inclusions further to the right, e) section of crystal 4 (sample SD20) showing two types of melt inclusions, the reddish-brown coloured inclusions are probably altered in comparison to the brown inclusions to the right; note again the irregular outline of the inclusions, f) section of crystal 8 (sample SD9D); abundant sheet-like inclusions probably oriented along crystallographic planes; the inclusions around the Fe-Ti oxide inclusions (black) appear to be connected. Scale bars are 100 µm in a), c), and e), 50 µm in d) and f), and 10 µm in b).

Figure 6-16…….218
Preliminary results of the thermal analysis studies. a) trial and error series of sample SD20, b) reproducibility results of different pumice samples; it is noted that for the same sample the maximum weight loss is often observed at similar temperatures.

Figure 7-1……...229
Groundmass texture (a-d) and crystallinity (e-h) of clasts from pyroclastic flow deposits. a and c) two groundmass glasses, b-d) differences in degree of groundmass crystallisation in clear translucent and brown glasses, e) semi- to hyaline, clear translucent glass; note microvesicularity, f) same image as in e) under crossed polarised light, g) semi- to holocrystalline brown glass, h) same image as in g) under crossed polarised light.

Figure 7-2……...231
Bulk rock composition of selected Maero eruptives. Block-and-Ash Flow deposits are not differentiated and the Pyramid Dome and the Turtle are omitted for clarity. For comparison, selected lava flows of the upper main cone and Fanthams Peak are plotted. Mg#=100[Mg^{2+}/(Mg^{2+}+Fe^{2+})]; all iron as Fe^{2+}.

Figure 7-3……...233
Analytical totals of all EMP glass analyses (a) and sample averages (b) are plotted against silica content. Estimated glass water contents using the water-by-difference method (WBD) are shown on the right axis. The terms andesite, dacite, and rhyolite refer to the TAS-classification scheme of Le Maitre et al. (1989).

Figure 7-4……...236
Calculated melt viscosities, η, are plotted against silica abundances. Values of the models of Shaw (1972) and Hui and Zhang (2007) are shown for H_2O contents of 0.1 wt.%, 1 wt.% and WBD at T=900 °C and P=1 bar. Solid and dashed lines are regression lines of η at WBD for the Hui-and-Zhang- and Shaw-models, respectively.

Figure 7-5……...237
Calculated magma viscosities, η_a, are plotted against SiO_2 contents. Lower and upper crystal volume fractions of 30% (a) and 55% (b), respectively are used for the calculation based on the calculated melt viscosities (see Fig. 7-4). Viscosities are calculated using H_2O contents of 0.1 wt.%, 1 wt.% and WBD at constant T=900 °C and P=1 bar. Solid and dashed lines are regression lines of η_a at WBD for the Hui-and-Zhang- and Shaw-models, respectively.

Figure 7-6……...238
Bulk SiO_2 contents (a) and Mg# (b) are plotted against K_2O in chronological appearance of eruption episodes.

Figure 7-7……...241
Calculated Mt. Taranaki melt viscosities are compared to calculated melt viscosities of Merapi volcano (Indonesia), Soufrière volcano (St. Vincent), and Soufrière Hills Volcano (Montserrat), using the same parameters. Solid lines are regression lines for Taranaki data.

Figure 7-8……...242
Calculated Mt. Taranaki magma viscosities plotted against SiO_2 are compared to other andesite to rhyolite volcanoes. Since Taranaki viscosity calculations are based on glass chemical compositions of the Maero Eruptive Period, the range in bulk silica contents of rocks erupted during this period are used to allow comparison to published data. Upper and lower viscosity abundances are taken from Fig. 7-5. Taranaki data are illustrated by two parallelograms with upper and lower limits representing crystal volume fractions of 55% and 30%, respectively. The grey parallelogram corresponds to 1 wt.% melt water content, whereas the dashed parallelogram relates to water contents determined by WBD. Data source: silicic lava flows (Murase and McBirney, 1973; Fink, 1980; Navarro-Ochoa et al., 2002; Manley, 1996; Harris et al., 2004; and McKay et al., 1998); Mt. St. Helens (Murase et al., 1985; Scandone and Malone, 1985); Unzen volcano (Suto et al., 1993; Goto, 1999; Sato et al., 1999); Soufrière Hills Volcano, Montserrat (Voight et al., 1999; Sparks et al., 2000); Soufrière volcano, St. Vincent (Huppert et al., 1982); Merapi volcano (Siswowidjoyo et al., 1995).

Chapter 1 Introduction

Chapter 1 provides information as to why this study was undertaken and what was known about Mt. Taranaki prior to this study.

1.1 Introduction

The unpredictable eruption behaviour of volcanoes erupting intermediate to silicic magmas makes them exceptionally hazardous to surrounding populations. Typically, andesitic volcanoes erupt only small volumes during any one episode (<1 km^3). Despite this, they can be extremely explosive and during the course of an eruption, the style and types of activity can change rapidly, unexpectedly and repeatedly. A number of cataclysmic eruptions in the last century have underscored this point. Three key eruptions underscored how little we knew about such volcanoes, before focussing world scientific attention on andesite systems and their eruption mechanisms: Mt. Pelée, Martinique, Mt. St. Helens, USA, and Soufrière Hills Volcano, Montserrat.

Within a few minutes on the morning of May 8, 1902, a single violent phase of an ongoing dome-building eruption at Mt. Pelée (Martinique) took the lives of over 23,000 people in the town of St. Pierre (Lacroix, 1904). This event changed forever our awareness of volcanic hazards and raised the spectre of the hitherto unknown

phenomenon of *nuées ardentes*. Since then "pyroclastic density currents" have been recognised as a common and worldwide volcanic process involving hot (often >300 °C), rapidly flowing (often >100 ms^{-1}) mixtures of gas and particles, with a range in particle sizes and particle/gas ratios (Moore and Melson, 1969; Nairn and Self, 1978; McClelland and Druitt, 1989; Scott and Glasspool, 2005; Zanella et al., 2007). Following this, physical volcanology research has focussed on understanding the driving mechanisms behind the variety of "pyroclastic density currents", such as pyroclastic flows and surges, along with specific sub-categories of these, including ash flows, Block-and-Ash Flows and scoria-and-ash flows (e.g. Smith and Bailey, 1966; Schmincke, 1974; Rodríguez-Elizarrarás et al., 1991; Bourdier et al., 1997). In addition, detailed sedimentological studies of the deposits of pyroclastic density currents (e.g. Walker et al., 1980; Wright and Walker, 1981; Wilson and Walker, 1982; Boudon and Lajoie, 1989; Boudon et al., 1993; Cas and Wright, 1991; Fisher et al., 1993; Abdurachman et al., 2000; Lube et al., 2007), have been used to interpret (and debate) a variety of eruptional, transportational and depositional processes (Sparks, 1976; Branney and Kokelaar, 1992; 2002; Dade and Huppert, 1996). Furthermore, physical and numerical models are under ongoing development to better describe and simulate flow and transport mechanisms based on observational and experimental studies of deposits (Battaglia, 1993; Giordano and Dobran, 1994; Fujii and Nakada, 1999; Choux and Druitt, 2002; Freundt, 1998; 2003; Freundt and Bursik, 1998; Lube et al., 2004).

A stupendous "blast", triggered in only a few seconds at 8:32 am marked the onset of the 18 May 1980 Mt. St. Helens eruption and caused 57 fatalities, despite the intense focus of scientists on this re-awakening volcano (cf. Lipman and Mullineaux, 1981). This event fundamentally changed our understanding of how eruptions are triggered and how rapidly andesitic volcanoes can generate explosive phases (e.g. Swanson et al., 1983; Blake, 1984; Pallister et al., 1992; Klug and Cashman, 1994; Aldibirov and Dingwell, 1996; Gardner et al., 1996; Blundy and Cashman, 2001; Scandone et al., 2007). Precursors of the 18 May 1980 eruption were known for three months but the size of the eruption and its outbreak mechanism were unforeseen. The intense scientific focus on this eventually 6-year long eruptive episode has resulted in a new generation of models that combine magma ascent processes (Scandone and Malone, 1985; Rutherford and Hill, 1993) with physico/chemical conduit and eruption processes (Dobran, 1992; Melnik and Sparks, 2002; Cashman and Hoblitt, 2004; Cashman and McConnell, 2005; Blundy et al., 2006), as well as providing an understanding of the physical dynamics of

sub-Plinian eruptions (Carey and Sigurdsson, 1985; Papale and Dobran, 1994), and a variety of mass flows. This long and complex episode also allowed detailed description of the emplacement, growth and destruction mechanisms of lava domes (Moore et al., 1981; Anderson and Fink, 1989; Fink et al., 1990; Swanson and Holcomb, 1990; Fink et al., 1992; Anderson et al., 1995).

The now 12-year long eruption episode of Soufrière Hills Volcano on Montserrat, has also repeatedly and tragically demonstrated the destructive potential of andesite volcanism, even whilst under the intense observation of scientists and local authorities. The most devastating activity occurred on June 25, 1997, when a retrogressive partial collapse of the dome generated pulsatory Block-and-Ash Flows and pyroclastic surges that killed 19 people and injured 7 others (Sparks and Young, 2002). This demonstrated that even with our increased knowledge of these systems, andesite volcanoes remain enigmatically diverse, unpredictable and intensely hazardous. Ongoing studies on this and other recent long-term dome-forming eruptions with similar tragic results from sudden state-changes (from Mts. Unzen, Merapi, and Colima) have helped to derive a new understanding of dome-forming eruption processes. A wealth of data have been collected on the dynamics of long-term and often sporadic lava-dome growth (e.g., Sparks, 1997; Sparks et al., 1998; Nakada et al., 1995; 1999; Voight et al., 1999; Sparks et al., 2000; Harford et al., 2003;), as well as on the variety of products related to dome collapse and destruction (e.g., Cole et al., 1998; 2002; Ui et al., 1999; Camus et al., 2000; Grunewald et al., 2000; Voight and Elsworth, 2000; Saucedo et al., 2002; Carn et al., 2004; Simmons et al., 2004; 2005; Voight et al., 2006). The major advance generated as a result of study into these eruptions, however, has been the combination of petrological, geochemical, geophysical and physical methods to comprehend the rise, evolution and eruption of dome-forming magmas from within the crust to the dome surface (e.g., Sato et al., 1999; Power et al., 2002; Couch et al., 2003; Devine et al., 2003; Higgins and Roberge, 2003; Rutherford and Devine, 2003; Cashman and McConnell, 2005). Experimental and numerical modelling inspired by these events have also lead to major advances in understanding the dynamics and rheology of these complex magmas (e.g., Alidibirov et al., 1997; Navon et al., 1998; Alidibirov and Dingwell, 2000; Massol et al., 2001; Lyman et al., 2004; Mueller et al., 2005). Despite this, however, the sudden interruption of “quiet” dome eruptions by violent Vulcanian and sub-Plinian events is not always well understood. These sudden transitions between eruptive styles remain difficult to forecast.

At historically and pre-historically active andesite volcanoes, sequences of pyroclastic deposits attributed to the same types of processes are commonly preserved in the geological record. These sequences also often demonstrate apparent rapid changes in deposition mode and hence inferred eruption style. Such sequences and transitions can be now better interpreted in relation to the insights gained from historic eruption sequences (as described above) to provide hazard assessments. On the other hand, over longer periods of the geological record, where deposits of many eruption sequences are exposed, there is also a potential to interpret a wider range and diversity of eruption sequences and transitions that can help to predict sudden changes during future ongoing eruptions.

Eruption styles and types similar to those exhibited during the three catastrophic eruptions described above have been used to interpret the depositional record of the past 1000 years at Mt. Taranaki, New Zealand (Topping, 1972; Neall, 1979; Platz, 2001; Cronin et al., 2003). The main features of this record have been the identification of a range of highly variable eruption styles that surprisingly resulted from eruption of very similar magma compositions. Important transitions in the style of eruptions have been noted, including (1) an initially extrusive, lava dome-forming event to an explosive, sub-Plinian event (Burrell Lapilli AD1655), (2) a dome emplacement punctuated by a highly explosive lateral blast (Newall episode, ~AD1400), as well as (3) a variety of less violent emplacement, growth and destruction episodes involving lava-domes. Pyroclastic deposits recording this series of eruption episodes are well exposed on the flanks of Mt. Taranaki, along with the most recent dome (previously thought to have been associated with the Tahurangi eruption) which remains in half-section at the volcano’s summit. These conditions present an excellent example and location to examine some aspects of the physico-chemical controls on eruption episodes, including transitions between effusive and explosive phases. Through a combined physical and petrological approach, estimates can be given about magma storage depths, ascent and extrusion rates. These data, in combination with reconstruction of detailed physical eruption processes through field studies, can be used to help constrain some of the controls on eruption dynamics at andesitic stratovolcanoes such as Mt. Taranaki. On a local scale, an improvement in the hazard assessments for Mt. Taranaki can be achieved by reconstructing in detail the course of previous eruption episodes. The variety of data sets provide a sound foundation for understanding eruption precursors, and possibly also precursors for anticipating rapid changes in state during eruption episodes.

1.2 Objectives and Strategy

The aim of this study is to investigate the causes and characteristics of differing eruptive mechanisms experienced during the last 1000 years of activity at Mt. Taranaki. To carry this out, robust stratigraphic, geochemical, petrological, and physical investigations were required to firstly reconstruct the past volcanic episodes at Mt. Taranaki. This also involved developing methods for geochemically and otherwise correlating pyroclastic units emplaced in diverse sectors of the volcano by a range of eruptive processes.

From this reconstructed record, specific periods and deposits/extrusives were chosen to concentrate on the major sub-aims of the thesis work:

1. understanding causes for rapid shifts from extrusive to explosive eruptive styles during eruptive episodes,
2. interpreting causes of lava dome emplacement and failure,
3. developing models for magma assembly and rise, and constraining late-stage (high-level, conduit, dome) magmatic processes and their impacts on eruption style and the texture/petrology of eruptive products.

Sub-objective 1 work focussed on the AD1655 sub-Plinian Burrell Lapilli eruption, the largest event of the Maero Eruptive Period. The remnants of the present summit dome were the focus for completing sub-objective 2, since this allowed a detailed view through a section of a dome that apparently collapsed without related explosive activity. For deposits of the entire sequence, detailed analyses of different mineral and glass phases along with whole rock analyses were carried out toward answering the third sub-objective. In addition, physical properties such as porosity and permeability of pumice and dense dome rocks were investigated. To further constrain late-stage eruption processes, estimates of water contents in glass inclusions (hosted in minerals) and in matrix glass were also made.

1.3 Thesis Outline

The remainder of this chapter provides a background to Taranaki volcanism, and this is followed by another six chapters comprising this thesis. Chapter 2 outlines the methods applied in this study and the strategy for determining choice of methods (within the constraints of available analytical tools). Chapter 3 outlines the reconstruction of the Maero Eruptive Period stratigraphy and interpreted sequence of eruptive episodes. This study resulted in a re-interpretation of the previously defined eruption sequence and enabled collection of many new age determinations of eruption episodes and events. Chapter 4 describes the problems and reasons in fingerprinting andesitic tephra layers and introduces a new procedure to identify contaminated electron microprobe glass analyses. As a result, correlation of andesite tephras using glass chemistry may facilitate a new degree of resolution in tephrostratigraphic records. The remnant summit dome is the subject of Chapter 5. The lava dome is interpreted to represent a single eruptive event following the AD1755 Tahurangi eruption. Physico-chemical conditions of dome formation are investigated and implications are given for magma storage depth(s), magma extrusion and ascent rates. Chapter 6 describes the AD1655 Burrell Lapilli eruption in detail, which began with an effusive, dome-forming phase and terminated in an explosive, sub-Plinian eruption. A model is proposed that explains the diversity of erupted ejecta. In Chapter 7 petrographic and geochemical data are used and interpreted to reconstruct the variety of eruption mechanisms that occurred during the Maero Eruptive Period.

All collected datasets are documented in the electronic appendices (on DVD). The printed appendix contains stratigraphic columns and all geochemical analyses collected by electron microprobe, XRF analysis, and Laser-ICP MS analysis.

1.4 Background Geology

1.4.1 Regional Geological Setting

New Zealand is located on the convergent plate boundary of the Pacific and Australian Plates. The North Island is situated where the oceanic Pacific Plate is subducted beneath the continental crust of the Australian Plate. The Hikurangi Trough marks the southernmost extremity of the Tonga-Kermadec trench and begins offshore to the east of the most southern part of the North Island (Fig. 1-1). Along the trench the relative plate motion decreases from north to south with relative plate convergence rates of up to 98 mm yr^{-1} in the Tonga trench and 42-50 mm yr^{-1} in the Hikurangi Trough (Minister and Jordan, 1978; de Mets et al., 1994). The occurrence of an oceanic plateau, the Hikurangi Plateau, to the east of the lower North Island causes resistance to subduction. The collisional resistance of the Hikurangi Plateau in the south and subduction of normal oceanic crust in the north of the Hikurangi Trough, forces clockwise rotation of microplates in the forearc, the region between the trough and the axial ranges, also creating a spreading centre beyond the axial ranges where volcanism in the North Island is concentrated (Wallace et al., 2004). South of the Hikurangi Trough, the plate movement contains a greater margin-parallel component and passes into a strike-slip fault system that accommodates most of the relative plate motion in the South Island (van Dissen and Yeats, 1991; de Mets et al., 1994).

Under the North Island, the Pacific Plate plunges steeply into the mantle with an approximate depth of 100 km below the c.40 km thick continental crust beneath Mt. Ruapehu (central North Island) at a distance of c.280 km from the trench (Reyners et al., 2006). The depth of the subducted slab beneath the Taranaki region (western North Island), located about 400 km from the trench, is approximately 250 km (Boddington et al., 2004; Reyners et al., 2006). However, the Taranaki volcanoes are not directly overlying the slab since it is only traceable to the southeastern part of the Taranaki region, c.35 km SE of Mt. Taranaki (pers. comm. S. Sherburn, 2006). Isolated deep earthquakes with foci centred beneath Mt. Taranaki occur at depths of c.600 km and are interpreted to be derived from a horizontal lying, detached sliver of the plate (Boddington et al., 2004).

Quaternary volcanism in the North Island is generated in two regions within the subduction zone: the Taupo Volcanic Zone (TVZ), including the Tongariro Volcanic Centre (TgVC) and the Taranaki Volcanic Lineament (Fig. 1-1). The TVZ is one of the

most productive rhyolitic magmatic systems on Earth caused by high heat flows up to 700 mWm^{-2} in a rapidly extending region (e.g. Stern, 1987, Wilson et al., 1995). The TVZ can be subdivided into three zones based on the main eruptive rock types: the NE (e.g. White Island) and SW (TgVC) are characterised by andesite provenance, whereas the central part is dominated by rhyolites (Wilson et al., 1995). The TgVC is located at the apex of the extending TVZ (i.e. lowest spreading rate) and consists of Mts Ruapehu and Tongariro with the satellite cone of Mt. Ngauruhoe (Donoghue et al., 1995; Cronin and Neall, 1997; Hobden et al., 2002). The Taranaki Volcanic Lineament is located 130 km to the west of Mt. Ruapehu and is geochemically and tectonically distinct from the TVZ setting. Other Cenozoic off- and onshore basalt and andesite volcanic centres are located farther north of Taranaki volcanism, for instance the Alexandra, Okete and Ngatutura Volcanics as well as the offshore Awhitu volcanic centre (Briggs, 1983; Briggs et al., 1989; Stagpoole, 1999).

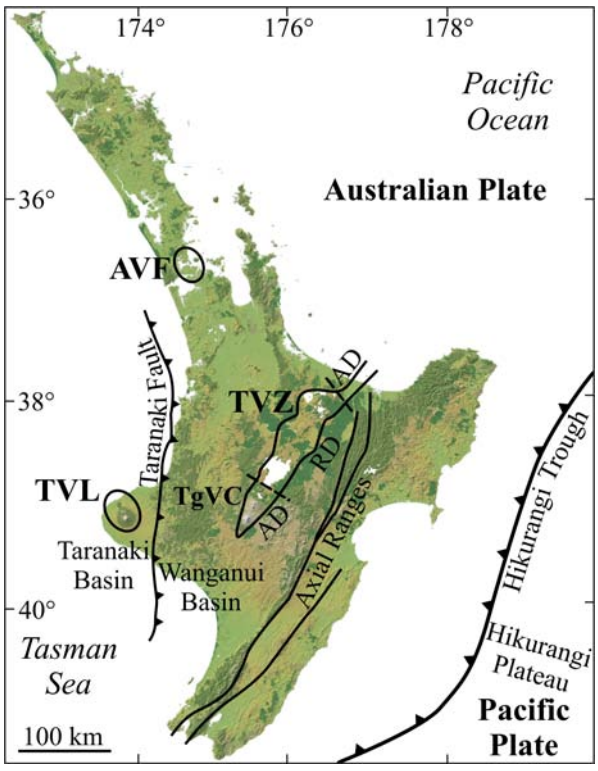


Figure 1-1: Tectonic setting and its relation to Holocene volcanism in the North Island, New Zealand. Area between the Hikurangi Trough and the axial ranges is the forearc. Arrow indicates Pacific Plate movement with a rate of 42 mm yr^{-1}. AVF – Auckland Volcanic Field; TgVC – Tongariro Volcanic Centre; TVL – Taranaki Volcanic Lineament; TVZ – Taupo Volcanic Zone. AD and RD refers to andesite and rhyolite dominance within TVZ, respectively. Modified after Reyners et al. (2006) and Wilson et al. (1995).

1.4.2 Taranaki Basin

The Taranaki peninsula, on the west coast of the North Island, lies within the Taranaki Basin (Fig. 1-2). The eastern boundary of the basin is marked by the Taranaki Fault, a crustal thrust fault that has accommodated a dip-slip displacement of 12-15 km in the last 80 Ma and vertically offsets the basement by about 6 km (King and Thrasher, 1996; Nicol et al., 2004). The Cape Egmont Fault Zone (CEFZ) to the west of the peninsula divides the basin into the Eastern Mobile Belt dominated by subduction related extension and compression processes, and the Western Stable Platform (King and Thrasher, 1996). The offshore Taranaki CEFZ represents the limit of deformation related to the convergence of the Pacific and Australian Plates. It is marked by extension and shows a 53 km long and 1-5 m high scarp on the seafloor; average dip-slip movement for the last 225,000 yrs is c.0.8 mm yr^{-1} (Nodder, 1993). Three active onshore NE-SW-trending faults are identified: the Oaonui Fault to the SW and the Inglewood and Norfolk Faults to the NE of Mt. Taranaki (Fig. 1-2). The Oaonui Fault shows a vertical displacement of 5 m over the last 6500 yrs, whereas the Inglewood has a 3 m scarp with >1 m vertical displacement in the last 13,000 yrs (Hull and Dellow, 1993; Hull, 1994). The three active faults are oblique normal slip faults and are interpreted to be related to magmatic intrusions at Mt. Taranaki (Sherburn and White, 2005). Sherburn and White (2005) speculate whether the last Inglewood Fault movement, 3-3.5 ka, is related to the formation of the satellite cone (Fanthams Peak) and two lava domes on the south flanks of Mt. Taranaki, since they appear to be of similar age.

The Taranaki Basin is on average 6 km thick, reaching 8 km 22 km SSE of Mt. Taranaki (King and Thrasher, 1996). It is composed of a Cretaceous to Cenozoic sedimentary sequence of limestones, coals, silt-, and sandstones, which in onshore sequences are covered by volcaniclastic deposits up to 300 m thick (cf. King and Thrasher, 1996). On- and offshore oil and gas reserves within the sediment sequence have led to extensive geophysical studies providing invaluable stratigraphic and lithologic data on the upper to middle crust. In two oil-exploration wells, two andesite sills of 5-8 m thickness are found near New Plymouth at depths of c.2800 m (Allis et al., 1995). However, the basement geology beneath Taranaki is less well constrained and interpretations are mainly based on seismic profiles, basement rocks drilled offshore, and inferred related rocks that are exposed in the South Island. Mortimer et al. (1997) interpreted the Taranaki basement as mainly composed of calc-alkaline

subduction-related plutonic rocks which are part of a major terrane boundary unit, the Median Tectonic Zone.

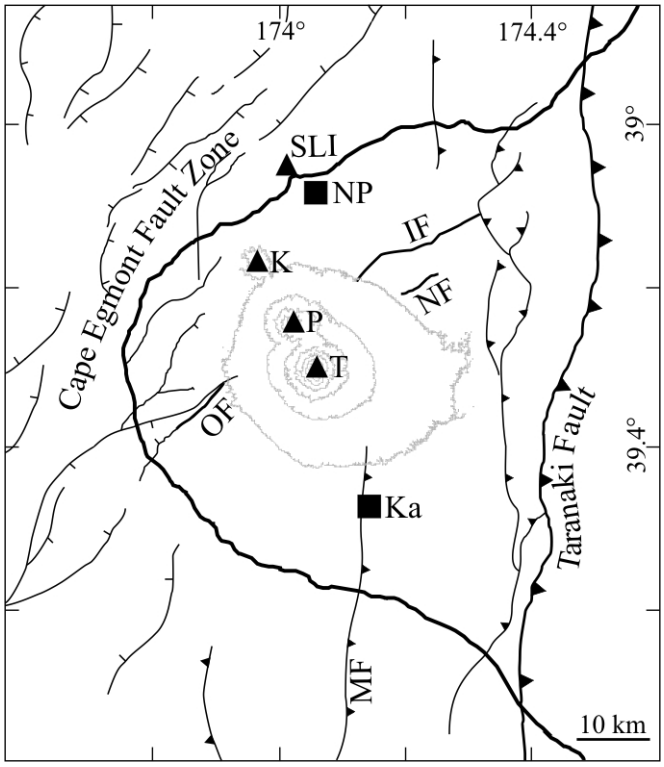


Figure 1-2: Regional tectonic setting of the Taranaki peninsula. The Taranaki Volcanic Lineament comprises the Sugar Loaf Islands (SLI), Kaitake (K), Pouakai (P) and Mt. Taranaki (T). Major onshore (thick lines) and offshore (thin lines) faults are indicated: IF-Inglewood Fault, MF-Manaia Fault, NF-Norfolk Fault, OF-Oaonui Fault. Contours are at 300 m intervals for the volcanic edifices only. New Plymouth (NP) as the major settlement is identified. Ka-Kapuni Gas Field. Modified after Sherburn and White (2005).

Heat flow measurements in oil exploration wells on- and offshore Taranaki peninsula revealed an anomalous high heat flow zone rising to 73 mWm^{-2} in New Plymouth with an average heat flow of c.60 mWm^{-2} for the entire Taranaki Basin (Allis et al., 1995; Funnel et al., 1996). Geotherms calculated for 50 mWm^{-2} (Kapuni, SSE of Mt. Taranaki) and 70 mWm^{-2} (New Plymouth) correspond to temperatures of 138 °C at 6 km depth and 160 °C at 5 km depth, respectively (Allis et al., 1995). A higher heat flow than 50 mWm^{-2} for two Kapuni wells (>5 km) is suggested and could be explained by cooling effects of cross-flowing ground water in the upper 3 km of sediments (Allis et al., 1995). Thermal modelling showed that the heat anomaly beneath New Plymouth is either caused by 5 km of crustal underplating over the last 2-4 Ma or by mid-crustal intrusions up to 500 m thick over the last 0.2-0.5 Ma. Recent crustal intrusions could be

indicated by a conductive heat pulse in a Kapuni well with an observed increase in the temperature gradient below 4 km (Allis et al., 1995).

Groundwater flow modelling beneath Mt. Taranaki predicts water circulation down to 3 km below sea level with lateral meteoric flow between 2-3 km b.s.l. due to presence of sandstone units (Allis et al., 1997). Although Allis et al. (1997) did not discuss the groundwater circulation in the context of heat flow variations within the Taranaki Basin, a decrease in observed heat flow along the Taranaki Volcanic Lineament towards Mt. Taranaki could also be caused by superimposed cooling effects of groundwater flows. The recent "disappearance" of warm springs such as Arawhata Spring (Mongillo and Clelland, 1984), c.19 km SW of Mt. Taranaki near/at the Oaonui Fault, the Waiweranui Stream (literally meaning "large hot water"), and the existence of a hot spring near The Dome (between Mt. Taranaki and Pouakai) until at least 1882 (The Taranaki Herald, 1871; Scanlan, 1961), may be evidence for temporal lateral groundwater and heat transfers following volcanic activity. High permeabilities of volcaniclastic deposits of the ring plain and Tertiary sandstones, with groundwater flow rates of 5 cm day^{-1} (Allis et al., 1997), may be able to disguise heat flows and reduce them to the observed 60 mWm^{-2} at Mt. Taranaki by lateral groundwater movements. The cold Kokowai Springs (c.1200 m a.s.l.) located c.2.5 km NNE of the summit of Mt. Taranaki contain magmatic carbon dioxide and hydrogen sulphide (Childs et al., 1986).

Gravity and aeromagnetic studies along the Taranaki Volcanic Lineament show large intrusive bodies beneath the volcanoes, probably reflecting complex, multiple dyke intrusions (Locke et al., 1993; 1994; Locke and Cassidy, 1997). The solidified andesite dyke complex beneath Mt. Taranaki can be modelled as a cylindrical intrusive body of approx. 5 km in diameter with a density of 2.7 gcm^{-3} compared to densities of 2.25-2.6 gcm^{-3} of the surrounding sedimentary rocks. If the intrusive body is modelled to where the density contrast is only 0.1 gcm^{-3}, the intrusive body extends down to 15 km, i.e. into the basement (Locke and Cassidy, 1997). A c.5 km diameter intrusive region beneath Mt. Taranaki extending to 10 km depth is also inferred by 3-D models of P-wave velocity, P- to S-wave velocity ratios, and P-wave quality factors. However, no magma storage was imaged within the upper 16 km, probably due to the 5 km spatial resolution of the models (Sherburn et al., 2006).

Geophysical studies (2001-2002) using 75 three-component, broad-band seismographs revealed a shallow crustal brittle-ductile transition zone (BDTZ) at 10 km depth beneath Mt. Taranaki with an increase in depth to 25 and 35 km to the west and east,

respectively (Sherburn and White, 2005). The shallow BDTZ caused by magmatic intrusions is consistent with observed high heat flows (up to 73 mWm^{-2}; Allis et al., 1995). The temperature at the top of the BDTZ is calculated at about 300 °C if the onset of plastic flow occurs in a quartz-dominated crust (Sherburn and White, 2005).

1.4.3 Taranaki Volcanic Lineament

Quaternary volcanism in the west of the North Island is expressed by the Taranaki Volcanic Lineament (Fig. 1-2) a succession of four NNW-SSE aligned individual andesite volcanoes consisting of the Sugar Loaf Islands (1.75 Ma), Kaitake (0.75 Ma), Pouakai (0.5 Ma) and Mt. Taranaki/Egmont (c.0.15 Ma) where volcanism has migrated to the SSE (Neall, 1979; Neall et al., 1986). The Sugar Loaf Islands are remnants of a former volcano where the pinnacles, such as Paritutu, represent volcanic dykes and plugs (Grant-Taylor, 1964). This former volcano is offset by c.12 km to the NNW of Kaitake. Kaitake and Pouakai are andesite volcanoes at different stages of erosion, although Pouakai appears considerably larger – although not approaching the basal diameter of the present Mt. Taranaki. The locus of volcanism for at least the last 150,000 yrs has been Mt. Taranaki.

The Taranaki peninsula with its near semi-circular coastline is made up of overlapping fans of volcaniclastic sediments, including debris-avalanche, debris-flow, pyroclastic-flow, and fluvial deposits which form the Egmont and Pouakai ring plains (lowland below c.300 m; Gibson and Morgan, 1927). Most of the western and southern parts of the peninsula are characterised by deposits representing several collapse episodes of Mt. Taranaki and subsequent reworked material (Neall, 1979; Newnham and Alloway, 2004; Alloway et al., 2005; Zernack et al., 2005).

1.4.4 Mount Taranaki/Egmont

Mount Taranaki/Egmont (2518 m), henceforth called Mt. Taranaki, is volumetrically the largest andesite volcano in New Zealand, although it is lower than Mt. Ruapehu (2797 m). The Taranaki edifice is a nearly perfectly shaped stratovolcano whose symmetry is only slightly disfigured by Fanthams Peak, a 1967 m high parasitic cone to

the south (Fig. 1-3). The volcanic history of Mt. Taranaki began more than 150,000 years ago with the earliest known deposits lying directly above an uplifted marine-cut surface (Alloway et al., 1995, 2005). The volcano's history has been characterised by several cone-building and collapse episodes with the current edifice having been predominantly constructed over the last c.10 ka (Neall et al., 1986). Grant-Taylor (1964) described Mt. Taranaki as a somma volcano with the symmetrical upper cone (i.e. above 1100 m) grown 400 m SW off-centre from the lower part of the edifice. His observation is based on erosion features and slope differences with a pronounced "plateau" on the eastern side of the edifice marking the pre-collapse structure.

Four lava domes are recognised on the lower flanks of Mt. Taranaki: the two Beehive domes on the south flank between 800-900 m are in alignment with Fanthams Peak on a NNE trend, whereas the other two domes, The Dome and Skinner Hill, are located on the northern flank at elevations of 900 m and c.1100 m, respectively (Fig. 1-3). Although the latter two domes are not aligned with the summit, they are also considered to be located on radial faults extending from the summit of Mt. Taranaki (Neall, 1971).

The eruptive activity over the last c.18 ka was characterised by moderate to large sized sub-Plinian eruptions on c.330 yr intervals, interspersed with more frequent effusive, dome-forming and destructive events and lava flows (Alloway et al., 1995). A brief summary of the succession of volcanic events in the last c.10,000 yrs follows based on Neall, 1979 and Neall et al. (1986):

- 12,000-7,000 yrs B.P.: major period of dome-producing and collapse episodes with BAF deposition on the western flank (e.g. Okahu Gorge, Pyramid and Waiweranui Streams) and the eastern flank (e.g. Manganui Gorge); immediately following this period was the extrusion of lava flows forming the core of the upper present day cone
- c.7000 yrs B.P.: sector collapse of the southern flank forming the Opua Formation comprising debris-avalanche, debris-flow and lahar deposits
- subsequent re-building phase of the cone by lava flow extrusion, most of them probably younger than 3500 yrs
- interspersed sub-Plinian eruptions with the Korito Tephra (4150 yrs B.P.) and the Inglewood Tephra (3690 yrs B.P.) being the most distinct eruptions (Alloway et al., 1995)

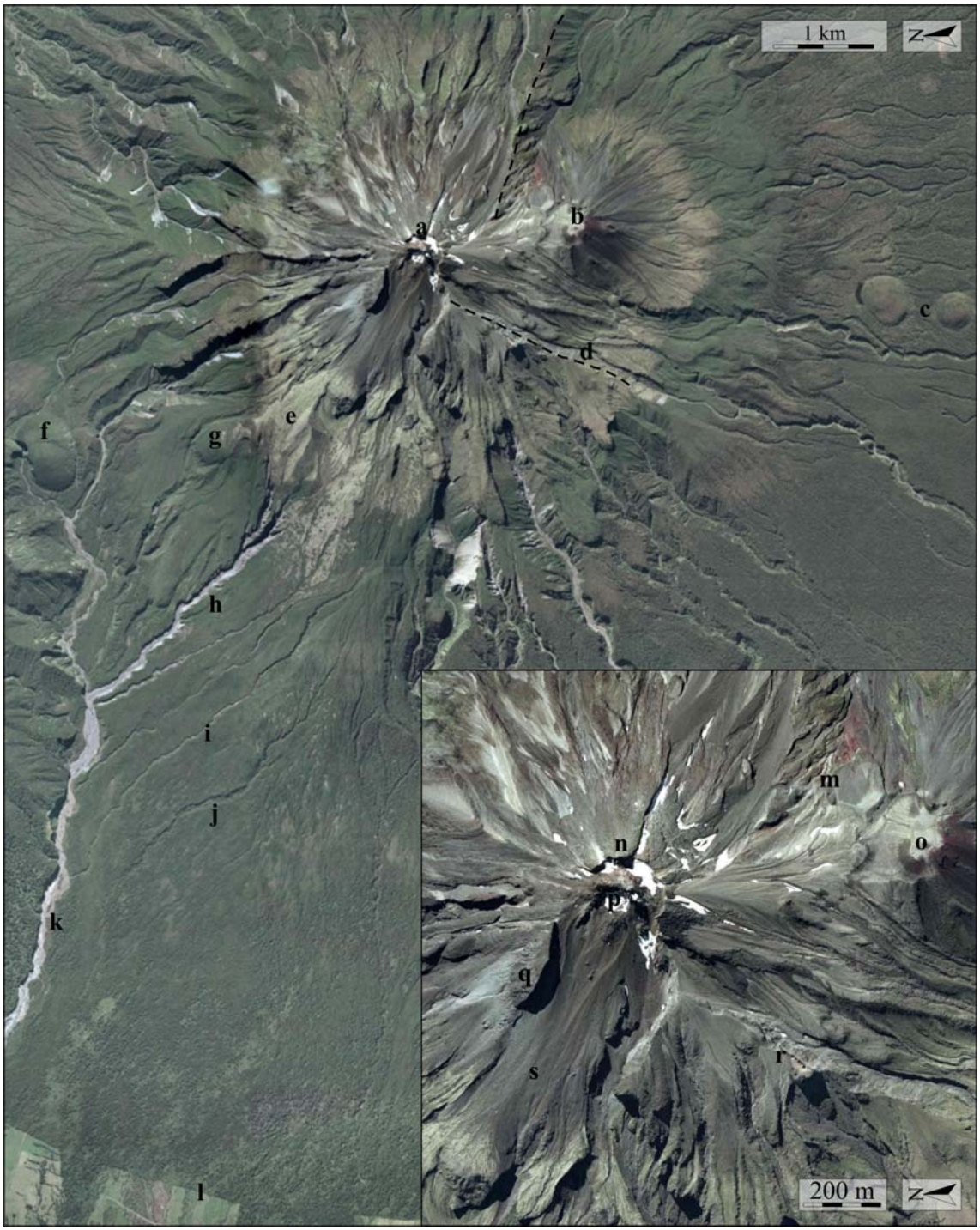


Figure 1-3: Orthophotograph of Mt. Taranaki including the lower northwestern flanks. Inset shows upper cone area including Fanthams Peak. Major morphological features are indicated by letters: a-summit crater of Mt. Taranaki, b-Fanthams Peak, c-the Beehives (two lava domes), d-scarp of the Opua amphitheatre, e-Big Pyramid, f-The Dome, g-Skinner Hill (probably a buried dome structure), h-Pyramid Stream, i-Maero Stream, j-Waiweranui Stream, k-Hangatahua River, l-Egmont National Park boundary (forest/pasture border, here 390 m), m-Kapuni Gorge (marks the eastern border of the amphitheatre), n-Sharks Tooth (second highest peak, 2510 m), o-Fanthams Peak (comprising multiple vents), p-remnant summit dome, q-Turtle, r-Bobs Ridge (western border of the Opua amphitheatre), s-NW flank and main path for BAFs.

- 3300 yrs B.P.: final construction of the parasitic cone (Fanthams Peak) with a major and distinct eruption c.2900 yrs ago
- extrusion of lava domes from subsidiary vents on the lower flanks (The Dome, Skinner Hill and the Beehives)
- 2000 yrs B.P.: dome-producing and collapse episode with BAF deposition on the eastern flanks
- climactic construction phase of the uppermost present day cone by lava flows
- 1400 yrs B.P.: sub-Plinian Kaupokonui eruption with widespread pumice deposition throughout the eastern sector of the edifice
- 600 yrs B.P.: Maero Eruptive Period characterised by dome-forming and collapse episodes and one sub-Plinian eruption in AD1655 (Burrell Lapilli eruption). The "last" known event at Mt. Taranaki, the Tahurangi eruption, was considered to be in AD1755 (Druce, 1966).

1.4.5 Petrology of Mt. Taranaki Rocks

The volcanic rocks of the Taranaki Volcanic Lineament were first described by Hutton (1889) as being hornblende-, augite-, and olivine andesites. Although petrographical, and later geochemical studies were subsequently made (Marshall, 1907; Clarke, 1912; Gibson and Morgan, 1927), it was not until Gow (1968) that the first classification scheme for Mt. Taranaki rocks, based on ferromagnesian mineral phases, was made. He recognised five rock types: 1) augite andesite, 2) augite – hornblende andesite (augite > hornblende), 3) augite – hornblende andesite (augite ~ hornblende), 4) augite – hornblende andesite (augite < hornblende), and 5) augite – olivine andesite (up to 7% modal olivine). This rock classification has been applied since then and was only modified by the addition of other mineral phases, such as plagioclase and biotite, where further distinction was needed (e.g. Neall et al., 1986, Stewart et al., 1996, Price et al., 1999).

Common phenocrysts in Mt. Taranaki rocks are plagioclase, clinopyroxene, hornblende, Fe-Ti oxides, and minor olivine with additional microphenocryst and groundmass phases of orthopyroxene and biotite (Gow, 1968; Neall et al., 1986). Rare accessories are apatite and zircon (Neall et al., 1986). Complex mineral textures such as zoning and

resorption are described in more detail by Gow (1968), Neall et al. (1986) and Stewart et al. (1996).

Igneous and sedimentary inclusions within Mt. Taranaki rocks have long been recognised and recently Gründer (2006) classified them into: 1) sedimentary rocks, 2) garnet-gneiss – granodiorite – granite suite, 3) mafic hornfels, 4) banded amphibolitic gneiss, 5) gabbros, and 6) ultramafic rocks. The latter two types are referred to as being of co-magmatic origin whereas the first two are considered to be exotic inclusions. Types 3 and 4 cannot be clearly assigned to either source but their metamorphic character could suggest an affiliation to deformed MTZ basement (Gründer, 2006).

The Mt. Taranaki rocks are classified as a high-K suite (Fig. 1-4) based on whole rock geochemistry, and comprise basalt – low-Si andesite – high-Si andesite (Price et al., 1992) according to the classification of Gill (1981). The same rock assemblage can also be classified as high-K basalts – basaltic andesites – andesites after Le Maitre et al. (1989). Further, a positive relationship within the rock suite between potassium and silica contents (Fig. 1-4) and time has been recognised; generally, the younger the volcanic rocks the higher potassium and mean silica abundances (cf. Price et al., 1992; Stewart et al., 1996). An increase of alkalis and silica within a rock suite with no iron enrichment is also referred to as a calc-alkaline trend. All Mt. Taranaki rocks are highly evolved based on Mg#, which is in general <53, and low whole rock Cr and Ni contents (Price et al., 1992).

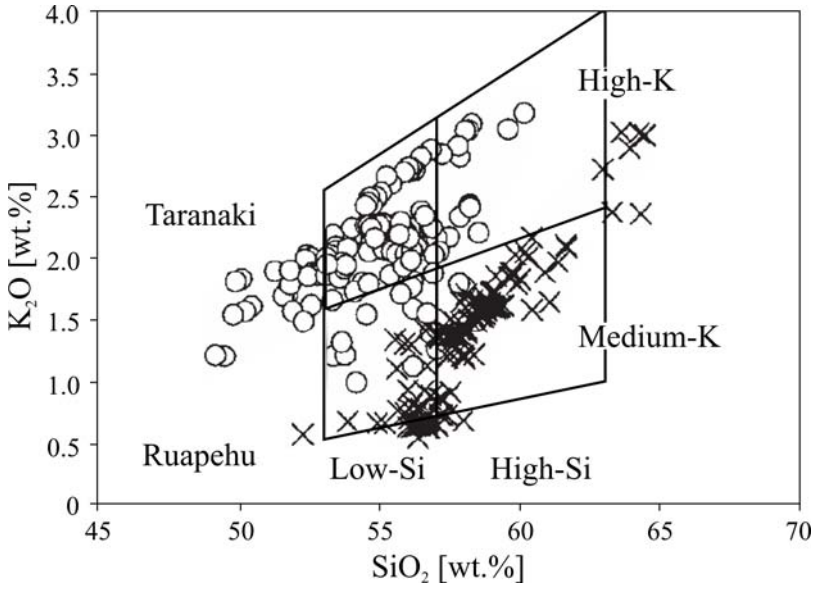


Figure 1-4: Classification of Mt. Taranaki and Mt. Ruapehu rocks after Gill (1981). Modified after Price et al. (1999).

Trace element abundances are characterised by relatively high proportions of large ion lithophile elements (LILE; e.g. Rb, Cs, Sr, Ba) and light rare earth elements (LREE) with deficiencies in high field strength elements (HFSE; Ta, Nb, Zr; cf. Price et al., 1992, 1999, 2005). These, as well as other trace element characteristics, such as depletion of Nb relative to La, and enrichment of Pb and Sr relative to Ce, are typical arc-signatures (Fig. 1-5).

Isotope studies carried out by Price et al. (1992; 1999; 2005) show that Mt. Taranaki rocks display a tight range of $^{143}Nd/^{144}Nd$ and $^{87}Sr/^{86}Sr$ ratios. However, $^{87}Sr/^{86}Sr$ ratios along the Taranaki lineament centres indicate a weak positive relationship with decreasing age although no relationship with SiO_2 is present. Lead and oxygen isotope data indicate that significant assimilation of crustal material or material rich in ^{18}O was not involved in the genesis of Mt. Taranaki magmas.

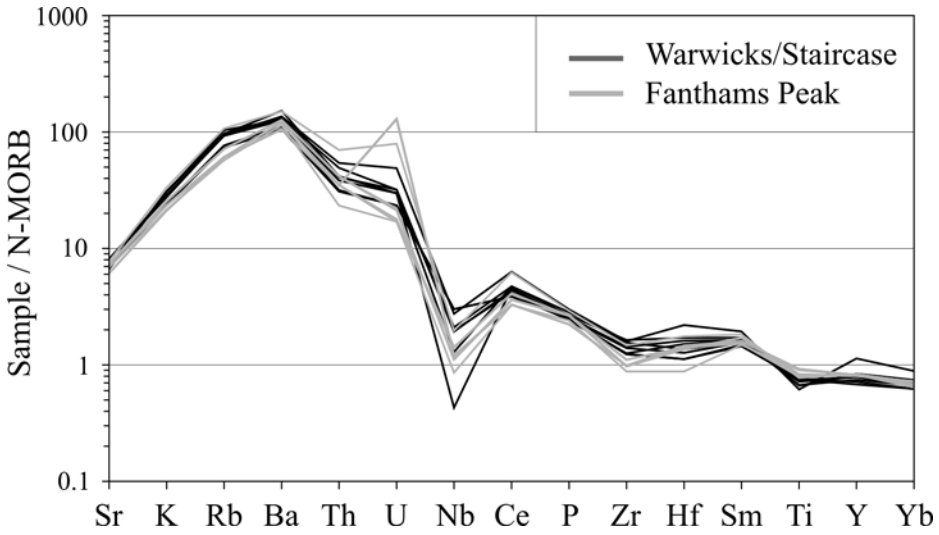


Figure 1-5: Trace element patterns of selected Mt. Taranaki rocks. Warwicks/Staircase refers to lava flow groups of the main cone of Mt. Taranaki; Fanthams describes lava flows of the satellite vent Fanthams Peak. Data compiled from Price et al. (1992, 1999). Normalisation after Sun and McDonough (1989).

The enrichment of LILE and depletion of HFSE in Mt. Taranaki magmas is attributed to low-degree partial melts of a depleted mantle as well as a significant component of slab-derived fluids (Price et al., 1999). Parental magmas were therefore interpreted to be relatively undersaturated, hydrous, high-Mg basalts. Stewart et al. (1996) introduced a model based on Foden and Green (1992) which suggests progressive underplating of these basalts at the base of the crust which then evolved to high-Al basalts. The high-Al basalts eventually intersect the amphibole stability field and interact with upper mantle/lower crust amphibolitic material, buffering the melt composition to basaltic

andesite. These magmas ascend and erupt as dry, mainly plagioclase-, olivine-, pyroxene-bearing magmas. However, these magmas may re-enter the amphibole stability field at higher crustal levels to crystallise amphibole driving the melt composition through andesite and dacite. The incongruent melting of amphibole at depth and/or through dyke – wall rock interaction is probably the main source for K-enrichment in the melt phase (Stewart et al., 1996).

In a comparison of andesite volcanism in the Tongariro Volcanic Centre and Taranaki, Price et al. (2005) proposed that andesite magmas are produced through the interaction of mantle-derived magmas and the lower crust. From this zone upward migrating magmas are crystal- and lithic-rich and their melt phases of rhyolite and dacite composition. High level crustal storage and the presence of a dispersed, complex plumbing systems was thought to cause the observed geochemical and mineral textural variations within andesitic rocks through time (Price et al., 2005).

1.5 References

Abdurachman, E.K., Bourdier, J.-L. and **Voight, B.** 2000. Nuées ardentes of 22 November 1994 at Merapi volcano, Java, Indonesia. *Journal of Volcanology and Geothermal Research* 100, 345-361.

Alidibirov, M. and **Dingwell, D.B.** 1996. Magma fragmentation by rapid decompression. *Nature* 380, 146-148.

Alidibirov, M. and **Dingwell, D.B.** 2000. Three fragmentation mechanisms for highly viscous magma under rapid decompression. *Journal of Volcanology and Geothermal Research* 100, 413-421.

Alidibirov, M., Dingwell, D.B., Stevenson, R.J., Hess, K.U., Webb, S.L. and **Zinke, J.** 1997. Physical properties of the 1980 Mount St. Helens cryptodome magma. *Bulletin of Volcanology* 59, 103-111.

Allis, R.G., Armstrong, P.A. and **Funnell, R.H.** 1995. Implications of a high heat flow anomaly around New Plymouth, North Island, New Zealand. *New Zealand Journal of Geology and Geophysics* 38, 121-130.

Allis, R.G., Zhan, X., Evans, C. and **Kroopnick, P.** 1997. Groundwater flow beneath Mt Taranaki, New Zealand, and implications for oil and gas migration. *New Zealand Journal of Geology and Geophysics* 40, 137-149.

Alloway, B., Neall, V.E. and **Vucetich, C.G.** 1995. Late Quaternary (post 28,000 year B.P.) tephrostratigraphy of northeast and central Taranaki, New Zealand. *Journal of the Royal Society of New Zealand* 25, 385-458.

Alloway, B., McComb, P., Neall, V., Vucetich, C., Gibb, J., Sherburn, S. and **Stirling, M.** 2005. Stratigraphy, age, and correlation of voluminous debris-avalanche events from an ancestral Egmont Volcano: implications for coastal plain construction and regional hazard assessment. *Journal of the Royal Society of New Zealand* 35, 229-267.

Anderson, S.W. and **Fink, J.H.** 1989. Hydrogen-isotope evidence for extrusion mechanisms of the Mount St Helens lava dome. *Nature* 341, 521-523.

Anderson, S.W., Fink, J.H. and **Rose, W.I.** 1995. Mount St. Helens and Santiaguito lava domes: the effect of short-term eruption rate on surface texture and degassing processes. *Journal of Volcanology and Geothermal Research* 69, 105-116.

Battaglia, M. 1993. On pyroclastic flow emplacement. *Journal of Geophysical Research-Solid Earth* 98, 22269-22272.

Blake, S. 1984. Volatile oversaturation during the evolution of silicic magma chambers as an eruption trigger. *Journal of Geophysical Research-Solid Earth* 89, 8237-8244.

Blundy, J. and **Cashman, K.** 2001. Ascent-driven crystallisation of dacite magmas at Mount St Helens, 1980-1986. *Contributions to Mineralogy and Petrology* 140, 631-650.

Blundy, J., Cashman, K. and **Humphreys, M.** 2006. Magma heating by decompression-driven crystallization beneath andesite volcanoes. *Nature* 443, 76-80.

Boddington, T., Parkin, C.J. and **Gubbins, D.** 2004. Isolated deep earthquakes beneath the North Island of New Zealand. *Geophysical Journal International* 158, 972-982.

Boudon, G. and **Lajoie, J.** 1989. The 1902 Peléean deposits in the Fort Cemetery of St. Pierre, Martinique: a model for the accumulation of turbulent nuées ardentes. *Journal of Volcanology and Geothermal Research* 38, 113-129.

Boudon, G., Camus, G., Gourgaud, A. and **Lajoie, J.** 1993. The 1984 nuée-ardente deposits of Merapi volcano, Central Java, Indonesia: stratigraphy, textural characteristics, and transport mechanisms. *Bulletin of Volcanology* 55, 327-342.

Bourdier, J.L., Pratomo, I., Thouret, J.C., Boudon, G. and **Vincent, P.M.** 1997. Observations, stratigraphy and eruptive processes of the 1990 eruption of Kelut volcano, Indonesia. *Journal of Volcanology and Geothermal Research* 79, 181-203.

Branney, M.J. and **Kokelaar, P.** 1992. A reappraisal of ignimbrite emplacement: progressive aggradation and changes from particulate to non-particulate flow during emplacement of high-grade ignimbrite. *Bulletin of Volcanology* 54, 504-520.

Branney, M.J. and **Kokelaar, P.** 2002. Pyroclastic density currents and the sedimentation of ignimbrites. *Geological Society of London Memoir* 27.

Briggs, R.M. 1983. Distribution, form, and structural control of the Alexandra Volcanic Group, North Island, New Zealand. *New Zealand Journal of Geology and Geophysics* 26, 47-55.

Briggs, R.M., Itaya, T., Lowe, D.J. and **Keane, A.J.** 1989. Ages of the Pliocene-Pleistocene Alexandra and Ngatutura Volcanics, western North island, New Zealand, and some geological implications. *New Zealand Journal of Geology and Geophysics* 32, 417-427.

Camus, G., Gourgaud, A., Mossand-Berthommier, P.C. and **Vincent, P.M.** 2000. Merapi (Central Java, Indonesia): an outline of the structural and magmatological evolution, with a special emphasis to the major pyroclastic events. *Journal of Volcanology and Geothermal Research* 100, 139-163.

Carey, S. and **Sigurdsson, H.** 1985. The May 18, 1980 eruption of Mount St. Helens; II - modeling of dynamics of the Plinian phase. *Journal of Geophysical Research-Solid Earth* 90, 2948-2958.

Carn, S.A., Watts, R.B., Thompson, G. and **Norton, G.E.** 2004. Anatomy of a lava dome collapse: the 20 March 2000 event at Soufriére Hills Volcano, Montserrat. *Journal of Volcanology and Geothermal Research* 131, 241-264.

Cas, R.A.F. and **Wright, J.V.** 1991. Subaqueous pyroclastic flows and ignimbrites: an assessment. *Bulletin of Volcanology* 53, 357-380.

Cashman, K.V. and **Hoblitt, R.P.** 2004. Magmatic precursors to the 18 May 1980 eruption of Mount St. Helens, USA. *Geology* 32, 141-144.

Cashman, K.V. and **McConnell, S.M.** 2005. Multiple levels of magma storage during the 1980 summer eruptions of Mount St. Helens, WA. *Bulletin of Volcanology* 68, 57-75.

Childs, C.W., Wells, N. and **Downes, C.J.** 1986. Kokowai Springs, Mount Egmont, New Zealand: chemistry and mineralogy of the ochre (ferrihydrite) deposit and analysis of the waters. *Journal of the Royal Society of New Zealand* 16, 85-99.

Choux, C.M. and **Druitt, T.H.** 2002. Analogue study of particle segregation in pyroclastic density currents, with implications for the emplacement mechanisms of large ignimbrites. *Sedimentology* 49, 907-928.

Clarke, E. de C. 1912. The geology of the New Plymouth Subdivision, Taranaki Division. *New Zealand Geological Survey Bulletin* 14.

Cole, P.D., Calder, E.S., Druitt, T.H., Hoblitt, R., Robertson, R., Sparks, R.S.J. and **Young, S.R.** 1998. Pyroclastic flows generated by gravitational instability of the 1996-97 lava dome of Soufriere Hills Volcano, Montserrat. *Geophysical Research Letters* 258, 3425-3428.

Cole, P.D., Calder, E.S., Sparks, R.S.J., Clarke, A.B., Druitt, T.H., Young, S.R., Herd, R.A., Harford, C.L. and **Norton, G.E.** 2002. Deposits from dome-collapse and fountain-collapse pyroclastic flows at Soufrière Hills Volcano, Montserrat. *Geological Society, London, Memoirs* 21, 231-262.

Couch, S., Sparks, R.S.J. and **Carroll, M.R.** 2003. The kinetics of degassing-induced crystallization at Soufrière Hills Volcano, Montserrat. *Journal of Petrology* 44, 1477-1502.

Cowan, J. 1930. Fairy folk tales of the Maori. Whitcombe and Toombs. Auckland.

Cronin, S.J. and **Neall, V.E.** 1997. A late Quaternary stratigraphic framework for the northeastern Ruapehu and eastern Tongariro ring plains, New Zealand. *New Zealand Journal of Geology and Geophysics* 40, 185-197.

Cronin, S.J., Stewart, R.B., Neall, V.E., Platz, T. and **Gaylord, D.** 2003. The AD1040 to present Maero eruptive period of Egmont Volcano, Taranaki, New Zealand. Abstract. *Geological Society of New Zealand Miscellaneous Publication* 116A, 43.

Dade, W.B. and **Huppert, H.E.** 1996. Emplacement of the Taupo ignimbrite by a dilute turbulent flow. *Nature* 381, 509-512.

Devine, J.D., Rutherford, M.J., Norton, G.E. and **Young, S.R.** 2003. Magma storage region processes inferred from geochemistry of Fe-Ti oxides in andesitic magma, Soufrière Hills Volcano, Montserrat, W.I. *Journal of Petrology* 44, 1375-1400.

Dissen, R. van and **Yeats, R.S.** 1991. Hope fault, Jordan thrust and uplift of the Seaward Kaikoura Range, New Zealand. *Geology* 19, 393-396.

Dobran, F. 1992. Nonequilibrium flow in volcanic conduits and application to the eruptions of Mt. St. Helens on May 18, 1980, and Vesuvius in AD 79. *Journal of Volcanology and Geothermal Research* 49, 285-311.

Donoghue, S.L., Neall, V.E. and **Palmer, A.S.** 1995. Stratigraphy and chronology of late Quaternary andesitic tephra deposits, Tongariro Volcanic Center, New Zealand. *Journal of the Royal Society of New Zealand* 25, 115-206.

Druce, A.P. 1966. Tree-ring dating of recent volcanic ash and lapilli, Mt Egmont. *New Zealand Journal of Botany* 4, 3-41.

Fink, J.H., Malin, M.C. and **Anderson, S.W.** 1990. Intrusive and extrusive growth of the Mount St Helens lava dome. *Nature* 348, 435-437.

Fink, J.H., Anderson, S.W. and **Manley, C.R.** 1992. Textural constraints on effusive silicic volcanism - beyond the permeable foam model. *Journal of Geophysical Research-Solid Earth* 97, 9073-9083.

Fisher, R.V., Orsi, G., Ort, M. and **Heiken, G.** 1993. Mobility of a large-volume pyroclastic flow-emplacement of the Campanian ignimbrite, Italy. *Journal of Volcanology and Geothermal Research* 56, 205-220.

Foden, J.D. and **Green, D.H.** 1992. Possible role of amphibole in the origin of andesite: some experimental and natural evidence. *Contributions to Mineralogy and Petrology* 109, 479-493.

Freundt, A. 1998. The formation of high-grade ignimbrites, I: experiments on high- and low-concentration transport systems containing sticky particles. *Bulletin of Volcanology* 59, 414-435.

Freundt, A. 2003. Entrance of hot pyroclastic flows into the sea: experimental observations. *Bulletin of Volcanology* 65, 144-164.

Freundt, A. and **Bursik, M.** 1998. Pyroclastic flow transport mechanisms. In: **Freundt, A.** and **Rosi, M.** (eds.) From magma to tephra: modelling physical processes of explosive volcanism. Elsevier. Amsterdam. pp. 151-222.

Fujii, T. and **Nakada, S.** 1999. The 15 September 1991 pyroclastic flows at Unzen Volcano (Japan): a flow model for associated ash-cloud surges. *Journal of Volcanology and Geothermal Research* 89, 159-172.

Funnell, R., Chapman, D., Allis, R. and **Armstrong, P.** 1996. Thermal state of the Taranaki Basin, New Zealand. *Journal of Geophysical Research-Solid Earth* 101, 25197-25215.

Gardner, J.E., Thomas, R.M.E., Jaupart, C. and **Tait, S.** 1996. Fragmentation of magma during Plinian volcanic eruptions. *Bulletin of Volcanology* 58, 144-162.

Gibson, W. and **Morgan, P.G.** 1927. The geology of the Egmont Subdivision, Taranaki. *New Zealand Geological Survey Bulletin* 29.

Gill, J.B. 1981. Orogenic andesites and plate tectonics. Springer Verlag. Berlin.

Giordano, G. and **Dobran, F.** 1994. Computer simulations of the Tuscolano-Artemisio's second pyroclastic flow unit (Alban Hills, Latium, Italy). *Journal of Volcanology and Geothermal Research* 61, 69-94.

Gow, A.J. 1968. Petrographic and petrochemical studies of Mt. Egmont andesites. *New Zealand Journal of Geology and Geophysics* 11, 166-190.

Grant-Taylor, T.L. 1964. Volcanic history of western Taranaki. *New Zealand Journal of Geology and Geophysics* 7, 78-86.

Gründer, K. 2006. Petrography and mineral chemistry of a xenolith suite from Mt. Taranaki, New Zealand: insights into the sub-volcanic lithosphere of an arc volcano. Unpublished Diploma thesis. Johannes Gutenberg Universität, Mainz, Bundesrepublik Deutschland.

Grunewald, U., Sparks, R.S.J., Kearns, S. and **Komorowski, J.C.** 2000. Friction marks on blocks from pyroclastic flows at the Soufriere Hills volcano, Montserrat: implications for flow mechanisms. *Geology* 28, 827-830.

Harford, C.L., Sparks, R.S.J. and **Fallick, A.E.** 2003. Degassing at the Soufrière Hills Volcano, Montserrat, recorded in matrix glass compositions. *Journal of Petrology* 44, 1503-1523.

Higgins, M.D. and **Roberge, J.** 2003. Crystal size distribution of plagioclase and amphibole from Soufrière Hills volcano, Montserrat: evidence for dynamic crystallization-textural coarsening cycles. *Journal of Petrology* 44, 1401-1411.

Hobden, B.J., Houghton, B.F. and **Nairn, I.A.** 2002. Growth of a young, frequently active composite cone: Ngauruhoe volcano, New Zealand. *Bulletin of Volcanology* 64, 392-409.

Hull, A.G. 1994. Past earthquake timing and magnitude along the Inglewood fault, Taranaki, New Zealand. *Bulletin of the New Zealand National Society for Earthquake Engineering* 27, 155-162.

Hull, A.G. and **Dellow, G.** 1993. Earthquake hazards in the Taranaki region. Institute of Geological and Nuclear Sciences Client Report 1993/03.

Hutton, F.W. 1889. The eruptive rocks of New Zealand. *Journal and Proceedings of the Royal Society of New South Wales* 23, 102-56.

King, P.R. and **Thrasher, G.P.** 1996. Cretaceous-Cenozoic geology and petroleum systems of the Taranaki Basin, New Zealand. *Institute of Geological and Nuclear Sciences Monograph* 13.

Klug, C. and **Cashman, K.V.** 1994. Vesiculation of May 18, 1980, Mount St. Helens magma. *Geology* 22, 468-472.

Lacroix, A. 1904. La Montagne Pelée et ses éruptions. Masson et Cie. Paris.

Le Maitre, R.W., Bateman, P., Dudek, A., Keller, J., Lameyre, J., Le Bas, M.J., Sabine, P.A., Schmid, R., Sorensen, H., Streckeisen, A., Woolley, A.R. and **Zanettin, B.** 1989. A classification of igneous rocks and glossary of terms. Blackwell Scientific Publications. Oxford.

Lipman, P.W. and **Mullineaux, D.R.** (eds.) 1981. The 1980 eruptions of Mount St. Helens, Washington. *U.S. Geological Survey Professional Paper* 1250.

Locke, C.A. and **Cassidy, J.** 1997. Egmont Volcano, New Zealand: three-dimensional structure and its implications for evolution. *Journal of Volcanology and Geothermal Research* 76, 149-161.

Locke, C.A., Cassidy, J. and **Macdonald, A.** 1993. Three-dimensional structure of relict stratovolcanoes in Taranaki, New Zealand: evidence from gravity data. *Journal of Volcanology and Geothermal Research* 59, 121-130.

Locke, C.A., Cassidy, J. and **Macdonald, A.** 1994. Constraints on the evolution of the Taranaki volcanoes, New Zealand, based on aeromagnetic data. *Bulletin of Volcanology* 56, 552-560.

Lube, G., Huppert, H.E., Sparks, R.S.J. and **Hallworth, M.A.** 2004. Axisymmetric collapses of granular columns. *Journal of Fluid Mechanics* 508, 175-199.

Lube, G., Cronin, S.J., Platz, T., Freundt, A., Procter, J.N., Henderson, C. and **Sheridan, M.F.** 2007. Flow and deposition of pyroclastic granular flows: a type example from the 1975 Ngauruhoe eruption, New Zealand. *Journal of Volcanology and Geothermal Research* 161, 165-186.

Lyman, A.W., Koenig, E. and **Fink, J.H.** 2004. Predicting yield strengths and effusion rates of lava domes from morphology and underlying topography. *Journal of Volcanology and Geothermal Research* 129, 125-138.

Marshall, P. 1907. Geology of centre and north of North Island. *Transactions and Proceedings of the Royal Society of New Zealand* 40, 79-98.

Massol, H., Jaupart, C. and **Pepper, D.W.** 2001. Ascent and decompression of viscous vesicular magma in a volcanic conduit. *Journal of Geophysical Research-Solid Earth* 106, 16223-16240.

McClelland, E.A. and **Druitt, T.H.** 1989. Paleomagnetic estimation of emplacement temperatures of pyroclastic deposits on Santorini, Greece. *Bulletin of Volcanology* 51, 16-27.

Melnik, O. and **Sparks, R.S.J.** 2002. Dynamics of magma ascent and lava extrusion at Soufrière Hills Volcano, Montserrat. In: **Druitt, T.H.** and **Kokelaar, B.P.** (eds.) The eruption of Soufrière Hills Volcano, Montserrat, from 1995 to 1999. *Geological Society, London, Memoirs* 21, 153-171.

Mets, C. de, Gordon, R.G., Argus, D.F. and **Stein, S.** 1994. Effect of recent revisions to the geomagnetic reversal time scale on estimates of current plate motions. *Geophysical Research Letters* 21, 2191-2194.

Minister, J.B. and **Jordan, T.H.** 1978. Present day plate motions. *Journal of Geophysical Research-Solid Earth* 83, 5331-5354.

Mongillo, M.A. and **Clelland, L.** 1984. Concise listing of information on the thermal areas and thermal springs of New Zealand. Department of Scientific and Industrial Research. Wellington. *DSIR geothermal report* 9.

Moore, J.G. and **Melson, W.G.** 1969. Nuées ardentes of the 1968 eruption of Mayon volcano, Philippines. *Bulletin of Volcanology* 33, 600-620.

Moore, J.G., Lipman, P.W., Swanson, D.A. and **Alpha, T.R.** 1981. Growth of lava domes in the crater, June 1980-January 1981. In: **Lipman, P.W.** and **Mullineaux, D.R.** (eds.) The 1980 eruptions of Mount St. Helens, Washington. *U.S. Geological Survey Professional Paper* 1250, 541-548.

Mortimer, N., Tulloch, A.J. and **Ireland, T.R.** 1997. Basement geology of Taranaki and Wanganui Basins, New Zealand. *New Zealand Journal of Geology and Geophysics* 40, 223-236.

Mueller, S., Melnik, O., Spieler, O., Scheu, B. and **Dingwell, D.B.** 2005. Permeability and degassing of dome lavas undergoing rapid decompression: an experimental determination. *Bulletin of Volcanology* 67, 526-538.

Nairn, I.A. and **Self, S.** 1978. Explosive eruptions and pyroclastic avalanches from Ngauruhoe in February 1975. *Journal of Volcanology and Geothermal Research* 3, 39-60.

Nakada, S., Miyake, Y., Sato, H., Oshima, O. and **Fujinawa, A.** 1995. Endogenous growth of dacite dome at Unzen Volcano (Japan), 1993-1994. *Geology* 23, 157-160.

Nakada, S., Shimizu, H. and **Ohta, K.** 1999. Overview of the 1990-1995 eruption at Unzen Volcano. *Journal of Volcanology and Geothermal Research* 89, 1-22.

Navon, O., Chekhmir, A. and **Lyakhovsky, V.** 1998. Bubble growth in highly viscous melts: theory, experiments, and autoexplosivity of dome lavas. *Earth and Planetary Science Letters* 160, 763-776.

Neall, V.E. 1971. Volcanic domes and lineations in Egmont National Park. *New Zealand Journal of Geology and Geophysics* 14, 71-81.

Neall, V.E. 1979. Sheets P19, P20, and P21. New Plymouth, Egmont and Manaia. 1st ed. Geological map of New Zealand 1:50,000. 3 maps and notes. New Zealand Department of Scientific and Industrial Research. Wellington.

Neall, V.E., Stewart, R.B. and **Smith, I.E.M.** 1986. History and petrology of the Taranaki volcanoes. In: **Smith, I.E.M.** (ed.) Late Cenozoic volcanism. *Royal Society of New Zealand Bulletin* 23, 251-263.

Newnham, R. and **Alloway, B.** 2004. A terrestrial record of last interglacial climate preserved by voluminous debris avalanche inundation in Taranaki, New Zealand. *Journal of Quaternary Science* 19, 299-314.

Nicol, A., Stagpoole, V. and **Maslen, G.** 2004. Structure and petroleum potential of the Taranaki fault play. Abstract. *2004 New Zealand Petroleum Conference Proceedings*. Ministry of Economic Development, Wellington, New Zealand.

Nodder, S.D. 1993. Neotectonics of the offshore Cape Egmont Fault Zone, Taranaki Basin, New Zealand. *New Zealand Journal of Geology and Geophysics* 36, 167-184.

Pallister, J.S., Hoblitt, R.P. and **Reyes, A.G.** 1992. A basalt trigger for the 1991 eruptions of Pinatubo volcano? *Nature* 356, 426-428.

Papale, P. and **Dobran, F.** 1994. Magma flow along the volcanic conduit during the Plinian and pyroclastic flow phases of the May, 18, 1980, Mount St. Helens eruption. *Journal of Geophysical Research-Solid Earth* 99, 4355-4373.

Platz, T. 2001. Mapping and characterisation of the volcaniclastic Maero formation deposits on the northwestern sector of Egmont volcano (Mt. Taranaki), New Zealand. Unpublished Diploma mapping thesis. Ernst-Moritz-Arndt Universität, Greifswald, Bundesrepublik Deutschland.

Power, J.A., Jolly, A.D., Nye, C.J. and **Harbin, M.L.** 2002. A conceptual model of the Mount Spurr magmatic system from seismic and geochemical observations of the 1992 Crater Peak eruption sequence. *Bulletin of Volcanology* 64, 206-218.

Price, R.C., McCulloch, M.T., Smith, I.E.M. and **Stewart, R.B.** 1992. Pb-Nd-Sr isotopic compositions and trace element characteristics of young volcanic rocks from Egmont Volcano and comparisons with basalts and andesites from the Taupo Volcanic Zone, New Zealand. *Geochimica et Cosmochimica Acta* 56, 941-953.

Price, R.C., Stewart, R.B., Woodhead, J.D. and **Smith, I.E.M.** 1999. Petrogenesis of high-K arc magmas: evidence from Egmont Volcano, North Island, New Zealand. *Journal of Petrology* 40, 167-197.

Price, R.C. Gamble, J.A., Smith, I.E.M., Stewart, R.B., Eggins, S. and **Wright, I.C.** 2005. An integrated model for the temporal evolution of andesites and rhyolites and crustal development in New Zealand's North Island. *Journal of Volcanology and Geothermal Research* 140, 1-24.

Reyners, M., Eberhart-Phillips, D., Stuart, G. and **Nishimura, Y.** 2006. Imaging subduction from the trench to 300 km depth beneath the central North Island, New Zealand, with Vp and Vp/Vs. *Geophysical Journal International* 165, 565-583.

Rodríguez-Elizarrarás, S., Siebe, C., Komorowski, J.-C., Espíndola, J.M. and **Saucedo, R.** 1991. Field observations of pristine block- and ash-flow deposits emplaced April 16-17, 1991 at Volcán de Colima, Mexico. *Journal of Volcanology and Geothermal Research* 48, 399-412.

Rutherford, M.J. and **Hill, P.M.** 1993. Magma ascent rates from amphibole breakdown - an experimental study applied to the 1980-1986 Mount St Helens eruptions. *Journal of Geophysical Research-Solid Earth* 98, 19667-19685.

Rutherford, M.J. and **Devine, J.D.** 2003. Magmatic conditions and magma ascent as indicated by hornblende phase equilibria and reactions in the 1995-2002 Soufriére Hills magma. *Journal of Petrology* 44, 1433-1453.

Sato, H., Nakada, S., Fujii, T., Nakamura, M. and **Suzuki-Kamata, K.** 1999. Groundmass pargasite in the 1991-1995 dacite of Unzen volcano: phase stability experiments and volcanological implications. *Journal of Volcanology and Geothermal Research* 89, 197-212.

Saucedo, R., Macias, J.L., Bursik, M.I., Mora, J.C., Gavilanes, J.C. and **Cortes, A.** 2002. Emplacement of pyroclastic flows during the 1998-1999 eruption of Volcán de Colima, México. *Journal of Volcanology and Geothermal Research* 117, 129-153.

Scandone, R. and **Malone, S.D.** 1985. Magma supply, magma discharge and readjustment of the feeding system of Mount St. Helens during 1980. *Journal of Volcanology and Geothermal Research* 23, 239-262.

Scandone, R., Cashman, K.V. and **Malone, S.D.** 2007. Magma supply, magma ascent and the style of volcanic eruptions. *Earth and Planetary Science Letters* 253, 513-529.

Scanlan, A.B. 1961. Egmont - the story of a mountain. A.H. & A.W. Reed. Wellington.

Schmincke, H.-U. 1974. Volcanological aspects of peralkaline silicic welded ash-flow tuffs. *Bulletin of Volcanology* 38, 594-636.

Scott, A.C. and **Glasspool, I.J.** 2005. Charcoal reflectance as a proxy for the emplacement temperature of pyroclastic flow deposits. *Geology* 33, 589-592.

Sherburn, S. and **White, R.S.** 2005. Crustal seismicity in Taranaki, New Zealand using accurate hypocentres from a dense network. *Geophysical Journal International* 162, 494-506.

Sherburn, S., White, R.S. and **Chadwick, M.** 2006. Three-dimensional tomographic imaging of the Taranaki volcanoes, New Zealand. *Geophysical Journal International* 166, 957-969.

Simmons, J., Elsworth, D. and **Voight, B.** 2004. Instability of exogenous lava lobes during intense rainfall. *Bulletin of Volcanology* 66, 725-734.

Simmons, J., Elsworth, D. and **Voight, B.** 2005. Classification and idealized limit-equilibrium analyses of dome collapses at Soufiere Hills volcano, Montserrat, during growth of the first lava dome: November 1995-March 1998. *Journal of Volcanology and Geothermal Research* 139, 241-258.

Smith, R.L. and **Bailey, R.A.** 1966. The Bandelier Tuff: a study of ash-flow eruption cycles from zoned magma chambers. *Bulletin of Volcanology* 29, 83-103.

Sparks, R.S.J. 1976. Grain size variations in ignimbrites and implications for the transport of pyroclastic flows. *Sedimentology* 23, 147-188.

Sparks, R.S.J. 1997. Causes and consequences of pressurisation in lava dome eruptions. *Earth and Planetary Science Letters* 150, 177-189.

Sparks, R.S.J. and **Young, S.R.** 2002. The eruption of Soufrière Hills Volcano, Montserrat (1995-1999). In: **Druitt, T.H.** and **Kokelaar, B.P.** (eds.) The eruption of Soufrière Hills Volcano, Montserrat, from 1995 to 1999. *Geological Society, London, Memoirs* 21, 45-69.

Sparks, R.S.J., Young, S.R., Barclay, J., Calder, E.S., Cole, P., Darroux, B., Davies, M.A., Druitt, T.H., Harford, C., Herd, R., James, M., Lejeune, A.M., Loughlin, S., Norton, G., Skerrit, G., Stasiuk, M.V., Stevens, N.S., Toothill, J., Wadge, G. and **Watts, R.** 1998. Magma production and growth of the lava dome of the Soufriere Hills Volcano, Montserrat, West Indies: November 1995 to December 1997. *Geophysical Research Letters* 25, 3421-3424.

Sparks, R.S.J., Murphy, M.D., Lejeune, A.M., Watts, R.B., Barclay, J. and **Young, S.R.** 2000. Control on the emplacement of the andesite lava dome of the Soufriere Hills volcano, Montserrat by degassing-induced crystallization. *Terra Nova* 12, 14-20.

Stagpoole, V. 1999. The Awhitu volcanic complex, an offshore Pliocene volcano in the northern Taranaki Basin, New Zealand. *New Zealand Journal of Geology and Geophysics* 42, 327-334.

Stern, T.A. 1987. Asymmetric back-arc spreading, heat flux and structure beneath the central volcanic region of New Zealand. *Earth and Planetary Science Letters* 85, 265-276.

Stewart, R.B., Price, R.C. and **Smith, I.E.M.** 1996. Evolution of high-K arc magma, Egmont volcano, Taranaki, New Zealand: evidence from mineral chemistry. *Journal of Volcanology and Geothermal Research* 74, 275-295.

Sun, S.-S. and **McDonough, W.F.** 1989. Chemical and isotopic systematics of oceanic basalts: implications for mantle composition and processes. *Geological Society, London, Special Publications* 42, 313-345.

Swanson, D.A. and **Holcomb, R.T.** 1990. Regularities in growth of the Mount St. Helens dacite dome, 1980-1986. In: **Fink, J.H.** (ed.) Lava flows and domes: emplacement mechanisms and hazard implications. *IAVCEI Proceeding in Volcanology* 2, 3-24.

Swanson, D.A., Casadevall, T.J., Dzurisin, D., Malone, S.D., Newhall, C.G. and **Weaver, C.S.** 1983. Predicting eruptions at Mount St. Helens, June 1980 through December 1982. *Science* 221, 1369-1376.

The Taranaki Herald 1871. 25 March.

Topping, W.W. 1972. Burrell Lapilli eruptives, Mount Egmont, New Zealand. *New Zealand Journal of Geology and Geophysics* 15, 476-490.

Ui, T., Matsuwo, N., Sumita, M. and **Fujinawa, A.** 1999. Generation of block and ash flows during the 1990-1995 eruption of Unzen Volcano, Japan. *Journal of Volcanology and Geothermal Research* 89, 123-137.

Voight, B. and **Elsworth, D.** 2000. Instability and collapse of hazardous gas-pressurized lava domes. *Geophysical Research Letters* 27, 1-4.

Voight, B., Sparks, R.S.J., Miller, A.D., Stewart, R.C., Hoblitt, R.P., Clarke, A., Ewart, J., Aspinall, W.P., Baptie, B., Calder, E.S., Cole, P., Druitt, T.H., Hartford, C., Herd, R.A., Jackson, P., Lejeune, A.M., Lockhart, A.B., Loughlin, S.C., Luckett, R., Lynch, L., Norton, G.E., Robertson, R., Watson, I.M., Watts, R. and **Young, S.R.** 1999. Magma flow instability and cyclic activity at Soufriere Hills Volcano, Montserrat, British West Indies. *Science* 283, 1138-1142.

Voight, B., Linde, A.T., Sacks, I.S., Mattioli, G.S., Sparks, R.S.J., Elsworth, D., Hidayat, D., Malin, P.E., Shalev, E., Widiwijayanti, C., Young, S.R., Bass, V., Clarke, A., Dunkley, P., Johnston, W., McWhorter, N., Neuberg, J. and **Williams, P.** 2006. Unprecedented pressure increase in deep magma reservoir triggered by lava-dome collapse. *Geophysical Research Letters* 33, L03312.

Walker, G.P.L., Wilson, C.J.N. and **Froggatt, P.C.** 1980. Fines-depleted ignimbrite in New Zealand: the product of a turbulent pyroclastic flow. *Geology* 8, 245-249.

Wallace, L.M., Beavan, J., McCaffrey, R. and **Darby, D.** 2004. Subduction zone coupling and tectonic block rotations in the North Island, New Zealand. *Journal of Geophysical Research-Solid Earth* 109, B12406.

Wilson, C.J.N. and **Walker, G.P.L.** 1982. Ignimbrite depositional facies: the anatomy of a pyroclastic flow. *Journal of the Geological Society* 139, 581-592.

Wilson, C.J.N., Houghton, B.F., McWilliams, M.O., Lanphere, M.A., Weaver, S.D. and **Briggs, R.M.** 1995. Volcanic and structural evolution of Taupo Volcanic Zone, New Zealand: a review. *Journal of Volcanology and Geothermal Research* 68, 1-28.

Wright, J.V. and **Walker, G.P.L.** 1981. Eruption, transport and deposition of ignimbrite - a case study from Mexico. *Journal of Volcanology and Geothermal Research* 9, 111-131.

Zanella, E., Gurioli, L., Pareschi, M.T. and **Lanza, R.** 2007. Influences of urban fabric on pyroclastic density currents at Pompeii (Italy): 2. temperature of the deposits and hazard implications. *Journal of Geophysical Research-Solid Earth* 112, B05214.

Zernack, A.V., Procter, J.N. and **Cronin, S.J.** 2005. Cyclic growth and destruction of stratovolcanoes. Abstract. *Geological Society of New Zealand Miscellaneous Publication* 119A, 99-100.

Chapter 2 Methodology

In this chapter the overall strategy for the research is outlined and all methods that were used in this study and applied by the author are described.

2.1 Brief Outline

In this study the following activities were undertaken toward fulfilling the aims outlined in Chapter 1:

- Development of an overall stratigraphy of eruptive units during the Maero Eruptive Period, including mapping deposit distribution, systematic sampling of bulk units, primary lithologies (clasts), and organic material between and within units that could be used for radiocarbon dating.
- Concentration of studies on the deposition record of two eruption episodes with contrasting eruptive styles from the Maero Eruptive Period: the explosive Burrell episode and the effusive Pyramid lava dome-forming eruption. Deposits resulting from these episodes and the surrounding deposits were mapped in the field and sampled systematically.

In order to complete the task of stratigraphic correlation of separate eruptive units in the Maero Period, glass chemistry (using electron microprobe) was analysed from ash samples of fall units, surge deposits and Block-and-Ash Flow (BAF) matrix materials

(Platz, 2001; S.J. Cronin, unpubl. data). In addition to mineralogical and geochemical analyses (bulk rock and mineral chemistry), physical properties (density, porosity, permeability) of erupted rocks were investigated. Further, water contents in melt inclusions were analysed to examine the role of volatiles in the explosivity of past eruptions. This was supplemented by other means of estimating water contents of glasses (through microprobe and differential scanning calorimetry and thermal gravimetric analysis).

2.2 Field Studies

Field studies carried out in the summers of 2004 and 2005 were focussed primarily on the fan of deposits making up the NW volcano flanks, expanding later to other areas, including the summit lava dome, and soil/tephra sections around the upper flanks of the remaining volcano flanks. Sampling and description of the main BAF units were carried out in order to later characterise their mineralogical and geochemical composition. Some of the samples from the NW sector of Mt. Taranaki used for mineralogical and geochemical studies were described by Platz (2001). All deposits were described and sampled following standard procedures, i.e. description of main characteristics of deposits at each location including thickness, clast componentry, maximum clast diameters for pumice and lithics, average diameters of about 10 clasts (pumice and lithics), bedding, grading, and sorting. Bulk samples and/or individual clasts were collected if necessary for grain size analysis. Similar techniques were applied to pumice flow deposits. In addition, 109 pumice clasts of various textures and sizes were collected for porosity, permeability measurements and bulk rock chemical analysis; typically pumice clasts of fall deposits were too small and fragile for these methods. At some sites measurement of the natural remanent magnetisation (NRM) of larger primary clasts was carried out using a portable fluxgate magnetometer. This method is considered a rapid and reliable indicator of whether pyroclastic deposits were emplaced above Curie Point temperatures (Hoblitt and Kellog, 1979). Ten oriented and marked clasts of at least 5 cm in diameter were taken out of each outcrop. With the portable fluxgate magnetometer the positive or negative alignment in 6 orientations (x, y, z) were measured. If more than 8 out of 10 clasts indicated the same pattern in all six directions it was assumed that deposition occurred above the Curie Point (c.350 °C) or blocking temperature, where ferromagnesian microlites are able to orientate in a uniform

direction (McClelland and Erwin, 2003). If only seven or eight clasts showed the same pattern, less confidence could be placed in the result, but it could be equally valid since some clasts could be xenoliths entrained from the bed by the BAF, or represent already cooled outer parts of a collapsing dome. Where less than seven clasts showed a common orientation in their magnetic directions, the deposits were interpreted as random and therefore emplaced below Curie Point temperatures.

The summit lava dome remnant was mapped in detail for internal-structures, geometry and related deposits such as blocky lava flows and rock-avalanche deposits. Samples were collected from various portions of the dome for comparison of petrographic and bulk chemical compositions. In addition, stratigraphic relationships of lavas around the summit area were investigated and several potentially Maero-aged lava flows were sampled in the standard way for petrographic/geochemistry studies. Outcrop positions were collected using a Garmin hand-held GPS and all maps were constructed using the GIS program ArcView. Samples taken for further laboratory processing were brush-cleaned or cleaned in a sonic bath prior to drying at 50-70 °C.

2.3 Mineralogy

2.3.1 Sample Preparation

Dense rock clasts of lapilli size or greater were sliced into 1 cm thick tablets to fit petrographic slides (27×46 mm) using a Struers Discoplan-TS or a coarse rock saw. Progressively finer silicon carbide grits (200 to 1000 grit) were used to grind the basal surface of the rock samples. A two component epoxy (EpoTek) was used to impregnate the samples and, if porous, to glue them onto the pre-roughened glass slide surface. After 24 hrs the tablets were cut close to the slide and the thin-section was ground to approximately 30 µm thickness using varying sizes of silicon carbide. For EMPA and SEM studies, thin sections were polished using a Struers Planopol-3 and increasingly finer grades of diamond paste (6, 3, and 1 µm).

Glass shards selected for EMPA were separated using a Frantz isodynamic magnetic separator. The 125-250 µm grain size fraction proved best for magnetic separation and was chosen for further processing. Grains for particle and glass compositional studies were first embedded in epoxy and if porous, air bubbles were removed by repeated vacuum extractions. The epoxy plugs were later ground until the majority of clasts were

intersected. The intersected grain surfaces were glued onto petrographic slides and thin-sectioned for microscopic studies and polished as above for EMP analysis.

Pumice clasts received special treatment due to their fragility. For petrographic, mineral chemistry, and textural studies, pumice samples were cut into cubes and impregnated with low viscosity methyl methacrylate (ρ=0.943 gcm^{-3} at 20 °C a clear, colourless and low-viscosity polymer η=0.58 mPas at 50 °C) before thin sectioning. The samples were repeatedly evacuated until no further bubbles were released from the sample, and then the fluid was polymerised using Cobalt-60 gamma radiation.

2.3.2 Microscopic Studies

Petrographic studies were carried out using a polarising microscope (NIKON Eclipse E600W POL) with integrated 5 Mega-Pixel Digital Camera. Proportions of minerals to groundmass are based on 500 counts per thin section and are calculated on a vesicle-free basis. Microlites were classified as groundmass. The following categories were used to classify crystal sizes: macrocrysts (>1 mm), phenocrysts (1 mm to 150 μm), microphenocrysts (150-50 μm), and microlites (<50 μm). Hornblende reaction rim thicknesses were only measured on crystals that were cut parallel to a, b or c-axes. Thickness analyses were carried out on 6-15 crystals per thin section with 10-23 measurements per crystal, depending on crystal size. For particle textural studies a binocular microscope (Leica Wild MZ8) was also utilised.

2.4 Geochemistry

2.4.1 X-ray Fluorescence Spectroscopy

Samples from individual units were collected to obtain a representative suite of clast types from one deposit and were then studied for their bulk rock geochemistry. Hence, 84 pumice and lithic clast specimens were crushed and ground using a tungsten carbide ring mill. Major element concentrations were determined by X-ray fluorescence (XRF) spectrometry (Siemens SRS 3000; The University of Auckland) on fused glass discs following a method of Norrish and Hutton (1969), and calibrated to a suite of 36 international standards at Victoria University of Wellington and The University of Auckland. In general, the precision is ±1% (1σ). Trace elements were analysed using

pressed powder pellets according to methods based on Norrish and Chappell (1977). Theoretical detection limits are 1-2 ppm and reproducibility ±5% (1σ). Some samples of the Burrell episode and Pyramid eruptives show considerably lower Ba values. This discrepancy is the result of an analytical error, indicated by the low-Ba samples being confined to one XRF sample batch, with low values not shown by parallel laser ICP-MS analysis.

2.4.2 Electron Microprobe Analysis

Mineral chemical studies were focussed on the pheno- and microcryst phases of clinopyroxene, hornblende, and Fe-Ti oxides, and in addition to minor groundmass constituents of apatite, biotite, olivine, and orthopyroxene. Inclusions of glass, Fe-Ti oxides and plagioclase in different host minerals were also studied. The matrix glass within tephra clasts was also analysed. Plagioclase was only analysed as a microlite phase within some pumice samples; it was not analysed in phenocryst or groundmass phases because the distinction of plagioclase and groundmass as well as zonation within crystals were impossible to identify on backscatter electron imagery on the University of Auckland electron microprobe.

Mineral and glass electron microprobe analyses (EMPA) were carried out with a JEOL JXA-840 equipped with an energy dispersive spectrometer at the University of Auckland. Analytical conditions were an accelerating voltage of 15kV, a beam current of 600 pA and 100 seconds live-time. It has been recognised that K and particularly Na are mobile in natural as well as synthetic glasses and can be strongly underrepresented in the analysis, especially if another oxide such as SiO_2 dominates the bulk glass composition (Nielsen and Sigurdsson, 1981). For glass EMPA, a defocused beam of 20 µm diameter was hence used to minimise alkali loss. At least 10 glass shards per sample were measured and where possible, two analyses per shard were collected. For mineral EMPA a focused beam was applied. Where possible, analysed glass shards and minerals were documented using backscatter electron imagery.

All glass EMPA are normalised to 100%. Since there is no agreement among geochemists regarding the use of normalised vs. unnormalised glass compositional data, normalised data are used in this study for further calculations. If unnormalised glass data were used for calculations and the difference to 100% is solely attributed to the presence of H_2O then the matrix used to calculate weight percentages of element oxides

must be modified, i.e. the matrix effect difference is about 1% absolute in the 5% water range (J.J. Donovan, person. comm., 2006). Depending on the difference of the totals to 100%, the effect of normalisation can be large, especially if one component is dominant (i.e. SiO_2). In this case, silica abundances can increase up to several wt.%. However, normalised and unnormalised sample populations still show a similar trend in bivariate diagrams.

Detection limits for EMP analysis are given Table 2-1. As part of an inter-laboratory EMPA project (64 participating laboratories) basaltic glass was analysed with deviation from its accepted composition listed in Table 2-1 (R. Sims, unpubl. data).

Table 2-1. Detection limit of element oxides measured at the EMP (University of Auckland) including the deviation from a reference glass composition.

Detection limit	SiO_2	TiO_2	Al_2O_3	FeO	MnO	MgO	CaO	Na_2O	K_2O	P_2O_5	SO_3	Cl	Cr_2O_3	NiO
1σ [wt.%]	0.11	0.08	0.06	0.07	0.07	0.07	0.04	0.11	0.03	0.07	0.06	0.03	0.06	0.10
3σ [wt.%]	0.32	0.23	0.18	0.20	0.20	0.21	0.13	0.32	0.10	0.20	0.19	0.08	0.17	0.30

International Round-Robin Inter-lab EPMA project (64 participating labs):
Difference to reference values of re-fused basaltic glass composition

SiO_2	TiO_2	Al_2O_3	FeO	MnO	MgO	CaO	Na_2O	K_2O	P_2O_5
-0.18	0.12	-0.05	-0.04	-0.01	0.17	-0.02	0.05	0.02	0.01

2.4.3 Laser Inductively Coupled Plasma Mass Spectrometry

For trace element studies, 46 samples from the Maero Formation and four lava flows were chosen as a representative suite of the youngest eruptive period of Taranaki.

Rock powders produced for XRF analysis were also used for trace element analyses using an Agilent 7500ce quadrupole inductively-coupled plasma mass-spectrometer (ICP-MS) coupled with a NewWave Research UP-213 laser-ablation unit at the Department of Geosciences, University of Mainz, Germany. Instrumental and analytical procedures are described in Nehring et al., (in press). Glass beads were prepared by using an iridium strip heater equipped with an argon atmosphere chamber to prevent oxidation and volatile loss. Approximately 30 mg of powder was placed on the iridium strip and melted for 10 s using a 110-120 A current at 1100-1400 °C. Three analyses per glass bead were performed using a 100 µm beam with a 10 Hz frequency and 60 s count time. Plasma torch conditions were kept at an oxide ThO/Th ratio below 1%. As a carrier and nebulizer gas, argon was used. Detection limits are 0.001-0.5 $\mu g g^{-1}$ (Nehring et al., in press). After nine analyses (i.e. three samples), certified glass reference

materials NIST SRM 612, NIST SRM 610 or BCR-2 were measured with reproducibilities of <10% (1σ) and all values were within 10% of published analyses (Pearce et al., 1997). Data evaluation was carried out using Glitter software and ^{43}Ca and ^{44}Ca as internal standards.

An initially observed Ta anomaly (four samples had elevated values) was later related to use of a tungsten grinder in the preparation process. Tantalum is an important high field strength element and indicative of magma mixing and fractionation processes since it is compatible in biotite and hornblende. Three samples were re-analysed after preparation using an agate mill, and no elevated Ta concentrations were found. Due to this potential contamination in the XRF dataset, Ta was not used further for geochemical data interpretation from this suite of analyses.

2.5 Porosity and Permeability

Porosity and permeability measurements were carried out at the Department of Geological Sciences, University of Oregon, USA. Cores (approx. 2.54 cm diameter and height) of clasts were drilled, in two or three mutually perpendicular orientations where sample size allowed (Fig. 2-1). From the known volume of the core (V_c), measured with a sliding calliper, and the mass of the cores (mc), the bulk density, ρ_{bulk} ($\rho_{bulk}=m_c/V_c$) was determined. A Micromeritics multi-volume He-pycnometer was used to determine the helium-accessible volume (V_{He}) of the sample by measuring the pressures in the sample chamber (P1) and the reference chamber (P2). The V_{He} results in an estimate of skeletal density, $\rho_{skeletal}$ ($\rho_{skeletal}=m_c/V_{He}$) and connected porosity, φ_{conn}, ($\varphi_{conn}=V_{He}/V_c$).

However, even rocks of dense appearance commonly possess non-accessible, isolated cavities and cracks, and vesiculated rocks usually have both isolated pores and interconnected pores, and therefore $\rho_{skeletal}$ is always lower than the solid density, ρ_{solid}. In order to determine ρ_{solid}, representative samples were powdered and their volume (V_p) determined by He-pycnometry ($\rho_{solid}=m_p/V_p$). The bulk vesicularity ($\varphi_{bulk}=1-(\rho_{bulk}/\rho_{solid})$ can then be used to calculate the isolate porosity ($\varphi_{iso}=\varphi_{bulk}-\varphi_{conn}$).

Long drilled cores of pumice were cut into two to examine reproducibility and homogeneity along a specific orientation. This showed that pumice samples were mostly homogeneous, with differences in φ_{bulk} of 0.1 to 8% over the range of φ_{bulk}=34-84%. However, in single larger pumice clasts with up to seven drilled cores per sample in multiple orientations, differences in φ_{bulk} of up to 20% were noted.



Figure 2-1: The specimen illustrates how pumice cores were obtained. As in this case, six cores in three mutually perpendicular orientations were drilled.

Error analysis of φ_{conn} for the entire data set was assessed by evaluating V_c using diameter and height variations, and V_{He} by using pressure variations. The core diameter and height were measured five times each and then used for volume calculations resulting in 25 individual V_c. The standard deviations vary between 0.005 and 1.171 cm^3. Pressures P1 and P2 were measured at least three times in consecutive runs giving at least 9 results for V_{He} with standard deviations between 0.009 and 0.588 cm^3. Standard deviations for V_c and V_{He} indicate a concentration of data points below 0.1 cm^3 with most data points enveloped by the 0.3 cm^3 border (Fig. 2-2b). The latter border is also regarded as the maximum accepted standard deviation for both V_c and V_{He}.

The standard deviation of 225 individual φ_{conn} per sample (25 V_c × 9 V_{He}) ranges between 0.12% and 6.20% (Fig. 2-3). Using the 0.3 cm^3 border, the upper range reduces to 3.07%. There is no relationship between standard deviation and vesicularity, although highest deviations are observed for φ_{conn}=44-73%. For each specimen a standard deviation of 1% for φ_{conn} is adopted (average 0.87%).

As demonstrated in Fig. 2-3, two sources of error are apparent. The core drilling carried out in New Zealand was not as precise as that in Oregon. Further, the standard deviation of sample volumes measured by He-pycnometry varies especially for highly porous samples and could have been caused by, for example, 1) incorrect purging of the sample chamber to remove all present air with He prior to analysis, 2) residual water in vesicles which adds vapour pressure to the gas pressure, and 3) pressures were not equilibrated

either in the sample or reference chamber, or both. The latter can be excluded because the analysis was only performed after pressures did equilibrate.

For future measurements, two changes are recommended based on experience gained in this study. Firstly, cores to be analysed should be stored in a desiccator to avoid water absorption due to varying room temperatures and/or air moisture. This potentially inhibits the development of any vapour pressure during analysis. Secondly, a minimum of five sample runs is recommended. In this study it is observed that the first of three runs record (in most instances) the highest pressures with runs 2 and 3 being similar. This strongly implies that pulsatory purging of the sample chamber prior to analysis was insufficient. Over five runs, data from the first or the first two runs should be disregarded, and only the last three should be averaged and used for further calculations. Errors made during pycnometry measurements at the University of Oregon were avoided when additional samples were analysed using the recently available He-pycnometer (Quantachrome Ultrapycnometer 1000) at Massey University. The density of powderised samples from XRF-analysis (n=32) was determined by measuring at least 5 runs where only the last three were averaged. Averaged analyses were only accepted if the standard deviation was below 0.005 vol.%.

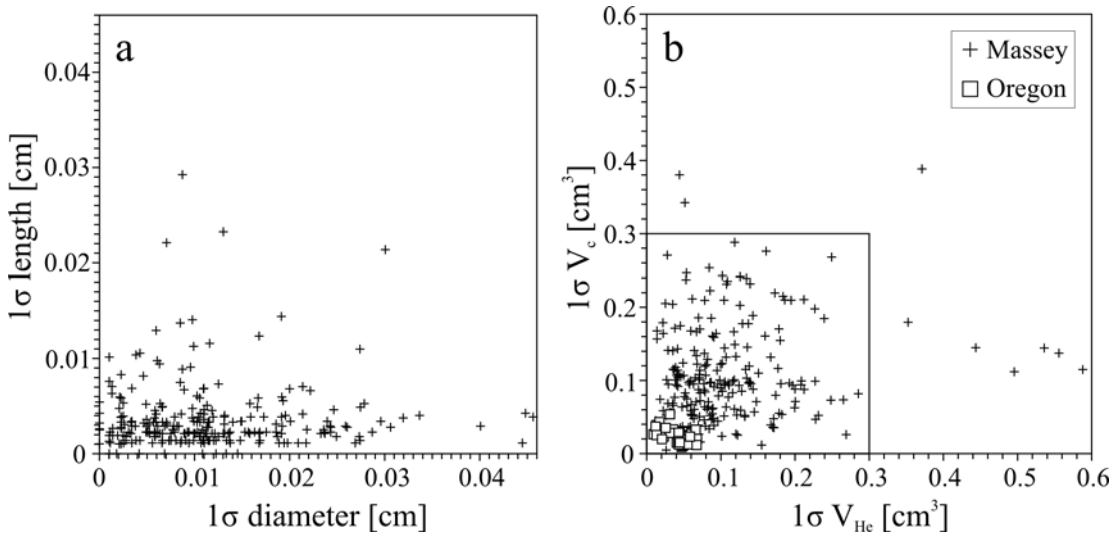


Figure 2-2: Standard deviations for diameter and length of the cores (a) and for volumes V_c and V_{He} (b). It is noted that one sample in a) is off the chart at a standard deviation of 0.1321 cm. b) Samples are differentiated into those drilled in Oregon and at Massey. Oregon samples show smaller variations for both V_c and V_{He}.

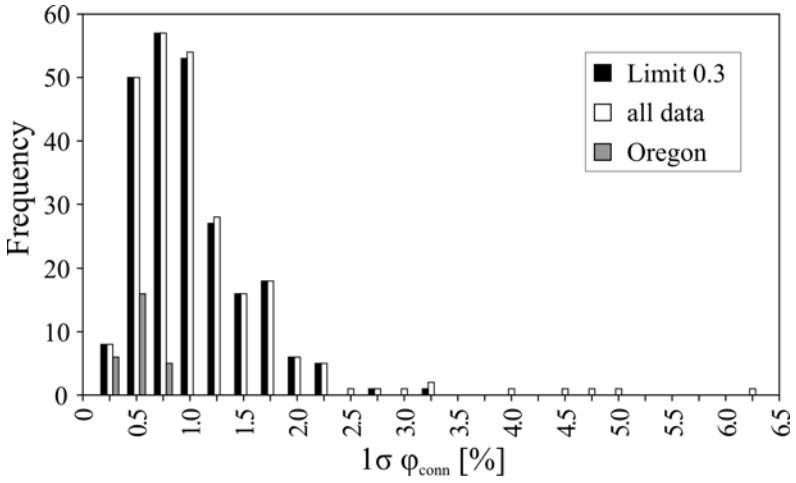


Figure 2-3: Standard deviation for connected porosities. The limit of 0.3 cm3 for Vc and VHe in Fig. 2-2b is used as maximum limit. Cores drilled in Oregon are shown for comparison.

The gas permeability of cores was measured in a capillary flow porometer (Porous Materials, Inc.) with air as the working gas. Permeability of the sample core is measured by applying successively increasing flow rates and measuring the differential pressures at each flow rate increment. Different flow rates were applied depending on the vesicularity (i.e. low flow rate for less vesicular samples). Three to six runs per sample were performed to demonstrate reproducibility (Fig. 2-4).

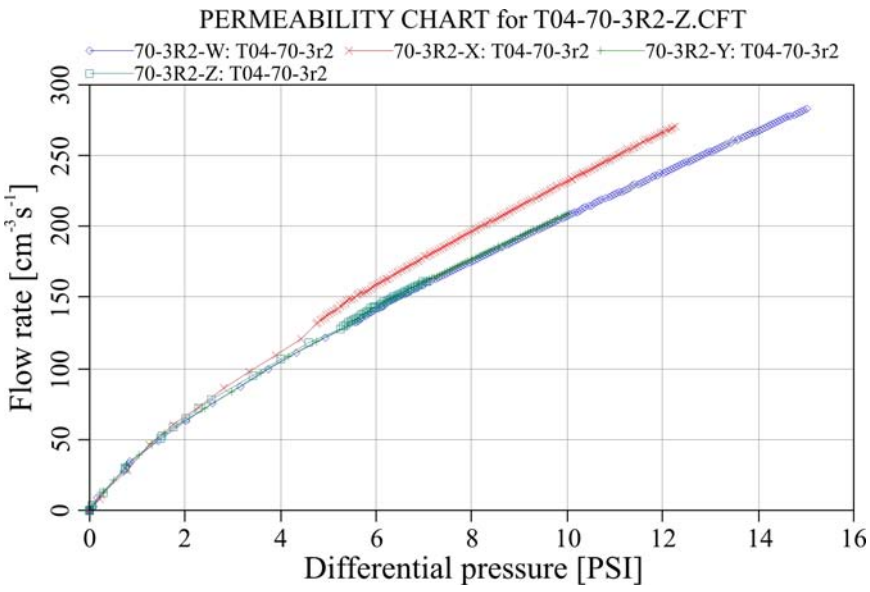


Figure 2-4: Permeability measurements of individual cores were performed three to six times, partially using multiple flow rates, in order to assess reproducibility. In this case, the red graph suggests higher flow rates compared to the other three runs and was excluded from further calculations.

Data were calculated as described by Wright et al. (2007) and Rust and Cashman (2004). A modified form of Darcy's Law known as the Forchheimer's equation is used to account for the energy loss in non-laminar flows. The viscous (Darcian) permeability, k_1, and the inertial (non-Darcian) permeability, k_2, can be calculated by:

$$\frac{P_i^2 - P_0^2}{2PL_C} = \frac{\mu}{k_1}\nu_s + \frac{\rho}{k_2}\nu_s^2 \qquad \text{[Eq. 2-1]}$$

where P_i and P_0 are the entrance and exit pressures at the sample core, respectively. In addition, the viscosity (μ) and density (ρ) of air, and the core length (L_c) are needed. The superficial velocity (υ_s) is calculated by dividing the flow rate by the cross-sectional area. The pressure P refers to the fluid pressure at which the velocity and viscosity are measured; in the Forchheimer equation $P=P_0$ so that μ and ρ correspond to values at atmospheric pressure.

2.6 Scanning Electron Microscopy

Scanning electron images were obtained from carbon coated thin and thick section samples at HortResearch, Palmerston North (Cambridge 250 Mark III) and the University of Oregon (JEOL 6300). Operating conditions were an accelerating voltage of 20 kV and 10 kV, respectively. Secondary electron images and backscatter images were obtained in analogue and digital form. For textural studies, SEM images were partially binarised; white represents the groundmass glass and minerals and whereas black constitutes void space (i.e. vesicles and cavities).

2.7 Fourier Transform Infrared Spectroscopy

Fourier Transform Infrared Spectroscopy (FTIR) was used for studies of dissolved water contents in andesite melt inclusion hosted in mineral phases. The three major mineral phases present in andesite rocks, plagioclase, clinopyroxene and hornblende, all have good to very good cleavage which makes them less suitable as an inclusion host. During decompression (i.e. magma ascent) volatiles dissolved in melt inclusions within these phases may escape along cleavage planes, and hence any measured volatile content may or may not reflect the melt volatile content at the time of capture. Despite this constraint, clinopyroxene phenocrysts were targeted since, being translucent, shape

and locations of inclusions could easily be seen and those appearing intact focussed upon. In addition, the clinopyroxene was more robust than plagioclase and hornblende.

Selected pumice and lithic samples of the Burrell Lapilli eruption were crushed in an agate mortar and clinopyroxene crystals were hand picked. Crystals were then checked for glass inclusions using a polarising microscope. Selected crystals were glued on a petrographic slide using crystal bond (a resin that is worked and reworked by melting at about 100 °C), and gently ground using 600 grit paper until glass inclusions were intersected on one side. The surface was polished using 6 µm and 1 µm diamond paste. The wafer was then turned and glued with the polished surface onto the slide by heating the crystal bond. The exposed side was also ground and polished. Most melt inclusions, however, were not intersected on both sides since they were too small.

The double-polished wafers were analysed using a Thermo Nicolet Nexus 670 FTIR spectrometer attached to an IR microscope at the Department of Geological Sciences, University of Oregon. Infrared spectra were obtained in the mid-infrared and near-infrared area of 650-6000 cm^{-1} with a resolution of 0.09 cm^{-1}. Water and CO_2 species were investigated at the absorbance bands 1630 cm^{-1}, 2350 cm^{-1}, 3550 cm^{-1}, 4520 cm^{-1} and 5230 cm^{-1} (Table 2-2). Due to the size of melt inclusions, apertures of 10-20 µm by 10-20 µm were often applied, which is near the minimum limit of instrumental detection, however, analysis time was increased from 256 s for larger inclusions to 1024 s for the smallest inclusions.

Because melt inclusions in clinopyroxene are small and irregular in shape, they were mostly exposed only on one face. In these cases, their thicknesses were estimated optically using a polarising microscope, and thus total H_2O concentrations are approximations. Where the inclusion was intersected at both sides, the thickness was determined by using a micrometer. The error involved in the analysis is difficult to determine but it is assumed that water estimates may have an error of up to 20%.

Infrared spectra of intersected and partially truncated melt inclusions only show a broad asymmetric peak at the infrared band 3550 cm^{-1}, which is assigned to total H_2O absorbance (molecular H_2O plus OH^-). Although the molecular water absorbance peak at 1630 cm^{-1} is present, peaks at 5230 cm^{-1} and 4520 cm^{-1} are in most cases absent. In order to determine peak heights, appropriate baselines had to be defined by applying a straight baseline for Abs_{3550} and a curved line (using a hand-fitted curve) was applied for Abs_{1630}, Abs_{4520} and Abs_{5230}, where present (Silver et al., 1990; Luhr, 2001).

Total water concentrations are determined using the Beer-Lambert Law:

$$Abs_{3550} = \frac{C_{H_2O} d \rho \varepsilon_{3550}}{18.0152} \quad \text{[Eq. 2-2]}$$

$$C_{H_2O} = \frac{Abs_{3550} 18.0152}{d \rho \varepsilon_{3550}} \quad \text{[Eq. 2-3]}$$

where d is the thickness [cm] of the melt inclusion, ρ is the density of glass [gL^{-1}] at 20 °C and 1 bar, ε_{3550} is the molar absorption coefficient [$Lmol^{-1}cm^{-1}$], Abs_{3550} is the absorbance at the wavelength 3550 cm^{-1} and C_{H2O} is the weight fraction of molecular water.

Table 2-2. Water and carbon dioxide peaks on the FTIR spectra including their bonds within glasses.

Peak [cm^{-1}]	Species	Mode[1]
3550	molecular H_2O_{total}	OH stretching vibration
4520	OH	stretching and bending of Si-OH groups
5230	molecular H_2O	stretching and bending
1630	molecular H_2O	symmetrical bending mode
2350	molecular CO_2	asymmetric stretch

[1] Nakamoto (1978), Stolper (1982), Fine and Stolper (1985).

The glass composition of most inclusions was measured by EMPA and their density calculated as described in Best (2003). Data for partial molar volume of oxides, their thermal expansivity and compressibility are from Lange and Carmichael (1990), Lange (1997), and Ochs and Lange (1997). Since the dissolved water content affects the density of melt, the density is iteratively determined. Molar absorptivities ε [$Lmol^{-1}cm^{-1}$] for IR absorption bands of Fe-bearing andesites were applied (Mandeville et al., 2002).

2.8 Thermal Analysis

Simultaneous Differential Scanning Calorimetry and Thermal Gravimetric Analysis (DSC-TGA) was carried out on pumice matrix glasses using a SDT Q600 (TA Instruments Waters-LLC). This device measures heat flow and weight changes with transitions and reactions in materials to temperature of up to 1500 °C. Reactions and transitions comprise endothermic and exothermic reactions with changes in weight (e.g. degradation) or without weight changes (e.g. melting and crystallisation). For this study DSC-TGA was used to determine whether it was possible to measure total volatile

concentrations by weight difference since FTIR spectroscopy cannot be applied to highly vesicular samples.

In order to obtain pure matrix glass, single grey and brown pumice clasts were crushed using a mortar and sieved to obtain the <125 µm fraction and afterwards ground to coarse silt. The glass fraction was isolated using sodium polytungstate (ρ=2.52 gcm^{-3}) and centrifuged, then dried at 70 °C for at least 12 hours. The glass fractions (<<5 g) were checked for purity using a polarising microscope (Fig. 2-5). Prior to DSC-TGA analysis, glass samples were powdered using an agate mortar and 20-30 mg were placed into the sample holder. For glass DSC-TGA analysis the following method was progressively developed: the sample was first heated to 110 °C at 20 $°Cmin^{-1}$ and kept isothermal at 110 °C for 15 min, then heated to 850 °C or 1000 °C at 5 $°Cmin^{-1}$ and then cooled. The experiments were carried out in a nitrogen atmosphere to prevent iron oxidation, however, some samples experienced some degree of oxidation.

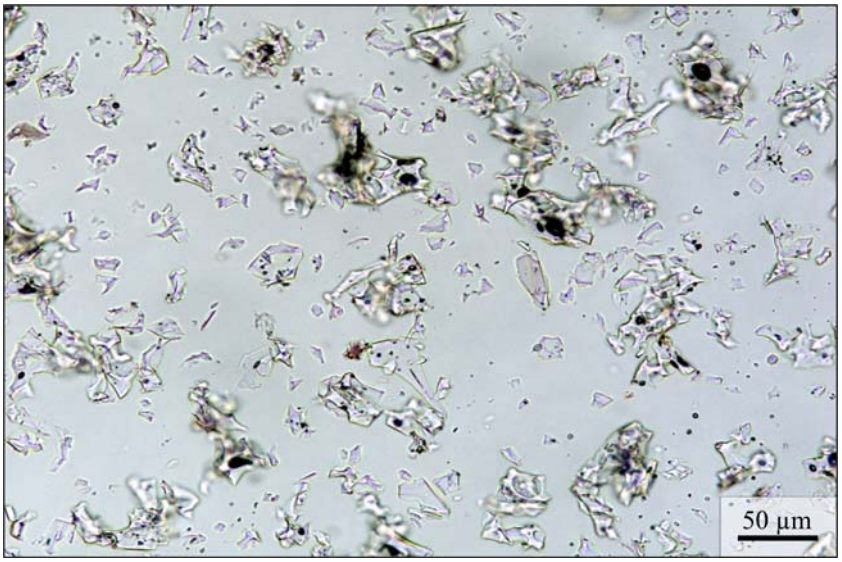


Figure 2-5: Separated groundmass glass fraction from a pumice clast (SD32).

The output of the analysis is a graph showing the weight difference (in %), heat flow (Wg^{-1}) and the temperature difference ($°Cmg^{-1}$) over the temperature range (Fig. 2-6). A sharp peak is observed at about 105-110 °C for heat flow and temperature difference. These peaks are evidence of an endothermic reaction and are related to the release of water from the surface of the glass. A drop in weight at this temperature is clearly observed. With increasing temperature the weight continuously decreases, first at a high rate and then the slope gradually flattens with higher temperatures. The difference in weight was measured between the maximum and minimum point of the graph in the

interval of c.110 °C to the maximum temperature using the software TA Universal Analysis 2000. The graphs for heat flow and temperature difference proceed evenly and show no sign for further endothermic or exothermic reactions.

One sample was analysed using a Stanton Redcroft DTA 673-674 coupled with infrared H_2O and CO_2 detectors using the procedures described by Morgan (1977) and Lindgren et al. (2002). The sample was heated at 5 °Cmin^{-1} in a gas flow of 300 ml N_2 min^{-1}. The analysis was carried out by H.B. Lindgren (Geological Survey of Denmark and Greenland).

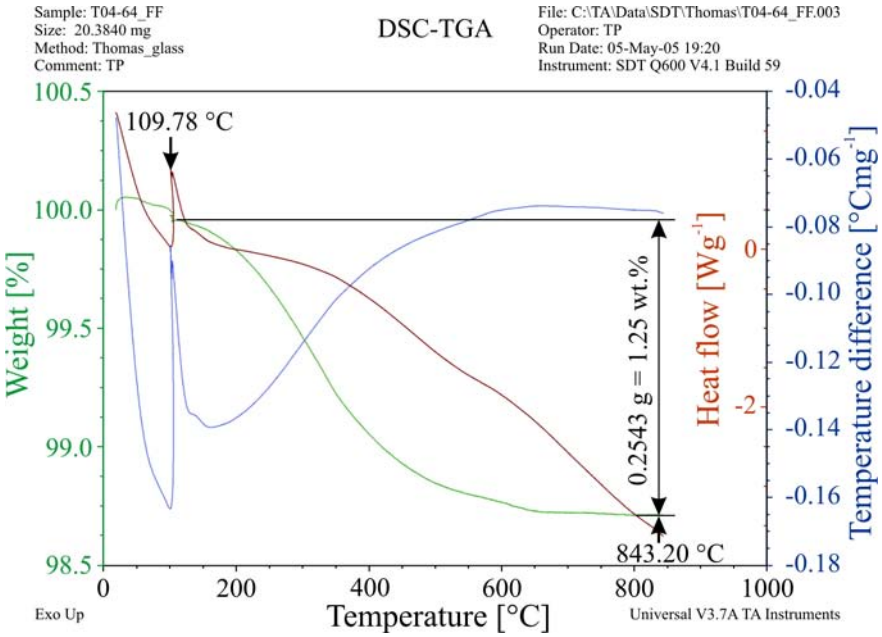


Figure 2-6: Thermal analysis of volcanic glass to 850 °C. The change in weight (green axis) was measured after the isothermal break at 110 °C.

2.9 References

Best, M.G. 2003. Igneous and metamorphic petrology. Blackwell Science. Malden.

Fine, G. and **Stopler, E.** 1985. The speciation of carbon dioxide in sodium aluminosilicate glasses. *Contributions to Mineralogy and Petrology* 91, 105-121.

Hoblitt, R.P. and **Kellog, K.S.** 1979. Emplacement temperature of unsorted and unstratified deposits of volcanic rock debris as determined by paleomagnetic techniques. *Geological Society of America Bulletin* 90, 633-642.

Lange, R.A. 1997. A revised model for the density and thermal expansivity of K_2O-Na_2O-CaO-MgO-Al_2O_3-SiO_2 liquids between 713 and 1896 K: extension to crustal magmatic temperatures. *Contributions to Mineralogy and Petrology* 130, 1-11.

Lange, R.A. and **Carmichael, I.S.E.** 1990. Thermodynamic properties of silicate liquids with emphasis on density, thermal expansion, and compressibility. In: **Nicholls, J.** and **Russell, J.K.** (eds.) Modern methods of igneous petrology: understanding magmatic processes. *Reviews in Mineralogy* 24, 25-64.

Lindgren, H., Drits, V.A., Sakharov, B.A., Jakobsen, H.J., Salyn, A.L., Dainyak, L.G. and **Krøyer, H.** 2002. The structure and diagenetic transformation of illite-smectite and chlorite-smectite from North Sea Cretaceous-Tertiary chalk. *Clay Minerals* 37, 429-450.

Luhr, J.F. 2001. Glass inclusions and melt volatile contents at Parícutin Volcano, Mexico. *Contributions to Mineralogy and Petrology* 142, 261-283.

Mandeville, C.W., Webster, J.D., Rutherford, M.J., Taylor, B.E., Timbal, A. and **Faure, K.** 2002. Determination of molar absorptivities for infrared absorption bands of H_2O in andesitic glasses. *American Mineralogist* 87, 813-821.

McClelland, E. and **Erwin, P.S.** 2003. Was a dacite dome implicated in the 9,500 B.P. collapse of Mt Ruapehu? A palaeomagnetic investigation. *Bulletin of Volcanology* 65, 294-305.

Morgan, D.J. 1977. Simultaneous DTA-EGA of mineral and natural mineral mixtures. *Journal of Thermal Analysis* 12, 245-263.

Nakamoto, K. 1978. Infrared and Raman spectra in inorganic and coordination compounds. 3rd ed. Wiley. New York.

Nehring, F., Jacob, D.E., **Barth, M.G.** and **Foley, S.F.** (in press). Laser-ablation ICP-MS analysis of siliceous rock glasses fused on an iridium strip heater using MgO dilution. *Microchimica Acta*.

Nielsen, C.H. and **Sigurdsson, H.** 1981. Quantitative methods for electron microprobe analysis of sodium in natural and synthetic glasses. *American Mineralogist* 66, 547-552.

Norrish, K. and **Hutton, J.T.** 1969. An accurate method for the analysis of a wide range of geological samples. *Geochimica et Cosmochimica Acta* 33, 431-451.

Norrish, K. and **Chappell, B.W.** 1977. X-ray fluorescence spectroscopy. In: **Zussman, J.** (ed.) Physical methods in determinative mineralogy. Academic Press. New York. pp. 201-272.

Ochs, F.A., III and **Lange, R.A.** 1997. The partial molar volume, thermal expansivity, and compressibility of H_2O in $NaAlSi_3O_8$ liquid: new measurements and an internally consistent model. *Contributions to Mineralogy and Petrology* 129, 155-165.

Pearce, N.J.G., Perkins, W.T., Westgate, J.A., Gorton, M.P., Jackson, S.E., Neal, C.R. and **Chenery, S.P.** 1997. A compilation of new and published major and trace element data for NIST SRM 610 and NIST SRM 612 glass reference materials. *Geostandards Newsletter* 21, 115-144.

Platz, T. 2001. Mapping and characterisation of the volcaniclastic Maero formation deposits on the northwestern sector of Egmont volcano (Mt. Taranaki), New Zealand. Unpublished Diploma mapping thesis. Ernst-Moritz-Arndt Universität, Greifswald, Bundesrepublik Deutschland.

Rust, A.C. and **Cashman, K.V.** 2004. Permeability of vesicular silicic magma: inertial and hysteresis effects. *Earth and Planetary Science Letters* 228, 93-107.

Silver, L.A., Ihinger, P.D. and **Stolper, E.** 1990. The influence of bulk composition on the speciation of water in silicate glasses. *Contribution to Mineralogy and Petrology* 104, 142-162.

Stolper, E. 1982. Water in silicate glasses: an infrared spectroscopic study. *Contributions to Mineralogy and Petrology* 81, 1-17.

Wright, H.M.N., Cashman, K.V., Rosi, M. and **Cioni, R.** 2007. Breadcrust bombs as indicators of Vulcanian eruption dynamics at Guagua Pichincha volcano, Ecuador. *Bulletin of Volcanology* 69, 281-300.

Chapter 3 The Maero Eruptive Period

This chapter describes the distribution and nature of the diverse eruptives and related deposits emplaced during the Maero Eruptive Period. Lava domes were the predominant extrusive product of this period; hence associated volcaniclastic units include Block-and-Ash-Flow and pyroclastic-surge deposits. The previous stratigraphy of the Maero Eruptive Period is revised to include four new eruption episodes. A new tephrostratigraphy of the Maero Formation is introduced, its reference sections are defined and the type section described.

3.1 Introduction

In the past four decades the tephrostratigraphy of Mt. Taranaki has been studied in detail, with the predominant focus being on medial and distal deposits of the largest sub-Plinian eruptions (Neall, 1972; Topping, 1972; Franks, 1984; Alloway et al., 1995). As the chronology of tephra eruptions and intervening lahar and debris avalanche events became increasingly better understood, attention has now turned to improving the dating of lava flow and dome-forming episodes. The focus on mappable, mainly distal fall deposits excluded detailed studies of the small, apparently more-frequent eruptions, whose deposits are only preserved on or near the edifice itself (Turner et al., 2007). This is particularly true for the Maero Eruptive Period, where many of the eruptions were of small scale or low-explosivity and hence tephra deposits are only preserved in proximal areas (Druce, 1966). Typically during this period, Block-and-Ash Flow (BAF) and surge deposition occurred on the NW sector of the mountain, whereas thin ash layers associated with these events were predominantly deposited on the northern, eastern, and

southern flanks (Neall, 1979). These thin ash layers are impossible to distinguish from one another based on their physical properties and appearances (Druce, 1966). Hence geochemical correlation techniques are required.

Glass chemistry has proven to be one of the most useful tools for correlating rhyolite tephra units within New Zealand (e.g. Lowe, 1988; Shane, 2000). Hence, this method was also applied to correlating proximal andesite tephras on Mt. Taranaki. In this instance glass chemistry of fall deposits from the northern, eastern and southern flanks were compared to fall, surge and BAF deposits on the NW sector. Early attempts to use glass chemistry for tephra correlation at Mt. Taranaki were unsuccessful (May, 2003; Platz et al., 2004) mainly due to the poor knowledge of the tephra sequence and the apparent broad compositional diversity in glass within individual units. The problems in studying the glass chemistry of andesitic tephras at Taranaki are described further in Chapter 4, along with a procedure of optimising this method by identifying and removing contaminated data points from the analyses.

This chapter introduces the range of volcanic deposits erupted in the last 1000 yrs and summarises type and reference sections representing this. Emphasis will be given to deposits of pyroclastic density currents (in particular BAF deposits) and their distribution and flow paths. These are volumetrically the predominant deposits representative of the eruptive period. By means of field studies and glass chemical analyses, a revised stratigraphy is introduced for the last c.1000 yrs of volcanic activity at Mt. Taranaki.

For a better comprehension of the volcanic history of Mt. Taranaki, two new terms are presented here. Previously, volcaniclastic deposits in the latest 500 years of volcanic activity at Mt. Taranaki were mapped under the informal term “Maero debris flows” (Neall, 1979). Investigations since have shown that these units are primarily Block-and-Ash Flow deposits. Additionally, older eruptions have also been shown to belong to this mapping unit due to their stratigraphic position, similar composition, style and distribution (Platz, 2001; Cronin et al., 2003). As a result of this, the term “Maero Eruptive Period” is here introduced to describe the latest period of volcanic eruptions at Mt. Taranaki, where since c.1000 yrs B.P. activity has been of a similar style and affected primarily the NW sector of the volcano. Associated with this is the “Maero Formation” – here defined to represent all volcanic products erupted during the Maero Eruptive Period.

3.1.1 Previous Studies

The first person to realise that Mt. Taranaki was comparatively recently active was Mr A.W. Burrell who found scoria clasts in tree forks in 1883 (Oliver, 1931). The discovery of a Maori umu (earth oven) buried by volcanic deposits on the upper eastern slope of Mt. Taranaki was also described by Oliver (1931). It was covered by a c.38 cm pumice layer (later named Burrell Lapilli). This discovery clearly testified that Mt. Taranaki was active during the colonisation of New Zealand by Maori. Further, other recent ash layers were described as Newall Ash [recognised by L.I. Grange and N.H. Taylor in the 1930s (Druce, 1966)], Burrell Ash [described by Taylor (1953)] and Puniho Grit [described by Grant-Taylor (1964)].

The detailed stratigraphic and botanical work of Druce (1966) showed that Burrell Ash and Newall Ash could be further subdivided into multiple events, and hence revealed that more eruptions occurred during the volcano's recent history. Druce (1966) recognised that considerable variations in vegetation and soil development related to the distribution of volcanic deposits from one side of the volcano to the other. Although he described fundamental differences in the character of deposits between eastern and the northwestern slopes of Mt. Taranaki, he described all volcanic deposits as tephra layers. Most deposits on the NW sector contained charcoal fragments as well as a poorly sorted mix of lapilli to block sized clasts set in an ash matrix, according to Druce (1966). He also recognised that these particular units were confined to the W-NW flank within c.14 km from the volcano's summit. On the basis of three soil-forming breaks, Druce (1966) grouped 10 "tephra" layers into three Formations: Newall Formation, Burrell Formation, and Tahurangi Formation (Table 3-1). The Burrell Lapilli eruption was dated by Druce at AD1655 using dendrochronology of trees presumably killed and/or damaged by the eruption. The Tahurangi Ash was determined by dendrochronology (of possibly damaged trees) and peat accumulation rates more loosely around the age of AD1755 (Druce, 1966).

The discovery of another Maori umu on the SE flank revealed further age details. Charcoal from the oven was dated at 470 ± 55 yrs B.P. (i.e. c.AD1480), which is indicative for the presence of Maori prior to the Newall eruptions (Topping, 1974). In addition, two ash layers previously not recognised were found between the Kaupokonui Tephra and Newall Ash (Topping, 1974).

Neall (1979) was the first to interpret the charcoal-containing units on the NW sector as being related to *nuées ardentes*[1]. The type section for a succession of these units is located in the Maero Stream (Neall, 1979). Here at least 14 debris and pyroclastic flow deposits considered to be emplaced over the past c.500 yrs were collectively mapped and termed the Maero Debris Flows (Neall, 1979). These deposits overlie a peat dated at c.1975 yrs B.P., which Neall (1979) used to interpreted a 1500 yrs period of relative quiescence in the NW sector of the volcano (Neall, 1979).

Table 3-1. Stratigraphy of the youngest deposits of Mt. Taranaki (Druce, 1966).

Formation	Member	Date [AD]
Tahurangi	Tahurangi Ash	1755
Burrell	Puniho Lapilli 2 Puniho Lapilli 1 Burrell Lapilli Burrell Ash	1655
Newall	Waiweranui Ash Waiweranui Lapilli Newall Lapilli Newall Ash	1604
	unnamed ash	1500?

Studies on the destruction and recovery of vegetation around the volcano during individual eruptions, as well as pollen analysis, added further details to the eruptive history, particularly in determining the length of some of the repose periods (Clarkson, 1990; McGlone, 1982; McGlone et al., 1988; Lees and Neall, 1993; McGlone and Neall, 1994; Table 3-2). McGlone et al. (1988) also implied that the youngest eruption, the Tahurangi Ash, could have occurred at any time between AD1700 and AD1900. This was further refined by studies of Lees and Neall (1993) who found *Pinus* pollen beneath the Tahurangi Ash indirectly indicating that the age of the Tahurangi eruption could have been closer to AD1860.

Platz (2001) confirmed that the deposits exposed on the northwestern sector were primarily deposited by pyroclastic flow deposits and confirmed that some units travelled more than 13.5 km from source, and hence well beyond the National Park boundary. In addition, a poorly sorted blast-like deposit was mapped extending at least 14 km from source with a sharp lateral confinement to the area W-NW of the summit of Mt. Taranaki (Cronin et al., 2003). Fall deposits in the NW sector are mainly thin ash layers,

[1] *Nuée ardente* (French: incandescent cloud) is described as a fast moving, highly destructive ground-hugging pyroclastic density current (cf. Lacroix, 1904).

Table 3-2. Stratigraphy of the youngest deposits at Mt. Taranaki until 2003 (Druce, 1966; Neall, 1972; Neall, 1979; McGlone et al., 1988; Lees and Neall, 1993).

Formation	Member	Date		Estimated breaks between eruptions [yrs]
		AD	yrs B.P.	
Tahurangi	Tahurangi Ash	1755/1700-1900/1860	145/90	← c.100
Burrell	Puniho Lapilli 2 Puniho Lapilli 1 Burrell Lapilli Burrell Ash	1655	295	← c.70 ← c.70
Newall	Waiweranui Ash Waiweranui Lapilli Newall Lapilli Newall Ash	1500-1550	c.450	← <1 ← c.100
	unnamed ash charcoal from umu unnamed ash unnamed ash	1500? 1480	450? 470	
Kaupokonui Tephra		400-1050[1]		

[1] based on radiocarbon age 1350 ± 150 yrs BP.

which are mostly genetically related to pyroclastic density currents (i.e. co-ignimbrite ashes). Due to the difficulties in reliably correlating the fall sequence on the east and south flanks with deposits of pyroclastic density currents on the W-NW sector, Cronin et al. (2003) made a first attempt to discard the partially confusing nomenclature for eruptive units and introduced a new stratigraphy on the basis of fall layers and pyroclastic flow deposits. According to this and new radiocarbon dates, six eruptive episodes (M1-M6; M=Maero) were defined which occurred after AD1040 (Table 3-3; Cronin et al., 2003). Cronin et al. (2003) thus defined this period as being characterised by effusive to explosive events producing lava domes, lava flows and pumice fall deposits.

Table 3-3. Current stratigraphy of the last 1000 yrs of activity at Mt. Taranaki (modified after Cronin et al., 2003).

Eruption Episode	^{14}C dates [yrs B.P.]	N and W flank expression	E and S flank expression	Previously recognised units within episodes
M6	225 ± 55 <250	2+ BAF[1] deposits with associated surge deposits	grey, fine to medium co-ignimbrite ash	Tahurangi Ash
M5	305 ± 39	2+ BAF deposits with associated surge deposits	grey, fine to medium co-ignimbrite ash	Puniho Lapilli 1 & 2
M4	387 ± 43 382 ± 39 404 ± 44	2+ BAF deposits with associated surge deposits	pumice pyroclastic flow deposits; lapilli fall; co-ignimbrite ash	Burrell Lapilli & Burrell Ash
M3	447 ± 40 453 ± 43 475 ± 42	2+ BAF deposits with associated surge deposits	grey, fine to medium co-ignimbrite ash	Waiweranui Lapilli 1 & 2
M2	605 ± 42 620 ± 74 649 ± 46	several BAF deposits; voluminous, widespread surge deposits	surge deposits; minor BAF deposits; grey, fine co-ignimbrite ash; lava flows	Newall Ash & Newall Lapilli
M1	878 ± 39	2+ BAF deposits	grey, fine co-ignimbrite ash and scattered lithic lapilli; lava flows?	

[1] BAF - Block-and-Ash flow.

3.1.1.1 Previous Work on Lava Flow Stratigraphy

The interrelation of tephra fall sequences exposed on the eastern to southern flanks and the successions of pyroclastic density currents in the W-NW sector of Mt. Taranaki is poorly known. In addition, the formation of lava flows of the upper cone of Mt. Taranaki including Fanthams Peak is also not well understood or correlated to other eruptive episodes. Paleomagnetic studies imply the formation of several of the summit lava flows in two periods approximately 400 and 700 yrs ago (Downey et al., 1994), which corresponds with the young coverbed sequences on many of the flows. The succession of lava flows forming the upper portion of Mt. Taranaki (Fig. 3-1) was subdivided into five age/geographic groups:

1. The Warwicks Castle Group, representing the oldest lava flows that form the present upper cone of Mt. Taranaki. They include distinct landscape features around the edifice such as Warwicks Castle and Bobs Ridge, and extend between a major break in slope at

about 1000 m up to 2000 m elevation. This group has an inferred maximum age of 8 ka (Stewart et al., 1996).

2. Neall (2003) introduced the Peters Group, the extent of which is limited to the W-NW sector. The age of this group is inferred to be between 3.3-7 ka (Neall, 2003).

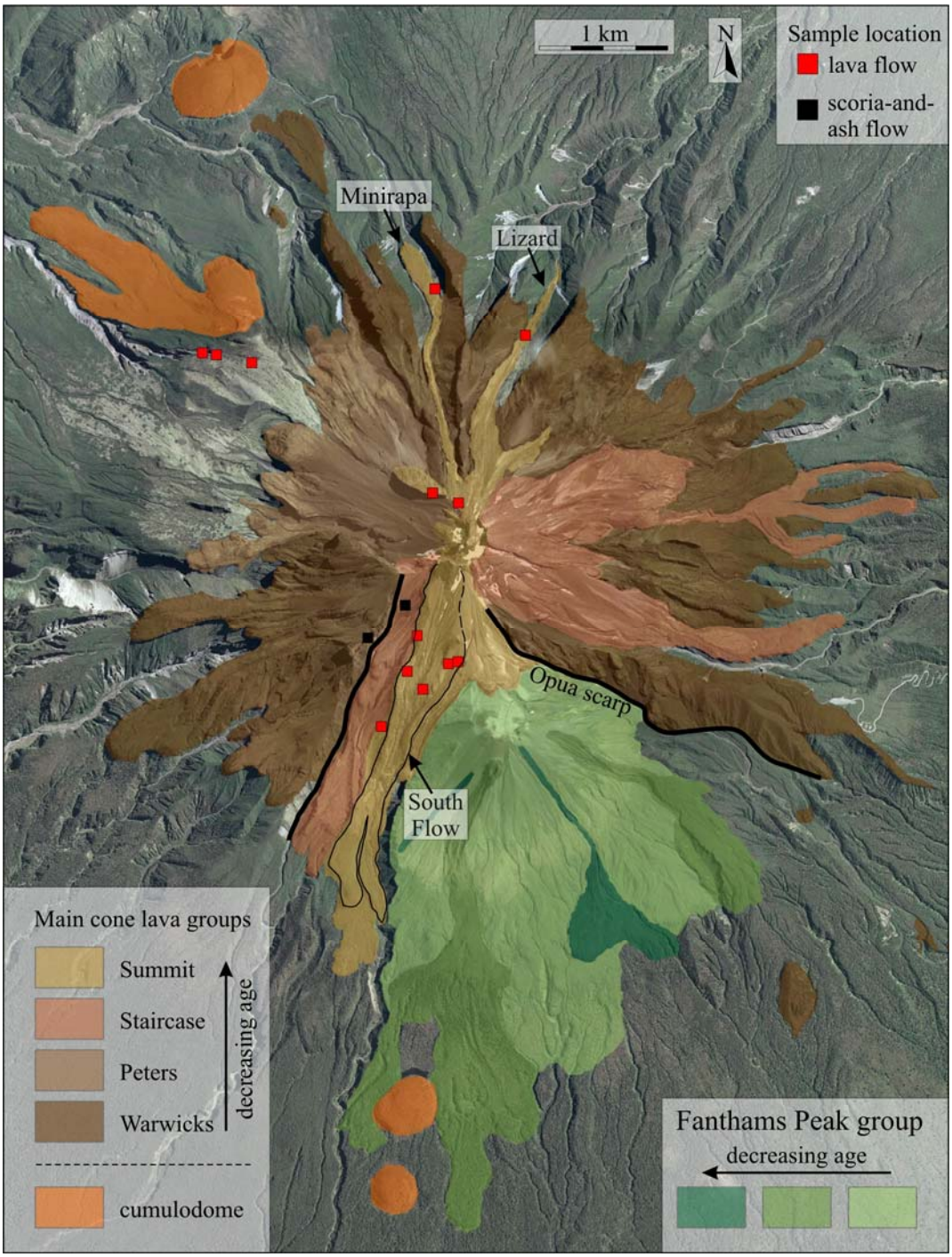


Figure 3-1: Distribution of lava flows on the Mt. Taranaki main cone and Fanthams Peak. Sampled lava flows and scoria-and-ash flow units are highlighted. The thick solid line represents the Opua amphitheatre scarps. The map has been modified after Neall (2003); map details were kindly provided by J.N. Procter.

3. The Fanthams Peak Group comprises lava flows solely emitted from the satellite cone to the south of the main summit. The minimum age of these lava flows is not yet well constrained but Neall et al. (1986) and Downey et al. (1994) showed that the youngest flows are 3.3 ka old or less. Later work on their coverbed stratigraphy would suggest that some lava flows on the east side of Fanthams Peak could be as young as 1400 yrs B.P. (Rosenthal, 2005).

4. The Staircase Group is exposed on the eastern to northeastern slopes overlying the Warwicks Castle Group and partially filling an amphitheatre in the south that was created by a sector-collapse that formed the Opua Debris Avalanche (Neall et al., 1986). Stratigraphic and paleomagnetic evidence suggest an age of 1.7 ka for this group (McGlone et al., 1988; Downey et al., 1994).

5. The youngest lava flows form the uppermost cone and are known as the Summit Group (Stewart el al., 1996). Neall (2003) further subdivided this group into Skeet Group and Summit Group, where the latter only comprises the present summit dome and the Turtle. These flows directly overlay the Staircase Group and predominantly fill the Opua amphitheatre in the south, but also extend to the North and East. No Summit lava flows are exposed on the west to northwest flank. The exception may be the remnant thick lava flow or coulée (known as the Turtle) of unknown age which is partially collapsed on its southern and upstream side. From paleomagnetic and stratigraphic evidence the Summit Group is younger than 1.7 ka and some flows have been estimated at 400 and 700 years old (Downey et al., 1994). The youngest lava flows could be correlatives to events of the Newall Formation (Stewart et al., 1996).

3.2 Results

3.2.1 Stratigraphic Type and Reference Sections

Representative sections around Mt. Taranaki were chosen to highlight the diversity of volcanic deposits at different sites of the mountain and within each locality (Fig. 3-2). A new chronostratigraphy for the Maero Eruptive Period and a new lithostratigraphy for the respective Maero Formation are here established with new type and reference sections being defined. At least 10 eruptive episodes occurred during the Maero Eruptive Period producing a diversity of volcaniclastic deposits around the flanks of Mt. Taranaki. In order to avoid confusion, previously established and used stratigraphic terms are partially substituted by new names. The Maero Eruptive Period started with the Hooker eruptive episode followed by the episodes of Te Popo, Waingongoro, Newall, Waiweranui, Puniho, Burrell, Mangahume, Tahurangi, and Pyramid. The formal members of the Maero Formation maintain the same nomenclature, along with the broad lithostratigraphic terms of Ash, Lapilli or Breccia.

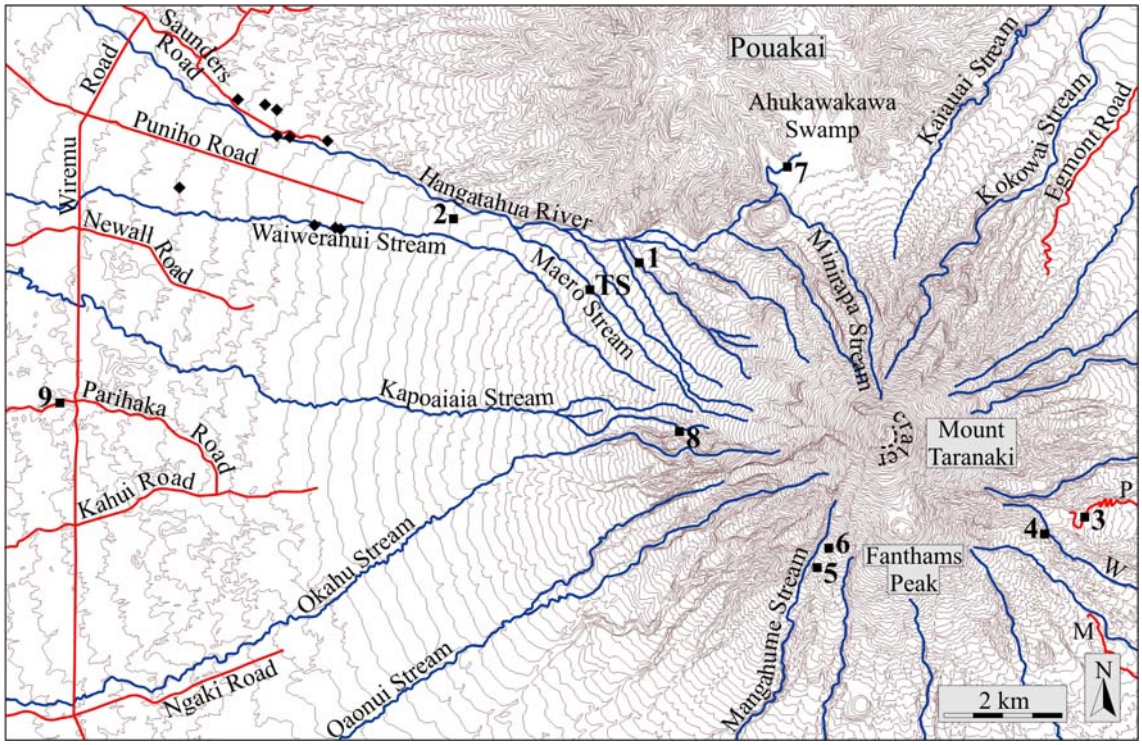


Figure 3-2: Location of type and reference sections around the edifice of Mt. Taranaki. TS-type section, P-Pembroke Road, W-Waingongoro Stream, M-Manaia Road. Numbered black squares refer to reference sections. Black diamonds mark distal locations of pyroclastic flow deposits in the area of Saunders Road – Wiremu Road – Waiweranui Stream.

3.2.1.1 Type Section of the Maero Formation

A new type section for the Maero Formation is defined (Fig. 3-3). It is located in Maero Stream near the former type section of the Maero debris flows of Neall (1979) which is now obscured by colluvium. The new type section comprises a succession of pyroclastic flow deposits of at least seven eruptive episodes. It can be correlated to nearby reference sections in Pyramid Stream (Fig. 3-3; Fig. 3-4) and Hangatahua River (Fig. 3-3). Individual exposed units can be grouped into sequences based on the occurrence of paleosols and were correlated with the new chronosequence of the Maero Eruptive Period. A detailed description of the type section is given below (cf. Platz, 2001).

The Maero Formation overlies the Oakura Tephra (<6970 ± 76 yrs B.P.; Neall, 1973), a cumulative unit of 1.4 m thickness, that represents cumulative accretion of fine-grained medial ash fall. A >2.5 m thick bouldery BAF deposit is exposed below this unit. Directly above the Oakura Tephra occur units of the Te Popo eruptive episode. A lower pyroclastic surge deposition sequence is overlain by a BAF deposit (Te Popo Breccia). The pyroclastic surge deposition sequence is composed of a pocketing 0-5 cm thick grey medium ash, up to a 10 cm thick layer of pale brown and pale olive brown ash with wavy bedding, up to a 10 cm layer of coarse to medium ash with rip-up clasts of fine brown ash, overlain by a 2-5 cm thick unit of pale grey medium ash with 4 cm diameter rip-ups of fine brown ash, and capped by a 1-5 cm pale brown ash containing charcoal fragments. The charcoal fragments were dated at 878 ± 39 yrs B.P. (Cronin et al., 2003). The pyroclastic surge sequence is overlaid by a 1.1 m thick brownish grey and strong brown and red-oxidised BAF deposit (Te Popo Breccia). It consists of approx. 70% clasts with maximum diameter of 20-30 cm set in a medium to coarse ash matrix of the same lithology. The clasts were subdivided into grey (60%), orange-coloured (30%), and greyish brown and pale grey (10%) andesite clasts. The clast-rich unit (c.70%) shows magnetic alignment indicating deposition temperature above 350 °C (after the method of Hoblitt and Kellog, 1979). The upper portion of the unit is overlain by a 4-5 cm dark brown humic-stained ash soil.

The overlying sequence was deposited during the Newall eruptive episode. It is composed of a pyroclastic surge and a BAF deposit (Newall Breccia). The pyroclastic surge unit overlies the paleosol, is about 4.5 cm thick, and comprises four sub-units: a c.1 mm thick fine pale brown ash passing up to coarse to medium, poorly sorted ash (c.4 cm) that normally grades into pale grey medium ash (5 mm) containing common fine charcoal fragments. The charcoal fragments were dated at 387 ± 43 yrs B.P. (Cronin et

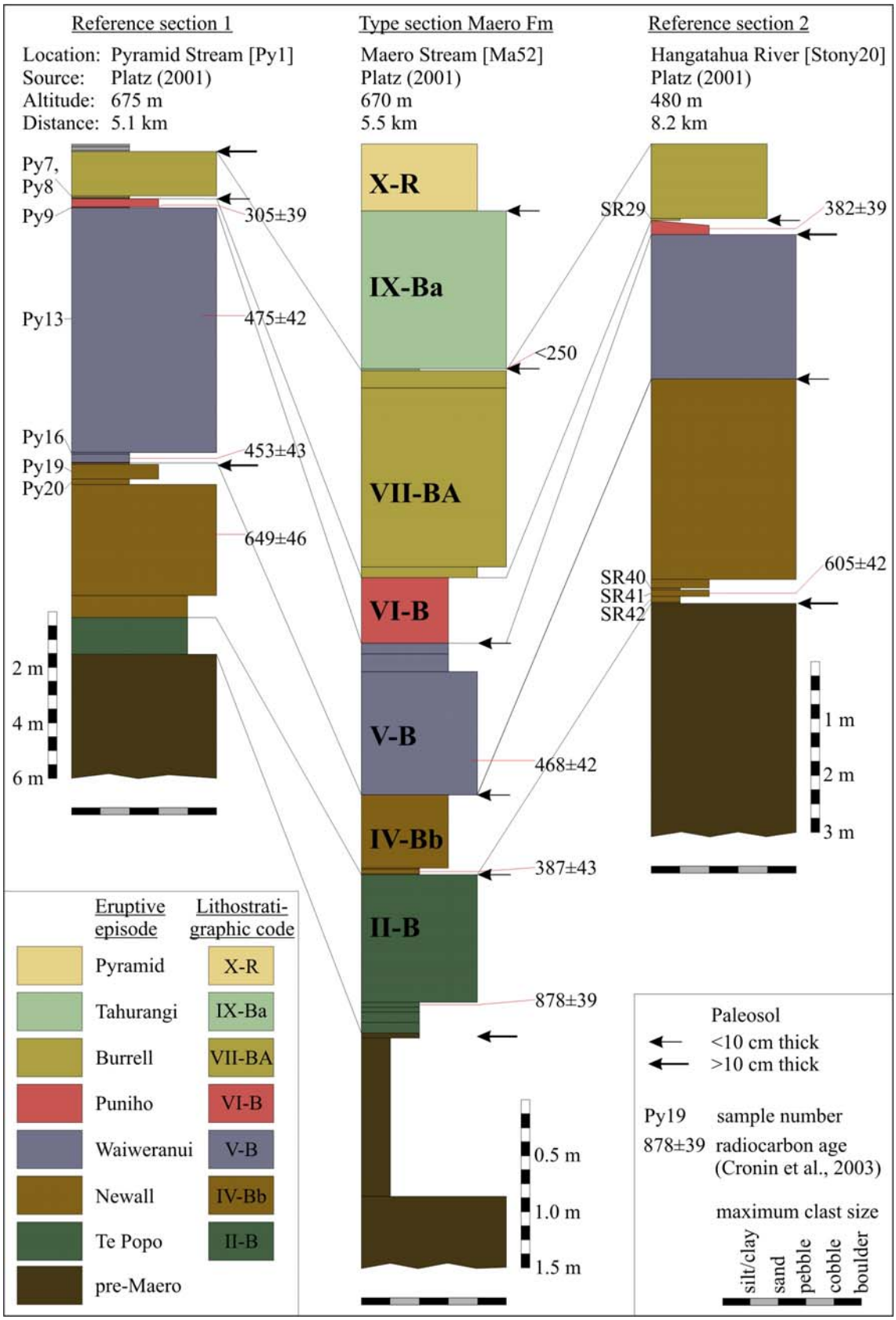


Figure 3-3: Type section of the Maero Formation located in Maero Stream, NW sector of Mt. Taranaki. Reference sections Nos. 1 and 2 are located in Pyramid Stream and Hangatahua River, respectively. The outcrops comprise deposits of BAFs, surges and pumice flows as well as co-ignimbrite ashes. Debris flow-, lahar-, and fluvial deposits are also exposed but not always differentiated. For further details see text and appendices. Labels Py7 etc refer to sample numbers. See also Fig. 3-4 for field photographs.

al., 2003). The uppermost unit (5 mm), above a gradational contact consists of pale brown and pale greyish-brown pocketing fine ash. The pyroclastic surge unit is overlain by a 68 cm thick BAF deposit (Newall Breccia), which is composed of a grey ash matrix supporting c.30% lapilli-sized, grey andesite clasts with maximum diameters of 4 cm. The unit is massive or with weak planar fabric in places. Large charcoalised logs are aligned parallel to bedding. The lower portion of the BAF deposit is clast-poor with orange-stained clasts concentrated near the lower erosive contact. The unit is capped by a 5 cm thick dark humic-stained soil.

Overlying this soil are three individual units that were deposited during the Waiweranui eruptive episode. The lower 1.1 m thick, matrix-supported BAF deposit (Waiweranui Breccia) is composed of a grey ash (50%) and cobble-sized clasts of dominantly grey and minor pale-grey andesite. The clasts show magnetic alignment and the largest clasts occur near the top. The upper 15 cm of the unit shows pervasive dark-red oxidation of matrix and clasts. A weak planar fabric of clast strings is observed and charcoal logs lie parallel to this, approx. 15 cm above the basal contact. These were dated at 468 ± 42 yrs B.P. (Cronin et al., 2003). The lower portion of the BAF unit (30-40 cm) is characterised by the absence of coarse clasts (maximum diameter 4 cm) and a grey medium ash matrix. The lower erosive contact is sharp and wavy. The next unit above is a 30 cm thick, massive, matrix-supported lapilli-breccia with a grey ash matrix and embedded fine lapilli clasts (up to 6 cm in diameter). Clast lithologies include grey (60%), orange (30%), and pale grey (10%) andesite. The grey andesite clasts show magnetic alignment. The basal 5 cm is fines-poor and clast-supported whereas the upper 20 cm is a grey-ash matrix diamicton with lapilli-sized clasts. A weak soil is developed on top of this unit.

The next unit above was emplaced during the Puniho eruption episode. The deposit (Puniho Breccia) is approx. 60 cm thick, is matrix-supported and clast poor (20%) comprising grey and up to 15% orange-stained andesite clasts. The upper 10 cm has pervasive red oxidation (matrix and clasts).

The sequence above this consists of four individual units and was deposited during the Burrell eruption episode (AD1655). The lower unit pinches and swells between 0 and 10 cm thick. Grey (90%) and orange-stained (up to 10%) lapilli- to cobble-sized clasts are the major constituents of this ash-poor unit. The major unit [Burrell Breccia (A)] is interpreted to represent a BAF deposit associated with the explosive removal of the

Burrell dome (cf. Chapter 6). It is 1.6 m thick and consists of a grey medium ash matrix, with up to boulder size clasts (maximum 40 cm diameter) near the top. The upper 30-40 cm show pervasive red oxidation of matrix and clasts. The unit is clast-supported in places, with grey and pale-grey andesite clasts being most common lithologies, along with minor pumice (2%) and orange-stained (3-5%) clasts. Grey andesite clasts show magnetic alignment and many of them are jig-saw fractured *in situ*. The basal 10 cm of the deposit is clast poor. The Burrell Breccia (A) is overlaid by a c.15 cm thick strong brown and red-coloured medium to coarse ash with interspersed rare boulder clasts. The uppermost unit in this sequence comprises a 1-3 cm thick pale brown to pale brownish grey medium to fine ash, and represents a fall deposit either directly from the sub-Plinian eruption column or from ash clouds associated with pyroclastic pumice flows which are deposited further downstream.

The next major unit overlying the Burrell sequence, is a direct correlative to Tahurangi Ash of AD1755 (cf. Chapter 5). The Tahurangi Breccia (a) is a bouldery 1.4 m thick unit: unusual in having a matrix-supported upper portion and a clast-supported base. A total of 30% ash matrix is estimated in the upper portion with the majority of clasts being highly angular, black to dark grey andesite (98%) and minor pale grey and orange-stained andesite. The major clast constituents show magnetic alignment. The upper 30-40 cm of the unit is oxidised to a pervasive reddish and purplish colour. The basal 5 cm is characterised by brown-stained ash matrix with fine tussock and charcoal fragments. Charcoal from this unit proved too young for radiocarbon dating (<250 yrs B.P.; Cronin et al., 2003). A weak soil is developed on top of the unit with weak weathering extending into the upper 10 cm of deposits.

The uppermost unit of the type section is a rock-avalanche deposit (Pyramid Rock Avalanche). This deposit represents most of the missing portion of the remnant summit lava dome, which was erupted post-AD1839 (Pyramid eruptive episode; cf. Chapter 5). The unit here is 60 cm thick and consists of brownish grey medium ash. It is matrix-supported with up to cobble-sized, subangular to subrounded predominantly grey and brownish grey andesite clasts. Rare (<5%) strong brown and orange clasts are noted.

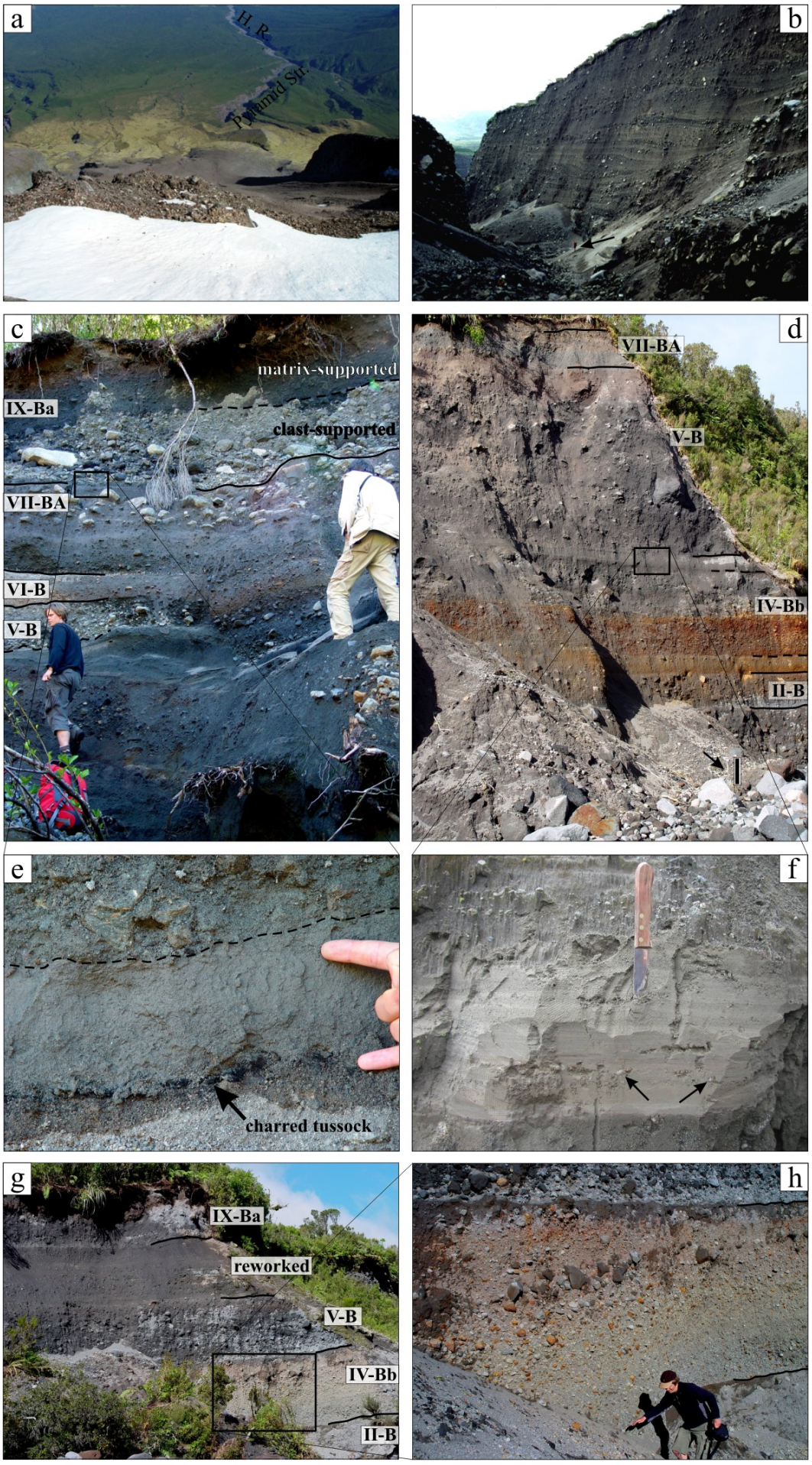

a
H. R.
Pyramid Str.
b
c
matrix-supported
IX-Ba
clast-supported
VII-BA
VI-B
V-B
d
VII-BA
V-B
IV-Bb
II-B
e
charred tussock
f
g
IX-Ba
reworked
V-B
IV-Bb
II-B
h



Figure 3-4: Field photographs of deposits from the NW sector of Mt. Taranaki. a) NW sector of Mt. Taranaki as viewed from the summit. Note the depression in vegetation caused by an avalanche (see Chapter 5). H. R. - Hangatahua River . b) exposure in the upper right Pyramid fork. Cliff section is approx. 30 m high and shows mainly lahar and hyperconcentrated flow deposits. Note Shane Cronin for scale (arrow). c) outcrop on the true left side of the Maero Stream near the intersection of Puniho and Holly Hut track. The upper unit shows the Tahurangi Block-and-Ash Flow deposit (unit a) with its upper matrix-supported and lower clast-supported zones. d) reference section No.1, lower Pyramid Stream, true right side. Only major units are labelled. Discolouration of units IV-Bb and II-B is caused by a raised iron-rich water table. Note the black bar has same height as the spate (arrow). e) close-up of c); basal portion of Tahurangi BAF (unit a) which consists of fine to medium ash. Dashed line marks the boundary between main body of the BAF and its basal portion. f) close-up of d); finely laminated and cross-bedded fine to medium ash surge deposit. Some pumice clasts (arrows) are present. g) exposure on the true right side of Maero Stream. Major units are labelled. The reworked section is 2.5 m thick and represents predominantly fluvial deposits. h) close-up of g); unit IV-Bb. Noteworthy are boulder trains and weak reverse grading of the lower to middle portion. i) distal blast deposit [Newall Breccia (a)] showing its typical pocketing appearance. j) stream exposure of a BAF deposit with pervasive red coloured top portion and grey bottom portion (Waiweranui Stream). k) in situ charcolised tree at a distal BAF exposure [Burrell Breccia (A)] near Saunders Road. l) degassing pipe originating at a charred log within the BAF deposit (same unit as in k). Note that the pipe branches at the centre of the photograph. Same unit as in k). Labelled units in c, d and g refer to the lithostratigraphic code. See discussion of Chapter 3 for further details. Detailed description of reference section No.1 can be found in the appendix. Photographs of f) and i) were taken by Shane Cronin.

3.2.1.2 Reference Sections of the Maero Formation

Tephra fall sequences on the eastern flank of Mt. Taranaki were well described by Druce (1966) and Topping (1974). Reference sections (No. 3 and 4) in this sector are located on Pembroke Road and near the intersection of the upper Round the Mountain Track (RTMT) and Waingongoro Stream (Fig. 3-5). The two sections are only about 600 m apart, but between them they exhibit differing sedimentological features which give valuable information about transport and eruption mechanisms.

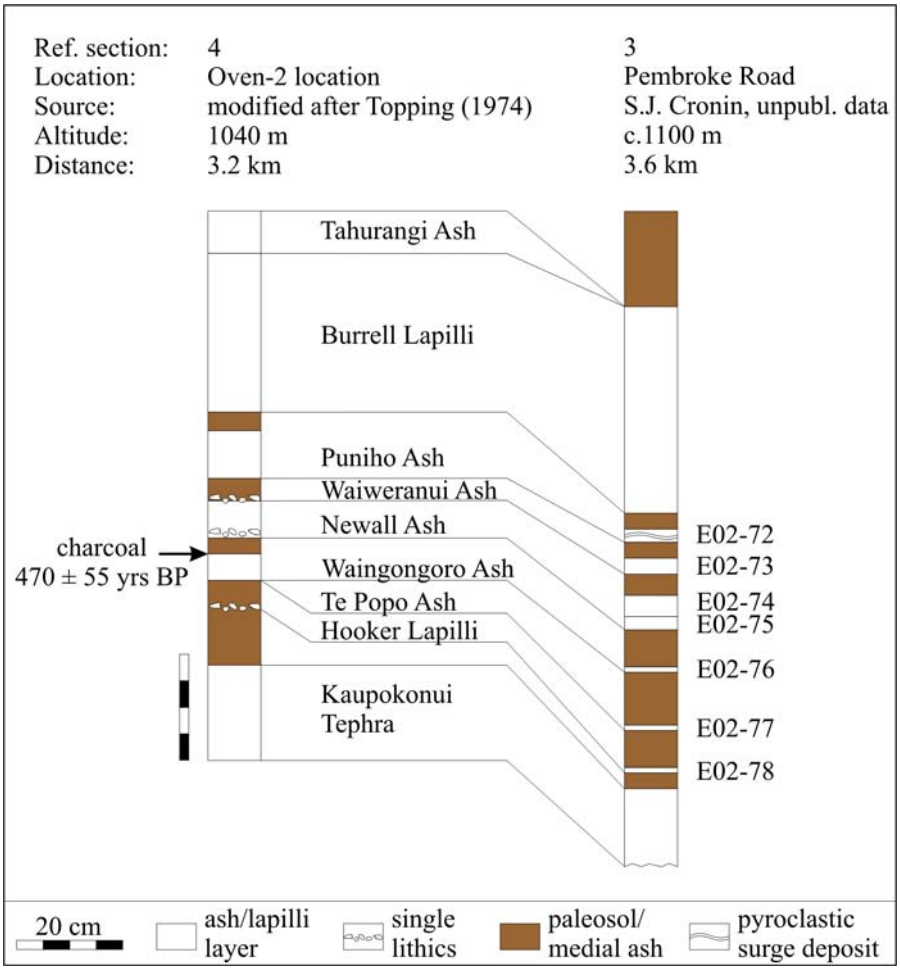


Figure 3-5: Reference sections Nos. 3 and 4 located on the east flank of Mt. Taranaki. Reference site: No.3–Pembroke Road cutting; No.4–intersection of Waingongoro Stream and Round-The-Mountain-Track. E02-72 etc are sample numbers.

At the Pembroke Road site, three units are distinctive: (1) the poorly sorted Puniho Ash which is preserved as a pyroclastic surge deposit, with wavy cross- and planar-bedding; (2) Newall Ash, which consists of twin ash layers; and (3) the oldest (unknown) tephra layer composed of a single layer of pumice and lithic lapilli clasts (Hooker Lapilli). All other units comprise single fall deposits of varying thicknesses. The Waingongoro section at similar altitude contains a buried Maori oven (umu), which is covered by

Newall Ash. Puniho Ash is thicker than at the previous section but shows no bedding. Waiweranui Ash is preserved only as grey lithic fragments. Newall Ash is apparently composed of two ash units, a and b; with grey lithic lapilli being scattered within the lower unit (a). The correlation of the two localities reveals a composite event record of eight erupted units. Charcoal in the umu was radiocarbon dated at 470 ± 55 yrs B.P. (Topping, 1974). Consequently, at these sites between the deposition of Kaupokonui Tephra and Newall Ash three eruptive events are recorded, whereas since 470 yrs B.P. at least five events are shown (Fig. 3-5).

Two closely spaced sections on the south flank of Mt. Taranaki form additional useful reference sections (Nos. 5 and 6) since they preserve additional eruptive units of this period. Here, near the site of the old Mangahume Hut, deposits from three eruptive events are preserved above the Burrell Lapilli (Fig. 3-6). A pale grey, fine to coarse ash correlates to Tahurangi Ash (AD1755; Druce, 1966). The unit above it constitutes a single layer of dark grey, highly crystalline lithic lapilli (Pyramid Lapilli) and corresponds to the Pyramid eruption (cf. Chapter 5). The unit below Tahurangi Ash also comprises a single layer of lithic lapilli (Mangahume Lapilli) and was erupted some time between AD1655 and AD1755. The tephra sequence upslope of the Old Mangahume Hut directly overlies one of the younger summit-group lava flows implying (together with the paleomagnetic age determinations of Downey et al., 1994) a possible emplacement during the Maero Eruptive Period. The next reference section (No. 7) is situated c.5 km NNW of the summit within the Ahukawakawa Swamp and contains deposits of tephra fall and pyroclastic flows (Fig. 3-7). The lower section is composed of a >1 m thick BAF deposit which is overlain by a pyroclastic surge unit. Four fall units are recognised which are separated by peat or peaty silt loams[2] (Tahurangi Ash, Waiweranui Ash, Newall Ash, and Te Popo Ash). The units comprise fine to medium ash; only one unit (Newall Ash; see reference section No. 3; Fig. 3-5) is composed of a pumice-rich surge deposit over- and underlain by a 2 cm thick fine ash.

West of the summit, two sections are exposed, at medial[3] (uphill of Kahui Hut; reference section No. 8) and distal[3] (Parihaka Road; reference section No. 9) locations

[2] Brownish clay to silty loams of varying thickness are derived from medial volcanic ash fall and/or colluvium.

[3] Proximal, medial and distal reaches describe distances from the present summit of Mt. Taranaki. The term proximal is used for areas <3 km from source, (i.e. in the range for ballistics), medial for a radius of 3-10 km from source (marked by the National Park boundary and also the normal limit for most pyroclastic flow and surge units), and distal at a radius >10 km, which only the rarer larger event reached.

(Fig. 3-7). Deposit types contrast with the previous sections since they were predominantly emplaced by pyroclastic density currents. The reference section exposed near Kahui Hut shows from bottom to top a sequence of three pyroclastic surge deposits followed by an alternating BAF-surge-BAF deposition sequence. In the upper portion of the section there are two ash layers, presumably correlatives to Newall Ash. Another ash layer (Tahurangi Ash) occurs at the top of the exposure which is overlain by the present-day topsoil.

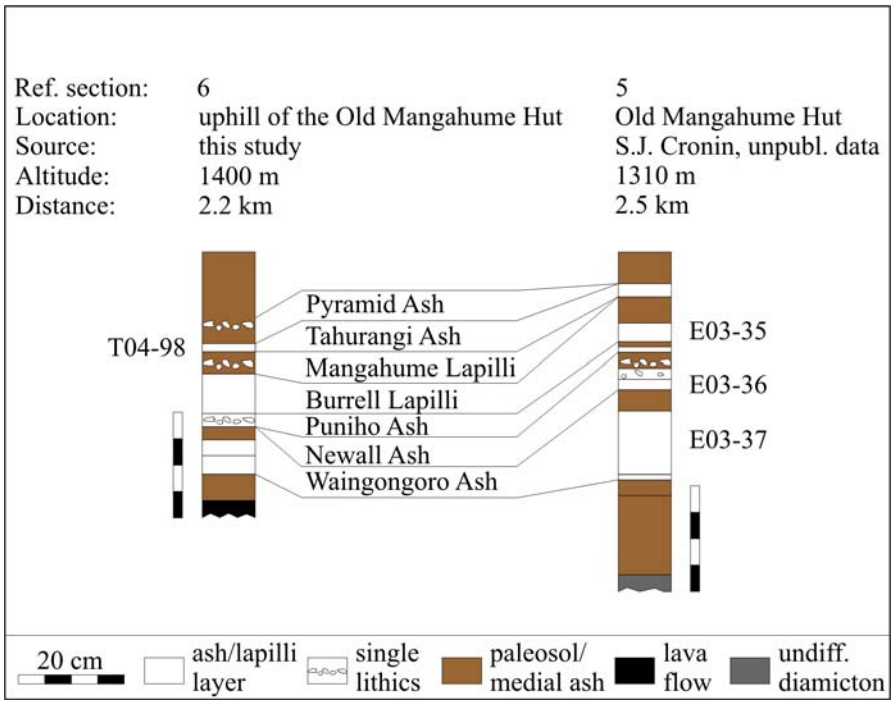


Figure 3-6: Reference sections Nos. 5 and 6 located on the south flank of Mt. Taranaki. Reference site: No.5–at the site of the Old Mangahume Hut; No.6–near the Old Mangahume Hut, upslope of No.5. Labels E03-35 etc are sample numbers.

The other reference section (No. 9) in this sector is located 14 km west of the summit and is a lateral blast-type deposit (Fig. 3-7). It comprises a poorly sorted, pocketing unit of firm grey and pale greyish-brown, medium to coarse ash with banding on a 1 cm scale. Fine lapilli lithic clasts and dense and vesicular ash occurs within two-thirds of the layers. Grey, blade-like angular dense clasts up to 4 cm long are also common. The correlation of this deposit to sections on the mountain is difficult due to an absence of other related beds, but it appears most likely to represent a correlative of a pyroclastic surge deposit sequence at the lower Kahui section (Waingongoro Ash). However, stratigraphic relation remains unknown.

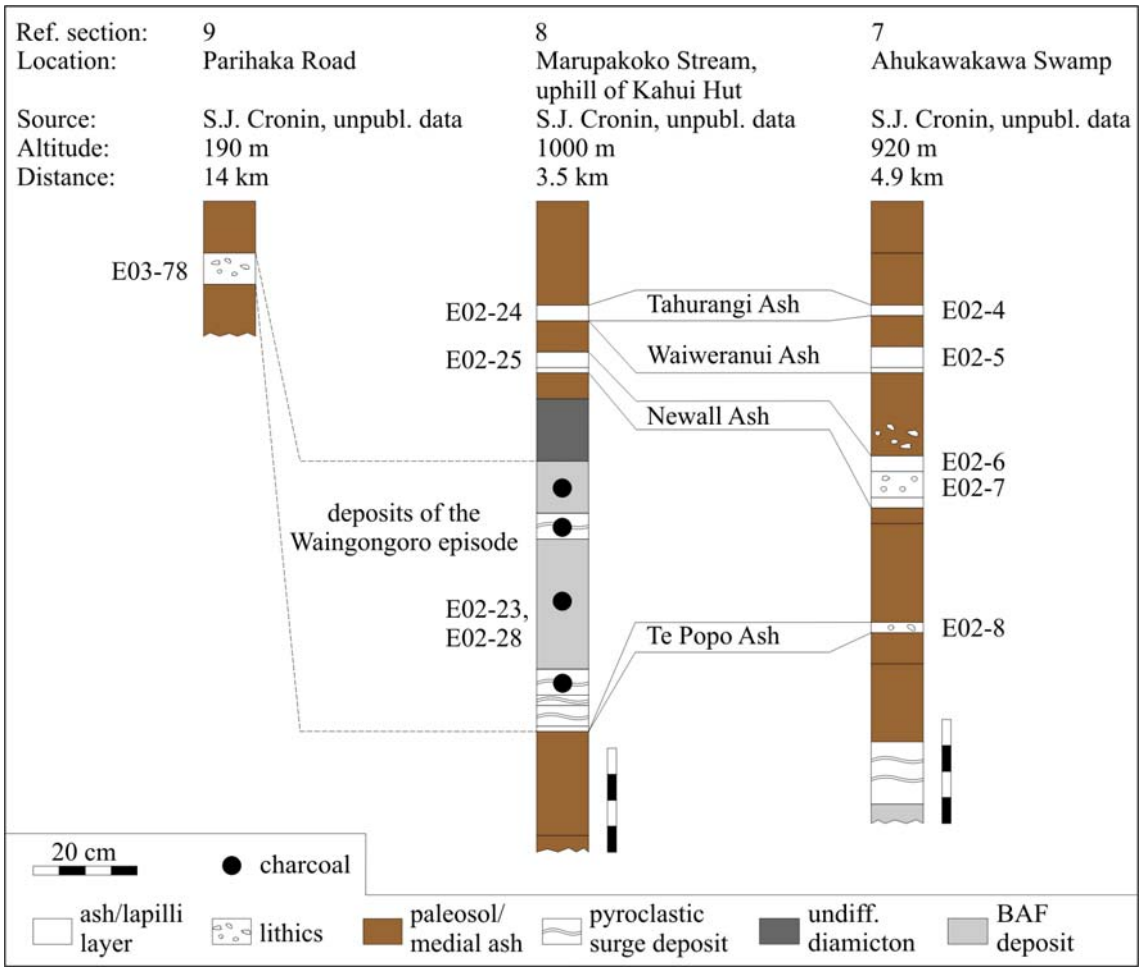


Figure 3-7: Reference sections Nos. 7, 8 and 9 located on the west and north sector of Mt. Taranaki. Reference site: No.7–Ahukawakawa Swamp; No.8–Marupakoko Stream near Kahui Hut; No.9–Parihaka Road cutting. Labels E02-4 etc refer to sample numbers.

Two locations in Pyramid Stream and Hangatahua River near the type section are defined as medial reference sites (Nos. 1 and 2) on the NW sector since they expand the record from the type section by two further units (Fig. 3-3).

Distal pyroclastic flow deposits in the NW sector are found outside the National Park in the area defined by Saunders Road – Wiremu Road – Waiweranui Stream (Fig. 3-2). Although other isolated exposures of pyroclastic flow deposits are known (cf. Platz, 2001), their correlation is difficult based on stratigraphic context alone. Even radiocarbon dating of two distal deposits did not elucidate their stratigraphic position due to their being more than one potential correlative within the standard error range of the radiocarbon method.

3.2.2 Block-and-Ash Flow Deposits

3.2.2.1 Distribution and Flow Paths

Block-and-Ash Flows (BAFs) generated by collapses from lava domes during the Maero Eruptive Period were predominantly directed towards the NW sector. Currently a continuous crater wall extends around the NE-E-SW sectors. The former W-SW crater rim was composed of a similar succession of at least four lava flows as exposed at the entrance of Okahu Gorge (Fig. 3-8). The distribution of BAF deposits allow the identification of three crater exit areas and flow paths for BAFs during Maero Eruptive Period. These are, in increasing order of importance the N, the SW (Okahu Gorge), and the W-NW sectors (Fig. 3-9, Fig. 3-10).

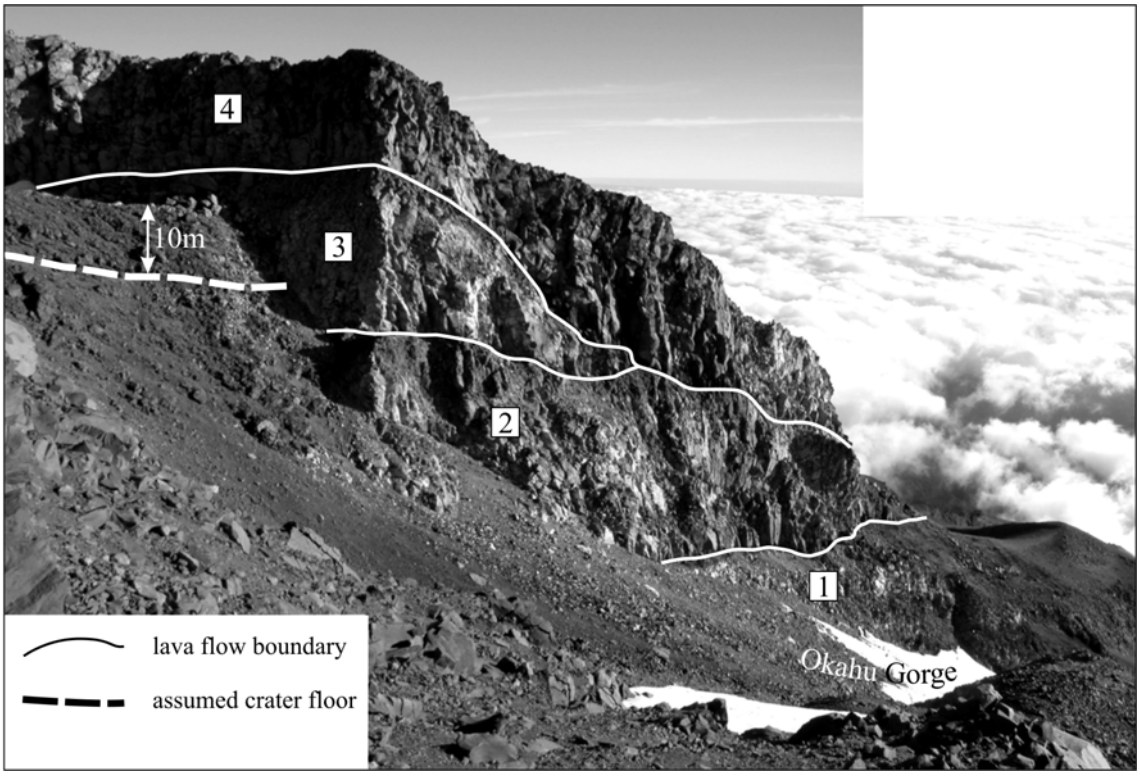


Figure 3-8: Crater rim stratigraphy as exposed on its SW side at the entrance of Okahu Gorge. Four lava flows are identifiable with the youngest flow (4) being known as South Flow.

North sector

The northern exit area includes the tributaries of Peters, Minirapa, and Kokowai Streams (Fig. 3-10). Exposures in these show BAF deposits and related debris flow deposits of Maero age, however, their detailed stratigraphy in relation to other units in the Maero catchment cannot be well constrained. In addition, coverbed sequences on ridges and lava flows contain numerous tephra layers; some of them are interpreted to be pyroclastic surge deposits related to BAFs.

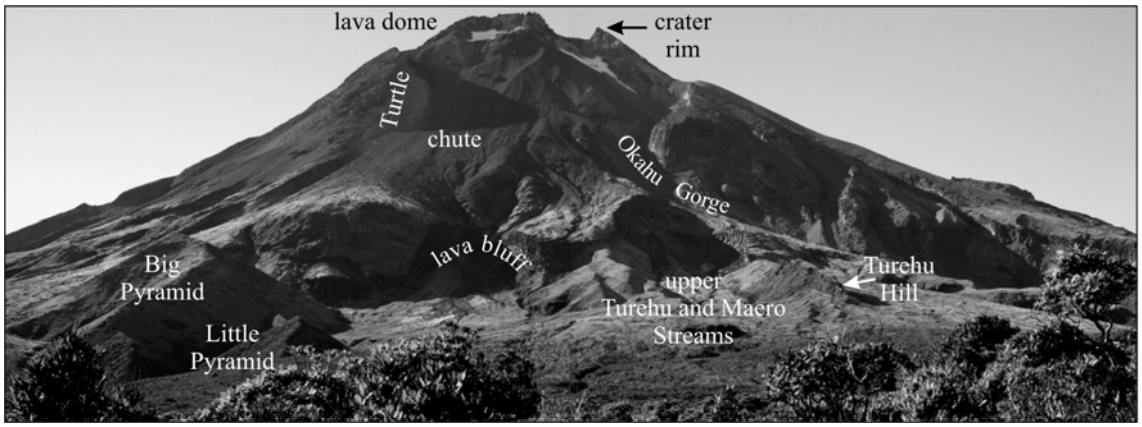


Figure 3-9: Composite photograph of the upper NW flank of Mt. Taranaki showing named and described morphological features.

Southwest sector

The present-day Okahu Gorge begins at a cliff on the SW side of the crater and deepens and widens downslope (Fig. 3-10). Many of the Maero Period dome-collapse related rockfalls and BAFs travelled this path. At about 1700 m altitude, the gorge turns sharply from W to SW. At this location BAFs either fully or partly flowed straight ahead (W) to enter the upper Maero/Turehu catchment, or they followed the SW course of the gorge. Those BAFs travelling W out of the gorge split further around Turehu Hill (remnants of two lava flows) and entered the upper catchments of one or more of the Turehu, Maero, Marupakoko or Kapoaiaia Streams. Puniho Hill does not appear to have been overtopped by BAFs. Farther downstream, in the Okahu Stream valley (at c.700 m altitude) some BAFs overtopped valley sides over a length of c.700 m and travelled up to 3 km through the forest. This deposition pattern is also indicated by vegetation zones seen in aerial photographs.

Northwest sector

This was the major travel path for BAFs during the Maero Eruptive Period. The upper NW flank forms a natural slightly concave shaped chute which is currently bordered by the Turtle to the north and by a low ridge to the south (Fig. 3-9). At the bottom end of the chute at c.1700 m altitude, BAFs were at times split to the NNW (W of the Big Pyramid) into the Upson Stream-Skinner Hill area, but mainly descended a steep bluff (Fig. 3-9). At the base of the bluff (1500 m altitude), local slope drops to 17°, from the typical 35° upslope. Block-and-Ash Flows descending the bluff were deflected off the “Big Pyramid” hill, traversed a broad low-relief surface before being channelled into

areas occupied by the present Pyramid, Unnamed, Turehu or Maero Streams. The bulk of passing BAFs were channelled into the Maero Stream area where they were confined on the southwest by a lava ridge. Only rarely could the basal dense avalanche parts of the BAFs overcome the lava barrier to form small, steeply inclined lobes. Block-and-Ash-Flow related surges, by contrast, travelled farther westward beyond the lava ridge.

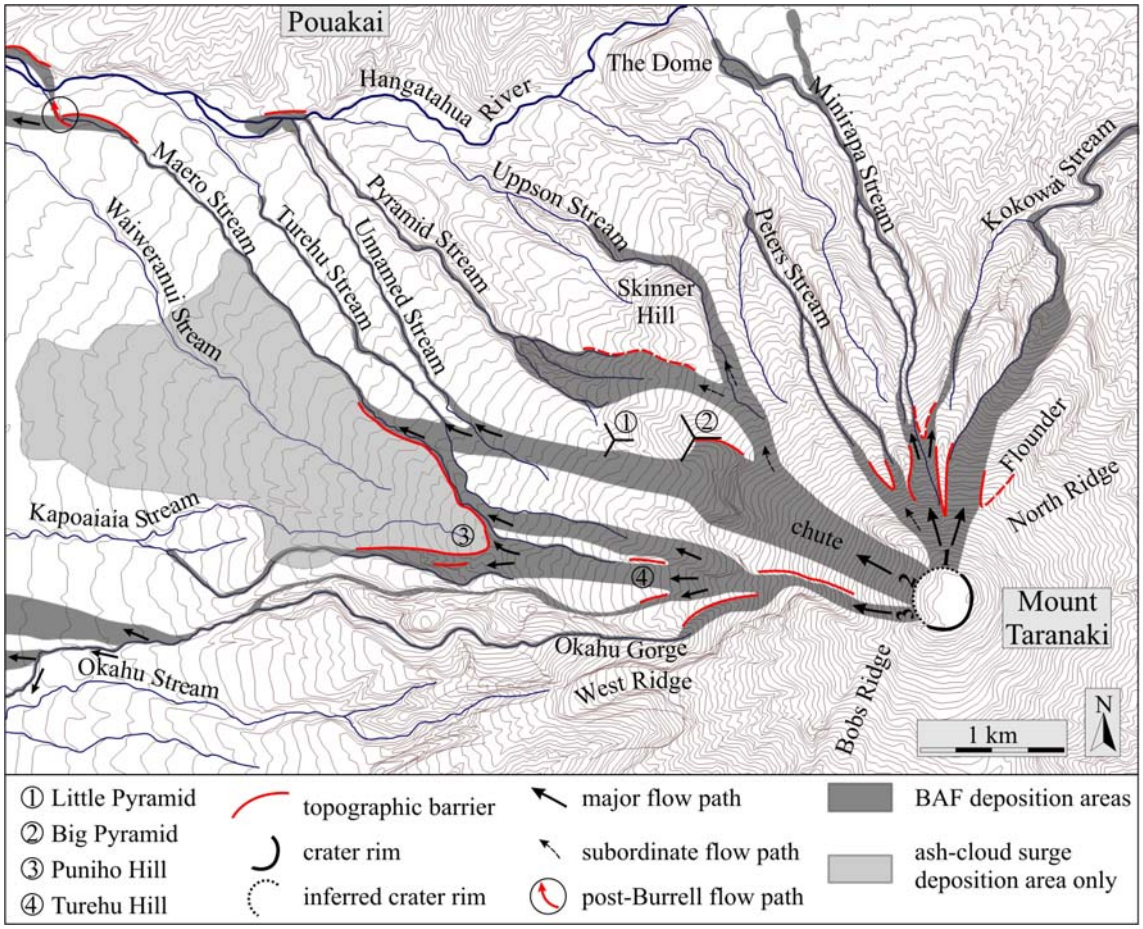


Figure 3-10: Flow paths and distribution of BAF and surge deposits on the N to W sectors. Crater exit areas: 1-north sector, 2-northwest sector, 3-southwest sector.

A fan containing the volumetric bulk of BAF deposits from the Maero Eruptive Period is bordered by Pyramid Stream, Maero Stream and Hangatahua River. This region as well as the area farther westward towards Kahui Hut, is characterised by the depression of current altitudinal vegetation zones by up to 300 m. The best exposures of these BAF deposits are found in Maero Stream where individual units can be traced over several km. Two breaks in slope occur at the 1000 m and 600 m contours, where the overall slope drops to 9° and 3°, respectively.

The present day Maero Stream valley has an immature box-shaped form, although from deposits preserved in the sides it appears that the valley may have remained in the same general position over the last 1000 years. Hence, there are subtle variations in the paths

of individual flows. Burrell-aged and older deposits (i.e. pre-AD1655) are exposed in the top section of a c.20 m high cliff at the true left side of the Hangatahua River, indicating the BAF travel path at that time was closer to the true left valley margin than the present river location (Fig. 3-10). The youthful forest vegetation of this area is still recognisable on aerial photographs. Initially, BAFs were diverted in a left-hand bend in the lower Maero Stream, before flowing, either parallel to the Hangatahua River, or entering the Waiweranui Stream at c.540 m altitude. Beyond the present National Park boundary, at the 400 m contour line, BAFs stalled in the relatively flat area defined by Waiweranui Stream – Saunders Road – Wiremu Road. Post Burrell-aged BAFs appear to have travelled down the Maero Stream and into the Hangatahua River valley. Deposits of these units are exposed in the Blue Rata Reserve, north of the Hangatahua River at a distance of 13 km from source.

The distribution of ash-cloud surges is generally bound to the travel paths and deposition areas of BAFs (Watanabe et al., 1999). This meant that ash-cloud surges were restricted to the W to NNE sector of Mt. Taranaki. Under some conditions, for example sharp valley bends, the turbulent ash cloud of a BAF is able to decouple from its basal avalanche (Fisher, 1995). A characteristic triangular region on the NW flanks shows evidence of being repeatedly devastated by ash-cloud surges, despite being protected by topography from the densest portion of BAFs (Fig. 3-10). The ash-cloud surges of Maero BAFs could overcome the morphological barrier and repeatedly destroy the vegetation in this region.

3.2.3 Lava Flows

Selected lava flows of the upper cone of Mt. Taranaki (Fig. 3-1) were studied, because cover bed stratigraphy and paleomagnetic studies suggested their emplacement at c.400 and 700 yrs ago (Downey et al., 1994), thus within the Maero Eruptive Period. Consequently, seven lava flows were sampled – Minirapa and Lizard lava flows to the north, two unknown lava flows to the west, the Turtle to the northwest, and two lava flows on the south flank within the Opua amphitheatre (Table 3-4).

The Lizard lava flow (short Lizard) originates on the north sector of the crater where the crater wall is collapsed. It splits at its uppermost portion above 2200 m altitude. The main portion flowed within the valley of the main tributary of Kokowai Stream down to an altitude of 1260 m, whereas a smaller lobe followed the Minirapa Stream valley. The

cover bed sequence on the Lizard at its termination is 50 cm thick and consists of a c.25 cm thick dark, greyish brown silt loam with increasing content of angular lava pebbles and cobbles with depth. It is overlain by two grey, fine to medium and medium ash layers of 2 and 3 cm thickness. The top unit is a dark brown sandy soil of 20 cm thickness. The current valley-confined flow path of the Lizard, along with the coverage of only two ash layers would suggest a relatively young emplacement age.

The Minirapa lava flow (short Minirapa) has a particularly distinctive-appearing. It is a low-viscosity flow that also originated from the north sector of the crater and followed the current Minirapa Stream valley (Fig. 3-1). It overlies the Lizard flow. The lava flow came to rest at 1200 m and formed a lobe up to 155 m wide: at its origin the flow is c.80 m wide and it narrows downhill to between 40 and 50 m.

In contrast to the Lizard, cover beds with a total thickness of at least 1 m are preserved on the Minirapa flow. The oldest unit is a diamicton containing greyish-brown pumice and grey and red lithics set in a sandy matrix, which appears most likely to be a pyroclastic flow deposit. This pumice-bearing unit may correspond to the youngest known pre-Maero pumice-producing event, the c.1350 ± 150 yrs B.P. Kaupokonui Tephra (McGlone et al., 1988), however, this unit is only known from the S and E flanks. Recent studies of tephra on the NE flanks have confirmed that the Kaupokonui is not present, but a younger pumice tephra and pyroclastic flow deposit does occur (M.B. Turner, unpubl. data). While not directly dated, this unit can be geochemically correlated to dated units within a fall sequence in Lake Rotokare, c.35 km SE of Mt. Taranaki. Ages of either 777 ± 36 or 885 ± 36 yrs B.P. (M.B. Turner, unpubl. data) relate to this Rotokare sample which in turn give a minimum age for the Minirapa flow. This implies that both Minirapa and Lizard flows could have been erupted only within the early Maero Eruptive Period prior to c.800 yrs B.P. Although Neall (2003) assigned the Lizard an age between 1.4 and 0.5 ka, the Minirapa was allocated to the Staircase Group (3.3-1.4 ka). In Stewart et al. (1996) both lava flows are classed as Summit Group lava flows, less than 0.7 ka old.

The Turtle is an up to c.15 m thick eroded lava coulée on the upper NW flank. Thick columnar joints are exposed at its southern and northern collapsed faces and a thin carapace occurs on its top. The only cover beds found on the flow surface, including within deep cracks, include rare dense grey, jig-saw jointed bombs and blocks (up to 20 cm in diameter). The absence of, for example, Burrell Lapilli pumice clasts on its surface could be evidence for post-AD1655 emplacement, although its steep upper

Table 3-4. Sample list, description and stratigraphy of studied lava flows and scoria-and-ash flow deposits.

Sample	East	North	Height [m]	Lava flow/ pyroclastic flow	Old Stratigraphy Group	Old Stratigraphy Age [ka]	New Stratigraphy Group	New Stratigraphy Age [ka]	Description
SD12	2601454	6212075	2200	Turtle	Summit Group [1,2]	c.0.7 [1]/ <0.5 [2]	Summit Group	?0.8	dense rock from top of the Turtle
T04-202	2600017	6213014	1319						dense rock; loose boulder on surface near Skinner Hill
MI5	2601511	6213626	1355	Minirapa	Summit Group [1]/ Staircase Group [2]	c.0.7 [1]/ 3.3-1.4 [2]	Summit Group	?0.8	dense rock from true right hand margin of lava lobe
SD11	2601709	6211875	2354						dense rock from top portion of lava flow
E03-77	2602245	6213250	1275	Lizard	Summit Group [1]/ Skeet Group [2]	c.0.7 [1]/ 1.4-0.5 [2]	Summit Group	?0.8	dense rock from lower portion of lava lobe
TO4-61	2601280	6210509	1873	South Flow	Summit Group [1]/ Skeet Group [2]	c.0.7 [1]/ 1.4-0.5 [2]	Summit Group	?0.4	dense rock of western flow margin
TO4-57	2601700	6210585	2016						dense rock from the eastern levee of the lava flow
TO4-58	2601418	6210366	1836						dense rock from the western levee of the lava flow
TO4-59	2601630	6210571	1999						dense rock from the central portion of the lava flow
TO4-62	2601080	6210063	1628	below South Flow/ unit 2 [3]	Summit Group [1]/ Skeet Group [2]	c.0.7 [1]/ 3.3-1.4 [2]	Summit Group	?0.4	dense rock from western levee of the lava flow beneath South Flow
TO4-63	2601359	6210790	2016						
TO4-200	2599732	6213082	1221	Pyramid lava flow 1	Warwick Castle Group [1]/ Peters Group [2]	c.8 [1]/ 3.3-7 [2]	Staircase Group?	?1.4	dense rock of central portion of the lava flow in upper central fork of Pyramid Stream upstream of RTMT [4]
TO4-199	2599623	6213095	1097	Pyramid lava flow 2					
TO4-52, T04-53	2601264	6211056	2081	scoria-and-ash flow deposit			Summit Group	?0.4	black, poorly sorted, monolithologic diamicton with semi-vesicular clast in a medium to coarse black ash matrix; western Opua amphitheatre
T04-56	2600966	6210782	1965	scoria-and-ash flow deposit			Staircase Group or older	?1.4	black, poorly sorted, monolithologic diamicton with semi-vesicular clasts in a medium to coarse black ash matrix; Bobs Ridge

[1] Stewart et al. (1996) [2] Neall (2003) [3] refers to the crater rim lava flow unit 2 [4] Round-The-Mountain-Track.

surface and the high altitude may have prevented the preservation of this and earlier tephra deposits. The distinct shape of the Turtle is that of a lava coulée and its emplacement was assumed to have been part of the former summit lava dome (Cronin, 1991). Other studies allocated the Turtle an age of 0.7 ka or younger (Stewart et al., 1996; Neall, 2003).

Two further (previously undescribed) lava flows are also exposed in the upper central fork of Pyramid Stream between 1100 and 1200 m (Fig. 3-1). Loose rockfall or BAF deposits are plastered onto and overlie the lava flows in places. The location and elevation of these lava flows suggests a stratigraphic affiliation to the Warwicks Castle Group, although, after Neall (2003) these flows would be assigned to Peters Group.

On the south flank between Bobs Ridge and Fanthams Peak two lava flows were sampled (Fig. 3-1). In addition, two distinct scoriaceous, black diamictons were observed which are interpreted to be proximal scoria-and-ash flow deposits. The deposits are poorly sorted and contain monolithologic scoria lapilli and blocks/bombs up to 25 cm in diameter that are set in medium to coarse black ash matrix. They are exposed on Bobs Ridge and east of it within the Opua amphitheatre.

The oldest sampled lava flow corresponds to unit 2 of the crater rim (see Fig. 3-8). It is overlain by the South Flow (lava flow unit 4; Fig. 3-8), which at 2100 m altitude forms two small bluffs before bifurcating into two lobes that extend down to c.1100 m. On the upper flanks only Burrell Lapilli-aged pumice pyroclastic flow deposits directly overlie the South Flow. This (and the dates of Downey et al., 1994) imply that South Flow extruded during the Maero Eruptive Period, possibly only 400 yrs ago.

The scoria-and-ash flow deposit that lies west of South Flow (still within the Opua amphitheatre; Fig. 3-1) is also overlain by Burrell-aged pyroclastic flow deposits. The stratigraphic relationship of the scoria-and-ash flow unit on Bobs Ridge is more difficult to interpret. It is overlain by only a thin (c.20 cm) poorly sorted lithic diamicton. Its exposed location on a ridge and its thickness of more than 20 cm in relation to its distance of about 900 m to the crater rim may suggest a larger eruptive event, perhaps one of the larger Staircase lava flow eruptions.

3.2.4 Glass Chemistry

Various sites around Mt. Taranaki described by Platz (2001), S. Cronin (unpubl. data), and this study were selected for glass compositional studies in order to chemically characterise the diversity of Maero-aged deposition types and to test the correlation of established units (Fig. 3-2).

The dataset of glass chemical compositions comprises 68 samples with a total number of 1016 analyses. Contaminated or hybrid analyses (i.e. EMP analyses comprising mixed proportions of glass and mineral phases) were identified by comparing intra-variations of two or more glass shard analyses and by applying the glass evaluation procedure presented in Chapter 4. A broad range in major element composition was observed: SiO_2 contents vary between 57.2 to 76.2 wt.% and K_2O from 2.3 to 7.2 wt.%. A near Gaussian distribution curve is observed for SiO_2 values between c.64-77 wt.%. with the mode at 68-69 wt.% SiO_2 and 5.5-6 wt.% K_2O (Fig. 3-11). However, there are also two weak secondary modes in the low-silica range. These modes should also occur in K_2O abundances if potassium behaves as an incompatible element, although the K_2O distribution curve does not have such distinct modes, and instead the distribution is skewed toward the low-K_2O range (Fig. 3-11).

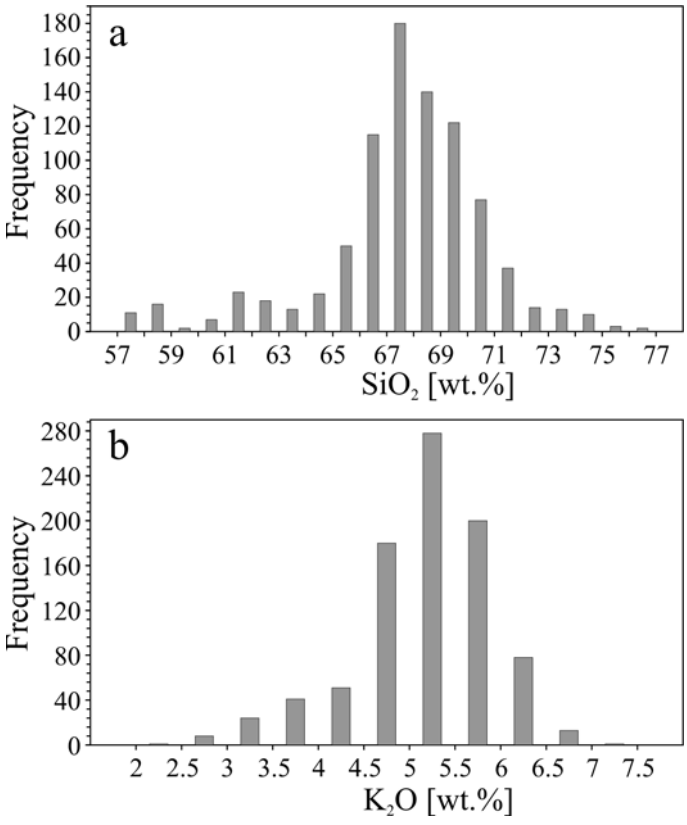


Figure 3-11: Histogram of all glass chemical analyses for SiO_2 (a) and K_2O (b).

Intra-sample variations can be large, for example up to 11.2 wt.% in SiO_2, although the majority are between 1-6 wt.% SiO_2. The largest intra-sample variations are observed for bimodal samples whereas the lowest often occur within tephra samples with rhyolitic glass compositions. Standard statistical methods (e.g., using standard deviations and 95% confidence intervals) as well as canonical discriminant function analysis (DFA) were used to group individual units to single eruptive events (cf. Shane and Froggatt, 1994; Cronin et al., 1996; 1997). Although DFA used seven independent variables, grouping proved difficult since the variance within samples is too strong. The probability of samples being classified into unique groups were in most cases <<75% (Platz et al., 2004). This means that the glass chemistry of individual units could only rarely be uniquely identified using DFA and other statistical methods. However, glass chemical characteristics (e.g. bimodality, andesitic vs. rhyolitic composition) of individual units were of support for field-based correlation of tephra and pyroclastic flow deposits.

3.2.4.1 Special Characteristics of Some Erupted Units

Intra-sample variations can be large and can have various reasons. Firstly, two or more glass populations (andesitic to rhyolitic) can be present within one tephra layer (Fig. 3-12; see also WW19 in Fig. 3-13). The compositional differences are often also reflected in different glass shard shapes (Fig. 3-12). However, even with similar glass compositions, the texture of glass shards also varied strongly. Even without distinctive populations being present, analyses on the same glass shard in some units showed silica variations of several wt.% (i.e. WW6: ΔSiO_2 = 3.5 wt.%; SR41: ΔSiO_2 = 3.5 wt.%; SR40: ΔSiO_2 = 2.8 wt.%). In addition, one of the units was contaminated by foreign glass shards (E03-35; Fig. 3-12). This tephra layer (of Burrell Lapilli) located at the old Mangahume Hut on the southern flank contains rhyolite glass shards with a chemistry typical of Taupo volcano (Taupo Volcanic Zone). These exotic shard compositions are a good match for the AD186 Taupo tephra or older Holocene Taupo tephras (P.A.R. Shane, pers. comm., 2007). However, it is impossible that these glass shards represent primary fall, and hence they either represent reworked Taupo tephra (unlikely since this unit was not deposited in this direction), or rare Taranaki glasses that coincidentally have the same compositions in major elements as Taupo.

Clasts of scoria-and-ash flow deposits, both within the Opua amphitheatre and on Bobs Ridge (Table 3-4), have glass compositions that contrast with dome-related and sub-Plinian eruptions of the Maero Eruptive Period. These have lower SiO_2 and higher TiO_2, MgO and partially higher FeO abundances (Fig. 3-14). Some tephra layers contain individual glass shard(s) that are similar in composition to scoria-and-ash flow producing eruptions (e.g. shards in samples E03-37, E02-28, E02-40, E02-41, E02-74/75/76, Py20, E03-78; Fig. 3-14).

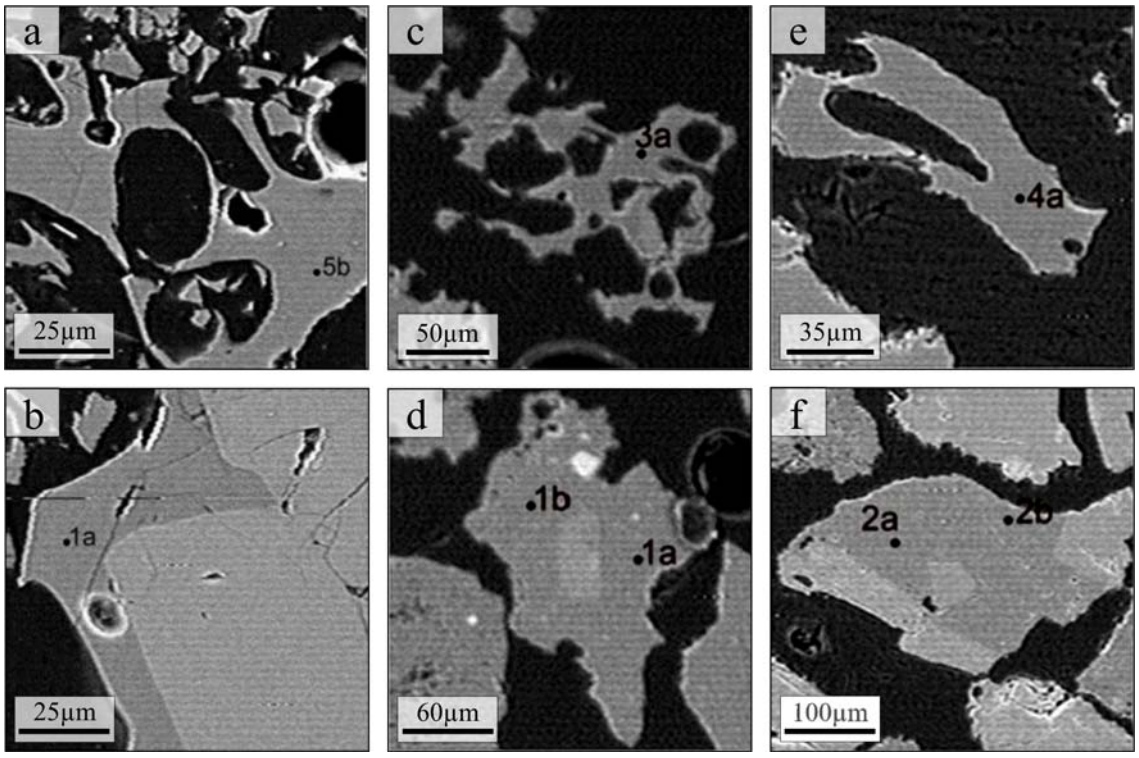


Figure 3-12: Backscatter-electron microscopy images of individual glass shards. Different glass shard shapes within individual samples are illustrated (top: vesicular, partially deformed; bottom: dense and angular). Label in images gives analysis number and approximate beam location (black dot). Grey=glass; light grey=minerals; black=epoxy. a-b) Tahurangi Ash sample (T04-98) with chemically homogenous glass shards but of different texture; a) deformed vesicles, b) dense angular. Note that the presence of large minerals (bottom) may alter vesicle distribution. c-d) Newall Ash sample (E02-75) with distinct shard textures; glass chemistry of shard (d) is similar to those of scoria-and-ash flow glass shard (c). Note regular to irregular vesicles in c). e-f) Burrell Lapilli sample (E03-35) with Taranaki glass shard (f) and Taupo volcano-derived glass shard (e), which shows a deformed vesicle.

3.2.4.2 Correlation of Tephra and Pyroclastic Flow Deposits

Deposits of the Burrell Lapilli eruption are used to illustrate how glass chemistry of various deposition types can be used as a back up tool for field-based correlation. Burrell-related fall, pumice flow, BAF, and pyroclastic surge deposits are discussed in Chapter 6; their range in glass composition is presented in Fig. 3-13.

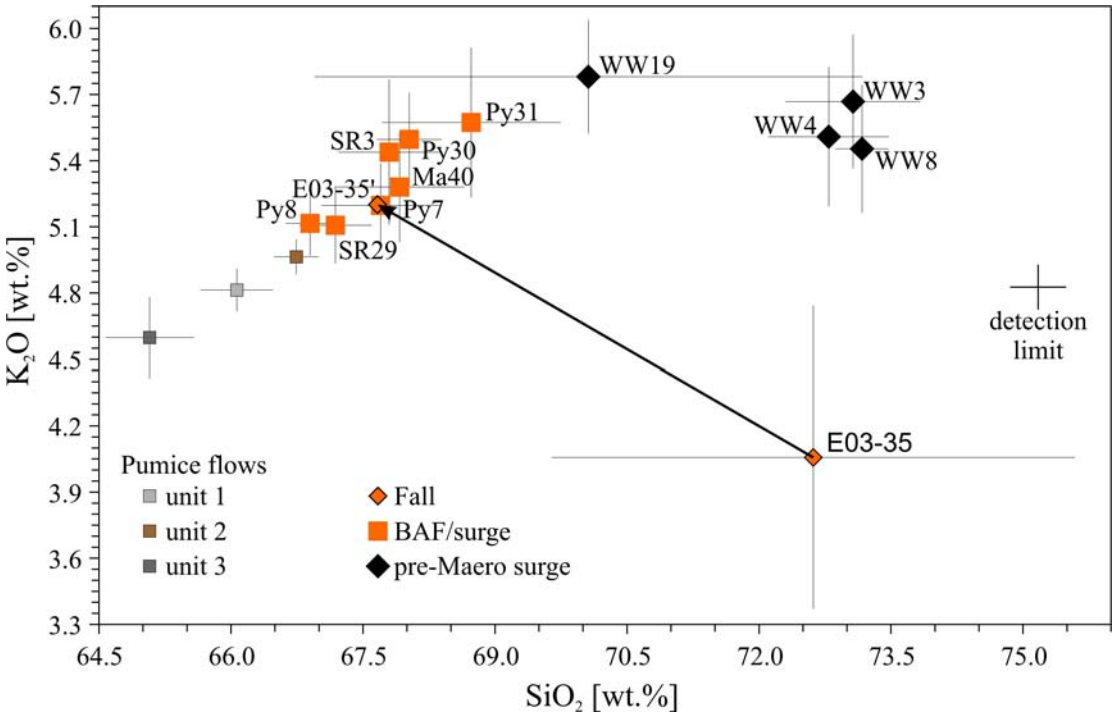


Figure 3-13: Glass chemistry of Burrell-aged deposits. The SiO_2 vs. K_2O diagram shows a general positive correlation. Highest mean silica and potassium contents are observed for BAF and surge deposits. The crosses represent the 95% confidence interval of the sample mean. The tephra sample E03-35 is bimodal containing glass shards with a signature similar to Taupo volcano (or atypical of Taranaki). If foreign glass shard analyses are excluded the sample mean is located within the field of BAF/surges (=E03-35'). Also included are sample means of a surge deposit pre-dating the Maero Eruptive Period showing a rhyolitic glass chemistry. It is noted that one sample (WW19) shows large variations and a bimodal sample population.

Individual BAF and surge deposits of the NW sector show compositional heterogeneities (e.g. Py31), however, their mean values are within 1.8 wt.% SiO_2 and 0.5 wt.% K_2O. Here the glass chemistry of medial as well as distal deposits supports the correlation based on field observations. Glass chemistry is, however, not always an effective tool as shown in two examples where two closely-spaced outcrops in Waiweranui Stream have comparable field characteristics, but their glass chemistry differs (WW19-WW8, WW20-WW6; Fig. 3-13).

Correlation of tephra deposits across different sectors of Mt. Taranaki is only partially possible, mainly due to the small-volume and restricted distribution of thin fall and surge deposits. Hence, sequences of fall and pyroclastic surge units within soils around Mt. Taranaki typically consist of thin fine to medium ash layers that are visually indistinguishable and highly variably preserved on scales of tens of metres. Correlation of some units using glass chemistry is possible, e.g. the youngest preserved tephra deposit exposed near Kahui Hut and in Ahukawakawa Swamp, both represent fall deposits of the Tahurangi Ash erupted in AD1755. Also correlated with this fall event

are surge deposits below a BAF unit of the same episode (Fig. 3-15). Similarly, tephra layers exposed on Pembroke Road and Ahukawakawa Swamp are also correlated to a BAF-related surge deposit in the Maero Stream area dated at 878 ± 39 yrs B.P. (Fig. 3-15). This correlation generates another important link between the BAF-dominated sequences of the NW flanks, with the fall-dominated sequences on northern, eastern, and southern flanks.

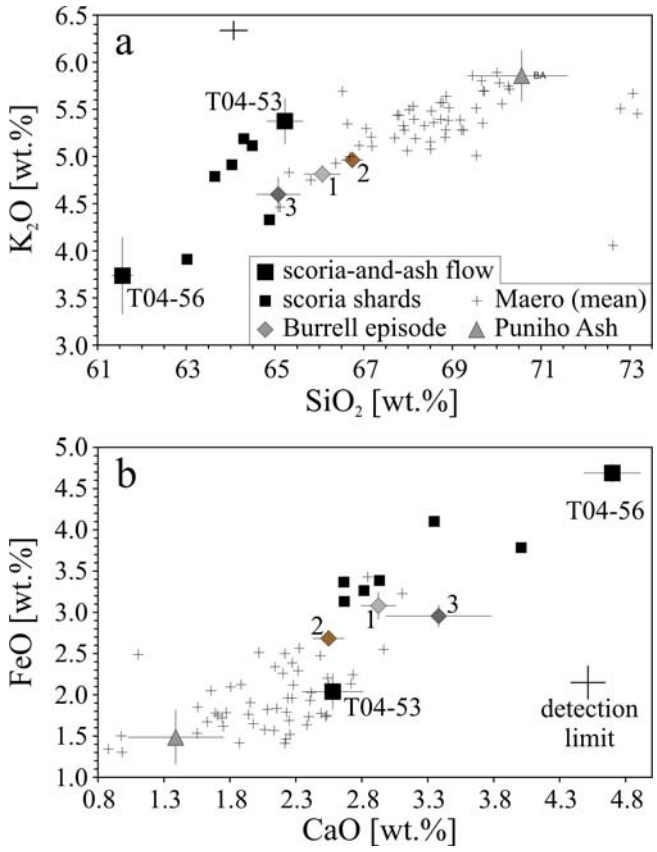


Figure 3-14: Comparison of mean sample values of scoria-and-ash flow units (T04-53, T04-56) to pyroclastic pumice flow deposits of the Burrell episode (units 1-3) and Puniho Ash, and other Maero deposits (crosses). Individual glass shards (small black squares) within deposits, other than T04-53 and T04-56, that have compositions similar to scoria-and-ash flows. a) SiO_2 vs. K_2O, b) CaO vs. FeO.

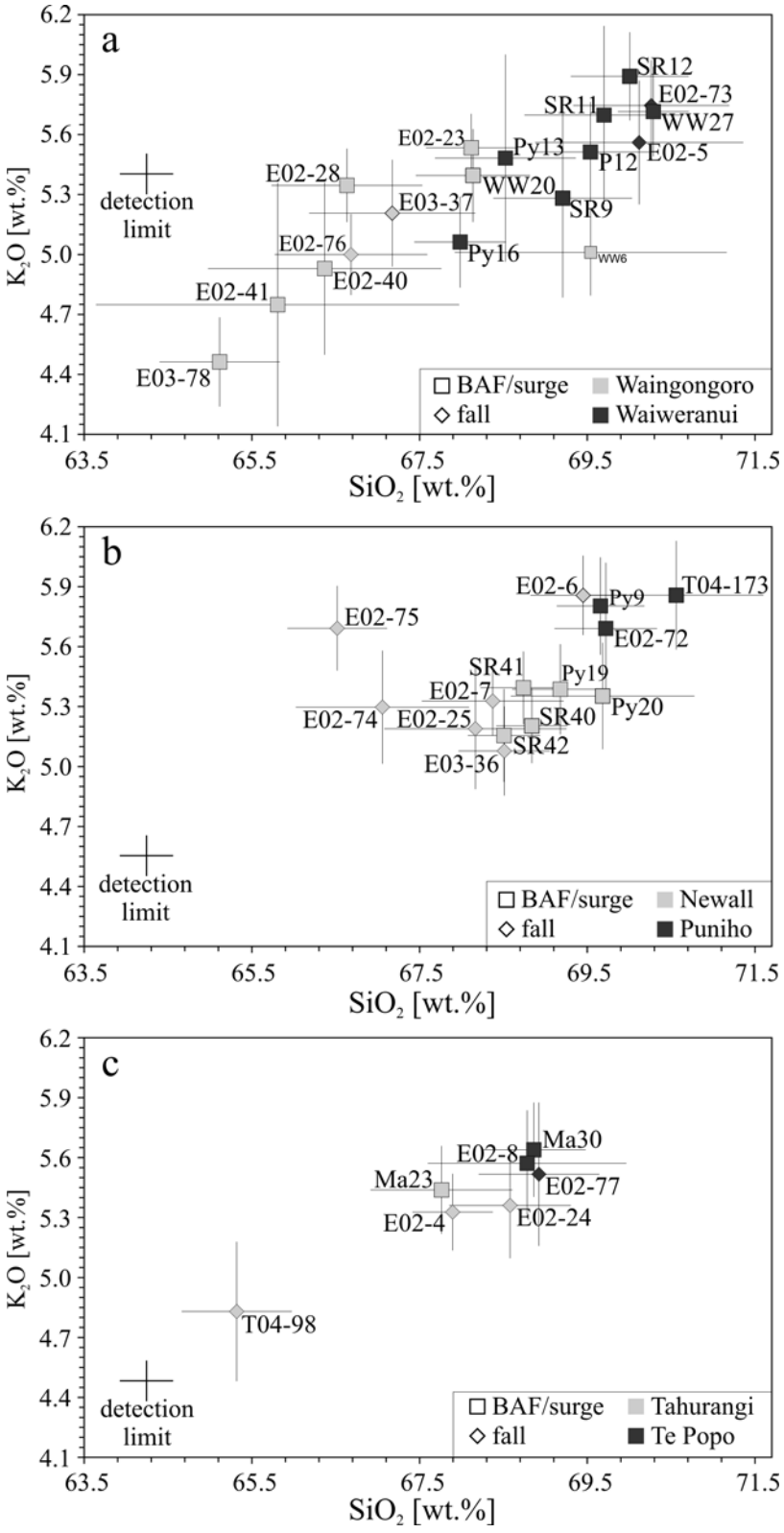


Figure 3-15: Correlation of individual tephra and pyroclastic flow units based on field studies and glass chemistry (SiO_2 vs. K_2O). a) Waingongoro and Waiweranui episodes, b) Newall and Puniho episodes, c) Tahurangi and Te Popo episodes.

3.3 Discussion

3.3.1 Eruption Frequency of the Maero Eruptive Period

Although not each individual tephra layer or pyroclastic flow deposit is uniquely characterised by its glass chemical composition, this method however greatly assisted the correlation of single eruptive units across large distances. Despite the broad glass compositional range within individual samples, tephra fall layers and pyroclastic flow and surge deposits can be correlated if field observations and stratigraphic positions within sequences are included. On this basis, tephra sequences on the northern, eastern, and southern flanks are first discussed and are then compared to pyroclastic flow and surge deposits of the western to northwestern sector of Mt. Taranaki.

On the northern, eastern and southern volcano flanks, 10 eruptive events are identified during the Maero Eruptive Period. These are represented by specific tephra units that are clearly separated by nine time breaks in the form of paleosols and/or variably clay/silt loams. The latest eruptive event is recorded within the present-day soil.

The beginning of the Maero Eruptive Period is herein defined by the first occurrence of a tephra unit stratigraphically above the Kaupokonui Tephra (on the SE flank). At reference section 3 on Pembroke Road (east sector), a single 1 cm-thick tephra layer (Hooker Lapilli) occurs 3-4 cm above Kaupokonui Tephra within a greyish-brown, weathered, fine medial ash. This tephra layer is considered representative for the first eruption of the Maero Eruptive Period. The next youngest tephra, Te Popo Ash, separated by 7 cm of greyish brown medial ash was geochemically correlated (see above) to a pyroclastic surge deposit in Maero Stream dated at 878 ± 39 yrs B.P. (Fig. 3-15). Upward toward the visually distinctive Burrell Lapilli pumice fall of AD1655, four intervening separate eruptive events (Waingongoro Ash, Newall Ash, Waiweranui Ash, and Puniho Ash) are preserved as ash fall units. In one instance, two consecutive tephra layers (Newall Ash [b], (E02-74) and Newall Ash [c], (E02-75)) have no intervening medial ash and hence are interpreted as two eruptive events belonging to a single episode (i.e. Newall episode). Above the Burrell Lapilli fall unit at this location, only one tephra is observed, the up to 10 cm-thick Tahurangi Ash erupted in AD1755. At a few other locations on the southern to southwestern sector of Mt. Taranaki, two layers comprising single layers of dense lithic lapilli occur above and below the Tahurangi ash. The youngest layer is attributed to the Pyramid eruptive episode (cf. Chapter 5).

The succession of tephra layers and their allocation into the stratigraphic sequence is summarised in Table 3-5. The dating of individual events has been approximated by combining results of botanical studies with thicknesses of paleosols and medial ash. The break between deposits of the previous members of Burrell Ash and Burrell Lapilli is marked by a 3 cm thick layer of medial ash with evidence of soil development (a paleosol), interpreted to represent a period of c.70 yrs (Lees and Neall, 1993). A similar period of repose is thought to occur between the previous members of Burrell Ash and Waiweranui Ash due to a 3 cm thick medial ash paleosol (Lees and Neall, 1993). Using a similar approach, the thicknesses of paleosols/medial ash accumulations at Pembroke Road can be used to give a rough idea of the period of repose between events. These estimates correlate well to those from botanical studies, at least for the last six eruptions. By adding the approximated periods of repose an age of c.AD860 results for Kaupokonui Tephra, which is in broad agreements to the mid point of calibrated calendar age range of AD400-1050 (Table 3-5).

The correlation of these fall and pyroclastic surge units around the volcano to BAF and surge units on the main NW depositional axis is more complicated. This is partly due to their restricted distribution and tight confinement near, or within valleys. While closely spaced outcrops can be correlated successfully, the correlation of BAFs over catchment boundaries and across distances of >400 m can be impossible, since their deposit characteristics may vary considerably, especially in distal reaches. In addition, soil development and accumulation of medial ash between eruptive events appears to have occurred much more slowly than on the eastern flanks and these horizons may be easily eroded by the violent and erosive BAFs. Hence, periods of repose may not always be recognised in these coarse BAF sequences. By consideration of field observations, glass chemical compositions and available ^{14}C dates, seven eruptive episodes can be identified from deposits in the medial area on the NW sector of Mt. Taranaki (cf. Maero type section). Deposits from four of these are recognised at distal reaches.

How the emplacement of lava flows fits into this sequence are not yet considered in this stratigraphy. Their effusion is probably not accompanied by significant ash fall. The generation of scoria-and-ash flows may be associated with lava flow eruptions or represent single eruptive events. ‘Foreign’ glass shards were found within blast/surge and tephra fall deposits (see above), which show silica compositions intermediate to the scoria-and-ash flow producing events and lava dome-producing eruptions. Individual

Table 3-5. New tephrostratigraphy of the Maero Eruptive Period .

Chronostratigraphy			Lithostratigraphy				Deposits		Age		
Eruptive Period	Episode number	Episode	Formation	Member	Units	Code	East-South sector	West-Northwest sector	AD	^{14}C [yrs B.P.] Tephra[1]	^{14}C [yrs B.P.] Pyroclastic flows[2]
Maero Eruptive Period	**X**	Pyramid	Maero Formation	Pyramid Rock Avalanche Pyramid Dome Pyramid Lapilli		X-R X-D X-L	single lithic layer; proximal	rock avalanche; medial remnant summit dome	1839-1866		
	IX	Tahurangi		Tahurangi Ash Tahurangi Breccia	 b a	IX-A IX-Bb IX-Ba	fine to medium ash layer; distal	2 major BAFs; surges; distal	1755[4]		225 ± 55, <250
	VIII	Mangahume		Mangahume Lapilli		VIII-L	single lithic layer; proximal	no correlation possible			
	VII	Burrell		Burrell Lapilli Burrell Breccia B Burrell Breccia A	 3 2 1 	VII-L VII-BB3 VII-BB2 VII-BB1 VII-BA	widespread pumice lapilli grey pumice flow; medial brown pumice flow; medial grey pumice flow; medial	grey pumice flow; medial brown pumice flow; medial grey pumice flow; medial 1 major BAF; surges; distal	1655[4]	300 ± 60 400 ± 60	 447 ± 40
	VI	Puniho		Puniho Ash Puniho Breccia		VI-A VI-B	fine to medium ash layer; surge; medial	1 major BAF; 1 pumice flow; surges; medial	1440-1660[5]		305 ± 39, 382 ± 39
	V	Waiweranui		Waiweranui Ash Waiweranui Breccia		V-A V-B	fine to medium ash layer; often shower-bedded; medial	1 major BAF; surges; distal	1390-1520[5]		447 ± 40; 453 ± 43; 475 ± 42; 468 ± 42
	IV	Newall		Newall Ash Newall Breccia	c b a b a	IV-Ac IV-Ab IV-Aa IV-Bb IV-Ba	fine ash layer; medial fine ash layer; medial single lithic layer; medial	1 major BAF; surges; distal 1 blast; distal	1270-1420[5]		605 ± 42, 649 ± 46, 387 ± 43
	III	Waingongoro		Waingongoro Ash		III-A	fine ash layer; medial	no correlation possible	1310-1630[5]	470 ± 55	
	II	Te Popo		Te Popo Ash Te Popo Breccia		II-A II-B	fine ash layer; medial	1 major BAF; surges; medial	1030-1260[5]		878 ± 39
	I	Hooker		Hooker Lapilli		I-L	single pumice/lithic layer; medial	no correlation possible			
			Kaupo-konui Tephra						400-1050[5]	1390 ± 150	

[1] radiocarbon data of Wellman (1962), Topping (1974), and McGlone et al. (1988).
[2] radiocarbon data from Cronin et al. (2003).
[3] see Table 3-2.
[4] Druce (1966).
[5] calibrated radiocarbon age (95.4% probability) using the software OxCal.

analyses were compared and arranged into two groups[4]. The tephra marker bed at 878 ± 39 yrs B.P. (Te Popo Ash) contains group 1 'foreign' shards whereas the next two younger units at the same location (Waingongoro Ash and Newall Ash) contain group 2 glass shards. If those analysed glass shards are juvenile and their chemistry is representative for their respective eruptions, then at least two additional eruptions must have occurred within the Maero Eruptive Period. The first event occurred at or just prior to 878 ± 39 yrs B.P. (i.e. Te Popo eruptive episode), the second one at or preceding the Waingongoro eruptive episode. Those 'foreign' shards within the next younger unit (Newall Ash c; sample E02-74) do not necessarily need to represent a separate effusive, lava flow-producing event and were likely picked up by this event. The two scoria-and-ash flow deposits on the upper south flank as well as the South Flow cannot be clearly integrated into the stratigraphic sequence, but field observations and glass chemical studies indicate that only the deposits within the Opua amphitheatre are related to the Maero Eruptive Period, possibly a correlative to the Waingongoro eruptive episode (post 878 ± 39 yrs B.P.). Since at high altitudes above the scrub line the scoria-and-ash flow deposits and the South Flow are only overlain by Burrell-aged deposits, lava flow emplacement may have occurred just prior to the sub-Plinian event [Burrell Breccia (B)].

By combining the frequency of eruptions in each sector, a total of at least 10, and possibly 12-14, events result. Ten tephra layers occur in the eastern to southern sector, which in parts can be correlated to the western to northwestern sector. In addition, at least two lava flow-producing eruptions and possibly two further eruptions producing scoria-and-ash flows may have occurred. This interpretation is based on the assumption that each dome-forming and explosive eruption produced a tephra layer(s), either as a single lithic layer (e.g. Pyramid Lapilli), as thin, and layered fine to medium ash close to source (e.g. Puniho Ash) or as widespread pumice tephra layer (Burrell Lapilli). Although 12-14 individual events could be identified, it is currently not known whether transitions occurred between lava flow- and lava dome-forming eruptions. Also, deposits of small events such as the Pyramid eruption may have not been preserved or found.

[4] Note the grouping is based only on a total of 19 analyses.

3.3.2 Comparison to the Previously Known Stratigraphy

The new versus old stratigraphy of the Maero Eruptive Period (Table 3-2) coincidentally implies no difference in the total number of events, if the minimum number of 12 eruptive events is used. There was a lack of knowledge of volcanic phenomena at the time of Grant-Taylor (1964) and Druce (1966). Hence, pyroclastic flow and surge deposits with/without carbonised wood were often described as lapilli beds and regarded as fall deposits. Consequently, some of those lapilli units only found in the NW sector were designated as individual eruptive events. The best examples are the previously known Puniho Lapilli 1 and 2 (see Table 3-1; Table 3-2) with the type section located within the triangular area NW of Puniho Hill (see Fig. 3-10; Druce, 1966). This type section is reinterpreted as a succession of pyroclastic surge deposits, which are predominantly related to BAFs. For instance, Puniho Lapilli 2 of Druce (1966) is reinterpreted to be related to a BAF deposit of the Tahurangi eruption (see Chapter 5). As described above, this triangular area was only inundated by pyroclastic surges due to its morphological characteristics. Therefore, this area is unsuitable as type locality for individual eruptions. It is difficult to correlate individual pyroclastic surge units found in this area to BAF deposits. Information such as componentry, glass shard morphology and composition and/or radiocarbon dating are needed.

Similar approaches led to the recognition of Newall and Waiweranui Lapilli as individual beds and hence eruptions, although there was only limited support by the tephrostratigraphic sequence known from the east flank of Mt. Taranaki. Type sections for those units again refer to pyroclastic surge and BAF deposits on the NW sector. Identification and correlation of deposit sets of very similar appearance generated an artificially high eruption frequency, e.g. Puniho Lapilli 1 and 2. As a consequence of Druce's (1966) established stratigraphy, eruption names were maintained. For example, Topping (1974) described a tephra sequence on the east flank of Mt. Taranaki (see Fig. 3-5) and correlated individual layers to those of Druce (1966). According to his correlations, a 0-10 mm thick layer of grey lithic fragments was identified as Newall or Waiweranui Lapilli. Yet 5 cm below it a similar lithic layer appears but was ignored in his interpretation (Topping, 1974).

In the episode-by-episode approach of Cronin et al. (2003), the results of botanical studies (cf. McGlone et al., 1988; Lees and Neall, 1993) were not considered leading to inconsistencies in their reconstruction of the eruptive sequence. For example, Burrell

Lapilli and Burrell Ash were grouped into one eruptive episode (see Table 3-3) although it was earlier interpreted that a period of c.70 years separates the events (see Table 3-2).

Paleomagnetic studies suggested the emplacement of lava flows on the NE sector at 700 and 400 yrs B.P. (Downey et al., 1994). These may be imprecise due to unavailability of a paleosecular variation curve available for New Zealand at that time (Downey et al., 1994), although it has since been found that the relevant curve is very similar to the one used in the analysis (R.B. Stewart, pers. comm., 2007). There may also be inconsistencies in the lava flow stratigraphy used in their studies because their classified 400/700 yrs B.P. lava flows of the NE flank are older than their Summit lava flow group. In addition, it was interpreted by Cronin (1991) that the youngest lava flow of the present intact crater rim is located in the south. Despite this, some lava flows were considered as Newall-equivalent eruptives (cf. Stewart et al., 1996; Cronin et al., 2003).

Based on the current study, only the South Flow and its underlying flow of the southern crater rim (i.e. units 1 and 2; see Fig. 3-8) appear to have been erupted with certainty during the Maero Eruptive Period. Further, no data are available which may indicate lava flow emplacement on the western flank in early Maero times because the western crater rim has been removed. The Turtle is the only remnant lava preserved here, likely representing part of a former coulée.

3.3.3 Tephrostratigraphy of the Maero Eruptive Period

During the Maero Eruptive Period, at least 10 eruptive episodes occurred that produced tephra fallout and/or pyroclastic BAF and surge deposits. Glass shard chemistry indicates that probably two eruptions producing scoria-and-ash flows may have occurred prior to the Newall eruptive episode. The tephrostratigraphy of the Maero Eruptive Period is presented in Table 3-5 with individual eruptive episodes. Former names have been retained where appropriate.

From the observed 10 tephra layers found on the eastern to southern flanks of Mt. Taranaki seven can be correlated to the NW sector. The oldest eruption of the Maero Eruptive Period, the Hooker[5] eruptive episode, is only preserved as a single incomplete layer of pumice and lithic fragments (Hooker Lapilli) on the eastern flank. A possible

[5] Named after L.O. Hooker (1873-1950); this lapilli layer was also found on the track towards Hooker Shelter.

correlative on the medial NW sector was not found, however, due to the limited extent and volume of the fall, surge and/or BAF deposits associated with this event may have been buried or eroded by subsequent events. Te Popo[6] Ash of the Te Popo eruptive episode is the most important marker bed for the early Maero Eruptive Period since it can be correlated to pyroclastic surge and BAF deposits on the NW sector dated at 878 ± 39 yrs B.P. These deposits directly overlie a >1 m thick brown clay loam soil, its upper portion dated at 1975 ± 50 yrs B.P. (Neall, 1979). The next youngest Waingongoro[7] eruptive episode produced a tephra layer (Waingongoro Ash) that was dated at 470 ± 55 yrs B.P. (Topping, 1974). The fine ash has been found on the eastern flank only in medial reaches; no correlative deposits were identified on the NW flank.

The Newall eruptive episode is of importance since it initiates the period of high magma discharge in this and subsequent eruptions. On the eastern flank this eruption is recognised as two medial fine to medium ash layers [Newall Ash (b) and (c)] partially overlying a single lithic layer [Newall Ash (a)]. On the NW sector a blast deposit [Newall Breccia (a)] is found up to 14 km from the summit. This event is likely to be the trigger for the Newall eruptive episode during which a major part of the western crater rim appears to have been removed. One major BAF sequence [Newall Breccia (b)] and several surge deposits were identified at medial to distal locations on the NW sector. The two tephra layers preserved on the east flank could be related to any of the event deposits of the NW and since no noticeable time gap is recorded they are considered as one eruptive episode. Radiocarbon dates suggest a calendar age between AD1270-1420 for the onset of the Newall eruptive episode.

The following Waiweranui eruptive episode is often represented by a bedded fine to medium ashfall unit (Waiweranui Ash) on the eastern flanks of Mt. Taranaki. The NW equivalent deposits comprise one major BAF deposit (Waiweranui Breccia) and several surge deposits preserved at medial to distal reaches. Although a brief period of repose between Newall Lapilli and Waiweranui Lapilli was indicated by Druce (1966), a much longer time break (90 yrs?) is interpreted from accumulation of medial ash at the Pembroke Road reference section (east sector). According to ^{14}C dates, an eruption time for Waiweranui episode between AD1390-1520 is suggested.

About 70 yrs later at c.AD1585 (^{14}C date: AD1440-1660) the Puniho eruptive episode began; the observed deposit on the east flank comprises medial fine to medium ash

[6] Named after Te Popo Stream on the east flank of Mt. Taranaki.
[7] Named after Waingongoro Stream where at its upper reaches a Maori oven was found (Topping, 1974).

(Puniho Ash), often related to a pyroclastic surge. One medial pyroclastic pumice flow deposit, a distal BAF (Puniho Breccia) and pyroclastic surge deposits found on the NW sector can also be related to this event. The Puniho episode was preceded and succeeded by periods of repose of approximately 70 yrs (McGlone et al., 1988; Lees and Neall, 1993).

The only sub-Plinian eruption within the Maero Eruptive Period is recorded as Burrell eruptive episode, which occurred in AD1655. Widespread pumice lapilli fallout (Burrell Lapilli) is observed on the NE-E-SE flanks including three distal pyroclastic pumice flows [Burrell Breccia (B) units 1-3; cf. Chapter 5]. On the NW sector this eruptive episode is recorded as a major BAF [Burrell Breccia (A)], pyroclastic surge and three pyroclastic pumice flow deposits [Burrell Breccia (B) units 1-3]. No fallout deposits are observed here. Pyroclastic flows are preserved >13 km from source.

Burrell Lapilli is overlain by a single lithic layer found near the old Mangahume Hut site (see Fig. 3-6). This proximal fall deposit is termed Mangahume Lapilli[8]. However, it cannot be correlated to any deposit found on the NW sector. It is possible that this eruptive event may only represent a minor lava dome-producing eruption similar to the youngest eruption of Mt. Taranaki (cf. Chapter 5). Due to an anticipated small erupted volume, associated deposits are probably only found in proximal reaches either represented by syn-eruptive rock falls or small BAFs, or post-eruptive by rock avalanche, debris flow or lahars.

The Tahurangi eruptive episode began at c.AD1755 based on tree ring dating and peat accumulation rates (Druce, 1966). On the eastern site of the mountain Tahurangi Ash is preserved in distal reaches as thin ash pockets; at medial locations it is composed of up to 10 cm thick, fine to medium ash, often constituting the thickest ash layer found. This may be explained by the observation that a distal and a medial BAF deposit [Tahurangi Breccia (a) and (b)] can be correlated to the Tahurangi episode indicating a possible higher total magma discharge.

The latest eruption of Mt. Taranaki, the Pyramid[9] eruptive episode (cf. Chapter 5), produced a lava dome (Pyramid Dome) partially preserved in the present summit crater. This episode is recorded in the tephrostratigraphic sequence on the southern flank as proximal single lithic layer (Pyramid Lapilli). In historic time (pre-AD1885), a cold lava

[8] Named after Mangahume Stream on the south flank of Mt. Taranaki.
[9] Named after the morphological features Big and Little Pyramid on the NW flank of Mt. Taranaki.

dome collapse occurred producing a rock-avalanche deposit (Pyramid Rock Avalanche) on the NW sector. Although the eruption date is poorly constrained, it is concluded that the eruption presumably took place between AD1840 and AD1866 based on dome cooling calculations and historical reports (cf. Chapter 5).

3.4 References

Alloway, B., Neall, V.E. and **Vucetich, C.G.** 1995. Late Quaternary (post 28,000 year B.P.) tephrostratigraphy of northeast and central Taranaki, New Zealand. *Journal of the Royal Society of New Zealand* 25, 385-458.

Clarkson, B.D. 1990. A review of vegetation development following recent (<450 years) volcanic disturbance in North Island, New Zealand. *New Zealand Journal of Ecology* 14, 59-71.

Cronin, S.J. 1991. The geology of the summit of Mt. Egmont. Unpublished BSc Honours thesis. Massey University, Palmerston North, New Zealand.

Cronin, S.J., Neall, V.E., Stewart, R.B. and **Palmer, A.S.** 1996. A multiple-parameter approach to andesitic tephra correlation, Ruapehu volcano, New Zealand. *Journal of Volcanology and Geothermal Research* 72, 199-215.

Cronin, S.J., Neall, V.E., Palmer, A.S. and **Stewart, R.B.** 1997. Methods of identifying late Quaternary rhyolitic tephras on the ring plains of Ruapehu and Tongariro volcanoes, New Zealand. *New Zealand Journal of Geology and Geophysics* 40, 175-184.

Cronin, S.J., Stewart, R.B., Neall, V.E., Platz, T. and **Gaylord, D.** 2003. The AD1040 to present Maero eruptive period of Egmont Volcano, Taranaki, New Zealand. Abstract. *Geological Society of New Zealand Miscellaneous Publication* 116A, 43.

Downey, W.S., Kellett, R.J., Smith, I.E.M., Price, R.C. and **Stewart, R.B.** 1994. New paleomagnetic evidence for the recent eruptive activity of Mt. Taranaki, New Zealand. *Journal of Volcanology and Geothermal Research* 60, 15-27.

Druce, A.P. 1966. Tree-ring dating of recent volcanic ash and lapilli, Mt Egmont. *New Zealand Journal of Botany* 4, 3-41.

Fisher, R.V. 1995. Decoupling of pyroclastic currents: hazards assessments. *Journal of Volcanology and Geothermal Research* 66, 257-263.

Franks, A.M. 1984. Soils of Eltham County and the tephrochronology of central Taranaki. Unpublished PhD thesis. Massey University, Palmerston North, New Zealand.

Grant-Taylor, T.L. 1964. Volcanic history of western Taranaki. *New Zealand Journal of Geology and Geophysics* 7, 78-86.

Hoblitt, R.P. and **Kellog, K.S.** 1979. Emplacement temperature of unsorted and unstratified deposits of volcanic rock debris as determined by paleomagnetic techniques. *Geological Society of America Bulletin* 90, 633-642.

Lacroix, A. 1904. La Montagne Pelée et ses éruptions. Masson et Cie. Paris.

Lees, C.M. and **Neall, V.E.** 1993. Vegetation response to volcanic eruptions on Egmont Volcano, New Zealand, during the last 1500 years. *Journal of the Royal Society of New Zealand* 23, 91-127.

Lowe, D.J. 1988. Stratigraphy, age, composition, and correlation of late Quaternary tephras interbedded with organic sediments in Waikato lakes, North Island, New Zealand. *New Zealand Journal of Geology and Geophysics* 31, 125-165.

May, D.J. 2003. The correlation of recent tephra with lava flows on Egmont volcano, Taranaki, New Zealand using evidence of mineral chemistry. Unpublished Masters thesis. The University of Auckland, Auckland, New Zealand.

McGlone, M.S. 1982. Modern pollen rain, Egmont National Park, New Zealand. *New Zealand Journal of Botany* 20, 253-262.

McGlone, M.S. and **Neall, V.E.** 1994. The late Pleistocene and Holocene vegetation history of Taranaki, North Island, New Zealand. *New Zealand Journal of Botany* 32, 251-269.

McGlone, M.S., Neall, V.E. and **Clarkson, B.D.** 1988. The effect of recent volcanic events and climatic changes on the vegetation of Mt Egmont (Mt Taranaki), New Zealand. *New Zealand Journal of Botany* 26, 123-144.

Neall, V.E. 1972. Tephrochronology and tephrostratigraphy of western Taranaki (N108-109), New Zealand. *New Zealand Journal of Geology and Geophysics* 15, 507-557.

Neall, V.E. 1973. Some aspects of western Taranaki geology and pedology. Unpublished PhD thesis. Victoria University of Wellington, Wellington, New Zealand.

Neall, V.E. 1979. Sheets P19, P20, and P21. New Plymouth, Egmont and Manaia. 1st ed. Geological map of New Zealand 1:50,000. 3 maps and notes. New Zealand Department of Scientific and Industrial Research. Wellington.

Neall, V.E. 2003. The volcanic history of Taranaki. Institute of Natural Resources, Massey University, *Soil & Earth Sciences Occasional Publication* 2.

Neall, V.E., Stewart, R.B. and **Smith, I.E.M.** 1986. History and petrology of the Taranaki volcanoes. In: **Smith, I.E.M.** (ed.) Late Cenozoic volcanism. *Royal Society of New Zealand Bulletin* 23, 251-263.

Oliver, W.R.B. 1931. An ancient Maori oven on Mount Egmont. *Journal of the Polynesian Society* 40, 73-80.

Platz, T. 2001. Mapping and characterisation of the volcaniclastic Maero formation deposits on the northwestern sector of Egmont volcano (Mt. Taranaki), New Zealand. Unpublished Diploma mapping thesis. Ernst-Moritz-Arndt Universität, Greifswald, Bundesrepublik Deutschland.

Platz, T., Cronin, S.J., Smith, I.E.M., Foley, S.F., Neall, V.E. and **Stewart, R.B.** 2004. Glass chemistry as a tool for tephra correlation: a new statistical approach on <1000 year old tephra deposits on Egmont volcano, Mt. Taranaki, New Zealand. Abstract. *Geological Society of Australia* 73, 284.

Rosenthal, A. 2005. Mapping and characterisation of the eastern Fanthams Peak lavas, Egmont Volcano, Taranaki, New Zealand. Unpublished Diploma mapping thesis. Technische Universität Bergakademie Freiberg, Freiberg, Bundesrepublik Deutschland.

Shane, P. 2000. Tephrochronology: a New Zealand case study. *Earth Science Reviews* 49, 223-259.

Shane, P.A.R. and **Froggatt, P.C.** 1994. Discriminant function analysis of glass chemistry of New Zealand and North American tephra deposits. *Quaternary Research* 41, 70-81.

Stewart, R.B., Price, R.C. and **Smith, I.E.M.** 1996. Evolution of high-K arc magma, Egmont volcano, Taranaki, New Zealand: evidence from mineral chemistry. *Journal of Volcanology and Geothermal Research* 74, 275-295.

Taylor, N.H. 1953. The ecological significance of the central North Island ash showers: the soil pattern. *Proceedings of the New Zealand Ecological Society* 1, 11-12.

Topping, W.W. 1972. Burrell Lapilli eruptives, Mount Egmont, New Zealand. *New Zealand Journal of Geology and Geophysics* 15, 476-490.

Topping, W.W. 1974. A 1480 A.D. Maori oven from Mount Egmont, New Zealand. *New Zealand Journal of Science* 17, 119-122.

Turner, M.B., Cronin, S.J., Bebbington, M.S. and **Platz, T.** 2007. Developing probabilistic eruption forecasts for dormant volcanoes: a case study from Mt Taranaki, New Zealand. *Bulletin of Volcanology* (DOI: 10.1007/s00445-007-0151-4).

Watanabe, K., Ono, K., Sakaguchi, K., Takada, A. and **Hoshizumi, H.** 1999. Co-ignimbrite ash-fall deposits of the 1991 eruptions of Fugen-dake, Unzen Volcano, Japan. *Journal of Volcanology and Geothermal Research* 89, 95-112.

Wellman, H.W. 1962. Holocene of the North Island of New Zealand: a coastal reconnaissance. *Transactions of the Royal Society of New Zealand Geology* 1, 29-99.

Chapter 4 Improving the Reliability of Microprobe-based Glass Analyses

This chapter addresses problems in correlating andesitic tephra units using glass chemistry. A simple evaluation procedure is presented to examine glass compositional datasets for contaminated hybrid glass-mineral analyses.

Chapter 4 represents the full version of a published journal paper. Its format has been altered to match the overall thesis.

Title Improving the reliability of microprobe-based analyses of andesitic glasses for tephra correlation.

Authors Thomas Platz, Shane J. Cronin, Ian E.M. Smith, Michael B. Turner, and Robert B. Stewart.

Status published in *The Holocene* 2007, vol. 17, 573-583.

Principal investigator	Thomas Platz
Carried out	- field description and sampling, - laboratory preparation of samples, - optical microscopy, - electron microprobe analysis. - manuscript preparation, writing and submission
Co-investigators	Shane J. Cronin, Robert B. Stewart, Ian E.M. Smith, and Michael B. Turner
Aided the study by	- providing Ruapehu glass analyses (Shane J Cronin) - providing access to and assistance with microprobe analysis - discussing results - editing and discussion of manuscript

4.1 Abstract

Andesite tephras have not been used in tephrostratigraphic studies to the same extent as rhyolitic units because they are seen as being chemically more complex than the latter. They are particularly difficult to “fingerprint” owing to apparent heterogeneity in glass analyses from single andesitic layers. Using case study tephras from two andesite volcanoes in New Zealand, Mts. Taranaki and Ruapehu, glass chemical heterogeneity is shown to be due predominantly to (1) differing particle types generated during closed- and open-vent phases of single eruption sequences, resulting in a broad range of glass compositions and (2) contaminated glass microprobe analyses by various proportions of microlite phase(s). A simple evaluation procedure using least-squares mixing calculations is presented to classify glass datasets for hybrid analyses and to estimate the proportions of the main contaminant microlite phase. By employing particle morphology studies as well as the glass-analysis evaluation procedure, variations in andesitic glass compositions can be significantly reduced. Hence this approach shows promise for enabling the use of some andesitic tephras for tephrostratigraphic correlation. This may facilitate the addition of a new degree of resolution in tephrostratigraphic records.

4.2 Introduction

Volcanic systems show behaviour that is fundamentally linked to the physico-chemical state of erupting magma. The variety of such states enables a petrological approach to be used to identify eruption sequences, as well as individual eruptions, by analyses of the products of eruptions. However, the eruptive history of a volcano is not represented equally by its different facies. The proximal or edifice part of the volcano represents accumulated lava flows erupted with little explosive violence. More widely distributed volcanic products are produced during explosive eruptions and transported up to hundreds of kilometres from the central volcano. These distal deposits are petrologically more variable (Shane and Hoverd, 2002), but they record the largest and most hazardous eruptions. Deriving a complete eruptive history requires integration of both proximal and distal records. Typically the distal deposits provide the most complete temporal record to link various parts of volcanic systems and their principal investigative tool is tephrostratigraphy. Tephra is the collective term for solid particles

ranging in size from ash to block that were erupted from a volcano and deposited from the air.

Tephrostratigraphy has underpinned our understanding of volcanic systems since Thorarinsson (1944) showed that single widespread tephra layers can be used as marker beds, and when well dated, as isochrons. The application of such isochrons as a dating tool is known as tephrochronology. Precise age determination and correlation of tephra layers are important not only for the establishment of eruption recurrence intervals at volcanoes, but are also essential for dating events such as earthquake ground motion (Kelsey et al., 1998), tsunami inundation (Nanayama et al., 2003), global/regional climate changes (Björck et al., 1992), human history (Hogg et al., 2003), and the petrological evolution of volcanic systems (e.g. Gamble et al., 1999; Andreastuti et al., 2000).

In the North Island of New Zealand, the sequence of rhyolitic tephras erupted from volcanoes of the Taupo Volcanic Zone (TVZ) is generally well established for the past c.60 ka (Froggatt and Lowe, 1990; Shane et al., 2002). Major and minor element compositions of glass and minerals have been successfully applied to the routine identification and correlation of distal eruptive units to their sources (Lowe 1988a; Eden and Froggatt, 1996; Shane, 1998). Some large volume (>>1 km^3) rhyolite tephras show homogeneous glass compositions making this characteristic one of the easiest means of correlation. In others, however, bimodal glass compositions have been identified in a number of rhyolite tephras (Shane et al., 2002; Smith et al., 2005).

Andesitic tephra units are interbedded with the rhyolite tephras in many sequences in New Zealand. In sequences younger than c.60 ka, these units erupted from either the Tongariro Volcanic Centre (TgVC, comprising Mts. Ruapehu, Tongariro and Ngauruhoe), or Mt. Taranaki (Fig. 4-1). Determining the source of these tephras as well as unequivocally correlating them to dated proximal units would add a new degree of resolution to the tephrostratigraphic record of the North Island. Shane (2005) renewed the focus on distal andesitic tephra layers, but correlating these with proximal deposits has been difficult because of the heterogeneity of the glass major element compositions and because there are few published reliable analyses of glass for proximal tephras (partly due to the problems outlined below).

The present limited use of andesite tephra layers for correlation purposes can be attributed to three prime factors. Firstly, andesitic glass rapidly alters to allophanic clay and is often poorly preserved, especially in soil-forming environments (Lowe, 1986).

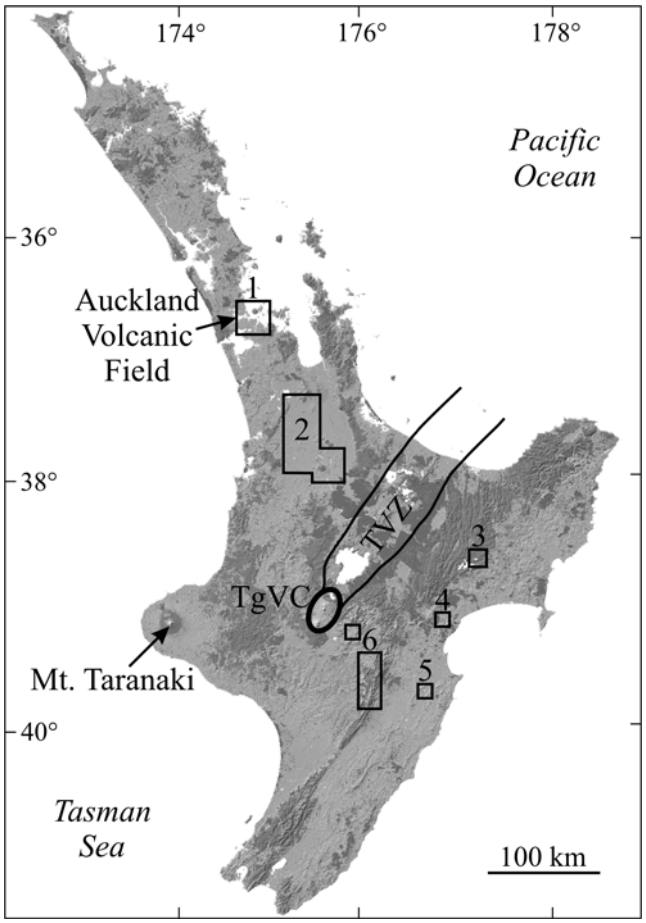


Figure 4-1: Locations of Holocene volcanic centres in the North Island of New Zealand: Auckland Volcanic Field, Taupo Volcanic Zone (TVZ), Tongariro Volcanic Centre (TgVC), Mt. Taranaki. Numbers 1-4 refer to distal andesite tephra sites: 1-Onepoto Basin/Pukaki Lagoon/Lake Pupuke (Sandiford et al., 2001; Shane and Hoverd, 2002; Shane, 2005), 2-Waikato lakes (Lowe, 1988b), 3-Kaipo Bog (Lowe et al., 1999), 4-Lake Tutira (Eden and Froggatt, 1996), 5-Lake Poukawa (Shane et al., 2002), 6-Kaimanawa Mts. and Ruahine Ranges (Froggatt and Rogers, 1990).

Secondly, andesitic volcanoes produce relatively small volume tephras (mostly <0.1 km^3) compared with those from rhyolitic centres. These low eruption volumes lead to narrowly distributed fallouts, often of very low thickness, and hence, poor preservation potential (Cronin et al., 1998). Thirdly, geochemical studies of andesitic glasses have commonly shown heterogeneous compositions. These variations are predominantly attributed to a strong influence of late-stage magma mixing/mingling and/or fractionation/crystallisation processes in the complex conduits of andesitic systems (Venezky and Rutherford, 1997; Hammer et al., 2000; Price et al., 2005). Some studies have shown that andesitic units can, in some cases, be distinguished, sourced and identified on the basis of their mineral chemistry (Donoghue and Neall, 1996), but

canonical discriminant function analysis is necessary (Cronin et al., 1996a,b). In these studies Fe-Ti oxides have proved especially useful for proximal to medial tephra distributions. However, gravity settling and winnowing within the atmosphere reduces the dispersion of denser Fe-Ti oxides and mineral particles to distal sites. As a result only glass and light minerals are typically present in distal andesitic tephras. Generally, their sources (TgVC vs. Taranaki) can be distinguished (Lowe, 1988a; Shane and Hoverd, 2002), but individual, discrete eruptives have been difficult to identify uniquely. Distinction between sources is based on the observation that Mt. Taranaki magmas have generally (although not always) high potassium contents, whereas Ruapehu eruptives have generally (with exceptions), lower K contents (Price et al., 1999). Because of these limitations, there have been very few attempts to match glass compositions to specific dated andesitic tephras (Lowe, 1988b; Eden and Froggatt, 1996; Shane, 2005).

In this paper we sound a note of warning and suggest a new way forward for the use of glass compositions in tephra correlation studies that are based on andesitic systems. The main reasons for heterogeneous glass populations in andesites are explored and, through case studies of specific tephra units from two well studied volcanoes, the difficulties of identification and correlation using glass composition are demonstrated. A new simple procedure is introduced to enable electron microprobe analysis of andesitic glass to be critically evaluated so that spurious data can be detected and discarded. Our aim is to develop sound, glass-analysis based datasets useful for correlating andesite tephras. Using the criteria proposed here, we see great potential for robust proximal-proximal and proximal-distal correlation of andesitic tephra.

4.2.1 Andesitic Volcanism, Tephra Generation and Dispersal

Tephra layers are produced at andesitic volcanoes through a wide a variety of eruptive styles, which can be summarised into two main types: (1) coeval ash associated with the effusion of lava flows and lava domes, and (2) explosive eruptions. A combination of lava emission and pumice production during the course of an eruption sequence is a common feature among andesite volcanoes (e.g. Santa Maria, Guatemala; Bezymianny, Kamchatka).

Lava flow emplacement is often associated with very small eruption columns and only minor ash is produced as thin layers, mostly on the upper flanks of the volcano (Hobden

et al., 2002). Such tephras are commonly of little use for correlation because they are poorly preserved, difficult to identify and not widely distributed. During extrusion of lava domes, tephras are produced through phreatic explosions and during dome-collapses where Block-and-Ash Flows (BAFs) are generated. BAFs are pyroclastic flows, consisting of a dense, coarse grained basal avalanche overlain by a billowing cloud of elutriated ash and gas that can decouple from the flow and travel as a separate ash cloud surge (Fisher, 1995). This elutriated cloud of ash may rise several kilometers vertically to produce regional thin fallout deposits of "co-ignimbrite" ash (Gardner et al., 1994).

Eruptions involving the explosive expansion of gas-charged magma produce the largest volumes of tephra and highest eruption columns. These types of events at NZ andesitic volcanoes have typically generated >10 km-high plumes with fall deposits covering several thousand square kilometres (Alloway et al., 1995; Donoghue, et al., 1999). Often such highly explosive events at andesitic volcanoes are immediately preceded by the emplacement of a lava dome, such as at Merapi, Indonesia (Boudon et al., 1993) and Redoubt volcano, Alaska (Gardner et al., 1994).

The style of eruption is governed by the physical properties of erupted magma (i.e. viscosity, temperature, melt composition, water content, vesicularity) as well as the range of processes that occur as andesitic magma approaches the surface. The most important of these processes is the mixing or mingling of magma batches, enabled by the relatively low viscosity of andesitic magmas in comparison to rhyolitic ones (Murphy et al., 1998; Roman et al., 2006). Mixing or mingling may be of distinct magmas, but because there are commonly many small batches of melt accumulating under similar conditions in andesitic edifices (Gamble et al., 1999; Price et al. 2005), mixed compositions may only have subtle differences. In addition, the hot and low-viscosity melts enable high rates of fractionation/crystallisation during magma ascent (Blundy and Cashman, 2001), along with syn-eruptive degassing (Wolf and Eichelberger, 1997).

Pre- and syn-eruptive crystallisation, especially during the extrusion of lava domes, has a pronounced impact on melt composition and viscosity. As the magma progressively ascends and degasses, groundmass microlite crystallization is induced (Cashman, 1988). Most commonly, needle-like plagioclase crystals form (<10 µm in length). Their number density and distribution in the upper conduit and the lava dome are dependent on local temperature and pressure gradients, and as a result the behaviour of the

remaining melt is altered by varying degrees. As well as these processes, because andesitic magmas are generally erupted at higher temperatures than those of rhyolitic composition, post-eruptive crystallisation and microlite formation may also occur and generate fine-scale heterogeneity, for example, as a result chemical diffusion and concentration gradients in areas near (<100 µm from the solid-liquid interface) growing crystals (Best, 2003).

All of these processes are active to varying extents during the eruption of individual tephras, with rapid ascent rates and short periods of high-level pre-eruption storage imparting the lowest degrees of glass heterogeneity. If these processes operate on longer time scales, major differences in glass composition, vesicularity and even bulk rock composition can be produced (e.g. Hammer et al., 2000; Platz et al., 2007). Hence magmatic/eruptive factors may produce variable glass compositions in andesite eruptions, and also fine-scale microtextures of andesitic glass may give rise to analytical errors in its measurement by the most common method of electron microprobe analysis.

The difficulty in achieving reliable glass electron microprobe results lies in being able to distinguish clearly between groundmass glass and microlites. Plagioclase and Fe-Ti oxide minerals are the most common late-stage crystallising phases in andesitic glasses. On backscatter electron images (BSE) there is little contrast between the very similar grey-tones of tiny plagioclase microlites and glass, because both are composed predominantly of light elements (i.e. Si, Al, Ca, Na). In addition, despite the clear contrast between Fe-Ti oxide phenocrysts/microphenocrysts and groundmass-glass on BSE images, minute, nanolite oxide-crystals (200-1000 nm) are also hardly resolvable (Schlinger et al., 1986).

Particles with a hypocrystalline groundmass contain abundant needle-like plagioclase microlites of <10 µm lengths. To find a pure glass area within the groundmass for a defocused 20 µm electron beam can be highly challenging. Similar problems occur in highly vesicular samples where bubble walls can be as thin as 6 µm, and the intersection of bubble walls are often occupied by microlites and microphenocrysts. If the electron-beam diameter is only slightly less than the thickness of bubble walls, analyses often have low totals.

The interpretation and evaluation of glass compositional data also proves difficult because most tephras, especially andesites, show large variations commonly in SiO_2, Al_2O_3, CaO and alkali (Sandiford et al., 2001; Shane et al., 2002). Shane (2005), for example, reported a range in silica content of up to 10 wt.%, and consequently a high

range in values for other element oxides within a single tephra layer. Such wide ranges were attributed to magma fractionation/crystallization processes, a compositionally zoned magma chamber, or mixing magma batches prior to and during the eruption. The potential for contamination of glass analyses by microcrystalline phases has been considered by many scientists (e.g. Lowe, 1988a, b) but no thorough evaluation of such contamination has been made, nor has a procedure been developed to identify hybrid glass data. Hunt and Hill (2001) provided guidelines for electron microprobe analysis evaluation, but our study considers further analytical as well as volcanological aspects.

4.2.2 Sample Sites

We chose tephras from two well studied New Zealand andesite volcanoes, Mts. Ruapehu and Taranaki. One individual andesite tephra from each of these volcanoes was chosen to demonstrate the problems inherent in using andesitic tephras for stratigraphic correlation and to introduce a glass data evaluation procedure that can circumvent some of these problems. The selected tephra units are: (1) the Burrell Lapilli sub-Plinian eruption (AD1655) of Mt. Taranaki (Platz et al., 2007), and (2) the 14 October 1995 tephra of Mt. Ruapehu (Cronin et al., 2003).

4.3 Results

4.3.1 Contrasts in Particle Texture

Thin-sectioning and microscopic analysis of tephras allows differentiation of petrographic textures within individual particles. Such a study is demonstrated in a sample from the sub-Plinian, Burrell Lapilli eruption of Mt. Taranaki. A reconstruction of the eruptive sequence of the Burrell Lapilli eruption (AD1655) shows that there were two phases to the eruption: (1) extrusion of a lava dome, followed by (2) an explosive, sub-Plinian event. Tephra fallout from the sub-Plinian eruption column was first deposited towards the SE and then as the wind shifted, the dispersal axis progressively shifted north-eastwards. Distal ash from this event has been found as far as Lake Tutira, 250 km east of Mt. Taranaki (Eden and Froggatt, 1996).

In grain-mount thin sections of Burrell tephra collected from medial locations, three types of ash particle textures were distinguished:

Type 1 - pumice particles that are highly vesicular with a glassy groundmass (Fig. 4-2a).

Type 2 - dense lithic particles that have a hypocrystalline textured groundmass dominated by plagioclase microlites and tiny Fe-Ti oxide crystals (Fig. 4-2b).

Type 3 - semi-vesicular particles with a pale brown glassy groundmass containing fewer microlites compared with type 2 (Fig. 4-2c). These particles are least common.

Type 2 and 3 particles were generated during the initial extrusive phase of the eruption and represent parts of the dome (type 2) and the upper conduit (type 3). The highly vesicular pumice clasts are clearly associated with the subsequent explosive phase. Despite the youth of these eruptive products, many of the pumice particles are slightly weathered and show a characteristic pale brown to brown appearance.

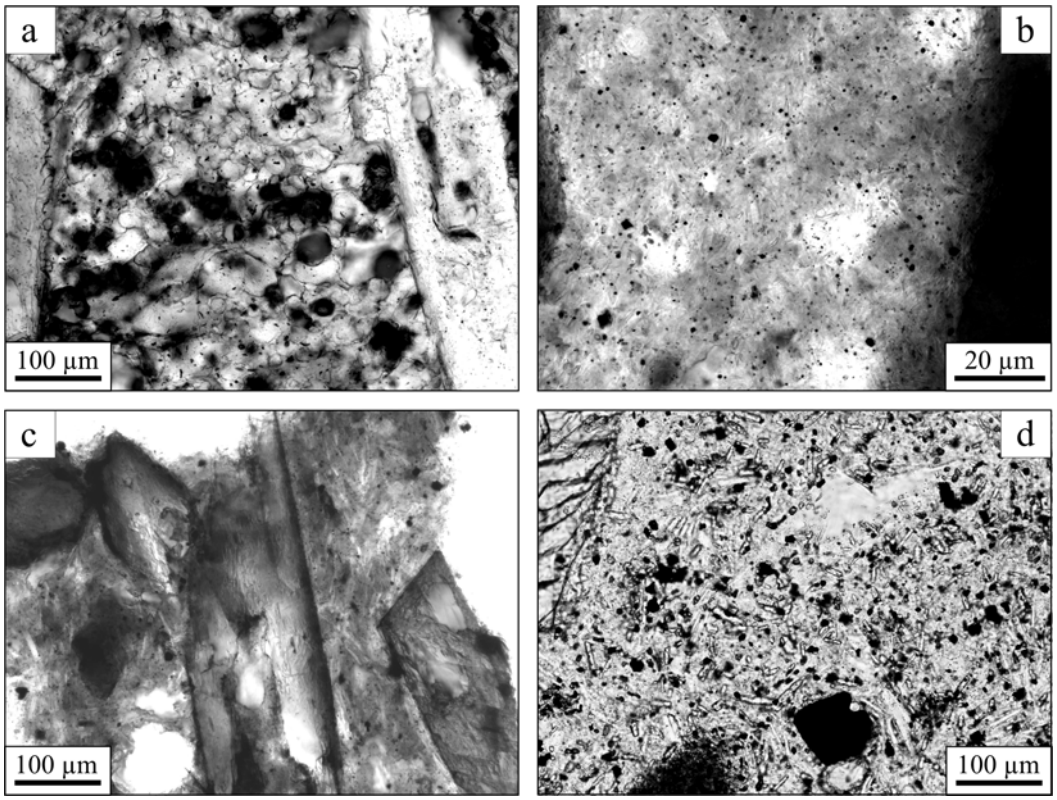


Figure 4-2: Particle textures found in Burrell Lapilli sub-Plinian fall deposits. a) pumice clast, type 1, with clear to pale brownish glass; b) hypocrystalline groundmass texture of type 2 clast showing plagioclase, Fe-Ti oxide and minor clinopyroxene microlites; c) semi-vesicular type 3 clast with brown groundmass glass, large crystals are hornblende; d) for comparison, hypocrystalline groundmass of the present summit dome of Mt. Taranaki with abundant microlites of plagioclase, Fe-Ti oxides and minor clinopyroxene. Scale bars are in µm.

4.3.2 Glass Chemistry and Data Evaluation

Compared to andesitic glass (Table 4-1), plagioclase has higher abundances of Al_2O_3 and CaO, and to some degree Na_2O, whereas SiO_2 is consequently lower (Table 4-2). If plagioclase contamination is suspected, the analyses should therefore have elevated values in Al_2O_3, CaO, and possibly Na_2O, but slightly lower values of SiO_2. In addition, the glass data population should display a broad range in these oxides compared with the restricted and complementary variation imposed by the stoichiometric limitations arising from the crystallographic structure of minerals. Standard deviations in glass compositions are typically highest for SiO_2, Al_2O_3 and CaO (Fig. 4-3), where high standard deviations for these three oxides show that contamination by plagioclase is evident.

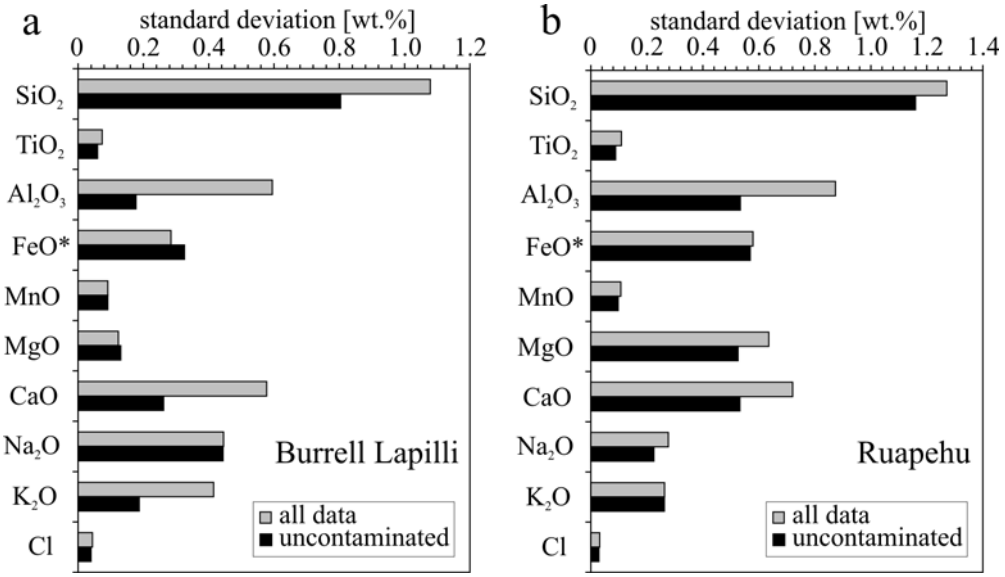


Figure 4-3: Standard deviations of all major oxides are shown for the original glass EMPA dataset and the glass dataset classed as uncontaminated by plagioclase for the Taranaki (a) and Ruapehu (b) samples. A clear reduction in SiO_2, Al_2O_3 and CaO variations is observed. See text for further details. All Fe expressed as FeO.

Two variation diagrams illustrate that glass compositions of both tephras show a generally negative correlation of Al_2O_3 with increasing SiO_2 and a positive relationship between K_2O and SiO_2 (Fig. 4-4). It is apparent that in both examples the glass population is generally oriented towards the mean compositions of the respective associated plagioclase. In both examples, data points with lowest silica contents show a strong linear relationship and plot on a glass-plagioclase mixing line (Fig. 4-4).

If contamination of glass EMPA data by a mineral phase is suspected, the best way to test the dataset is to use bivariate compositional diagrams, where an incompatible and a compatible oxide of the mineral phase are plotted. Because plagioclase consists of only

Table 4-1. Glass EMPA of Taranaki (Burrell Lapilli eruption) and Ruapehu (14. October 1995 eruption) sorted by classed uncontaminated and contaminated data points. Detection limits for Taranaki glass EMPA only. All data in wt. %.

Oxides	Detection limit	Standard deviation from a basaltic glass**	Taranaki glass classed uncontaminated															
SiO_2	0.32	-0.18	67.27	66.80	65.69	66.31	66.08	65.74	66.70	65.89	67.64	67.13	65.58	65.47	64.83	65.17	65.11	65.65
TiO_2	0.23	0.12	0.49	0.44	0.68	0.60	0.61	0.55	0.51	0.57	0.59	0.56	0.54	0.52	0.58	0.68	0.60	0.58
Al_2O_3	0.18	-0.05	16.69	16.64	16.86	16.81	16.56	16.52	16.84	16.66	16.80	16.57	17.06	16.82	16.90	16.46	17.10	16.76
FeO*	0.20	-0.04	2.93	3.06	2.86	2.99	2.72	3.32	2.75	2.79	2.79	2.50	3.48	3.34	3.52	3.62	3.33	3.30
MnO	0.20	-0.01	0.04	0.04	0.14	0.15	0.25	0.17	0.01	0.30	0.05	0.17	0.25	0.14	0.32	0.23	0.14	0.21
MgO	0.21	0.17	0.95	0.72	0.91	1.06	0.99	1.04	1.05	0.96	0.85	0.72	1.14	1.09	1.13	1.17	1.02	0.98
CaO	0.13	-0.02	2.79	2.64	3.17	2.65	2.79	2.83	2.61	2.92	2.95	2.50	3.46	3.12	3.27	2.96	3.27	2.89
Na_2O	0.32	0.05	3.72	4.30	4.87	4.04	4.88	4.57	4.35	4.89	3.61	4.45	3.44	4.60	4.68	4.72	4.50	4.58
K_2O	0.10	0.02	4.91	5.01	4.60	5.07	4.91	4.97	4.95	4.79	4.50	5.14	4.81	4.66	4.50	4.73	4.72	4.76
Cl	0.08	n.a.	0.21	0.36	0.23	0.31	0.21	0.28	0.23	0.23	0.23	0.27	0.25	0.24	0.27	0.27	0.21	0.29
Total			96.95	98.64	96.62	97.35	95.98	97.03	95.8	96.36	96.03	96.76	95.15	97.30	97.31	97.71	97.57	98.14

Oxides	Taranaki glass classed contaminated						Mean and standard deviation [uncontaminated]		Mean and standard deviation [all analyses]	
SiO_2	64.10	63.36	65.43	64.39	64.99	63.99	66.07	0.83	65.61	1.10
TiO_2	0.55	0.46	0.52	0.45	0.37	0.63	0.57	0.06	0.55	0.08
Al_2O_3	18.18	18.67	17.71	17.88	17.38	17.92	16.75	0.18	17.08	0.61
FeO*	2.97	2.81	3.04	3.03	3.09	3.11	3.08	0.34	3.06	0.29
MnO	0.16	0.00	0.00	0.16	0.12	0.18	0.16	0.09	0.15	0.09
MgO	0.87	1.03	0.81	0.85	0.91	1.00	0.99	0.13	0.97	0.13
CaO	4.03	4.74	3.73	3.86	3.61	4.26	2.93	0.27	3.23	0.59
Na_2O	4.86	4.77	4.76	4.87	4.92	5.17	4.39	0.46	4.52	0.46
K_2O	4.09	3.95	3.84	4.23	4.37	3.56	4.81	0.19	4.59	0.43
Cl	0.20	0.21	0.15	0.28	0.24	0.19	0.25	0.04	0.24	0.04
Total	96.95	97.17	98.13	97.7	97.97	98.53				

* all iron expressed as FeO.

** Inter-laboratory EMPA project (64 participating laboratories).

n.a. not analysed.

Table 4-1. (continued).

Oxides	Ruapehu glass classed uncontaminated																Ruapehu glass classed contaminated			
SiO_2	63.29	62.85	64.40	62.45	61.65	61.46	62.69	62.55	62.54	64.04	64.16	62.59	62.83	65.86	61.63	62.32	62.36	64.05	61.18	60.39
TiO_2	0.99	0.98	1.24	0.97	0.90	1.07	0.98	0.95	0.95	0.93	1.03	1.06	1.08	0.88	1.09	1.01	0.84	1.27	1.08	0.93
Al_2O_3	15.07	15.46	14.32	15.37	15.43	15.99	15.11	13.84	15.29	14.92	14.67	15.83	15.10	14.72	15.31	14.99	17.08	16.47	16.55	17.25
FeO*	6.44	6.24	7.19	6.24	7.31	6.50	6.48	7.26	6.03	5.98	6.13	6.02	6.43	5.15	7.12	6.54	5.51	6.02	6.00	5.67
MnO	0.21	0.33	0.23	0.21	0.22	0.38	0.09	0.20	0.21	0.28	0.32	0.37	0.37	0.12	0.41	0.14	0.07	0.18	0.16	0.41
MgO	2.32	2.58	1.77	2.72	2.81	2.79	2.49	4.16	2.68	2.48	2.33	2.26	2.71	1.82	2.65	2.77	1.32	1.06	2.46	2.19
CaO	5.34	5.39	4.03	6.05	5.75	6.00	5.99	5.05	5.90	5.48	5.36	5.68	5.56	4.67	5.70	5.75	6.24	4.21	6.52	7.08
Na_2O	3.74	3.86	3.48	3.56	3.57	3.55	3.60	3.22	3.66	3.34	3.67	3.80	3.53	4.13	3.61	3.97	4.15	4.26	3.67	4.08
K_2O	2.52	2.19	3.23	2.26	2.26	2.19	2.45	2.67	2.59	2.43	2.24	2.21	2.24	2.51	2.35	2.36	2.30	2.43	2.27	1.89
Cl	0.09	0.12	0.10	0.16	0.09	0.07	0.12	0.11	0.15	0.12	0.10	0.18	0.16	0.14	0.13	0.14	0.15	0.05	0.11	0.10
Total	100.27	97.61	94.15	98.16	99.20	96.93	98.96	98.52	98.13	100.20	100.34	98.65	97.36	100.60	100.88	99.40	98.31	98.47	97.80	99.28

Oxides	Mean and standard deviation [uncontaminated]		Mean and standard deviation [all analyses]	
SiO_2	63.25	1.73	62.71	1.91
TiO_2	1.03	0.09	1.00	0.12
Al_2O_3	15.04	0.63	15.60	1.19
FeO*	6.38	0.58	6.22	0.60
MnO	0.24	0.09	0.24	0.10
MgO	2.43	0.63	2.35	0.63
CaO	5.36	0.79	5.67	1.01
Na_2O	3.68	0.23	3.73	0.25
K_2O	2.45	0.33	2.36	0.34
Cl	0.13	0.04	0.12	0.04

* all iron expressed as FeO

Table 4-2. Plagioclase microlite rim and centre compositions (Burrell Lapilli eruption, Mt. Taranaki). All data in wt. %.

Oxides	xtl 1 centre	xtl 2 centre	xtl 2 rim	xtl 3 centre	xtl 3 rim	xtl 4 centre	xtl 4 rim	xtl 5 centre	xtl 6 centre	xtl 6 rim	xtl 7 centre	xtl 7 rim	xtl 8 centre	xtl 8 rim	xtl 9 centre	xtl 9 rim	Mean and standard deviation of core and rim	
SiO_2	52.13	54.34	52.85	51.24	54.02	51.84	51.10	53.69	49.46	53.42	52.91	55.10	54.70	54.42	54.28	54.63	53.13	1.60
TiO_2	0.00	0.11	0.14	0.19	0.09	0.06	0.03	0.00	0.01	0.16	0.12	0.06	0.02	0.18	0.07	0.00	0.08	0.07
Al_2O_3	28.90	28.03	28.34	29.71	28.06	29.15	29.73	28.51	30.90	28.63	28.43	27.18	28.17	28.03	27.53	27.87	28.57	0.93
FeO*	0.61	0.56	0.46	0.57	0.51	0.77	0.70	0.52	0.53	0.50	0.47	0.65	0.31	0.36	0.57	0.56	0.54	0.11
MnO	0.06	0.00	0.03	0.16	0.07	0.01	0.00	0.17	0.15	0.00	0.02	0.00	0.00	0.04	0.00	0.23	0.06	0.08
MgO	0.13	0.00	0.07	0.00	0.22	0.00	0.02	0.05	0.04	0.04	0.04	0.19	0.08	0.00	0.00	0.04	0.06	0.07
CaO	12.09	10.81	11.83	13.16	11.40	12.81	13.33	11.71	14.67	11.65	11.97	10.62	11.11	11.10	10.67	11.13	11.88	1.12
Na_2O	4.52	5.05	4.55	3.64	4.65	4.08	3.89	4.72	3.04	4.66	4.42	5.02	4.84	4.94	4.88	5.16	4.50	0.58
K_2O	0.36	0.48	0.49	0.29	0.48	0.36	0.26	0.43	0.24	0.50	0.41	0.56	0.44	0.49	0.53	0.63	0.43	0.11
Total	98.80	99.38	98.76	98.96	99.50	99.08	99.06	99.80	99.04	99.56	98.79	99.38	99.67	99.56	98.53	100.25		

* all iron expressed as FeO.

four major oxides, all other analysed oxides could be considered. In practice, it is best to use those that are well above detection limits, associated with low analytical errors and that are concentrated in the glass phase. In this case K_2O and FeO are considered as incompatible oxides although minor iron (as Fe^{3+}) can also be substituted for Si^{4+} in the plagioclase lattice.

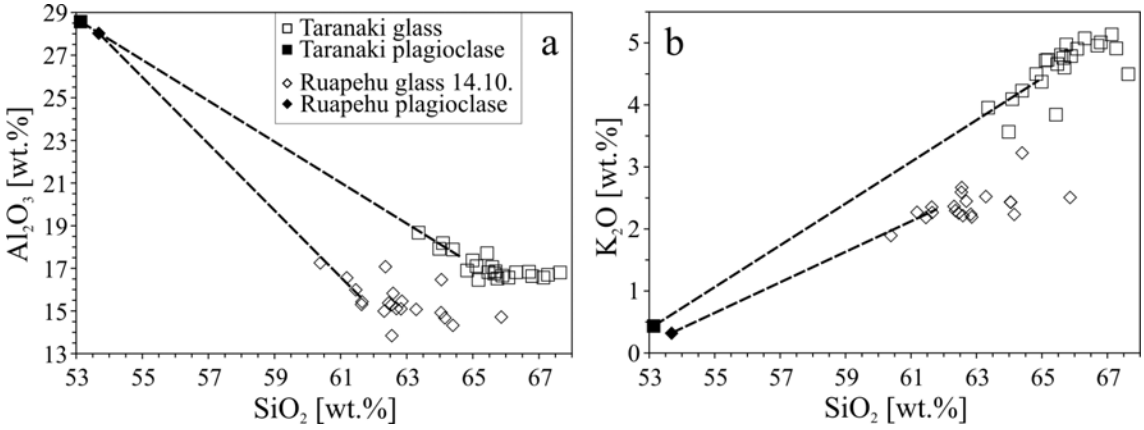


Figure 4-4: Bivariate plots of Al_2O_3 and K_2O vs. SiO_2 for Burrell Lapilli (Taranaki) and Ruapehu glass data. Data points with lowest SiO_2 show linear relationship towards mean plagioclase compositions (dashed lines).

Using this empirical approach, the Burrell dataset can be classified into contaminated and uncontaminated analyses (Fig. 4-5a-d). Iron vs. aluminium oxides proved most helpful in classifying the data and an upper threshold value of 17.1 wt.% Al_2O_3 appears to represent the limit for uncontaminated analysis. Analyses with higher alumina contents plot off the bulk population and towards the mean plagioclase composition (Fig. 4-5a). This threshold value is also notable on plots of K_2O vs. SiO_2, CaO and Na_2O with contaminated data mostly converging toward the mean plagioclase composition. In the same way, upper threshold values can be identified for CaO (3.5 wt.%) and K_2O (4.4 wt.%) corresponding to the threshold value found for Al_2O_3 (17.1 wt.%). Agreement of the data points classed as contaminated using all three threshold values gives confidence that the contamination is due to plagioclase. Hence these data must be erased from the dataset.

After applying this technique there are two points slightly off the plagioclase-glass mixing line (Fig. 4-5d-c). These likely represent a case of overlapping contamination, in this instance probably by minute Fe-Ti oxide nanolites. Data offsets from the ideal plagioclase-glass mixing line can also be due to variations in plagioclase microlite compositions, i.e. variations, especially in SiO_2 and Al_2O_3, between rim and centre of the microlites caused by substitution of Al^{3+} for Si^{4+} in tetrahedral position (Table 4-2).

Using this approach to identifying contaminated glass EMPA, the variation within the Burrell dataset can be significantly reduced as shown by the decrease in standard deviations for SiO_2, Al_2O_3, CaO and K_2O (Fig. 4-3a).

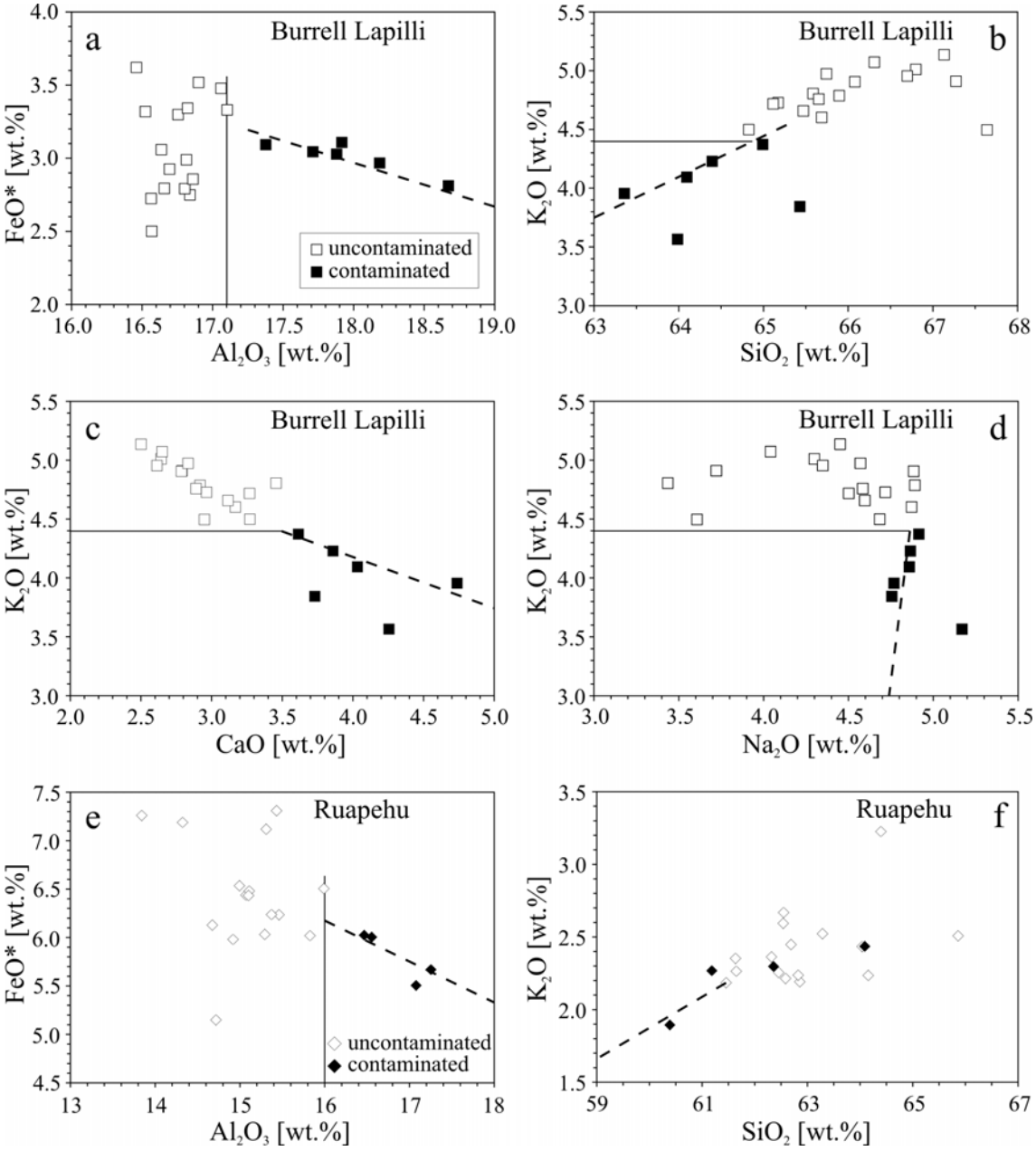


Figure 4-5: Bivariate oxide plots for Burrell Lapilli eruption, Taranaki (a-d) and 14. October 1995 eruption, Ruapehu (e-f) demonstrate how contaminated glass analyses were identified. Open symbols are classed uncontaminated, closed symbols represent hybrid glass-plagioclase analyses. Dashed lines point towards mean plagioclase compositions.

Tephra erupted during the major phase of the 1995 Ruapehu eruption on 14 October (Cronin et al., 2003) also show similar trends (Fig. 4-5e-f), despite representing a simple type of eruption event without the major differences in style identified for the Burrell event. In this case an upper threshold value of 16 wt.% Al_2O_3 appears to identify the limit of uncontaminated data. This threshold value is supported by other major oxides

with the exception of Na_2O. In this case Na_2O shows no trend towards the mean plagioclase composition. The applied procedure reduced the variation, especially in Al_2O_3, however, a large range in SiO_2 still remains (Fig. 4-3b). High standard deviations for CaO, FeO and MgO remain which may be due to contamination from microlites and nanolites of clinopyroxene, orthopyroxene and/or Fe-Ti oxide. These are common groundmass constituents in Ruapehu tephras (Cronin et al., 1997) and common microlites of orthopyroxene, although showing more contrast than plagioclase, are still difficult to distinguish from glass.

4.3.3 Estimating Plagioclase Proportions in Contaminated Analyses

Once hybrid glass-plagioclase analyses are identified, the proportion of plagioclase within the composite analysis should be calculable. In the Taranaki example a procedure is demonstrated by using four data points that plot closest to the assumed plagioclase-glass mixing line (Fig. 4-5b-c). To calculate mixing proportions requires the assumption of a composition where mixing between glass and plagioclase is thought to start. In this case, the Al_2O_3 threshold value of 17.1 wt.% is expected to equal the starting composition, and the oxides of all four contaminated data points were linearly extrapolated back to Al_2O_3 = 17.1 wt.% (Table 4-3). Mass balance calculations are then used to best fit the mixing proportion. In this example, the maximum portion of plagioclase within the hybrid analysis is estimated to be 13.7%. There is a strong linearity displayed by contaminated data points that can be used to constrain their mixing proportions. Low standard deviations (<0.21) for all oxides indicate very good agreement between analysed and calculated data points (Table 4-3).

Table 4-3. Calculation of various plagioclase mixing proportions within Taranaki hybrid glass EMPA. EMPA data in wt.%. See text for explanation.

	Plagioclase [Plg]		R^2 value of mixed data points	Starting composition[a]	Mixing proportion of plagioclase and glass including standard deviation between observed and calculated data points							
Oxides	Mean [wt.%]	1σ			2.4% Plg	1σ	6.8% Plg	1σ	9.4% Plg	1σ	13.7% Plg	1σ
SiO_2	53.13	1.60	0.9965	65.36	65.07	0.06	64.53	0.10	64.21	0.08	63.69	0.23
TiO_2	0.08	0.07	0.4078	0.38	0.37	0.00	0.36	0.07	0.35	0.14	0.34	0.09
Al_2O_3	28.57	0.93	-	17.10	17.38	0.00	17.88	0.00	18.18	0.00	18.67	0.00
FeO[b]	0.54	0.11	0.9542	3.18	3.11	0.01	3.00	0.02	2.93	0.03	2.81	0.00
MnO	0.06	0.08	0.4323	0.19	0.19	0.05	0.18	0.01	0.18	0.02	0.17	0.12
MgO	0.06	0.07	0.3768	0.83	0.81	0.07	0.78	0.05	0.76	0.08	0.73	0.21
CaO	11.88	1.12	0.9196	3.27	3.48	0.10	3.86	0.00	4.08	0.03	4.45	0.20
Na_2O	4.50	0.58	0.9290	4.95	4.94	0.02	4.92	0.04	4.91	0.04	4.89	0.09
K_2O	0.43	0.11	0.9926	4.47	4.37	0.00	4.19	0.02	4.09	0.00	3.92	0.03
Cl	0.01	0.02	0.2783	0.27	0.26	0.02	0.25	0.02	0.24	0.03	0.23	0.02
Total	99.27			100.00	99.98		99.95		99.93		99.90	

[a] obtained by extrapolation of contaminated data points to Al_2O_3=17.1 wt.%.

[b] all iron expressed as FeO.

4.4 Discussion

In our experience, before tephra deposits are analysed by EMPA for their glass composition, the bulk sample should be examined for particle textures. The three types of particles identified in the Burrell Lapilli fall deposit (Taranaki) occurred during different phases of the eruption, with lithic and poorly vesicular types 2 and 3 from initial dome-forming events, and pumice clasts from a climactic final sub-Plinian phase (Platz et al., 2007). The proportions of highest-density type 2 and 3 clasts reduce rapidly with distance from source in the fall deposit, however, small fragments are still commonly found in distal reaches. This range of particle types is not just confined to this event, but has also been recognised in other eruptions of Taranaki (Turner et al., in press) and at other centres (Hammer et al., 2000).

The mineralogical composition of distal andesite tephras is commonly reported to aid in correlation (e.g. Lowe, 1988a, b; Eden and Froggat, 1996). However, detailed descriptions of particle types in the tephra fall deposits have been conspicuously absent, despite the fact that these can be simply determined from SEM or optical microscopy methods. Analysing glass without knowing the context of particle types in a tephra unit

may lead to wide ranges in composition that are related to different phases of an eruption and are difficult to use for correlation purposes. By analysing each particle type as a separate sub-population for any given unit, correlation studies can proceed with "like" being compared to "like".

Similarly, previous authors have stated the possibility of plagioclase contamination (e.g. Lowe, 1988a, b; Shane, 2005). Our study has shown that checking glass compositional data for impurities, especially plagioclase, can tighten the compositional range for individual tephra units significantly. This in turn improves their potential for correlation purposes. If analyses of the contaminating phase are available, the proportion of contamination can also be evaluated, and this may be of use in determining the physical characteristics, such as microlite content, of individual tephras.

The evaluation of broad glass populations must not only take into account particle type and potential microlite contamination in EMPA data, but there are additional features of some types of andesitic eruptions that make their tephras unsuitable for correlation. Tephras that result from pyroclastic surges, phreatic/phreatomagmatic blasts or BAFs generated from a lava dome collapse are dominated by type 2 and 3 lithic particles (Fig. 4-2b-c). In these cases, variable crystallisation/cooling rate environments (i.e. temperature, water content, pressure) in different parts of the lava dome and upper conduit gives rise to variable glass compositions (Hammer et al., 2000; Platz et al., 2004). In addition, lava dome rocks are characterised by very high abundances of plagioclase microlites as well as Fe-Ti oxides in the groundmass (see Fig. 4-2d). The very late stage crystallising microlites may lead to strong variations in surrounding melt composition on a micro-scale. Hence analysis of glasses in such dome-derived particles can lead to a broad compositional range for any single tephra unit. The strongest variation is still expected to be a sub-linear relationship between late-stage plagioclase-microlite and melt compositions. Using an example from the Burrell Lapilli eruption, the glass compositions of type 1 and 2 particles in a BAF deposit of this sequence (Fig. 4-6) show a broad compositional range including hybrid analyses. In this instance, upper threshold values could be set at 17.9 wt.% Al_2O_3. This is in contrast to the value of 17.1 wt.% Al_2O_3 used for the type 1 particles of the stratigraphically equivalent Burrell pumice-rich fall. The analyses between these two thresholds, show a further degree of transition, and could arguably be also excluded from the "true" glass population. However, this may not be appropriate on grounds of contamination, instead they show that many of the points analysed in type 2 and 3 particles are from glass that

is fractionated to higher degrees than in type 1 shards (i.e. by a greater degree of late-stage microlite formation). In addition, the presence of more-common minute Fe-Ti oxides may also contribute to creating these transitional compositions. Hence, precise mean values and tight ranges of true "glass" compositions for type 2 or 3 particles can be difficult to derive, and may not relate at all to correlative deposits made up mostly of type 1 pumice shards.

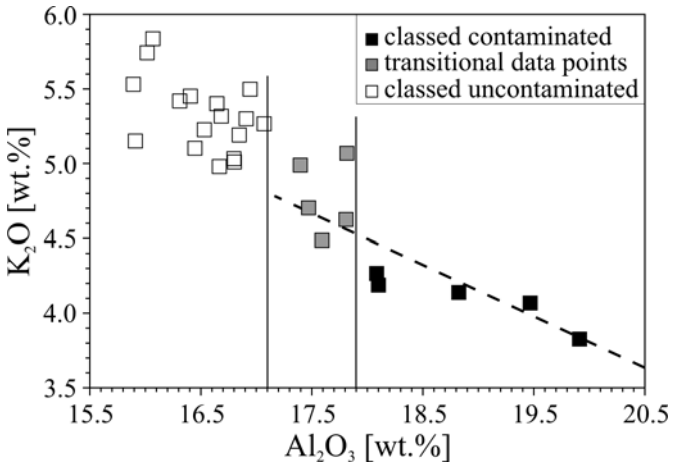


Figure 4-6: The glass evaluation procedure cannot be directly applied to BAF deposits as demonstrated for the Burrell Lapilli equivalent BAF deposit. Although data points above a threshold value of 17.9 wt.% Al_2O_3 clearly embrace contaminated glass analyses, the transitional data between 17.1 and 17.9 wt.% Al_2O_3 cannot be uniquely classified. Dashed line points toward mean plagioclase composition.

A review of all andesite glass compositions used for correlation purposes is required. In New Zealand, the published data from TgVC and Taranaki centres may be unreliable because they include both microlite-contaminated analyses as well as particles from different cooling/eruption histories. The published mean compositions of Al_2O_3 and K_2O (Lowe, 1988b; Lowe et al., 1999; Eden and Froggatt, 1996 and Shane and Hoverd, 2002) for a range of distal TgVC and Taranaki tephras, when taken with their standard deviations (Fig. 4-7), show no possibility for discrimination of individual units, and difficult discrimination even between individual eruptive centres. The data from the Burrell Lapilli eruption (Taranaki) have been plotted for comparison (in grey, Fig. 4-7). Although the previously stated authors acknowledged difficulties in glass analyses and the shortfall in application, it is apparent that the large variation in Al_2O_3 is a clear indicator for plagioclase contamination in the published datasets, and that the removal of hybrid data points could significantly improve the use for correlation purposes.

A further problem in published glass analyses is the use of glass analyses with low total oxide sums. Shane and Hoverd (2002) and Sandiford et al. (2001) reported mean total oxide sums as low as 91.6 wt.% with individual analyses lower than 86.5 wt.%. These differences clearly cannot be accounted for by water dissolved in glass. Even though secondary hydration of glass takes place after deposition (water absorption starts immediately as hot tephra particles come in contact with air), this cannot explain the very low totals. Therefore, these data should be discarded from the dataset.

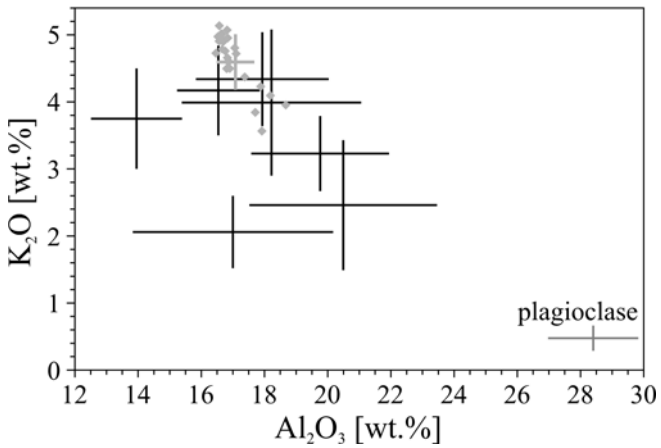


Figure 4-7: Glass compositions of Taranaki and TgVC tephras (Lowe 1988b; Lowe et al., 1999; Eden and Froggatt, 1996 and Shane and Hoverd, 2002) show large variations, here shown for the means and standard deviations of K_2O and Al_2O_3. Contaminated plagioclase-glass analyses and/or the analysis of two or more particle types may have caused the apparent glass compositional heterogeneity. The small variation in the unmodified Burrell Lapilli dataset (Taranaki) is shown for comparison (in grey).

Estimates of glass water contents using the weight-by-difference (WBD) method is commonly used and at times can be highly questionable, for instance, 13.5 wt.% H_2O in andesite glass (as described above) is unrealistic. Hydrogen cannot be measured by EMPA and the difference in analyses totals from 100% is commonly attributed to dissolved H_2O in glass, despite the fact that other volatiles can contribute significant proportions, for instance SO_3 and F (Luhr et al., 1984; Cronin et al., 1998). In addition, Roman et al. (2006) demonstrated that water contents in glass inclusions estimated by WBD are approximately 1 wt.% higher than water contents measured by Fourier Transform Infrared analysis.

Hence, low analysis totals for glass are more likely to represent measurement error which could result from a number of sources, including: (1) the exposed glass surface

not being as large as the beam spot; (2) the beam being placed incorrectly - e.g. overlapping the edge of a grain; (3) poor polish and scratches on the grain; (4) glass vesicles within the beam spot, or (5) errors in the detection/counting of one or more oxides. Given these possibilities, covering the missing fractions of the analyses by simply calculating ratios from each of the components will produce questionable results at best. This type of practice is more likely to lead to broader compositional ranges and consequent greater difficulties in unique correlations.

4.5 Conclusions

Although glass EMPA are carefully executed by avoiding visible inclusions (i.e. mineral phases, vesicles) and common guidelines are followed (cf. Froggatt, 1983; Hunt and Hill, 2001) a sensible error analysis is a final step that should be taken, one that has often been neglected. Also, previous studies on andesite eruptions commonly have lacked particle textural studies which are considered a major factor for contributing to large variations in glass compositional datasets.

This study highlights the fact that hybrid mineral-glass EMP analyses are common in datasets that are thought to contain “pure” glass compositional analyses. By thoroughly reviewing those datasets by using bivariate oxide diagrams (comprising a compatible and an incompatible oxide of the most common groundmass mineral phase) hybrid data points can be identified and excluded from the set. Proportions of the mineral phase(s) in hybrid analyses can be estimated by extrapolating the classed contaminated data back to the identified threshold value.

While working on andesite tephra sequences, it should always be kept in mind that tephra units are deposited through a variety of processes, and single eruptive events can switch between eruptive styles producing various particle types, and hence, different glass compositions.

4.6 References

Alloway, B., Neall, V.E. and **Vucetich, C.G.** 1995. Late Quaternary (post 28,000 year B.P.) tephrostratigraphy of northeast and central Taranaki, New Zealand. *Journal of the Royal Society of New Zealand* 25, 385-458.

Andreastuti, S.D., Alloway, B.V. and **Smith, I.E.M.** 2000. A detailed tephrostratigraphic framework at Merapi Volcano, Central Java, Indonesia: implications for eruption predictions and hazard assessment. *Journal of Volcanology and Geothermal Research* 100, 51-67.

Best, M.G. 2003. Igneous and metamorphic petrology. Blackwell Science. Malden.

Björck, S., Ingólfsson, Ó., Haflidason, H., Hallsdóttir, M. and **Anderson, N.J.** 1992. Lake-Torfadalsvatn: a high-resolution record of the North Atlantic ash zone I and the last glacial-interglacial environmental changes in Iceland. *Boreas* 21, 15-22.

Blundy, J. and **Cashman, K.** 2001. Ascent-driven crystallisation of dacite magmas at Mount St Helens, 1980-1986. *Contributions to Mineralogy and Petrology* 140, 631-650.

Boudon, G., Camus, G., Gourgaud, A. and **Lajoie, J.** 1993. The 1984 nuée-ardente deposits of Merapi volcano, Central Java, Indonesia: stratigraphy, textural characteristics, and transport mechanisms. *Bulletin of Volcanology* 55, 327-342.

Cashman, K.V. 1988. Crystallization of Mount St. Helens 1980-1986 dacite: a quantitative textural approach. *Bulletin of Volcanology* 50, 194-209.

Cronin, S.J., Neall, V.E., Stewart, R.B. and **Palmer, A.S.** 1996a. A multiple-parameter approach to andesitic tephra correlation, Ruapehu volcano, New Zealand. *Journal of Volcanology and Geothermal Research* 72, 199-215.

Cronin, S.J., Wallace, R.C. and **Neall, V.E.** 1996b. Sourcing and identifying andesitic tephras using major oxide titanomagnetite and hornblende chemistry, Egmont volcano and Tongariro Volcanic Centre, New Zealand. *Bulletin of Volcanology* 58, 33-40.

Cronin, S.J., Neall, V.E., Palmer, A.S. and **Stewart, R.B.** 1997. Methods of identifying late Quaternary rhyolitic tephras on the ring plains of Ruapehu and Tongariro volcanoes, New Zealand. *New Zealand Journal of Geology and Geophysics* 40, 175-184.

Cronin, S.J., Hedley, M.J., Neall, V.E. and **Smith, R.G.** 1998. Agronomic impact of tephra fallout from the 1995 and 1996 Ruapehu Volcano eruptions, New Zealand. *Environmental Geology* 34, 21-30.

Cronin, S.J., Neall, V.E., Lecointre, J.A., Hedley, M.J. and **Loganathan, P.** 2003. Environmental hazards of fluoride in volcanic ash: a case study from Ruapehu volcano, New Zealand. *Journal of Volcanology and Geothermal Research* 121, 271-291.

Donoghue, S.L. and **Neall, V.E.** 1996. Tephrostratigraphic studies at Tongariro volcanic centre New Zealand: an overview. *Quaternary International* 34-6, 13-20.

Donoghue, S.L., Palmer, A.S., McClelland, E., Hobson, K., Stewart, R.B., Neall, V.E., Lecointre, J.A. and **Price, R.C.** 1999. The Taurewa Eruptive Episode: evidence for climactic eruptions at Ruapehu volcano, New Zealand. *Bulletin of Volcanology* 60, 223-240.

Eden, D.N. and **Froggatt, P.C.** 1996. A 6500-year-old history of tephra deposition recorded in the sediments of Lake Tutira, eastern North Island, New Zealand. *Quaternary International* 34/36, 55-64.

Fisher, R.V. 1995. Decoupling of pyroclastic currents: hazards assessments. *Journal of Volcanology and Geothermal Research* 66, 257-263.

Froggatt, P.C. 1983. Toward a comprehensive upper Quaternary tephra and ignimbrite stratigraphy in New Zealand using electron-microprobe analysis of glass shards. *Quaternary Research* 19, 188-200.

Froggatt, P.C. and **Lowe, D.J.** 1990. A review of late Quaternary silicic and some other tephra formations from New Zealand - their stratigraphy, nomenclature, distribution, volume, and age. *New Zealand Journal of Geology and Geophysics* 33, 89-109.

Froggatt, P.C. and **Rogers, G.M.** 1990. Tephrostratigraphy of high-altitude peat bogs along the axial ranges, North Island, New Zealand. *New Zealand Journal of Geology and Geophysics* 33, 111-124.

Gamble, J.A., Wood, P., Price, R.C., Smith, I.E.M., Stewart, R.B. and **Waight, T.** 1999. A fifty year perspective of magmatic evolution on Ruapehu volcano, New Zealand: verification of open-system behaviour in an arc volcano. *Earth and Planetary Science Letters* 170, 301-314.

Gardner, C.A., Neal, C.A., Waitt, R.B. and **Janda, R.J.** 1994. Proximal pyroclastic deposits from the 1989-1990 eruption of Redoubt Volcano, Alaska: stratigraphy, distribution, and physical characteristics. *Journal of Volcanology and Geothermal Research* 62, 213-250.

Hammer, J.E., Cashman, K.V. and **Voight, B.** 2000. Magmatic processes revealed by textural and compositional trends in Merapi dome lavas. *Journal of Volcanology and Geothermal Research* 100, 165-192.

Hobden, B.J., Houghton, B.F. and **Nairn, I.A.** 2002. Growth of a young, frequently active composite cone: Ngauruhoe volcano, New Zealand. *Bulletin of Volcanology* 64, 392-409.

Hogg, A.G., Higham, T.F.G, Lowe, D.J., Palmer, J.G., Reimer, P.J. and **Newnham, R.M.** 2003. A wiggle-match date for Polynesian settlement of New Zealand. *Antiquity* 77, 116-125.

Hunt, J.B. and **Hill, P.G.** 2001. Tephrological implications of beam size - sample-size effects in electron microprobe analysis of glass shards. *Journal of Quaternary Science* 16, 105–117.

Jarosewich, E., Nelen, J.A. and **Norberg, J.A.** 1980. Reference samples for electron microprobe analysis. *Geostandards Newsletter* 4, 43-47.

Kelsey, H.M., Hull, A.G., Cashman, S.M., Berryman, K.R., Cashman, P.H., Trexler, J.H. and **Begg, J.G.** 1998. Paleoseismology of an active reverse fault in a forearc setting: the Poukawa fault zone, Hikurangi forearc, New Zealand. *Geological Society of America Bulletin* 110, 1123-1148.

Lowe, D.J. 1986. Controls on the rates of weathering and clay mineral genesis in airfall tephras: a review and New Zealand case study. In: **Coleman, S.M.** and **Dethier, D.P.** (eds.) Rates of chemical weathering of rocks and minerals. Academic Press, Dordrecht. pp. 265-330.

Lowe, D.J. 1988a. Late Quaternary volcanism in New Zealand: towards an integrated record using distal airfall tephras in lakes and bogs. *Journal of Quaternary Science* 3, 111-120.

Lowe, D.J. 1988b. Stratigraphy, age, composition, and correlation of late Quaternary tephras interbedded with organic sediments in Waikato lakes, North Island, New Zealand. *New Zealand Journal of Geology and Geophysics* 31, 125-165.

Lowe, D.J., Newnham, R.H. and **Ward, C.M.** 1999. Stratigraphy and chronology of a 15 ka sequence of multi-sourced silicic tephras in a montane peat bog, eastern North Island, New Zealand. *New Zealand Journal of Geology and Geophysics* 42, 565-579.

Luhr, J.F, Carmichael, I.S.E. and **Varekamp, J.C.** 1984. The 1982 eruptions of El Chichon Volcano, Chiapas, Mexico - mineralogy and petrology of the anhydrite-bearing pumices. *Journal of Volcanology and Geothermal Research* 23, 69-108.

Murphy, M.D., Sparks, R.S.J., Barclay, J., Carroll, M.R., Lejeune, A.M., Brewer, T.S., Macdonald, R., Black, S. and **Young, S.** 1998. The role of magma mixing in triggering the current eruption at the Soufriere Hills volcano, Montserrat, West Indies. *Geophysical Research Letters* 25, 3433-3436.

Nanayama, F., Satake, K., Furukawa, R., Shimokawa, K., Atwater, B.F., Shigeno, K. and **Yamaki, S.** 2003. Unusually large earthquakes inferred from tsunami deposits along the Kuril trench. *Nature* 424, 660-663.

Nielsen, C.H. and **Sigurdsson, H.** 1981. Quantitative methods for electron microprobe analysis of sodium in natural and synthetic glasses. *American Mineralogist* 66, 547-552.

Platz, T., Cronin, S.J., Smith, I.E.M., Foley, S.F., Neall, V.E. and **Stewart, R.B.** 2004. Glass chemistry as a tool for tephra correlation: a new statistical approach on <1000 year old tephra deposits on Egmont volcano, Mt. Taranaki, New Zealand. Abstract. *Geological Society of Australia* 73, 284.

Platz, T., Cronin, S.J., Cashman, K.V., Stewart, R.B. and **Smith, I.E.M.** 2007. Transition from effusive to explosive phases in andesite eruptions - a case-study from the AD1655 eruption of Mt. Taranaki, New Zealand. *Journal of Volcanology and Geothermal Research* 161, 15-34.

Price, R.C., Stewart, R.B., Woodhead, J.D. and **Smith, I.E.M.** 1999. Petrogenesis of high-K arc magmas: evidence from Egmont Volcano, North Island, New Zealand. *Journal of Petrology* 40, 167-197.

Price, R.C., Gamble, J.A., Smith, I.E.M., Stewart, R.B., Eggins, S. and **Wright, I.C.** 2005. An integrated model fro the temporal evolution of andesites and rhyolites and crustal development in New Zealand's North Island. *Journal of Volcanology and Geothermal Research* 140, 1-24.

Roman, D.C., Cashman, K.V., Gardner, C.A., Wallace, P.J. and **Donovan, J.J.** 2006. Storage and interaction of compositionally heterogeneous magmas from the 1986 eruption of Augustine Volcano, Alaska. *Bulletin of Volcanology* 68, 240-254.

Sandiford, A., Alloway, B. and **Shane, P.** 2001. A 28000-6600 cal yr record of local and distal volcanism preserved in a paleolake, Auckland, New Zealand. *New Zealand Journal of Geology and Geophysics* 44, 323-336.

Schlinger, C.M., Smith, R.M. and **Veblen, D.R.** 1986. Geologic origin of magnetic volcanic glasses in the KBS tuff. *Geology* 14, 959-962.

Shane, P. 1998. Correlation of rhyolitic pyroclastic eruptive units from the Taupo volcanic zone by Fe-Ti oxide compositional data. *Bulletin of Volcanology* 60, 224-238.

Shane, P. 2005. Towards a comprehensive distal andesitic tephrostratigraphic framework for New Zealand based on eruptions from Egmont volcano. *Journal of Quaternary Science* 20, 45-57.

Shane, P. and **Hoverd, J.** 2002. Distal record of multi-sourced tephra in Onepoto Basin, Auckland, New Zealand: implications for volcanic chronology, frequency and hazards. *Bulletin of Volcanology* 64, 441-454.

Shane, P., Lian, O.B., Augustinus, P., Chisari, R. and **Heijnis, H.** 2002. Tephrostratigraphy and geochronology of a ca. 120 ka terrestrial record at Lake Poukawa, North Island, New Zealand. *Global and Planetary Change* 33, 221-242.

Smith, V.C., Shane, P. and **Nairn, I.A.** 2005. Trends in rhyolite geochemistry, mineralogy, and magma storage during the last 50 kyr at Okataina and Taupo volcanic centres, Taupo Volcanic Zone, New Zealand. *Journal of Volcanology and Geothermal Research* 148, 372-406.

Thorarinsson, S. 1944. Tefrokronologiska studier på Island. *Geografiska Annaler* 26, 1-217.

Turner, M.B., Cronin, S.J., Bebbington, M.S. and **Platz, T.** 2007. Developing probabilistic eruption forecasts for dormant volcanoes: a case study from Mt Taranaki, New Zealand. *Bulletin of Volcanology* (DOI: 10.1007/s00445-007-0151-4).

Venezky, D.Y. and **Rutherford, M.J.** 1997. Preeruption conditions and timing of dacite-andesite magma mixing in the 2.2 ka eruption at Mount Rainier. *Journal of Geophysical Research* 102, 20069-20086.

Wolf, K.J. and **Eichelberger, J.C.** 1997. Syneruptive mixing, degassing, and crystallization at Redoubt Volcano, eruption of December, 1989 to May 1990. *Journal of Volcanology and Geothermal Research* 75, 19-37.

Chapter 5 Non-explosive, Dome-forming Eruptions

Chapter 5 demonstrates that the Tahurangi eruption in AD1755 was followed by a small, extrusive dome-forming event. In order to evaluate the physico-chemical conditions of dome formation at Taranaki, the structure and composition of the summit dome was investigated in detail. Magma storage depths, extrusion and ascent rates, and eruption duration were interpreted for the first time ever at Taranaki. In addition, the age of the latest eruption at Mt. Taranaki, the Pyramid eruption, is discussed.

5.1 Introduction

Lava dome-forming eruptions can last from a few days up to several decades. In most cases, the impacts of these typically small volcanic eruptions are forgotten within years or decades after the event. This leads to complacency within the surrounding population and a consequent underestimation of volcanic hazards. This is particularly the case where population pressures are high and the level of government regulation low. A lava dome located at high altitudes within a summit crater and in parts emplaced onto the outer steep flanks is in a metastable state. If the dome is growing, parts of it can collapse forming devastating Block-and-Ash Flows (BAFs). This hazard has been known for centuries and is included in hazard risk analysis. However, the hazard potential of a cool lava dome is mostly not regarded because the volcano is inherently considered dormant or even extinct. But a cool metastable lava dome could in fact collapse at any time, decades to centuries after its emplacement. In addition, if volcanoes are going to erupt

most people expect large eruptions and major impacts on the environment and the community. But eruptions may not be that devastating and could be short-termed. Hence, hazard analysis should also take these events into consideration and eruption scenarios and conditions for these types of eruption need also to be investigated.

Studies on the lava dome forming the current summit of Mt. Taranaki were carried out to reconstruct its original geometry, growth dynamics and also zones of weakness within it. This in part enables a view into the possibly very common, but non-dramatic dome effusion events possible at Mt. Taranaki. Alongside studies of the typically hazardous sub-Plinian events, it is important to examine the conduit and eruption conditions that lead to non-explosive dome-forming events. From the properties of the summit dome eruptive parameters such as magma storage depth(s), magma ascent rates, and eruption duration can be interpreted. Field observations and geochemical studies will show that the remnant summit dome represents an individual event and postdates the Tahurangi eruption of AD1755. The youngest eruption of Mt. Taranaki is here named the Pyramid eruptive event which produced the summit lava dome (i.e. Pyramid Dome).

5.1.1 Lava Domes

Lava domes are typically hemispherical mounds of volcanic rock representing one or more lava units extruded above a vent and too viscous to flow far (Fink and Anderson, 2000). The extrusion of lava domes can occur above the central vent of a volcano (e.g. Mt. Taranaki, New Zealand; Gunung Merapi, Indonesia; Mt. St. Helens, USA), on the lower slopes of volcanoes either in isolation or in groups (e.g. Mt. Taranaki, New Zealand; South Sisters, Oregon, USA), and along fault lines or caldera ring faults (Mono Lake - Inyo Craters, California, USA; Cerro Chascon-Runtu Jarita Dome Complex, Bolivia; Pago, New Guinea). Lava domes were initially subdivided into four categories based on their morphology (Blake, 1990): up-heaved plugs; Pelean domes; low lava domes; and coulées. Additional consideration of dome surface textures and eruptive style were used to classify them into spiny or Pelean domes, lobate domes, platy domes and axisymmetric domes (Fink and Anderson, 2000). Spiny domes are steep-sided with smooth upper surfaces penetrated by tall near-vertical spines (Fig. 5-1a). These domes often grow horizontally and are largely confined by the geometry of

their vents to display near-circular outlines (e.g. Mont Pelée, Martinique; Soufrière Hills, Montserrat, 1995-1996). Lava domes with lower side-slopes that consist of individual lava lobes with an irregular plan outline are characterised as lobate domes (Fig. 5-1b). Their surfaces are partially smooth or covered by small blocks (e.g. Pinatubo, Philippines; Unzen volcano, Japan, 1991-1993). Platy domes (Fig. 5-1c) are represented by a low cross-sectional profile, a blocky carapace, with shallower fractures and more abundant surface ridges (e.g. Gunung Merapi, Indonesia, 1994-1995; Obsidian Dome, Inyo Craters, California). A further type, axisymmetric domes, are characterised by a relatively low relief with near-level upper surface, an irregular plan outline and small blocks on their surfaces (e.g. Dacite Flow and Little Glass Mountain, Californian, USA). These morphologies can be related to eruptive conditions, where a series can be recognised following the trend of increasing extrusion/cooling rates and yield strengths from: axisymmetric, platy, lobate to spiny forms (Griffiths and Fink, 1997; Fink and Griffiths, 1998). Common to all lava domes is that they were formed by highly viscous lava. Within a restricted range, however, they vary in their viscosity and rheology depending on their composition, phenocryst, microphenocryst and microlite content, along with their dissolved water concentrations.



Figure 5-1 : Lava dome types: a) spiny (Rock Mesa ENE, Oregon), b) spiny-lobate (Mt. St. Helens lava dome, Washington, July 2004), c) lobate-platy (Big Obsidian Flow, Newberry, Oregon).

5.1.1.1 Lava Dome Distribution in Taranaki

Four lava domes occur on the lower slopes of Mt. Taranaki: The Dome to the NNW, Skinner Hill to the NW, and the Beehives (two lava domes) on the southern flank (Grant-Taylor, 1964; Neall, 1971; see Fig. 1-3). The lava domes on the lower flanks are probably located on radial fissures of Mt. Taranaki (Neall, 1971). Two other domes occur farther from the stratocone: Pukeiti (between Kaitake and Pouakai) and German Hill (13.5 km to the NNE of Mt. Taranaki). Pukeiti and The Dome are directly situated along the overall volcanic lineament defined by Kaitake, Pouakai and Mt. Taranaki. Also, the Sugar Loaf Islands and German Hill are aligned parallel to this lineament. The present summit of Mt. Taranaki is part of a lava dome structure, partially filling a crater form. This has been attributed to the latest eruption of the volcano, thought to be a correlative of the Tahurangi tephra fall dated at AD1755 (Stewart et al., 1996).

5.2 Field Observations

5.2.1 Tahurangi Eruptive Deposits

Previous workers (Druce, 1966; Neall, 1972; Neall et al., 1986; Platz, 2001; Cronin et al., 2003) interpreted the AD1755 Tahurangi tephra, as either a fall deposit or ash cloud surge deposits related to the emplacement of the summit dome. Although Neall et al. (1986) and Cronin et al. (2003) recognised that individual Block-and-Ash Flow (BAF) units on the northwestern sector of Mt. Taranaki are genetically related to the established tephrostratigraphy (cf. Druce, 1966), they did not consider the present summit dome to be a separate event.

Field observations (Platz, 2001; this study) identified two BAF deposits on the NW sector as being associated with the Tahurangi eruption (Fig. 5-2). The older Tahurangi BAF A is characterised by distinctive features compared to both Tahurangi BAF B and other BAF deposits of the Maero Eruptive Period. It extends over the entire NW sector, primarily within the Pyramid, Maero and Hangatahua catchments and is exposed from proximal (3.5 km) to distal reaches (12 km; planimetric distance). The Tahurangi BAF A deposit is very poorly sorted and varies in thickness from >12 m at proximal locations to about 0.4 m at more distal locations. The angular to subangular clasts are predominantly grey to dark grey, dense andesite lithics with minor reddish, orange or

brown-coloured accessory clasts. The most distinguishing sedimentological feature of the deposit is its subdivision into a clast-supported, virtually matrix-free, lower portion and a matrix- to clast-supported upper portion with matrix contents of about 30-35% (see Fig. 3-4c and e). The internal boundary is transitional and the proportions of the two parts vary considerably. The upper massive portion also often displays coarse-tail reverse grading. Observed clast diameters vary considerably within and between described sections and reach boulder size up to 2 m in diameter. Only at two distal locations (outcrops 21 and 29; Fig. 5-3) the maximum clast size are cobbles (i.e. <256 mm) compared to boulder at proximal to medial sections. The clasts show magnetic alignment[1] at most locations, indicating a deposition temperature above 350 °C (Hoblitt and Kellog, 1979). The distinct twofold zoning of the deposit is apparent even at its most distal occurrence c.12 km from source.

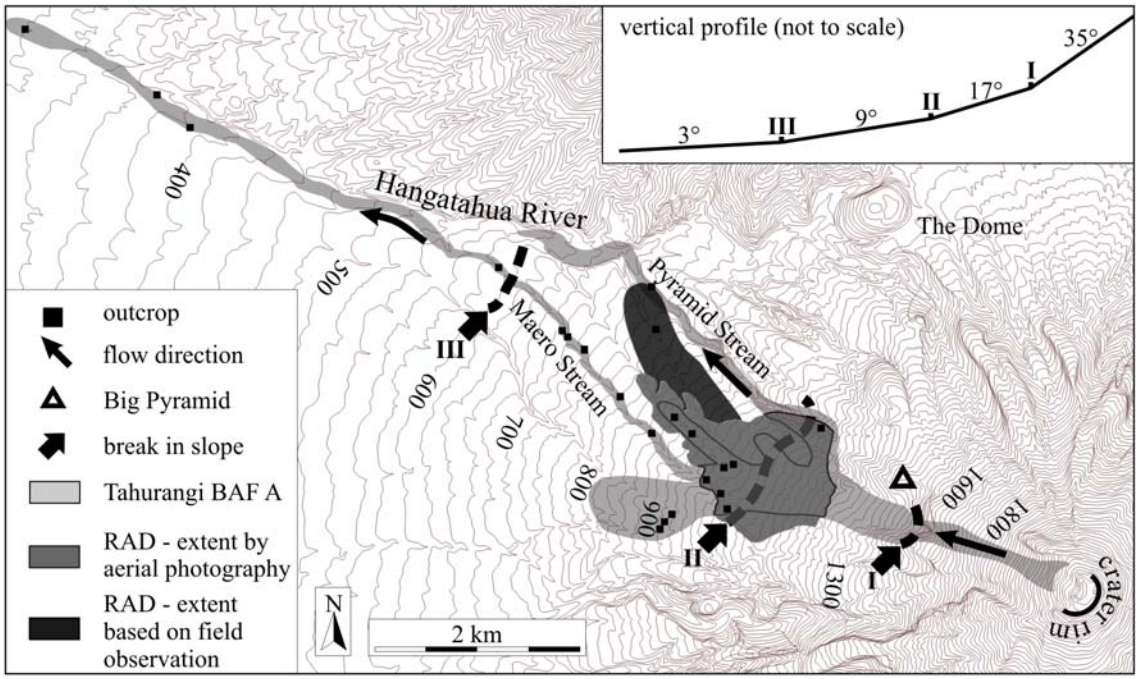


Figure 5-2 : NW sector of Mt. Taranaki showing the main deposition area of Maero BAF deposits. The extent of the Tahurangi BAF A is outlined (light grey); unit B is only observed in the Maero Stream and is omitted for clarity. The rock-avalanche deposit (RAD) is outlined as observed on aerial photographs from 1959 (mid-grey) with an additional area based on field observations (dark grey). Contour interval is 20 m. The upper right inset shows the general slope inclinations. The squares are the locations of the sections reproduced in Figure 5-3.

The basal contact of Tahurangi BAF A is sharp and erosive in places. Where it is not erosive, it consists of a few centimetres of fine to medium grey ash overlying a black, humic paleosol. Charcoaled twigs or in situ charred tussock have been found in some

[1] The natural remanent magnetisation (NRM) was measured using a portable fluxgate magnetometer (Platz, 2001).

locations. Two substantially different degrees of development of directly underlying paleosols (0.5 cm humus layer vs. up to 30 cm of weathering) were observed which represent soil development on surfaces of different ages. A radiocarbon age (NZ5593) of charred tussock in the basal portion of the deposit was too young for the method at <250 yrs B.P. (V.E. Neall, unpubl. data).

Three proximal sections (Ma 17-19; Fig. 5-3) located at slightly elevated positions on top of a buried lava ridge contain a poorly sorted, 0.5-0.7 m thick ash and lapilli unit with sharp lower erosive contacts that contain rip-up clasts and charred tussock stems. A thin (<0.5-1 cm) basal pocketing grey fine ash is also observed. Mapping the distribution of the deposit, together with examination of lithologies and distribution on paleomorphic surfaces, indicates that these fine-grained units probably represent an "overbank" or surge-like deposit, resulting from deflection of the main body of the Tahurangi BAF A by a major underlying lava ridge. The axial flow travelled from WNW to NW due to this deflection.

At three locations (Ma 16, 44, and 46) the Tahurangi BAF A is overlain by another BAF unit. This unit has a more restricted distribution both in terms of runout (<6.5 km from source) and lateral extent, being only exposed in the Maero Stream (Fig. 5-3). The unit varies in thickness from 0.6 to 1.1 m and consists of a grey to greyish brown ashy predominantly matrix-supported lapilli to block breccia. In comparison to the Tahurangi BAF A, it has consistently smaller maximum clast sizes (< 20 cm). The majority of clasts comprise grey angular, dense andesites (80-95%) along with reddish and brown coloured variants (5-20%). The aligned magnetic orientation of eight clasts at location 10 suggests a depositional temperature above 350 °C. The absence of soil development between the BAF A and B deposits as well as their similar lithologies supports their being derived from the same source. The consistently smaller maximum clast diameter in BAF B could also be caused by a different exposed cross-sectional area than for BAF A, i.e. centre vs. marginal flow facies or thermal fracturing of more coherent dome material where clast size is controlled by physical properties of the dome rocks. Both BAF deposits are younger than 250 yrs B.P. and represent the youngest BAFs known on the mountain. This corresponds to the youngest known ashfall unit on the volcano (potentially in part a co-ignimbrite ash), the AD1755 Tahurangi Ash.

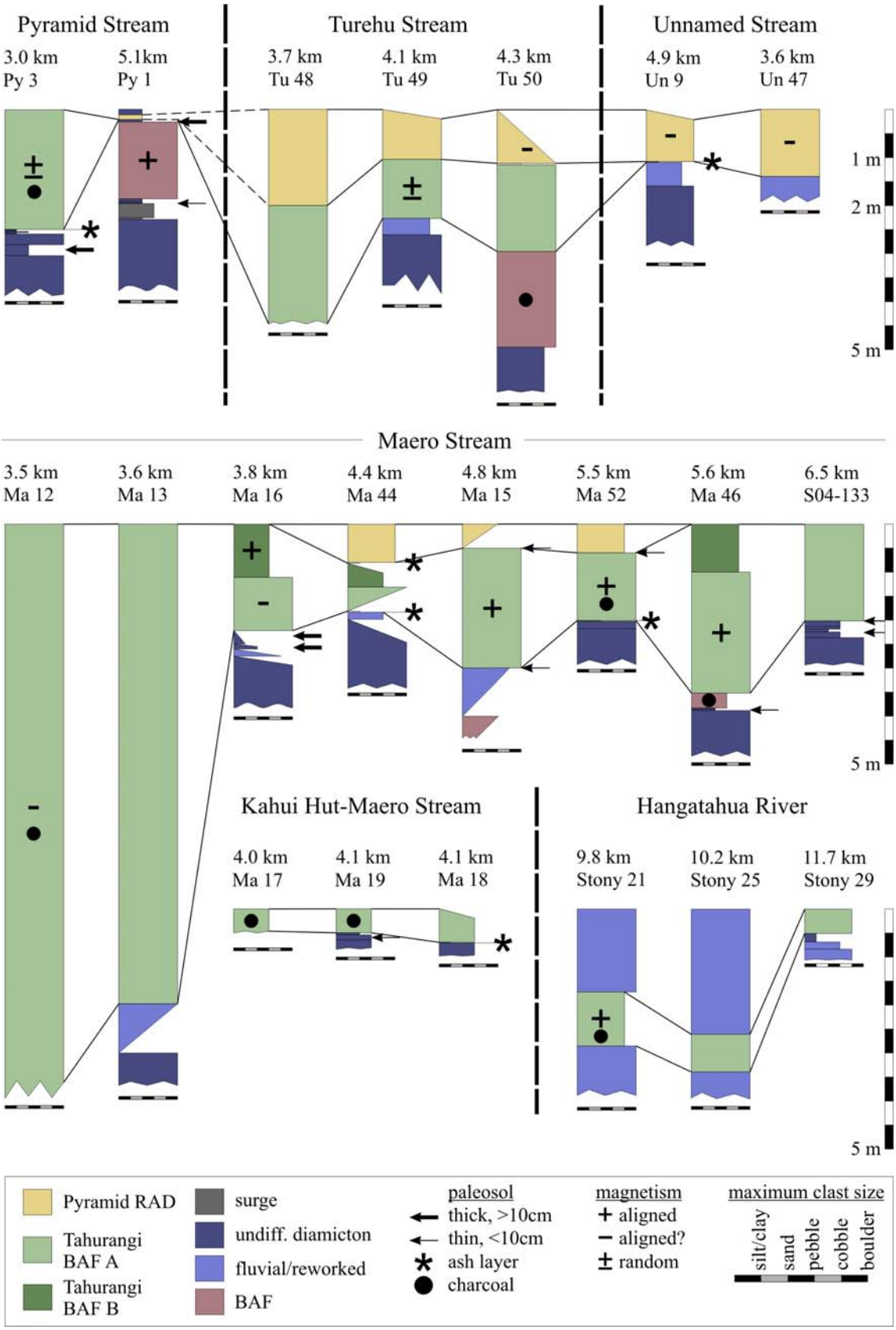


Figure 5-3: Correlation of Tahurangi BAF A and B units and the rock-avalanche deposit across the Pyramid-Maero-Hangatahua area. The exposures are sorted by stream and planimetric distance from source (filled squares in Fig. 5-2). See figure legend for further details (RAD – rock-avalanche deposit). Magnetism was measured by a portable fluxgate magnetometer. For clarity, older exposed units were omitted. Outcrop numbers and profiles refer to Platz (2001) except S04-133.

5.2.2 The Present Summit Lava Dome

The summit lava dome of Mt. Taranaki is located within a 420 m diameter partial crater with intact walls preserved from the NE through E to SW. The summit of the lava dome at 2518 m constitutes the highest point of Mt. Taranaki. When viewed from the southeast, the lava dome appears hemispheric with an extrapolated original diameter of 320 m (Fig. 5-4a). The crater floor is usually obscured by semi-permanent ice and snow but is exposed at the south entrance of the crater at the Okahu Gorge. Here the brown vesicular dome carapace directly overlies older hydrothermally altered rocks of the crater rim. The dome fills the crater to varying depths governed by how it impinges on the crater walls. The dome height is therefore estimated to be c.105 m above the crater floor level (assuming a flat crater floor rather than a funnel shape). The south side of the dome at the Okahu Gorge is modified by a small, wedge shaped collapse zone, about 25 m wide at the top and 50 m wide at the bottom, with the collapsed material deposited within the crater.

The western margin of the dome forms the wall of a horseshoe-shaped amphitheatre open to the west (Fig. 5-4b-c). This implies >50% of the original dome is missing. The collapse scarp exposes the upper 45 m of the dome, with wall inclinations ranging from 55°-83° in a parabolic form (Fig. 5-4c). The scarp reveals a central 80 m-wide zone of hydrothermal alteration comprising white- to yellowish-brown rock; the lithologies at the northern and southern sides are grey to dark grey with reddish stained surfaces (Fig. 5-4b). A succession of three small coulée flows extend from the northern side of the amphitheatre and an unstable bouldery field of talus from the scarp drapes the surface below the western face. On the northern side of the dome, two blocky lava flows each 4-6 m thick occur between remnants of the former northern crater rim with a blocky flow field extending down to 2230 m altitude.

The carapace of the dome is characterised by brown, vesicular scoria that is mostly <1.5 m thick. The thin, vesicular lava dome rind is often penetrated by grey to dark grey, dense micro-vesicular lava which was extruded laterally and sub-vertically. The summit itself is located on a sub-vertical extrusion which shows weak columnar jointing (Fig. 5-4d). Other pinnacles are remnants of dense interior dome rock exposed by partial collapse, e.g. in the southern part of the dome. The eastern side of the dome is smooth and is characterised by a thicker carapace (c.2 m).

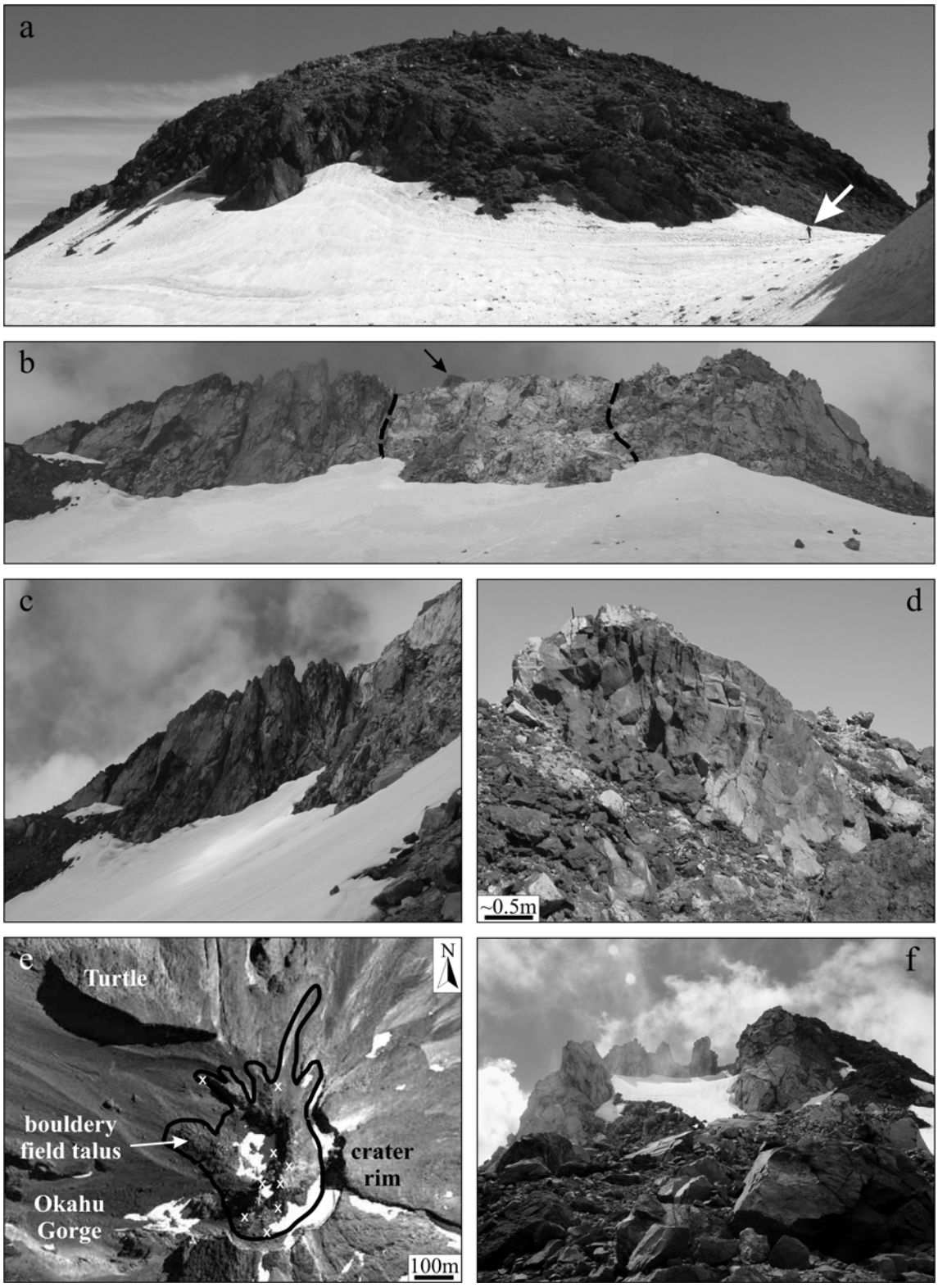


Figure 5-4: The remnant present summit dome. a) hemispherical shape of the dome as viewed from the SE; arrow points to a person for scale. Photographed by S.J. Cronin. b) dome amphitheatre as viewed from the W; the arrow points to the summit marker (2518 m); the dashed lines mark the hydrothermally altered central dome portion. c) northern scar of the amphitheatre showing listric faults. d) the summit marker is a sub-vertical extrusion penetrating the carapace; note weak columnar jointing; summit marker is highest point of the dome. e) orthophotograph of the summit region of Mt. Taranaki; outline shows mapped deposits associated with the lava dome; note the blocky lava flow to the N; crosses mark sample locations. f) the 'Three Sisters' (background) mark the NW border of the intra-crater collapse zone with resulting deposit still preserved in the crater (foreground).

5.2.3 Rock-Avalanche Deposit

A widespread bouldery deposit confined to the upper Pyramid – Maero Stream catchments on the NW flank of Mt. Taranaki (Fig. 5-2) has been photographed by the surveyor H.M. Skeet between 1898-1901 showing a still fresh bouldery surface (Fig. 5-5). On present-day aerial photographs the suppression of vegetation is clearly visible with the depression of the tussock zone marking the extent of this deposit (see Fig. 3-4a). From 1959 aerial photographs an extent to 4.8 km from the summit is indicated, although the maximum extent is 5.3 km, based on exposed and correlated units in Pyramid Stream (Fig. 5-3). The maximum depositional area is estimated at c.2×10^6 m^2.



Figure 5-5: Black and white photograph taken between 1898 and 1901 showing the fresh bouldery rock-avalanche deposit (centre to right). The photograph is taken from the Round-The-Mountain-Track just west of Maero Stream from the top of a buried lava ridge. The view is NNW towards Pouakai. Photographed by the surveyor H.M. Skeet.

The poorly sorted, predominantly matrix-supported deposit is up to 2 m thick, consisting of a brownish grey, sandy matrix and angular to subrounded clasts with the largest (up to 4 m in diameter) concentrated at or near the surface often in boulder trains (Fig. 5-3). Maximum grain sizes range between pebbles and boulders, often with reverse coarse-tail grading through the unit. Weak planar fabric is observed in longitudinal exposures, including clast long-axes being aligned in a down-flow direction. The unit has a polylithologic clast assemblage, comprising mainly dense grey,

greyish brown, pale brown and reddish andesite clasts. The lowermost 20-30 cm is lithologically similar, but is separated from the main body of the deposit by a pocketing pale brown, 0.5 cm thick fine ash layer. The deposits overlie either BAF deposits from the Tahurangi eruption (AD1755), separated by an 4-5 cm thick medial ash paleosol, or reworked volcaniclastic material (Fig. 5-3).

The presence of a bouldery deposit and dome remnants in the summit crater indicate that the former intact dome collapsed with the bouldery unit being the resultant deposit. Based on the NRM of clasts from the deposit, which show a random orientation, it can be concluded that the deposition temperature was below 350 °C (Platz, 2001). This conclusion also implies that at least a portion of the dome that collapsed also had a temperature below 350 °C at the time of collapse.

The precise date of the lava dome collapse is not known but it may have occurred in the 1880s. This is supported by Davis and Carrington's summit crater map of AD1885 which shows a similar crater configuration to the present day (Neall, 1973). The deposit does not result from a BAF, and is more appropriately termed a rock-avalanche deposit. The deposit has a more polylithologic and subrounded clast assemblage than the typical predominantly monolithologic angular to subangular BAF units exposed in the area.

5.3 Sample Sites and Methods

For a detailed study of the dome composition, 15 samples at various sites – dome top, margin and centre - were chosen (Table 5-1). The following methods were used in the investigation: polarised microscopy (mineralogy and textural studies); XRF, Laser ICP-MS, EMPA (geochemistry); He-pycnometry, porosimeter, binocular microscopy (physical rock properties); GPS and ArcGIS (mapping and volume calculations). Detailed descriptions of the methodologies applied are listed in Chapter 2.

Table 5-1. Sample location and description of studied summit dome rocks.

Sample	East	North	Height[1] [m]	Rock description	Location description
SD1	2601790	6211537	2497	large grey, dense boulder split along cooling fractures	south of summit on broad flat top of dome
SD2	2601814	6211578	2513	grey, moderately vesicular lava	immediately below summit marker
SD3	2601814	6211578	2513	reddish oxidised, moderately vesicular lava	immediately below summit marker
SD4	2601760	6211411	2432	dark grey, dense boulder; collapsed dome material	southern end of dome; opposite south crater entrance
SD5	2601784	6211471	2454	grey, dense lava; outer skin of dome	southern dome flank near Three Sisters
SD6	2601745	6211535	2474	grey, dense lava	Middle sister (inner dome part, collapse zone south side)
SD7	2601702	6211447	2408	grey, dense lava	Okahu Gorge; central dome facies on S flank
SD10	2601786	6211780	2396	grey, dense boulder; bouldery dome surface	lower northern dome face
SD13	2601595	6211801	2345	grey, dense lava	lower coulee flow, upper NW flank
SD14	2601774	6211613	2473	purplish grey, dense lava	central west face of dome below summit marker
SD15	2601660	6211514	2432	grey, dense boulder; collapsed dome material	southwestern part of dome
T04-39	2601814	6211578	2513	grey and dark grey, dense pebble; parallel bands visible	loose pebble next to summit marker

[1] approximate height using GPS, ArcGIS and handheld theodolite.

5.4 Results

5.4.1 Dome Volume Calculations

The remains of the dome have been mapped using GPS and aerial photographs (Fig. 5-6a). Its original geometry and that of the crater was extrapolated from the intact portions. The pre-collapse crater rim is inferred to have had near-circular dimensions of 420×405 m. The dome remnants occur within the crater as well as on the upper outer NW-flank. The portion of the dome within the crater is hemispherical with a near semi-circular base, whereas the portion on the flank is elongated, forming a strong semi-elliptical base. To fit the original 3-dimensional elliptical paraboloids were combined with an assumed even underlying surface. The elliptical paraboloids were combined to simulate the crater- and flank-portions of the original dome (Fig. 5-6b, c). The linkage of both halves coincides with the break in slope/crater rim. In addition, the centre point

of the combined paraboloid (i.e. centre of the linkage line) roughly coincides with the centre point of the inferred crater geometry.

The modelled dome has a maximum volume of 5.9×10^6 m^3, whereas from a 20 m resolution DEM[2], the remnants of the dome comprise only 1.5×10^6 m^3 (Fig. 5-6b, c). Bulk vesicularity of eight dome rock samples ranged between 12.4 – 22.8%. Using the mean bulk vesicularity (18.3%), a dense rock equivalent (DRE) volume for the modelled dome is 4.9×10^6 m^3. It should be noted that the depositional volume of the rock avalanche is approximately 2×10^6 m^3, if an average thickness of 1 m is assumed (deposition thickness varies between 0.5-2 m). This disparity with the missing dome volume (c.4.3×10^6 m^3) could be due to a portion of the collapse having entered the Okahu Gorge or it may relate to an overestimation of the original dome volume.

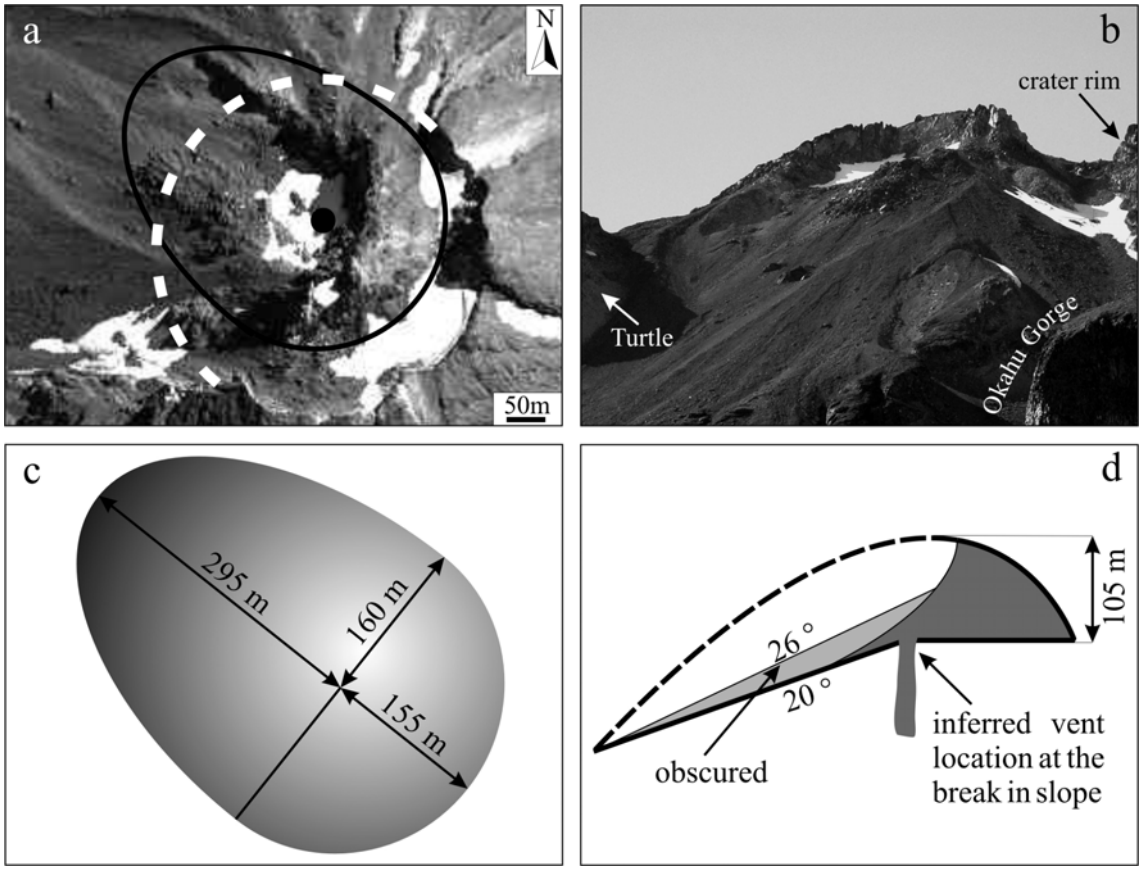


Figure 5-6: Reconstruction of the Pyramid Dome geometry. a) dashed white line illustrates the former ideal crater wall position; the solid line marks the inferred dome outline; the black dot is the assumed vent location at the break in slope. b) view of the remnant summit dome from the W. c) top view of the combined paraboloid with a composite elliptical base; dimensions of elliptical radii are given. d) side view of the inferred dome geometry; the dome remnants are in dark grey; the inferred underlying slope on the upper flank is estimated to be c.20°.

[2] The remnant dome volume was calculated by J.N. Procter using ArcGIS software.

Direct comparison of the Taranaki dome to published studies of dome extrusions is difficult since most domes rest on a flat or slightly inclined surface often with a near circular base. Moriya (1978) defined a relationship between height (h), diameter (d), and radius (r) of lava domes where the maximum dome height is calculated at:

$h = 0.32\ d = 0.32\ (2r)$ [Eq. 5-1]

Equation 1 can also be expressed as

$h/r = 0.64$ and the tangent being [Eq. 5-2]

$\tan 0.64 = 32.6°$ [Eq. 5-3]

where the corresponding angle is close to the angle of repose for loose rubble (Swanson and Holcomb, 1990). Although not all lava domes can be compared to a pile of loose material, this ratio can be used to assess whether a dome is metastable (Swanson and Holcomb, 1990). The dimensions of the remnant dome of Mt. Taranaki (here the dimensions of the hemispherical SE part of the dome: h=105 m, d=320 m), only slightly exceed the maximum h/d ratio with h/d = 0.33 (= 33.3°**)**. For comparison, the dimension of other Taranaki flank domes are listed in Table 5-2.

Table 5-2. Comparison of the modelled summit dome to other Taranaki flank lava domes.

Lava dome	Radii [m]	Height [m]	Inferred geometrical shape	Slope [°]	Calculated maximum	
					Basal area [m^2]	Volume [m^3]
Pyramid Dome	155/160/295	105	combined elliptical paraboloid	0/20[1]	2.3×10^5	5.9×10^6
The Dome	277.5/397.5	177	scalene ellipsoid	25[2]	3.5×10^5	4.1×10^7
Northern Beehive	200/265	91	scalene ellipsoid	8[3]	1.7×10^5	1.0×10^7
Southern Beehive	190	92	spherical dome	6[3]	1.1×10^5	5.6×10^6

[1] estimated from the present crater morphology.
[2] measured by Neall (1971).
[3] calculated underlying minimum slope.

5.4.2 Mineralogy and Mineral Chemistry

The mineral assemblage of the lava dome comprises plagioclase (19-30%), hornblende (5-18%), clinopyroxene (4-14%), Fe-Ti oxides (c.1-4%), biotite (up to 1%), and traces of orthopyroxene and apatite. The major phases (plg, hbl, cpx) range in grain size from macrocrysts to microlites. The rocks are porphyritic, holo- to hypocrystalline with partly fluidal textures, and crystal contents ranging between 36 and 49% (vesicle free). The

most abundant mineral phase, plagioclase (up to 31%), is euhedral to subhedral with both normal and reversed zoning, and partly sieved-textured cores. Hornblende (5-18%) is commonly observed as brown to reddish-brown, euhedral to subhedral pheno- and microphenocrysts and frequently contains Fe-Ti oxide, and plagioclase, as well as minor melt inclusions. Weak zoning of greenish-brown cores outward to brown rims are sometimes observed within single phenocrysts.

Three types of hornblende can be distinguished, based on their degree of decomposition and opacitisation (Fig. 5-7). The most common (type 1) hornblende shows black crystal rims composed of minute Fe-Ti oxides, plagioclase and pyroxene. Type 2 only occurs in sample SD1 and shows hornblende decomposition rims in an earlier stage, where individual Fe-Ti oxide crystals can still be identified and are not entirely fringing the crystal. Type 3 hornblende is partially or fully replaced by minute grains of plagioclase, Fe-Ti oxide, and pyroxene and is present as a minor constituent in all dome rocks. In one sample (SD6), type 1 hornblende shows a rim of pale brown glass approx. 9 µm thick, surrounding the reaction rim. Type 1 rim thicknesses are approx. 10 µm. A near Gaussian distribution for the mean reaction rim thickness was noted (Fig. 5-8).

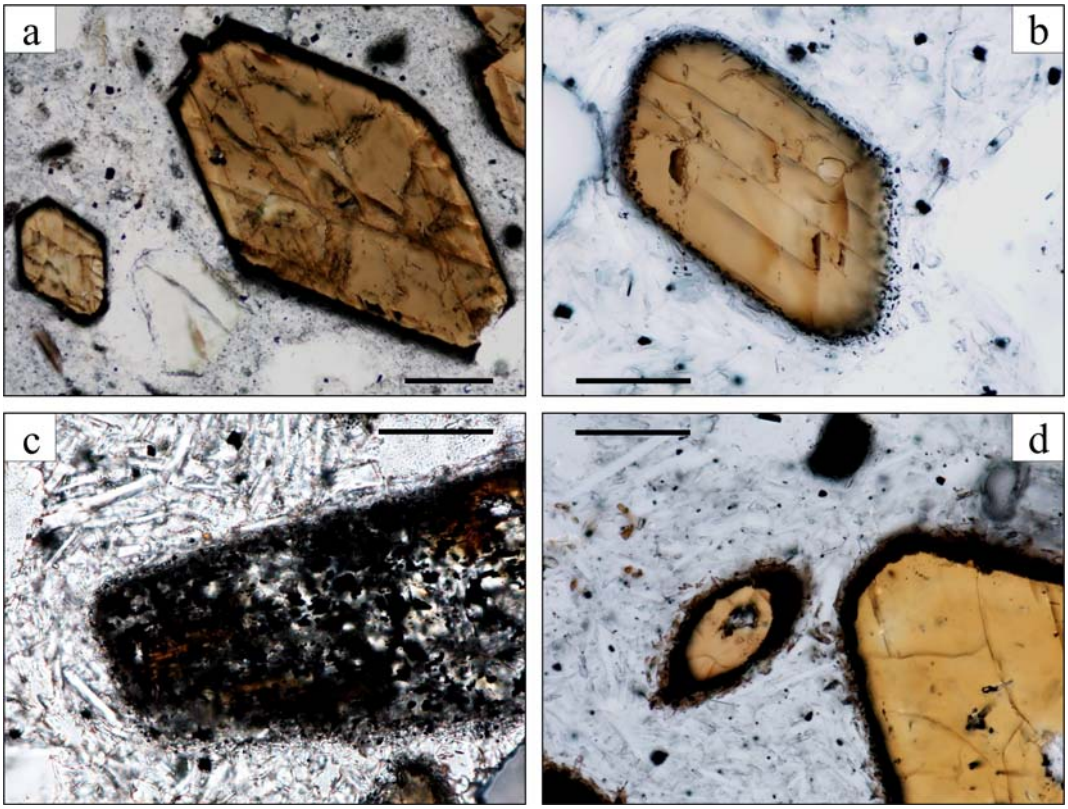


Figure 5-7: Hornblende types. a) type 1 with continuous reaction rim. b) type 2 with discontinuous reaction rim; present only in sample SD1; note individual Fe-Ti oxide crystals are visible. c) type 3 partial to fully replaced hornblende crystals. d) type 1 with observed brown glass fringing the reaction rim; only observed in sample SD6. Scale bar is 100 µm in a) otherwise 25 µm.

Geochemically, the hornblende phenocrysts and microphenocrysts are pargasite and titanian pargasite (Leake et al., 1997a, b, 2003), although core and rim compositions differ in all major element oxides. Octahedral Al^{VI}, the Mg#[3] and the abundance of Na and K in the A-site is usually higher in cores than in rims. Microphenocrysts, on the other hand, have higher Mg# and tetrahedral Al^{IV} and are substantially lower in Na and K than phenocrysts (Fig. 5-9). The increase of Mg# in microphenocrysts is likely caused by progressive oxidation of the magma where ferrous iron is converted to ferric iron.

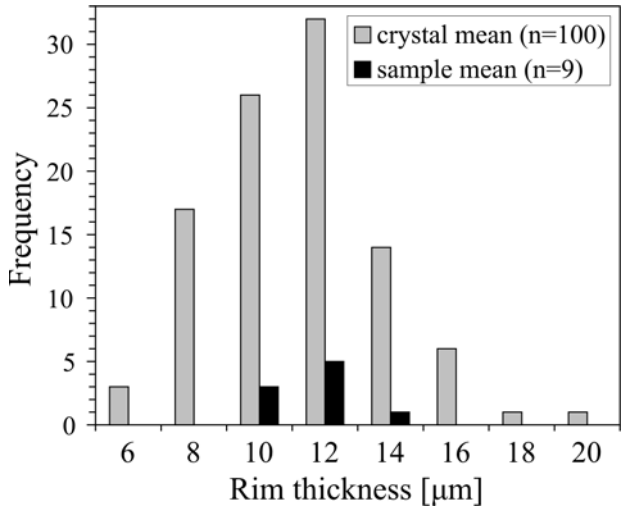


Figure 5-8: Histogram of type 1 hornblende reaction rim thicknesses averaged for crystals and entire samples.

Clinopyroxene in Taranaki dome rocks usually occurs as green to pale green, euhedral to subhedral crystals or as coherent glomerocrysts with attached Fe-Ti oxides of varying sizes from macro- to microphenocrysts. Glass, plagioclase and Fe-Ti oxides are common inclusions. Clinopyroxenes are predominantly augitic in composition and some are diopsides (Morimoto, 1989). Generally, clinopyroxene cores show higher SiO_2, MgO and CaO, and lower TiO_2, Al_2O_3 and FeO abundances than their rims.

Fe-Ti oxides are either present as phenocrysts, groundmass constituents, or as inclusions in clinopyroxene and hornblende. Three distinct groups are recognised according to their appearance as phenocrysts or inclusions (Fig. 5-10). Fe-Ti oxides in hornblende show a large range in Fe^{3+}# from 76.1-90.0 with correspondingly increasing Ti/Al ratios up to 1.7. Inclusions in clinopyroxene, however, show a narrow range in Fe^{3+}# predominantly between 91.1 and 94.4 in a narrow Ti/Al interval of 1.3-1.9. One outlier is noted with a Ti/Al ratio of 7.1. Phenocrysts, on the other hand, display a large variation in Ti/Al ratios from 1.2 to 5.4 over only a minor range in Fe^{3+}# (90.1 to 96.6).

[3] Mg# = $100[Mg^{2+}/(Mg^{2}+Fe^{2+})]$; minimum Fe^{3+} estimated after Schumacher (1997).

It is noted that phenocryst rim and core compositions generally remain nearly constant but this can be masked by cross-sectional effects.

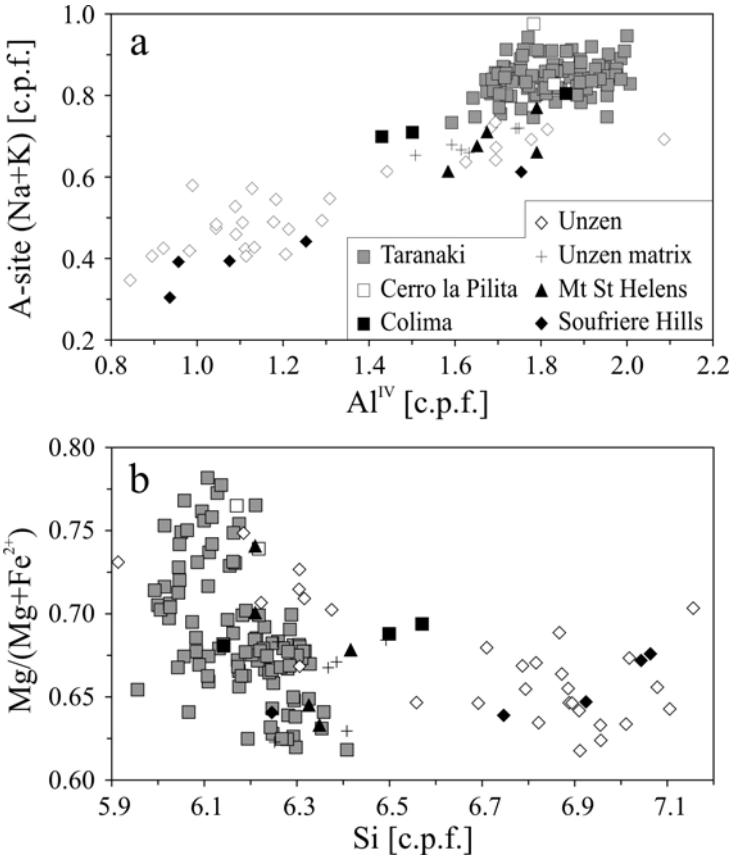


Figure 5-9: Hornblende compositions of the summit lava dome, Mt. Taranaki. a) Na+K (A-site) vs. Al^{IV}. b) Mg# vs. Si; (c.p.f.– cation per formula unit). For comparison are shown recalculated pargasitic hornblende compositions of Unzen volcano, Japan (Sato et al., 1999; Browne et al., 2006; Nakada and Motomura, 1999) [Unzen matrix refers to groundmass crystals], Soufrière Hills Volcano, Montserrat (Barclay et al., 1998; Rutherford and Devine, 2003), Mt. St. Helens, USA (Rutherford and Hill, 1993), Colima, Mexico (Luhr, 2002) and Cerro la Pilita, Mexico (Barclay and Carmichael, 2004).

Biotite is a minor pheno- and microphenocryst often showing reaction rims or rounded margins. Based on Al^{IV} and Mg# contents biotite lies close to the annite-phlogopite series and has 62-81% phlogopite component (Rieder et al., 1998). Orthopyroxene is a subordinate groundmass constituent and rarely observed as a microphenocryst. The general appearance is of weak brownish to translucent colour and is slightly pleochroic with rounded margins. Orthopyroxene cores are sometimes composed of olivine. Apatite is commonly observed as an inclusion in clinopyroxene, hornblende and Fe-Ti oxides but is also a trace constituent in the groundmass. Its composition is relatively uniform with Cl and SO_3 contents ranging between 0.8-3 wt.% and 0.3-1.7 wt.%,

respectively. Since F was not measurable, apatite crystals cannot be clearly classified as chlor- or perhaps fluorapatite.

The dome groundmass is mostly hypocrystalline, consisting predominantly of plagioclase and minor clinopyroxene microlites with small proportions of interstitial colourless glass. Large xenocrystic clusters up to 1.5 cm in diameter are also present in dome samples and predominantly comprise plagioclase, clinopyroxene, Fe-Ti oxide ± hornblende and interstitial pale brown glass.

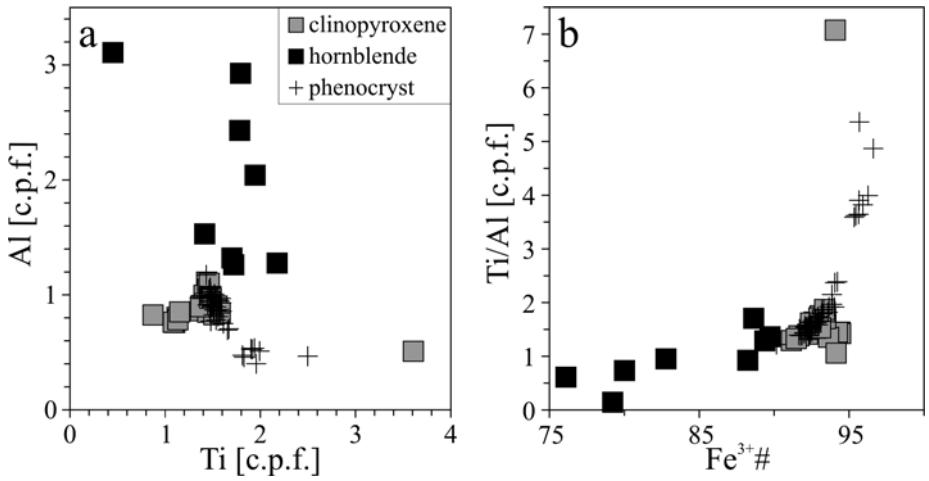


Figure 5-10: Compositions of Fe-Ti oxide phenocrysts and inclusions in clinopyroxene and hornblende. a) Al vs. Ti. b) Ti/Al vs. Fe^{3+}# (c.p.f. – cations per formula unit). Cations are calculated on the basis of 32 oxygens.

Major element compositions of melt inclusions trapped in hornblende and clinopyroxene were determined. Hornblende melt inclusions (n=7) are distinct from clinopyroxene melt inclusions (n=21; Fig. 5-11). Melt inclusions in clinopyroxene show higher silica contents from 64.5-71.6 wt.% compared to 59.7-66.3 wt.% SiO_2 in hornblende melt inclusions.

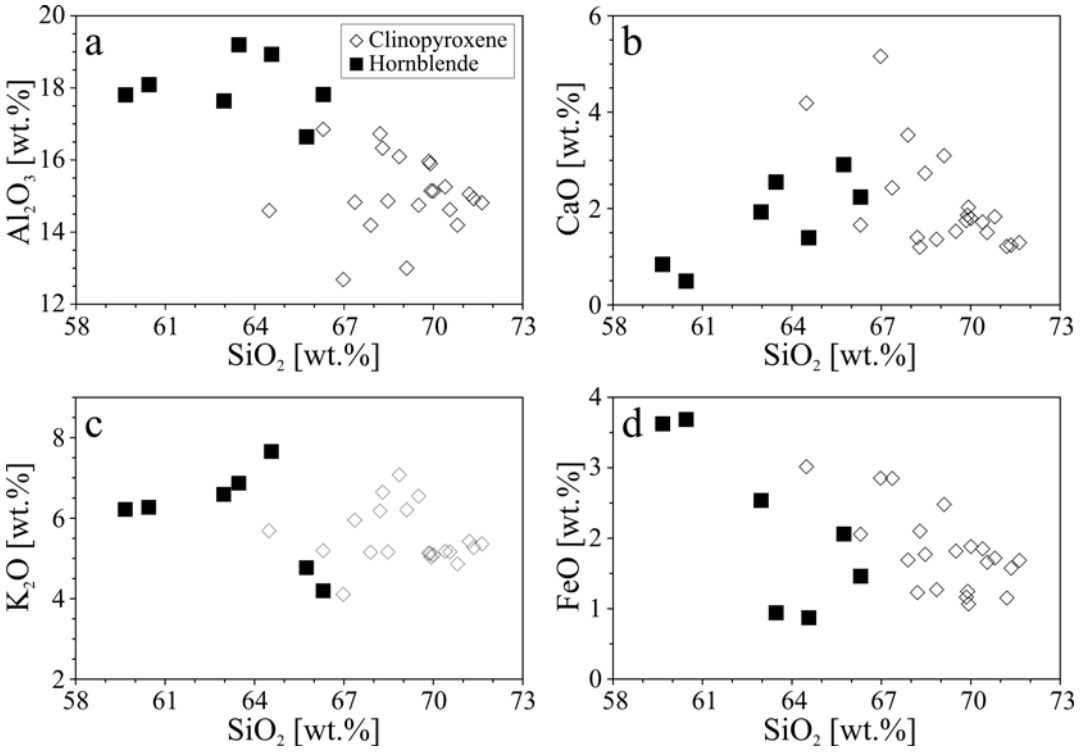


Figure 5-11: Glass compositions of inclusions in clinopyroxene and hornblende. Silica is used as differentiation index. Note that inclusions in different host minerals form separate groups.

5.4.3 Bulk Rock Composition

Volcanic rocks erupted in the past 10 ka at Mt. Taranaki are high-K, low-Si and high-Si andesites from the main summit cone, with minor high-K basalts erupted from the parasitic cone of Fanthams Peak. The general geochemical trend over the past 130,000 yrs of Mt. Taranaki's history shows that the rocks became progressively more potassic and siliceous (Zernack et al., 2006), but within any given eruptive period variations across the whole spectrum of compositions may occur, as will be shown for the youngest products. Major, trace element and isotopic compositions of the broad Mt. Taranaki rock suite are described in more detail by Price et al. (1992), Stewart et al. (1996) and Price et al. (1999).

The present summit lava dome is homogeneous in its major element chemistry (Fig. 5-12) with only minor variations in SiO_2 (56.4-57.5 wt.%), CaO (6.9-7.1 wt.%), Fe_2O_3 (6.6-7.1 wt.%), and Al_2O_3 (17.4-17.8 wt.%). The dome rocks can be classified as a high-K, low-Si andesite (Gill, 1981; Le Maitre et al., 1989). Trace element abundances are also uniform across the sample suite with minor variations for Cr (<1-28 ppm) and Sr (591-627 ppm). A single sample stands out from the suite because of its higher

values of Mg#, Cr, Cu and Zr values, and lowest Sr content (lower coulée flow, sample SD13).

Barium abundances appear bimodal with four samples containing 755-789 ppm Ba and six samples in the range of 982-1019 ppm. This variation, however, was the result of an analytical error in the XRF data; the four samples were analysed as one batch which gave consistently similar but lower abundances in Ba. Subsequent Laser ICP-MS analysis confirmed that the results were anomalous. In addition, if the Ba anomaly was real, K_2O and/or Rb should show similar covariance with Ba due to their similar ionic radii and affinity for certain mineral phases. They do not.

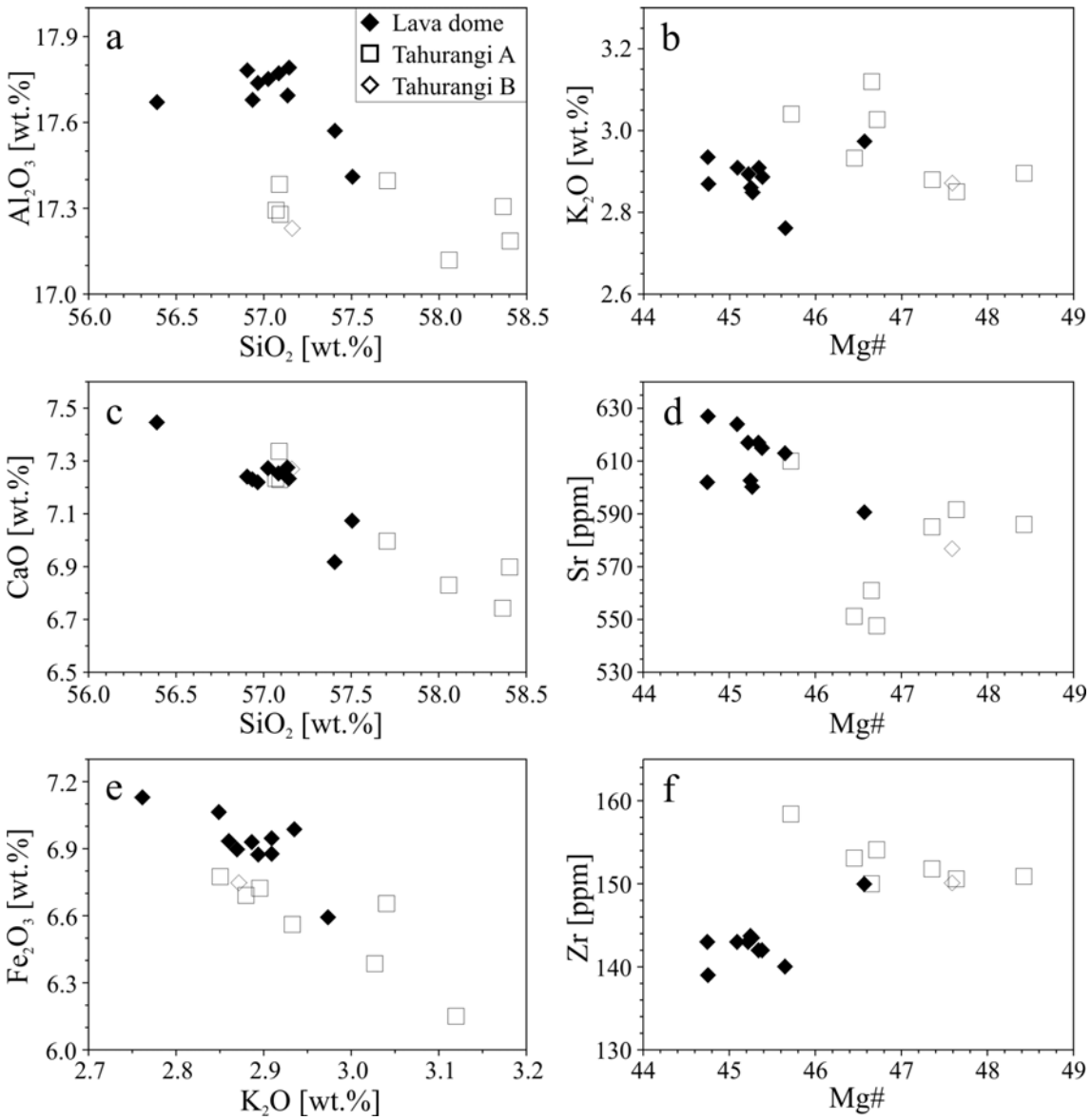


Figure 5-12: Bulk rock compositions of the summit lava dome and the Tahurangi BAF A and B deposits. Dome compositions are distinct to Tahurangi rocks as illustrated for Al_2O_3 (a), Mg# (b, d) Fe_2O_3 (e) and Zr (f).

The chondrite normalised REE pattern (Fig. 5-13b) is smooth with a negative slope for elements La to Er (La_N/Er_N = 6.04-7.38) with a sub-horizontal progression from Er to Y. Normalised La_N/Y_N ratios vary between 6.15 and 7.21 indicative of relative enrichment of LREE over HREE. The patterns of trace elements normalised to N-type MORB (mid ocean ridge basalt; Fig. 5-13a) show greater abundances for the large-ion-lithophile elements (LILE – Sr-U) compared to more compatible and high field strength elements (HFSE – Nb, Zr, Hf, Ti). It is observed that high field-strength (HFS) elements Nb, Zr and Hf have similar values; Ti is offset to lower abundances. The elements Ti to Yb are depleted in comparison to MORB (i.e. <1). On the relatively smooth Ba-Yb line Nb forms a negative trough. It is noted that Pyramid Dome and Tahurangi BAF rocks show higher Rb abundances than older Mt. Taranaki rocks (see Fig. 1-5). The comparison of summit dome rocks and Tahurangi BAF A+B rocks show clear differences in Al_2O_3, Mg#, Zr (Fig. 5-12) and Cr, although normalised trace element patterns are virtually identical (Fig. 5-13).

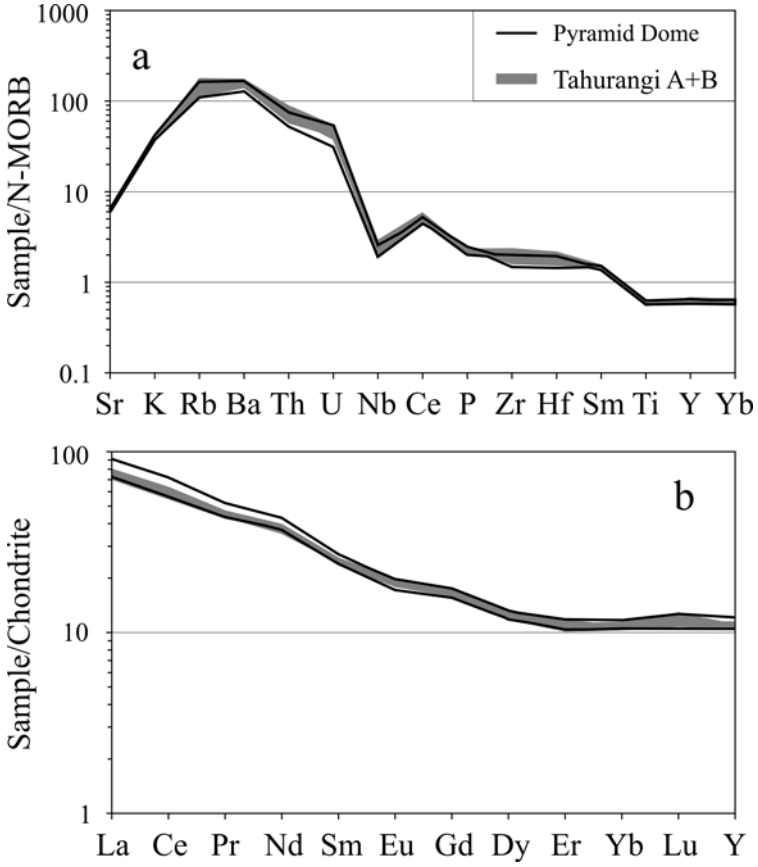


Figure 5-13: Trace element patterns of the Pyramid Dome and Tahurangi BAF deposits normalised to N-MORB (a) and chondrite (b). Pyramid Dome rocks and Tahurangi BAF deposits show nearly identical trace element patterns. For the light rare earth elements slightly higher abundances in Tahurangi BAF deposits are noted. Normalisation after Sun and McDonough (1989).

5.4.4 Microstructure, Density and Permeabilitiy of Dome Rocks

Textural studies of dome rocks revealed micro-cracks that occur around individual crystals and a succession of sub-parallel cracks within the groundmass also occur (Fig. 5-14).

The bulk density of eight dome rock samples ranged from 2.19 to 2.49 gcm^{-3} with bulk vesicularities of 12.4 to 22.8%. The mean solid density of five powdered samples is 2.84 gcm^{-3}. The permeability ranges over one order of magnitude between 6.8×10^{-13} m^2 and 5.8×10^{-14} m^2. This permeability is similar to that of dome rocks inferred from decompression experiments (Melnik and Sparks, 2002; Mueller et al., 2005).

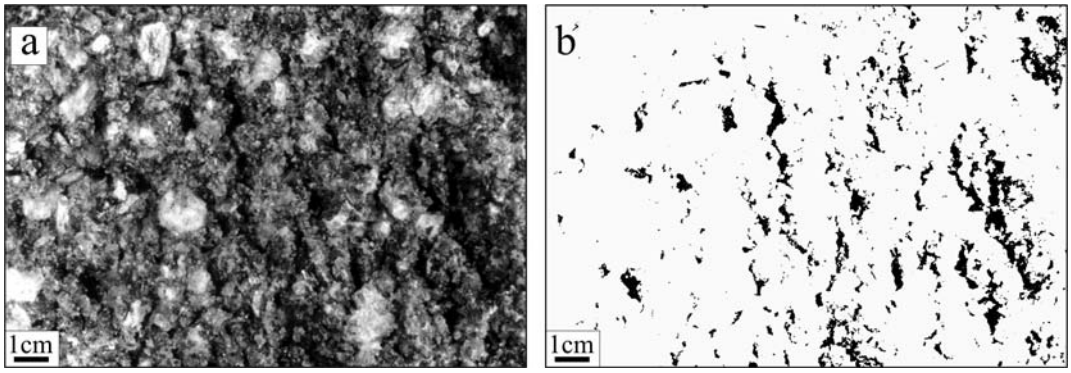


Figure 5-14: Texture of rock sample SD6. a) photograph shows sub-vertical, near parallel crack patterns and cavities. b) modified image of a) highlighting cracks and cavities in black.

5.5 Discussion

5.5.1 Lava Dome Emplacement and Growth

In order to reconstruct emplacement mechanisms of the Pyramid Dome, the underlying surface needs to be modelled. From the inferred dome dimensions, a SE-NW cross-section is created to calculate the underlying slope. A planar inner-crater floor is assumed. The centre point of the body represents the inferred vent location and is positioned at the break in slope. The underlying slope of the upper flank of the volcano is calculated at c.20° (Fig. 5-6c), from the distribution of the dome remnants around the present-day amphitheatre surface (c.26°).

The presence of a coulée lava flow to the north of the amphitheatre and two thick lava flows on the northern dome side, along with the hemispherical shape of the SE side of the dome, suggest combined exogenous (extrusive) and endogenous (intrusive) dome

growth. Exogenous and endogenous phases are thought to be related to changes in magma extrusion and/or magma ascent rates, such as those observed at Mt. St. Helens (Anderson et al., 1995). At Mt. Taranaki, both phases of growth occurred, either simultaneously or alternately. This is primarily caused by the vent location at or near the break in slope where the downslope side favours the formation of stacked lava lobes, whereas the "upslope" or crater side promotes growth by inflation. Endogenous dome growth is promoted by the development of a thick cooled dome crust that hinders the breakout of lava, and endogenous dome growth probably occurred at a very slow rate. Exogenous growth by fast downslope extrusion of lava lobes and endogenous growth with a slowly inflating inner crater dome side therefore probably proceeded simultaneously.

Even though a reconstruction of all dome growth phases and their relative duration is not possible from the exposed dome remnants, it is likely that dome emplacement and growth took place during a single sustained event (Fig. 5-15). Single lava lobes extruded onto the upper W-NW flanks advanced at least 300 m (true distance) downslope from the vent. With continuous lava production lava lobes were stacked on top of each other. At the same time, smaller volumes of lava were extruded onto the inferred crater floor to form a near hemispherical shape. The scars of the amphitheatre reveal relatively smooth upper rock faces which may be indicative for the predominant endogenous growth in this part of the dome (Fig. 5-4b). Penetration of the dome carapace is observed on the NE side, about 120 m from the inferred vent location, where lava extruded forming two block lava flows. The smooth rock faces only c.30 m from the discharge point, however, do not show any textural changes which may indicate exogenous growth. Based on field observation it is likely that the two NE lava flows as well as the small spine forming the highest point of the remnant dome were extruded during the final growth stage (Fig. 5-15e). The blocky flow field to the north is an indirect indication for high extrusion rates of the two lava flows where rapid fracturing of the flow surfaces generated abundant small blocks. A correlation between block size distribution and extrusion rate was observed at Mt. St. Helens and Unzen volcano where low extrusion rates cause less intense flow surface fragmentation promoting the development of large slabs. By contrast, high extrusion rates cause the formation of more abundant smaller blocks (Anderson et al., 1998). However, the steep north slopes of c.32° may have caused additional fracturing due to mechanical and thermal processes.

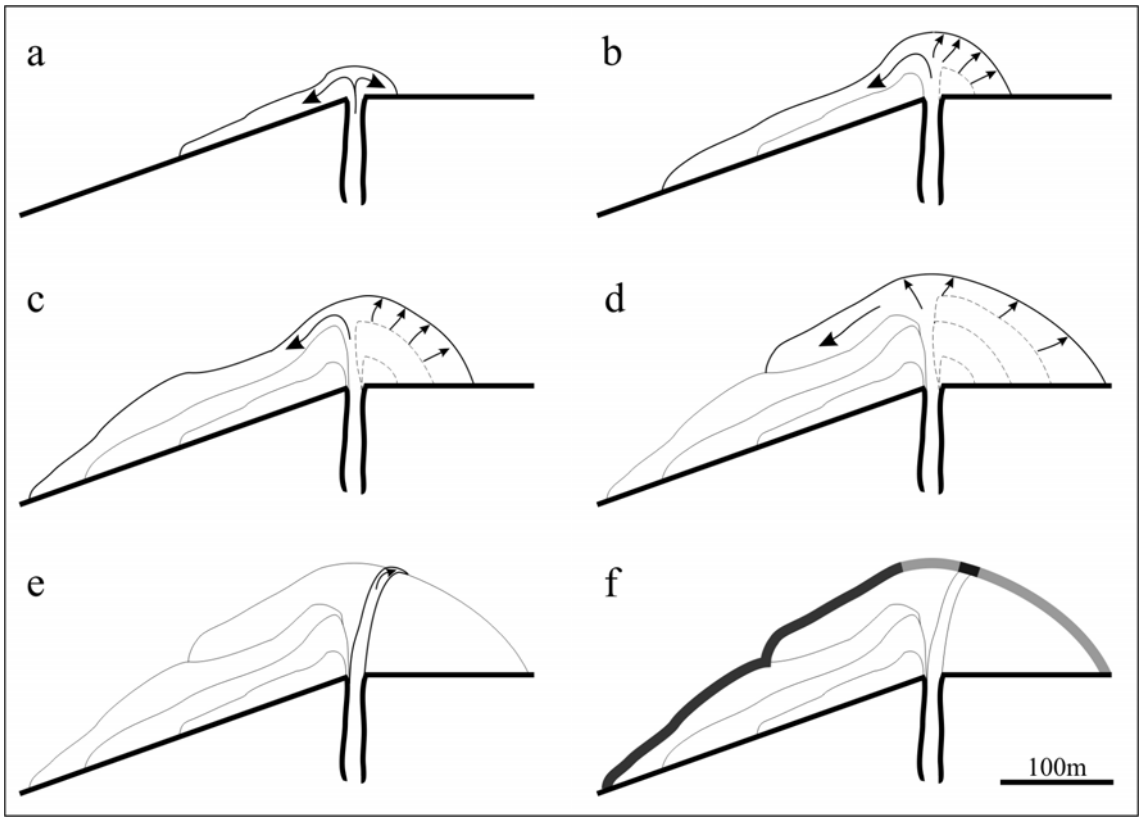


Figure 5-15: Lava dome growth patterns are illustrated in a-e. Exogenous and endogenous dome growth occurred simultaneously. f) demonstration of the inferred exogenously (dark grey) and endogenously (light grey) formed surfaces as observed on the dome remnants.

The development of a vesicular dome carapace (SE-E dome portion) leads to two potential conclusions. Firstly, the vesiculation of the lava surface at atmospheric pressure proves that the magma ascent was at a sufficient high rate to retain magmatic gases which later exsolved from the carapace. This implies that even the endogenous growth may have occurred relatively rapidly. Secondly, inferred high magma ascent and extrusion rates point to a low viscosity magma. Studies of lava dome surface textures during dome formation at Mt. St. Helens (1980-1986) conclude that at high magma extrusion rates, the lava does not degas completely which later promotes vesiculation of the surfaces and the formation of a carapace (Anderson et al., 1995).

The hemispherical dome shape was probably not only caused by endogenous growth but was also influenced by the confining crater wall. Here the initially extruded lava impinged on the crater wall (see title photograph), forcing itself upwards and hence contributing to endogenous growth. The assumption of a relatively low viscosity of the magma is born out by the presence of two lava flows near the top of the dome.

In summary, the homogenous interior structure and chemical composition implies that the Pyramid Dome was formed during a single and short extrusive event. Associated

lava flows and lobes superimposed on a dominantly hemispherical shape indicate simultaneous exogenous and endogenous dome growth, although the latter seems to have been dominant. The formation of a vesicular dome rind (carapace) along with inferred relatively high growth rates point to a low viscosity (and hot) magma extruded at relatively high magma ascent and extrusion rates.

5.5.2 Lava Dome Collapse

Evidence from the natural remanent magnetisation of clasts within the youngest rock-avalanche deposit suggests deposition temperatures <350 °C. This implies that since the summit dome is the obvious source of the landslide, it must have cooled to below 350 °C before the collapse occurred. This implies a considerable time lapse between emplacement and collapse. Additionally, some time is also implied by the presence of an extensive hydrothermally altered central zone in the central dome portions. The presence of fractures and faults transecting the entire dome is a further indication for its brittle state and hence relatively low temperature at the time of collapse (see Fig. 5-4c and below). If they were created while the dome had a ductile interior then those fractures would likely be annealed or possibly deformed by subsequent flow. The presence of listric faults also implies formation in a brittle near-solid state, which is most likely in a post-eruption cooled condition (ie. a ductile dome interior can be excluded). The northern part of the collapsed amphitheatre along with the curvature of the amphitheatre itself indicates that the dome failure and disintegration occurred along these predefined fault planes (see Fig. 5-4c).

Micro-cracks described around crystals in dome-rock samples are interpreted to represent rapid contraction of groundmass and crystals during cooling. Sub-parallel crack patterns are likely to be the result of stretching, indicating ductile failures rather than brittle fractures (cf. Smith et al., 2001). Large gravitational forces (e.g. extrusion on steep slopes), viscosity increase during cooling, and strain intensification around rigid crystals are probably the main reasons for such crack development (also known as cavitation by Smith et al., 2001). Hence, these micro-cracks developed both syn- and post-eruptively. Physical weathering (including water and ice interaction) may have also enhanced crack development. With the presence of abundant micro-cracks the measured permeability (and porosity) values shown above are probably much higher than the

actual permeability at the time of emplacement. This supports the interpretation of the observed dome carapace. At the time of emplacement, gas escape was low, hence a vesicular dome rind could develop, which is probably also linked to high extrusion rates.

The arcuate amphitheatre on the western summit dome face could have been formed syn- or post-eruptive. A similar arcuate surface structure is observed on The Dome. Both lava domes are resting on steep slopes and these downslope opened arcuate structures may reflect subsidence, from the upper vent area by magma withdrawal. In the case of the summit dome, the arcuate shape could also trace the underlying collapsed western crater structure[4].

The reasons for dome failure may have included the development of a weak inner core structure through hydrothermal alteration above the vent zone. This instability was probably also exacerbated by cooling and post-emplacement subsidence fractures. The steep and unconsolidated substrate beneath the up to 100 m thick dome was likely an important pre-conditioning factor for dome instability. The failure event could have been triggered by an earthquake, heavy rain or even climatic disturbance (e.g. snow load). Distant tectonic earthquakes (up to 100 km) have been shown to destabilise growing lava domes (Walter et al., 2007). The occurrence of frequent earthquakes within a 25 km radius SW-NW of Mt. Taranaki could have caused sudden fracture initiation and propagation within the western part of the dome.

Based on the location and curvature of the amphitheatre scar and the erosion gullies on the slope, four collapsed sectors are identified (Fig. 5-16) in an anticlockwise direction: I-northwest, where only the upper portion was removed; II-WNW with a collapse over the total dome depth; III-SSW with a smaller collapse through the entire depth; and IV-south with only a superficial collapse with collapsed material remaining in the crater (see Fig. 5-4f). These sectors may have failed independently. Multiple deposition episodes are indicated by a thin pocketing fine ash layer within the rock-avalanche deposit observed at only two proximal locations (outcrops 47 and 48; Fig. 5-3). This demonstrates a small time break occurred between avalanches that allowed an elutriated cloud of ash from the initial collapse to settle. The thin silt layer is absent in distal deposits, which may indicate that the initial collapse was only minor.

[4] Although the western crater rim is breached and at least in parts collapsed to depths of >100 m (see Okahu Gorge) there is no other field evidence which may indicate a pre-dome, arcuate collapse structure of the western crater area.

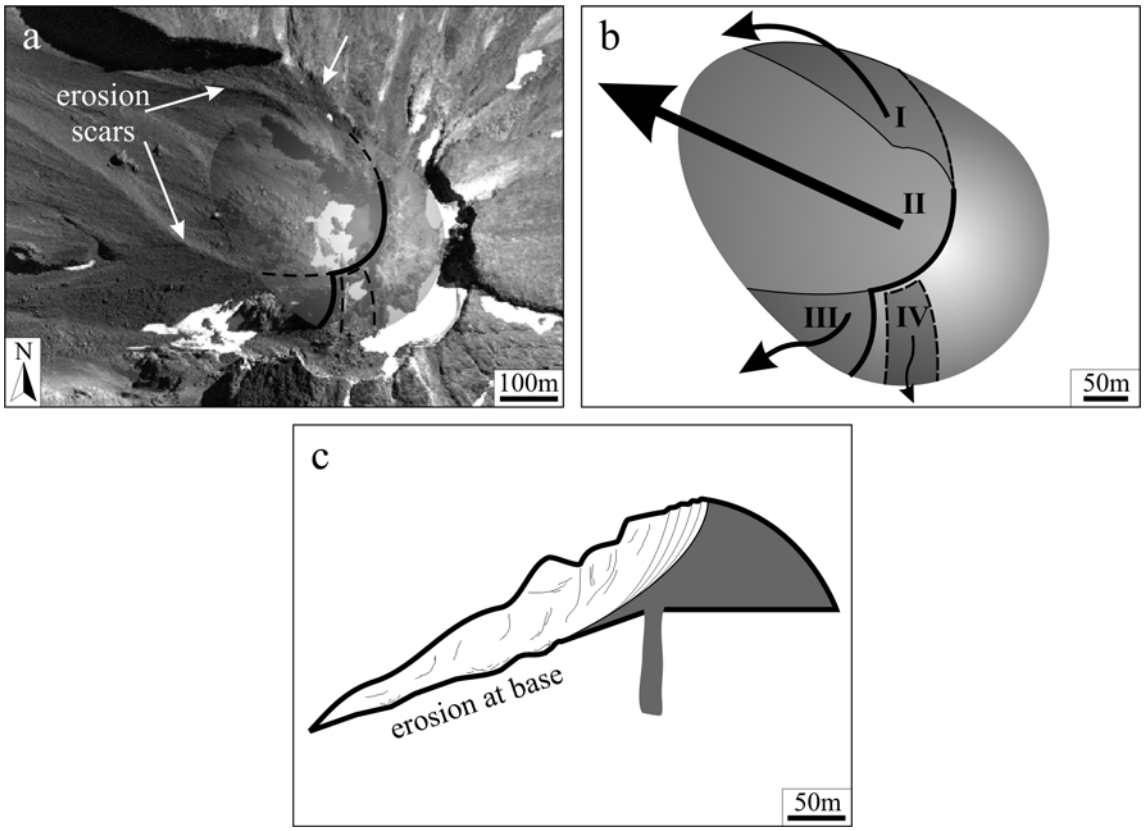


Figure 5-16: Reconstruction of the summit dome failure. a) erosion scars on upper flank (white arrows) as well as the curvatures of the amphitheatre, and the scars to the SW and S define the geometry of individual collapse sectors. b) dome geometry with individual sectors I-IV and their flow directions. c) cross-section of the dome showing the dome remnants (grey), and the disintegration of dome rocks along listric faults.

Although it is impossible to fully reconstruct a time frame for the dome collapse process, the sequence of dome collapse events can be hypothesised. Partial sector collapse (from sector I) likely occurred before the major collapse from sector II because the erosion scars of collapse II are not obliterated or modified by collapse I (Fig. 5-16a). This is also consistent with the assumption from deposit evidence above that stage 1 deposits are derived from a lower volume, partial sector collapse. The collapse of zones III and IV are probably concurrent with the major collapse event. The collapse of sector III is closely related to the partial collapse of the older underlying, hydrothermally altered crater lava flow deposits at the entrance of the Okahu Gorge (Fig. 5-4e). The unstable bouldery talus field within the amphitheatre postdates the major collapse (II). Similar arcuate amphitheatres developed as a result of dome collapses have also been observed, for example, at Dikii Greben' volcano, Kamchatka (Ponomareva et al., 2006). Here arcuate, concave uphill ridges are also observed which are against flow direction. The dome collapse is interpreted to have occurred after the main dome-building phase (Ponomareva et al., 2006).

The polylithologic character of the resulting rock-avalanche deposit is primarily due to firstly, the variety of rock domains within the dome that have undergone different degrees of vesiculation, oxidation, cooling and hydrothermal alteration. Some dome substrate material and also surficial accidental clasts may have also been incorporated into the avalanche (Fig. 5-16c). In contrast, many of the BAF deposits are monolithologic (e.g. Tahurangi BAFs A and B) and emplaced at temperatures above the Curie Point. The monolithologic nature of these units testifies to collapse during dome growth, soon after lava effusion that allowed little time for hydrothermal alteration and differential degrees of oxidation.

5.5.3 Estimation of Eruption Parameters

5.5.3.1 Magma Source Areas

The brittle-ductile transition zone (BDTZ) recognised at 10 km beneath Mt. Taranaki is interpreted to represent magmatic intrusions (Sherburn and White, 2005). This implies magma storage at mid-crustal levels. The BDTZ represents a rheological boundary and often coincides with the level of neutral buoyancy explained by density equilibration between magma and its surrounding country rock (e.g. Holm, 1995; Marquez et al., 2001).

Possible magma storage depth(s) can also be inferred from hornblende crystallisation pressures by applying the aluminium-in-hornblende geobarometer. This geobarometer for calc-alkaline plutonic complexes was first empirically developed by Hammarstrom and Zen (1986) and progressively experimentally refined by Hollister et al. (1987), Johnson and Rutherford (1989), Blundy and Holland (1990), Thomas and Ernst (1990), Schmidt (1992), Anderson and Smith (1995). The barometer is experimentally calibrated to the mineral assemblage quartz + K-feldspar + plagioclase + biotite + Fe-Ti oxide + sphene over a pressure range of 2-8 kbar with an estimated error of ± 1 kbar. Because the required conditions for this geobarometer are not met for Mt. Taranaki rocks (quartz, K-feldspar, and sphene are microscopically absent; the exception is sphene in some xenoliths; Gründer, 2006), the total pressure estimates yielded are maxima for K-feldspar-absent samples. The role of sphene still remains unknown; an overestimation in calculated pressure may therefore be up to 1.5 kbar (c.f. Hollister et al., 1987; Johnson and Rutherford, 1989; Anderson and Smith, 1995).

The data show a total calculated maximum pressure range for hornblende between 4.5 and 6.7 kbar based on minimum ferric estimates in hornblende after Schumacher (1997) [hornblende calculations based on 23 oxygens yield lower pressures by 0.42 kbar]. Assuming an overestimation of 1.5 kbar, hornblende crystallisation pressures of 3-5 kbar[5] would correspond to depths of 9.5-17 km[5]. Two maxima are observed for hornblende core formation, the first between 4 and 4.5 kbar and a second between 3 and 3.5 kbar (Fig. 5-17). Hornblende growth continues to pressures down to 3 kbar as calculated from rim compositions. Highest crystallisation pressures are recorded for some rim compositions and are the result of reverse zoning in some hornblende phenocrysts, probably caused by an increase in pH_2O (Luhr and Carmichael, 1980).

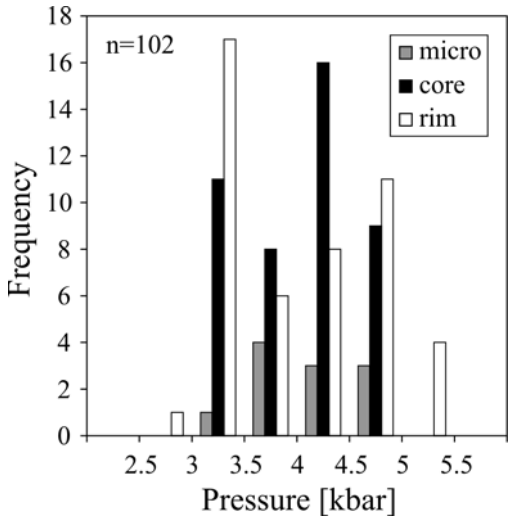


Figure 5-17: Aluminium-in-hornblende geobarometer shown as histogram for hornblende phenocrysts (core and rim) and microphenocrysts. Calculated after Johnson and Rutherford (1989) and corrected by -1.5 kbar.

For temperature estimates of hornblende formation, the amphibole-plagioclase thermometer of Holland and Blundy (1994) is used, which can be applied over a temperature range of 400-1000 °C at 1, 5, 10 and 15 kbar. The uncertainty of this thermometer is ±30-40 °C, however, it may be higher if the iron-rich hornblendes are oxidised and the ferrous/ferric ratio in hornblende is not well defined. Temperature estimates for 19 hornblende-plagioclase pairs range between 867-928 °C at an assumed pressure of 5 kbar (c.17 km). Eight pairs are restricted between 900-920 °C. It is

[5] Calculations of the lithostatic pressure include a 2000 m high edifice, i.e. 1.1 kbar correspond to 2 km depth below sea level (see Fig. 5-18).

assumed that hornblende and plagioclase are in equilibrium since no rounded edges or resorption of plagioclase inclusions were observed.

The data of this study are consistent with the literature (see above), and suggest that hornblende in the dome rocks started crystallising at approximately 17 km depth (see also Fig. 5-18). The two hornblende populations likely reflect two crystallisation pressures, and hence, two storage levels at c.9.5 and 14.5 km depth, at temperatures of about 900 °C. The crystallisation of hornblende at mid-crustal levels is generally in agreement with the proposed model of the Mt. Taranaki magma evolution by Stewart et al. (1996) where ascending hydrous basaltic andesite melts re-enter the hornblende stability field at shallower depths.

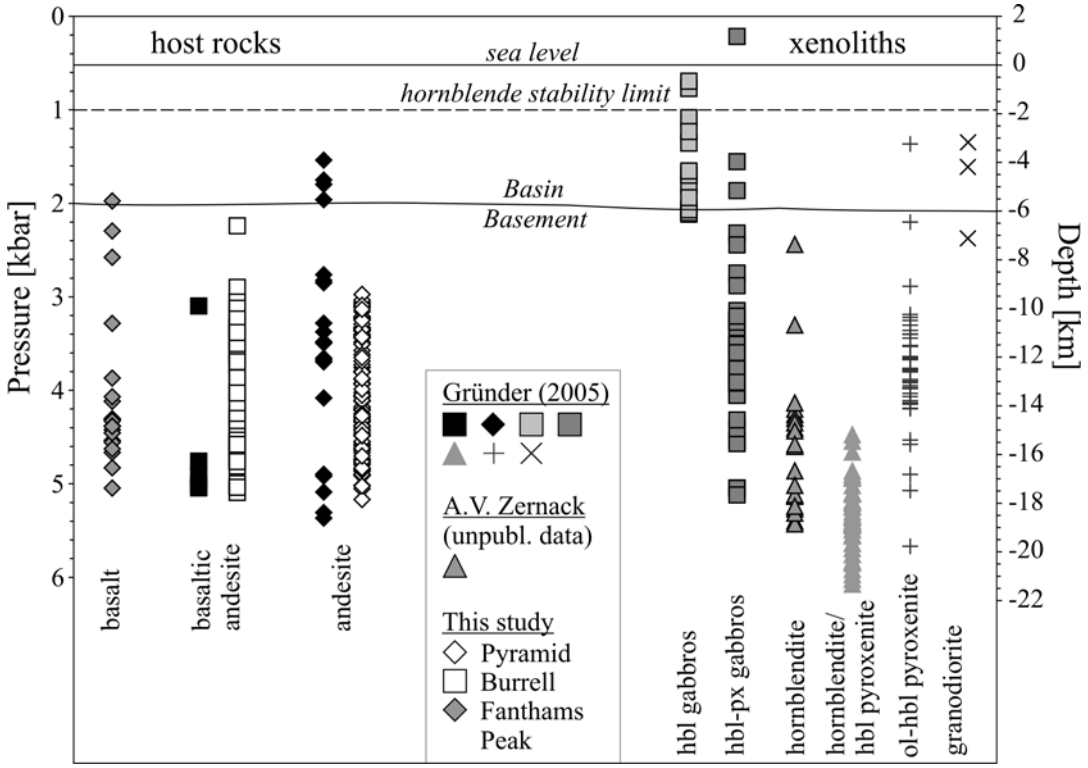


Figure 5-18: Comparison of calculated hornblende crystallisation pressures for various Mt. Taranaki rocks and xenoliths. Granodiorite xenoliths contain all required mineral phases for the Al-in-hornblende geobarometer (Johnson and Rutherford, 1989) and therefore were not corrected. Note that some hornblende crystals of hornblende gabbros and hornblende-pyroxene gabbros indicate crystallisation below (<1 kbar) the inferred hornblende stability limit. Data of Gründer (2005) and A.V. Zernack were recalculated using the procedure described above.

There are two possibilities to explain the presence of two hornblende populations within an erupted magma: 1) the two hornblende populations belong to the same magma which stagnated at two different levels within the lower and middle crust, or 2) it represents mixing of two hornblende-phyric magma batches where the deeper-stored magma intrudes into the high-level source area. Although scenario 1 appears to be the simplest

explanation, its disadvantage is that the final ascent to the surface from the high storage level has to be initiated by internal processes, i.e. the threshold of neutral buoyancy must be overcome by internal processes such as crystal segregation and fractional crystallisation processes. The most common trigger of mobilising magma is, however, the input of heat by a more buoyant magma (e.g. Soufrière Hills Volcano, Montserrat [Murphy et al., 1998], Mt. Pinatubo, Indonesia [Pallister et al., 1992], Augustine volcano, Alaska [Roman et al., 2006]), and this favours scenario 2. Scenario 2 requires homogenous mixing since neither macroscopic nor microscopic textures imply the existence of two magmas. Despite this, scenario 2 is favoured. Magma mixing of two magmas at depth can be petrographically indistinguishable because the mineral assemblage in hornblende-phyric magmas of basalts, basaltic andesites and andesites is nearly identical (see Chapter 7). Homogenous mixing is even more likely when the melts of both batches contain sufficient water (indicated by hornblende crystallising), and hence have relatively low viscosities. In addition, the extruded Pyramid magma is geochemically distinct from any other dome rocks extruded during the Maero Eruptive Period, including the immediately preceding eruption. Given the general trend of K_2O enrichment in Mt. Taranaki rocks over time the latest magma is anticipated to have highest values for K_2O (and also SiO_2). Instead it has relatively low K_2O and SiO_2 contents, along with higher Al_2O_3 wt.% and lower Mg# than other dome-forming magmas (see also Fig. 7-2 and Fig. 7-6). This suggests mixing of at least two geochemically distinct magmas: 1) a low-level magma (c.14.5 km depth) basalt/basaltic andesite magma with high Al_2O_3 and Mg# and low SiO_2 and K_2O abundances (similar to those observed at Fanthams Peak); and 2) a high-level more evolved (probably andesitic) magma. The mixing of these two appears to generate the unique properties of the Pyramid lava dome within the Maero series. The low dome volume may be consistent with a small volume, but mobile magma at depth.

5.5.3.2 Magma Storage at the Level of Neutral Buoyancy

Magma storage depths are often controlled by their level of neutral buoyancy. In order to overcome this threshold and rise to the surface, the magma has to reduce its density. On the basis of hornblende-geobarometry and geophysical evidence, the mid-crustal storage region occurs at c.9.5 km depth at or near the BDTZ. Although smaller magma

batches may be stored temporarily at even lower pressures within a 5 km-diameter dyke complex inferred below the volcano (Locke and Cassidy, 1997; Sherburn et al., 2006), a major magma source area at shallower depths is unlikely since there were no geophysical indicators in the 1993 and 2001-2002 surveys (Cavill et al., 1997; Sherburn and White, 2005).

The main reason for final magma ascent was likely the injection of hot and probably less evolved magma from depth, as discussed in the previous chapter. However, another process may have preceded this event. Fractional crystallisation may also reduce magma density, although it requires more time than the injection process. The crystallisation and separation of mafic mineral phases (i.e. hornblende and clinopyroxene) would significantly change the remaining melt density. The presence of abundant microscopic and macroscopic cumulates of hornblende and clinopyroxene ± plagioclase show that this process was at least partly in operation.

Extensive hornblende crystallisation is evident by geochemical changes of melt and Fe-Ti oxide phases. Three compositionally distinct groups of Fe-Ti oxides are recognised with increasing Fe^{3+}#, as inclusions in hornblende and clinopyroxene, and as phenocrysts (Fig. 5-10). The same grouping is reflected in Al contents. Fe-Ti oxides are sensitive to changes in the magmatic system, especially fO_2 and temperature, which are geochemically recorded even on short eruptive time scales, similar to reaction rim formation of hornblende crystals during decompression (e.g. Rutherford and Hill, 1993; Venezky and Rutherford, 1999). The rapid drop of Al_2O_3 in Fe-Ti oxides at near constant TiO_2 contents is primarily caused by hornblende crystallisation, since it is composed of 11.0-13.5 wt.% Al_2O_3. Clinopyroxene, co-crystallising at a later time, contains Fe-Ti oxide inclusions of an intermediate Al_2O_3-TiO_2 composition (Fig. 5-10). The suite of Fe-Ti oxide phenocrysts has a wide range in Ti/Al ratios, and the progressively lower Al_2O_3 contents signal the onset of plagioclase crystallisation and simultaneously the cessation of hornblende formation. Plagioclase crystallisation is sensitive to water pressures and could indicate an advanced stage of magma degassing, also supported by increased Fe^{3+}#. The sharp change in Ti/Al ratios for groundmass Fe-Ti oxides probably indicates crystallisation at reduced pressures and water contents, i.e. crystallisation during magma ascent. It appears that melt inclusions record a similar history; first the melt experiences dominant hornblende crystallisation evolving from c.60 to 66 wt.% SiO_2, then hornblende crystallisation and growth ceased and dominant clinopyroxene (and plagioclase) crystallisation governs the melt evolution, shifting melt

silica contents to higher values up to 72 wt.% (Fig. 5-11). Fractionation by gravitational settling of both mafic phases produces a restite layer at the bottom of the magma body; observed microscopic and macroscopic cumulates could therefore represent either co-genetic assemblages or xenoliths if in the latter case the ascending magma penetrates other source areas.

5.5.3.3 Inferences for Hornblende Stability

The occurrence of hornblende in many subduction-related volcanic rocks is associated with water-rich magmas, and hence higher potential for explosivity. Understanding these magmatic conditions has been a focus in experimental petrology over the past two decades. Studies were directed towards well documented eruptions of hornblende-andesite (e.g. Soufrière Hills Volcano, Montserrat; Barclay et al., 1998; Rutherford and Devine, 2003) and dacitic volcanoes such as Mt. St. Helens, USA (Rutherford and Devine, 1988; Rutherford and Hill, 1993), Mt. Unzen, Japan (Sato et al., 1999; Holtz et al., 2005), and Mt. Pinatubo, Philippines (Prouteau and Scaillet, 2003). However, experimental studies on natural hydrous, hornblende-bearing basalts, basaltic andesites and andesite are less common (Moore and Carmichael, 1998; Barclay and Carmichael, 2004). Experiments based on natural rocks with pargasitic hornblende by Rutherford and Devine (1988), Foden and Green (1992), Rutherford and Hill (1993), Moore and Carmichael (1998), Sato et al. (1999) and Barclay and Carmichael (2004) are used for comparative purposes in this study.

The stability of synthesized pargasite was first studied by Boyd (1959) and later by Holloway (1973) who determined a minimum stability of 1 kbar at 1000 °C. In contrast to the conclusions of Westrich and Holloway (1981), Lynkins and Jenkins (1992) found that the stability of pargasite in equilibrium with olivine and orthopyroxene in the system Na_2O-CaO-MgO-Al_2O_3-SiO_2-H_2O was stable at low pressures (0.4 kbar) at 750 °C. The crystallisation of groundmass pargasite during the 1991-1995 Unzen eruption also occurred at a relatively low stability limit of 0.98 kbar at 900 °C and 0.48 kbar at 820 °C (Sato et al., 1999), whereas Mt. St. Helens pargasite was shown to be stable above c.1.1 kbar and 1.7 kbar at 830 °C and 910 °C, respectively (Rutherford and Devine, 1988). Sato et al. (1999) argue that the reduction in pargasite stability in dacite

systems at Unzen volcano relative to Mt. St. Helens are probably due to higher SiO_2 contents and higher K_2O/Na_2O ratios in the Unzen groundmass compositions.

Andesites (Colima volcano, Mexico) and basaltic andesites (Mascota volcanic field, Mexico) were investigated by Moore and Carmichael (1998) who determined hornblende stability limits of 0.5 kbar at 950 °C and 1 kbar at 1000 °C, respectively. Barclay and Carmichael (2004) determined hornblende stability limits of 0.5 kbar at c.1010 °C, or 0.5 kbar at 950 °C in the presence of biotite, in the hydrous basalt of Cerro la Pilita, Mexico.

Taranaki hornblende is characterised by a considerable range in Mg# but with much narrower variations in Al^{IV} compared with hornblende compositions from Unzen volcano (Fig. 5-9). Taranaki hornblende also has higher K_2O contents with high Na and K cation occupancy of the A-site vacancy (Fig. 5-9). Only Colima volcano and Cerro la Pilita (Mexico) have hornblende with similar compositions. In terms of hornblende as well as whole rock composition, Mt. Taranaki magmas are closest to Mascota basaltic andesites than to any other previously listed volcanic centres. It is therefore assumed that Taranaki hornblendes are stable to similar pressures of as low as 1 kbar (i.e. 2 km depth; Fig. 5-18). This hornblende stability limit is therefore compatible with temporary magma storage between c.9.5 and 2 km depth.

5.5.3.4 Magma Ascent Rate

The formation of hornblende reaction rims was investigated in decompression experiments using Mt. St. Helens dacite compositions, and these clearly showed a correlation between rim thickness and increasing time spent outside the hornblende stability field (Rutherford and Hill, 1993). Hornblende crystals in isothermal decompression experiments developed 11 µm thick rims after 7 days at 1.6-0.02 kbar and 10 days at 2.2-0.02 kbar, and rim thicknesses of 15 µm after 8 and 11 days, respectively (Rutherford and Hill, 1993). Recent experiments on dacites (840 °C) of Redoubt volcano, Alaska (Browne and Gardner, 2006) indicate that hornblende could linger much longer outside its stability field, about twice the time given by Rutherford and Hill (1993). Observed average rim thickness per sample of Taranaki dome rocks is approximately 12 µm. If compared to the above experiments, this would correspond to a period of about 7 or 10 days outside the stability field (cf. Rutherford and Hill, 1993) or

17 days (cf. Browne and Gardner, 2006). The conversion of hornblende rim thickness into time (i.e. time for reaction formation) and the subsequent estimate of magma ascent rate (assuming the hornblende pressure limit is known) requires one further condition: that the hornblende stored within a dome must cool immediately to prevent further reaction rim formation. In other words, if the lava forming the summit dome contained hornblende crystals with 12 μm thick rims, it would have had to collapse immediately (forming a BAF) so that it cooled quickly enough to preserve the hornblende texture and to prevent further reaction rim growth. However, given that the samples analysed are from the intact portion of the lava dome, they might have cooled to ambient temperatures quickly. Hence, the observed hornblende rims could have been formed within the dome after extrusion, rather than during ascent. This is supported by the fact that only one sample (SD1; small spine penetrating the dome rind – and hence rapidly cooled) shows a weak breakdown reaction (type 2, Fig. 5-7b). In Rutherford and Hills' (1993) constant-rate decompression experiments (1.6-0.02 kbar), hornblende first showed reaction rims after 4 days outside the stability field. Browne and Gardner (2006) suggest that a time of 7 days is required for reaction rim formation. In the latter case, single-step and multi-step experiments were carried out, including stalling times at various pressures in order to investigate various hornblende textures, e.g. crystal size variations and crystal rounding (Browne and Gardner, 2006). However, Taranaki hornblende compositions and inferred magma temperatures are closer to Mt. St. Helens than to Redoubt volcano so the data from Rutherford and Hill is considered to be more applicable here. Hence, if Taranaki hornblendes are stable up to 1 kbar and are able to spend up to 4 days outside the stability limit before showing any signs of decompression-breakdown reactions, then the magma ascended in a 4 km long dyke or conduit at rates of 0.012 ms^{-1}. In this scenario the magma ascent rate calculation (1000 md^{-1}) is a minimum.

5.5.4 Eruption Duration

Effusive, lava dome-producing eruptions with or without explosive, phreatic, vulcanian to sub-Plinian phases, are often long-term, ongoing events that may last for several months to years, or even up to decades, as recently observed at many volcanoes, e.g. Mt. Merapi (Indonesia; 1992-2002), Santa Maria (Guatemala; 1922-today), Soufrière

Hills Volcano (Montserrat; 1995-today), Unzen volcano (Japan; 1991-1995), Mt. St. Helens (USA; 1980-1986, 2005-today), and Mt. Lamington (Papua New Guinea; 1951-1956). However, some lava dome-producing eruptions can instead be short, lasting for only a few weeks, or even for only a few days (Table 5-3).

Table 5-3. Historic lava dome eruptions compiled from Newhall and Melson (1983) and the Smithsonian Institution Catalogue[1].

Volcano/area of activity	Island, Country	Year	Duration of eruption [d]	Volume of dome [m^3]	Dome growth rate [m^3d^{-1}]	SiO_2 [wt.%]	VEI[2]
Komagatake	Hokkaido, Japan	1856	1?				4
Novarupta	Alaska peninsula, USA	1912	7				
Great Sitkin	Aleutian Islands, USA	1945	7	1×10^7?			2
Galunggung/ Gunung Jadi	Java, Indonesia	1918	14	1×10^7	6×10^4	56	1
Ruang	Sangihe, Indonesia	1949	15				2
Usu	Hokkaido, Japan	1822	21				4
Nea Kameni	Santorini, Greece	1950	24	7×10^{4a}	c.1×10^5	63	2
Teneguia	La Palma, Spain	1971	24	1.2×10^{7a}	2×10^3?		2
Paluweh	Lesser Sunda Islands, Indonesia	1928	53	8×10^6	1.4×10^5	58	3

[1] www.volcano.si.edu.
[2] Volcanic Explosivity Index.
[a] total lava volume.

Laboratory experiments by Blake (1990), Griffiths and Fink (1997), Fink and Griffiths (1998) and Lyman et al. (2004) show that lava dome morphologies can be related to eruptive conditions. If the initial parameters such as morphology, extrusion rate, rock composition and underlying slope are known, then the yield strength of an active lava dome can be estimated. However, the study of historic lava domes is more complicated since only the geometry and composition is known. Since the yield strength of the Mt. Taranaki lava dome is unknown, the assumption must be made that the inferred dome geometry reflects its yield strength (Blake, 1990). Based on a homogenous dome composition and a short emplacement duration, the yield strength σ_o is estimated using the equation (Blake, 1990):

$$\sigma_0 = (0.323 \pm 0.016)\frac{H^2 \rho g}{R} \qquad \text{[Eq. 5-4]}$$

where H and R are dome height and radius, ρ density and g gravitational acceleration. The density needs to be estimated carefully since it has a considerable impact on the resulting yield strength. Solid densities as well as bulk densities of dome rocks are assumed to over- and underestimate the lava density at the time of extrusion, i.e. at 900

°C. The mean bulk density of 2321 kgm^{-3}, approximately equal to the density of the andesitic glass[6], is not realistic and should be closer to the solid density. The lava density (at 900 °C and 1 bar) should be 10% less than the solid density to account for thermal expansion of glass and crystals and the presence of cavities and/or vesicles. A lava emplacement density of 2555 kgm^{-3} will therefore be used for further calculations. Since the studied dome is resting in part flat and in part inclined surface, and its surface area was described by three radii, a mean radius of 203 m and a height of 105 m were applied to estimate a yield strength of $\sigma_0 = 4.4\times10^5 \pm 2.2\times10^4$ Pa. This estimate is in the same order of magnitude to that of other andesitic dome-forming lavas (Fink and Griffiths, 1998).

Recent laboratory experiments of Lyman et al. (2004) show that effusion rates and hence, the eruption duration of historic domes can be estimated. To calculate the effusion rate Q and eruption duration t_e, the following equations are used based on Lyman et al. (2004):

$$Q = \frac{1}{\psi_B} \frac{t_s}{(g\Delta\rho / \sigma_0)^3} \qquad \text{[Eq. 5-5]}$$

$$t_e = \frac{V}{Q} \qquad \text{[Eq. 5-6]}$$

where g is the gravitational acceleration, $\Delta\rho$ is the density difference between magma/lava and the environment, σ_0 is the isothermal yield strength, ψ_B is the dimensionless ratio of the timescale of solidification (t_s) and advection (t_a), and V is the volume of the lava dome. The values of parameters used in the equations are listed in Table 5-4.

The minimum extrusion rate, Q_{min}, for the modelled summit dome is estimated to be 6.0 m^{3}s^{-1} (5.2×10^5 m^{3}d^{-1}) which gives a maximum eruption duration of 11.5 days. The calculated extrusion rate compares well with recent dome-forming eruptions of Mt. St. Helens, Washington (1980-1983: Q_{max}=20.1 m^{3}s^{-1} =1.74×10^6 m^{3}d^{-1}; Anderson and Fink, 1990), Mt. Lamington, Papua New Guinea (Q_{max}=22.2 m^{3}s^{-1} =1.92×10^6 m^{3}d^{-1}; Taylor, 1958) and Unzen volcano, Japan (Q_{max}=15.1 m^{3}s^{-1} =1.3×10^6 m^{3}d^{-1}; BGVN 17:11). If a maximum time of 4 days is assumed (from the lack of decompression-induced reaction rims of hornblende; Rutherford and Hill, 1993) then a minimum extrusion rate of 17.2

[6] The Tahurangi Ash glass composition is inferred to be similar to the dome glass composition. Its mean density is calculated to be 2355 kgm^{-3} at 900 °C, 1 bar and 1 wt.% H_2O.

m^3s^{-1} (1.5×10^6 m^3d^{-1}) is estimated. Hence, the calculated extrusion rates using the two different methods are consistent.

Another eruptive parameter, the vent diameter, may be estimated on the basis of magma extrusion and ascent rates. Using the minimum values of 0.012 ms^{-1} and 6.0 m^3s^{-1}, a cylindrical vent diameter of 26 m immediately below the dome results (Table 5-4). The vent diameter is about one third the size of the c.80 m wide hydrothermally altered zone within the amphitheatre. It is impossible to estimate the vent-shape changes with depth, but if a narrower conduit diameter of 10 m was present, much higher magma ascent rates of 0.189 ms^{-1} result.

Table 5-4. Physical parameters and results for equations 5-4 to 5-6.

Physical parameters		Results	
Dome morphology[a]	lobate	Extrusion rate, min Q^c	6.0 m^3s^{-1}
Underlying slope, α	20°	Eruption duration, max t_e	11.5 days
Gravitational acceleration, g	9.81 ms^{-2}	Extrusion rate, max Q^c	39.3 m^3s^{-1}
Isothermal yield strength, mean σ_o[b]	4.4×10^5 Pa	Eruption duration, min t_e	1.7 days
Timescale for solidification, t_s[a]	90 s		
Min ψ_B[c]	0.247	Magma ascent rate, $v^{d,e}$	?0.012 ms^{-1}
Max ψ_B[c]	1.262	Conduit diameter, d	?26 m
Density contrast rock-air, ρ	2554 kgm^{-3}	Extrusion rate, min Q^e	17.2 m^3s^{-1}
Lava dome volume, V	5.9×10^6 m^3		
Conduit length, min l[d]	4000 m		

[a] Fink and Griffiths (1998).
[b] calculated after Blake (1990).
[c] calculated after Lyman et al. (2004).
[d] corresponds to the inferred hornblende stability of 100 MPa.
[e] using 4 days as maximum before hornblende breakdown reaction begins (Rutherford and Hill, 1993).

5.5.5 Approximation of the Time of Eruption

Although it has been shown that the present summit dome represents a single eruptive event, the date of the eruption still remains unknown. It is thought that the collapse of the dome may have occurred prior to AD1885 according to Davis and Carrington's summit crater map (Neall, 1973). Druce (1964) argued that a major landslide occurred in the early 1880s: "Stability on this side of the mountain has not been regained since; successive landslides, initiated in the area between the Turtle and Bobs Ridge by torrential falls of rain have poured down the upper slopes building new fan surfaces".

According to this it can be assumed that the eruption date occurred between AD1755 and 1885.

The timing of eruption can be further constrained by examining the cooling history of the dome. It is inferred that the dome collapse occurred when its temperature was below 350 °C, as determined by NRM of clasts within the rock avalanche deposit. To approximate the time required to cool the dome centre to 350 °C, a simple conductive cooling model can be applied. Jaeger (1968) proposed a non-dimensional time for heat transfer across a static body:

$$t_D = \frac{\kappa t}{a^2} \qquad \text{[Eq. 5-7]}$$

where κ is the thermal diffusivity, t is the transfer time (i.e. the time elapsed since extrusion) and a is the radius of the sphere (i.e. the radius simulating the dome). The value of t_D=0.2 corresponds to 50% cooling by ambient air (Simmons et al., 2004) whereas t_D>10 describes the heat transfer to be practically complete (Jaeger, 1968). Using the parameters listed in Table 5-5, approximately 26 years are needed for the dome to cool to half its initial temperature. As the dome emplacement temperature was probably around 900 °C, it would correspond to c.450 °C, or 17.1 °Cyr^{-1}. If this rate is also applied to the remaining 100 °C (i.e. 450 °C-100 °C=350 °C), then a cooling time of c.32 years is necessary. An important factor for accelerated cooling is rainfall-quenching, especially at Mt. Taranaki. Here the mean annual rainfall at the North Egmont Visitors Centre (852 m) is 7.5 myr^{-1}, with a maximum of 10.6 myr^{-1} in the period 1991-2003. Hence, rainfall would have had a significant impact on the cooling history of the dome. Simmons et al. (2004) estimated the quenching potential of rain (ΔT_R - change in rock temperature) by assuming rain falls in a single event over an entire surface resulting in the equation

$$\Delta T_R = \frac{\Delta T_W \rho_W c_W i}{\rho_R c_R h} \qquad \text{[Eq. 5-8]}$$

where ΔT_w represents the temperature change of water between ambient and boiling temperature, ρ and c are the densities and specific heats for water and rock, i is the height of rain, and h is the thickness of the dome. From this, the rainfall-quenching rate for Taranaki is estimated to be 11.5 °Cyr^{-1}. If both rates are combined a rate of 28.6 °Cyr^{-1} would imply that the summit dome would cool to 350 °C in approximately 19 years. It is noted that the simple conductive cooling model does not include thermal radiation, which would further increase the annual cooling rate. In addition, the applied

dimension of a spherical dome results in maximum cooling times since the dome on the upper slope is less than 100 m thick. From the estimated maximum cooling time of c.19 years, it is here inferred that the dome was emplaced some time between AD1755 and AD1866. If complete cooling of the dome is considered and the same conditions are applied then about 74 years needed to elapse placing the date of extrusion before c.AD1811.

Table 5-5. Physical parameters used for conductive cooling and rainfall-quenching of the lava dome.

Conductive cooling		Rain-quenching	
Radius of the sphere, r	160 m	Change in water temperature, ΔT_W	90 °C
Thermal diffusivity, κ[a]	6.17×10^{-6} m^2s^{-1}	Density of water, ρ_W	1000 kgm^{-3}
		Rock density	2555 kgm^{-3}
		Specific heat of water, c_W	4187 $Jkg^{-1}K^{-1}$
		Specific heat of rock, c_R[a]	918 $Jkg^{-1}K^{-1}$
		Thickness, h	105 m
		Height of rainfall, i[b]	7.5 m

[a] Elsworth (1989).
[b] Taranaki Regional Council (www.trc.govt.nz).

Field studies showed that the rock-avalanche deposit overlies the Tahurangi BAF A deposit at two locations (outcrops 15 and 52; Fig. 5-3) and shows a weakly developed 4-5 cm thick soil. Revegetation and pedogenesis on bare rock-avalanche deposits take considerable time, especially at high altitudes. The lack of clay minerals along with the high porosity and permeability of those deposits further delay the recolonisation of those deposits. If there were better data on pedogenesis in montane regions after devastating debris flow or rock avalanche events, the eruption time of the Pyramid event may even be better constrained. The photograph of H.M. Skeet was taken more than 13 years after the rock-avalanche deposition. The fresh bouldery surface is still recognisable at the time of the photograph with no indication of a vegetation cover (Fig. 5-5). This may indicate that revegetation and pedogenesis occurred within decades after deposition. As an hypothetical example, if revegetation and pedogenesis on widespread rock-avalanche deposits under local conditions take at least 30 years then and considering the dome cooling time of 19 years it can be estimated that the Pyramid eruption began c.11 years following the Tahurangi eruption, i.e. the time window for the Pyramid eruption could then be narrowed down to occurring between c.AD1766 and 1866.

5.5.6 Historic References to Volcanic Activity in the 19th Century

Although Maori were living in Taranaki since the c.14th century and potentially witnessed most eruptions of the Maero period, their oral traditions contain few references to some but not all of the eruptions of Mt. Taranaki (Faulkner-Blake, 1977). This is probably due to the predominantly extrusive, lava dome-producing, style of activity in that period with only one sub-Plinian event in AD1655. The first ascent by Europeans to the summit of Mt. Taranaki was by the German geologist Ernst Dieffenbach and the whaler James Herberley on the 23 December 1839 (Dieffenbach, 1843). Although no volcanic activity was observed by them on the summit of Mt. Taranaki, their brief description of the summit region gives important clues. Dieffenbach (1843) entered the crater from the north and estimated the crater area at approximately one square mile (c.1.61 km^2). This is clearly overestimated since given the ideal crater dimensions an area of only 0.52 km^2 results. However, the circumstances for Dieffenbach's estimate can be more closely examined. Anyone who enters the summit of Mt. Taranaki today from the north (as Dieffenbach), would never estimate the crater area to be a square mile, even if viewed from the highest point of the present summit dome. An explanation for his overestimation could be that the crater area was just composed of a field of snow with some protruding rocks as he described (Table 5-6; Dieffenbach, 1843). From this perspective (i.e. in the absence of the summit dome), the crater area can easily be overestimated if it is considered that the snow field gently dips to the west with the western crater rim missing. Further, if there was a summit dome at the time of Dieffenbachs ascent then this important morphological feature would have been described by him, for example, as a conical hill composed of ash, scoria and lava. Even if intensive snow cover made it more difficult to recognise the dome as positive relief, no "protruding rocks" should be recognisable (see above).

In addition, reports stating that Mt. Taranaki was an active volcano have not been previously known. The first citation is given by Hay (1832), others are from 1848 and 1862 by Daubeney and Scrope, respectively (Table 5-6). Although these references are not supported by other sources, they clearly raise the question as to whether an eruption of Mt. Taranaki during European settlement occurred unnoticed.

Before European settlement started in the early 1840s on the Taranaki peninsula (New Plymouth was founded in 1841), only whalers were present in this area. Since a very short time of dome emplacement is indicated, it may be possible that this small eruption was unnoticed in the early years of colonisation. Paintings, diaries and eyewitness

reports (1841-1890) record useful observations (Table 5-6) which could refer to volcanic activity at Mt. Taranaki, but information provided is not precise. Earthquakes felt in Taranaki are often accompanied by sound and explosions from Mts. Tongariro and Ngauruhoe and are frequently heard. These common occurrences may have led to either any unusual sounds or shocks being ignored or that they were instantly related to other phenomena "outside" Taranaki. Only one observation from 1854 appears to describe volcanic activity at Mt. Taranaki (Table 5-6). Although Dieffenbach's observations of the crater area and various other eyewitness reports offer only weak evidence, a post-AD1839 date for the Pyramid eruption cannot be excluded. This assumption is supported by the only known scientific evidence. Lees and Neall (1993) reported *Pinus* pollen at two locations below Tahurangi Ash, indicative for an eruption that occurred during early colonisation of the Taranaki peninsula. An eruption date for the Tahurangi eruption close to AD1860 has been suggested (Lees and Neall, 1993). If this finding is considered the Pyramid eruption occurred later.

All that can be definitely stated about the Pyramid eruption are the following facts:

1) the collapse of the Pyramid Dome occurred prior to AD1885;
2) the temperature of the rock-avalanche deposit was below 350 °C;
3) the development of faults within the dome implies they were created while the dome was entirely in a brittle state, when the dome interior was probably also below the temperature of 350 °C;
4) from the inferred dome dimensions, the dome needed at least 19 years to cool to about 350 °C, or about 74 years to cool completely;
5) the date of the dome-emplacing eruption was after the Tahurangi eruption and prior to c.AD1866. A precise date of the Tahurangi eruption is needed, i.e. AD1755 (Druce, 1966) vs. AD1860 (Lees and Neall, 1993).

Table 5-6. Selected eyewitness reports of the 18th and 19th century.

Date and location	Eyewitness reports
13 Jan 1770, Tasam Sea	"At five o'clock in the mornig we saw, for a few minutes, the summit of the Peak, towering above the clouds, and covered with snow; it now bore N.E. It lies in latitude 39° 16' S. longitude 185° 15' W. and I named it Mount Egmont, in honour of the Earl; it seems to have a large base, and to rise with a gradual ascent." Hawkesworth (1775), p.199.
Comment by the author	The peak of Mt. Taranaki was already observed by Captain James Cook on the 10. January and compared to the Peak of Tenerife. This is the first description of Mt. Taranaki.
9 April 1832, Mt. Taranaki	"Mount Egmont is an active volcano." Hay (1832), p.135.
Comment by the author	First reference found that describes Mt. Taranaki as a volcano, and in addition, also as an active volcano. Note that numerous references are available portraying Mt. Taranaki as an extinct or dormant volcano, which are omitted in this list.
23 Dec 1839, Mt. Taranaki	"However, we at length reached the summit, and found that it consisted of a field of snow about a square mile in extent. Some protruding blocks of scoriæ, of a reddish-brown colour, and here and there slightly vitrified on the surface, indicated the former existence of an active volcano." Dieffenbach (1843), p.154-155.
Comment by the author	Description of the first ascent of Mt. Taranaki by Ernst Dieffenbach and James Herberley. No volcanic activity was observed. For further remarks regarding the description of the crater area see text.
18 Sep 1841, New Plymouth	"A rather severe shock of an earthquake occurred on Friday night…the motion resembled that which we experience in the interior of a flour mill, but in greater degree: and a noise was very like sives at work. It lasted about a minute, and, as some say, terminated with a pop, but this I did not hear."; "This was accompanied with the rattling of china and bottles, as well as general noise, which appeared to pervade the atmosphere... The motion gradually ceased and the sound died away..." J. Newland (1841-1873), p.6.
Comment by the author	The earthquake appears to be greater than MM6 (MM=modified Mercalli scale; Eiby, 1966, Eiby, 1968). This appears to be a common observation in Taranaki. Explosions of Tongariro and Ngauruhoe are frequently heard in Taranaki. Apparently, the sound of the explosions is reflected in strata of the upper atmosphere. An ash eruption of Ngauruhoe occurred in 1841 which truncated the top, however, the precise date is unknown (Crawford, 1880).
13 Sep 1845, New Plymouth	"…I for the first time felt the shock of an earthquake. It was preceded by a sound, apparently coming from the direction of the mountain (Egmont), like a distant report of a very heavy piece of ordinance, but without any echo. And then the earth trembled for a second or two, about as fast as a person moves his hand when shading a drawing - a queer measure of time - but I cannot think of any other which so well represents the character as well as the rate of the motion." W.C. Cotton (1845-1846), p.138.
Comment by the author	Intensity of the earthquake was above MM4 (Eiby, 1973). Although there was a report of an eruption of Ngauruhoe in January 1845 (Taylor, 1833-1873), no further eruptions of Ngauruhoe were reported until 1857 (Gregg, 1960). In addition, no eruptions from Tongariro or Ruapehu were reported (Cole and Nairn, 1975).
1848	"New Zealand itself seems to be indebted to volcanos for much of its formation. The southern and middle islands indeed have as yet been but little explored, but in the northern we recognise an active vent in Mount Egmont, a mountain no less than 8829 feet in height, according to Dieffenbach, which rises from a table-land, and consists of clinkstone covered over on the summit with scoriæ." Daubeney (1848), p.428.

Table 5-6. (continued).

Date and location	Eyewitness reports
9 April 1848, New Plymouth	"…while Natives and self were at tent door talking a smart shock of earthquake was felt, preceded by a loud report; the vibration of the earth lasted some time; instantly all struck silent" W. Colenso (1846-1848).
Comment by the author	The earthquake was slightly felt in Wellington and more strongly in Hawera (Eiby, 1973). It appears to be very common that earthquakes are accompanied by sounds making it even more difficult to distinguish the reports from those that may be related to volcanic activity at Mt. Taranaki.
1 Jan 1853, New Plymouth	"On 1st January 1854 (?), at half past 8 pm a severe shock of earthquake was felt in New Plymouth. The afternoon had been hazy, and a remarkable round cloud, which sent out a long tail-like streamer, hovered near the peak of the mountain." J Newland (1841-1873). "On Saturday night last the town of New Plymouth and its vicinity was visited by a more severe shock of earthquake than the oldest settlers in this place remember. The first and strongest shock took place about 20 minutes past 8 pm, and appeared to come from seaward, and to take a south-easterly direction across the island lasting two minutes..." The Taranaki Herald (1853).
Comment by the author	The two statements describe the same event at the same time although the former states 1854. The additional comment on the cloud shape near the summit may refer to some kind of volcanic activity at the summit of Mt. Taranaki.
2 May 1854, New Plymouth	"… at quarter past 6 o'clock this morning felt a smart shock of an earthquake, it lasted for several seconds and was accompanied in the first instant by an explosion like a cannon at a distance but it subsided into a rumbling noise like a loaded Waggon passing over a wooden bridge..." W. Messenger (1853-1858).
Comment by the author	It was an earthquake of at least MM4, and possibly a rather distant shock (Eiby, 1973). The rumbling noise described could be attributed to an avalanche travelling downhill with the preceding earthquake being the trigger. No eruptions are known to have occurred at Tongariro, Ngauruhoe or Ruapehu.
23 Jan 1855, New Plymouth	"… quarter past nine o'clock in the evening a smart shock of an earthquake, it lasted about 3 minutes and appeared to come from East to West accompanied with loud explosions like Artillery at a distance, in the direction of Tongariro, several slight shocks during the night, perhaps as many as 9 or 10..." W. Messenger (1853-1858).
Comment by the author	These comments could describe a possible eruption of Mt. Taranaki, but further investigations revealed that the Red Crater, Tongariro erupted at this time (Hochstetter, 1864). In addition, a M8.2 earthquake hit Wellington at 9.11 pm explaining the shocks experienced in Taranaki (Eiby, 1973).
1862	"New Zealand contains several active volcanos, and a considerable area is covered by the products of very recent eruptions. In the Northern Isle, Mount Egmont (8960 feet) - a truncated cone, with a smaller ash-cone on its summit - is occasionally active: its mass consists of clinkstone lavas and scoriæ." Scrope (1862), p.470.
Comment by the author	It is the most precise description of the summit region of Mt. Taranaki.

Table 5-6. (continued).

Date and location	Eyewitness reports
1862, Cook Strait	"...the snowy mountains upon the North Island were all tinged with the pink, the woods near the shore looking almost black, while, just on the horizon, a faint white pillar of smoke rose from the volcano of Mount Egmont. ... The pillar of smoke had become a crown of fire, above which, hung a thick and dreadfully dark cloud. The sides of the mountain, though at such a great distance, were distinctly visible, and looked as sharp as if cut with a knife. ... They were still gazing, and neither had spoken, when a low, rumbling sound crept along the water; it only lasted a minute, and might have been the echo of distant thunder, or the firing of cannon (refers to an earthquake) ...the pillar of fire growing sometimes brighter, sometimes almost disappearing; not a sound broke the stillness, except the straining and groaning of the labouring vessel... As the morning advanced, the heat became almost unbearable, and once or twice the same low, grumbling sound broke the stillness. Presently the great pillar of smoke rushing up from the volcano disappeared…" Aylmer (1862).
Comment by the author	The novel is based on letters written by Rev. W.E. Aylmer of Akaroa (Moffat, 2000). Reverend William E. Aylmer arrived at Lyttelton, New Zealand on the 18 Sept 1851 and was vicar of Akaroa from 1851-1872 (Blain, 2000). The novel was written by Mrs. J.E. Aylmer (a distant relative of Rev. W.E. Aylmer) who never visited New Zealand, and her novel appears erroneous i.e due to the description of an eruption of Mt. Taranaki coinciding with an earthquake in Cooks Strait. Many observations of Rev. W.E. Aylmer were recorded in letters and later integrated into this novel. Interestingly, an earthquake occurred in Cook Strait on the 7 Sept 1851 (Eiby, 1973) just prior to Rev. Aylmer's arrival in Canterbury. The Graham family portrayed in the novel also arrives in Lyttelton and most likely represents the Aylmer family. Based on the passenger list of the vessel "Lady Nugent" Rev. W.E. Aylmer arrives with 7 family members, among them 3 children. The earthquake described in the novel caused alarm and destruction in Wellington due to the sudden ebb and flow of the tide. There may be a possibility that the novel describes real events, which perhaps only occurred at different times. Since the novel is based on Rev. W.E. Aylmer's letters, only those may shed light in the reliability of these descriptions.
December 1883 or 1884, Mt. Taranaki	"Old hands tell the top (the summit of Mt. Taranaki) has altered very much since they first remember it….Tongariro was smoking…" Pownall (1885).
Comment by the author	This is the only direct hint on changes of the crater morphology. It is possible that the statement relates to the partial dome collapse or the emplacement of the dome or both. Tongariro was active from 1885 ± 1 yr, Ngauruhoe in 1881 and 1883 (Gregg, 1960; Cole and Nairn, 1975) making this statement reliable.

5.6 Conclusions

The dome remnants within the crater of Mt. Taranaki were extruded after the AD1755 Tahurangi eruption, and hence, represent a distinct eruptive event, the youngest known from the volcano, here termed the Pyramid eruption. This event resulted in the extrusion of a lava dome at the volcano's summit, without any apparent collapse to form Block-and-Ash Flows. Importantly from a hazard perspective, once the dome had cooled – at least two decades (c.19 yrs) after eruption, it collapsed to generate a large rock avalanche, extending over 5 km from source.

Studies of the summit dome structure, mineralogy, chemical compositions, and geometrical shape show that its emplacement occurred rapidly, probably within days. Exo- and endogenous growth occurred due to part of the dome extending over a break in slope and onto the steep outer flank. The portion emplaced within the crater developed a lobate-platy dome shape. Two methods using independent parameters showed that minimum magma extrusion rates were in the order of 6 to 17 m^3s^{-1}. Magma ascent rates of $\geq$0.012 ms^{-1} are estimated on the basis of hornblende breakdown reaction rims. A mid-crustal magma source area is identified near the BDTZ at c.9.5 km depth. It may also be possible that temporary magma stalling also occurred below 2 km depth, within the inferred hornblende stability limit.

The cooling of the dome to ambient temperatures was complete in less than 74 years; while cooling to the inferred maximum dome temperature of 350 °C at the time of the collapse could have been within c.19 years.

5.7 References

Anderson, J.L. and **Smith, D.R.** 1995. The effects of temperature and fO_2 on the Al-in-hornblende barometer. *American Mineralogist* 80, 549-559.

Anderson, S.W. and **Fink, J.H.** 1990. The development and distribution of surface textures at the Mount St. Helens Dome. In: **Fink, J.H.** (ed.) Lava flows and domes: emplacement mechanisms and hazard implications. *IAVCEI Proceeding in Volcanology* 2, 25-46.

Anderson, S.W., Fink, J.H. and **Rose, W.I.** 1995. Mount St. Helens and Santiaguito lava domes: the effect of short-term eruption rate on surface texture and degassing processes. *Journal of Volcanology and Geothermal Research* 69, 105-116.

Anderson S.W., Stofan, E.R, Plaut, J.J. and **Crown, D.A.** 1998. Block size distributions on silicic lava flow surfaces; implications for emplacement conditions. *Geological Society of America Bulletin* 110, 1258-1267.

Aylmers, J. E. 1862. Distant homes; or the Graham Family in New Zealand. Griffith and Farran. London.

Barclay, J. and **Carmichael, I.S.E.** 2004. A hornblende basalt from western Mexico: Water-saturated phase relations constrain a pressure-temperature window of eruptibility. *Journal of Petrology* 45, 485-506.

Barclay, J., Rutherford, M.J., Carroll, M.R., Murphy, M.D., Devine, J.D., Gardner, J. and **Sparks, R.S.J.** 1998. Experimental phase equilibria constraints on pre-eruptive storage conditions of the Soufriere Hills magma. *Geophysical Research Letters* 25, 3437-3440.

BGVN 17:11. Smithsonian Institution, 1992. Unzen Volcano. *Bulletin of the Global Volcanism Network* vol. 17, no. 11.

Blain, M. 2000. The Canterbury Association: a study of its members connections: a tribute on the 150th anniversary of the Canterbury settlement. Occasional Paper 4, The Archives Committee, Anglican Diocese of Canterbury.

Blake, S. 1990. Viscoplastic models of lava domes. In: **Fink, J.H.** (ed.) Lava flows and domes: emplacement mechanisms and hazard implications. *IAVCEI Proceeding in Volcanology* 2, 88-126.

Blundy, J.D. and **Holland, T.J.B.** 1990. Calcic amphibole equilibria and a new amphibole-plagioclase geothermometer. *Contributions to Mineralogy and Petrology* 104, 208-224.

Boyd, F.R. 1959. Hydrothermal investigations of amphiboles. In: **Abelson, P.H.** (ed.) Researches in Geochemistry. Wiley. New York. pp.377-396.

Browne, B.L. and **Gardner, J.E.** 2006. The influence of magma ascent path on the texture, mineralogy, and formation of hornblende reaction rims. *Earth and Planetary Science Letters* 246, 161-176.

Browne, B.L., Eichelberger, J.C., Patino, L.C., Vogel, T.A., Dehn, J., Uto, K. and **Hoshizumi, H.** 2006. Generation of porphyritic and equigranular mafic enclaves during magma recharge events at Unzen volcano, Japan. *Journal of Petrology* 47, 301-328.

Cashman, K.V. and **McConnell, S.M.** 2005. Multiple levels of magma storage during the 1980 summer eruptions of Mount St. Helens, WA. *Bulletin of Volcanology* 68, 57-75.

Cavill, A.W., Cassidy, J. and **Brennan, B.J.** 1997. Results from the new seismic monitoring network at Egmont Volcano, New Zealand: tectonic and hazard implications. *New Zealand Journal of Geology and Geophysics* 40, 69-76.

Cole, J.W. and **Nairn, I.A.** 1975. Catalogue of the active volcanoes of the world including solfatara fields. Part 22: New Zealand. International Association of Volcanology and Chemistry of the Earth's Interior. Rome.

Colenso, W. 1846-1848. Journal, Paper Vol. 2.

Cotton, W.C. 1845-1846. Diary of W.C. Cotton.

Crawford, J.C. 1880. Recollections of travel in New Zealand and Australia. Trubner & Co. London.

Cronin, S.J., Stewart, R.B., Neall, V.E., Platz, T. and **Gaylord, D.** 2003. The AD1040 to present Maero eruptive period of Egmont Volcano, Taranaki, New Zealand. Abstract. *Geological Society of New Zealand Miscellaneous Publication* 116A, 43.

Daubeny, C. 1848. A description of active and extinct volcanos, of earthquakes, and of thermal springs; with remarks on the causes of these phænomena, the character of their respective products, and their influence on the past and present condition of the globe. 2nd ed. Richard and John E. Taylor. London.

Dieffenbach, E. 1843. Travels in New Zealand; with contributions to the Geography, Geology, Botany, and natural history of that country. Vol. I. John Murray. London.

Druce, A.P. 1964. The vegetation. In: **Scanlan, A.B.** (ed.) Egmont National Park Handbook. Egmont National Park Board. New Plymouth. pp. 41-56.

Druce, A.P. 1966. Tree-ring dating of recent volcanic ash and lapilli, Mt Egmont. *New Zealand Journal of Botany* 4, 3-41.

Eiby, G.A. 1966. The modified Mercalli scale of earthquake intensity and its use in New Zealand. *New Zealand Journal of Geology and Geophysics* 9, 122-129.

Eiby, G.A. 1968. A descriptive catalogue of New Zealand earthquakes. Part 1 Shocks felt before the end of 1845. *New Zealand Journal of Geology and Geophysics* 11, 16-40.

Eiby, G.A. 1973. A descriptive catalogue of New Zealand earthquakes. Part 2 Shocks felt from 1846 to 1854. *New Zealand Journal of Geology and Geophysics* 16, 857-907.

Elsworth, D. 1989. Thermal permeability enhancement of blocky rocks: plane and radial flow. *International Journal of Rock Mechanics and Mining Sciences* 26, 329-339.

Faulkner-Blake, J. 1977. Nga maunga Tarewarewa or the restless mountains. 7 audiotapes and brochure. Radio New Zealand, New Plymouth.

Fink, J.H. and **Griffiths, R.W.** 1998. Morphology, eruption rates, and rheology of lava domes: insights from laboratory models. *Journal of Geophysical Research - Solid Earth* 103, 527-545.

Fink, J.H. and **Anderson, S.W.** 2000. Lava domes and coulees. In: **Sigurdsson, H.** (ed.) Encyclopedia of Volcanoes. Academic press. London. pp. 307-319.

Foden, J.D. and **Green, D.H.** 1992. Possible role of amphibole in the origin of andesite: some experimental and natural evidence. *Contributions to Mineralogy and Petrology* 109, 479-493.

Gill, J.B. 1981. Orogenic andesites and plate tectonics. Springer Verlag. Berlin.

Grant- Taylor, T.L. 1964. Volcanic history of western Taranaki. *New Zealand Journal of Geology and Geophysics* 7, 78-86.

Gregg, D.R. 1960. Volcanoes of Tongariro National Park. *New Zealand Department of Scientific and Industrial Research Information series* 28.

Griffiths, R.W. and **Fink, J.H.** 1997. Solidifying Bingham extrusions: a model for the growth of silicic lava domes. *Journal of Fluid Mechanics* 347, 13-36.

Gründer, K. 2006. Petrography and mineral chemistry of a xenolith suite from Mt. Taranaki, New Zealand: insights into the sub-volcanic lithosphere of an arc volcano. Unpublished Diploma thesis. Johannes Gutenberg Universität, Mainz, Bundesrepublik Deutschland.

Hammarstrom, J.M. and **Zen, E.A.** 1986. Aluminum in hornblende: an empirical igneous geobarometer. *American Mineralogist* 71, 1297-1313.

Hawkesworth, J. 1775. An account of the voyages undertaken by the order of His present Majesty for making discoveries in the Southern Hemisphere, and successively performed by Commodore Byron, Captain Wallis, Captain Carteret and Captain Cook in the Dolphin, the Swallow, and the Endeavour; to which is added: A voyage to the North Pole by Commodore Phipps. Vol. II. James Williams. Dublin.

Hay, R.W. 1832. Notices of New Zealand. From original documents in the Colonial Office. In: *The Royal Journal of Geographical Society of London*. Vol. II. 133-135.

Hoblitt, R.P. and **Kellog, K.S.** 1979. Emplacement temperature of unsorted and unstratified deposits of volcanic rock debris as determined by paleomagnetic techniques. *Geological Society of America Bulletin* 90, 633-642.

Hochstetter, F von 1864. Geologie von Neu-Seeland. Beiträge zur Geologie der Provinzen Auckland und Nelson. Reise der österreichischen Fregatte Novara um die Erde in den Jahren 1857, 1858, 1859. Geologische Theil, Band 1, Abteilung 1 und 2. Hof- und Staatsdruckerei. Wien.

Holland, T. and **Blundy, J.** 1994. Non-ideal interactions in calcic amphiboles and their bearing on amphibole-plagioclase thermometry. *Contributions to Mineralogy and Petrology* 116, 433-447.

Hollister, L.S., Grissom, G.C., Peters, E.K., Stowell, H.H. and **Sisson, V.B.** 1987. Confirmation of the empirical correlation of Al in hornblende with pressure of solidification of calc-alkaline plutons. *American Mineralogist* 72, 231-239.

Holloway, J.R. 1973. The system pargasite-H_2O-CO_2: a model for melting of a hydrous mineral with a mixed-volatile fluid, I. experimental results to 8 kbar. *Geochimica et Cosmochimica Acta* 37, 651-666.

Holm, D.K. 1995. Relation of deformation and multiple intrusion in the Death Valley extended region, California, with implications for magma entrapment mechanism. *Journal of Geophysical Research-Solid Earth* 100, 10495-10505.

Holtz, F., Sato, H., Lewis, J., Behrens, H. and **Nakada, S.** 2005. Experimental petrology of the 1991-1995 Unzen dacite, Japan. Part I: Phase relations, phase composition and pre-eruptive conditions. *Journal of Petrology* 46, 319-337.

Jaeger, J.C. 1968. Cooling and solidification of igneous rocks. In: **Hess, H.H.** and **Poldervaart, A.** (eds.) Basalts: The Poldervaart treatise on rocks of basaltic composition. Wiley. New York. pp. 503-536.

Johnson, M.C. and **Rutherford, M.J.** 1989. Experimental calibration of the aluminum-in-hornblende geobarometer with application to Long Valley Caldera (California) volcanic rocks. *Geology* 17, 837-841.

Le Maitre, R.W., Bateman, P., Dudek, A., Keller, J., Lameyre, J., Le Bas, M.J., Sabine, P.A., Schmid, R., Sorensen, H., Streckeisen, A., Woolley, A.R. and **Zanettin, B.** 1989. A classification of igneous rocks and glossary of terms. Blackwell Scientific. Oxford.

Leake, B.E., Woolley, A.R., Arps, C.E.S., Birch, W.D., Gilbert, M.C., Grice, J.D., Hawthorne, F.C., Kato, A., Kisch, H.J., Krivovichev, V.G., Linthout, K., Laird, J., Mandarino, J., Maresch, W.V., Nickel, E.H., Rock, N.M.S., Schumacher, J.C., Smith, D.C., Stephenson, N.C.N., Ungaretti, L., Whittaker, E.J.W. and **Youzhi, G.** 1997a. Nomenclature of amphiboles: report of the Subcommittee on amphiboles of the International Mineralogical Association Commission on new minerals and mineral names. *Mineralogical Magazine* 61, 295-321.

Leake, B.E., Woolley, A.R., Arps, C.E.S., Birch, W.D., Gilbert, M.C., Grice, J.D., Hawthorne, F.C., Kato, A., Kisch, H.J., Krivovichev, V.G., Linthout, K., Laird, J., Mandarino, J.A., Maresch, W.V., Nickel, E.H., Rock, N.M.S., Schumacher, J.C., Smith, D.C., Stephenson, N.C.N., Ungaretti, L., Whittaker, E.J.W. and **Guo, Y.Z.** 1997b. Nomenclature of amphiboles: report of the Subcommittee on amphiboles of the International Mineralogical Association Commission on new minerals and mineral names. *American Mineralogist* 82, 1019-1037.

Leake, B.E. Woolley, A.R., Birch, W.D., Burke, E.A.J., Ferraris, G., Grice, J.D., Hawthorne, F.C., Kisch, H.J., Krivovichev, V.G., Schumacher, J.C., Stephenson, N.C.N. and **Whittaker, E.J.W.** 2003. Nomenclature of amphiboles: additions and revisions to the International Mineralogical Association's 1997 recommendations. *Canadian Mineralogist* 41, 1355-1362.

Lees, C.M. and **Neall, V.E.** 1993. Vegetation response to volcanic eruptions on Egmont Volcano, New Zealand, during the last 1500 years. *Journal of the Royal Society of New Zealand* 23, 91-127.

Locke, C.A. and **Cassidy, J.** 1997. Egmont Volcano, New Zealand: three-dimensional structure and its implications for evolution. *Journal of Volcanology and Geothermal Research* 76, 149-161.

Luhr, J.F. 2002. Petrology and geochemistry of the 1991 and 1998-1999 lava flows from Volcán de Colima, México: implications for the end of the current eruptive cycle. *Journal of Volcanology and Geothermal Research* 117, 169-194.

Luhr, J.F. and **Carmichael, I.S.E.** 1980. The Colima Volcanic Complex, Mexico. I. Post-caldera andesites from Volcán Colima. *Contributions to Mineralogy and Petrology* 71, 343-372.

Lykins, R.W. and **Jenkins, D.M.** 1992. Experimental determination of pargasite stability relations in the presence of orthopyroxene. *Contributions to Mineralogy and Petrology* 112, 405-413.

Lyman, A.W., Koenig, E. and **Fink, J.H.** 2004. Predicting yield strengths and effusion rates of lava domes from morphology and underlying topography. *Journal of Volcanology and Geothermal Research* 129, 125-138.

Marquez, A., Oyarzun, R., Ignacio, C. de and **Doblas, M.** 2001. Southward migration of volcanic activity in the central Mexican Volcanic Belt: asymmetric extensions within a two-layer crustal stretching model. *Journal of Volcanology and Geothermal Research* 112, 175-187.

Melnik, O. and **Sparks, R.S.J.** 2002. Dynamics of magma ascent and lava extrusion at Soufrière Hills Volcano, Montserrat. In: **Druitt, T.H.** and **Kokelaar, B.P.** (eds.) The eruption of Soufrière Hills Volcano, Montserrat, from 1995 to 1999. *Geological Society, London, Memoirs* 21, 153-171.

Messenger, W. 1853-1858. Diary of W. Messenger.

Moffat, K. 2000. The Puritan paradox: an annotated bibliography of Puritan and Anti-Puritan New Zealand fiction, 1860-1940. Part 1: The Puritan legacy. *Kōtare: New Zealand Notes and Queries* 3, 36-86.

Moore, G. and **Carmichael, I.S.E.** 1998. The hydrous phase equilibria (to 3 kbar) of an andesite and basaltic andesite from western Mexico: constraints on water content and conditions of phenocryst growth. *Contributions to Mineralogy and Petrology* 130, 304-319.

Morimoto, N. 1989. Nomenclature of pyroxenes. *Canadian Mineralogist* 27, 143-156.

Moriya, I. 1978. Morphology of lava domes. *Bulletin of the Department of Geography - The University of Kanazawa* 14, 55-69.

Mueller, S., Melnik, O., Spieler, O., Scheu, B. and **Dingwell, D.B.** 2005. Permeability and degassing of dome lavas undergoing rapid decompression: an experimental determination. *Bulletin of Volcanology* 67, 526-538.

Murphy, M.D., Sparks, R.S.J., Barclay, J., Carroll, M.R., Lejeune, A.M., Brewer, T.S., Macdonald, R., Black, S. and **Young, S.** 1998. The role of magma mixing in triggering the current eruption at the Soufriere Hills volcano, Montserrat, West Indies. *Geophysical Research Letters* 25, 3433-3436.

Nakada, S. and **Motomura, Y.** 1999. Petrology of the 1991-1995 eruption at Unzen: effusion pulsation and groundmass crystallization. *Journal of Volcanology and Geothermal Research* 89, 173-196.

Neall, V.E. 1971. Volcanic domes and lineations in Egmont National Park. *New Zealand Journal of Geology and Geophysics* 14, 71-81.

Neall, V.E. 1972. Tephrochronology and tephrostratigraphy of western Taranaki (N108-109), New Zealand. *New Zealand Journal of Geology and Geophysics* 15, 507-557.

Neall, V.E. 1973. Some aspects of western Taranaki geology and pedology. Unpublished PhD thesis. Victoria University of Wellington, Wellington, New Zealand.

Neall, V.E., Stewart, R.B. and **Smith, I.E.M.** 1986. History and petrology of the Taranaki volcanoes. In: **Smith, I.E.M.** (ed.) Late Cenozoic volcanism. *Royal Society of New Zealand Bulletin* 23, 251-263.

Newhall, C.G. and **Melson, W.G.** 1983. Explosive activity associated with the growth of volcanic domes. *Journal of Volcanology and Geothermal Research* 17, 111-131.

Newland, J. 1841-1873. Journal of John Newland, Vol. 2, New Plymouth.

Pallister, J.S., Hoblitt, R.P. and **Reyes, A.G.** 1992. A basalt trigger for the 1991 eruptions of Pinatubo volcano? *Nature* 356, 426-428.

Platz, T. 2001. Mapping and characterisation of the volcaniclastic Maero formation deposits on the northwestern sector of Egmont volcano (Mt. Taranaki), New Zealand. Unpublished Diploma mapping thesis. Ernst-Moritz-Arndt Universität, Greifswald, Bundesrepublik Deutschland.

Ponomareva, V.V., Melekestsev, I.V. and **Dirksen, O.V.** 2006. Sector collapses and large landslides on Late Pleistocene-Holocene volcanoes in Kamchatka, Russia. *Journal of Volcanology and Geothermal Research* 158, 117-138.

Pownall, R.W. 1885. Illustrated guide to the west coast of the North Island, N.Z., describing the various towns and adjacent land available for settlement. A.D. Willis. Wanganui.

Price, R.C., McCulloch, M.T., Smith, I.E.M. and **Stewart, R.B.** 1992. Pb-Nd-Sr isotopic compositions and trace element characteristics of young volcanic rocks from Egmont Volcano and comparisons with basalts and andesites from the Taupo Volcanic Zone, New Zealand. *Geochimica et Cosmochimica Acta* 56, 941-953.

Price, R.C., Stewart, R.B., Woodhead, J.D. and **Smith, I.E.M.** 1999. Petrogenesis of high-K arc magmas: evidence from Egmont Volcano, North Island, New Zealand. *Journal of Petrology* 40, 167-197.

Prouteau, G. and **Scaillet, B.** 2003. Experimental constraints on the origin of the 1991 Pinatubo dacite. *Journal of Petrology* 44, 2203-2241.

Rieder, M., Cavazzini, G., D'Yakonov, Y., Frank-Kamenetskii, V.A., Gottardi, G., Guggenheim, S., Koval', P.V., Müller, G., Neiva, A.M.R., Radoslovich, E.W., Robert, J.-L., Sassi, F.P., Takeda, H., Weiss, Z. and Wones, D.R. 1998. Nomenclature of the micas. *Canadian Mineralogist* 36, 905-912.

Roman, D.C., Cashman, K.V., Gardner, C.A., Wallace, P.J. and **Donovan, J.J.** 2006. Storage and interaction of compositionally heterogeneous magmas from the 1986 eruption of Augustine Volcano, Alaska. *Bulletin of Volcanology* 68, 240-254.

Rutherford, M.J. and **Devine, J.D.** 1988. The May 18, 1980, eruption of Mount St. Helens 3. Stability and chemistry of amphibole in the magma chamber. *Journal of Geophysical Research-Solid Earth* 93, 11949-11959.

Rutherford, M.J. and **Devine, J.D.** 2003. Magmatic conditions and magma ascent as indicated by hornblende phase equilibria and reactions in the 1995-2002 Soufrière Hills magma. *Journal of Petrology* 44, 1433-1453.

Rutherford, M.J. and **Hill, P.M.** 1993. Magma ascent rates from amphibole breakdown - an experimental study applied to the 1980-1986 Mount St Helens eruptions. *Journal of Geophysical Research-Solid Earth* 98, 19667-19685.

Sato, H., Nakada, S., Fujii, T., Nakamura, M. and **Suzuki-Kamata, K.** 1999. Groundmass pargasite in the 1991-1995 dacite of Unzen volcano: phase stability experiments and volcanological implications. *Journal of Volcanology and Geothermal Research* 89, 197-212.

Schmidt, M.W. 1992. Amphibole composition in tonalite as a function of pressure: an experimental calibration of the Al-in-hornblende barometer. *Contributions to Mineralogy and Petrology* 110, 304-310.

Schumacher, J.C. 1997. The estimation of ferric iron in electron-microprobe analysis of amphiboles. Appendix 2. In: **Leake, B.E. Woolley, A.R., Arps, C.E.S., Birch, W.D., Gilbert, M.C., Grice, J.D., Hawthorne, F.C., Kato, A., Kisch, H.J., Krivovichev, V.G., Linthout, K., Laird, J., Mandarino, J.A., Maresch, W.V., Nickel, E.H., Rock, N.M.S., Schumacher, J.C., Smith, D.C., Stephenson, N.C.N., Ungaretti, L., Whittaker, E.J.W.** and **Youzhi, G.** Nomenclature of amphiboles: report of the Subcommittee on amphiboles of the International Mineralogical Association, Commission on new minerals and mineral names. *Canadian Mineralogist* 35, 238-246.

Scrope, G.P. 1862. Volcanos. The character of their phenomena, their share in the structure and composition of the surface of the globe, and their relation to its internal forces. With a descriptive catalogue of all known volcanos and volcanic formations. 2nd ed. Longman, Green, Longmans, and Roberts. London.

Sherburn, S. and **White, R.S.** 2005. Crustal seismicity in Taranaki, New Zealand using accurate hypocentres from a dense network. *Geophysical Journal International* 162, 494-506.

Sherburn, S., White, R.S. and **Chadwick, M.** 2006. Three-dimensional tomographic imaging of the Taranaki volcanoes, New Zealand. *Geophysical Journal International* 166, 957-969.

Simmons, J., Elsworth, D. and **Voight, B.** 2004. Instability of exogenous lava lobes during intense rainfall. *Bulletin of Volcanology* 66, 725-734.

Smith, J.V., Miyake, Y. and **Oikawa, T.** 2001. Interpretation of porosity in dacite lava domes as ductile-brittle failure textures. *Journal of Volcanology and Geothermal Research* 112, 25-35.

Stewart, R.B., Price, R.C. and **Smith, I.E.M.** 1996. Evolution of high-K arc magma, Egmont volcano, Taranaki, New Zealand: evidence from mineral chemistry. *Journal of Volcanology and Geothermal Research* 74, 275-295.

Sun, S.-S. and **McDonough, W.F.** 1989. Chemical and isotopic systematics of oceanic basalts: implications for mantle composition and processes. *Geological Society, London, Special Publications* 42, 313-345.

Swanson, D.A. and **Holcomb, R.T.** 1990. Regularities in growth of the Mount St. Helens dacite dome, 1980-1986. In: **Fink, J.H.** (ed.) Lava flows and domes: emplacement mechanisms and hazard implications. *IAVCEI Proceeding in Volcanology* 2, 3-24.

Taylor, R. 1833-1873. Journal of Rev. Richard Taylor. 14 vol. Typescript in Alexander Turnbull Library, Wellington.

Taylor, G.A.M. 1958. The 1951 eruption of Mount Lamington, Papua. *Australian Bureau of Mineral Resources, Geology and Geophysics Bulletin* 38.

The Taranaki Herald 1853. 5 January.

Thomas, W.M. and **Ernst, W.G.** 1990. The aluminum content of hornblende in calc-alkaline granitic rocks: a mineralogic barometer calibrated experimentally to 12 kbars. In: **Spencer, R.J.** and **Chou, I.-M.** (eds.) Fluid-mineral interactions: a tribute to H. P. Eugster. *Geochemical Society Special Publication* 2, 59-63.

Venezky, D.Y. and **Rutherford, M.J.** 1999. Petrology and Fe-Ti oxide reequilibration of the 1991 Mount Unzen mixed magma. *Journal of Volcanology and Geothermal Research* 89, 213-230.

Walter, T.R., Wang, R., Zimmer, M., Grosser, H., Lühr, B. and **Ratdomopurbo, A.** 2007. Volcanic activity influenced by tectonic earthquakes: static and dynamic stress triggering at Mt. Merapi. *Geophysical Research Letters* 34, L05304.

Westrich, H.R. and **Holloway, J.R.** 1981. Experimental dehydration of pargasite and calculation of its entropy and Gibbs energy. *American Journal of Science* 281, 922-934.

Zernack, A., Stewart, R.B. and **Price, R.C.** 2006. Slab or crust - K_2O enrichment at Egmont volcano, New Zealand. *Geochimica et Cosmochimica Acta Supplement* 70, 614.

Chapter 6 Transition to Explosive Eruptions

Long-term dome growth by extrusion of viscous andesitic magma can be interrupted or terminated by explosive activity. To understand the driving forces behind sudden changes from extrusive to explosive behaviour at andesitic volcanoes, a study of the AD1655 Burrell Lapilli eruption episode at Mt Taranaki was carried out. Individual phases of the eruption have been reconstructed and a model is proposed that explains the diversity of erupted ejecta.

Chapter 6 represents the full version of a published journal paper. Its format has been altered to match the overall thesis. Additional data collected in the context of the Burrell episode are presented in the appendices of this chapter.

Title Transition from effusive to explosive phases in andesite eruptions – a case-study from the AD1655 eruption of Mt. Taranaki, New Zealand.

Authors Thomas Platz, Shane J. Cronin, Katharine V. Cashman, Robert B. Stewart and Ian E.M. Smith.

Status published in *Journal of Volcanology and Geothermal Research* 2007, vol. 161, 15-34.

Principal investigator	Thomas Platz
Carried out	- field description and sampling, - laboratory preparation of samples, - optical microscopy, - electron microprobe analysis. - scanning electron microscopy, - porosity and permeability measurements, - FTIR spectroscopy - manuscript preparation, writing and submission
Co-investigators	Shane J. Cronin, Katharine V. Cashman, Robert B. Stewart, and Ian E.M. Smith
Aided the study by	- field assistance (Shane J. Cronin) - discussing results - editing and discussion of manuscript

6.1 Abstract

The extrusion of viscous andesite lava forming domes can terminate in explosive activity. To understand the driving forces behind this behaviour, a study of an AD1655 eruption episode at Mt Taranaki was carried out. We propose that simple changes in magmatic conditions of a single hydrous melt during ascent caused sudden changes in explosivity and gave rise to the highly variable pumice with highly variable vesicularities and colour. Fractionation of hornblende + plagioclase + clinopyroxene + Fe-Ti oxide at the onset of magma ascent, and step-wise crystallisation of plagioclase ± clinopyroxene in different parts of a single melt within the conduit was controlled by rates of initial rise, capping by an impermeable lava dome, and differential rates of vesiculation and volatile exsolution. This resulted in a vertical stratification in the conduit, comprising a viscous, hypo-crystalline lava cap, that overlay alternating zones of grey, brown and grey magma-foams. Horizontal gradients in geochemistry in the conduit are also indicated by different clast textures. The eruption consisted of an initial extrusive phase followed by three pulses of sub-Plinian activity. Each phase or pulse, corresponded to individual layers within the conduit. Ejecta included Block-and-Ash Flow deposits, three pyroclastic pumice-flow deposits of alternating grey, brown and grey pumice, as well as fallout deposits dominated by grey pumice. The brown magma foam contained more microlites, had a more-evolved matrix glass, and a higher temperature than the grey magma foams above and below. Its eruption destabilised the sub-Plinian eruption column because it was more degassed. It fragmented less efficiently than the grey magma foams due to its lower viscosity, preventing pressure build-up in bubbles. Incomplete mixing at interfaces between brown and grey magma phases gave rise to banded pumices.

6.2 Introduction

In many historic eruptions of andesitic and dacitic volcanoes an initially effusive lava emission phase was abruptly terminated by an explosive phase, often with highly hazardous consequences. Such shifts in eruptive style have been related to many complex sub-surface processes such as, decompression-induced crystallisation (Hammer et al., 2000), increase in magma viscosity by increased crystallinity (predominantly microlites) and vesicularity, water-loss, temperature gradients (Stevenson et al., 1996; Manga et al., 1998), as well as conduit shear processes within vesicular magmas (Stasiuk et al., 1996; Massol et al., 2001; Rust et al., 2003; Tuffen et al., 2003), and viscous dissipation at conduit walls (Polacci et al., 2001, 2005; Rosi et al., 2004). These sudden transitions in andesite eruptions are accompanied by the presence of ejecta with a wide range in vesicularity and permeability (Klug and Cashman, 1994; Gardner et al., 1998; Rosi et al., 2004). This includes strongly banded pumice clasts, with grey to brown bands, interpreted as mingled compositions, or products of shear processes within conduits.

Emplacement and destruction of lava domes is very common at subduction-related andesitic and dacitic volcanoes. Partial dome collapse is commonly caused by [1] over-steepening (Sparks et al., 2000), [2] gas over-pressurisation (Elsworth and Voight, 2001), and [3] rainfall (Matthews et al., 2002). However, dome collapse and partial unroofing of the vent does not always trigger a shift in eruptive style. This was true for most of the eruptions over the last c.1000 years at Mt. Taranaki, where several lava domes were emplaced, forming Block-and-Ash Flows (BAFs) through dome collapse. However, one of these dome-effusion periods was terminated by an explosive sub-Plinian eruption (Druce, 1966). These sub-Plinian deposits, and all other known from sub-Plinian events at this volcano, contain notably high contents (10-30%) of monolithologic dense lithics, which appear to be juvenile.

Understanding the causes of such transitions in eruptive style is critical for constructing hazard models for andesitic volcanoes and hence developing realistic eruption scenarios and volcanic emergency plans. Here we propose an alternative model to explain some types of transitions from effusive to explosive activity, primarily through changes of magmatic conditions during ascent. This model also helps explain the production of a variety of pumice textures as well as the origin of some types of banded pumice. We base this study on the AD1655 Burrell Lapilli eruption of Mt. Taranaki, an episode in which a small-scale dome effusion event was suddenly terminated by an explosive sub-

Plinian eruption that covered several 100's of km^2 of New Zealand's central North Island in fall deposits.

6.2.1 Geological Setting

Mount Taranaki/Egmont volcano is located in the west of the North Island of New Zealand and is the youngest edifice in a 0.75-0.13 Ma SE-trending volcanic alignment [Fig. 6-1; (Neall et al., 1986; Stewart et al., 1996)]. The volcanic history of Mt. Taranaki began c.130,000 years ago and has been characterised by several cone-building and collapse episodes (Alloway et al., 1995). The current edifice was constructed over the last c.10 ka (Neall et al., 1986) with activity characterised by 0.1-2 km^3 sub-Plinian eruptions on c.330 yr intervals, interspersed with more frequent effusive dome-and BAF-forming events and lava flows (Alloway et al., 1995).

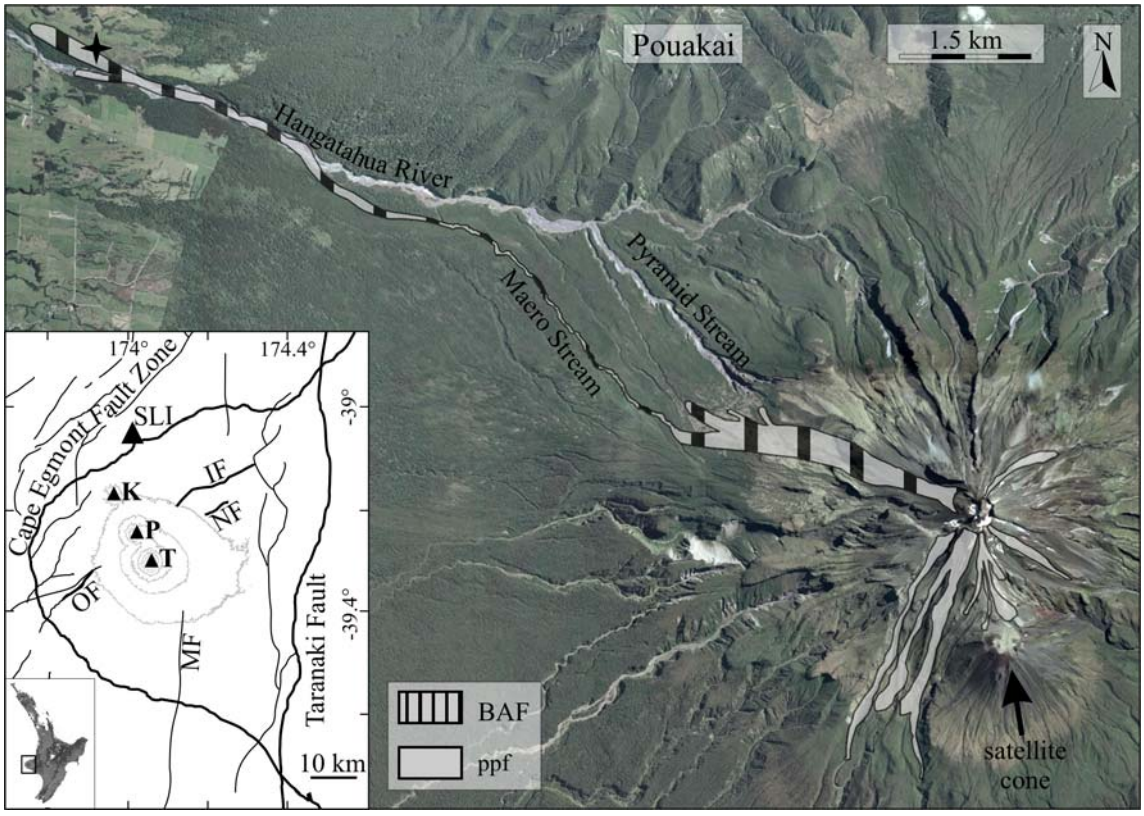


Figure 6-1: Mount Taranaki (lower right) has produced mainly lava dome eruptions in the past 800 years with Block-and-Ash Flow deposits making up the fan between the Maero and Pyramid Stream and in the Hangatahua River (BAF – Block-and-Ash Flow, ppf – pumice pyroclastic flow). Star (top left) indicates the most distal outcrop discussed in the text. To the NNW of Mt. Taranaki are the south flanks of Pouakai volcano. The inset shows the Taranaki peninsula with the Taranaki Volcanic Lineament (SLI-Sugar Loaf Islands, K-Kaitake, P-Pouakai, T-Taranaki). Major onshore and offshore faults: IF-Inglewood Fault, MF-Manaia Fault, NF-Norfolk Fault, OF-Oanui Fault. Contours are 300 m. Modified after Sherburn and White (2005).

The latest eruptive sequence of Mt. Taranaki comprises at least nine separate episodes, collectively mapped as the Maero Formation (Druce, 1966; Neall et al., 1986). Each episode was characterised by effusion of highly-viscous andesitic magma to form lava domes within the summit crater and through a breach in the crater onto the uppermost NW flank. Collapses and small explosions from these lava domes generated BAFs and surges, with the largest BAFs travelling up to 13.5 km down the Hangatahua River.

The Burrell Lapilli eruption episode took place in AD1655, according to ^{14}C dating of charcoal in a Maori oven that was buried by tephra fall (Wellman, 1962) and dendrochronology dating of trees damaged by the fall (Druce, 1966). In earlier descriptions of this eruption, pumice fallout deposits were mapped to the ESE (Druce, 1966). Three lobes, directed to the NE, SE, and ESE, were recognised based on grain size analyses (Topping, 1972). The pumice flows and BAFs associated with the Burrell Lapilli are newly described in this study.

6.3 Methodology

For petrographic, mineral chemistry, and textural studies, pumice samples were impregnated with the low viscosity polymer, methyl methacrylate and polymerised by Cobalt-60 gamma radiation. Glass and mineral microprobe analyses were carried out on polished thin sections of impregnated pumices and dense clasts using an energy dispersive spectrometer (JEOL JXA-840) with an accelerating voltage of 15kV, a beam current of 600 pA and 100 seconds live time. Glass analyses were performed with a beam defocused to 20 μm diameter.

For bulk rock geochemistry, pumice and lithic clast specimens were crushed and ground using a tungsten carbide mill. Major and trace elements were measured on prepared glass discs and powder pellets, respectively, using X-ray fluorescence spectrometry (Siemens SRS 3000) and calibrated to a suite of 36 international standards at the University of Auckland.

Porosity and permeability measurements were made using cores (approx. 2.54 cm diameter and height) of clasts that were drilled in two or three mutually perpendicular orientations (depending on sample size; Fig. 6-2). From the known volume ($V_{cylinder}$) and mass of the cores, the bulk density (ρ_{bulk}) was determined. A He-pycnometer was used to measure the helium accessible volume (V_{He}) of the sample, resulting in an

estimate of skeletal density ($\rho_{skeletal}$). However, even rocks of dense appearance commonly possess isolated cavities and cracks, and vesiculated rocks usually have isolated pores (V_{iso}) in addition to a connected pore network, and therefore $\rho_{skeletal}$ is always lower than ρ_{solid}. In order to determine ρ_{solid}, representative samples of grey (n=6), brown (n=4) and black (n=2) clasts were powdered and their volume determined by He-pycnometry. The isolated pore volume, V_{iso}, can then be calculated and the bulk vesicularity determined by $\varphi = (V_{He} + V_{iso})/V_{cylinder}$.

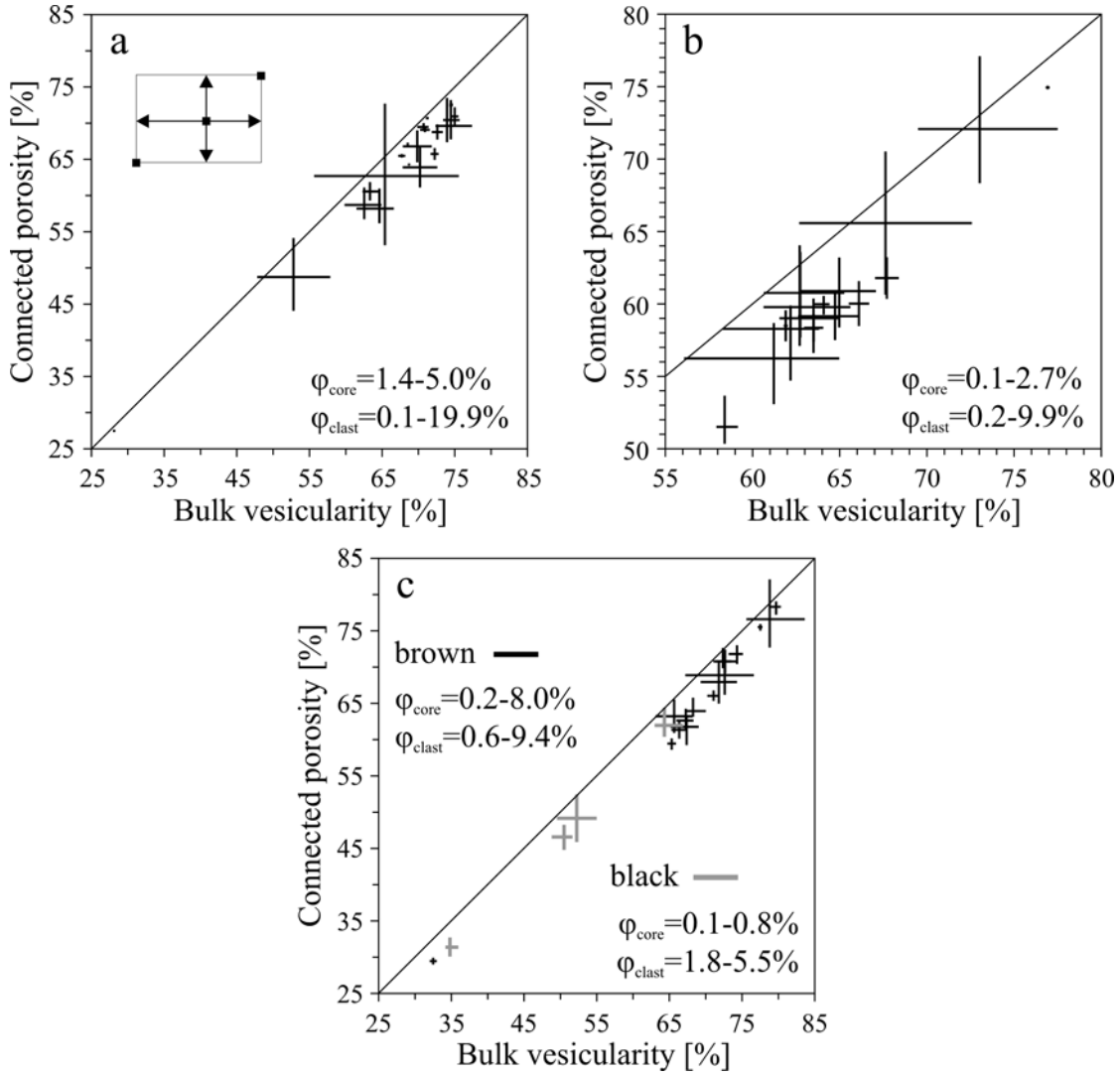


Figure 6-2: Variations in bulk vesicularity and connected porosity of single clasts for grey pumice (a), banded pumice (b), and black and brown pumice (c). Crosses represent the range in vesicularity per clast using minimum, mean and maximum values (see inset in a). Variations in bulk vesicularity refer to single cores cut in two (φ_{core}) and overall clast variations with multiple cores (φ_{clast}). Note different scale in b). See text for details.

Long drilled cores cut into two were analysed for reproducibility and homogeneity in a specific orientation. Pumice samples appear homogeneous, with differences in φ of 0.1 to 8.0% over the range of φ=34.2-83.6%. However, single larger pumice clasts with up

to seven drilled cores per sample in multiple orientations showed differences in φ of up to 19.9% (Fig. 6-2). The gas permeability of pumice cores was measured in a capillary flow porometer with air as the working gas using calculations after Rust and Cashman (2004) and Wright et al. (2007).

Scanning electron microscopy images of carbon-coated samples were collected at Massey University and the University of Oregon using accelerating voltages of 20 kV and 10 kV, respectively.

6.4 Results

6.4.1 Field Observations

6.4.1.1 Fall Deposits

The pumice fall deposits are well exposed on the steeper parts of the mountain near walking tracks, whereas outside the National Park boundary on flatter terrain, exposures are rare or the unit is disturbed by soil tillage.

The proximal to medial deposits (within 10 km) are characterised by pale grey and pale brown (weathered) subrounded to subangular pumice and darker grey angular to subangular lithics (commonly dense grey andesite). Overall, between 10-15% lithic clasts are scattered throughout the fall unit, with fewer, larger clasts near the base and finer, more-abundant clasts near the top. Reverse grading of the whole unit is also occasionally observed. Rare accessory clasts also occur, including iron-stained, weathered, and hydrothermally altered andesites. While lithic clast abundances vary greatly between exposures, there is an overall decrease with distance from dispersal axis and source.

6.4.1.2 Pumice Pyroclastic Flow Deposits

Pumice pyroclastic flows associated with the Burrell Lapilli eruption travelled predominantly down the southern flanks (Fig. 6-3a), but were also deposited on the upper southeastern and northeastern sectors (Fig. 6-4b). Three flow units are preserved on the southern flank.

The basal unit (1) is up to 1.5 m thick and comprises pale grey pumice of up to 70 cm in diameter in a medium- to coarse-ash matrix. The subrounded to rounded pumice blocks and lapilli are uniform in colour or contain patches or bands of darker grey. They also commonly contain inclusions of grey, angular, dense lithic lapilli. Larger pumice blocks are concentrated at or near the upper surface of the unit. Lithic clasts up to 50 cm diameter are present throughout the unit, most commonly as grey and dark grey dense andesites. The dense grey andesites are often bread-crusted, jigsaw-jointed or fractured (Fig. 6-3c). Occasionally, their concentration increases upwards through the unit. Rare hydrothermally altered and other dense andesite lithologies are present.

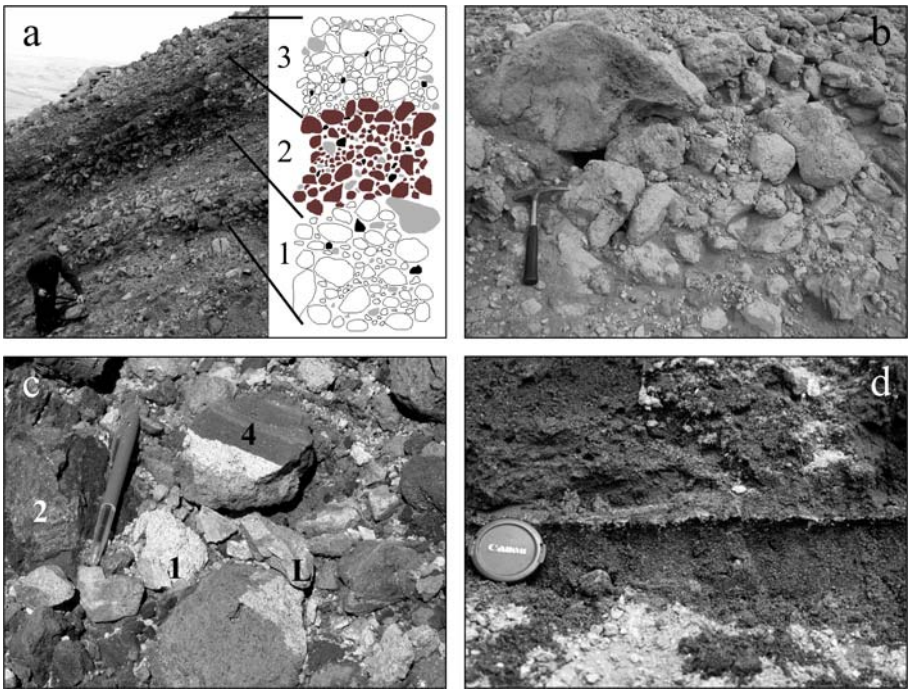


Figure 6-3: Field photographs of a) succession of three pumice pyroclastic flow deposits on the upper south flanks; sketch shows a general assembly of pumice types and grey dense lithics, b) grey pumice clasts of unit 3, c) eroded surface into unit 2 showing the scattered grey pumice [1] from airfall, brown pumice [2], banded pale grey to dark brown pumice [4], and the dense fractured andesite clasts [L]; d) lower contact of a distal BAF deposit, c.13.5 km from source (star in Fig. 6-1). See text for field description.

The middle unit (2) is up to 2 m thick and comprises subangular to rounded, brown to dark-brown pumice up to 45 cm in diameter. Common lithics of grey and dark-grey dense andesites are concentrated toward the base of the unit (c.10% by volume), while glassy black, vesicular to semi-vesicular clasts are evenly distributed throughout it (c.5% by volume). Grey, dense, bread-crusted and jointed blocks are rare. Accidental lithics comprise hydrothermally altered or weathered andesite and iron-stained clasts. The lower and upper contacts are gradational and marked by concentrations of banded

pumice (Fig. 6-3c). Unit 2 is in part consolidated and is the only unit to show partial welding textures. In places, it is also strongly oxidised. The partially welded parts of the unit form small ridges on the volcano flanks above 1900 m, capping and preserving the friable unit 1. Deposits of unit 2 are more restricted than the others and are found only within 1.2 km of the crater rim.

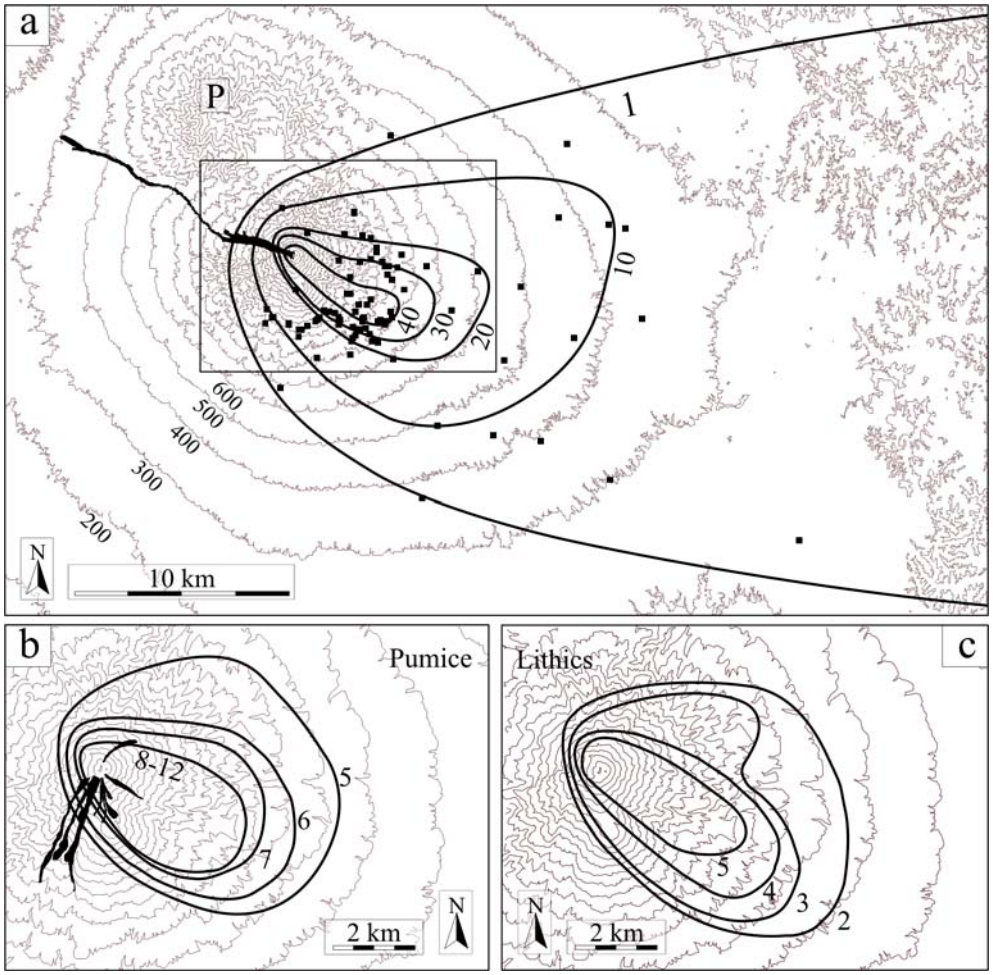


Figure 6-4: Distribution of Burrell Lapilli deposits: a) isopachs in cm including the BAF deposit (black) to the NW for reference, black squares represent mapping locations for fall deposits only, P-Pouakai, contours 100 m; b) isopleths for pumice clasts and pumice pyroclastic flow deposits on the upper flanks (black), see inset in a) for location; c) isopleths for lithic clasts, same outline as in b). Numbers in b) and c) are clast diameters in cm.

The uppermost unit (3) is >1 m thick, but often partly eroded. Near the summit, it contains pumice clasts up to 70 cm in diameter, which are usually concentrated on the surface, along with dense grey bombs and blocks (Fig. 6-3b). Units 1 and 3 are generally similar in clast composition and texture and occur separately or together up to 3.3 km from the crater rim.

6.4.1.3 Block-and-Ash Flow Deposits

A fan of Maero Formation BAF and related deposits occur on the NW sector of Mt. Taranaki. Since the last events in AD1755 and c.1860, box-canyons of up to 80 m wide and deep have been eroded into the unconsolidated volcaniclastics (see Fig. 3-4b).

The primary BAF deposits often contain charcoalised twigs, branches or logs, hence the stratigraphic sequence is well constrained by radiocarbon dates (see Appendix A and Fig. 3-4k-l). One sub-set of the deposits can be related to the Burrell Lapilli event. The most distal exposed Burrell-related BAF deposit is found 13.5 km from source beside Hangatahua River (Fig. 6-4a). It consists of a brownish-grey, 1.75 m thick, medium ash matrix-supported diamicton with 45% lapilli to fine block-sized clasts of dense grey andesite, with rare weathered and hydrothermally altered andesite and occasional grey pumice. Pumice is not strongly represented in the -1.5 to -1 φ fractions, comprising c.6% by volume.

The deposit drapes a 1 cm charred humus layer containing charcoal twigs (Fig. 6-3d), and charcoal logs are imbricated throughout the unit. The natural remanent magnetism of 10 clasts measured with a portable fluxgate magnetometer shows coherent alignment in six directions for 8 clasts, indicating a deposition temperature above or near the Curie Point.

This deposit can be correlated upstream through a succession of units in the Maero Stream (see Appendix A and B). Characteristics of these nearer-source deposits are similar, with only very rare pumice clasts present.

6.4.2 Volume Estimates

The minimum fall volume was estimated as 3.2×10^8 m^3, by applying $V=13.08T_0b_t^2$ (based on Cole and Stephenson, 1972) to the mapped isopachs (Table 6-1) where T_0 is the extrapolated maximum thickness and b_t the distance over which the thickness of the deposit halves (see also Pyle, 1989).

ArcGIS was used to calculate the minimum bulk volume of pumice flow and BAF deposits, at 1.3×10^6 m^3 and 2.5×10^6 m^3, respectively (Table 6-1). On a volumetric basis, the Burrell Lapilli eruption is classified as a VEI 4 sub-Plinian eruption (cf. Newhall

and Self, 1982). Applying the model of Carey and Sparks (1986) the eruption column is estimated to have been up to 14 km.

Lithic contents of the fall deposit were counted in the -4 to 0 φ grain size fractions of 5 samples at varying distances from source. The volumetric lithic content shows an exponential decrease with distance, with maximum lithic contents between 28 and 39 wt.% (approx. 13-20 vol.%) at distances of 2.5 to 2.9 km. By 9.8 km, it had dropped to 19 wt.% (approx. 8 vol.%). These estimates include a combination of juvenile and accidental clasts, since distinguishing them was difficult optically. Using an overall lithic population of 14%, a lithic volume of 1.7×10^7 m^3 (Table 6-1) is contained in the fall, corresponding closely to the theoretical maximum volume that a dome could occupy in the present crater dimensions (c.2×10^7 m^3). Given that some of the dome is probably also contained in the BAF, the lithics in the fall probably also derive from the upper conduit.

Table 6-1. Minimum volume and mass calculations of erupted tephra.

	Bulk volume [m^3]	Mass [kg]	DRE volume [m^3]	Lithic content [%]	DRE Pumice [m^3]	DRE Lithics [m^3]
Fall	3.2×10^8	2.8×10^{11}	1.1×10^8	14 wt.%[b]	9.6×10^7	1.6×10^7
BAF	1.7×10^6	3.6×10^9	1.5×10^6	90 vol.%[c]	1.5×10^5	1.3×10^6
Pumice PF[d]	1.3×10^6	1.7×10^9	7.1×10^5	10 vol.%[c]	6.4×10^5	7.1×10^4
Total	3.3×10^8	2.8×10^{11}	1.2×10^8		9.7×10^7	1.8×10^7

Bulk density Fall	850	[kgm^{-3}]
Bulk density BAF	2100	[kgm^{-3}]
Bulk density Pumice PF[d]	1300	[kgm^{-3}]
Bulk density Pumice	900	[kgm^{-3}]
Bulk density Lithics	2300	[kgm^{-3}]
Magma density	2450	[kgm^{-3}]

[a] Dense Rock Equivalent.
[b] Estimates based on lithic-pumice counts in wt.% from grain size fractions -4 to 0 φ.
[c] Overall deposit estimate.
[d] Pumice pyroclastic flow.

6.4.3 Clast Types and Textures

The different clast types of the Burrell Lapilli eruption episode provide insights into the eruptive processes and the mechanisms of pumice formation. For simplicity, all clasts that developed individual vesicles within their groundmass are termed pumice, regardless of whether an interconnected bubble network is developed or not. Those clasts that only display cracks and cavities are collectively termed lithics. For

quantitative analyses, pumice samples were categorized into four groups based on their colour; [1] uniform pale grey, [2] brown, [3] black, and [4] banded to transitional pumice clasts ranging from pale grey to dark brown.

Dense grey clasts present in BAF and fall deposits have a hypocrystalline groundmass with abundant plagioclase microlites and Fe-Ti oxides, and very rare minor cracks (Fig. 6-5a). Pumice clasts [1], [2], and [4] have a well-developed, interconnected vesicle network with areas of coalesced vesicles that are often a few centimetres long (Fig. 6-5d). Black pumice clasts [3] show two vesicularity populations; semi-vesicular, with minor isolated vesicles in a glassy, microlite containing matrix (Fig. 6-5b), and vesicular, with more abundant isolated vesicles that display partial coalescence (Fig. 6-5c).

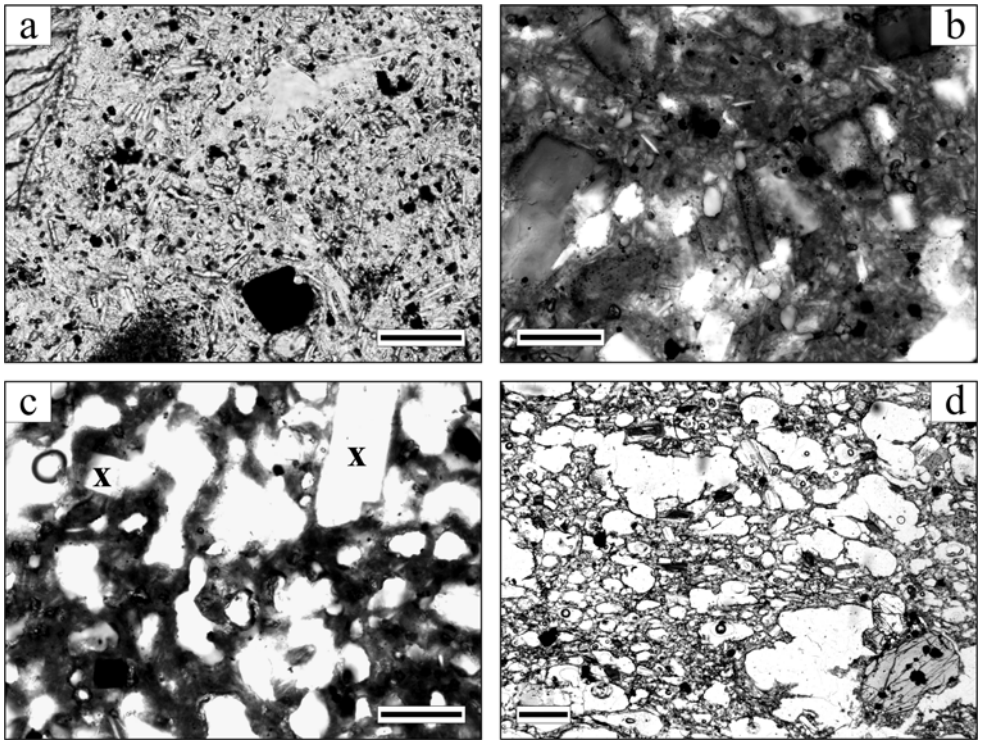


Figure 6-5: Thin-section photographs illustrating basic vesicularity differences of juvenile clasts. a) dense grey lithic, b) semi-vesicular black pumice, c) vesicular black pumice with isolated and coalesced vesicles, crosses mark plagioclase crystals; d) grey pumice with isolated large single vesicles as well as larger coalesced vesicle. Scale bar is 100 µm in a-c and 500 µm in d. See text for details.

Type 1 pumice has a broad range in vesicle-size distributions (Fig. 6-6a) with large single and coalesced bubbles (Fig. 6-6c). Larger bubbles are elongated but show no deformation, and only few microlites occur in the glass. By contrast, brown pumice [2] has a broad but bimodal range in vesicle sizes (Fig. 6-6b). Large, coalesced bubbles are

present, but simple large bubbles are absent. The bubble network is often deformed and bubbles walls are thicker with microlites in the glass.

Banded pumices [4] contain types [1] and [2] (Fig. 6-6d). The grey bands within them are often coarsely vesicular with interconnected vesicles. Black vesicular clasts [3] have comparatively small bubbles of uniform size, which also appear in thin sections to be commonly isolated (Fig. 6-5c).

The difference in pumice types is also expressed in their solid densities (grey: 2.74 gcm^{-3}; brown: 2.79 gcm^{-3}).

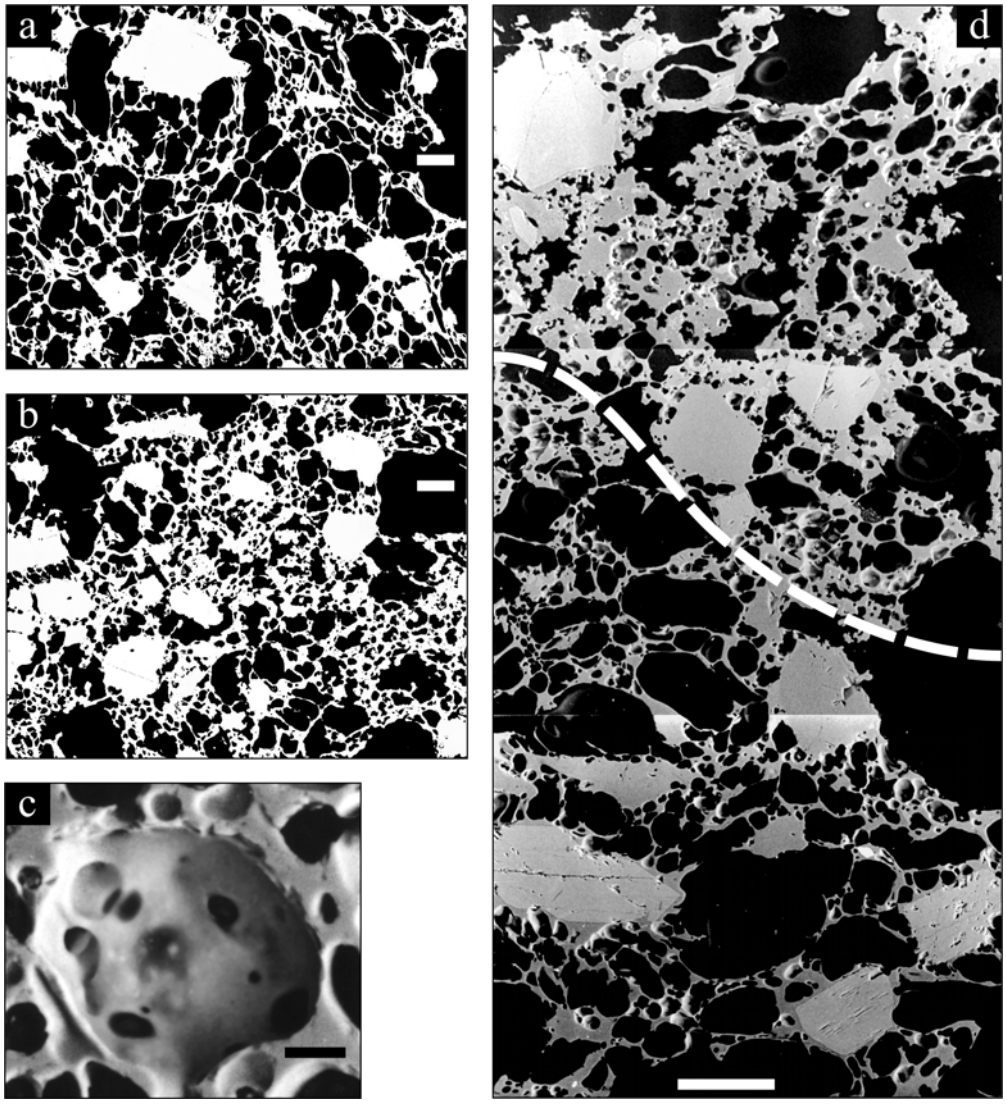


Figure 6-6: SEM images of grey (a) and brown (b) pumice (note a and b are binarised; black=vesicles, white=glass + crystals); c) shows a large coalesced vesicle; d) consists of three SEM images showing the transition from grey to brown in banded pumice. Scale bar is 10 µm in c), otherwise 100 µm.

6.4.4 Mineralogy and Mineral Chemistry

All pumice clasts contain common euhedral crystals of plagioclase, clinopyroxene, hornblende, Fe-Ti oxides, and minor biotite. Often crystals are broken fragments. In the glassy, highly vesiculated rocks, microlites of plagioclase, and to a lesser extent clinopyroxene, appear predominantly at the intersection of adjacent vesicles or next to phenocrysts. In addition, hornblende and biotite crystals are fresh, showing no oxidation or breakdown reaction rims (Fig. 6-7a).

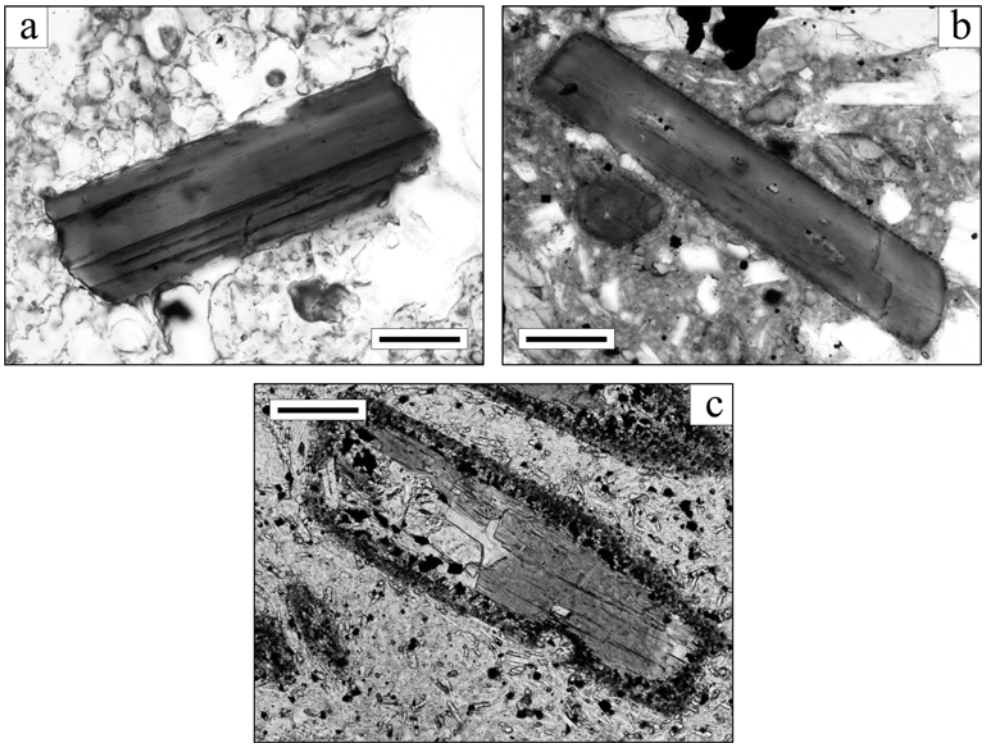


Figure 6-7: Hornblende reaction textures in different clast types: a) fresh hornblende with no reaction rims in pumice, b) single Fe-Ti oxide crystals are attached to the hornblende rims in black semi-vesicular pumice, c) hornblende in dense grey lithic clast shows resorption textures and is partially replaced by clinopyroxene, plagioclase and Fe-Ti oxide crystals or is fully replaced (lower left); note abundant plagioclase microlites in groundmass. Scale bar is 100 µm.

Grey lithics, the most abundant lithic clast type within pumice flow and fall deposits, are dense, hypocrystalline, and comprise plagioclase, clinopyroxene, hornblende, Fe-Ti oxides, and biotite. Hornblende and biotite are partially oxidised, with Fe-Ti oxide reaction rims; in some cases the crystals are replaced by minute plagioclase, clinopyroxene and Fe-Ti oxides (Fig. 6-7c).

Black dense and vesicular clasts, common in the pumice pyroclastic flow deposits, are glassy with the same mineral assemblage as grey, dense lithics, except with lower biotite contents. Hornblende appears fresh, with minor Fe-Ti oxide rim alteration (Fig. 6-7b).

6.4.5 Bulk Rock Geochemistry

Whole rock analyses of pumice clasts and juvenile lithics from the pumice pyroclastic flow, BAF and fall deposits are shown in Table 6-2. Pumice clasts from units 1 to 3 and black dense and vesicular lithics show very little variation in major and minor element geochemistry. Silica contents range between 55.5 and 56.0 wt.% (Fig. 6-8). The common grey dense lithics in the deposits show a broader range in composition, with silica varying between 56.4 and 59.5 wt.%.

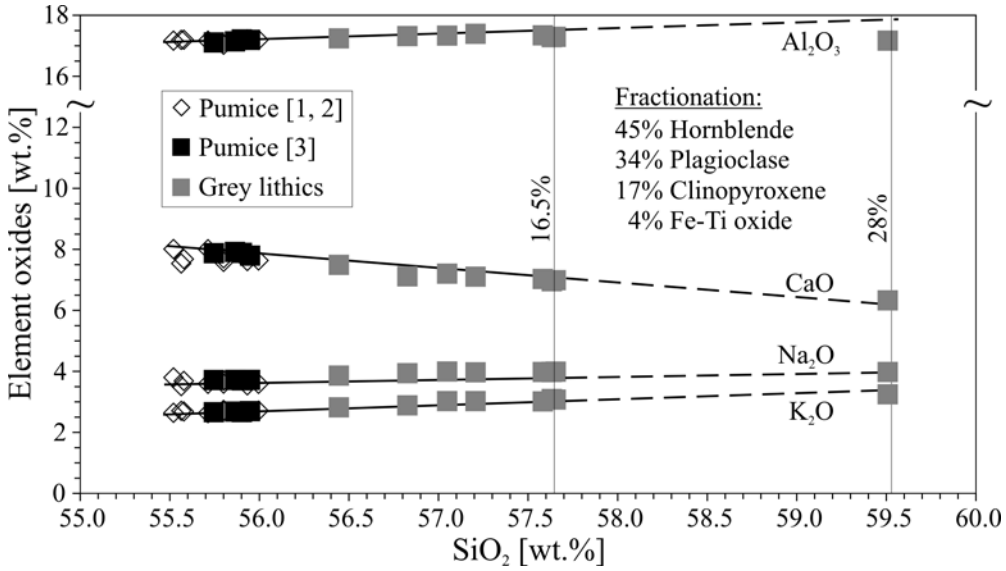


Figure 6-8: Bulk rock geochemistry of pumice and grey andesite clasts in a multi element oxide vs. SiO_2 diagram. The calculated fractionation trend pumice – grey lithics is in good agreement for the majority of clasts (solid line) with some variation for the most evolved clast (dashed line). See Table 6-3 for details.

Data for all major elements show linear relationships (Fig. 6-8) with the trends being best explained by fractionation from pumice to grey lithics involving 45% hornblende, 34% plagioclase, 17% clinopyroxene, and 4% Fe-Ti oxides. This mineral assemblage represents common macroscopic and microscopic cumulates within Mt. Taranaki rocks. Sample P10 has been used as a starting composition based on its highest Mg# of 49.9. From this assumed magma composition, crystals have been subtracted from the magma composition using average mineral compositions for plagioclase and Fe-Ti oxides and average rim compositions for hornblende and clinopyroxene obtained by electron microprobe (Table 6-3). The modelled fractionation is in very good agreement with observed rock compositions up to 16.5% of fractionation, however, there is a considerable deviation for Al_2O_3, FeO and MgO contents between the model and the

Table 6-2. XRF bulk rock geochemistry of Burrell Lapilli clasts. Samples are mostly from pumice flow deposits with one BAF deposit sample (P10).

Sample	SD20	SD35	TO4-22	TO4-96	P10	SD24	TO4-19	TO4-65	SD9a	SD9c	SD28	TO4-1	TO4-21	TO4-24
Rock type	pumice	pumice	pumice	pumice	pumice	pumice	pumice	pumice	grey lithic	grey lithic	grey lithic	grey lithic	grey lithic	grey lithic
SiO_2	55.56	55.58	56.00	55.52	55.71	55.80	55.93	55.80	56.44	57.65	57.21	57.58	56.83	59.51
TiO_2	0.770	0.761	0.768	0.770	0.780	0.753	0.754	0.757	0.772	0.760	0.772	0.749	0.756	0.669
Al_2O_3	17.19	17.20	17.19	17.17	17.17	17.05	17.20	17.04	17.24	17.29	17.40	17.35	17.32	17.17
Fe_2O_3	7.31	7.09	7.17	7.25	7.21	7.01	7.18	7.15	6.92	6.54	6.65	6.62	6.98	5.97
MnO	0.15	0.15	0.15	0.15	0.15	0.15	0.15	0.15	0.15	0.14	0.14	0.15	0.16	0.14
MgO	3.45	3.49	3.35	3.61	3.62	3.44	3.45	3.47	3.17	2.91	2.96	2.88	3.20	2.54
CaO	7.54	7.68	7.64	8.01	8.00	7.59	7.62	7.71	7.49	6.99	7.11	7.03	7.12	6.33
Na_2O	3.52	3.69	3.59	3.80	3.59	3.70	3.54	3.59	3.86	3.99	3.97	3.98	3.94	3.98
K_2O	2.71	2.69	2.71	2.64	2.63	2.74	2.67	2.71	2.82	3.07	3.02	3.02	2.89	3.25
P_2O_5	0.27	0.27	0.27	0.27	0.26	0.27	0.26	0.27	0.28	0.28	0.29	0.28	0.28	0.24
H_2O	0.12	0.12	0.16	0.19	0.22	0.09	0.18	0.30	0.00	0.00	0.02	0.10	0.13	0.04
LOI	1.12	1.04	0.84	0.55	0.47	0.78	0.85	0.85	-0.08	-0.02	-0.05	-0.03	0.11	-0.08
Total	99.70	99.75	99.84	99.93	99.81	99.36	99.80	99.78	99.28	99.83	99.70	99.70	99.71	99.75
Sc	18.8	18.8	13.0	16.2	18.7	19.8	15.6	22.5	17.0	17.0	17.0	10.8	9.5	11.7
V	201	197	202	214	202	194	199	206	192	183	187	184	179	151
Cr	42.5	44.5	48.9	54.3	56.2	51.5	45.2	47.0	29.4	22.9	21.9	22.4	22.5	24.2
Ni	11.9	8.9	10.1	13.5	13.7	17.8	11.6	12.6	7.7	8.1	9.6	7.2	9.1	7.9
Cu	76.0	81.0	26.1	77.1	42.6	110.0	51.2	111.3	47.0	62.2	33.5	44.0	34.3	31.1
Ga	18.8	20.8	19.4	19.4	19.5	19.8	19.0	19.1	21.4	22.5	21.1	20.6	21.0	20.0
Rb	70.1	68.2	72.4	68.8	69.8	70.4	71.5	71.2	69.9	77.7	76.7	77.2	76.1	87.2
Sr	584	569	574	573	574	569	566	558	602	597	610	608	619	550
Y	21.7	21.7	21.6	22.2	21.9	21.8	21.3	21.6	22.6	23.3	23.4	23.6	22.1	20.7
Nb	5.9	5.9	4.9	4.5	4.3	5.9	5.0	4.9	7.0	6.5	7.3	5.6	5.3	5.6
Ba	701	706	990	944	961	705	977	965	777	797	811	1128	1181	1173
La	20.7	19.8	19.6	15.7	22.4	18.8	21.7	20.2	0.0	0.0	0.0	20.5	18.9	17.2
Ce	41.5	38.5	38.9	38.0	40.4	32.7	40.7	37.7	0.0	0.0	0.0	45.0	38.0	37.2
Pb	13.8	12.8	15.8	16.1	15.9	15.9	15.7	16.7	12.0	15.0	12.0	16.1	17.5	20.3
Th	13.8	8.9	7.1	8.7	7.2	11.9	6.8	7.3	0.0	0.0	0.0	9.3	8.5	9.2
U	b.d.	b.d.	2.8	4	4.2	<1	2.1	2.8	b.d.	b.d.	b.d.	1.8	2.2	2.4

Table 6-2. (continued).

Sample	SD34	SD39	SD9b	SD27	SD29	SD33
Rock type	grey lithic	grey lithic	black pumice	black pumice	black pumice	black pumice
SiO_2	57.05	57.63	55.86	55.95	55.75	55.90
TiO_2	0.792	0.766	0.767	0.757	0.752	0.757
Al_2O_3	17.34	17.28	17.15	17.20	17.11	17.21
Fe_2O_3	6.75	6.58	7.14	7.09	7.14	7.09
MnO	0.15	0.15	0.15	0.15	0.15	0.15
MgO	3.01	2.89	3.61	3.51	3.62	3.57
CaO	7.20	6.95	7.91	7.80	7.88	7.89
Na_2O	3.99	3.98	3.72	3.72	3.72	3.70
K_2O	3.02	3.09	2.68	2.70	2.66	2.67
P_2O_5	0.31	0.28	0.26	0.27	0.26	0.27
H_2O	0.00	0.00	0.00	0.06	0.11	0.00
LOI	-0.03	-0.02	0.26	0.37	0.48	0.42
Total	99.79	99.81	99.73	99.57	99.62	99.63
Sc	17.0	14.0	19.0	17.9	19.2	16.9
V	196	183	201	195	197	196
Cr	23.9	24.9	47.7	46.8	45.6	48.8
Ni	4.1	6.0	11.0	11.0	11.7	12.9
Cu	56.0	89.3	67.5	103.6	73.9	92.6
Ga	22.0	19.8	18.6	18.9	20.0	21.9
Rb	75.6	81.1	68.7	70.7	66.4	68.7
Sr	627	597	576	577	572	578
Y	23.1	23.7	22.2	21.9	22.1	21.9
Nb	6.6	6.1	5.6	5.0	5.2	5.0
Ba	784	830	720	736	996	703
La	0.0	0.0	0.0	18.9	17.7	14.9
Ce	0.0	0.0	0.0	38.8	37.3	20.9
Pb	15.0	15.0	12.0	13.9	15.3	14.9
Th	0.0	0.0	0.0	11.9	6.3	12.9
U	b.d.	b.d.	b.d.	b.d.	b.d.	b.d.

b.d. below detection limit.

Table 6-3. Mass balance calculation for the inferred fractionation process for pumice-lithics.

Oxides [wt.%]	Start composition	Fractionating phases: Hornblende (n=23)	Clinopyroxene (n=33)	Plagioclase (n=50)	Fe-Ti oxides (n=27)	Cumulate composition	Comparison Model - Observation: Model at 16.5% fractionation	Observed	1σ	Model at 28% fractionation	Observed	1σ
Mineral Proportion		45%	17%	34%	4%							
Sample	P10						SD9C			T04-24		
SiO_2	55.71	41.90	51.62	53.07	0.13	45.94	57.64	57.65	0.01	59.51	59.51	0.00
TiO_2	0.78	2.65	0.49	0.07	6.45	1.30	0.68	0.76	0.06	0.58	0.67	0.06
Al_2O_3	17.17	11.81	2.30	27.80	2.59	15.39	17.52	17.29	0.16	17.86	17.17	0.49
FeO[a]	6.49	12.04	7.38	0.63	83.24	10.19	5.76	5.89	0.09	5.05	5.37	0.23
MnO	0.15	0.22	0.48	0.01	0.61	0.21	0.14	0.14	0.00	0.13	0.14	0.01
MgO	3.62	13.64	14.75	0.10	2.14	8.76	2.61	2.91	0.22	1.62	2.54	0.65
CaO	8.00	11.60	21.72	11.23	0.05	12.64	7.09	6.99	0.07	6.20	6.33	0.09
Na_2O	3.59	2.09	0.30	4.57	0.05	2.63	3.78	3.99	0.15	3.96	3.98	0.01
K_2O	2.63	1.14	0.04	0.56	0.02	0.69	3.01	3.07	0.04	3.38	3.25	0.10
Total[b]	98.15	97.08	99.08	99.04	95.27	97.76	98.22	98.70		98.30	98.96	
Mg#[c]	49.9					60.5	44.6	46.9		36.4	45.8	

[a] Fe_2O_3 of XRF analysis converted to FeO.

[b] Totals are different to published values because Fe_2O_3 abundances have been mistakenly used.

[c] $Mg\# = 100[Mg^{2+}/(Mg^{2+}+Fe^{2+})]$; all iron as Fe^{2+}.

single rock at 59.5 wt.% SiO_2 (Table 6-3). An alternative explanation for these trends could also be mixing or mingling of magmas, although glass compositions (see below) do not support this.

6.4.6 Glass Composition

Glass compositions were analysed for brown (unit 2), grey pumice clasts (unit 1 and 3), and black pumice present throughout units 1-3 (Fig. 6-9; Table 6-4). The grey pumices of unit 1 range in silica content from 64.6-67.4 wt.% whereas the same pumice type of unit 3 only varies between 64.4 to 65.8 wt.% SiO_2. Brown pumices (unit 2) have a higher silica content, ranging from 64.5-68.2 wt.%. Black pumice glass compositions differ from units 1 and 3 pumice in their higher range in silica values (64.9-69.3 wt.%), but show a very similar trend in Al_2O_3 vs. SiO_2 as observed in brown pumice with a slightly steeper slope. Glass compositions of individual lapilli are homogeneous as illustrated in the inset of Figure 6-9.

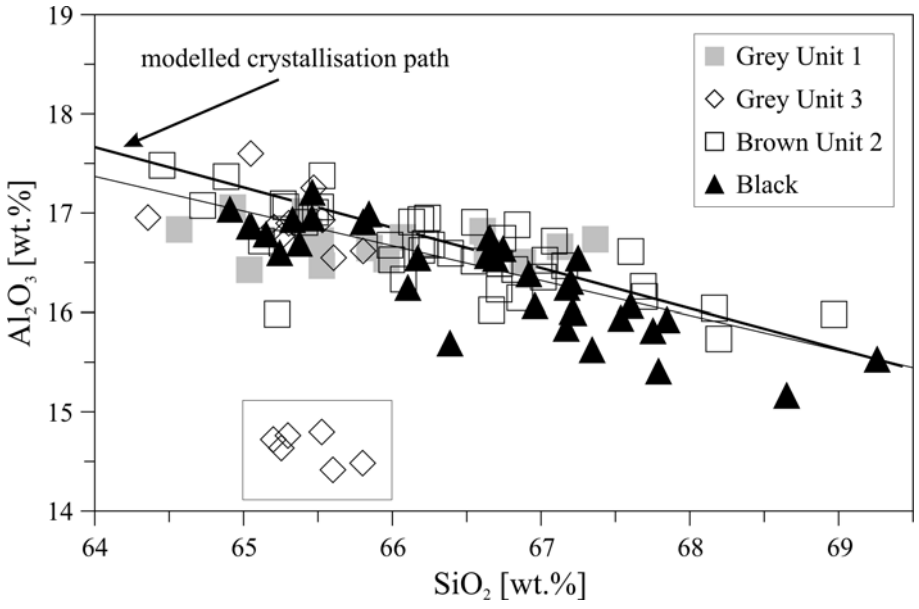


Figure 6-9: Groundmass glass compositions of pumice types presented in the Al_2O_3 vs. SiO_2 diagram. Modelled glass composition changes due to plagioclase and clinopyroxene crystallisation (thick solid line) and is in good agreement with linear regression line (thin solid line). The small inset shows six data points of one lapillus (SD20) demonstrating relative glass homogeneity. The dimensions of the box are 1 wt. % for Al_2O3 and SiO_2.

Table 6-4. Representative normalised matrix glass compositions. All data in wt. %.

Unit	Unit 1	Unit 1	Unit 1	Unit 1	Unit 1	Unit 2	Unit 2	Unit 2	Unit 3	Unit 3	Unit 3	Unit 3	Unit 3	Unit 2	Unit 1	Unit 2	Unit 2
Pumice type	grey	grey	grey	grey	grey	brown	brown	brown	grey	grey	grey	grey	grey	black	black	black	black
Sample	SD21	SD21	SD20	SD20	SD20	SD23a	SD25a	SD25a	SD31a	SD31a	SD32a	SD32a	SD32b	T04-66	SD27	SD33	SD33
SiO_2	65.58	65.21	65.65	65.36	65.59	68.31	66.85	67.07	65.11	65.65	67.64	67.13	66.80	68.78	65.11	66.92	65.84
TiO_2	0.66	0.47	0.62	0.59	0.43	0.34	0.60	0.44	0.60	0.58	0.59	0.56	0.44	0.63	0.62	0.64	0.55
Al_2O_3	17.28	17.64	16.96	16.90	16.85	15.76	16.88	16.37	17.10	16.76	16.80	16.57	16.64	15.19	17.09	16.39	16.99
FeO	2.87	2.86	3.08	3.19	2.97	2.54	2.69	2.68	3.33	3.30	2.79	2.50	3.06	2.66	3.17	2.67	2.45
MnO	0.00	0.11	0.00	0.13	0.17	0.07	0.00	0.20	0.14	0.21	0.05	0.17	0.04	0.17	0.07	0.06	0.19
MgO	1.04	0.79	1.05	1.17	1.06	0.63	0.85	0.91	1.02	0.98	0.85	0.72	0.72	0.70	0.89	0.79	0.69
CaO	3.17	3.64	3.03	3.20	3.23	2.31	2.65	2.27	3.27	2.89	2.95	2.50	2.64	1.70	3.46	2.43	2.88
Na_2O	4.75	4.73	4.61	4.62	4.60	4.45	4.07	4.72	4.50	4.58	3.61	4.45	4.30	4.06	4.68	4.52	5.22
K_2O	4.47	4.28	4.76	4.57	4.82	5.26	5.07	5.11	4.72	4.76	4.50	5.14	5.01	5.95	4.63	5.38	5.00
Cl	0.18	0.26	0.24	0.26	0.27	0.34	0.33	0.24	0.21	0.29	0.23	0.27	0.36	0.15	0.28	0.19	0.19
Unnormalised Total	95.18	96.98	96.63	95.82	96.89	98.03	96.3	97.33	97.29	97.94	95.64	96.39	98.4	96.95	97.72	98.44	99.13

The general trend of all data (thin solid line in Fig. 6-9) can be modelled using plagioclase microlite and clinopyroxene rim analyses. The thick line in Figure 6-9 represents the change in glass compositions by crystallisation of 76% plagioclase and 24% clinopyroxene calculated by mass balance. It is noted that unit 1 pumice data lie on a flatter slope, although still situated within the entire data set. This may suggest a stronger involvement of clinopyroxene during late stage evolution of glass chemistry.

6.4.7 Porosity and Permeability

Porosity (n=221) and permeability (n=83) were measured on cores of grey, brown and banded pumices and black vesicular clasts. There is a wide range in connected porosity and bulk vesicularity for all analysed clast types (Fig. 6-10). The dataset clearly illustrates a concentration of bulk vesicularities between c.57-77%, with a broader range in isolated pore volume up to 10%. Clasts with φ <54% have similar isolated pore volumes in a restricted range and these seem to decrease with decreasing φ. The gap in the dataset (36.0< φ <47.8%) may be due to low sample numbers but is more likely to be real (see discussion). The highest φ values (up to 83.6%) are observed for brown pumices.

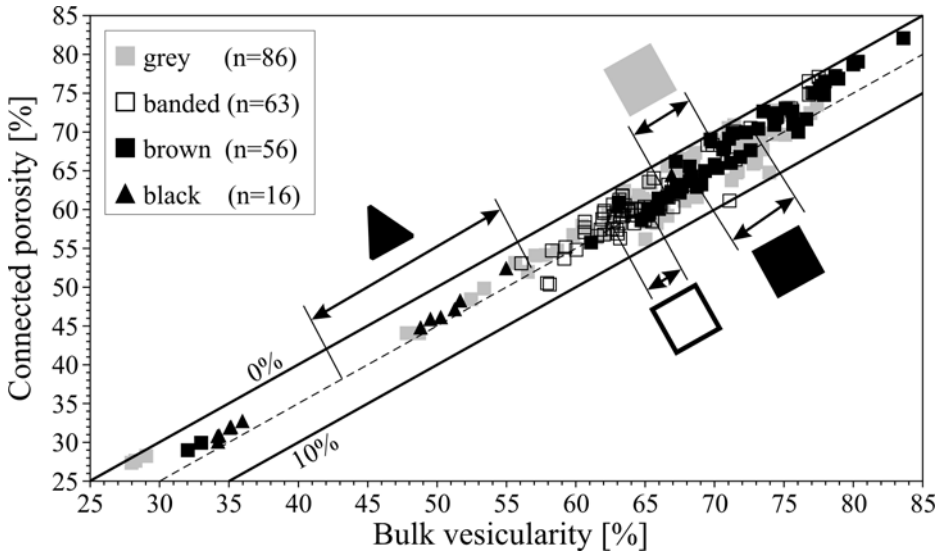


Figure 6-10: Connected porosity vs. bulk vesicularity of all pumice types. Brackets represent 95% confidence limit for the mean of each pumice population. Solid lines represent 0% and 10% and dashed line 5% isolated pore volume.

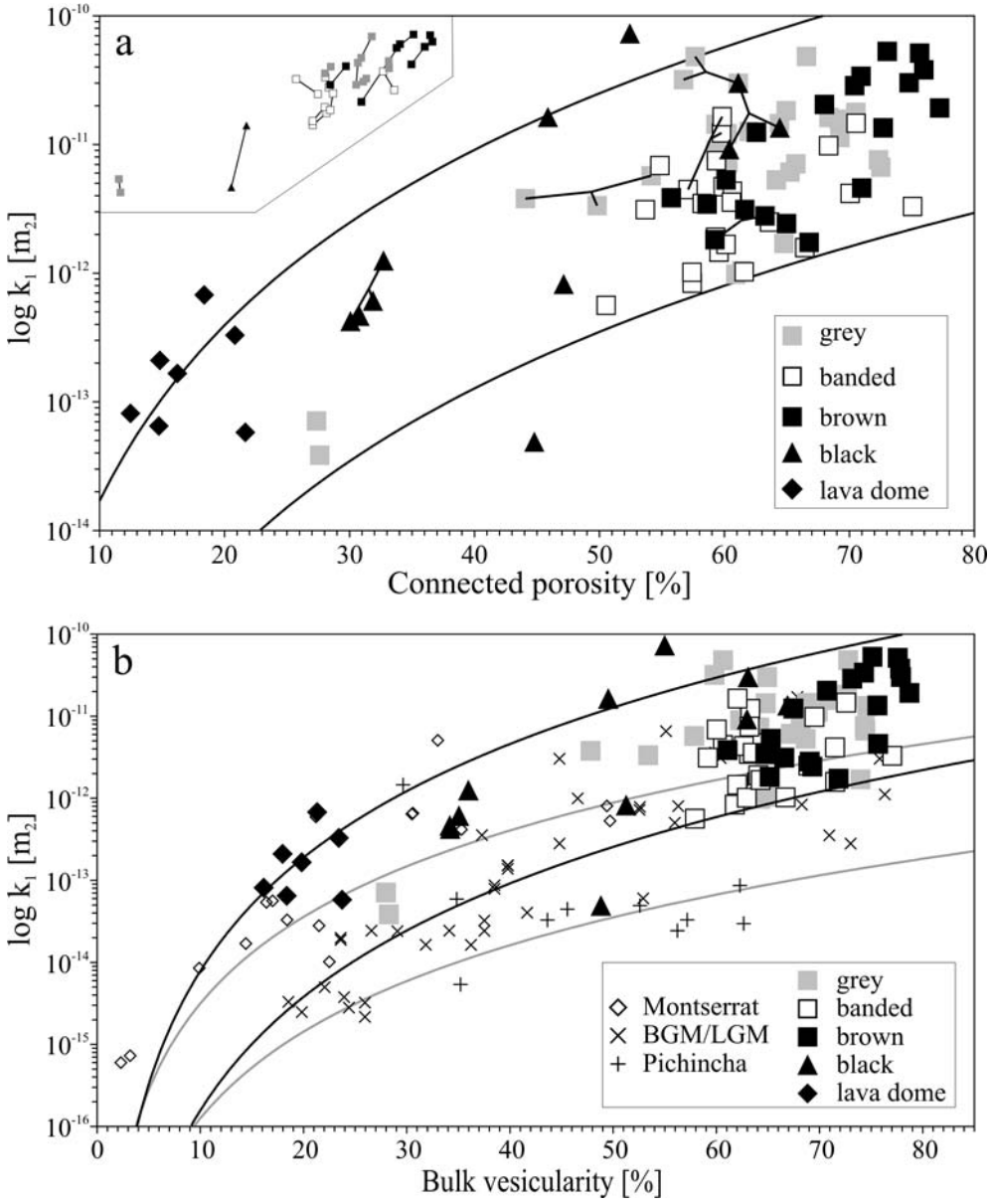


Figure 6-11: Connected and bulk vesicularity vs. permeability. a) data of this study with upper and lower data limits (black lines) of $y=5\times10^{-19}\ x^{-4.5314}$ and $y=6\times10^{-21}\ x^{-4.5314}$, respectively. Note there are six specimens with three cores cut in three mutually perpendicular directions. Upper inset shows cores cut in two perpendicular directions. b) comparison of our data with published literature: Montserrat (Melnik and Sparks, 2002), Big and Little Glass Mountains (Rust and Cashman, 2004), Pichincha (Wright et al., 2007); grey lines are limits of Klug and Cashman (1996).

Grey pumice clasts of unit 1 and 3 show similar ranges in connected porosities from 53.1-73.5% and 44.1-72.7%, respectively, with isolated pore volumes, varying between 2.0-8.8% (unit 1) and 2.0-4.6% (unit 3). There is an overall positive correlation of permeability and connected porosity (Fig. 6-11a), despite the fact that permeability ranges over three orders of magnitude. For example, two grey pumice clasts with φ=64.8 and 64.9% differ considerably in permeability (1.0×10^{-11} m^2 and 3.0×10^{-12} m^2). However, data from three mutually perpendicular cores per sample show no positive

correlation of porosity with permeability (Fig. 6-11a). Above φ=59.8%, all four investigated clast types show that the highest permeability occurs in the core samples having an intermediate bulk vesicularity value. Combining these data with the observations on pumice core samples in two mutually perpendicular directions (see inset in Fig. 6-11a), suggest that this is the result of an anisotropic bubble network which is present in all pumice types. In banded pumice clasts this effect is particularly strong, where coarsely vesicular bands were probably able to effectively channel the pre- and syn-eruptive gas flows.

Unusually, the permeability data for Burrell Lapilli pumice are on average one log unit higher than other silicic pumice (Fig. 6-11b). This could be caused by larger aperture sizes of connected bubbles and may be related to lower viscosities in the Burrell magmas (e.g. Saar and Manga, 1999). If lower viscosities cause higher permeability of pumice clasts, then greater post-fragmentation bubble expansion (and coalescence) is highly likely.

6.5 Discussion

The ejecta of this eruption span a range of vesicularity, bulk silica content and colour, with systematic variations in hornblende phenocryst rim morphologies, microlite contents and glass compositions. These variations are related to the order of eruption in the following way:

1. Grey lithic clasts, which probably represent the earliest-extruded magma of the AD1655 episode, are incorporated in ejecta from all phases of the eruption. These are hypo-crystalline rocks of low vesicularity and low permeability (the latter mostly represents cooling-induced micro-cracks). They have bulk rock silica contents that are 0.4 to 4 wt.% higher than co-erupted pumice clasts, contain hornblende and biotite phenocrysts with strongly altered/resorbed rims and a groundmass dominated by plagioclase and clinopyroxene.

2. Pale grey pumice with porosities of between 53-74% and the highest isolated pore volumes (up to 8.8%) represent the earliest explosive phase of the episode. This pumice contains a number of elongated large, single and coalesced vesicles within an overall broad pore-size distribution.

3. Brown pumice, displaying the highest porosities (up to 84%) was next erupted. The large single vesicles are absent from these pumices, which, compared with the early pale-grey pumice, show a more restricted pore size-distribution, a more strongly deformed network, thicker walls between bubbles, and a higher microlite content. These differences are also observed between the different coloured zones within banded clasts. Both brown and the initial pale-grey pumice have identical ranges in glass composition, between 64-68 wt.% SiO_2.

4. Black clasts, erupted as a minor concomitant component during the middle stages of the explosive phase, are either low- or moderately-vesicular, and are characterised by having isolated pores in a glassy microlite-rich matrix. They have a similar range in glass compositions to the brown and initial pale grey pumice, although extending slightly higher to 69 wt.% SiO_2.

5. Banded pumice clasts predominantly comprise grey and brown pumice networks and show macroscopically complex textures of stretching, banding and folding.

6. The final explosive phase is represented by a pale grey pumice of similar appearance to that firstly erupted. Like the initial pumice, it has a low-moderate porosity range (<73%), but shows lower isolated pore volumes than the earliest pale-grey ejecta. This pumice also has the lowest silica glass (64-66 wt.% SiO_2), with the most restricted composition range, compared to earlier ejecta.

To understand the phases of this eruption, its transitions in eruptive style and the range in physical and chemical properties of the ejecta, a range of magmatic processes within the upper conduit need to be considered. The factors causing different clast types are discussed in chronological order and divided into pre-climactic and syn-climactic processes, which form the basis for reconstructing the eruption dynamics.

6.5.1 Pre-climactic Conditions

6.5.1.1 Grey Lithics

No large-scale magma reservoirs are evident in the upper crust at Taranaki (Sherburn and White, 2005), suggesting that the final magma storage level is at about 10-11 km depth. Magmas ascend through 6 km of Tertiary sediments into the 2.5 km high edifice.

Gravity measurements indicate that multiple dyke intrusions have created a c.5 km-wide dyke/stock complex below Mt. Taranaki (Locke and Cassidy, 1997).

Dyke propagation provides a first-order control of ascent rates of the initial rising magma. Rise rate controls a series of physical and chemical processes, including degree of crystallisation, fractionation, degassing, vesiculation, viscosity and fragmentation that can be seen in the final ejecta. During rise, the typically hydrous Taranaki melts move outside the pressure/temperature and pH_2O stability fields for hornblende and hence varying degrees of disequilibrium and hornblende breakdown occur that may be used to constrain magma rise processes. Decompression experiments (130-4 MPa) on Soufrière Hills andesites showed that hornblende can spend up to 6 days outside its stability field before showing any breakdown reactions (Rutherford and Devine, 2003). The upper pressure boundary for hornblende stability at Taranaki corresponds to c.5.2 km below the summit (using densities of 2400 kgm^{-3} for the edifice and 2700 kgm^{-3} for the dyke/stock complex; Locke and Cassidy, 1997). However, Sato et al. (1999) also showed that groundmass pargasitic hornblende in Unzen dacite is stable up to 70 MPa at c.880 °C, which is equivalent to >3 km depth in a Taranaki conduit. These data imply that hornblende-breakdown reactions in Mt. Taranaki rocks likely occurred in the upper conduit and/or within a dome.

The grey, dense, dome-derived lithics have evolved from the same magma as co-erupted pumice. The difference in SiO_2 content can be modelled by fractionation of hornblende, plagioclase, clinopyroxene, and Fe-Ti oxides (see Fig. 6-8). The major involvement of hornblende in the fractionation process is essential because it is the only major, low-silica mineral phase (average 41.7 wt.% SiO_2) to be able to move the bulk rock silica content by 4 wt.% during ascent.

Although crystallisation and fractionation processes during ascent influences the ability of a magma to flow due to an increase in crystallinity and silica contents in the melt phase (Hammer et al., 1999), another profound impact on magma evolution is the degree of degassing. Gas escape through dyke walls is important (e.g. Tuffen et al., 2003), especially if the dyke intrudes into porous media, although degassing along marginal shear zones is usually dominant (Jaupart and Allegre, 1991; Stasiuk et al., 1996).

Once the fractionated “grey” magma enters shallower levels, magma processes are governed by rheological changes due to increasing gas loss, particularly within the edifice, and subsequent, degassing- and decompression-induced groundmass

crystallisation (Blundy and Cashman, 2001). Nucleation and growth of predominantly plagioclase microlites within the groundmass (Fig. 6-5) considerably increases melt and magma viscosities, thus reducing the ascent rate. As soon as a dome or cryptodome is emplaced on top of a conduit, it has such extremely low gas permeability that it forms an effective cap (Melnik and Sparks, 2002; Mueller et al., 2005). The remnant summit dome at Mt Taranaki (erupted approximately AD1850-60) has permeability that ranges between 6.7×10^{-13} and 5.8×10^{-14} m^2 at φ=16.1-23.7% (Fig. 6-11b). However, these already low values are dominated by cooling-induced micro-cracks (as seen macroscopically) and the permeability at the time of emplacement would have been much lower.

6.5.1.2 Grey Pumice (Unit 1)

Sealing and/or capping the conduit leads towards a closed-degassing system and also a partial stagnation of the magma in the upper conduit. Slow rates of vesicle nucleation and growth may still occur in the upper conduit (Fig. 6-12a, b, to level 1) over extended periods. This slowly forces the viscous overlying magma upwards, and drives dome growth (Fig. 6-12b). At the same time, crystallisation continues, especially the growth of microlites. Should magma in the slowly vesiculating level 1 domain be explosively ejected during these slow vesiculation periods, the ejecta (pumice) should display a heterogeneous bubble network, containing a large range in vesicle sizes (cf. Klug et al., 2002).

The upper-conduit processes of water loss/bubble growth and decompression encourages late-stage microlite crystallisation of mostly plagioclase and clinopyroxene. This, in turn, shifts liquid-compositions to higher silica contents (Fig. 6-9), and subsequently increases melt and magma viscosities (Richet et al., 2000; Sparks et al., 2000). This leads to stretching of originally spherical bubbles as they expand, under steadily-applied shear stress. Melt films between bubbles also thin and rupture as vesicles grow (cf. Manga et al., 1998; Klug et al., 2002). Any onset of vesicle coalescence within the upper conduit increases permeability of the magma foam. This eventually leads to an increased storage of additional volatiles supplied from underlying magma and a progressively higher gas pressure below the dome/plug (cf. Cashman et al., 2000).

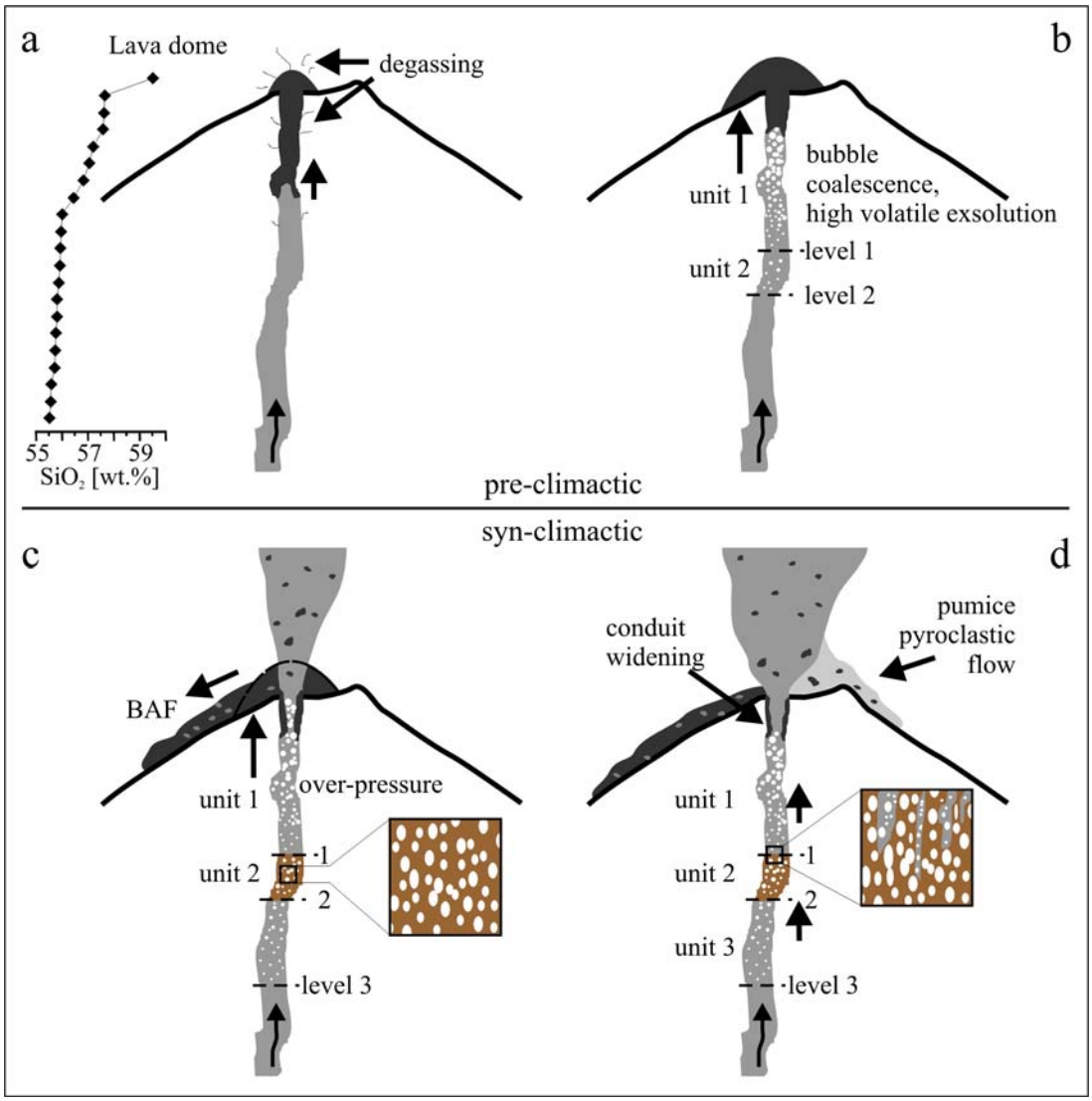


Figure 6-12: Reconstruction of eruptive events during the Burrell Lapilli eruption. Changes in bulk rock silica contents are illustrated in Stage a. Bubble nucleation levels 1-3 correspond with erupted units 1-3. See text for further details.

Once uncapped, magma following from deeper in the conduit, rises rapidly, hence the time for crystallisation is short and the melt viscosity changes little. Under rapid depressurisation, vesiculation also proceeds rapidly, leading to pumice ejecta with narrow ranges in bulk silica content (i.e., 0.5 wt.%; Fig. 6-8), and a relatively homogenous size-distribution of vesicles.

6.5.1.3 Brown Pumice (Unit 2)

As slow dome growth continues or stagnates and the overlying pressure slowly but steadily reduces, the nucleation level propagates downwards. Here, slower gas-exsolution and hence slower bubble-nucleation and growth rates promote microlite

crystallisation at higher magma temperatures as the degree of undercooling of the melt is less pronounced (Hammer and Rutherford, 2002; D'Oriano et al., 2005). Hence, the gradually formed (brown) magma foam (Fig. 6-12b) is characterised by thicker bubble walls containing more microlites, which concomitantly grew with the bubbles. The bubble-size distribution has generally a smaller, narrower range. In addition, abundant microlites form, causing a broader range in glass composition compared to the (grey) magma foam above. The difference between brown and colourless matrix pumice glasses is likely caused by submicroscopic Fe^{3+}-rich oxide "nanolites" (hematite and/or magnetite), which also increase magnetic susceptibility in brown pumice (Schlinger et al., 1988; Paulick and Franz, 1997). Nucleation and growth of Fe^{3+}-rich oxide "nanolites" predominantly in the brown magma is probably induced by slower volatile exsolution and hence, a higher oxidation state of the magma (Paulick and Franz, 1997). Post-depositional precipitation of Fe-Ti oxides probably led to further glass colouring but it could not have affected the glass composition (see Fig. 6-9).

It is inferred that, despite higher microlite contents, the brown magma foam retained a higher temperature and hence had a lower viscosity than the earlier formed grey magma foam.

6.5.2 Syn-climactic Conditions

6.5.2.1 Black, Banded, and Unit 3 Grey Pumice Clasts

Initiation of the explosive phase caused instant vesiculation and further bubble growth in the grey (unit 1) and brown magma foams (Fig. 6-12c). Further, an immediate pressure drop, as well as magma ascent within the conduit caused rapid downward progression of the bubble nucleation to level 3. Here, the grey pumice of unit 3 was developed. Rapid volatile exsolution caused high degrees of undercooling of the melt, permitting syn-crystallisation of plagioclase ± clinopyroxene, however, rapid ejection and cooling meant that the melt silica content was only driven up to 65.8 wt.%. The unit 3 pumice has slightly higher isolated pore volume, also suggesting a less mature bubble network than unit 1 pumice.

As the three domains of magma rose within the conduit, the slightly different viscosities contributed to further differences in clast textures. For example, the brown magma foam was easily plastically deformed, and bubbles coalesced more rapidly due to shearing of

the ascending magma (Fig. 6-12d). Higher connected porosities and permeabilities compared to the grey magma foams seems to be controlled by larger aperture size rather than greater vesicle size (cf. Saar and Manga, 1999). The occurrence of black pumice clasts predominantly within unit 2 pyroclastic flows and their glass composition being similar to brown pumice (Fig. 6-9) suggests a genetic link. The poorly vesicular texture of black pumice and its low abundance in the pyroclastic flow deposit (c.5% by volume) suggests that it could represent a conduit-margin variant of the brown pumice. They may have been derived under higher temperature conditions developed by friction during shearing of magma along the conduit walls (cf. Rosi et al., 2004). Black clasts show the highest difference in permeability per clast (Fig. 6-11a) with only medium connected porosities of 44.8% and 47.1%, but strongly anisotropic permeable clasts with differences of 1.2 log units. The large difference between semi-vesicular and vesicular pumice clasts (φ=36.0-47.8%; Fig. 6-10) could be due to their genetic position in respect to the conduit margins, with an abrupt transition between a dense marginal facies and a porous interior facies.

In addition, due to variable ascent velocities across and along the conduit, the lower-viscosity brown magma could partly intrude and mingle into the upper grey magma (unit 1) to produce flow banding (Fig. 6-12d). The same process occurred at the base of the brown magma. The banded pumices also clearly show an anisotropic bubble network (Fig. 6-11a). Contrary to a horizontal textural zonation of a conduit, where banded pumice forms in the outer margins and coarsely vesicular pumice occupies the core (as proposed by Polacci et al., 2001, Rosi et al., 2004, and D'Oriano et al., 2005), banded pumices of the Burrell Lapilli eruption are thought to be the result of vertical gradients within the conduit. Although D'Oriano et al. (2005) also argue for a vertical zonation of a conduit, they apply it only to the degassed and variably crystalline plug of the upper conduit.

6.5.3 Eruption Dynamics

Evolution of magmas in the dome and the upper conduit were governed by decompression-induced microlite crystallisation and growth in the melt fraction. This caused a large pressure gradient, due to excess fluid pressure in the melt as well as large viscosity differences by increasing crystallinity and melt silica content, and decreasing

dissolved water contents (Sparks, 1997). Over-pressurisation from below the dome was probably an additional contributing factor for dome rupture and collapse (Fig. 6-12a). The dome collapse generated a large BAF, which due to the pre-existing crater morphology, was directed down the NW flank and travelled up to 13.5 km. The presence of primary grey pumice clasts within the BAF deposit further suggests over-pressurisation of the dome from below was a major factor. The explosive removal of lava dome material was accompanied by a vertically-directed sub-Plinian eruption of the fragmented grey pumice foam (unit 1) with dome clasts and associated conduit rocks incorporated and transported through the column. The strength of fragmentation was maintained until the fragmentation front reached a change in vesicularity. Variable degrees of vesicularity, viscosity and temperature down and across the stratified conduit were caused by the formation of three distinct magma foams.

The partially vesiculated brown magma foam had the lowest melt viscosity and hence the lowest pressure build-up by vesiculation. This in turn led to lower exit velocities and lower eruption column heights. In static experiment Burgisser and Gardner (2004) showed that bubble coalescence is time-dependent and had already occurred by porosities of c.43%. A sufficiently coalesced bubble network prior to fragmentation may decrease fragmentation rates, and hence could produce the low, unstable eruption columns inferred for the eruption of the brown pumice (unit 2). However, this does not exclude post-fragmentation bubble expansion and bubble deformation during emplacement as a further contributing factor to changes in bubble shapes and therefore permeabilities (e.g. Thomas et al., 1994).

Fluctuations in column height and explosive energy are common during sub-Plinian and Plinian eruptions where the column partially, or completely, collapses to produce pumice pyroclastic flows. This was observed, for example, during the 22nd July 1980 eruptions at Mt. St. Helens where three individual sub-Plinian pulses with column heights to 14 km removed half of the pre-existing dome of 4.7×10^6 m^3 (Christiansen and Peterson, 1981; Moore et al., 1981).

At Mt. Taranaki, no brown pumice is found in preserved fall deposits, which indicates that the brown magma was not fragmented and ejected as efficiently as the grey magma foam above and below it. The sudden drop in exit velocity associated with the eruption of brown magma foam caused instabilities within the eruption column, implying a lower energy, “boiling-over” type eruption (cf. Taylor, 1958). Hence, grey pumice pyroclastic flows were generated before and after the brown unit (Fig. 6-12d). The minimum

estimate of erupted brown magma is approximately 6.9×10^4 m^3 (DRE) corresponding to a cylindrical conduit length of c.880 m (r=5 m), a sufficient segment within the conduit to affect magma ascent and fragmentation rates. Another potential means to alter exit velocity, fragmentation rate and hence column height is to widen the vent, but this can only be achieved at the very top of the vent and, it would also have affected the fragmentation of the grey, unit 3 magma. The boiling-over type of eruption at Mt. Taranaki is also consistent with higher emplacement temperatures of brown pyroclastic flows (unit 2) compared to units 1 and 3.

Isopach and isopleth mapping suggests that the eruption column was initially directed towards the SE, and then the dispersal axis progressively rotated northeastwards. Lithic isopleths and a normal followed by inverse grading of lithic clasts in the fall deposit may also suggest that the eruption occurred in two sub-Plinian pulses, or, perhaps more likely, was interrupted by a transient waning in the magma ascent rate. Pulsatory, sub-Plinian eruptive periods have been observed for example at the June/July eruptions at Mt. St. Helens (Christiansen and Peterson, 1981; SEAN 05:06; 05:07) at the 1991 pre-climactic eruptions at Mt. Pinatubo, Philippines (Hoblitt et al., 1996) and at El Chichon, Mexico (SEAN 07:03).

The total eruption column height at its highest energy phases was probably up to 14 km above the crater (based on application of the isopach and isopleth data to models from Carey and Sparks, 1986) and transported fine ash more than 250 km east and northeastwards over the North Island (Eden and Frogatt, 1996).

6.6 Conclusions

It has been demonstrated through this AD1655 Burrell eruption case-study that simple changes in magmatic conditions of a single hydrous andesitic magma during ascent can explain sudden changes in eruptive explosivity and hazard potential. Our model of a stratified conduit with varying magma composition, vesicularity and viscosity can explain all observed pumice variations.

Transitions from effusive to explosive phases within these types of andesitic eruption appear to be mainly governed by internal/magmatic factors, including 1) dyke propagation and sealing, 2) degree of fractionation of magma, and 3) magma ascent rate and magma volume. The faster the magma ascends and the faster the dyke is sealed to

reduce gas loss, the more effectively a magma foam is developed that can fragment explosively.

Textural and colour variations of pumice clasts have been recognised at other volcanoes (Donoghue et al., 1995; Bourdier et al., 1997; Gardner et al., 1998; Clynne, 1999; Polacci et al., 2001; Rosi et al., 2004 and D'Oriano et al., 2005). Where these clast variations occur within individual stages of eruptive sequences (e.g. within layered fall deposits), they could also be explained by a similar model to that described here.

6.7 References

Alloway, B., Neall, V.E. and **Vucetich, C.G.** 1995. Late Quaternary (post 28,000 year B.P.) tephrostratigraphy of northeast and central Taranaki, New Zealand. *Journal of the Royal Society of New Zealand* 25, 385-458.

Anderson, A.T. 1979. Water in some hypersthenic magmas. *Journal of Geology* 87, 509-531.

Blundy, J. and **Cashman, K.** 2001. Ascent-driven crystallisation of dacite magmas at Mount St Helens, 1980-1986. *Contributions to Mineralogy and Petrology* 140, 631-650.

Blundy, J., Cashman, K. and **Humphreys, M.** 2006. Magma heating by decompression-driven crystallization beneath andesite volcanoes. *Nature* 443, 76-80.

Bourdier, J.L., Pratomo, I., Thouret, J.C., Boudon, G. and **Vincent, P.M.** 1997. Observations, stratigraphy and eruptive processes of the 1990 eruption of Kelut volcano, Indonesia. *Journal of Volcanology and Geothermal Research* 79, 181-203.

Burgisser, A. and **Gardner, J.E.** 2004. Experimental constraints on degassing and permeability in volcanic conduit flow. *Bulletin of Volcanology* 67, 42-56.

Carey, S. and **Sparks, R.S.J.** 1986. Quantitative models of the fallout and dispersal of tephra from volcanic eruption columns. *Bulletin of Volcanology* 48, 109-125.

Cashman, K.V. and **McConnell, S.M.** 2005. Multiple levels of magma storage during the 1980 summer eruptions of Mount St. Helens, WA. *Bulletin of Volcanology* 68, 57-75.

Cashman, K.V., Sturtevant, B., Papale, P. and **Navon, O.** 2000. Magmatic fragmentation. In: **Sigurdsson, H., Houghton, B., McNutt, S.R., Rhymer, H.** and **Stix, J.** (eds.) Encyclopedia of Volcanoes. Academic Press. San Diego. pp. 419-430.

Christiansen, R.L. and **Peterson, D.W.** 1981. Chronology of the 1980 eruptive activity. In: **Lipman, P.W.** and **Mullineaux, D.R.** (eds.) The 1980 eruptions of Mount St. Helens, Washington. *U.S. Geological Survey Professional Paper* 1250, 17-30.

Clynne, M.A. 1999. A complex magma mixing origin for rocks erupted in 1915, Lassen Peak, California. *Journal of Petrology* 40, 105-132.

Cole, J.W. and **Stephenson, T.M.** 1972. Calculation of the volume of a tephra deposit. Appendix. In: **Cole, J.W.** Distribution of high-alumina basalts in the Taupo Volcanic Zone. *Geology Department Victoria University of Wellington Publication* 1, 13-15.

DeGroat-Nelson, P.J., Cameron, B.I., Fink, J.H. and **Holloway, J.R.** 2001. Hydrogen isotope analysis of rehydrated silicic lavas: implications for eruption mechanisms. *Earth and Planetary Science Letters* 185, 331-341.

Donoghue, S.L., Gamble, G.A., Palmer, A.S. and **Stewart, R.B.** 1995. Magma mingling in an andesite pyroclastic flow of the Pourahu Member, Ruapehu volcano, New Zealand. *Journal of Volcanology and Geothermal Research* 68, 177-191.

D'Oriano, C., Poggianti, E., Bertagnini, A., Cioni, R., Landi, P., Polacci, M. and **Rosi, M.** 2005. Changes in eruptive style during the A.D. 1538 Monte Nuovo eruption (Phlegrean Fields, Italy): the role of syn-eruptive crystallization. *Bulletin of Volcanology* 67, 601-621.

Druce, A.P. 1966. Tree-ring dating of recent volcanic ash and lapilli, Mt Egmont. *New Zealand Journal of Botany* 4, 3-41.

Eden, D.N. and **Froggatt, P.C.** 1996. A 6500-year-old history of tephra deposition recorded in the sediments of Lake Tutira, eastern North Island, New Zealand. *Quaternary International* 34/36, 55-64.

Elsworth, D. and **Voight, B.** 2001. The mechanics of harmonic gas pressurization and failure of lava domes. *Geophysical Journal International* 145, 187-198.

Friedman, I. and **Long, W.** 1976. Hydration rate of obsidian. *Science* 191, 347-352.

Gardner, C.A., Cashman, K.V. and **Neal, C.A.** 1998. Tephra-fall deposits from the 1992 eruption of Crater Peak, Alaska: implications of clast textures for eruptive processes. *Bulletin of Volcanology* 59, 537-555.

Grove, T.L., Elkins-Tanton, L.T., Parman, S.W., Chatterjee, N., Müntener, O. and **Gaetani, G.A.** 2003. Fractional crystallisation and mantle-melting controls on calc-alkaline differentiation trends. *Contributions to Mineralogy and Petrology* 145, 515-533.

Hammer, J.E. and **Rutherford, M.** 2002. An experimental study of the kinetics of decompression-induced crystallization in silicic melt. *Journal of Geophysical Research - Solid Earth* 107, 1-24.

Hammer, J.E., Cashman, K.V., Hoblitt, R.P. and **Newman, S.** 1999. Degassing and microlite crystallization during pre-climactic events of the 1991 eruption of Mt. Pinatubo, Philippines. *Bulletin of Volcanology* 60, 355-380.

Hammer, J.E., Cashman, K.V. and **Voight, B.** 2000. Magmatic processes revealed by textural and compositional trends in Merapi dome lavas. *Journal of Volcanology and Geothermal Research* 100, 165-192.

Hoblitt, R.P., Wolfe, E.W., Scott, W.E., Couchman, M.R., Pallister, J.S. and **Javier, D.** 1996. The preclimactic eruptions of Mount Pinatubo, June 1991. In: **Newhall, C.G.** and **Punongbayan, R.S.** (eds.) Fire and mud: eruptions and lahars of Mount Pinatubo, Philippines. University of Washington Press. Seattle. pp. 457-511.

Jaupart, C. and **Allegre, C.J.** 1991. Gas content, eruption rate and instabilities of eruption regime in silicic volcanoes. *Earth and Planetary Science Letters* 102, 413-429.

Klug, C. and **Cashman, K.V.** 1994. Vesiculation of May 18, 1980, Mount St. Helens magma. *Geology* 22, 468-472.

Klug, C. and **Cashman, K.V.** 1996. Permeability development in vesiculating magmas: implications for fragmentation. *Bulletin of Volcanology* 58, 87-100.

Klug, C., Cashman, K.V. and **Bacon, C.R.** 2002. Structure and physical characteristics of pumice from the climactic eruption of Mount Mazama (Crater Lake), Oregon. *Bulletin of Volcanology* 64, 486-501.

Laursen, T. and **Lanford, W.A.** 1978. Hydration of obsidian. *Nature* 276, 153-156.

Locke, C.A. and **Cassidy, J.** 1997. Egmont Volcano, New Zealand: three-dimensional structure and its implications for evolution. *Journal of Volcanology and Geothermal Research* 76, 149-161.

Manga, M., Castro, J., Cashman, K.V. and **Loewenberg, M.** 1998. Rheology of bubble-bearing magmas. *Journal of Volcanology and Geothermal Research* 87, 15-28.

Massol, H., Jaupart, C. and **Pepper, D.W.** 2001. Ascent and decompression of viscous vesicular magma in a volcanic conduit. *Journal of Geophysical Research-Solid Earth* 106, 16223-16240.

Matthews, A.J., Barclay, J., Carn, S., Thompson, G., Alexander, J., Herd, R. and **Williams, C.** 2002. Rainfall-induced volcanic activity on Montserrat. *Geophysical Research Letters* 29, 1644.

McMillan, P., Peraudeau, G., Holloway, J. and **Coutures, J.P.** 1986. Water solubility in a calcium aluminosilicate melt. *Contributions to Mineralogy and Petrology* 94, 178-182.

Melnik, O. and **Sparks, R.S.J.** 2002. Dynamics of magma ascent and lava extrusion at Soufrière Hills Volcano, Montserrat. In: **Druitt, T.H.** and **Kokelaar, B.P.** (eds.) The eruption of Soufrière Hills Volcano, Montserrat, from 1995 to 1999. *Geological Society, London, Memoirs* 21, 153-171.

Moore, J.G., Lipman, P.W., Swanson, D.A. and **Alpha, T.R.** 1981. Growth of lava domes in the crater, June 1980-January 1981. In: **Lipman, P.W.** and **Mullineaux, D.R.** (eds.) The 1980 eruptions of Mount St. Helens, Washington. *U.S. Geological Survey Professional Paper* 1250, 541-548.

Mueller, S., Melnik, O., Spieler, O., Scheu, B. and **Dingwell, D.B.** 2005. Permeability and degassing of dome lavas undergoing rapid decompression: an experimental determination. *Bulletin of Volcanology* 67, 526-538.

Neall, V.E., Stewart, R.B. and **Smith, I.E.M.** 1986. History and petrology of the Taranaki volcanoes. In: **Smith, I.E.M.** (ed.) Late Cenozoic volcanism. *Royal Society of New Zealand Bulletin* 23, 251-263.

Newhall, C.G. and **Self, S.** 1982. The Volcanic Explosivity Index (VEI) – an estimate of explosive magnitude for historical volcanism. *Journal of Geophysical Research-Solid Earth* 87, 1231-1238.

Paulick, H. and **Franz, G.** 1997. The color of pumice: case study on a trachytic fall deposit, Meidob volcanic field, Sudan. *Bulletin of Volcanology* 59, 171-185.

Platz, T. 2001. Mapping and characterisation of the volcaniclastic Maero formation deposits on the northwestern sector of Egmont volcano (Mt. Taranaki), New Zealand. Unpublished Diploma mapping thesis. Ernst-Moritz-Arndt Universität, Greifswald, Bundesrepublik Deutschland.

Polacci, M., Papale, P. and **Rosi, M.** 2001. Textural heterogeneities in pumices from the climactic eruption of Mount Pinatubo, 15 June 1991, and implications for magma ascent dynamics. *Bulletin of Volcanology* 63, 83-97.

Polacci, M., Rosi, M., Landi, P., Di Muro, A. and **Papale, P.** 2005. Novel interpretation for shift between eruptive styles in some volcanoes. *Eos, Transactions, American Geophysical Union* 86, 333-336.

Pyle, D.M. 1989. The thickness, volume and grainsize of tephra fall deposits. *Bulletin of Volcanology* 51, 1-15.

Richet, P., Whittington, A., Holtz, F., Behrens, H., Ohlhorst, S. and **Wilke, M.** 2000. Water and the density of silicate glasses. *Contributions to Mineralogy and Petrology* 138, 337-347.

Rosi, M., Landi, P., Polacci, M., Di Muro, A. and **Zandomeneghi, D.** 2004. Role of conduit shear on ascent of the crystal-rich magma feeding the 800-year-B.P. Plinian eruption of Quilotoa Volcano (Ecuador). *Bulletin of Volcanology* 66, 307-321.

Rust, A.C. and **Cashman, K.V.** 2004. Permeability of vesicular silicic magma: inertial and hysteresis effects. *Earth and Planetary Science Letters* 228, 93-107.

Rust, A.C., Manga, M. and **Cashman, K.V.** 2003. Determining flow type, shear rate and shear stress in magmas from bubble shapes and orientations. *Journal of Volcanology and Geothermal Research* 122, 111-132.

Rutherford, M.J. and **Devine, J.D.** 2003. Magmatic conditions and magma ascent as indicated by hornblende phase equilibria and reactions in the 1995-2002 Soufrière Hills magma. *Journal of Petrology* 44, 1433-1453.

Saar, M.O. and **Manga, M.** 1999. Permeability-porosity relationship in vesicular basalts. *Geophysical Research Letters* 26, 111-114.

Sato, H., Nakada, S., Fujii, T., Nakamura, M. and **Suzuki-Kamata, K.** 1999. Groundmass pargasite in the 1991-1995 dacite of Unzen volcano: phase stability experiments and volcanological implications. *Journal of Volcanology and Geothermal Research* 89, 197-212.

Schlinger, C.M., Rosenbaum, J.G. and **Veblen, D.R.** 1988. Fe-oxide microcrystals in welded tuff from southern Nevada; origin of remanence carriers by precipitation in volcanic glass. *Geology* 16, 556-559.

SEAN 05:06. Smithsonian Institution, 1980. Mount St. Helens. *Scientific Event Alert Network* vol. 5, no. 6.

SEAN 05:07. Smithsonian Institution, 1980. Mount St. Helens. *Scientific Event Alert Network* vol. 5, no. 7.

SEAN 07:03. Smithsonian Institution, 1982. El Chichon. Scientific *Event Alert Network* vol. 7, no. 3.

Sherburn, S. and **White, R.S.** 2005. Crustal seismicity in Taranaki, New Zealand using accurate hypocentres from a dense network. *Geophysical Journal International* 162, 494-506.

Sparks, R.S.J. 1997. Causes and consequences of pressurisation in lava dome eruptions. *Earth and Planetary Science Letters* 150, 177-189.

Sparks, R.S.J., Murphy, M.D., Lejeune, A.M., Watts, R.B., Barclay, J. and **Young, S.R.** 2000. Control on the emplacement of the andesite lava dome of the Soufriere Hills volcano, Montserrat by degassing-induced crystallization. *Terra Nova* 12, 14-20.

Stasiuk, M.V., Barclay, J., Carroll, M.R., Jaupart, C., Ratté, J.C., Sparks, R.S.J. and **Tait, S.R.** 1996. Degassing during magma ascent in the Mule Creek vent (USA). *Bulletin of Volcanology* 58, 117-130.

Steen-McIntyre, V. 1975. Hydration and superhydration of tephra glass: a potential tool for estimating age of Holocene and Pleistocene ash beds. In: **Suggate, R.P.** and **Cresswell, M.M.** (eds.) Quaternary Studies. *Royal Society of New Zealand Bulletin* 13, 271-278.

Stevenson, R.J., Dingwell, D.B., Webb, S.L. and **Sharp, T.G.** 1996. Viscosity of microlite-bearing rhyolitic obsidians: an experimental study. *Bulletin of Volcanology* 58, 298-309.

Stewart, R.B., Price, R.C. and **Smith, I.E.M.** 1996. Evolution of high-K arc magma, Egmont volcano, Taranaki, New Zealand: evidence from mineral chemistry. *Journal of Volcanology and Geothermal Research* 74, 275-295.

Taylor, G.A.M. 1958. The 1951 eruption of Mount Lamington, Papua. *Australian Bureau of Mineral Resources, Geology and Geophysics Bulletin* 38.

Thomas, N., Jaupart, C. and **Vergniolle, S.** 1994. On the vesicularity of pumice. *Journal of Geophysical Research-Solid Earth* 99, 15633-15644.

Topping, W.W. 1972. Burrell Lapilli eruptives, Mount Egmont, New Zealand. *New Zealand Journal of Geology and Geophysics* 15, 476-490.

Tuffen, H., Dingwell, D.B. and **Pinkerton, H.** 2003. Repeated fracture and healing of silicic magma generate flow banding and earthquakes? *Geology* 31, 1089-1092.

Wellman, H.W. 1962. Holocene of the North Island of New Zealand: a coastal reconnaissance. *Transactions of the Royal Society of New Zealand Geology* 1, 29-99.

Wright, H.M.N., Cashman, K.V., Rosi, M. and **Cioni, R.** 2007. Breadcrust bombs as indicators of Vulcanian eruption dynamics at Guagua Pichincha volcano, Ecuador. *Bulletin of Volcanology* 69, 281-300.

6.8 Appendix

6.8.1 Appendix A: Correlation of Burrell Deposits, NW Sector

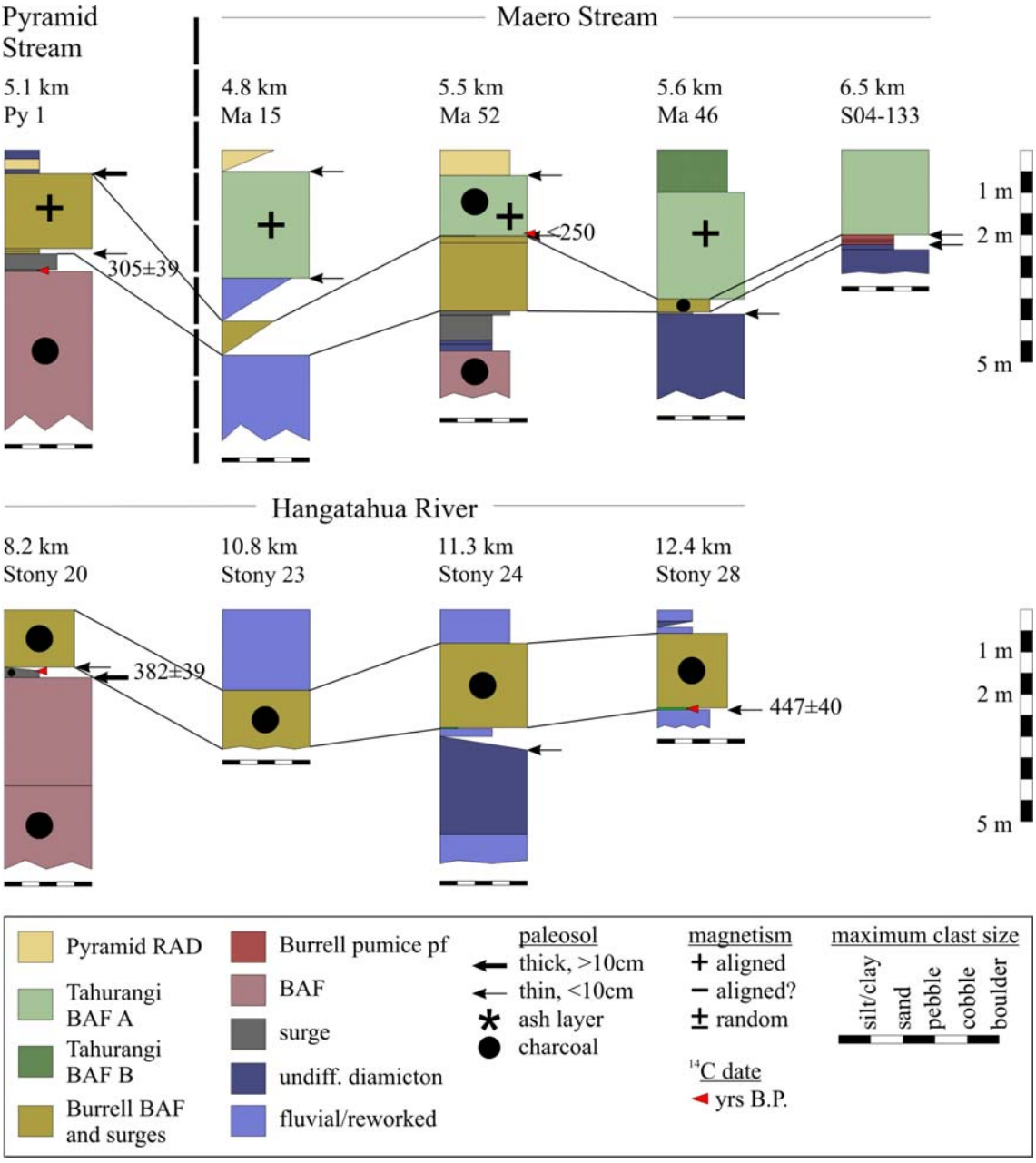


Figure 6-13: Correlation of pyroclastic flow deposits associated with the Burrell episode. Note that the major unit from medial to distal represents the Burrell Breccia (A). In section S04-133, the thin pyroclastic pumice flow deposits represent Burrell Breccia (B) units 1-3. Exposures are sorted by stream and planimetric distance from source. See figure legend for further details (RAD – rock-avalanche deposit). Magnetism was measured by a portable fluxgate magnetometer. For clarity, older exposed units were omitted. Outcrop numbers and profiles refer to Platz (2001) except S04-133. For list of samples and coordinates of outcrops see Appendix B.

6.8.2 Appendix B: Location of Pyroclastic Flow Deposits

Table 6-5. Location of pyroclastic flow deposits on the NW and S sector of Mt. Taranaki.

Section	North	East	Height	Type of deposit[1] and unit		Samples	Location
Py1[2]	6214537	2597581	700	BAF		T04/167	Pyramid Stream
Ma15[2]	6213466	2597286	780	BAF			Maero Stream
Ma52[2]	6214019	2596823	680	BAF		DS16	Maero Stream
Ma46[2]	6214056	2596746	680	BAF			Maero Stream
Stony20[2]	6215287	2594429	480	BAF		NZ1	Hangatahua River
Stony23[2]	6216610	2592195	360	BAF			Hangatahua River
Stony24[2]	6216669	2591647	330	BAF			Hangatahua River
Stony28[2]	6217310	2590762	290	BAF		P10	Hangatahua River
S04-133	6214739	2596099	649	PPF	1-3	T04/175-176	Maero Stream
S03-7	2601927	6210701	2050	PPF	1 or 3	SD8	upslope of Rangitoto Flat
S03-8	2601906	6210746	2065	PPF	1-2	SD9A-H, K	upslope of Rangitoto Flat
S03-25	2601895	6210810	2119	PPF	1-3	SD20-35	upslope of Rangitoto Flat
S03-26	2601452	6210567	1966	PPF	1 or 3	SD36-39	between R. Flat and B. Ridge
S03-27	2601453	6210621	1947	PPF	2		between R. Flat and B. Ridge
S03-28	2601500	6210688	1990	PPF	1 or 3		between R. Flat and B. Ridge
S04-1	2601168	6209620	1448	PPF	1 or 3	T04/1-4	between F. Peak and B. Ridge
S04-2	2601138	6209654	1445	PPF	1 or 3		between F. Peak and B. Ridge
S04-3	2600901	6209788	1445	PPF	1 or 3	T04/5	between F. Peak and B. Ridge
S04-4	2600656	6209739	1376	PPF	1 or 3	T04/6-9	Mangahume Gorge
S04-8	2601289	6210198	1750	PPF	1 or 3		between F. Peak and B. Ridge
S04-9	2601298	6210283	1785	PPF	1 or 3	T04/10-11	between F. Peak and B. Ridge
S04-10	2601234	6210344	1806	PPF	1 or 3	T04/12, 14-18	between F. Peak and B. Ridge
S04-11	2601480	6211325	2310	PPF	1-2	T04/19-24	Bobs Ridge
S04-12	2601461	6211288	2294	PPF	1-2	T04/25-28	Bobs Ridge
S04-18	2601264	6211056	2081	PPF	1-2	T04/45-51	between R. Flat and B. Ridge
S04-81	2601607	6210926	2150	PPF	2-3	T04/64-71	between R. Flat and B. Ridge
S04-82	2601455	6209055	1403	PPF	1 or 3	T04/75	between F. Peak and B. Ridge
S04-87	2601335	6209334	1409	PPF	1 or 3	T04/87	on Bell Falls track near F. Peak
S04-88	2600976	6209456	1321	PPF	1 or 3	T04/95	between F. Peak and B. Ridge
S04-89	2601079	6209350	1267	PPF	1 or 3	T04/96-97	between F. Peak and B. Ridge
S04-93	2600920	6209719	1440	PPF	1 or 3	T04/105-106	between F. Peak and B. Ridge

[1] BAF-Block-and-Ash Flow; PPF-pyroclastic pumice flow.
[2] section described by Platz (2001).
R. Flat = Rangitoto Flat between Fanthams Peak and the summit.
B. Ridge = Bobs Ridge.
F. Peak = Fanthams Peak.

6.8.3 Appendix C: Volatile Contents in Glass – Preliminary Results and Conclusions

6.8.3.1 FTIR Spectroscopy

The total H_2O concentrations (measured from the 3550 cm^{-1} peak; see Chapter 2) of glass inclusions hosted in clinopyroxene crystals vary considerably from 0.74 to 6.16 wt.% with one outlier at 9.15 wt.%, and appear to correlate linearly with molecular H_2O at 1630 cm^{-1} on a positive slope (Fig. 6-14a). It is noted that one matrix glass was analysed with 0.28 wt.% H_2O. Molecular CO_2 peaks were only present in some samples and calculated concentrations range between 19 and 82 ppm. If total H_2O and CO_2 concentrations are plotted, the data appear to correlate linearly although on a negative slope, i.e. smaller H_2O concentrations seem to contain more CO_2. Two data points off the linear trend are noted (Fig. 6-14b).

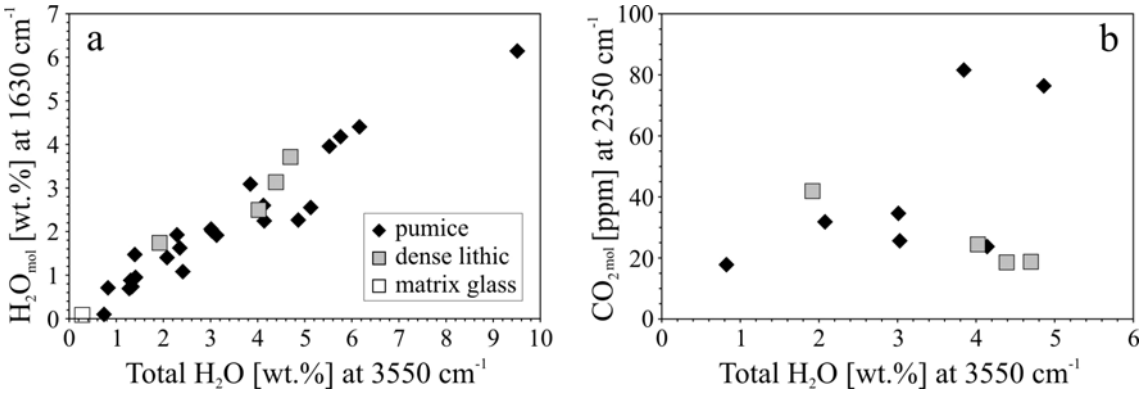


Figure 6-14: Estimates of total water and carbon dioxide contents in melt inclusions. a) total H_2O at 3550 cm^{-1} vs. molecular H_2O at 1630 cm^{-1}, and b) molecular CO_2 at 2350 cm^{-1} vs. total H_2O at 3550 cm^{-1}.

The FTIR data of these melt inclusions must be considered cautiously, particularly with respect to the host mineral and the shape of melt inclusions. Clinopyroxene exhibits good cleavage due to its crystallographic habit. It has been frequently observed that melt inclusions can leak during ascent, especially in crystals with good to very good fissility such as plagioclase and clinopyroxene (Cashman and McConnell, 2005; Blundy et al., 2006). Due to rapidly changing pressure conditions during ascent, melt inclusions can partially re-equilibrate by loosing water which can be possibly detected from the shape of the melt inclusion (Fig. 6-15). Melt inclusions in clinopyroxene normally exhibit irregular outlines and are positioned along cleavage planes, making them mostly unsuitable for analysis (Fig. 6-15). These sheet-like shapes make it difficult to intersect the inclusions from both sides and therefore to measure their thicknesses. The measurement of 9.15 wt.% H_2O in one inclusion appears too high, although

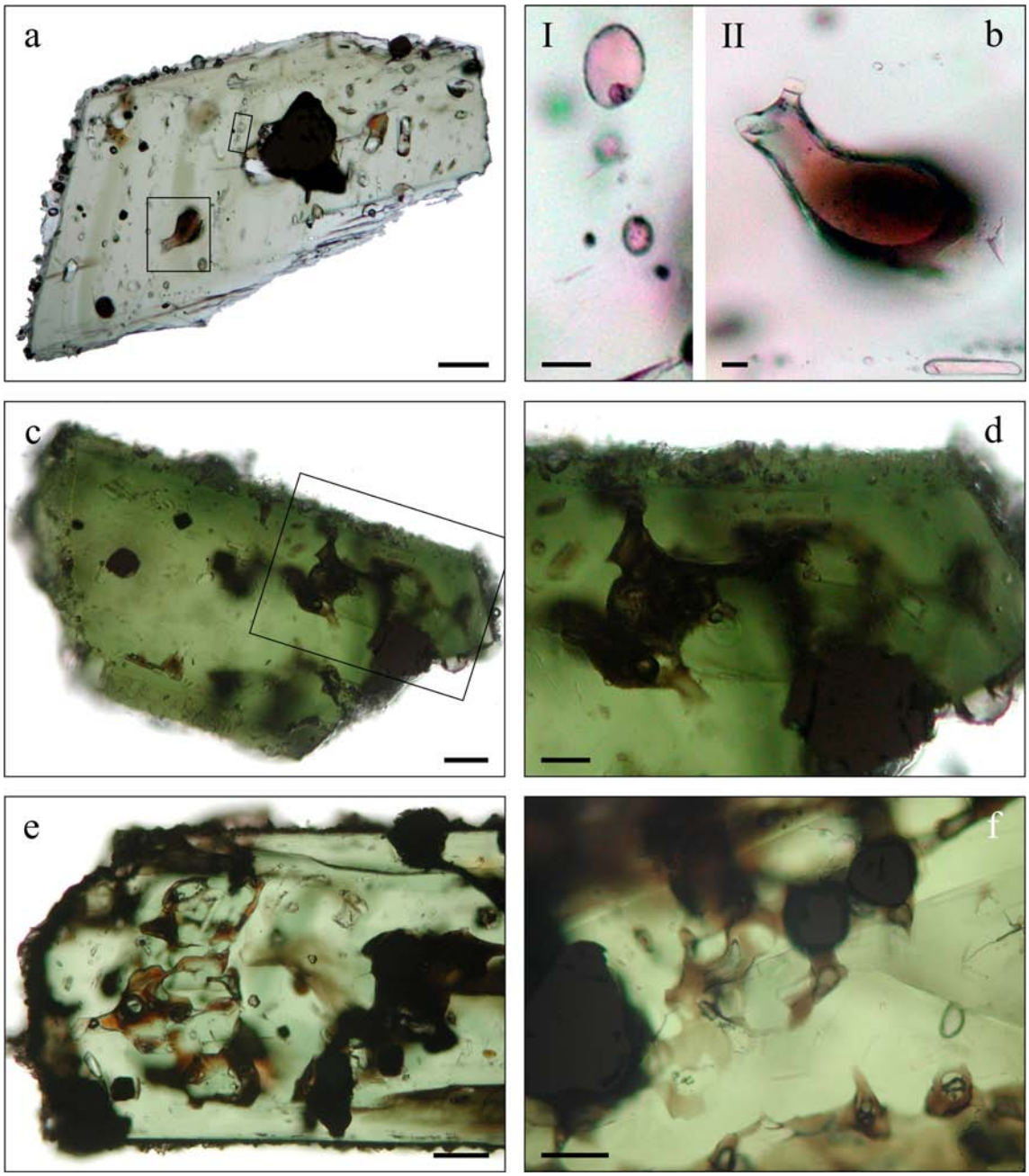


Figure 6-15: Different shapes of melt inclusions in clinopyroxene. a) overview of crystal 2 (sample SD20); note the many inclusions of glass, plagioclase, apatite and Fe-Ti oxide which are mostly oriented along crystallographic planes, b) two close-ups as marked in a); I - represents common but very small melt inclusions found in clinopyroxene, which are unsuitable for FTIR analysis. Their shape is near spherical to ovate; II - the bottle-neck shape is typical for leaked melt inclusions, c) overview of crystal 11 (sample SD32) showing a large irregular shaped melt inclusion, d) close-up of c) showing the impossibility of using these inclusions for FTIR analysis; it can be assumed that the inclusion extends further into the crystals as indicated by the diffuse outline of the melt inclusions further to the right, e) section of crystal 4 (sample SD20) showing two types of melt inclusions, the reddish-brown coloured inclusions are probably altered in comparison to the brown inclusions to the right; note again the irregular outline of the inclusions, f) section of crystal 8 (sample SD9D); abundant sheet-like inclusions probably oriented along crystallographic planes; the inclusions around the Fe-Ti oxide inclusions (black) appear to be connected. Scale bars are 100 µm in a), c), and e), 50 µm in d) and f), and 10 µm in b).

concentrations of 10 wt.% in andesitic melt inclusions have been reported (Anderson, 1979; Grove et al., 2003). In addition, the apparent negative correlation of (very small) CO_2 and H_2O concentrations is contradictory because carbon dioxide is about one order of magnitude less soluble than water relating to melt and volatile composition, and prevailing pressure and temperature conditions, i.e. CO_2 is also released from the melt phase earlier (at greater depth). If the trend is real, it must be assumed that clinopyroxene host crystals tapped melt over a large pressure range, or alternatively, those crystals are derived from different magma batches.

Despite the difficulties experienced in this study, leaky melt inclusions can provide important information about changes of physical properties of the magma during ascent and therefore eruption dynamics (Blundy et al., 2006).

6.8.3.2 Thermal Analysis

The study of water concentrations in natural glasses using FTIR spectroscopy demonstrated that this technique can only be applied to glass inclusions in minerals and quenched volcanic glasses (i.e. obsidian). Unfortunately, it cannot be applied to vesicular pumice rocks due to their thin bubble walls.

Earlier attempts were made to measure water contents by thermogravimetric analysis of quenched synthetic glass (McMillan et al., 1986) and obsidian (DeGroat-Nelson et al., 2001), however, the methods used may have not have been optimised to provide precise results. For example, (1) glass chips with/without inclusions were used, which modifies the glass weight fraction, and/or (2) step-heating occurred either at constant rates or incrementally in 4-5 steps which may lead to erroneous results, since volatile diffusion rates in glass chips are higher than in glass powders. In this study, powderised pure glass samples were used for thermal analysis since it enabled uniform heating across the sample as well as quick volatile diffusion through the glass. An optimal methodology of heating the sample was developed through iteration (Fig. 6-16a).

Preliminary results of this methodology are illustrated in Figure 6-16b. The low temperature experiments are most likely incomplete, because further weight loss is indicated by other runs (Fig. 6-16a). It is noted that some samples give a very good reproducibility while other samples display major differences in weight loss, mainly

caused by the difference in applied maximum temperatures (Fig. 6-16b). Nonetheless, these preliminary results encourage further pursuit of this method.

Hydration of glass is an inter-diffusion process where hydronium ions (H_3O^+) are substituted for mobile alkali ions, mainly Na^+ and K^+ (Laursen and Lanford, 1978). The process already starts once volcanic glass is exposed to the atmosphere and water is adsorpted on its surface. In earlier studies the rate of obsidian hydration was investigated, for example, to indirectly date obsidian artefacts based on the thickness of the hydration rind (Steen-McIntyre, 1975. Friedman and Long, 1976; Laursen and Lanford, 1978). Despite the large surface areas of pumice exposed to hydration compared to obsidian, no such effects (e.g. discolouration) were observed, and this method seems applicable, at least to historically erupted pumice.

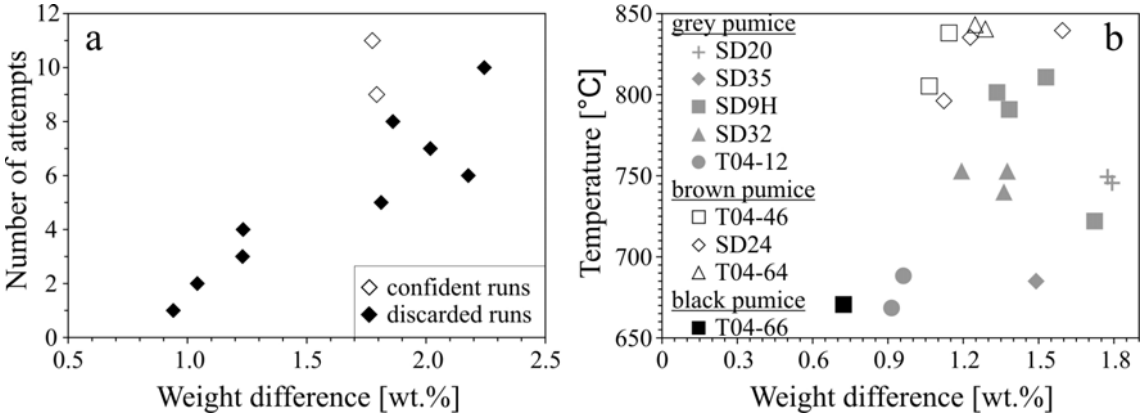


Figure 6-16: Preliminary results of the thermal analysis studies. a) trial and error series of sample SD20, b) reproducibility results of different pumice samples; it is noted that for the same sample the maximum weight loss is often observed at similar temperatures.

One sample (SD35) was used to quantify the weight change and a thermal analysis (to a temperature of 950 °C) coupled with infrared H_2O and CO_2 detectors was carried out (by H.B. Lindgren, Geological Survey of Denmark and Greenland, Copenhagen). The resulting DTA-EWA curve (Differential Thermal Analysis-Evolved Water Analysis) shows two prominent water release peaks at 355 °C and 635 °C, and a weak peak at 460 °C. However, if a larger amount of sample were used, the peaks would have been more intense (H.B. Lindgren, pers. comm., 2006). The analysis showed that only 6.5 ppm H_2O was released. No peaks on the CO_2 curve were observed. The measured 6.5 ppm H_2O of this sample is in gross contrast to the average weight change of 1.47 wt.% obtained by DSC-TGA (Fig. 6-16b). In addition, prominent water release peak at 635 °C only roughly coincides with the maximum weight changes at 657 °C, 685 °C, and 687 °C as observed on the DSC-TGA curves (Fig. 6-16b). This implies that most water bound in volcanic glass may be released at temperatures well below 900 °C. Further

studies need to be pursued to confirm these preliminary results and examine whether loss of other volatile phases (such as F and SO_4) could explain the enormous weight change observed in erupted pumice clasts.

Chapter 7 Reconstruction of Eruption Mechanisms Using Physico-chemical Data

Petrographic and geochemical data can be used for calculation of melt and magma conditions. In this chapter, physico-chemical data are interpreted to reconstruct eruption mechanisms during the Maero Eruptive Period. Between eruption episodes and events significant differences in eruptive style and processes occurred; through this physico-chemical dataset some of the controlling influence on these will be discussed.

7.1 Introduction

Reconstruction of eruption mechanisms is difficult if no observational datasets are available. Understanding the eruptive styles of a dormant volcano, deposits of historic eruptions need to be studied. In most cases, these studies are limited to petrographic and geochemical analyses. The datasets collected for the Maero Eruptive Period comprise petrography, glass and bulk rock chemistry, which are used to derive conclusions about the most important physical property of erupted magma: its melt and magma viscosities. It is then debated what propositions can be derived about each eruptive episode of the Maero Eruptive Period in respect of eruption style and mechanisms.

7.1.1 Viscosity of Magmas

Understanding the viscosity of silicate melts and the knowledge of its governing factors are particularly important for igneous processes including melt and crystal segregation, convection in magma chambers, melt migration in source regions, and magma ascent and fragmentation. Processes occurring in sub-surface regions are particularly important where melt and magma changes in the conduit control the dynamics and style of eruptions (i.e. magma flow dynamics and fragmentation).

Since the seminal works of Bottinga and Weill (1972) and Shaw (1972) numerous studies were carried out on the physical properties of a variety of anhydrous and hydrous silicate melts: rhyolite and granite (Neuville et al., 1993; Dingwell et al., 1996), andesite (Richet et al., 1996; Liebske et al., 2003), basalt (Toplis et al., 1994; Giordano and Dingwell, 2003; Sato, 2005), also including phonolite, trachyte, basanite, peridotite, and carbonatite (Dobson et al., 1996, Whittington et al., 2001; Romano et al., 2003; Dingwell et al., 2004; Giordano et al., 2004a; Liebske et al., 2005; Misiti et al., 2006).

There are three main factors controlling the viscosity of silicate melts: 1) melt structure and chemical composition, 2) temperature, and 3) volatile content. Most silicate melts are composed of tetrahedrally coordinated Si^{4+} and Al^{3+} and minor Fe^{3+} cations strongly bonded to four non-bridging oxygen anions, along with octahedrally coordinated Ca^{2+}, Mg^{2+} and Fe^{2+} cations weakly bonded to six bridging oxygen anions (Best, 2003). Interlinked polymers of mainly $(SiO_4)^{4-}$, $(Al^{3+}O_4)^{5-}$, and subordinate $(Fe^{3+}O_4)^{5-}$ tetrahedra form a three-dimensional melt structure or network. The higher the degree of polymerisation, i.e. the longer the string-like polymers with interspersed octahedra, the higher is the melt viscosity. Thus, the chemical melt components can generally be subdivided into 1) network-forming cations (Si^{4+}, Al^{3+}, Fe^{3+}), 2) bridging oxygens, 3) network-modifying cations (monovalent [Na^{+}, K^{+}] and divalent [Ca^{2+}, Mg^{2+}] cations including more highly charged high-field-strength cations [e.g. Ti^{4+}, P^{5+}] and low abundance trace elements [e.g. Mn^{2+}, Ba^{2+}, Sr^{2+}]; Best, 2003). It is noted that some mono- and divalent cations are needed to balance the charge of trivalent cations in tetrahedral coordination. Ferrous iron occurs exclusively as a network-modifying cation whereas ferric iron is either a network-former or network-modifier (Best, 2003). According to this, the oxidation state of a melt can influence its degree of polymerisation, and hence its viscosity.

The temperature is the second principal factor controlling the degree of polymerisation and thus viscosity. At higher temperatures polymers of silicon and aluminium cations with non-bridging oxygens (i.e. Si=O and Al=O bonds) can be stretched or broken due to the increase of kinetic energy of atoms. Silicate melts at high temperature behave as Newtonian fluids, whereas at low temperatures, their behaviour is strongly non-Newtonian due to polymerisation and crystallisation. Pressure, by contrast, does not have a significant direct impact on melt viscosities, at least not below 2 GPa (Pinkerton and Stevenson, 1992; Baker, 1996).

The effect of volatiles on viscosity of melts is still poorly known. Baker and Vaillancourt (1995), Dingwell et al. (1996), and Hess and Dingwell (1996) showed a strong non-linear increase in viscosity with decreasing water contents, particularly below 1 wt.%. Dissolved water occurs in silicate melts as OH^- ions and molecular water (Stolper, 1982). Hydroxyl ions are able to break polymers in melts, and hence act as network-modifiers. Consequently, the effect of water on viscosity is more drastic in silica-rich melts (i.e. andesites-rhyolites) compared to silica-poor melts (i.e. basalts). Fluorine (F^-) is probably the second most effective volatile in reducing melt viscosities. In contrast to water, fluorine remains in solution even at atmospheric pressure. Lavas of Mt. Nyiragongo (DR Congo), for example, contain large abundances of fluorine and phosphorus (Platz et al., 2004), which may have contributed to their extremely mobile nature reaching speeds of up to 60 kmh^{-1} (SEAN 02:03). Recent studies investigated the effect of volatiles such as fluorine, chlorine, phosphorus, and boron on melt viscosities; fluorine, for example, depolymerises the melt by replacing one oxygen with two fluorines (Toplis and Dingwell, 1996; Giordano et al., 2004b; Zimova and Webb, 2007).

Because the viscosity of hydrous and anhydrous natural melts is sensitive to chemical composition (cf. silica-factor) and temperature, a range in viscosity ($\log_{10}\eta$ in Pas) over 15 orders of magnitude is observed. Melt viscosities ($\log_{10}\eta$) relevant to this study (i.e. andesitic to rhyolitic melts) commonly range between 2-15 Pas for rhyolites in the temperature range of c.600-1200 °C (containing various proportions of H_2O and F) and 1-13 Pas for anhydrous andesites in the temperature range of c.650-1650 °C (Neuville et al., 1993; Baker and Vaillantcourt, 1995). Hydrous andesites have lower viscosities of $\log_{10}\eta$=0.7-13 Pas at temperatures between c.700-1650 °C and H_2O concentrations of 2 and 3.5 wt.% (Richet et al., 1996).

Magmas are even more complex, since they commonly represent three-phase mixtures of melt, crystals and bubbles (i.e. liquid-solid-gas), hence their rheological behaviour is

strongly non-Newtonian. In this case the "viscosity" of two-phase (liquid-solid) or three-phase magmas is termed apparent viscosity, η_a. The dependence of viscosity on crystal-content is important for modelling conduit and dome-growth processes (cf. Melnik and Sparks, 1999, 2002). For estimating apparent viscosities of crystal-bearing magmas relative to their equivalent melt viscosities, the Einstein-Roscoe equation (Einstein, 1906; Roscoe, 1952, Brinkman, 1952) can be used (Marsh, 1981):

$$\eta_a = \eta(1 - BX_\nu)^{-2.5} \qquad \text{[Eq. 7-1]}$$

where η is the melt visocisty (Pas), B=1.35 representative for uniformly sized spherical crystals and X_v is the crystal volume fraction suspended in the melt. Because magmas contain various crystal shapes and sizes, B is larger and approximated to 1.7. There is a non-linear positive relationship between crystal volume and apparent viscosity (Pinkerton and Stevenson, 1992; Lejeune and Richet, 1995) and the maximum crystal content a magma can bear before acting as a 'solid' is 70 vol.% (Lejeune and Richet, 1995).

The viscosity of melts (and magmas) is also influenced by the presence of suspended bubbles. The rheology of bubble-bearing melts varies depending on the bubble volume fraction and the Capillary number. The dimensionless Capillary number, Ca, is defined as the ratio of viscous stresses and surface tension stresses (Manga and Loewenberg, 2001):

$$Ca = \frac{\mu\eta a}{\sigma} \qquad \text{[Eq. 7-2]}$$

where μ, η, a, and σ are shear rate, suspending fluid viscosity (i.e. melt viscosity), bubble radius, and surface tension, respectively. If Ca is low (Ca<0.1), bubbles resist deformation and preserve their near spherical shape; if Ca is high (Ca>0.1), bubbles deform easily and elongate (Manga and Loewenberg, 2001). As a result, an increase in the shear rate will increase the Capillary number, and consequentially the viscosity of the bubble-melt mixture will decrease (Pal, 2003).

7.2 Methods and Approach

To understand differences between individual dome-forming episodes, petrographic and bulk rock chemical studies were carried out. Since eruptive conditions at the onset of dome emplacement are unknown, estimates of melt and magma viscosities are based on glass chemistry of studied tephra and pyroclastic flow samples with estimated constant parameters such as melt water contents, emplacement temperature, and crystal content. Using this approach, individual eruptive episodes can be compared and some conclusions be derived.

7.3 Results

7.3.1 Petrography

7.3.1.1 Pyroclastic Flow Deposits

The mineral assemblage within the studied BAF rocks (Table 7-1) is identical for both phenocrysts and groundmass constituents, including plagioclase, clinopyroxene, hornblende and Fe-Ti oxides. In addition, biotite is a common but minor microphenocryst and groundmass phase. Orthopyroxene (<1%) is a groundmass constituent observed in all samples, however, it is difficult to detect where brown groundmass glass is present. Due to this similarity in mineral assemblage, three petrographic features were used to distinguish individual samples and highlight major textural features within the sample set: 1) hornblende texture, 2) degree of groundmass crystallinity, and 3) groundmass texture. The observations are summarised in Table 7-2.

Hornblende crystals exhibit different degrees of decomposition and samples were subdivided into three categories showing 1a) fresh crystals with no reaction rim; 1b) distinct but relatively thin and continuous rim; and 1c) more advanced reaction with a thick reaction rim or entirely altered crystals (Table 7-2).

The degree of groundmass crystallinity varies between individual samples and is differentiated into five subgroups based on microlite content and glass colour: 2a) nearly holocrystalline groundmass with occasional clear, translucent interstitial glass; 2b) semi- to holocrystalline groundmass with clear, translucent glass; 2c) semicrystalline to hyaline groundmass with clear, translucent glass; 2d) semi- to holocrystalline groundmass with brownish glass; 2e) semicrystalline to hyaline

Table 7-1. Sample list and description of studied pyroclastic flow deposits.

Sample	Section[1]	North	East	Height [m]	Sample location	Deposition Type	Unit	Lithology	Eruptive Episode No.	Eruptive Episode Stratigraphy
T04-168	S04-131 [1]	6214537	2597581	700	Pyramid Stream	rock-avalanche		dense rock	X	Pyramid
T04-158a	S04-128 [15]	6213606	2597173	745	Maero Stream	BAF	A	dense rock	IX	Tahurangi
T04-158b	S04-128 [15]	6213606	2597173	745	Maero Stream	BAF	A	dense rock	IX	Tahurangi
T04-170	S04-132	6214119	2596723	671	Maero Stream	BAF	A	dense rock	IX	Tahurangi
T04-177	S04-133	6214739	2596099	649	Maero Stream	BAF	A	dense rock	IX	Tahurangi
T04-178	S04-133	6214739	2596099	649	Maero Stream	BAF	A	dense rock	IX	Tahurangi
DS6	[52]	6214019	2596823	680	Maero Stream	BAF	A	dense rock	IX	Tahurangi
P7	[52]	6214019	2596823	680	Maero Stream	BAF	A	pumice	IX	Tahurangi
T04-171	S04-132	6214119	2596723	671	Maero Stream	BAF	B	dense rock	IX	Tahurangi
SD9a	S03-8	6210746	2601906	2065	Opua amphitheatre	pumice flow	3	breadcrust bomb	VII	Burrell
SD9b	S03-8	6210746	2601906	2065	Opua amphitheatre	pumice flow	2	black dense rock	VII	Burrell
SD9c	S03-8	6210746	2601906	2065	Opua amphitheatre	pumice flow	1	grey dense rock	VII	Burrell
SD20	S03-25	6210810	2601895	2119	Opua amphitheatre	pumice flow	3	grey pumice	VII	Burrell
SD24	S03-25	6210810	2601895	2119	Opua amphitheatre	pumice flow	2	brown pumice	VII	Burrell
SD27	S03-25	6210810	2601895	2119	Opua amphitheatre	pumice flow	2	black dense rock	VII	Burrell
SD28	S03-25	6210810	2601895	2119	Opua amphitheatre	pumice flow	2	breadcrust bomb	VII	Burrell
SD29	S03-25	6210810	2601895	2119	Opua amphitheatre	pumice flow	2	black vesicular rock	VII	Burrell
SD33	S03-25	6210810	2601895	2119	Opua amphitheatre	pumice flow	1	black dense rock	VII	Burrell
SD34	S03-25	6210810	2601895	2119	Opua amphitheatre	pumice flow	1	grey dense rock	VII	Burrell
SD35	S03-25	6210810	2601895	2119	Opua amphitheatre	pumice flow	1	grey pumice	VII	Burrell
SD39	S03-26	6210567	2601452	1966	Opua amphitheatre	pumice flow	1 or 3	grey dense rock	VII	Burrell
T04-1	S04-1	6209620	2601168	1448	Opua amphitheatre	pumice flow	1 or 3	grey dense rock	VII	Burrell
T04-3	S04-1	6209620	2601168	1448	Opua amphitheatre	pumice flow	1 or 3	black dense rock	VII	Burrell
T04-19	S04-11	6211325	2601480	2310	Opua amphitheatre	pumice flow	2	brown pumice	VII	Burrell
T04-21	S04-11	6211325	2601480	2310	Opua amphitheatre	pumice flow	2	grey dense rock	VII	Burrell
T04-22	S04-11	6211325	2601480	2310	Opua amphitheatre	pumice flow	1	grey pumice	VII	Burrell
T04-24	S04-11	6211325	2601480	2310	Opua amphitheatre	pumice flow	1	breadcrust bomb	VII	Burrell
T04-65	S04-81	6210926	2601607	c.2154	Opua amphitheatre	pumice flow	2	brown pumice	VII	Burrell
T04-96	S04-89	6209350	2601079	1267	Opua amphitheatre	pumice flow	1 or 3	grey pumice	VII	Burrell

[1] Sections marked in brackets refer to section numbers of Platz (2001). S04-128 refers to Section2004-section number 128.

Table 7-1. (continued).

Sample	Section[1]	East	North	Height [m]	Sample location	Deposition Type	Unit	Lithology	Eruptive Episode No.	Eruptive Episode Stratigraphy
P10	[28]	6217310	2590762	290	Sanders Road	BAF		grey pumice	VII	Burrell
T04-167	S04-131 [1]	6214537	2597581	700	Pyramid Stream	BAF		dense rock	VII	Burrell
P1	S04-131 [1]	6214537	2597581	700	Pyramid Stream	BAF		dense rock	VII	Burrell
NZ1	[20]	6215287	2594429	480	Hangatahua River	BAF		dense rock	VII	Burrell
P6	[52]	6214019	2596823	680	Maero Stream	BAF		grey pumice	VII	Burrell
T04-174	S04-133	6214739	2596099	649	Maero Stream	pumice flow		grey pumice	VI	Puniho
T04-160	S04-128 [15]	6213606	2597173	745	Maero Stream	BAF		dense rock	V	Waiweranui
T04-166	S04-131 [1]	6214537	2597581	700	Pyramid Stream	BAF		dense rock	V	Waiweranui
NZ2	[20]	6215287	2594429	480	Hangatahua River	BAF		dense rock	V	Waiweranui
NZ4	[34]	6215148	2592732	390	Waiweranui Stream	BAF		dense rock	V	Waiweranui
DS22	[52]	6214019	2596823	680	Maero Stream	BAF		dense rock	V	Waiweranui
T04-162	S04-131 [1]	6214537	2597581	700	Pyramid Stream	BAF		pumice	IV	Newall
T04-163	S04-131 [1]	6214537	2597581	700	Pyramid Stream	BAF		dense rock	IV	Newall
T05-34	S05-179 [15.1]	6213606	2597182	732	Maero Stream	BAF		semi-vesicular rock	IV	Newall
NZ3	[20]	6215287	2594429	480	Hangatahua River	BAF		dense rock	IV	Newall
PY19	S04-131 [1]	6214537	2597581	700	Pyramid Stream	surge		dense rock	IV	Newall
E02-26	S02-13[2]	6211666	2598262	c.1005	Marupakoko Stream	BAF		dense rock	IV	Newall
T04-152	S04-128	6213606	2597173	745	Maero Stream	BAF		dense rock	II	Te Popo
T04-165	S04-131 [1]	6214537	2597581	700	Pyramid Stream	BAF		dense rock	II	Te Popo
T04-172	S04-133	6214739	2596099	649	Maero Stream	BAF		dense rock	VI or V?	Maero
T04-180	S04-133	6214739	2596099	649	Maero Stream	BAF		semi-vesicular rock	VI or V?	Maero
SR21	[24]	6216669	2591647	330	Hangatahua River	BAF		dense rock	?[3]	Maero
SD12	S03-11	6212075	2601454	c.2250	Turtle	lava flow		dense rock		Maero
T04-202	S04-147	6213014	2600017	1319	on top of Skinner Hill	loose rock from Turtle		dense rock		Maero
DS24a	[52]	6214019	2596823	680	Maero Stream	BAF		dense rock		pre-Maero[4]

[1] Sections marked in brackets refer to section numbers of Platz (2001). S04-128 refers to Section2004-section number 128.
[2] S.J. Cronin, unpubl. data.
[3] AD1000-1655.
[4] >7000 yrs BP.

groundmass with brownish glass. Semi- to holocrystalline glass has abundant microlites, predominantly plagioclase laths, with residual, interstitial glass and glass pockets still present. Semi-crystalline to hyaline glass is used to highlight the abundance of glass in comparison to microlites. No nearly holocrystalline groundmass with remnants of brownish glass was observed (Fig. 7-1).

The third category, groundmass texture, highlights those samples that could represent hybrid rocks, based on the presence of two different groundmass glasses, or may imply other emplacement and growth mechanisms (Fig. 7-1).

Table 7-2. Summary of petrographic studies of BAF samples.

Sample	Eruptive episode	Category 1 Hornblende texture			Category 2 Groundmass crystallinity					Category 3 Groundmass texture
					clear, translucent glass			brown glass		
		fresh	thin rim	thick rim/ replaced	nearly holo-crystalline	semi- to holo-crystalline	semicrystalline to hyaline	semi- to holo-crystalline	semicrystalline to hyaline	two glass populations
T04-152a	II	×				×				
T04-152b	II	×				×				
T04-154	IV	×				×				
T04-155a	IV	×			×					
T04-155b	IV	×			×					
T04-158	IX	×							×	×
T04-165	II	×							×	
T04-166	V	×						×		
T04-168	X	×					×			
T04-171	IX	×							×	×
T04-177	IX	×					×			
T04-193	?	×			×					
P1	VII	×				×				
SR21	?	×							×	
T04-160	V		×					×		
T04-163	IV		×		×					
T04-170	IX		×					×		
T04-172	V or VI		×		×					
DS6	IX		×		×					×
Py19	IV		×		×					
T04-178	IX			×	×					
NZ1	VII			×	×					×

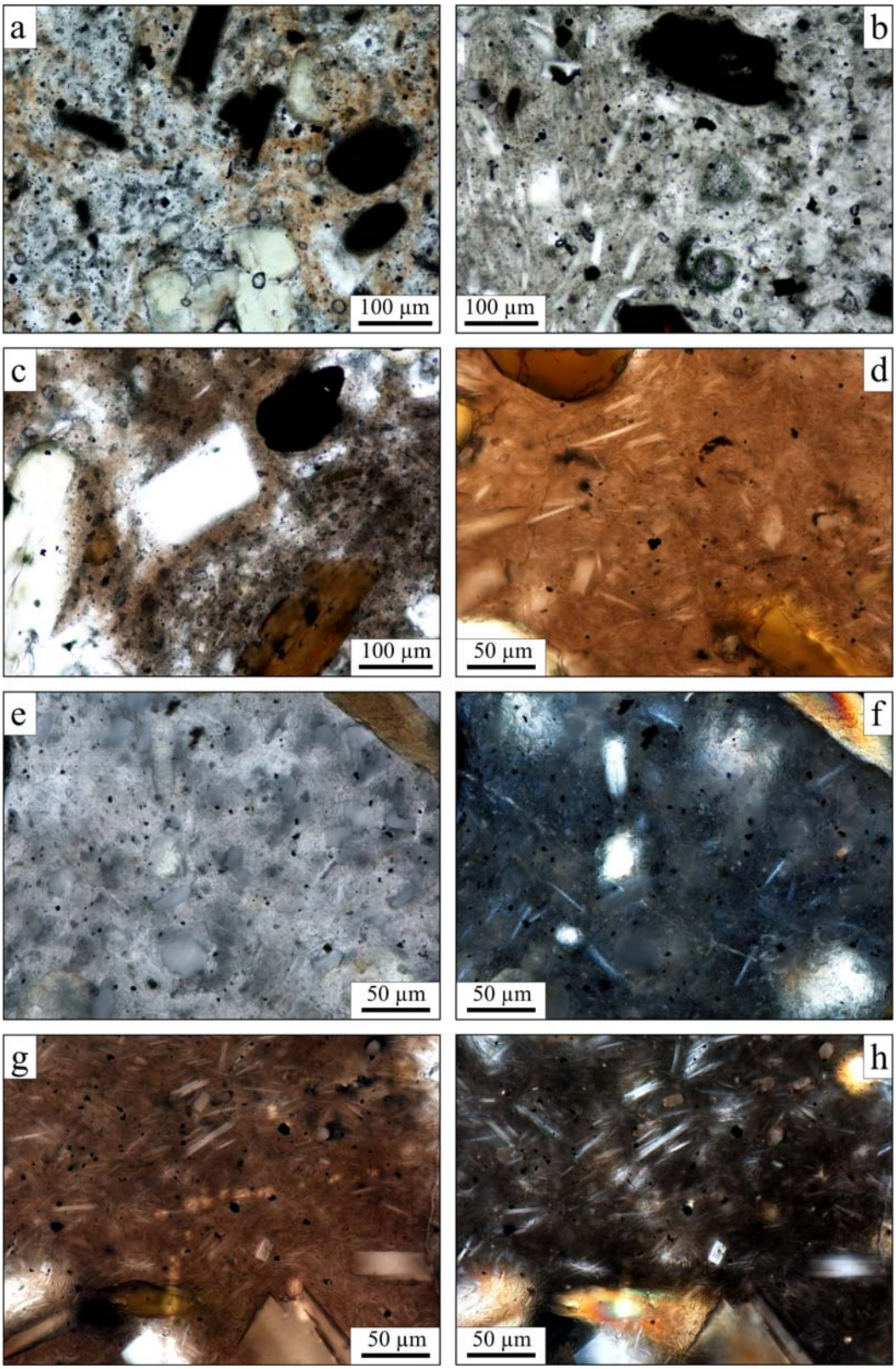


Figure 7-1: Groundmass texture (a-d) and crystallinity (e-h) of clasts from pyroclastic flow deposits. a and c) two groundmass glasses, b-d) differences in degree of groundmass crystallisation in clear translucent and brown glasses, e) semi- to hyaline, clear translucent glass; note microvesicularity, f) same image as in e) under crossed polarised light, g) semi- to holocrystalline brown glass, h) same image as in g) under crossed polarised light.

7.3.1.2 Lava Flows

The studied lava flows (see Table 3-4) contain phenocrysts of plagioclase and clinopyroxene with microphenocrysts and groundmass constituents of plagioclase, clinopyroxene, orthopyroxene, Fe-Ti oxides and traces of olivine. If hornblende crystals (<1%) are present either as phenocryst or microphenocryst they show thick decomposition reaction rims or are entirely decomposed. It is noted that cores of groundmass orthopyroxene crystals often represent olivine. The Turtle is an exception since it contains hornblende (6-7%) with varying degrees of reaction as well as minor biotite crystals. In mineralogy, the Turtle is similar to MacKays Rock, a lava flow forming the SE crater wall (Cronin, 1991).

7.3.2 Bulk Rock Chemistry

7.3.2.1 Pyroclastic Flow Deposits

The Maero eruptive sequence is unique in terms of bulk geochemistry within the erupted rock suite of Mt. Taranaki because they display the highest potassium contents known from the centre. Also within the succession of individual dome-forming events of this period, there is diversity in all major elements, especially SiO_2, Al_2O_3, Fe_2O_3 and MgO. Two eruptive events stand out: the remnant summit dome and the Turtle. The latter is a remnant coulée flow partially collapsed on its northern-southwestern side. Although it was speculated (Cronin, 1991) that the Turtle was part of the summit dome, this is not supported by differences in Sr, Mg#, and K_2O between the two. The summit dome composition is further described in detail in Chapter 5.

For the purpose of this section, the Maero BAF compositions are not distinguished individually but rather their compositional range within the Maero Eruptive Period are illustrated. Some of the BAF units are described in detail in subsequent sections. The dense, dome-derived clasts exhibit the highest silica and potassium contents of the Maero eruptive products although their SiO_2 contents are restricted between 56-60 wt.% (Fig. 7-2). Major element abundances of BAF rocks show positive correlation (e.g. for K_2O) or negative correlation (CaO, FeO, MgO, Al_2O_3) with increasing SiO_2 contents. In addition, considerable variation in trace element abundances (e.g., Sr, Zr, Ni) are observed within this group (Fig. 7-2). It is noted that one sample is distinct within this

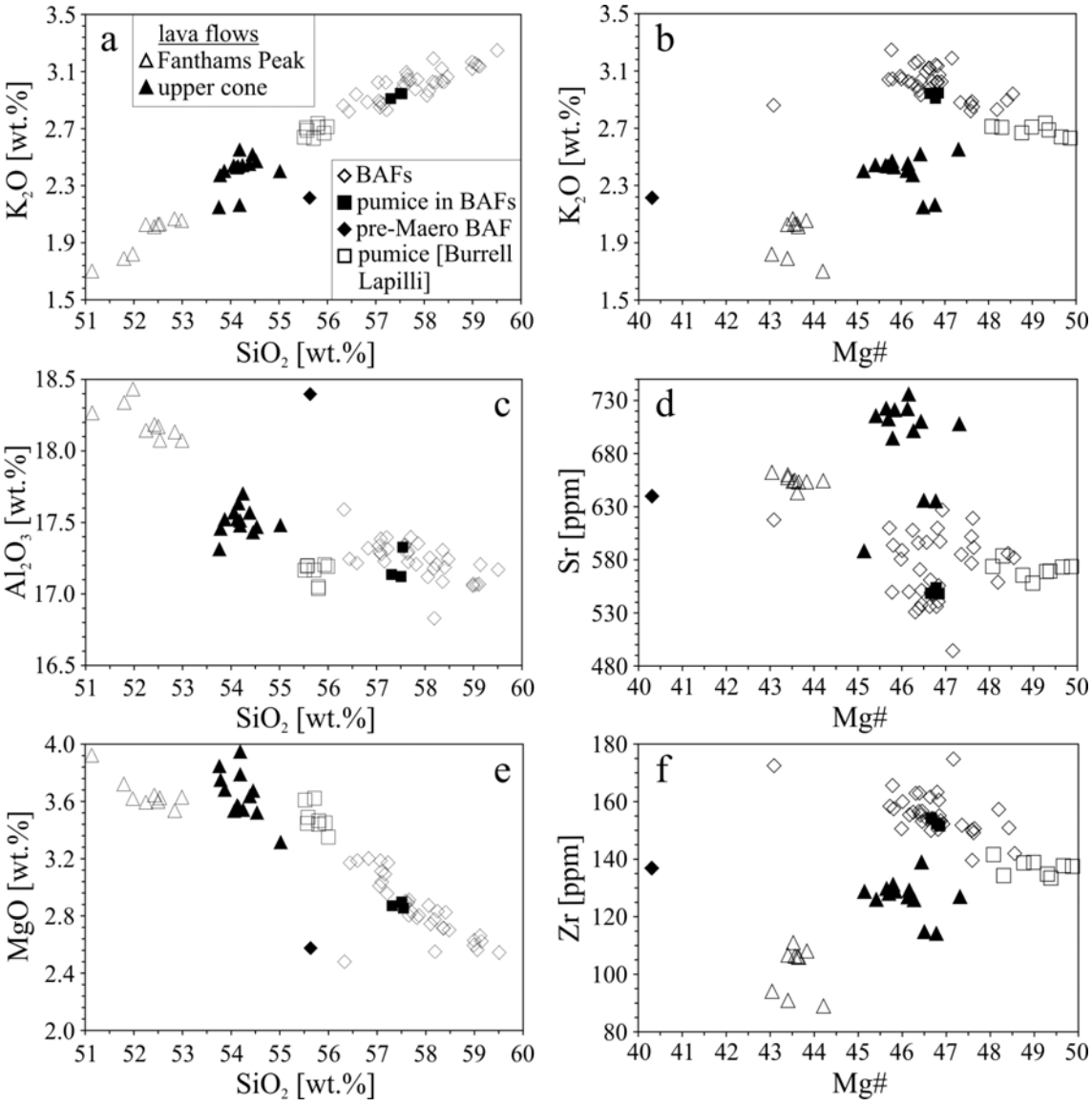


Figure 7-2: Bulk rock composition of selected Maero eruptives. Block-and-Ash Flow deposits are not differentiated and the Pyramid Dome and the Turtle are omitted for clarity. For comparison, selected lava flows of the upper main cone and Fanthams Peak are plotted. Mg#=100[Mg^{2+}/(Mg^{2+}+Fe^{2+})]; all iron as Fe^{2+}.

group with a considerable lower Mg# of 43.1. For comparison, one sample of a pre-Maero BAF deposit is shown that is distinct in nearly all elemental abundances (Fig. 7-2).

Three pumice samples collected from three BAF units showed nearly identical major and trace element compositions with silica values of 57.3-57.5 wt.%. These pumice clasts are 2 wt.% higher in silica, compared to the Burrell Lapilli fall deposits. It is noted that the collected samples were relatively small and also considering the porosity, the analysis may not represent their true bulk composition (e.g. the phenocryst assemblage may be underrepresented causing higher bulk silica contents due to higher proportions of high silica matrix glass).

7.3.2.2 Lava Flows

Bulk rock compositions of lava flows appear to arrange into distinct groups. The youngest lava flows (Summit Group) show highest K_2O contents. With increasing age, individual lava flow groups show progressively lower potassium contents and correlate positively with silica. Potassium is an incompatible element in lava flow rocks and its age-abundance ratio has already been recognised by Stewart et al. (1996) and Zernack et al. (2006). The scoria-and-ash flow deposit from Bobs Ridge (T04-56) cannot clearly be classed into either the Summit or Staircase Group, although its chemical signature leans more toward the former. Likewise, two lava flows in the upper Pyramid Stream have chemical similarities to the Staircase Group.

Chemical compositions of the Fanthams Group are also displayed to illustrate their differences to the central-vent Mt. Taranaki rocks. They are characterised by ≤53 wt.% SiO_2. Interestingly, Fanthams Peak lava flows describe a similar inclined linear slope as main cone lava flow groups (Fig. 7-2). If Mg# is plotted against SiO_2, it is observed that both main cone and Fanthams Peak Groups are clearly separated illustrating a complex petrogenetic evolution of Mt. Taranaki rocks.

Investigated lava flows show very similar trace element abundances if compared, for example, to Maero-aged BAF deposits (Fig. 7-2). Only a slightly greater range in abundances (e.g., Sr and V) are noted which may be owed to the fact that studied lava flows cover a much greater time span and therefore, exhibit greater variations.

7.3.3 Physical Properties

As described above, an understanding of eruption dynamics requires that the physical properties of the erupting melt (and magma) need to be estimated. Of these water content is probably the most influential constituent on the properties of silicate melts since it controls melt density and viscosity, and also the explosivity of a magma.

7.3.3.1 Water Estimates of Volcanic Glasses

The determination of water contents in silicate glasses is limited to two precise methods, Karl-Fisher-Titration (cf. Scholz, 1984; Behrens, 1995) and Fourier Transform Infrared spectroscopy (FTIR; cf. Mackenzie, 1988; Stuart. 2004). Other methods such as loss on ignition and the water-by-difference (WBD) method are widely used, however, their results are less precise. Since the WBD method is the difference from an electron microprobe analytical total and the ideal of 100% (Fig. 7-3), it also includes a summation of analytical errors and is highly dependent on the state of glass weathering, post-depositional hydration and the quality of shard polish. In addition, Roman et al. (2006) demonstrated that water contents in glass inclusions estimated by WBD are approximately 1 wt.% higher than when measured by Fourier Transform Infrared spectroscopy.

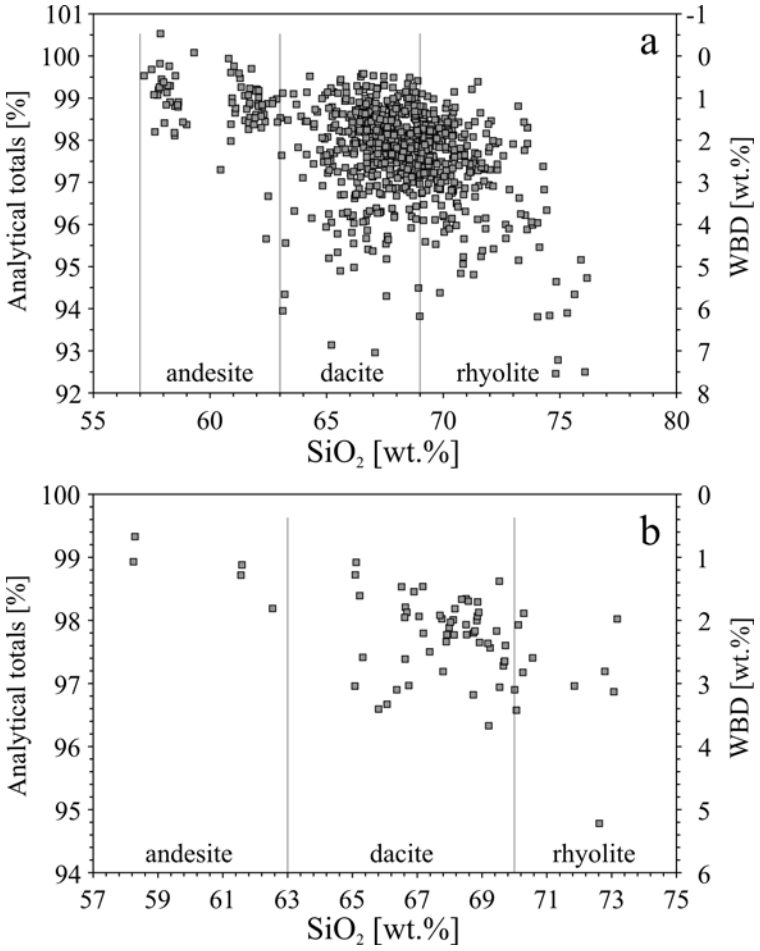


Figure 7-3: Analytical totals of all EMP glass analyses (a) and sample averages (b) are plotted against silica content. Estimated glass water contents using the water-by-difference method (WBD) are shown on the right axis. The terms andesite, dacite, and rhyolite refer to the TAS-classification scheme of Le Maitre et al. (1989).

Although the WBD method appears to overestimate water contents in silicate glasses, it represents a simple method to approximate water contents in glass shards at least to the first order. The typical high microlite content and small grain size of andesitic glass makes it difficult to apply FTIR or other techniques such as Ion Microprobe with confidence. The totals of uncontaminated glass analyses are highly variable and range between 92.5% and 100.5% with a mode at 98.0-98.5% (Fig. 7-3). The distribution curve is also skewed toward lower totals (left skewed by -1.3). Using only the difference to 100%, the mean value of 97.8% of all analyses (n=875) would correspond to an estimate of 2.2 wt.% H_2O. It is also observed that the sample mean analytical totals roughly negatively correlate with their mean silica contents (Fig. 7-3).

7.3.3.2 Viscosity

Melt viscosities are calculated after the models of Shaw (1972) and Hui and Zhang (2007). In the former model, melt viscosity, η, is determined following the equation:

$$2.303\log_{10}\eta = s\frac{10^4}{T} - 1.5s - 6.4 \qquad \text{[Eq. 7-3]}$$

where T is the temperature in K. The parameter s is calculated as

$$s = \sum X_i (S_i^{\circ} X_{SiO_2}) / (1 - X_{SiO_2}) \qquad \text{[Eq. 7-4]}$$

where X_i represents the mole fractions of oxides and S_i° is the partial molar activation energy of oxides (Shaw, 1972).

The model of Hui and Zhang (2007) uses the following formula:

$$\log\eta = A + \frac{B}{T} + e^{(C+\frac{D}{T})} \qquad \text{[Eq. 7-5]}$$

where T is the temperature in K, e is Euler number, and A, B, C, and D are linear functions of oxide mole fractions (except for H_2O). The parameters A-D are calculated as follows:

$$\begin{aligned} A = {} & -6.38X_{SiO_2} - 170.79X_{TiO_2} - 14.71X_{Al_2O_{3ex}} - 18.01X_{MgO} - 19.76X_{CaO} \\ & + 34.31X_{(Na,K)_2O} - 140.38Z + 159.26X_{H_2O} - 8.43X_{(Na,K)AlO_2} \end{aligned} \qquad \text{[Eq. 7-6]}$$

$$\begin{aligned} B = {} & 18.14X_{SiO_2} + 248.93X_{TiO_2} + 32.61X_{Al_2O_{3ex}} + 25.96X_{MgO} + 22.64X_{CaO} \\ & - 68.29X_{(Na,K)_2O_{ex}} + 38.84Z - 48.55X_{H_2O} + 16.12X_{(Na,K)AlO_2} \end{aligned} \qquad \text{[Eq. 7-7]}$$

$$C = 21.73X_{Al_2O_{3ex}} - 61.98X_{(Fe,Mn)O} - 105.53X_{MgO} - 69.92X_{CaO} - 85.67X_{(Na,K)_2O_{ex}} + 332.01Z - 432.22X_{H_2O} - 3.16X_{(Na,K)AlO_2} \quad \text{[Eq. 7-8]}$$

$$D = 2.16X_{SiO_2} - 143.05X_{TiO_2} - 22.10X_{Al_2O_{3ex}} + 38.56X_{(Fe,Mn)O} + 110.83X_{MgO} + 67.12X_{CaO} + 58.01X_{(Na,K)_2O_{ex}} + 384.77X_{P_2O_5} - 404.97Z + 513.75X_{H_2O} \quad \text{[Eq. 7-9]}$$

with Z being:

$$Z = (X_{H_2O})^{1/[1+(185.797/T)]}. \quad \text{[Eq. 7-10]}$$

Al_2O_{3ex} and $(Na,K)_2O_{ex}$ are excess oxides after forming $(Na,K)AlO_2$. The 2σ deviation is 0.61 $\log_{10}\eta$ units (Hui and Zhang, 2007).

For both models the melt composition and its temperature are required as variables. Lava dome temperatures at other volcanoes were measured at >900 °C (Santiaguito, Sahetapy-Engel et al., 2004), c.850 °C (Unzen volcano, Wooster et al., 2000), 720 °C (2004 Mt. St. Helens lava dome, Driedger et al., 2004), and 800 °C (1999 lava dome of Soufrière Hills Volcano, Taron et al., 2007). Since the majority of studied Taranaki glasses are derived from dome-forming eruptions a temperature of 900 °C is assumed. This estimate is based on applying the amphibole-plagioclase thermometer of Holland and Blundy (1994) to the rock suite (see section 5.5.3.1). Thus, using a consistent temperature for all melt viscosity calculations, comparison can be made between dome-forming and sub-Plinian eruptions. A similar approach was undertaken regarding the melt water content. Melt viscosities were determined 'anhydrous' (i.e. 0.1 wt.% H_2O) and using 1 wt.% H_2O. Glass water contents as estimated by WBD were also used, although the resulting melt viscosities are lower because WBD often overestimates the 'true' glass water content (see above). For calculation purposes only the mean sample compositions of studied glass analyses were used resulting in mean sample melt viscosities.

Calculated melt viscosities are plotted against silica contents (Fig. 7-4). In both models it is observed that with increasing silica contents, melt viscosities increase linearly with fixed water contents (i.e. 0.1 and 1 wt.% H_2O). Using estimated water contents (i.e. by WBD), the Shaw-model also shows increases in melt viscosities with increasing SiO_2 content, however, on a shallower slope, whereas melt viscosities decrease with increasing SiO_2 abundances in the Hui-and-Zhang model. In the silica range 58.2-73.2 wt.% melt viscosities ($\log_{10}\eta$) of Shaw (1972) range between 5.1-8.0 Pas (anhydrous), 4.5-7.0 Pas (1 wt.% H_2O), and 4.5-6.0 Pas (WBD). Melt viscosities ($\log_{10}\eta$) calculated

after Hui and Zhang (2007) are consistently higher in the same silica range varying between 7.3-9.0 Pas (anhydrous), 5.7-7.0 Pas (1 wt.% H_2O), and 5.6-4.7 Pas (WBD). It is noted that one outlier at 71.85 wt.% SiO_2 has elevated melt viscosities in the Hui and Zhang (2007) model which is mainly ascribed to a comparatively low potassium content.

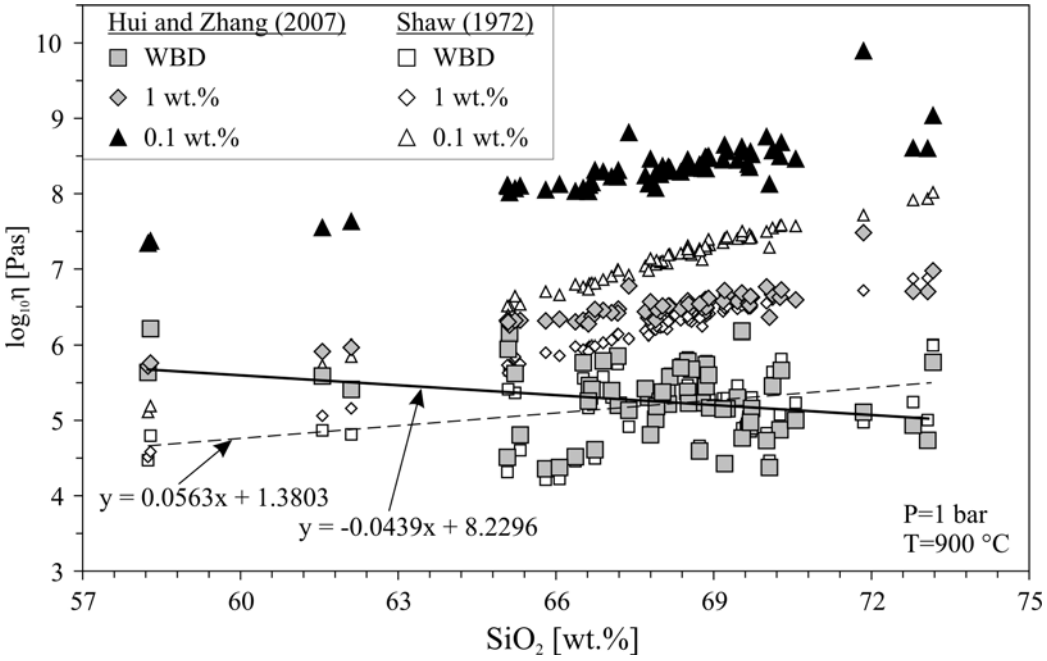


Figure 7-4: Calculated melt viscosities, η, are plotted against silica abundances. Values of the models of Shaw (1972) and Hui and Zhang (2007) are shown for H_2O contents of 0.1 wt.%, 1 wt.% and WBD at T=900 °C and P=1 bar. Solid and dashed lines are regression lines of η at WBD for the Hui-and-Zhang- and Shaw-models, respectively.

If the apparent viscosities of magmas (η_a) are to be estimated, the volume fraction of crystals and vesicles must be known. Rocks of the present summit dome exhibit an average crystallinity (excluding microlites) of 42 vol.% with lower and upper limits of 36 and 49 vol.%. Other studied rocks (mainly derived from BAF deposits) show crystallinities between 27 and 42 vol.%. The microlite content of rocks has not been determined because microlite nucleation and growth continues syn- and post-eruptively which makes it difficult to estimate its proportion at the time of eruption or just prior to it. Higgins (1996) measured lava flow crystallinities (only crystals larger than 150 μm) of 9.8-30.2 vol.% with an estimated average crystallinity of about 20 vol.%. Decompression-induced microlite crystallisation is an important process that significantly impacts on magma viscosities (Sparks, 1997). However, petrographic studies showed that rocks derived from BAF deposits can be semi-crystalline to hyaline (see Fig. 7-1). Hence, the microlite content can be very low, at least in some individual

eruptive deposits. On this basis, end-member magma viscosities ($\log_{10}\eta_a$) were calculated with total crystal volume fractions of 30% and 55%.

The Shaw-model predicts upper and lower apparent viscosity [$\log_{10}\eta_a$ in Pas] at 58.2 wt.% SiO_2 of 5.9-8.1 (anhydrous), 5.3-7.5 (1 wt.% H_2O), and 5.3-7.4 (WBD) and at 73.2 wt.% SiO_2 of 8.8-11.0 (anhydrous), 7.8-9.9 (1 wt.% H_2O), and 6.8-9.0 (WBD; Fig. 7-5). In contrast, upper and lower apparent viscosities of the Hui and Zhang model using the same crystal volume fractions of 30 and 55%, respectively, result at 58.2 wt.% SiO_2 in $\log_{10}\eta_a$ of 8.1-10.3 (anhydrous), 6.5-8.7 (1 wt.% H_2O), and 6.4-8.6 (WBD), and at 73.2 wt.% SiO_2 in $\log_{10}\eta_a$ of 9.8-12.0 (anhydrous), 7.8-9.9 (1 wt.% H_2O), and 6.6-8.7 (WBD; Fig. 7-5).

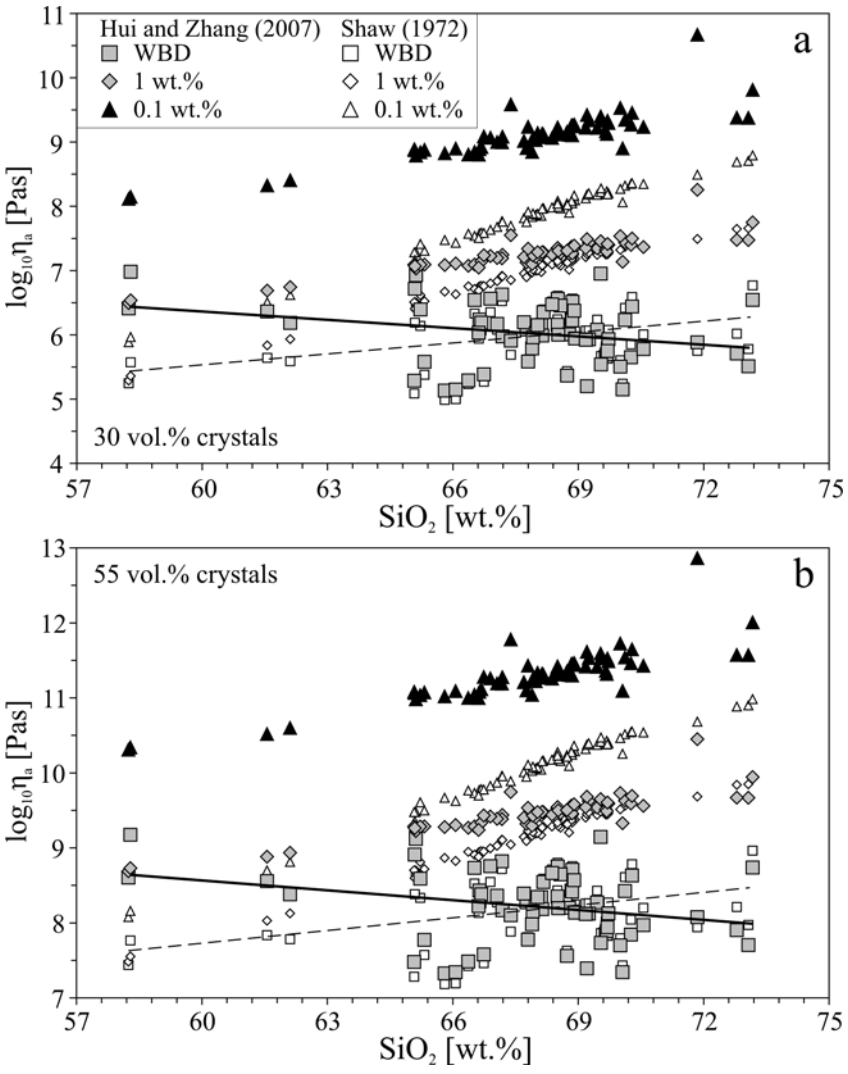


Figure 7-5: Calculated magma viscosities, η_a, are plotted against SiO_2 contents. Lower and upper crystal volume fractions of 30% (a) and 55% (b), respectively are used for the calculation based on the calculated melt viscosities (see Fig. 7-4). Viscosities are calculated using H_2O contents of 0.1 wt.%, 1 wt.% and WBD at constant T=900 °C and P=1 bar. Solid and dashed lines are regression lines of η_a at WBD for the Hui-and-Zhang- and Shaw-models, respectively.

7.4 Discussion

7.4.1 Comparison of Physico-chemical Properties

7.4.1.1 Bulk Rock Composition

Rocks erupted during the Maero Eruptive Period show bulk compositional variations, especially in SiO_2 and K_2O. Pumiceous clasts of the sub-Plinian Burrell Lapilli eruption exhibit lowest silica abundances in a tight range of 55-55.5 wt.% whereas the pre-climactic dome shows a broader compositional range (55.9-59.5 wt.% SiO_2). Products of other dome-forming eruptions also exhibit similar compositional variations, however, not as large as, for example, the Pyramid and Tahurangi eruption episodes. Silica contents and Mg# are plotted for individual eruptions (Fig. 7-6). It is noted that no bulk rock compositions are available for the eruptive events of Hooker Lapilli, Waingongoro Ash, and Mangahume Lapilli because identified fall deposits did not contain sufficient amounts of sample material. In addition, only 1-2 analyses are available for Puniho Ash and Te Popo Ash, which cannot reveal any compositional variations. No systematic compositional variation in time of Maero-aged products is observed. The only noteworthy observation is that rocks of Newall Ash show homogeneous Mg# (46.2-46.8) despite variations in SiO_2 (55.7-59.1 wt.%). This may be indicative of a homogenous source region and may exclude mixing/mingling processes during magma ascent.

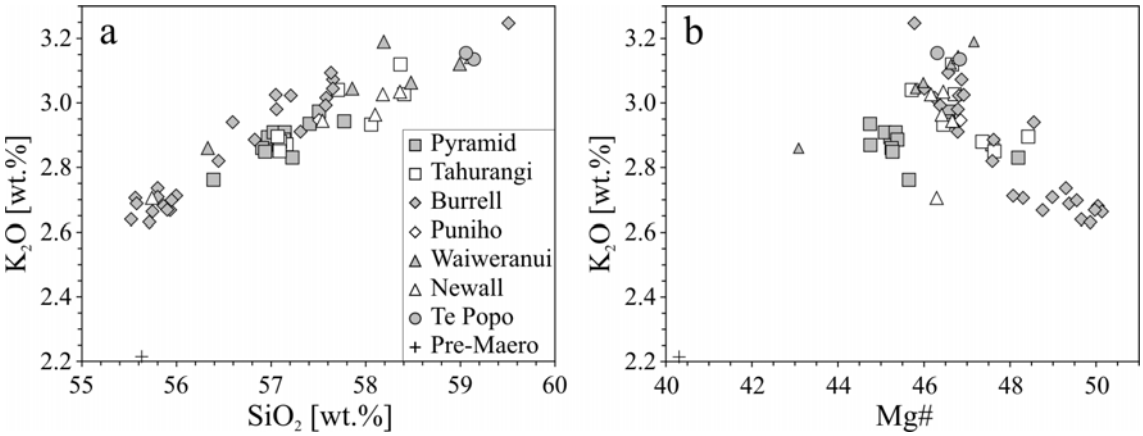


Figure 7-6: Bulk SiO_2 contents (a) and Mg# (b) are plotted against K_2O in chronological appearance of eruption episodes.

Although no systematic geochemical variations are apparent in this dataset, some remarks are made as to why the last erupted products of the Pyramid eruption do not show highest silica and potassium abundances as inferred from the overall geochemical behaviour of the Mt. Taranaki rock suite. It has been recognised that the major

processes at mid- to shallow crustal magma storage levels involve fractional crystallisation and mixing and mingling of compositionally distinct or similar magmas. Influx of primitive or less evolved magma into a source region containing a more evolved magma often causes eruption (Huppert and Sparks, 1980; Druitt et al., 1999). Time is required for the replenished primitive magma at mid- to upper crustal levels to differentiate to a more evolved magma. In the case of a long period of repose, the magma is able to differentiate at depth, however, in the case of two eruptions separated by a short period of repose, the second eruption may produce less evolved magma due to a lack of time for differentiation. In other words, the absence of eruptions allows magma differentiation in the crustal reservoir.

Cyclic variations of low and high eruptive frequencies are observed at Merapi volcano, Indonesia (Gertisser and Keller, 2003). Each magmatic cycle spans several hundreds of years and is characterised by the initial eruption of more evolved magmas (low eruption frequency) which then gradually decline to less evolved magmas due to a higher eruption frequency (Gertisser and Keller, 2003). Although the data of this study are insufficient to support or disprove such cyclic magmatic variation at Mt. Taranaki, it is noted that the latest two eruptions of Taranaki show declining silica abundances (Fig. 7-6).

7.4.1.2 Melt and Magma Viscosities

Viscosities of natural silicate melts have been frequently estimated using the model of Shaw (1972). However, this model extremely underestimates predicted viscosities at very low H_2O (<1 wt.%) contents and slightly underestimates viscosities of melt with high H_2O (>3.5 wt.%) contents (Dingwell et al., 1996; Hess and Dingwell, 1996). Thus, the model of Hui and Zhang (2007) is preferred for the following reasons. First, it is applicable to all natural hydrous and anhydrous silicate melts. Second, the model has a high accuracy with a 2σ deviation of 0.61 $\log_{10}\eta$ units. Third, the model should not be used for viscosities above 10^5 Pas, temperatures below 573 K, and for non-rhyolitic melts with >5 wt.% water which makes this model suitable for volcanological applications, and covers the entire range of prevailing conditions at andesite volcanoes. Fourth, it uses all major element oxides including trace abundances of MnO and P_2O_5. Fifth, iron is only used in the model as ferrous iron which makes an estimate of the iron

oxidation state redundant. Although it is known that the iron oxidation state has an impact on melt viscosity, especially at very low temperatures (Dingwell and Virgo, 1987), there is currently no information of how to estimate the ferric/ferrous ratio of melts, especially if analyses are derived by EMP. The only potential disadvantage of the Hui-and-Zhang model are the large amount of parameters involved.

Published matrix glass compositions from Merapi volcano, Indonesia (Bardintzeff, 1984; Berthommier, 1990; Hammer et al., 2000) and Soufrière Hills Volcano, Montserrat (Harford et al., 2003) were used to calculate melt viscosities using the same parameters (T=900 °C, 0.1 and 1 wt.% H_2O) in order to compare to calculated Mt. Taranaki melt viscosities. Here only the model of Hui and Zhang (2007) is used (see above). This shows that Mt. Taranaki melt viscosities are intermediate between the slightly lower melt viscosities (at similar SiO_2 abundances) of Merapi volcano and the higher melt viscosities of Soufrière Hills Volcano (Fig. 7-7). It is pointed out that the majority of Merapi dome clasts have glass silica contents above 71 wt.% and therefore exhibit similar melt viscosities as the majority of Taranaki glasses at lower SiO_2 contents. In contrast, Soufrière Hills glass silica abundances are exclusively above 76 wt.% and thus displaying highest melt viscosities of approx. 1 log unit above Mt. Taranaki melt viscosities. If magma viscosities, η_a, (T=900 °C, crystal fractions of 30% and 55%, 1 wt.% H_2O) between the three andesite volcanoes are compared then similar observations are made in comparison to melt viscosities. However, eruptive conditions (i.e. emplacement temperature, crystal and microlite content, residual water in matrix glass) differ from volcano to volcano. Viscosities of natural lava (either as flow or dome) are difficult to estimate and reliable viscosity measurements under natural conditions are rare. Fig. 7-8 illustrates lava viscosities of selected andesite, dacite, and rhyolite centres. Calculated Mt. Taranaki magma viscosities of the Maero Eruptive Period are based on matrix glass compositions. In order to compare Taranaki lavas to other centres, the range in magma viscosity with crystal fractions of 30% and 55% is used and plotted against the range of bulk SiO_2 abundances of Maero rocks. A linear relationship between bulk silica content and lava viscosity as observed for calculated melt and magma viscosities is assumed. In this context, studied Mt. Taranaki rocks appear to have lowest lava viscosities with estimated maximum viscosities (i.e. at crystal fractions of 55%) of $\log_{10}\eta_a$=9.2-9.8 Pas (T=900 °C; 1 wt.% H_2O). It is noted that if melt water estimates are used from WBD then even lower lava viscosities result with a negative relationship between $\log_{10}\eta_a$ and SiO_2. Only the 1979 Soufrière volcano

(St. Vincent) lava dome and lava flows from Colima volcano, Mexico, have similarly low viscosity. It is noted that Merapi lava dome rocks seem to possess lowest viscosities of $\log_{10}\eta_a$=6-7 Pas (which would roughly correspond to the estimated minimum Taranaki dome viscosities at similar SiO_2 contents and 1 wt.% H_2O) but these data were calculated on the basis of average extrusion rate and T=1000 °C (Siswowidjoyo et al., 1995). On this basis, reported Merapi dome viscosities may be regarded as minimum values.

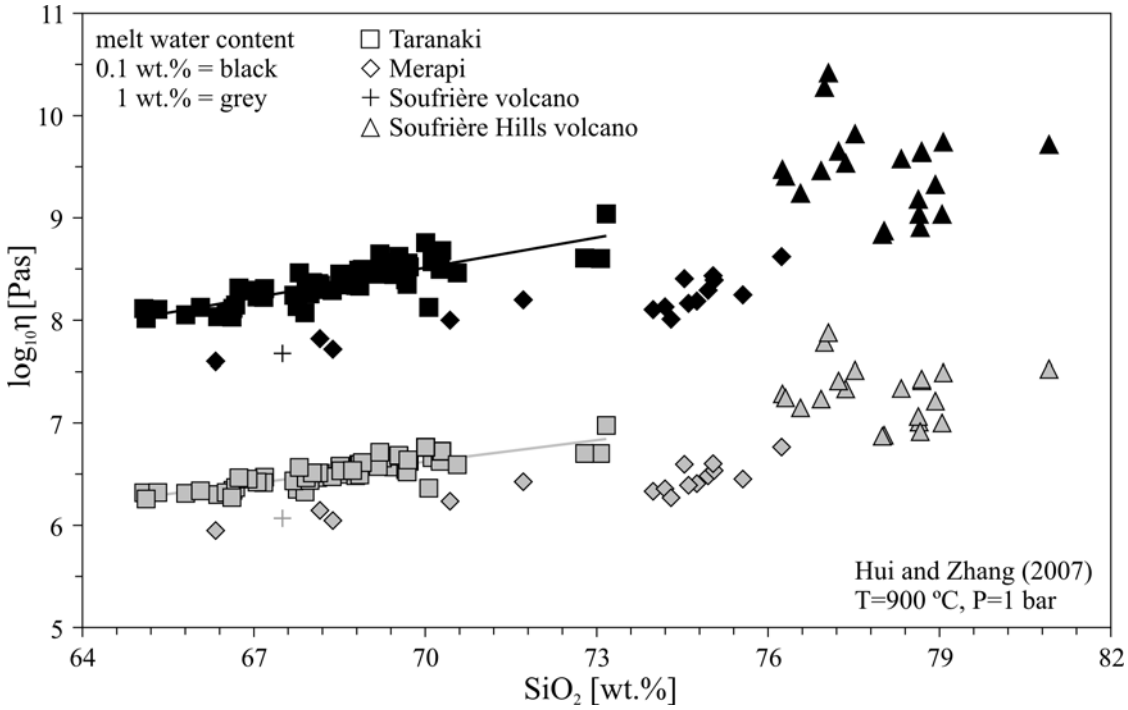


Figure 7-7: Calculated Mt. Taranaki melt viscosities are compared to calculated melt viscosities of Merapi volcano (Indonesia), Soufrière volcano (St. Vincent), and Soufrière Hills Volcano (Montserrat), using the same parameters. Solid lines are regression lines for Taranaki data.

The significance of calculated Mt. Taranaki melt and magma viscosities is that the magma erupted at any time during the Maero Eruptive Period had lower viscosities compared to recent eruptions (i.e. Soufrière Hills Volcano, Montserrat; Mt. St. Helens, USA). This means that emplacement and growth of Taranaki lava domes is limited in height and total volume. Therefore, the formation of spiny or Pelean domes within the Taranaki crater appears unlikely. Instead, lobate dome morphologies and coulée and block lava flows are expected (cf. Chapter 5).

This conclusion is supported by petrographic rock textures (Table 7-2). The dominance of fresh and pristine hornblende crystals observed in rocks of pyroclastic flow deposits clearly shows that magma ascent and extrusion occurred at relatively fast rates. It also demonstrates that dome collapses occurred syn-eruptively since resulting pyroclastic

flow deposits cooled quickly to preserve the observed pristine hornblende crystals. The observation of semi-crystalline groundmass textures also indicate fast magma ascent and extrusion rates also implying low strain rates and low magma viscosities due to presence of 'large' quantities of melt. Dome geometries with heights of c.100 m may represent the upper limit before deforming. The presence of semi-crystalline groundmass textures also support syn-eruptive dome collapses (see above).

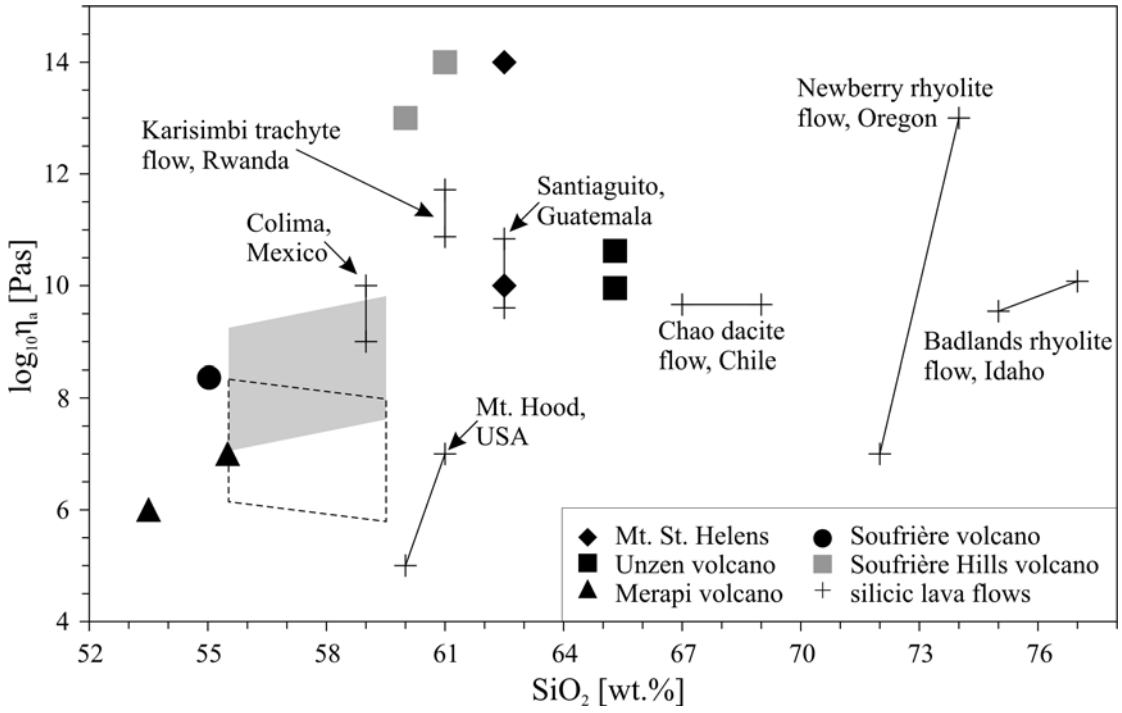


Figure 7-8: Calculated Mt. Taranaki magma viscosities plotted against SiO_2 are compared to other andesite to rhyolite volcanoes. Since Taranaki viscosity calculations are based on glass chemical compositions of the Maero Eruptive Period, the range in bulk silica contents of rocks erupted during this period are used to allow comparison to published data. Upper and lower viscosity abundances are taken from Fig. 7-5. Taranaki data are illustrated by two parallelograms with upper and lower limits representing crystal volume fractions of 55% and 30%, respectively. The grey parallelogram corresponds to 1 wt.% melt water content, whereas the dashed parallelogram relates to water contents determined by WBD. Data source: silicic lava flows (Murase and McBirney, 1973; Fink, 1980; Navarro-Ochoa et al., 2002; Manley, 1996; Harris et al., 2004; and McKay et al., 1998); Mt. St. Helens (Murase et al., 1985; Scandone and Malone, 1985); Unzen volcano (Suto et al., 1993; Goto, 1999; Sato et al., 1999); Soufrière Hills Volcano, Montserrat (Voight et al., 1999; Sparks et al., 2000); Soufrière volcano, St. Vincent (Huppert et al., 1982); Merapi volcano (Siswowidjoyo et al., 1995).

7.4.2 Course and Eruption Styles of the Maero Eruptive Period

7.4.2.1 Types of Lava Domes

The formation of either a dome shaped body or a lava flow is governed by prevailing magma viscosity and extrusion rates. By comparing magma viscosities of different volcanoes, inferences can be made about lava dome morphologies at Mt. Taranaki. Three basic dome types appear to have been formed during the Maero Eruptive Period: 1) composite lava domes, 2) coulée and block lava flows, and 3) homogenous lava domes.

Composite lava domes (type 1) preferentially form within an intact summit crater where short-lived lava extrusion episodes of different eruption periods amalgamate to a large dome complex or where a long-term extrusion episode forms a heterogeneous dome by ongoing vent migration, alternating growth episodes, and the extrusion of compositionally distinct magma domains. The best examples for this dome type are the 1980-1986 Mt. St. Helens and the 1995-present Soufrière Hills Volcano dome-forming eruptions.

Type 2 lava domes comprise coulée and block lava flows. The formation of a block lava flow occurred during the most recent summit dome producing eruption (see Chapter 5). The Turtle was also interpreted as a coulée (Cronin, 1991). The columnar-jointed thick remnants on the upper NW flank extend down to 770 m over a 450 m altitude difference. Coulée and block lavas are generated either once a lava lobe is spilled over the confining crater rim onto the upper flanks or, in the case of a breached crater, if they are extruded directly onto the upper flanks (cf. early stage of the summit dome formation). Recent block lava flows were observed, for example, at Santiaguito, Guatemala and Augustine volcano, USA).

The third lava-dome type represents the case where a simple homogenous dome is formed during a brief extrusion event. Typically a hemispherical shape develops with/without individual lava lobes being emplaced on the upper flanks. An example for this type is the remnant summit dome of Mt. Taranaki.

7.4.2.2 Causes of Dome Collapse and Associated Deposits

During recent and historic dome-forming eruptions at andesite and dacite volcanoes, different dome collapse types are recognised. At Mt. Taranaki, three end-member types of dome collapse generated diverse properties and magnitudes of associated deposits: gravitational collapse of 1) parts of individual lava lobes and 2) a major portion of the lava dome (sector dome collapse), and 3) dome disruption (or explosion) caused by over-pressurisation.

Gravitational dome failure is also known as Merapi-type dome collapse. It is here distinguished between two end-members of a spectrum; the gravitational failures of a lava lobe/dome margin vs. failure of a major portion of the dome (sector collapse). An advancing lava lobe on a steep slope will behave depending on a combination of the slope and its tensile strength. Within the lava body vertical velocity and hence deformation gradients occur with highest velocities and deformation rates at the top along with highest shear rates at the base near contact with substrate. Cracks develop preferentially at the surface due to cooling and are also induced by localised stress during flowage. Crack propagation is favoured by progressive deformation and hence flowage. Rainfall quenching is also another contributing factor to extend surface cracks causing further degradation of rock strength (Elsworth et al., 2004). Once the gravitational force exceeds the tensile strength of the lava, portions of the lobe can break off, forming either rock falls or BAFs depending on the volume lost in each event. Similar processes are involved during a sector dome collapse. A dominant factor also involved in gravitational instabilities of lava domes is the increasing pressure load due to extrusion of large masses of lava. Increasing weight acting on the basal dome portion causes progressively higher tensile stress. The delicate balance between downward- and upward-acting forces can be disrupted by volcano-tectonic earthquakes triggering failure. Over-steepening and subsequent collapse of the dome front is also achieved by inflation of the dome interior or inflation of the upper edifice due to increasing magma supply rates.

The collapse of an over-pressurised lava dome causing a lateral blast/explosion is known as Pelean-type dome collapse. Pressurisation of the dome interior is caused by increasing fluid pressures within the melt fraction or increasing gas pore pressures, both caused by ongoing microlite growth when the outer part of the dome is sealed. Pressurisation within a dome results at high melt and magma viscosities where over-pressures in bubbles can be developed. High melt viscosities are the result of degassing

and groundmass crystallisation. A dramatic increase in melt viscosity occurs if dissolved water contents are reduced; a change from 1 wt.% to 0.1 wt.% H_2O results in an increase in viscosity of more than 3 orders of magnitude (Hess and Dingwell, 1996). Viscosity and bubble over-pressures are apparently greatest in domes with minor water contents (Massol and Jaupert, 1998).

Pore pressures increase with increasing viscosities, i.e. the more viscous the lava is, the more pressure builds up in pores or vesicles due to the increasing forces resisting pore/vesicle expansion. Large fluid (melt) pressures can develop by rapid nucleation, crystallisation and growth of anhydrous microlites (Sparks, 1997). If the lava is already highly viscous, exsolution of residual dissolved water is reduced or inhibited, causing excess fluid pressures up to several tens of MPa (Sparks, 1997). Pressure gradients within the dome and between dome and upper conduit result. If more pressure is added to the system, for example by intrusion of (volatile-rich) magma into the dome, the tensile strength of rocks can be exceeded. It is still to be investigated to what extent meteoric water vapour impacts on dome failure. It may be possible that rain water percolates through the porous crater rim rocks, heats up and vapour is trapped underneath the emplaced, weakly permeable dome cap. Resulting phreatic explosions by instant vapour release either weaken metastable domes, or themselves generate/trigger lateral blasts and major dome collapses.

Large-scale failure of a pressurised dome, induced by either gravitational instability or excess internal overpressures, may cause lateral blasts or explosions. This is common when a dome is partially emplaced in a crater and partially onto the upper flanks. A sector collapse may expose the pressurised dome interior, while much still-hot lava remains directly above the vent. Sudden pressure reduction may induce rapid fragmentation by vesicle expansion and this near-instantaneous exsolution and expansion of pressurised melt pockets triggers an explosion(s). Unroofing of a gas-pressurised inner dome or conduit may also generate ejection of ballistics, fountaining or magmatic fragmentation (e.g. Newhall and Melson, 1983; Robertson, et al., 1998; Platz et al., 2007). The observed single lapilli lithics scattered around the volcano were most likely generated by such mechanisms. Fragmentation of highly viscous, vesicular rocks by rapid decompression was investigated by Alidibirov and Dingwell (1996) who showed that a decompression wave propagates downward at sonic speed. Sub-parallel fractures perpendicular to the wave front are generated due to large pressure gradients.

A variety of deposits are observed at Mt. Taranaki, which are associated with the three end-member types of dome collapse. Syn-eruptive gravitational lava dome collapses (1 and 2) produce (hot) rock falls, BAFs and pyroclastic surges. These deposits are primarily composed of magnetically aligned angular to subangular clasts. Other indicators for hot deposition are the presence of charred or charcoalised organic fragments (i.e. grass, twigs, or logs) or pervasive red-colourisation of matrix and clasts in the upper portion of the deposit [e.g. Tahurangi Breccia (a); cf. Chapter 5]. Block-and-Ash Flows can also be generated by post-eruptive gravitational dome collapses, however, if the dome has already cooled to ambient temperature then rock avalanches are triggered by gravitational failure (e.g. Pyramid Rock Avalanche; cf. Chapter 5).

The disruption of a pressurised lava dome (type 3) can involve the generation of a directed blast, BAFs, pyroclastic surges, and pumice flows depending on the magnitude of dome failure and whether the dome interior or the upper conduit is exposed. A blast deposit [Newall Breccia (a)] identified by Cronin et al. (2003) is confined to the W-NW sector of Mt. Taranaki (cf. Chapter 3 and Fig. 3-4i). The explosive removal of a pressurised lava dome occurred during the Burrell episode where a large BAF was initiated travelling more than 13 km from source (cf. Chapter 6). The generation of at least one pumice flow (exposed in Maero Stream) during the Puniho eruptive episode indirectly proves firstly, the failure of a pressurised dome triggering rapid magma vesiculation and fragmentation due to rapid decompression, and secondly, also the failure of a sustained explosive phase since no pumice fallout is recorded during Puniho times.

The extent of Maero-aged BAF deposit varies; only three BAF units are recorded outside the National Park boundary [Waiweranui Breccia, Burrell Breccia (A), and Tahurangi Breccia (a)]. Since all BAFs produced during the Maero Eruptive Period were initiated by lava domes located in the summit crater, the initial potential energy can be considered as constant (except for more advanced lava lobes/coulées collapsed at significantly lower altitude). Consequentially, only two factors can significantly influence the runout of BAFs (assuming similar travel paths): the initial volume of collapsing material and added kinetic energy into the system. Kinetic energy could have been added at the beginning through a directed blast or explosive removal of the dome. The latter case is envisaged to have occurred during the Burrell episode (cf. Chapter 5). In summary, the common Merapi-type dome collapse as well as Pelean-type failure occurred during the Maero Eruptive Period.

7.4.2.3 Reconstruction of the Maero Eruptive Period

The stratigraphy of the Maero Eruptive Period has been established in Chapter 3. It was shown that this period of activity is characterised by at least 10 eruptive episodes (see Fig. 3-6). All of these episodes are represented by fall deposits, however, exposed pyroclastic flow deposits on the NW sector are only recognised for seven of the eruptive episodes. A complete reconstruction of the Maero Eruptive Period is difficult, because lava flows thought to have been emplaced during the period cannot be clearly correlated to any of the known episodes nor can they be distinguished as individual eruptive events. Despite this, conclusions can be drawn about eruption styles and mechanisms based on field observations and measured and calculated physical rock and magma properties. Inferences about the course of each eruptive episode of the Maero Eruptive Period are discussed in chronological order.

The Maero Eruptive Period starts with the Hooker eruptive episode thought to have occurred at around AD930 (Table 3-5). Only a discontinuous pumice and lithic lapilli fallout layer (Hooker Lapilli) is preserved on the eastern flank of Mt. Taranaki. This implies that only a low volume of magma erupted causing a spatially limited tephra layer. Although the main dispersal axis could have been towards the W-NW (contrasting to the main NE-S dispersal axis), no fall deposits were found on the NW sector. The production of pumice and dense lithic clasts during this event may suggest the explosive removal of a lava dome or plug. Due to the apparent limited volume of erupted pumice, vesiculation and fragmentation of magma occurred probably only in the upper conduit by sudden decompression. Sustained fragmentation was probably prevented by limited magma supply rates.

After a period of c.150 years, the Te Popo episode produced fall- (Te Popo Ash), BAF- (Te Popo Breccia) and multiple pyroclastic surge deposits dated at 878 ± 39 yrs B.P. (Cronin et al., 2003). During this episode, the NW flank of Mt. Taranaki was extensively inundated by pyroclastic surges and BAFs with their deposits directly overlying a thick paleosol of Oakura Tephra. The confinement of pyroclastic flow deposits to the NW sector has three implications: (1) either a low-point in the western crater rim enabled the direction of dome-related BAFs and surges towards the west, or (2) parts of the western rim collapsed, for example, caused by excess load pressure due to emplacement of large volumes of lava within the crater, or (3) dome growth exceeded

the dimensions of the crater area and individual lava lobes were emplaced onto the upper NW flanks and successively collapsed forming BAFs and surges. The partial rim collapse scenario appears to be the simplest explanation since about 30% of the clast population found in the BAF deposit (Te Popo Breccia) are orange-coloured clasts likely representing parts of the altered crater rim lava flows (cf. Fig. 3-8).

Following an estimated 200-year-period of repose, the Waingongoro episode appears to have produced only a small fine ash layer on the eastern flanks; no pyroclastic flow deposits associated with this episode were found on the NW sector. The eruptive style producing this ash layer is unknown. Phreatic eruptions commonly produce thin, 2-3 cm thick, pale to dark grey ash layers of dense lithic ash (i.e. shards of crystalline rock). This style can be excluded for this eruption because the shards of the tephra were analysed and shown to be glassy, i.e. juvenile magma was erupted. The presence of abundant microlites in these glass shards and their dense and angular shape are similar to glass shards erupted during dome-forming events. In addition, Waingongoro Ash has a very similar appearance to Te Popo Ash also indicating a similar predominant extrusive eruption style. The absence of pyroclastic flow deposits on the NW sector may indicate that either the extruded lava dome did not collapse or if it failed it only produced rock falls and minor BAFs preserved at proximal areas.

The Newall eruptive episode initiated a period of increased activity following an estimated period of repose of c.150 years. The episode started in c.AD1430 and was initiated by a directed blast. This event and subsequent generated pyroclastic surges and BAFs devastated the NW sector as evident by abundant charcoalised organic fragments present in those deposits. The blast deposit [Newall Breccia (a)] is strongly confined to the W-NW area of Mt. Taranaki (Cronin et al., 2003). Medial and distal pyroclastic surge and BAF deposits are exposed, for example, in Maero, Pyramid, and Waiweranui Streams. Observed fine to medium ash layers on the northern through to southern flanks along with exposed BAF [Newall Breccia (b)] and pyroclastic surge deposits on the W-NW sector clearly indicate a lava dome-forming episode. The deposition of a single lithic lapilli layer [Newall Ash (a)] followed by two fine to medium ash layers [Newall Ash (b) and (c)] point towards three phases where the lapilli layer presumably represents a vent-clearing phase prior to lava extrusion. The two individual fall deposits are probably related to the lateral blast and later to ongoing dome growth and collapse events. The clear distinction of both ash layers may indicate that the Newall episode was a longer-term eruption. The evidence of a blast deposit implies failure of a

pressurised lava dome (type 3 dome collapse). The exposure of the dome interior or un-roofing of the upper conduit caused instantaneous magma vesiculation and fragmentation. This is supported by the presence of up to 15% pumice clasts within BAF and surge deposits, often rounded and concentrated near the top of the deposits. Since no pumice fall deposit is observed, it is assumed that only a small magma volume vesiculated and fragmented explosively. In addition, in parts significant portions of orange-coloured clasts inferred to be derived from crater-rim lava flows are also present in these deposits possibly indicating excavation and broadening of the breached western crater rim.

Less than 100 years later, another dome-forming eruption took place, the Waiweranui eruptive episode. Deposits associated with this episode comprise a fine to medium ash bed (Waiweranui Ash) on the eastern flanks and a distal BAF deposit (Waiweranui Breccia) along with a pyroclastic surge deposit on the NW sector. Based on deposition characteristics, it appears that this eruption is marked by ongoing lava extrusion forming a summit dome which subsequentially collapsed. The extent of the Waiweranui Breccia (>13 km from source) and the absence of significant amounts of pumice clasts within the deposit may be indicative of a simple gravitational sector dome collapse (i.e. type 2).

The next eruptive episode occurred about 70 years later (Lees and Neall, 1993) in c.AD1590. The Puniho episode is also recorded on the eastern flank as fine to medium ash (Puniho Ash) and partially as a surge deposit. On the contrary, a BAF deposit (Puniho Breccia), a pumice flow- as well as pyroclastic surge deposits are exposed on the NW flank of Mt. Taranaki. A predominant dome-forming eruptive style is assumed for this period. The collapse of the Puniho dome triggered a short-lived, presumably sub-horizontal directed, explosive fragmentation (type 3 dome collapse), which generated minor pumice flow(s). The failure to cause sustainable fragmentation could be due to insufficient time for the magma below to vesiculate to greater depth and possibly low magma extrusion rates during this period of dome growth.

The course and eruptive style of the Burrell episode of AD1655 is described in detail in Chapter 6. The Burrell episode is characterised by an initial lava dome extrusion followed by explosive removal of the dome triggering a large BAF. Un-roofing the vent caused a switch to an explosive, sub-Plinian eruption style, which itself can be distinguished into three phases each producing individual pumice flows. From a sub-Plinian eruption column widespread pumice lapilli fall was produced.

About 40 years later, the Mangahume eruption occurred, a presumably small eruption based on the observation of only a single lithic lapilli layer (Mangahume Lapilli) found on the southern flank. No correlatives were found on the NW sector. The presence of a scattered dense lithic layer alone only indicates an explosive event, perhaps a vent-clearing phase with the formation of ballistics (originating from a former dome/plug?). Therefore, due to the absence of ash particles associated with the lapilli layer other eruption styles such as Vulcanian explosions can be excluded. However, in the light of results derived from the Pyramid eruption (cf. Chapter 5), it is also possible that a lava dome was erupted in a single (short-term?) event and did not collapse, i.e. no pyroclastic flow and fine ash fall deposits were produced during this eruption.

The Tahurangi eruptive episode, tentatively dated at AD1755 (Druce, 1966), appears to be one of the bigger dome-forming episodes of the Maero Eruptive Period judged by the thickness of the fall deposit. Tahurangi Ash is a fine to medium, up to 10 cm thick ash deposit exposed on the NE-E flanks and is even in pockets found beyond the National Park boundary. Block-and-Ash Flow deposits [Tahurangi Breccia (a) and (b)] on the NW sector were correlated with Tahurangi Ash; charred tussock [Tahurangi Breccia (a)] proved to be too young for radiocarbon age determination (i.e. <250 yrs B.P.). Tahurangi Breccia (a) is exposed at distal reaches near Hangatahua River more than 12 km from source. The exposure of two major BAF deposits may be indicative for ongoing dome extrusion and simultaneous dome failure. Rock falls associated with dome growth are likely be only deposited at proximal reaches. The homogenous appearance of Tahurangi Ash does not indicate any major breaks in time (i.e. by bedding or grain size variations) and may therefore point to an ongoing extrusive event of constant intensity.

The last eruption of Mt. Taranaki, the Pyramid eruption, produced the summit dome whose remnants (Pyramid Dome) are still preserved within the crater (cf. Chapter 5). The preservation of a scattered lithic lapilli layer (Pyramid Lapilli) on the southern flank shows that this eruption occurred post-Tahurangi since there is a 2-3 cm thick paleosol between Tahurangi Ash and Pyramid Lapilli. A post-eruptive (cold?) Pyramid Dome collapse produced a rock avalanche (Pyramid Rock Avalanche) on the NW sector which is exposed >5 km from source. The date of the Pyramid eruption is poorly constrained but is thought to have occurred between AD1839 and AD1866 (cf. Chapter 5).

7.5 Conclusions

The Maero Eruptive Period is characterised by contrasting eruption styles and mechanisms. It appears that every eruptive episode (see Table 3-5) began with the extrusion of viscous lava forming domes. In some instances, an initial vent-clearing phase producing ballistics occurred as evident by the record of scattered single lithic layers at medial reaches [Newall Ash (a), Mangahume Lapilli, Pyramid Lapilli]. The type of dome failure (Merapi-type vs. Pelean-type dome collapse) then controlled successive eruptive phases. In the case of a Merapi-type dome collapse, dome growth continued or magma extrusion ceased shortly after the event (cf. Tahurangi episode). In contrast, Pelean-type dome failures can trigger a directed lateral blast-explosion (cf. Newall episode), instantaneous but short-lived magmatic fragmentation (cf. Newall and Puniho episodes), and sustained sub-Plinian eruptions (cf. Burrell episode). In addition, the emission of lava flows thought to have occurred during the Maero Eruptive Period is yet another eruptive style where also compositionally distinct magmas were erupted.

During the Maero Eruptive Period, arrival of viscous and degassed andesite magma in the upper conduit led to the formation of three types of lava domes described above. The dome type depended on melt and magma viscosity and the rate of extrusion where either lava lobes, block lava flows or lava domes are generated. Estimates of melt and magma viscosities at Mt. Taranaki have been derived in this study, based on glass chemistry, predominantly derived from shards of fall deposits. Important factors controlling viscosity are H_2O content and temperature; these parameters were estimated by glass WBD and amphibole-plagioclase thermometry, respectively. Upper and lower crystal volume fractions were quantified under petrographic microscope. Magma ascent rates were also indirectly estimated by hornblende decomposition reactions; if the dimensions of the lava dome are known, extrusion rates can also be evaluated using the model of Lyman et al. (2004). For the latest Pyramid eruption, minimum magma ascent and extrusion rates of 0.012 ms^{-1} and 6.0 m^3s^{-1} (5.2×10^5 m^3d^{-1}), were estimated, respectively. Pre- or syn-eruptive magma viscosity are unknown, however, the first-order viscosity can be estimated using the above parameters. Erupted rocks initially forming a lava dome have assumed maximum syn-eruptive viscosities in the order of $\log_{10}\eta$=9.2-9.8 Pas (T=900 °C, 1 wt.% H_2O, 55 vol.% crystals). If water estimates based on WBD are applicable, much lower maximum viscosities between $\log_{10}\eta$=8.3-8.0 Pas could have occurred.

7.6 References

Alidibirov, M. and **Dingwell, D.B.** 1996. Magma fragmentation by rapid decompression. *Nature* 380, 146-148.

Baker, D.R. 1996. Granitic melt viscosities: Empirical and configurational entropy models for their calculation. *American Mineralogist* 81, 126-134.

Baker, D.R. and **Vaillancourt, J.** 1995. The low viscosities of $F+H_2O$-bearing granitic melts and implications for melt extraction and transport. *Earth and Planetary Science Letters* 132, 199-211.

Bardintzeff, J. 1984. Merapi volcano (Java Indonesia) and Merapi-type nuée ardente. *Bulletin of Volcanology* 47, 433-446.

Behrens, H. 1995. Determination of water solubilities in high-viscosity melts: an experimental study on $NaAlSi_3O_8$ and $KAlSi_3O_8$ melts. *European Journal of Mineralogy* 7, 905-920.

Berthommier, P. 1990. Etude volcanologique du Merapi (Centre-Java): téphrostratigraphie et chronologie - produits éruptifs. Unpublished PhD thesis. Université Blaise Pascal, Clermont-Ferrand, France.

Best, M.G. 2003. Igneous and metamorphic petrology. Blackwell Science. Malden.

BGVN 29:09. Smithsonian Institution, 2004. Mount St. Helens. *Bulletin of the Global Volcanism Network*, vol. 29, no. 9.

Bottinga, Y. and **Weill, D.F.** 1972. The viscosity of magmatic silicate liquids: a model for calculation. *American Journal of Science* 272, 438-475.

Brinkmann, H. 1952. The viscosity of concentrated suspensions and solutions. *The Journal of Chemical Physics* 20, 571.

Cronin, S.J. 1991. The geology of the summit of Mt. Egmont. Unpublished BSc Honours thesis. Massey University, Palmerston North, New Zealand.

Cronin, S.J., Stewart, R.B., Neall, V.E., Platz, T. and **Gaylord, D.** 2003. The AD1040 to present Maero eruptive period of Egmont Volcano, Taranaki, New Zealand. Abstract. *Geological Society of New Zealand Miscellaneous Publication* 116A, 43.

Dingwell, D.B. and **Virgo, D.** 1987. The effect of oxidation state on the viscosity of melts in the system Na_2O-FeO-Fe_2O_3- SiO_2. *Geochimica et Cosmochimica Acta* 51, 195-205.

Dingwell, D.B., Romano, C. and **Hess, K.-U.** 1996. The effect of water on the viscosity of a haplogranitic melt under P-T-X conditions relevant to silicic volcanism. *Contributions to Mineralogy and Petrology* 124, 19-28.

Dingwell, D.B., Courtial, P., Giordano, D. and **Nichols, A.R.L.** 2004. Viscosity of peridotite liquid. *Earth and Planetary Science Letters* 226, 127-138.

Dobson, D.P., Jones, A.P., Rabe, R., Sekine, T., Kurita, K., Taniguchi, T., Kondo, T., Kato, T., Shimomura, O. and **Urakawa, S.** 1996. In-situ measurement of viscosity and density of carbonate melts at high pressure. *Earth and Planetary Science Letters* 143, 207-215.

Driedger, C.L., Schneider, D., Wessels, R. and **Ramsey, M.** 2004. Airborne thermal infrared observations during the first month of the 2004 eruption of Mount St. Helens volcano, Washington. Abstract. *American Geophysical Union* V31E-05.

Druce, A.P. 1966. Tree-ring dating of recent volcanic ash and lapilli, Mt Egmont. *New Zealand Journal of Botany* 4, 3-41.

Druitt, T.H., Edwards, L., Mellors, R.M., Pyle, D.M., Sparks, R.S.J., Lanphere, M., Davies, M. and **Barreiro, B.** 1999. Santorini Volcano. *Geological Society London Memoirs* 19, 1-176.

Einstein, A. 1906. Eine neue Bestimmung der Moleküldimension. *Annalen der Physik* 19, 289-306.

Elsworth, D., Voight, B., Thompson, G. and **Young, S.R.** 2004. Thermal-hydrologic mechanism for rainfall-triggered collapse of lava domes. *Geology* 32, 969-972.

Fink, J. 1980. Surface folding and viscosity of rhyolite flows. *Geology* 8, 250-254.

Gertisser, R. and **Keller, J.** 2003. Temporal variations in magma composition at Merapi Volcano (Central Java, Indonesia): magmatic cycles during the past 2000 years of explosive activity. *Journal of Volcanology and Geothermal Research* 123, 1-23.

Giordano, D. and **Dingwell, D.B.** 2003. Viscosity of hydrous Etna basalt: implications for Plinian-style basaltic eruptions. *Bulletin of Volcanology* 65, 8-14.

Giordano, D., Romano, C., Papale, P. and **Dingwell, D.B.** 2004a. The viscosity of trachytes, and comparison with basalts, phonolites, and rhyolites. *Chemical Geology* 213, 49-61.

Giordano, D., Romano, C., Dingwell, D.B., Poe, B. and **Behrens, H.** 2004b. The combined effects of water and fluorine on the viscosity of silicic magmas. *Geochimica et Cosmochimica Acta* 68, 5159-5168.

Goto, A. 1999. A new model for volcanic earthquake at Unzen Volcano: Melt rupture model. *Geophysical Research Letters* 26, 2541-2544.

Hammer, J.E., Cashman, K.V. and **Voight, B.** 2000. Magmatic processes revealed by textural and compositional trends in Merapi dome lavas. *Journal of Volcanology and Geothermal Research* 100, 165-192.

Harford, C.L., Sparks, R.S.J. and **Fallick, A.E.** 2003. Degassing at the Soufrière Hills Volcano, Montserrat, recorded in matrix glass compositions. *Journal of Petrology* 44, 1503-1523.

Harris A.J.L., Flynn L.P, Matias O., Rose W.I. and **Cornejo J.** 2004. The evolution of an active silicic lava flow field: an ETM+ perspective. *Journal of Volcanology and Geothermal Research* 135, 147-168.

Hess, K.-U. and **Dingwell, D.B.** 1996. Viscosities of hydrous leucogranitic melts: a non-Arrhenian model. *American Mineralogist* 81, 1297-1300.

Higgins, M.D. 1996. Crystal size distributions and other quantitative textural measurements in lavas and tuff from Egmont volcano (Mt. Taranaki), New Zealand. *Bulletin of Volcanology* 58, 194-204.

Holland, T. and **Blundy, J.** 1994. Non-ideal interactions in calcic amphiboles and their bearing on amphibole - plagioclase thermometry. *Contributions to Mineralogy and Petrology* 116, 433-447.

Hui, H. and **Zhang, Y.** 2007. Toward a general viscosity equation for natural anhydrous and hydrous silicate melts. *Geochimica et Cosmochimica Acta* 71, 403-416.

Huppert, H.E. and **Sparks, R.S.J.** 1980. The fluid dynamics of a basaltic magma chamber replenished by influx of hot, dense ultrabasic magma. *Contributions to Mineralogy and Petrology* 75, 279-289.

Huppert, H.E., Shepherd, J.B., Sigurdsson, H. and **Sparks, R.S.J.** 1982. On lava dome growth, with application to the 1979 lava extrusion of the Soufrière of St. Vincent. *Journal of Volcanology and Geothermal Research* 14, 199-222.

Le Maitre, R.W., Bateman, P., Dudek, A., Keller, J., Lameyre, J., Le Bas, M.J., Sabine, P.A., Schmid, R., Sorensen, H., Streckeisen, A., Woolley, A.R. and **Zanettin, B.** 1989. A classification of igneous rocks and glossary of terms. Blackwell Scientific. Oxford.

Lees, C.M. and **Neall, V.E.** 1993. Vegetation response to volcanic eruptions on Egmont Volcano, New Zealand, during the last 1500 years. *Journal of the Royal Society of New Zealand* 23, 91-127.

Lejeune, A.M. and **Richet, P.** 1995. Rheology of crystal-bearing silicate melts: an experimental study at high viscosities. *Journal of Geophysical Research* 100, 4215-4230.

Liebske, C., Behrens, H., Holtz, F. and **Lange, R.A.** 2003. The influence of pressure and composition on the viscosity of andesitic melts. *Geochimica et Cosmochimica Acta* 67, 473-485.

Liebske, C., Schmickler, B., Terasaki, H., Poe, B.T., Suzuki, A., Funakoshi, K., Ando, R. and **Rubie, D.C.** 2005. Viscosity of peridotite liquid up to 13 GPa: implications for magma ocean viscosities. *Earth and Planetary Science Letters* 240, 589-604.

Lyman, A.W., Koenig, E. and **Fink, J.H.** 2004. Predicting yield strengths and effusion rates of lava domes from morphology and underlying topography. *Journal of Volcanology and Geothermal Research* 129, 125-138.

Mackenzie, M.W. 1988. Advances in applied Fourier transform infrared spectroscopy. Wiley. New York.

Manga, M. and **Loewenberg, M.** 2001. Viscosity of magmas containing highly deformable bubbles. *Journal of Volcanology and Geothermal Research* 105, 19-24.

Manley, C.R. 1996. Physical volcanology of a voluminous rhyolite lava flow: the Badlands lava, Owyhee Plateau, southwestern Idaho. *Journal of Volcanology and Geothermal Research* 71, 129-153.

Marsh, B.D. 1981. On the crystallinity, probability of occurrence, and rheology of lava and magma. *Contributions to Mineralogy and Petrology* 78, 85-98.

Massol, H. and **Jaupart, C.** 1998. Gas overpressures in lava dome eruptions. Abstract. *American Geophysical Union* V32C-07.

McKay, M.E., Rowland, S.K., Mouginis-Mark, P.J. and **Garbeil, H.** 1998. Thick lava flows of Karisimbi Volcano, Rwanda: insights from SIR-C interferometric topography. *Bulletin of Volcanology* 60, 239-251.

Melnik, O.E. and **Sparks, R.S.J.** 1999. Nonlinear dynamics of lava dome extrusion. *Nature* 402, 37-41.

Melnik, O. and **Sparks, R.S.J.** 2002. Dynamics of magma ascent and lava extrusion at Soufrière Hills Volcano, Montserrat. In: **Druitt, T.H.** and **Kokelaar, B.P.** (eds.) The eruption of Soufrière Hills Volcano, Montserrat, from 1995 to 1999. *Geological Society, London, Memoirs* 21, 153-171.

Misiti, V., Freda, C., Taddeucci, J., Romano, C., Scarlato, P., Longo, A., Papale, P. and **Poe, B.T.** 2006. The effect of H_2O on the viscosity of K-trachytic melts at magmatic temperatures. *Chemical Geology* 235, 124-137.

Murase, T. and **McBirney, A.** 1973. Properties of some common igneous rocks and their melts at high temperatures. *Geological Society of America Bulletin* 84, 3563-3592.

Murase, T., McBirney, A.R. and **Melson, W.G.** 1985. Viscosity of the dome of Mount St. Helens. *Journal of Volcanology and Geothermal Research* 24, 193-204.

Navarro-Ochoa, C., Gavilanes-Ruiz, J.C. and **Cortes-Cortes, A.** 2002. Movement and emplacement of lava flows at Volcan de Colima, Mexico: November 1998-February 1999. *Journal of Volcanology and Geothermal Research* 117, 155-167.

Neuville, D.R., Courtial, P., Dingwell, D.B. and **Richet, P.** 1993. Thermodynamic and rheological properties of rhyolite and andesite melts. *Contributions to Mineralogy and Petrology* 113, 572-581.

Newhall, C.G. and **Melson, W.G.** 1983. Explosive activity associated with growth of volcanic domes. *Journal of Volcanology and Geothermal Research* 17, 111-131.

Pal, R. 2003. Rheological behavior of bubble-bearing magmas. *Earth and Planetary Science Letters* 207, 165-179.

Pinkerton, H. and **Stevenson, R.J.** 1992. Methods of determining the rheological properties of magmas at sub-liquidus temperatures. *Journal of Volcanology and Geothermal Research* 53, 47-66.

Platz, T. 2001. Mapping and characterisation of the volcaniclastic Maero formation deposits on the northwestern sector of Egmont volcano (Mt. Taranaki), New Zealand. Unpublished Diploma mapping thesis. Ernst-Moritz-Arndt Universität, Greifswald, Bundesrepublik Deutschland.

Platz, T., Foley, S.F. and **André, L.** 2004. Low-pressure fractionation of the Nyiragongo volcanic rocks, Virunga Province, D.R. Congo. *Journal of Volcanology and Geothermal Research* 136, 269-295.

Platz, T., Cronin, S.J, Cashman, K.V., Stewart, R.B. and **Smith, I.E.M.** 2007. Transition from effusive to explosive phases in andesite eruptions - a case-study from the AD1655 eruption of Mt. Taranaki, New Zealand. *Journal of Volcanology and Geothermal Research* 161, 15-34.

Richet, P., Lejeune, A.-M., Holtz, F. and **Roux, J.** 1996. Water and the viscosity of andesite melts. *Chemical Geology* 128, 185–197.

Robertson, R., Cole, P., Sparks, R.S.J., Harford, C., Lejeune, A.M., McGuire, W.J., Miller, A.D., Murphy, M.D., Norton, G., Stevens, N.F. and **Young, S.R.** 1998. The explosive eruption of Soufriere Hills Volcano, Montserrat, 17 September, 1996. *Geophysical Research Letters* 25, 3429-3432.

Roman, D.C., Cashman, K.V., Gardner, C.A., Wallace, P.J. and **Donovan, J.J.** 2006. Storage and interaction of compositionally heterogeneous magmas from the 1986 eruption of Augustine Volcano, Alaska. *Bulletin of Volcanology* 68, 240-254.

Romano, C., Giordano, D., Papale, P., Mincione, V., Dingwell, D.B. and **Rosi, M.** 2003. The dry and hydrous viscosities of alkaline melts from Vesuvius and Phlegrean Fields. *Chemical Geology* 202, 23-38.

Roscoe, R. 1952. The viscosity of suspensions of rigid spheres. *British Journal of Applied Physics* 3, 267-269.

Sahetapy-Engel, S.T.M., Flynn, L.P., Harris, A.J.L., Bluth, G.J., Rose, W.I. and **Matias, O.** 2004. Surface temperature and spectral measurements at Santiaguito lava dome, Guatemala. *Geophysical Research Letters* 31, L19610.

Sato, H. 2005. Viscosity measurement of subliquidus magmas: 1707 basalt of Fuji volcano. *Journal of Mineralogical and Petrological Sciences* 100, 133-142.

Sato, H., Nakada, S., Fujii, T., Nakamura, M. and **Suzuki-Kamata, K.** 1999. Groundmass pargasite in the 1991-1995 dacite of Unzen volcano: phase stability experiments and volcanological implications. *Journal of Volcanology and Geothermal Research* 89, 197-212.

Scandone, R. and **Malone, S.D.** 1985. Magma supply, magma discharge and readjustment of the feeding system of Mount St. Helens during 1980. *Journal of Volcanology and Geothermal Research* 23, 239-262.

Scholz, E. 1984. Karl Fischer Titration. Springer Verlag. Berlin.

SEAN 02:03. Smithsonian Institution, 1977. Mount Nyiragongo. Scientific Event Alert Network vol. 2, no. 3.

Shaw, H.R. 1972. Viscosities of magmatic silicate liquids: an empirical method of prediction. *American Journal of Science* 272, 870-893.

Siswowidjoyo, S., Suryo, I. and **Yokoyama, I.** 1995. Magma eruption rates of Merapi volcano, Central Java, Indonesia during one century (1890-1992). *Bulletin of Volcanology* 57, 111-116.

Sparks, R.S.J. 1997. Causes and consequences of pressurisation in lava dome eruptions. *Earth and Planetary Science Letters* 150, 177-189.

Sparks, R.S.J., Murphy, M.D., Lejeune, A.M., Watts, R.B., Barclay, J. and **Young, S.R.** 2000. Control on the emplacement of the andesite lava dome of the Soufriere Hills volcano, Montserrat by degassing-induced crystallization. *Terra Nova* 12, 14-20.

Stewart, R.B., Price, R.C. and **Smith, I.E.M.** 1996. Evolution of high-K arc magma, Egmont volcano, Taranaki, New Zealand: evidence from mineral chemistry. *Journal of Volcanology and Geothermal Research* 74, 275-295.

Stolper, E. 1982. The speciation of water in silicate melts. *Geochimica et Cosmochimica Acta* 46, 2609-2620.

Stuart, B.H. 2004. Infrared spectroscopy: fundamentals and applications. John Wiley and Sons Ltd. Chichester.

Suto, S., Sakaguchi, K., Watanabe, K., Saito, E., Kawanabe, Y., Kazahaya, K., Takarada, S. and **Soya, T.** 1993. Dynamics of flowage and viscosity of the 1991 lava of Unzen Volcano, Kyushu, Japan. *Bulletin of the Geological Survey of Japan* 44, 609-629.

Taron, J., Elsworth, D., Thompson, G. and **Voight, B.** 2007. Mechanisms for rainfall-concurrent lava dome collapses at Soufrière Hills Volcano, 2000-2002. *Journal of Volcanology and Geothermal Research* 160, 195-209.

Toplis, M.J. and **Dingwell, D.B.** 1996. The variable influence of P_2O_5 on the viscosity of melts of differing alkali/aluminium ratio: implications for the structural role of phosphorus in silicate melts. *Geochimica et Cosmochimica Acta* 60, 4107-4121.

Toplis, M.J., Dingwell, D.B. and **Libourel, G.** 1994. The effect of phosphorus on the iron redox ratio, viscosity, and density of an evolved ferro-basalt. *Contributions to Mineralogy and Petrology* 117, 293-304.

Voight, B., Sparks, R.S.J., Miller, A.D., Stewart, R.C., Hoblitt, R.P., Clarke, A., Ewart, J., Aspinall, W.P., Baptie, B., Calder, E.S., Cole, P., Druitt, T.H., Hartford, C., Herd, R.A., Jackson, P., Lejeune, A.M., Lockhart, A.B., Loughlin, S.C., Luckett, R., Lynch, L., Norton, G.E., Robertson, R., Watson, I.M., Watts, R. and **Young, S.R.** 1999. Magma flow instability and cyclic activity at Soufriere Hills Volcano, Montserrat, British West Indies. *Science* 283, 1138-1142.

Whittington, A., Richet, P., Linard, Y. and **Holtz, F.** 2001. The viscosity of hydrous phonolites and trachytes. *Chemical Geology* 174, 209-223.

Wooster, M.J., Kaneko, T., Nakada, S. and **Shimizu, H.** 2000. Discrimination of lava dome activity styles using satellite-derived thermal structures. *Journal of Volcanology and Geothermal Research* 102, 97-118.

Zernack, A., Stewart, R.B. and **Price, R.C.** 2006. Slab or crust - K_2O enrichment at Egmont volcano, New Zealand. Abstract. *Geochimica et Cosmochimica Acta Supplement* 70, 614.

Zimova, M. and **Webb, S.L.** 2007. The combined effects of chlorine and fluorine on the viscosity of aluminosilicate melts. *Geochimica et Cosmochimica Acta* 71, 1553-1562.

Chapter 8 Conclusions

Over the last 1000 yrs of activity at Mt. Taranaki, a range of eruption products were generated: from pyroclastic flow deposits (i.e. Block-and-Ash Flow deposits, pumice flow units and surge deposits), to ash, lapilli, and pumiceous tephra layers, along with lava flows and domes. The previous eruptive reconstruction of this period, (here newly defined as the Maero Eruptive Period), have been revised to comprise at least 10 eruptive episodes, including predominantly extrusive, lava dome- and lava flow-producing eruption episodes and one explosive, sub-Plinian eruption. Field-stratigraphy and glass chemical studies were used to correlate tephra units across different sectors of the mountain. A new stratigraphy of the Maero Formation is introduced, which correlates fall units of the eastern and southern flanks to pyroclastic flow and fall deposits of the western to northwestern sector. A replacement type section for the Maero Formation is defined in Maero Stream with an additional 9 reference sites positioned around the edifice. Despite the detailed knowledge of lava dome-forming episodes, the stratigraphic classification of lava flow-producing eruptions is still poorly constrained. Also, it remains unknown whether lava flow-forming eruptions represent individual eruptive events or were related to lava-dome eruptions.

As a result of analysing glass compositions of ash particles derived from flow and fall deposits, a new evaluation procedure has been developed that examines glass datasets for contaminated mineral-glass analyses. These hybrid analyses can be identified by using bivariate compositional diagrams where an incompatible and a compatible element oxide of the mineral phase is plotted. Because this is a simple mixing relationship, hybrid analyses are detectable if linear data trends point towards the composition of the mineral phase. Once potential hybrid analyses have been detected they must be checked for all other remaining element oxides. Although exclusion of contaminated glass analyses improves and clusters the glass dataset by reducing the sample variance, analysed ash/lapilli particle textures also need to be examined. It was

demonstrated that during any one eruption episode a range of particle types form during individual eruption phases. Hence, tephras at Mt. Taranaki commonly contain two or more particle populations, each having matrix glass of differing compositions. Hence, particle glass chemistry from the combined unit may be unusable for tephra correlation purposes. Through the study of particle textures, glass chemistry and the application of the glass data evaluation procedure, a higher degree of resolution of the tephrostratigraphic record can be achieved.

Detailed studies on the remnant summit dome of Mt. Taranaki were carried out to understand lava dome emplacement and destruction mechanisms. It has been shown that the remnant dome (Pyramid Dome) was not formed during the Tahurangi eruptive episode but extruded post-AD1755. The main evidence for this conclusion stems from bulk rock geochemistry and the internal structure of the dome. Identified Tahurangi Block-and-Ash flow (BAF) deposits have a different composition from the Pyramid Dome, particularly in Al_2O_3, Mg#, Cr and Zr contents. The homogenous dome composition, its simple structure, and the absence of former dome remnants in the crater, clearly indicate an individual eruption, the Pyramid eruptive episode. Reconstruction of the inferred original dome geometry implies extrusion of a maximum volume of 5.9×10^6 m^3 (4.9×10^6 m^3 DRE) of lava. Due to the crater morphology, the dome was emplaced partially onto the crater floor as well as on the upper steep north-western flank, where some lava lobes advanced up to 300 m downhill. The observation of individual lava lobes on the upper flank, the hemispherical eastern dome side within the crater and the occurrence of blocky lava flows imply simultaneous endogenous and exogenous dome growth. In consideration of the texture of hornblende crystals and the formation of a thin vesicular dome carapace, it is further concluded that emplacement duration was rapid. By comparing the dome hornblende compositions with other well-studied volcanoes, it is assumed that Taranaki hornblende is stable up to 1 kbar or c.2 km depth. The arrival of pristine hornblende within the lava dome suggests minimum magma ascent rates of 0.012 ms^{-1}. Hence, the Pyramid Dome emplacement could have taken place within days. The magma storage depth(s) are only poorly constrained and based only on the hornblende geobarometer. According to this geobarometer, hornblende crystallises at pressures between 3-5 kbar (c.9.5-17 km). The lower crystallisation limit coincides with depth estimates of the Brittle-Ductile Transition Zone beneath Mt. Taranaki. Hence, magmas may stagnate at this level due to reaching

the level of neutral buoyancy. However, it is emphasised that temporary shallower magma stalling levels may also exist, as evidenced from co-magmatic xenoliths.

The rock-avalanche deposit generated by the Pyramid (summit) Dome failure was interpreted to have occurred at or below c.350 °C, based on the random magnetic alignment of clasts. This also implies that the dome was at similar temperatures, i.e., cool. Hence, an important conclusion is that the dome probably failed years after its formation, implying a potentially unexpected post-eruptive hazard. By applying simple conductive cooling models, a period of about 19 yrs is required to cool the dome to c.350 °C, or 74 yrs for it to cool completely. Although the date of the Pyramid eruption cannot be well constrained, it most likely took place at some time in the period AD1839-1866.

Transitions from initially extrusive, dome-forming eruptions to explosive, sub-Plinian phases can occur suddenly and without any warning. This occurred during the AD1655 Burrell episode, which produced widespread deposits of pumice fallout, pyroclastic pumice flows, BAFs and surges. The fallout, which was initially directed towards E and then NE is dominated by grey, highly vesicular pumice clasts and a large (c.14%) component of dense lithic fragments. In contrast, pumice flow deposits show a variety of vesicular clasts ranging from brown and grey coloured pumice to semi-vesicular to vesicular black scoria. Dense lithics, breadcrust bombs, and accidental wall rock clasts are also common. Pumice flow deposits are restricted to the upper to mid flanks of the volcano, and are predominantly preserved on the steep volcano flanks. Block-and-Ash flow deposits are found predominantly on the NW sector; the major BAF unit during the Burrell episode travelled down the Hangatahua River more than 13.5 km from source. Pumice clasts at c.6 vol.% are the second most abundant component in this deposit. The total volume of erupted magma during the Burrell episode is estimated at 0.12 km^3 DRE. The formation of a variety of dense to vesicular clasts during this event was related to differing eruption phases. The grey lithic clasts likely represent the initial extrusive phase, where a dome within the summit crater was formed. Dome removal generated BAFs and triggered an explosive, sub-Plinian eruption. The sub-Plinian phase was further subdivided into three pulses in which grey, brown and grey pumice clasts erupted. Each pulse corresponded to individual layers in the conduit caused by different degrees of vesiculation and crystallisation. The magma producing brown pumice clasts contained more microlites and had a more evolved matrix glass composition compared to magmas above and below it, which produced grey pumice. Since there are no

geophysical indicators for large magma batches in the upper crust, magma ascent is assumed to start at depths of c.9.5 km. The bulk compositional variation of erupted clasts (pumice to dense dome rocks) can be modelled by fractionation of hornblende, plagioclase, clinopyroxene, and Fe-Ti oxides. The differentiation to more silicic dome rocks occurred during magma ascent up to depths of 2 km, where the inferred stability limit of hornblende is reached, i.e. at shallower depth hornblende is not a fractionating phase and hence, rock differentiation is significantly lowered.

The Maero Eruptive Period consists of at least 10 eruptive episodes of contrasting eruptive style. It appears that every eruptive period produced lava dome(s), some of them preceded by a vent-clearing phase producing single lithic layers around the edifice (Newall Ash a, Mangahume Lapilli, Pyramid Lapilli). The type of dome failure controlled successive eruptive phases in most instances. Gravitational dome failures did not cause a change in eruptive style, as inferred for the Tahurangi episode. By contrast, the destruction of a pressurised dome caused instantaneous but short-lived magmatic fragmentation (Newall and Puniho episodes) or triggered a directed blast-explosion (Newall episode), or initiated sustained magmatic fragmentation (Burrell Episode).

From a hazard and emergency management perspective, the above described results are important in showing the variety of courses a future eruption may take at Mt Taranaki. They also point out that eruptions at this volcano are often more than just “one-off” occurrences. Instead, some of the recent episodes (e.g. the Burrell Episode), involved a long and complex chain of events that may have taken place over several months of activity. If Mt Taranaki continues to behave as it has over the last 1000 years, the next eruption will very likely involve dome extrusion, probably preceded by vent clearing blasts. The course of events thereafter will be highly dependent on (1) the state of the dome and upper conduit – particularly its ability to degas and the supply rate of new magma, and (2) the stability of the crater area. These features should be intensely monitored, and samples of ash or dome material taken on many occasions to compare and contrast to the described Maero Period events. The results of this study show that a highly explosive event is a possibility, but by no means certain during any future eruption. In addition, since the most widespread and destructive events are likely to be dense pyroclastic flows or BAFs, the geometry of the summit area will be highly critical to determine areas at greatest risk.

8.1 Avenues of Future Research

In completing this study, it is recognised that it is only a step along the way to understanding the overall scientific questions of andesitic volcanism, as well as answering questions of likely volcanic risk at Mt Taranaki. Upon completion of this work, the following issues and questions are raised for subsequent studies:

1) The knowledge of water concentrations in silicate glasses is essential in order to understand degassing processes prior to and during volcanic eruptions. What is the total water budget dissolved in the pre-eruptive magma? How much water escapes during magma ascent through permeable wall rocks? How much water is released during the eruptions, and how much water remains in volcanic glasses? What other volatile components (e.g. F, Cl, CO_2, SO_3) are released during eruptions and what is their impact on surrounding areas. Preliminary results of using thermal analysis for water estimates in matrix glasses are encouraging and may answer some of the above questions.

2) For a better understanding of magmatic fragmentation, e.g. during sub-Plinian eruptions, porosity determinations of pumice clasts need to be complemented by studies on bubble aperture widths and tortuosities of vesicular samples (e.g. by electrical conductivity and high-resolution X-ray tomography). These results will help constrain timescales of degassing and fragmentation.

3) Tectonic aspects, such as the surrounding stress regime of volcanoes, need further consideration in understanding volcanic processes. At Mt. Taranaki, for example, this has not yet been concentrated on in detail. The occurrence of repeated edifice failure and the presence of faults near, and presumably beneath the volcano, may have impacts on the eruptible magma volume and composition. Sudden edifice collapse and hence, pressure release may promote the ascent and eruption of larger magma batches at depth. Changes in the prevailing crustal stress regime, for example from compressional to extensional, may enable and ease dyke initiation and propagation and thus trigger magma movement in the crust. Seismic monitoring techniques are the most reliable (and only) methods to identify precursors of magma movement within the mid-upper crust. Using the petrographic results from this study, critical areas to be focussed upon are potential mid-crustal ponding areas, where rising magmas may initially stall due to their initially high density. Hence, the collaboration between geophysicists, geologists, and

volcanologists need to be intensified and focussed on geophysical monitoring techniques.

4) What is the maximum load pressure of lava that Mt Taranaki's summit crater can resist before failure? The determination and assessment of the mechanical rock properties of crater-rim lava flows will aid hazard mitigation during future volcanic eruptions. For example, should a lava dome slowly grow within a summit crater, the hazard zone could be extended once the estimated threshold value for the structural stability of the crater walls is exceeded. Thus, the loss of lives can be prevented (or reduced) by sudden dome collapse due to flank instabilities and the possible triggering of a blast-explosion or sub-Plinian eruption.

5) During the Maero Eruptive Period many Block-and-Ash flows were generated by the destruction of lava domes but only a few of them travelled >10 km from source. What are the physical aspects controlling pyroclastic-flow runouts? What effect do topography, vegetation, and channelisation have on the runout of pyroclastic flows? Do the physical properties of the lava dome (e.g. temperature, rock strength, density) influence the flow behaviour of Block-and-Ash Flows?

Appendices

Type and Reference Sections **V**

Type Section of the Maero Formation – Maero Stream V

Reference Section 1 – Pyramid Stream XV

Reference Section 2 – Hangatahua River XXI

Electron Microprobe Analysis **XXV**

Amphibole XXV

Apatite XXXI

Biotite XXXIII

Clinopyroxene XXXIV

Fe-Ti Oxides XLI

Glass Inclusions XLVII

Matrix Glass LIII

Olivine LXXVII

Orthopyroxene LXXVIII

Plagioclase LXXIX

X-ray Fluorescence Spectroscopy **LXXXIII**

Major Element Oxides LXXXIII

Trace Elements XXXVI

Laser Inductively Coupled Plasma Mass Spectroscopy **LXXXIX**

Trace Elements LXXXIX

Appendices on DVD

Digital Copy of Thesis

Fourier Transform Infrared Spectroscopy

Graphs

Images

Geochemistry

Electron Microprobe Analysis

Original Data Files and Images

Amphibole

Apatite

Biotite

Clinopyroxene

Fe-Ti Oxides

Glass Inclusions

Matrix Glass

Olivine

Orthopyroxene

Plagioclase

Unknown Minerals

Laser Inductively Coupled Plasma Mass Spectroscopy

Original Data Files

Laser ICP-MS Data

X-ray Fluorescence Spectroscopy

Original Data Files

XRF Analyses

Permeability

Graphs

Original Data Files

Permeability_2003&2004

Porosity

Massey_2006

Oregon_2003&2004

Reference List

Selected References

Scanning Electron Microscopy

Massey

Oregon

Thermal Analysis

Original Data Files

DSC-TGA Analysis

Thin Section Photographs

Type and Reference Sections

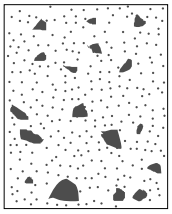
Reference Section 1

Reference Section 2

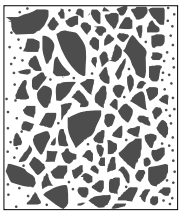
Type and Reference Sections

Type Section

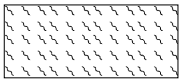
Key to Stratigraphic Columns



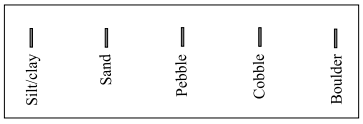
Poorly sorted diamicton,
matrix-supported



Poorly sorted diamicton,
clast-supported



Present or buried soil



Maximum clast size
present in deposit



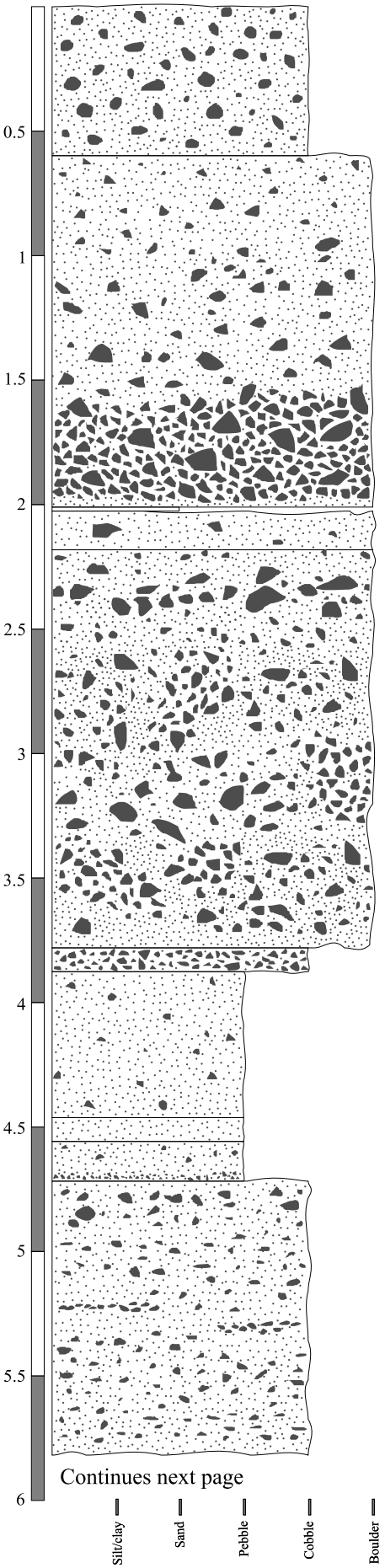
Scale given in meters;
Against geological convention, the reference level was chosen to be the present day surface for a better orientation in the field, i.e. field description occurred from top to bottom.

Type section of the Maero Formation

described by Platz (2001)

Maero Stream, approximately 50 m upstream of the previous type section of Neall (1979), true right side.

North: 6214019 East: 2596823 Height: c.680 m



60 cm brownish grey silty sandy matrix-supported diamicton, with present soil development, subangular to subrounded clasts, grey and brownish grey dominated, 5% strong brown and orange, matrix sample DS1, diagenic iron staining near base, sharp contact, sample T04-171 (dense grey lithic)
Dmax: 21, 20, 16, 15 [cm]

1.4 m, clast rich diamicton with weak soil development in upper 10 cm, weakly normally graded, clast supported near base, 30% matrix, pervasive reddish and purplish oxidised 30-40 cm top, 98% black/dark grey, 1% pale, 1% orange-stained clasts, highly angular clasts, loose friable unit, basal 5 cm, brown stained matrix and clast depleted zone with fine tussock charcoal fragments, charcoal DS2, matrix DS3, Lithic clast samples Ds6 and T04-170, sharp contact
Dmax: 42, 33, 30, 28, 27, 25, 30 [cm], mode 10 cm
Magnetism: aligned (9x)

1-3 cm pale brown-pale brownish grey med-fine sand, firm, grading into
15 cm strong brown and red med-coarse sand, between rare med-boulder clasts, grading into

1.6 m, bouldery diamicton, with large clasts concentrated near the top, but boulders throughout unit, grey dominant + pale grey pumice (2%), orange stained (3-5%), upper 30-40 cm pervasive red oxidation of matrix and clasts, highly angular and some sub-rounded clasts, sandy matrix clast rich (clast supported in places) diamicton, up to 70% clasts, matrix sample DS 4, Jig-saw fractured clasts, broken in place and undisrupted, pumice from unit sampled as DS 5, lithic clast sample DS 7
Dmax: 40, 35, 35, 40, 30, 30, 30 [cm]
Magnetism: aligned (10x)
Basal portion, clast depleted for 10 cm

0-10 cm pebble-cobble fines depleted (lag?) deposit, subangular grey (90%) and orange-stained, sharp contact

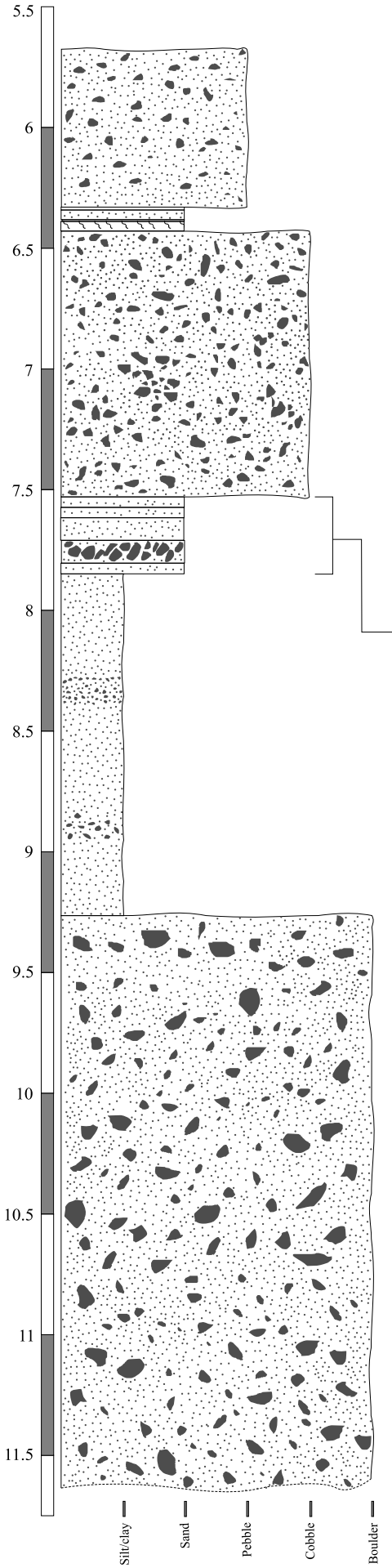
60 cm, sandy matrix-supported, clast poor (20%) diamicton, 15 % orange stained clasts, and upper 10 cm reddish pervasive oxidation of matrix and clasts, pebble dominant clasts Dmax: 4-5 cm

20 cm brownish grey sandy matrix diamicton, pebbly with weak soil development

30 cm, grey pebbly sandy matrix diamicton, up to fine-pebble clasts, massive and matrix supported, bulk sample DS 8, Dmax 6 cm, grey 60%, orange 30%, and pale grey, basal portion fines poor, clast-supported zone in lower 5 cm, sharp contact
Magnetism aligned (10x)

1.1 m, grey sandy matrix-supported diamicton, 50% matrix, grey 99% and pale grey, Dmax 12 cm near top, within unit, 6-8 cm, upper 15 cm pervasive dark red oxidation of matrix and clasts, bulk sample DS 9, weak planar fabric in parts with cobble strings and coarse fragment depleted layers, large charcoal log (DS 10) 15 cm above base, lying parallel with horizontal fabric, lower 30-40 cm coarse clast depleted and Dmax = 4 cm, no discolouration around the charcoal log., v rare orange clasts, lower 2-5 cm pale grey med sand, clast lithology sample Ds22, sharp erosional wavy contact
Magnetism: aligned (10x)

Type section of the Maero Formation (continued)



68 cm, fine grained diamicton with dark brown humic stained soil preserved in parts of the upper 5 cm, diamicton grey sandy matrix-supported, with 30% fine pebble clasts, Dmax 4 cm, 99% grey, massive and weak planar fabric in places, Large charcoal logs parallel to bedding , DS11 charcoal, DS 12 bulk sample, lower part particularly clast poor, rare orange stained clasts near lower contact, sharp erosive contact, undulating over 5-10 cm

5 mm pale brown and pale greyish brown fine ash, pocketing
grading into
4 cm normally graded pale grey med ash with common fine charcoal fragments, bulk DS13, grading into coarse-med poorly sorted ash (DS14 bulk sample), with common fine-grained charcoal (DS 15)
1mm pocketing fine pale brown ash, sharp contact

4-5 cm dark brown humic stained sandy soil

1.1 m brownish grey and strong brown and red stained sandy matrix diamicton, friable, with 50% grey, 30% orange, 10% greyish brown and pale grey subangular clasts, Dmax, 20-30 cm, modally pebbles and fine cobbles, clast rich 70%, matrix sample DS16, upper 40 cm dark brown humic staining, strong iron staining at base
Magnetism: aligned (10x)

1-5 cm pale brown fine ash with charcoal fragments, DS17
grading into
2-5 cm pale grey med ash with 4cm diameter rip up clasts of fine brown ash.
grading into
10 cm coarse-med ash, grey and pale brown (40%), fines depleted, with rip-up clasts of fine brown ash

0-10 cm, preserved only in pockets within swales, pale brown and pale olive brown ash, wavy bedding, with lenses of grey fine-med ash (fluvial)

0-5 cm grey med ash in base of swales

1.4 m, brown greasy clay loam, upper 40 cm dark brown humic stained with leaves, twigs, and branches along upper surface, at 40 cm a 15 cm reddish and grey coarse ash-fine lapilli, 40 cm above base pale yellow and pale brown single line of lapilli, irregular contact, sharp over 40 cm

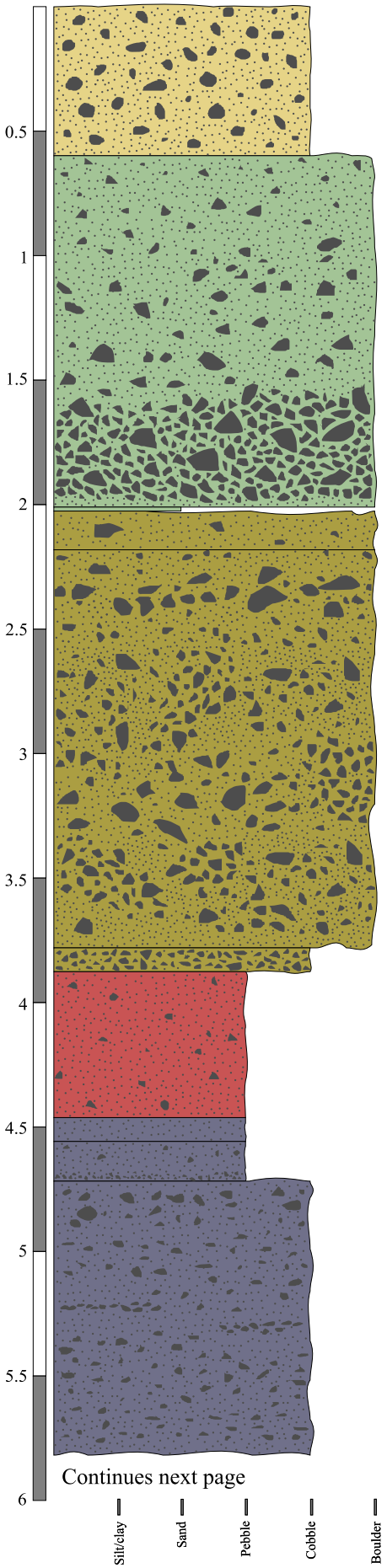
>2.5 m, diamicton, upper 60 cm pervasive reddish oxidation, below is grey and highly uniform with little contrast between clasts and matrix, clasts 30-40%, including large boulders, matrix med-coarse sand, Dmax: 1.5-0.4 m. matrix sample from basal half DS 20, clast lithology sample Ds24
Magnetism: aligned (10x)

Type section of the Maero Formation

described by Platz (2001)

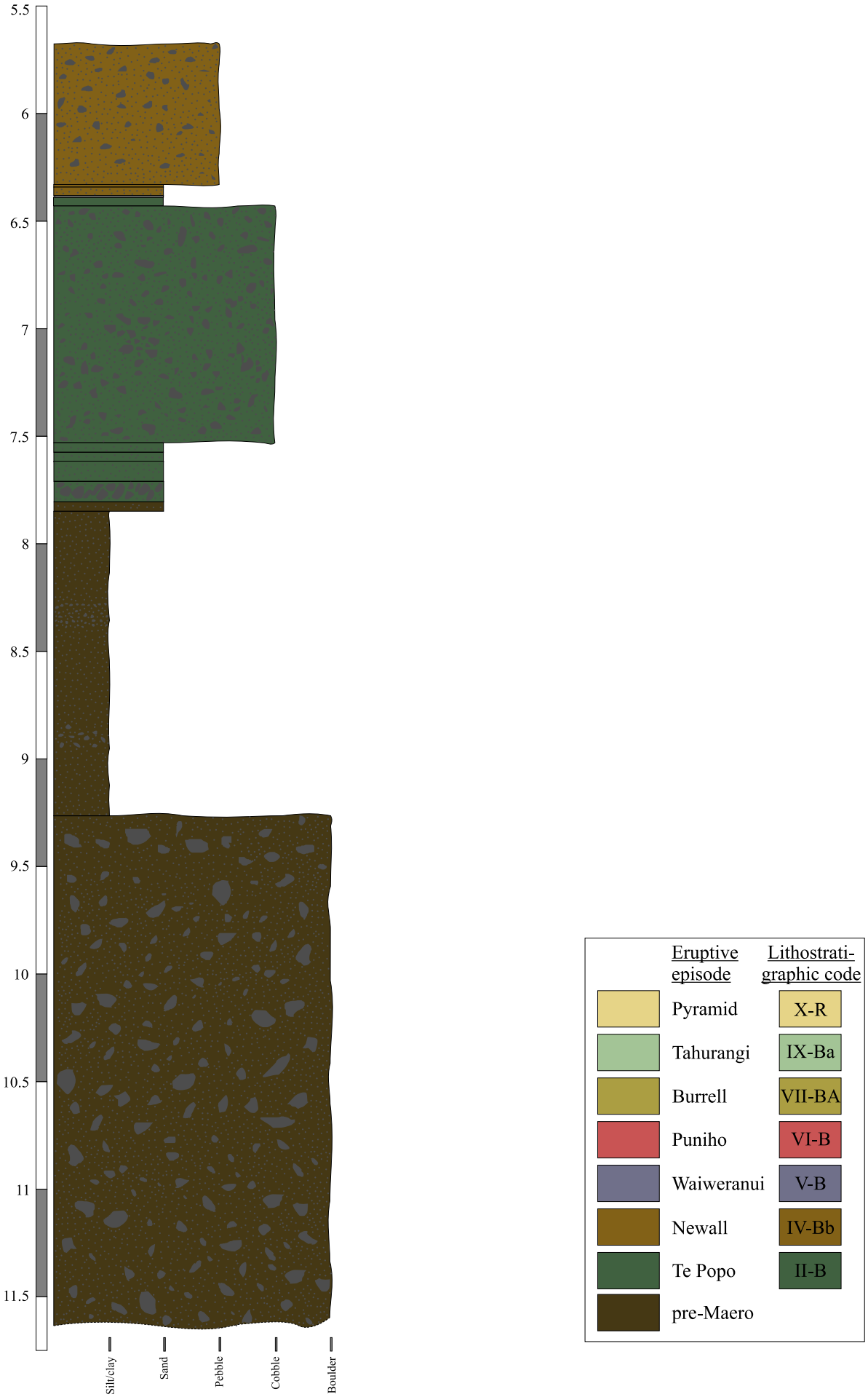
Maero Stream, approximately 50 m upstream of the previous type section of Neall (1979), true right side.

North: 6214019 East: 2596823 Height: c.680 m



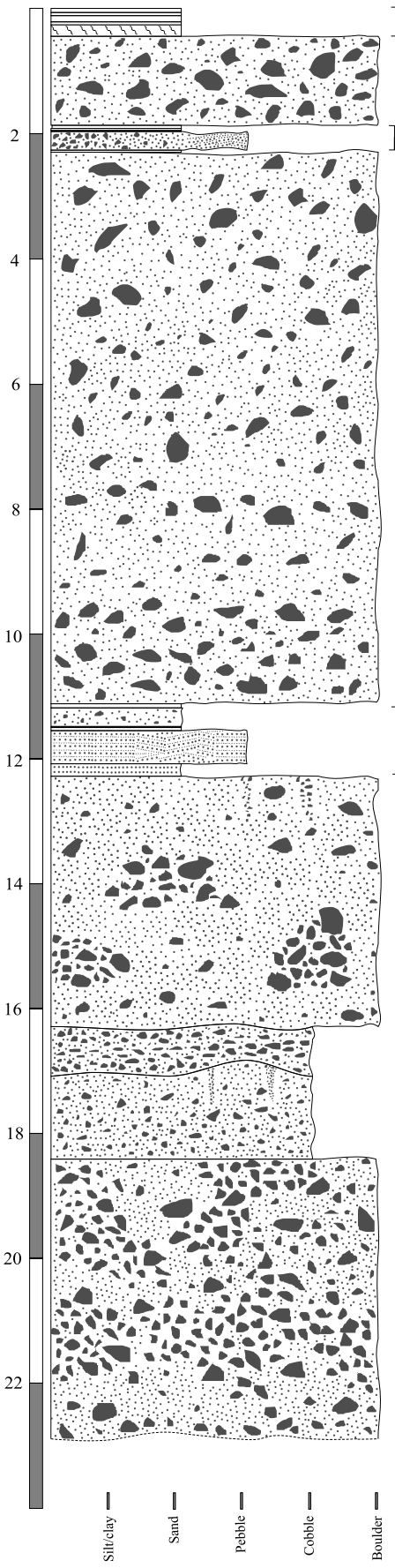
Eruptive episode	Lithostratigraphic code
Pyramid	X-R
Tahurangi	IX-Ba
Burrell	VII-BA
Puniho	VI-B
Waiweranui	V-B
Newall	IV-Bb
Te Popo	II-B
pre-Maero	

Type section of the Maero Formation (continued)



Reference section No. 1

described by Platz (2001)
lower Pyramid Stream, true right side
North: 6214537 East: 2597581 Height: c.700 m



Dark brown humic sandy loam, up to 10 cm thick

8 cm, strong brown sandy loam with 30% pebbles (max. diameter 5 cm)

Olive grey silty sand, varies 0-20 cm in thickness, 40% angular grey pebbles in thicker sections, sample T04-168 (grey dense lithic)

Olive grey fine sandy loam, 4 cm

15 cm, brown humified top of diamiction

Poorly sorted, massive diamicton, 1.4 m thick, lower 28 cm grey sandy matrix, dominantly pebble clasts, passes up into steel grey sandy matrix, 30-40% clasts up to 20 cm diameter (av. 5-10 cm), Lithology: dominantly grey andesite with rare reddish brown altered andesite, very rare rounded pumice
Dmax: 33, 24, 23, 22, 18, 17, 17, 16, 16, 16 [cm]
Lithology: dense ang grey andesite, 40; rounded pumice, 1; reddish br. hydrothermal, 5; matrix, 61
Magnetism: aligned (9x)
Py5-matrix, Py6-bulk sample from basal 28 cm, T04-167 (grey lithic clast)

Sharp contact, erosive, 2.5 cm thick, pocketing pale greyish brown, fine to medium ash, well sorted, underlain by 5 mm of very pale fine ash, drapes underlying layer
Py7-greyish brown ash, Py8-pale ash

1.5 cm black, fibrous moss, not charred (slightly lignified), 1-2 cm thickness variation

1 cm brown stained sand

27 cm, pale brown to yellowish brown, gravelly sand (clast-supported, 10% gravel); discontinuous bedding, low angle cross-stratification + planar bedding; some clasts are hydroth altered, rip-up clasts clay loam, discontinuous layers of fine ash and finer within deposit; pinches and swells

Pale greyish brown, fine ash, 0.5 cm thin, charcoal bearing, (coig ash with underlying), shower-bedded, pinches out to 0 over 10 m scale, Py9-ash, Py10-charcoal

Upper 2.4 m: reddish matrix, lower portion steel grey
Upper red: medium to coarse sandy matrix, reddish grey, colour pervasive into clasts, 2-3% hyd alt clasts, massive, clasts angular to subangular, hard andesite, grey lithic sampled as T04-166
Dmax: 60, 56, 55, 50, 40, 40, 40, 40, 28, 28 [cm]
Dmax (hydrothermal) 5-6 cm
Lithology: dense grey andesite, 40; hydro alt andesite, 5; black glassy andesite, 5; pumice <1 (noted); matrix, 50; Py12-matrix
Magnetism: aligned? (7x)
Middle (grey): coarse to medium ash matrix, uniform grey colour, clast assemblage similar to red portion, Py13-matrix
Dmax: 70, 70, 55, 50, 45, 40, 38, 35, 32, 32 [cm]
Lithology: dense grey, 42; hydro alt. andesite, 1; black glassy andesite, 2; matrix, 60
Lower (grey): coarse to medium ash, dark grey matrix, clast rich, angular, some subrounded, glassy and normal (grey) andesite, 60% clasts, massive, Py14-matrix
Lithology: black glassy, 1; normal, 64; hydro alt, 3; matrix, 41
Dmax: 80, 70, 60, 45, 35, 30, 30, 28, 26 [cm]
Magnetism: aligned? (7x)
Irregular, erosive basal contact, 5 cm relief

Brownish grey, massive, medium ash, 6 cm, Py16-ash, charcoal; underlain by 5 mm grey fine ash, down to 2 mm pale brown, fine ash, draping charcoal on underlying surface

30 cm, grey, massive, medium sand dominated unit, grades over 10 cm into pebbly diamicton, angular clasts, small charcoal fragments throughout, large oriented branches or stems at top (see later) (Py15-charcoal=Py2), clasts angular normal andesite, rare pumice and hydro alt red clasts, orientation: 5deg@295, 18@326, 5@298, <5@298, <5@294, <5@310, <5@299, 30@115(large), 25@230, 0@305, 0@324; Py17-bulk sample(middle), unit is vesiculated in upper 10 cm 2-5 mm vesicles
Charred litter layer, 10 mm, Py18-sample includes some of underlying unit

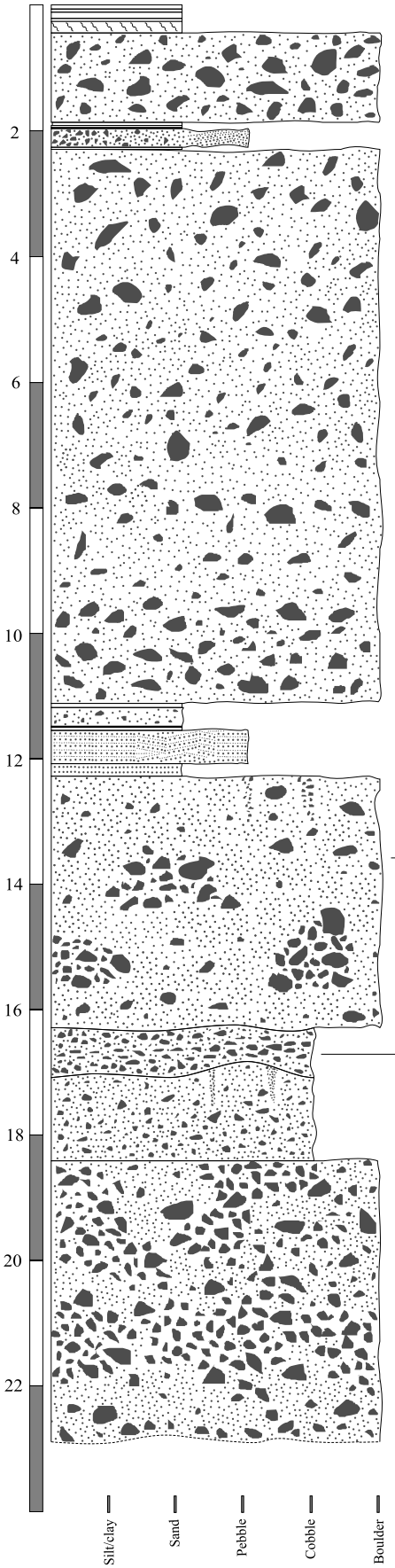
Dark brown humic pebbly sand, massive, 9cm

47 cm, brownish grey, friable, planar and cross-bedded sand with 1-3 cm scale beds, up to 30% pebbles, 80% clasts light-dk grey andesite, 10% rounded pumice, 10% hydro alt, Py19-bulk sample, fine layers vesiculated

Pale brown and greyish brown, fine to medium ash, pinching up to 23 cm, high-angle cross-stratified and laminated on a 1-5 mm scale, fine grained layers highly vesiculated (20-30%, 2-3 mm dia) incl. small charcoal fragments, Py20-cross-bedded coarser unit

Description continues next page

Reference section No. 1 (continued)



Top 20 cm: normally graded, reddish brown, medium to coarse sand (10 cm), grading to grey coarse ash, fines depleted gas pipes, 1.5 to 2 cm dia up to 15 cm through med sand, filled with grey coarse sand, charcoal throughout, Py21-charcoal, samples: T04-162 (pumice), T04-163 (lithic, T04-164 (matrix)
Massive, clast-rich diamicton, 4 m thick, varies laterally from matrix to clast-supported, angular to subangular pebbles to boulders, yellow/orange ochre staining in upper 2 m, lower dark grey, normal and significant pumice up to 10-15 cm, pumice concentration near top of unit, often subrounded
Dmax: 38, 27, 26, 26, 25, 25, 25, 25, 22, 20 [cm]
Lithology: normal, 71; pumice, 8; hydro alt, 3; matrix, 24
Magnetism: lithics: aligned? (7x); pumice upper: aligned ? (8x)
Py22-matrix middle

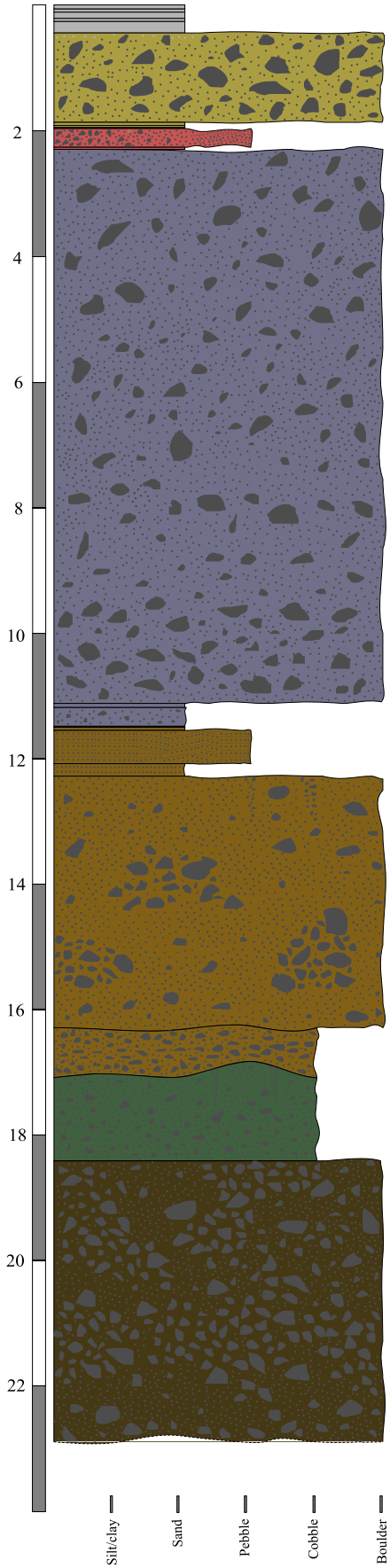
Clast-supported diamicton, 75 cm, coarse to medium sandy matrix, clasts to cobble size but dom pebble faint planar fabric+low angle faint cross bedding defined by clast lines ?pinches and swells, angular clasts, normal andesite, rare pumice and red hydro alt clasts, traces of charcoal throughout (did not sample), strongly ochre stained, strong brown/orange, Py23-bulk sample
Dmax: 15, 14, 12, 11, 10, 10, 10, 10, 9, 9 [cm]

Upper 15 cm medium to coarse ash with 2 cm wide and 15 cm long gas pipes, fines depleted and filled with coarse ash, passes onto grey and strong brown stained coarse sand/pebbly matrix, matrix-supported, clast rich diamicton, 1.4 m thick, clasts grey, angular, glassy andesite, massive, few hydrothermal clasts, no pumice, Py24-matrix, T04-165 (grey glassy lithic)
Lithology: normal, 59; hydrothermal, 3; matrix, 41;
Magnetism: aligned (10x)
Dmax: 38, 35, 25, 25, 23, 21, 20, 20, 19, 18, 17 [cm]

> 4.5 m thick, poorly sorted, massive diamicton, clast rich, largely clast-supported, strong iron-staining (ochre) of matrix and finer clasts; patchy grey, medium to coarse sandy matrix, relatively friable, Py34-matrix
Lithology: grey, 98; matrix, 11
Dmax: 2.1, 1.9, 1.7, 1.3, 1.2, 1.2, 1.2, 1.2, 1.1, 1.0 [m]

Reference section No. 1

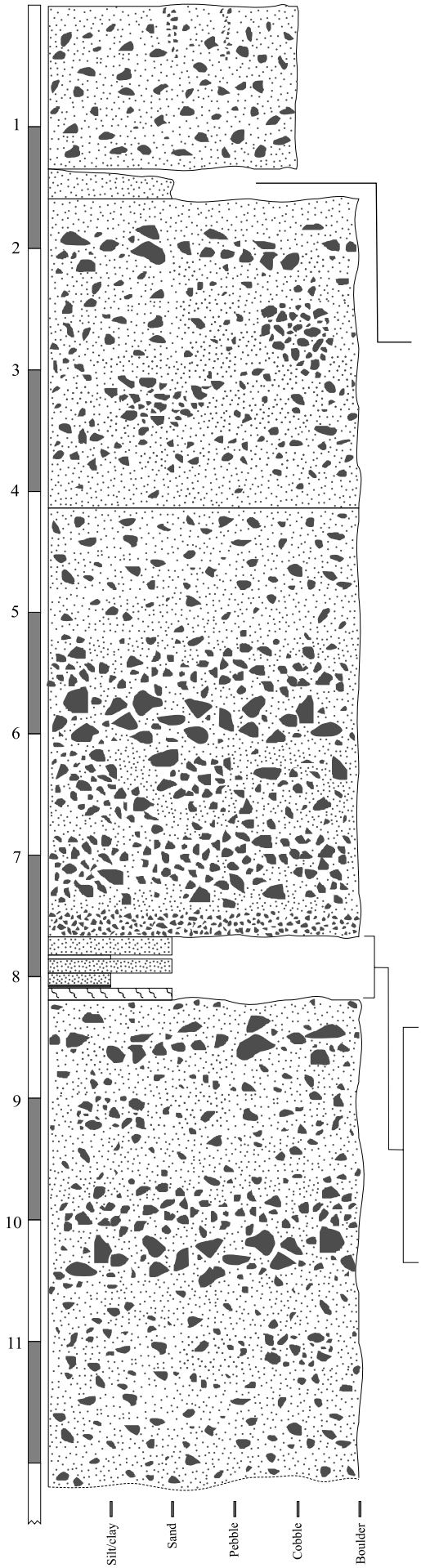
described by Platz (2001)
lower Pyramid Stream, true right side
North: 6214537 East: 2597581 Height: c.700 m



Eruptive episode	Lithostrati-graphic code
Pyramid	X-R
Tahurangi	IX-Ba
Burrell	VII-BA
Puniho	VI-B
Waiweranui	V-B
Newall	IV-Bb
Te Popo	II-B
pre-Maero	

Reference section No. 2

described by Platz (2001)
Hangatahua River, cliff section, true left side
North: 6215287 East: 2594429 Height: c.480 m



40 cm brown staining soil
Poorly sorted, massive diamicton, 80 cm thick, grey sandy matrix, matrix-supported, contains angular pebbly clasts, gas pipe app.50 cm high, SR27-matrix, NZ1 (grey andesite)
Lithology: grey, 23; pumice, 7; weathered/hydro, 3; matrix, 74
Dmax: 15, 14, 13, 11, 11, 11, 10, 10, 10, 10 [cm]
Magnetism: aligned? (8x)
Bottom 10 cm:
7 cm grey, fine to medium ash with rare coarse ash, massive, upper contact gradational, lower contact sharp and uneven, SR28
4-0 cm medium to coarse ash, clast-supported, pinches and swells, SR29
1-2 mm pale grey, fine ash, pocketing, sharp contacts
0-2 cm intermix of pale brown, fine ash and rip up humus, charcoal and sandy soil, contains charcoal fragments, in places 0-2 cm erosion into underlying unit

Sharp uneven, erosive contact onto 0-1 cm black humus, SR30
Poorly sorted, massive diamicton, 24-8 cm, greyish brown, fine to coarse ash, with charcoal fragments, at the bottom brown soil stained in upper 2 cm, diffuse, irregular lower contact, SR31-matrix, SR32-charcoal

2 cm dark brown stained, pebbly sand, poorly sorted
10 cm brown stained soil
30 cm red oxidation (hematite), rest is grey
Poorly sorted, massive diamicton, 1.6 m, grey, sandy matrix, matrix-supported, clast rich, large clasts (boulders) near top, dominantly angular dense andesite with rare pale brown angular pumice, looks in places clast-supported, SR33-matrix, NZ2 (grey andesite)
Lithology: grey, 82; pumice, 3; hydrothermal, 1; matrix, 35
Dmax: 31, 30, 23, 20, 13 [cm]
Magnetism: aligned (10x)
Lower 70 cm: clast depleted, medium to coarse sandy matrix, up to 10% clasts, sharp and relatively even lower contact, in places erosive contact (5 cm) into underlying unit, SR34-matrix

Poorly sorted, massive diamicton, 3.5 m thick
5 mm brownish stained, fine soil development, medium sand
1 m: grey, sandy matrix, matrix-supported, pebbles to cobbles, 30-40% clasts, subangular to subrounded, SR38-matrix, magnetism: random
2.5 m: grey, sandy matrix, in centre boulder clasts, clast rich, 50-60% clasts, subangular to subrounded, one pumice in cobble size, SR36-matrix, NZ3 (grey andesite)
Lithology: grey, 81; pumice, 2; weathered/hydro, 2; matrix, 29
Dmax: 66, 64, 63, 60, 50, 50, 48, 45, 38, 35 [cm]
Magnetism: aligned (9x)
Lower 1.5 m: dominated by dark grey andesite, clast rich and in places clast-supported
Basal 20 cm: iron-stained, strong brown, matrix depleted, large charcoal logs, dominantly pebbles onto erosive contact with 10 cm relief, SR37-charcoal

Up to 14 cm pockety, bedded, fine to medium ash, pale to mid grey (general stratigraphy)

3-4 cm pale grey, fine ash, gradational base into next unit, SR40-ash

7-10 cm grey, medium to coarse ash with 10cm x 3cm lenses, matrix-depleted, chaotic bedding with charcoal fragments, large ones not fully charcoalised, SR41-matrix, SR39-charcoal

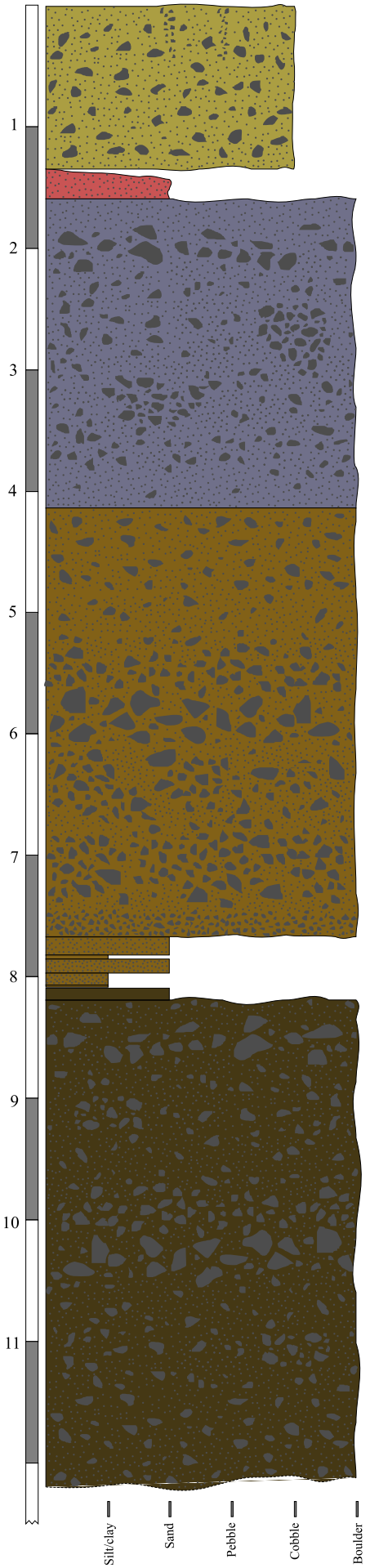
0-10 cm grey, fine to medium ash, cross and planar bedded, charcoal fragments, SR42-matrix
5 mm pale brown, fine to medium ash, appears to be rip up and erosive on 1-2 cm scale, sharp lower contact

4-10 cm humic, sandy loam, dark brown, burnt A-horizon, sharp even contact, SR43-soil

Poorly sorted, diamicton, >4 m thick
Upper portion: yellowish brown, pale grey brown, silty sand matrix, matrix-supported, large clasts concentrated near top and in a zone in the middle [could be reverse graded flow units], pebbles to boulders, subrounded, polylithic: pale to dark grey andesite, iron-stained, reddish
Dmax: 1.5, 1.2, 1.2, 1.1, 1.0, 1.0, 0.9, 0.8, 0.8, 0.7 [m]
Lower portion: matrix is grey and moderately friable sand, SR44-matrix
Lithology: grey, 44; reddish/hydro, 7, pumice, 1; matrix, 59
Magnetism: random (base)

Reference section No. 2

described by Platz (2001)
Hangatahua River, cliff section, true left side
North: 6215287 East: 2594429 Height: c.480 m



Eruptive episode	Lithostratigraphic code
Pyramid	X-R
Tahurangi	IX-Ba
Burrell	VII-BA
Puniho	VI-B
Waiweranui	V-B
Newall	IV-Bb
Te Popo	II-B
pre-Maero	

Sample	Description of Analysis	SiO_2	TiO_2	Al_2O_3	FeO	MnO	MgO	CaO	Na_2O	K_2O	Cl	NiO	V_2O_3	Cr_2O_3	SO_3	P_2O_5	Total
SD14	ID = 2065 SD14 hbl1-c	41.60	2.51	12.25	12.33	0.27	13.66	11.83	2.45	1.10	0.04	0.12		0.01	0.00	0.00	98.17
SD14	ID = 2076 SD14 hbl2-c	42.06	2.74	11.78	12.10	0.31	13.57	11.61	2.23	1.09	0.06	0.00		0.00	0.06	0.13	97.74
SD14	ID = 2081 SD14 hbl3-c	42.13	2.98	11.17	13.43	0.36	12.62	11.35	2.20	1.35	0.12	0.00		0.00	0.04	0.00	97.75
SD14	ID = 2082 SD14 hbl3-r	41.63	2.88	10.93	12.52	0.43	13.53	11.38	2.22	1.07	0.33	0.00		0.00	0.00	0.13	97.05
SD14	ID = 2093 SD14 hbl4-c	41.74	2.36	12.10	11.55	0.24	14.40	11.75	2.15	1.08	0.13	0.04		0.00	0.00	0.00	97.54
SD14	ID = 2095 SD14 hbl4-r	40.87	2.59	12.81	12.77	0.20	13.14	11.51	2.13	1.20	0.09	0.00		0.00	0.00	0.00	97.31
SD14	ID = 2097 SD14 hbl5-c	41.26	2.86	12.36	11.96	0.27	13.47	11.73	2.26	1.02	0.10	0.00		0.10	0.00	0.00	97.39
SD14	ID = 2098 SD14 hbl5-r1	40.46	2.60	13.26	11.92	0.22	13.15	11.75	2.42	1.05	0.00	0.00		0.05	0.08	0.09	97.05
SD14	ID = 2099 SD14 hbl5-r2	42.79	3.18	11.05	11.78	0.23	14.13	11.26	2.42	0.95	0.14	0.09		0.00	0.04	0.00	98.06
SD14	ID = 2101 SD14 hbl5-r3	41.73	2.58	12.18	13.28	0.48	12.41	11.73	2.18	1.14	0.06	0.22		0.11	0.14	0.17	98.41
SD14	ID = 2106 SD14 hbl6-r1	42.44	2.69	10.69	13.28	0.44	12.74	11.49	2.01	1.11	0.13	0.04		0.00	0.02	0.16	97.24
SD14	ID = 2107 SD14 hbl6-r2	42.31	2.88	11.01	12.57	0.31	13.09	11.63	2.57	1.00	0.13	0.00		0.18	0.01	0.07	97.76
SD14	ID = 2109 SD14 hbl6-r3	43.32	2.58	11.48	13.44	0.31	12.21	11.15	2.16	1.31	0.11	0.01		0.07	0.05	0.00	98.20
SD14	ID = 2110 SD14 hbl6-c?	42.05	3.01	11.87	11.88	0.29	13.64	11.35	2.35	1.01	0.12	0.08		0.00	0.01	0.16	97.82
SD14	ID = 2120 SD14 hbl7-c	41.83	2.13	12.82	11.42	0.07	14.59	11.79	2.18	1.11	0.00	0.03		0.16	0.14	0.00	98.27
SD14	ID = 2122 SD14 hbl7-r	41.57	2.07	13.02	10.83	0.03	14.47	11.92	2.14	1.13	0.11	0.06		0.00	0.12	0.00	97.47
SD14	ID = 2129 SD14 hbl8-c1	42.14	2.79	11.34	12.90	0.23	13.05	11.53	1.81	1.21	0.18	0.03		0.01	0.05	0.00	97.27
SD14	ID = 2130 SD14 hbl8-c2	42.17	2.99	11.22	13.73	0.36	12.55	10.99	1.99	1.39	0.19	0.00		0.07	0.08	0.08	97.81
SD14	ID = 2131 SD14 hbl8-r1	40.89	2.13	13.04	10.33	0.09	14.72	11.84	2.22	1.04	0.07	0.05		0.02	0.00	0.00	96.44
SD14	ID = 2132 SD14 hbl8-r2	40.80	2.28	13.46	12.83	0.15	12.50	12.09	2.25	1.19	0.05	0.08		0.00	0.17	0.13	97.98
SD14	ID = 2134 SD14 mhbl8-c	41.70	2.11	12.86	10.15	0.08	15.34	11.65	2.00	1.15	0.07	0.00		0.09	0.00	0.00	97.20
SD14	ID = 2135 SD14 mhbl8-r	40.58	2.79	12.91	17.84	0.45	11.30	11.35	1.09	0.24	0.00	0.00		0.00	0.07	0.00	98.62
SD14	ID = 2136 SD14 mhbl2-c	41.11	2.58	12.97	11.42	0.14	14.43	11.66	2.18	1.09	0.05	0.00		0.00	0.06	0.07	97.76
SD14	ID = 2137 SD14 mhbl2-r	41.46	2.24	12.84	10.21	0.09	14.74	11.84	2.05	1.14	0.00	0.06		0.10	0.00	0.00	96.77
SD14	ID = 2138 SD14 mhbl3-c	42.27	2.63	11.79	12.24	0.14	13.93	11.71	1.97	0.98	0.14	0.19		0.01	0.00	0.00	98.00
SD14	ID = 2141 SD14 mhbl3-r	41.85	2.77	11.59	12.04	0.39	13.63	11.54	2.18	1.07	0.07	0.00		0.00	0.00	0.00	97.13
SD5	ID = 2197 SD5 hbl1-c	42.01	2.27	12.69	10.80	0.03	14.38	11.89	2.09	1.01	0.06	0.17		0.18	0.00	0.00	97.58
SD5	ID = 2198 SD5 hbl1-r	42.44	2.98	11.37	11.76	0.15	13.97	11.46	2.16	1.09	0.04	0.08		0.17	0.00	0.04	97.71
SD5	ID = 2208 SD5 hbl2-c	41.41	2.17	13.23	11.31	0.09	14.18	11.85	2.06	1.11	0.09	0.05		0.04	0.07	0.02	97.68
SD5	ID = 2209 SD5 hbl2-r	40.73	2.52	13.38	11.90	0.22	13.36	12.10	2.26	1.15	0.07	0.00		0.01	0.00	0.00	97.70
SD5	ID = 2217 SD5 hbl3-c	41.52	2.21	12.80	10.70	0.07	15.05	11.59	2.14	1.11	0.00	0.00		0.07	0.07	0.00	97.33
SD5	ID = 2219 SD5 hbl3-r	41.16	2.35	13.46	11.99	0.14	13.83	11.61	1.92	1.07	0.00	0.03		0.11	0.19	0.00	97.86
SD5	ID = 2220 SD5 hbl4-c	41.82	2.18	12.74	11.21	0.04	14.06	11.66	2.26	1.12	0.00	0.00		0.16	0.07	0.00	97.32

Sample	Description of Analysis	SiO_2	TiO_2	Al_2O_3	FeO	MnO	MgO	CaO	Na_2O	K_2O	Cl	NiO	V_2O_3	Cr_2O_3	SO_3	P_2O_5	Total
SD5	ID = 2223 SD5 hbl4-r1	40.57	2.33	13.30	12.26	0.01	13.66	11.86	2.41	1.15	0.09	0.00		0.00	0.07	0.00	97.71
SD5	ID = 2224 SD5 hbl4-r2	42.27	2.93	11.06	12.30	0.31	13.82	11.39	2.04	1.20	0.14	0.00		0.00	0.07	0.10	97.63
SD5	ID = 2227 SD5 mhbl1-c	42.53	2.66	11.39	12.18	0.17	13.80	11.53	2.18	1.25	0.16	0.00		0.25	0.08	0.00	98.18
SD5	ID = 2249 SD5 hbl5-c	41.94	2.29	12.24	10.36	0.05	15.11	11.65	2.14	1.11	0.22	0.05		0.04	0.00	0.00	97.20
SD5	ID = 2252 SD5 hbl5-r	41.14	2.52	13.23	11.64	0.10	13.61	11.91	2.27	1.14	0.07	0.10		0.03	0.07	0.00	97.83
SD5	ID = 2262 SD5 mhbl2-c	40.86	2.02	12.95	11.14	0.00	14.45	11.66	2.21	1.08	0.06	0.12		0.00	0.00	0.00	96.55
SD5	ID = 2263 SD5 mhbl3-c	41.83	2.49	12.07	11.76	0.13	13.52	11.98	2.22	1.10	0.11	0.00		0.00	0.20	0.00	97.41
SD28	ID = 2268 SD28 hbl1-c	40.96	2.69	12.29	13.19	0.21	12.30	11.54	2.10	1.22	0.06	0.08		0.00	0.05	0.00	96.69
SD28	ID = 2270 SD28 hbl1-r1	42.08	2.89	11.17	13.09	0.33	12.94	11.39	2.01	1.22	0.11	0.05		0.04	0.08	0.00	97.40
SD28	ID = 2292 SD28 hbl2-c	42.01	3.01	11.13	13.82	0.20	12.39	11.48	2.14	1.36	0.10	0.00		0.17	0.09	0.00	97.90
SD28	ID = 2294 SD28 hbl2-r1	42.19	2.22	12.25	10.92	0.00	14.57	11.70	1.97	1.09	0.07	0.00		0.00	0.00	0.00	96.98
SD28	ID = 2295 SD28 hbl2-r2	41.93	3.15	11.02	13.61	0.51	12.56	11.38	2.14	1.36	0.18	0.00		0.00	0.00	0.00	97.84
SD28	ID = 2304 SD28 hbl3-c	40.95	2.40	13.16	12.39	0.00	13.30	11.88	2.32	1.12	0.11	0.03		0.12	0.11	0.00	97.89
SD28	ID = 2305 SD28 hbl3-r	44.63	2.80	8.77	11.24	0.25	14.37	14.15	1.53	0.86	0.22	0.00		0.04	0.16	0.00	99.02
SD28	ID = 2315 SD28 hbl4-c	40.92	2.55	12.61	11.20	0.03	14.39	11.87	2.37	1.18	0.04	0.09		0.05	0.00	0.11	97.41
SD28	ID = 2316 SD28 hbl4-r	41.55	2.80	11.46	12.96	0.29	12.81	11.78	2.17	1.32	0.07	0.04		0.05	0.09	0.16	97.55
SD32b	ID = 2377 SD32b hbl1-r1	41.80	3.09	11.76	12.91	0.32	13.16	11.52	2.46	1.17	0.13	0.01		0.13	0.08	0.12	98.66
SD32b	ID = 2378 SD32b hbl1-r2	41.21	2.07	12.84	12.06	0.27	13.81	11.42	2.07	1.08	0.06	0.00		0.00	0.00	0.00	96.89
SD32b	ID = 2379 SD32b hbl1-c	41.00	2.68	12.81	12.36	0.02	13.27	11.68	2.07	1.06	0.06	0.00		0.00	0.00	0.00	97.01
SD32b	ID = 2390 SD32b hbl2-r	41.16	2.16	13.24	10.83	0.18	14.50	11.82	1.99	1.12	0.03	0.00		0.21	0.00	0.00	97.24
SD32b	ID = 2392 SD32b hbl2-c	42.01	2.03	13.11	10.52	0.05	14.97	11.66	2.13	1.11	0.08	0.07		0.01	0.09	0.01	97.85
SD32b	ID = 2395 SD32b hbl3-c	40.89	2.55	12.40	13.27	0.10	12.64	11.69	2.17	1.19	0.10	0.04		0.09	0.09	0.19	97.41
SD32b	ID = 2397 SD32b hbl3-r	41.33	2.63	12.05	12.46	0.15	13.17	11.69	2.24	1.16	0.06	0.10		0.03	0.13	0.00	97.20
SD32b	ID = 2401 SD32b hbl4-c	43.99	2.79	9.80	13.64	0.36	13.42	11.30	2.17	1.01	0.09	0.00		0.00	0.00	0.05	98.62
SD32b	ID = 2403 SD32b hbl4-r	42.25	2.92	11.21	11.80	0.17	14.15	11.46	2.12	1.09	0.09	0.06		0.23	0.05	0.00	97.60
SD32b	ID = 2407 SD32b hbl5-c	42.90	2.07	11.94	10.21	0.13	15.46	11.65	2.06	1.00	0.08	0.01		0.00	0.10	0.00	97.61
SD32b	ID = 2408 SD32b hbl5-r	41.76	2.11	13.33	10.55	0.00	14.95	12.04	2.12	1.08	0.07	0.07		0.10	0.00	0.17	98.35
SD23a	ID = 2472 SD23a hbl1-c	41.27	1.86	13.25	11.19	0.10	14.18	11.70	2.10	1.19	0.05	0.00		0.00	0.00	0.00	96.89
SD23a	ID = 2473 SD23a hbl1-r	43.01	2.74	11.28	11.01	0.28	14.46	11.45	1.93	1.03	0.07	0.17		0.00	0.00	0.00	97.43
SD23a	ID = 2475 SD23a mhbl1-c	41.96	2.60	11.37	11.57	0.27	13.89	11.66	2.12	1.12	0.06	0.00		0.08	0.00	0.08	96.78
SD23a	ID = 2476 SD23a mhbl1-r	42.28	2.92	11.75	11.52	0.25	13.92	11.57	2.12	1.01	0.08	0.04		0.21	0.09	0.04	97.80
SD23a	ID = 2480 SD23a hbl2-c	41.82	2.99	11.45	12.36	0.31	13.12	11.28	2.27	1.19	0.05	0.00		0.04	0.00	0.00	96.88
SD23a	ID = 2481 SD23a hbl2-r	41.69	2.94	11.14	13.27	0.40	12.70	11.09	2.03	1.29	0.18	0.00		0.01	0.14	0.00	96.88

Sample	Description of Analysis	SiO_2	TiO_2	Al_2O_3	FeO	MnO	MgO	CaO	Na_2O	K_2O	Cl	NiO	V_2O_3	Cr_2O_3	SO_3	P_2O_5	Total
SD23a	ID = 2487 SD23a mhbl2	42.25	2.57	11.20	10.99	0.17	14.29	11.39	2.18	1.03	0.13	0.00		0.14	0.10	0.00	96.44
SD23a	ID = 2501 SD23a hbl3-c	42.13	3.14	10.92	12.96	0.30	12.78	11.17	1.87	1.24	0.04	0.13		0.00	0.00	0.08	96.76
SD23a	ID = 2502 SD23a hbl3-r	41.89	3.16	11.25	13.50	0.24	12.35	11.14	2.26	1.47	0.19	0.05		0.00	0.01	0.00	97.51
SD23a	ID = 2503 SD23a mhbl3	41.41	2.73	11.99	13.54	0.21	12.23	11.33	2.24	1.13	0.12	0.04		0.03	0.14	0.00	97.14
SD23a	ID = 2510 SD23a hbl4-c	42.75	2.95	10.82	11.39	0.23	14.07	11.45	2.08	1.07	0.11	0.00		0.05	0.12	0.13	97.22
SD23a	ID = 2511 SD23a hbl4-r	42.86	2.72	10.93	12.06	0.40	13.70	11.49	2.04	1.22	0.09	0.01		0.01	0.02	0.00	97.55
SD23a	ID = 2512 SD23a hbl5-c	40.77	2.04	13.49	11.65	0.02	13.86	11.85	1.92	1.12	0.03	0.00		0.00	0.11	0.00	96.86
SD23a	ID = 2513 SD23a hbl5-r	43.30	2.77	11.38	11.06	0.05	13.76	11.34	2.10	1.16	0.09	0.00		0.07	0.00	0.10	97.18
SD23a	ID = 2515 SD23a mhbl4-c	42.01	2.24	11.97	11.67	0.05	14.23	11.70	1.90	1.09	0.04	0.06		0.00	0.00	0.00	96.96
SD23a	ID = 2517 SD23a mhbl4-r	40.98	2.28	12.88	12.03	0.15	13.84	11.46	2.05	1.03	0.05	0.00		0.00	0.01	0.12	96.88
SD23a	ID = 2521 SD23a hbl6-c	41.73	2.10	12.96	11.00	0.12	14.83	11.58	2.05	0.97	0.10	0.00		0.18	0.00	0.00	97.62
SD23a	ID = 2522 SD23a hbl6-r	41.92	3.02	11.57	11.65	0.10	14.02	11.32	2.16	1.07	0.18	0.00		0.00	0.00	0.15	97.16
SD23a	ID = 2528 SD23a hbl7-c	41.68	2.19	12.97	11.47	0.02	14.53	11.34	1.81	1.00	0.06	0.01		0.14	0.00	0.00	97.22
SD23a	ID = 2529 SD23a hbl7-r	40.48	1.93	13.50	13.30	0.08	12.67	11.62	1.96	1.22	0.04	0.08		0.00	0.00	0.01	96.89
SD23a	ID = 2530 SD23a cpx8-hbl8	40.05	2.70	13.47	11.70	0.14	13.41	11.86	2.28	0.84	0.00	0.05		0.20	0.00	0.00	96.70
SD32a	ID = SD32a_amph1a-c_w	42.13	2.89	10.72	11.37	0.32	14.11	11.10	2.15	1.19	0.08	0.00		0.09	0.09	0.00	96.24
SD32a	ID = SD32a_amph1b-r_w	41.08	2.40	12.61	12.24	0.23	13.57	11.32	2.14	1.02	0.04	0.07		0.01	0.00	0.00	96.73
SD32a	ID = SD32a_amph1c=2-r_w	43.21	2.64	10.63	10.75	0.19	14.63	11.34	2.10	0.98	0.09	0.06		0.09	0.00	0.01	96.72
SD32a	ID = 10467 SD32a_amph1_b-c	40.50	2.10	12.73	11.29	0.07	13.78	11.29	2.27	1.23	0.06	0.00		0.04	0.00	0.00	95.36
SD32a	ID = 10468 SD32a_amph1b_b-r	40.48	2.01	13.51	11.83	0.10	14.00	11.53	2.11	1.07	0.06	0.06		0.00	0.00	0.00	96.76
SD25a	ID = 10499 SD25a_amph01m-c	41.61	2.81	11.29	11.51	0.13	13.64	11.00	2.00	1.06	0.14	0.03		0.17	0.00	0.00	95.39
SD25a	ID = 10507 SD25a_amph1m	41.07	1.95	13.13	10.64	0.07	14.54	11.45	2.16	1.05	0.03	0.03		0.07	0.12	0.00	96.31
SD25a	ID = 10519 SD25a_amph2?_c	40.71	2.83	12.25	12.85	0.22	12.95	11.13	2.28	1.10	0.00	0.10		0.00	0.14	0.05	96.61
SD25a	ID = 10520 SD25a_amph2?_c2	40.89	2.31	12.80	12.18	0.16	13.40	11.22	2.24	1.06	0.03	0.00		0.00	0.13	0.10	96.52
SD25a	ID = 10521 SD25a_amph2?_r	40.72	2.94	12.06	12.25	0.30	13.11	11.13	2.20	1.11	0.11	0.00		0.07	0.04	0.00	96.04
SD25a	ID = 10522 SD25a_amph2?_r2	42.13	2.97	10.97	11.44	0.35	13.94	11.07	2.14	1.15	0.14	0.00		0.00	0.04	0.08	96.42
SD25a	ID = 10531 SD25a_amph3?m-c	41.27	2.69	11.83	12.46	0.34	13.23	11.26	2.22	1.13	0.08	0.09		0.11	0.00	0.00	96.71
SD1	ID = 3121 SD1 hbl1-c	42.04	2.01	12.72	10.90	0.09	14.72	11.60	2.19	1.06	0.04	0.04	0.11	0.13	0.00	0.05	97.71
SD1	ID = 3122 SD1 hbl1-r	41.06	2.60	13.40	11.73	0.21	13.94	11.70	2.22	1.16	0.05	0.06	0.03	0.04	0.09	0.05	98.34
SD1	ID = 3135 SD1 hbl2-c	42.21	2.87	11.48	13.12	0.45	13.19	11.46	2.14	1.22	0.07	0.10	0.12	0.00	0.09	0.00	98.51
SD1	ID = 3138 SD1 hbl2-r	41.66	2.76	12.24	12.22	0.11	13.47	11.38	2.11	1.06	0.09	0.01	0.16	0.10	0.00	0.05	97.42
SD1	ID = 3147 SD1 hbl3-c	41.76	2.01	13.04	9.19	0.03	15.62	11.69	2.42	1.20	0.05	0.00	0.08	0.00	0.12	0.00	97.20
SD1	ID = 3148 SD1 hbl3-r	40.92	2.14	13.07	10.66	0.07	13.96	11.70	2.25	1.16	0.07	0.03	0.13	0.14	0.00	0.00	96.29

Sample	Description of Analysis	SiO_2	TiO_2	Al_2O_3	FeO	MnO	MgO	CaO	Na_2O	K_2O	Cl	NiO	V_2O_3	Cr_2O_3	SO_3	P_2O_5	Total
SD1	ID = 3149 SD1 hbl4-c	40.77	2.10	13.12	10.71	0.04	14.46	11.82	2.27	1.15	0.08	0.00	0.09	0.00	0.00	0.00	96.60
SD1	ID = 3150 SD1 hbl4-r	40.24	1.98	13.37	11.54	0.00	13.47	11.71	2.16	1.15	0.11	0.00	0.03	0.10	0.19	0.00	96.04
SD1	ID = 3151 SD1 hbl5-c	41.00	2.36	13.03	10.76	0.24	14.63	11.59	2.12	1.04	0.05	0.00	0.20	0.01	0.00	0.14	97.16
SD1	ID = 3152 SD1 hbl5-r	40.73	2.36	13.73	11.33	0.18	13.73	11.47	2.21	1.15	0.02	0.07	0.00	0.32	0.10	0.02	97.42
SD1	ID = 3164 SD1 hbl6-c	42.37	2.87	11.21	11.19	0.16	14.01	11.62	2.49	1.13	0.12	0.00	0.06	0.12	0.07	0.00	97.43
SD1	ID = 3166 SD1 hbl6-r	41.80	2.85	11.18	12.18	0.34	13.54	11.31	2.44	1.25	0.21	0.19	0.25	0.00	0.17	0.00	97.73
SD13	ID = 3191 SD13 hbl1-c	41.27	2.61	12.29	12.22	0.07	13.09	11.43	2.49	1.21	0.11	0.00	0.09	0.15	0.00	0.00	97.04
SD13	ID = 3192 SD13 hbl1-r	41.48	3.12	11.05	13.33	0.38	12.62	11.17	2.25	1.53	0.30	0.08	0.05	0.00	0.20	0.00	97.55
SD13	ID = 3193 SD13 hbl2-c	40.85	2.13	13.10	12.08	0.20	13.42	11.58	2.50	1.04	0.10	0.01	0.14	0.05	0.00	0.05	97.25
SD13	ID = 3194 SD13 hbl2-r	41.92	3.06	11.20	13.56	0.34	12.66	10.90	2.16	1.49	0.23	0.00	0.03	0.05	0.17	0.00	97.76
SD13	ID = 3195 SD13 hbl1-c	42.40	3.05	10.86	11.66	0.30	13.75	11.54	2.17	1.12	0.15	0.04	0.06	0.00	0.07	0.00	97.18
SD13	ID = 3199 SD13 hbl1-r	43.01	2.82	12.18	12.13	0.34	13.58	11.47	2.39	1.04	0.08	0.00	0.08	0.10	0.07	0.19	99.49
SD13	ID = 3200 SD13 hbl2-c	41.37	2.49	12.28	11.05	0.09	13.69	11.85	2.37	1.15	0.04	0.00	0.16	0.29	0.02	0.10	96.96
SD13	ID = 3201 SD13 hbl2-r	40.94	2.58	12.48	12.94	0.12	13.01	11.70	2.22	1.00	0.07	0.00	0.05	0.06	0.00	0.07	97.23
SD13	ID = 3209 SD13 hbl3-c	42.66	2.82	10.86	13.02	0.25	13.04	11.22	2.22	1.13	0.16	0.01	0.00	0.11	0.13	0.00	97.63
SD13	ID = 3210 SD13 hbl3-r	41.11	2.75	12.72	12.11	0.12	13.35	11.70	2.33	1.11	0.08	0.00	0.06	0.10	0.00	0.07	97.61
SD13	ID = 3211 SD13 hbl4-c	41.65	2.27	12.93	10.33	0.25	14.91	11.73	2.24	1.11	0.04	0.12	0.11	0.00	0.07	0.00	97.76
SD13	ID = 3212 SD13 hbl4-r	40.46	2.17	13.52	12.28	0.16	13.51	11.75	2.20	1.04	0.04	0.00	0.06	0.07	0.09	0.00	97.35
SD13	ID = 3215 SD13 hbl5-c	41.59	2.56	12.26	12.23	0.17	13.41	11.76	2.31	0.99	0.12	0.00	0.12	0.00	0.00	0.06	97.59
SD13	ID = 3216 SD13 hbl5-r	42.35	2.95	10.69	11.67	0.44	13.92	11.46	2.26	1.24	0.13	0.00	0.07	0.17	0.04	0.00	97.40
SD13	ID = 3223 SD13 hbl6-c	41.83	2.76	11.44	11.37	0.17	13.77	11.57	2.35	1.12	0.07	0.00	0.08	0.00	0.00	0.00	96.54
SD13	ID = 3225 SD13 hbl6-r	42.43	2.83	11.80	11.90	0.31	13.43	11.33	2.51	1.08	0.13	0.00	0.08	0.17	0.00	0.00	98.01
SD13	ID = 3226 SD13 hbl7-c	41.65	2.42	12.56	11.79	0.18	14.04	11.49	2.24	1.16	0.02	0.00	0.07	0.00	0.01	0.00	97.63
SD13	ID = 3227 SD13 hbl7-r	41.34	2.49	12.37	11.86	0.07	13.47	11.61	2.34	1.04	0.04	0.01	0.11	0.09	0.11	0.00	96.96
SD13	ID = 3242 SD13 hbl8-c	41.65	2.32	12.35	11.78	0.15	13.75	11.39	2.44	1.09	0.10	0.04	0.01	0.01	0.00	0.00	97.09
SD13	ID = 3243 SD13 hbl8-r	41.49	2.77	11.18	13.16	0.48	12.67	11.32	2.51	1.18	0.19	0.00	0.13	0.00	0.04	0.08	97.20
SD13	ID = 3244 SD13 mhbl1-c	41.69	2.73	11.95	12.73	0.23	13.42	11.51	2.28	1.02	0.12	0.01	0.00	0.21	0.00	0.00	97.90
SD13	ID = 3245 SD13 mhbl1-r	40.95	2.52	13.05	11.99	0.15	13.28	11.81	2.13	1.17	0.11	0.10	0.03	0.07	0.15	0.00	97.51
SD13	ID = 3255 SD13 hbl9-c	42.18	2.67	11.93	11.63	0.32	13.95	11.61	2.29	1.01	0.06	0.09	0.16	0.19	0.07	0.00	98.17
SD13	ID = 3256 SD13 hbl9-r	42.14	2.80	11.23	12.00	0.36	14.09	11.40	2.29	1.07	0.14	0.00	0.05	0.13	0.00	0.00	97.71
SD13	ID = 3300 SD13 hbl3-c	41.67	2.19	12.51	11.21	0.12	14.05	11.60	2.28	1.07	0.10	0.00	0.05	0.04	0.00	0.00	96.89
SD13	ID = 3301 SD13 hbl3-r	42.09	2.74	11.09	11.87	0.31	13.72	11.07	2.16	1.12	0.12	0.00	0.02	0.14	0.00	0.00	96.45
SD13	ID = 3302 SD13 hbl4-c	40.79	2.28	13.18	12.63	0.22	13.01	11.81	2.31	1.06	0.12	0.00	0.12	0.12	0.00	0.00	97.65

Sample	Description of Analysis	SiO_2	TiO_2	Al_2O_3	FeO	MnO	MgO	CaO	Na_2O	K_2O	Cl	NiO	V_2O_3	Cr_2O_3	SO_3	P_2O_5	Total
SD13	ID = 3303 SD13 hbl4-r1	41.85	1.90	12.78	9.78	0.15	15.56	11.52	2.30	1.14	0.06	0.08	0.06	0.00	0.01	0.00	97.19
SD13	ID = 3304 SD13 hbl4-r2	41.85	2.67	11.85	11.51	0.19	14.01	11.46	2.48	1.14	0.13	0.09	0.06	0.12	0.02	0.00	97.58
SD13	ID = 3305 SD13 hbl5-c	40.81	2.38	12.87	12.02	0.30	13.42	11.22	2.37	1.05	0.12	0.00	0.08	0.05	0.08	0.02	96.79
SD13	ID = 3309 SD13 hbl5-r	41.76	2.97	10.98	12.83	0.53	12.69	11.10	2.09	1.25	0.15	0.08	0.03	0.19	0.00	0.00	96.65
SD13	ID = 3322 SD13 hbl6-c	41.75	2.16	11.94	11.36	0.21	14.28	11.25	2.68	0.88	0.05	0.00	0.07	0.00	0.16	0.00	96.79
SD13	ID = 3323 SD13 hbl6-r	42.34	2.88	10.83	11.78	0.18	13.88	11.39	2.35	1.05	0.15	0.00	0.08	0.12	0.14	0.00	97.17
SD13	ID = 3325 SD13 hbl7-c	40.22	2.20	12.86	11.86	0.16	13.69	11.59	2.21	1.31	0.03	0.12	0.22	0.16	0.00	0.00	96.63
SD13	ID = 3326 SD13 hbl7-r	41.73	3.20	11.10	13.39	0.36	12.51	11.32	2.09	1.47	0.21	0.00	0.00	0.00	0.00	0.00	97.38
SD13	ID = 3334 SD13 hbl8-c	42.30	1.95	11.96	10.56	0.09	15.45	11.43	2.20	0.94	0.11	0.00	0.08	0.06	0.00	0.00	97.13
SD13	ID = 3335 SD13 hbl8-r1	40.70	2.24	13.29	10.64	0.17	14.65	11.62	2.26	1.02	0.07	0.00	0.16	0.00	0.10	0.07	96.99
SD13	ID = 3336 SD13 hbl8-r2	41.10	1.94	12.35	10.30	0.26	14.78	11.17	2.27	1.04	0.40	0.00	0.07	0.03	0.07	0.00	95.78
SD4	ID = 3372 SD4 hbl1-c	41.87	2.74	10.93	13.05	0.38	12.96	11.42	2.55	1.11	0.09	0.01	0.09	0.04	0.02	0.00	97.26
SD4	ID = 3387 SD4 hbl2-c	42.52	3.04	10.86	11.78	0.37	14.12	11.43	2.33	1.19	0.11	0.00	0.00	0.00	0.17	0.06	97.98
SD4	ID = 3389 SD4 hbl2-r	41.45	2.85	12.14	12.16	0.16	13.56	11.46	2.30	1.04	0.08	0.00	0.03	0.00	0.01	0.00	97.24
SD4	ID = 3406 SD4 hbl3-c	42.29	2.59	11.16	11.86	0.31	13.50	11.27	2.31	1.19	0.15	0.00	0.10	0.00	0.11	0.00	96.84
SD4	ID = 3407 SD4 hbl3-r	42.43	2.76	11.09	11.88	0.31	13.84	11.51	2.29	1.14	0.18	0.07	0.06	0.03	0.15	0.00	97.74
SD4	ID = 3408 SD4 hbl4-c	42.18	2.98	10.81	11.12	0.27	14.52	11.30	2.40	1.04	0.09	0.00	0.05	0.00	0.13	0.00	96.89
SD4	ID = 3411 SD4 hbl4-r	41.83	2.90	10.81	11.82	0.35	13.86	11.42	2.19	1.13	0.12	0.00	0.08	0.00	0.00	0.00	96.51
SD4	ID = 3420 SD4 hbl5-c	40.52	2.30	13.31	11.31	0.10	14.13	11.66	2.48	1.24	0.02	0.04	0.12	0.17	0.00	0.14	97.54
SD4	ID = 3422 SD4 hbl5-r	41.37	2.56	11.92	11.93	0.28	13.53	11.53	2.10	1.10	0.10	0.00	0.01	0.22	0.00	0.07	96.72
SD4	ID = 3425 SD4 hbl6-c	42.32	2.83	11.27	12.51	0.48	12.97	10.89	2.24	1.35	0.10	0.00	0.03	0.09	0.04	0.00	97.12
SD4	ID = 3430 SD4 hbl6-r	41.48	2.68	11.46	12.01	0.13	13.59	11.55	2.09	1.12	0.00	0.00	0.13	0.02	0.00	0.00	96.26
T04-56	ID = 3520 T04-56 hbl1-c	42.06	2.81	12.74	11.96	0.11	13.99	11.71	2.51	1.11	0.21	0.08	0.02	0.10	0.04	0.00	99.45
T04-56	ID = 3521 T04-56 hbl1-r	41.42	2.81	12.98	11.44	0.11	13.75	11.78	2.30	1.03	0.09	0.18	0.00	0.31	0.13	0.00	98.33
T04-56	ID = 3522 T04-56 hbl2-c	41.70	2.67	12.76	12.92	0.13	13.10	11.56	2.33	0.96	0.07	0.00	0.00	0.15	0.10	0.18	98.63
T04-56	ID = 3523 T04-56 hbl2-r	41.48	2.75	13.18	11.30	0.11	14.08	11.80	2.72	0.98	0.04	0.00	0.14	0.02	0.01	0.12	98.73
T04-56	ID = 3524 T04-56 hbl3-c	42.37	3.44	11.20	11.92	0.29	13.95	10.93	2.41	1.13	0.14	0.05	0.15	0.07	0.00	0.00	98.05
T04-56	ID = 3525 T04-56 hbl3-r	41.23	2.67	13.01	11.43	0.20	13.77	11.72	2.38	1.01	0.07	0.00	0.06	0.05	0.05	0.00	97.65
T04-56	ID = 3530 T04-56 hbl4-c	41.37	2.68	13.01	11.50	0.07	14.44	11.53	2.27	1.07	0.01	0.10	0.11	0.02	0.00	0.00	98.18
T04-56	ID = 3531 T04-56 hbl4-r	40.68	2.85	13.27	11.84	0.18	13.59	11.55	2.44	0.97	0.06	0.00	0.14	0.14	0.00	0.00	97.71
E02-117	ID = 8348 E02-117 hbl1-c	41.44	2.84	12.25	12.21	0.32	13.29	11.73	2.46	0.82	0.06	0.00	0.07	0.00	0.00	0.07	97.56
E02-117	ID = 8352 E02-117 hbl1-r	39.82	2.81	13.49	11.19	0.28	13.47	12.20	2.31	0.84	0.00	0.16	0.09	0.04	0.00	0.00	96.70
E02-117	ID = 8360 E02-117 hbl2-c	43.39	2.52	9.23	13.40	0.67	12.81	11.19	2.26	0.94	0.11	0.00	0.00	0.06	0.02	0.00	96.60

Sample	Description of Analysis	SiO_2	TiO_2	Al_2O_3	FeO	MnO	MgO	CaO	Na_2O	K_2O	Cl	NiO	V_2O_3	Cr_2O_3	SO_3	P_2O_5	Total
E02-117	ID = 8363 E02-117 hbl2-r	42.56	2.71	10.03	13.36	0.51	12.60	11.28	2.40	1.06	0.12	0.00	0.10	0.04	0.05	0.00	96.82
E02-117	ID = 8368 E02-117 hbl2-r2	42.69	2.71	9.66	13.49	0.53	12.73	11.50	2.42	1.08	0.12	0.00	0.00	0.04	0.00	0.00	96.97
E02-117	ID = 8369 E02-117 hbl3-c	41.26	2.87	12.50	12.56	0.35	12.94	11.44	2.58	0.87	0.04	0.16	0.08	0.01	0.00	0.01	97.67
E02-117	ID = 8372 E02-117 hbl3-r1	40.58	2.88	12.40	12.85	0.36	12.68	11.60	2.50	0.92	0.06	0.00	0.13	0.00	0.05	0.02	97.03
E02-117	ID = 8374 E02-117 hbl3-r	41.28	2.93	11.73	12.54	0.29	12.46	11.58	2.42	0.84	0.05	0.00	0.00	0.03	0.00	0.01	96.16
E02-117	ID = 8375 E02-117 hbl4-c	40.22	2.90	12.32	11.87	0.38	12.77	11.54	2.51	0.79	0.07	0.00	0.00	0.07	0.04	0.01	95.49
E02-117	ID = 8378 E02-117 hbl4-r	41.21	2.76	12.05	11.60	0.37	13.32	11.51	2.50	0.83	0.02	0.00	0.00	0.00	0.00	0.00	96.17
E02-117	ID = 8405 E02-117 hbl5-r	40.37	2.93	12.52	11.84	0.38	12.97	11.61	2.55	0.95	0.02	0.00	0.07	0.03	0.00	0.02	96.26
E02-117	ID = 8406 E02-117 hbl5-c	40.75	2.78	12.54	11.27	0.30	13.75	11.65	2.63	0.83	0.05	0.07	0.02	0.00	0.00	0.07	96.71

[all data in wt.%]

Sample	Description of Analysis	SiO_2	TiO_2	Al_2O_3	FeO	MnO	MgO	CaO	Na_2O	K_2O	Cl	NiO	V_2O_3	Cr_2O_3	SO_3	P_2O_5	Total
SD11	ID = 2060 SD11 cpx3ap	1.73	0.00	0.03	0.55	0.27	0.84	52.38	0.18	0.09	1.17	0.00		0.00	0.60	42.31	100.15
SD14	ID = 2073 SD14 ox2-ap	0.05	0.00	0.00	1.71	0.21	0.22	52.53	0.01	0.01	1.50	0.09		0.00	0.68	43.11	100.12
SD14	ID = 2075 SD14 ox3-ap	0.25	0.00	0.08	1.74	0.00	0.34	52.67	0.00	0.00	1.46	0.00		0.00	0.60	43.27	100.41
SD14	ID = 2078 SD14 cpx2-ap	0.13	0.07	0.06	0.57	0.00	0.22	53.06	0.13	0.00	1.54	0.00		0.00	0.81	43.27	99.86
SD14	ID = 2080 SD14 ap1	0.21	0.00	0.01	0.57	0.00	0.18	52.83	0.03	0.01	1.03	0.00		0.00	0.80	43.47	99.14
SD14	ID = 2096 SD14 ap2	0.38	0.00	0.00	0.50	0.15	0.22	52.90	0.00	0.00	0.85	0.03		0.00	0.00	43.08	98.11
SD14	ID = 2100 SD14 hbl5-ap1	0.08	0.01	0.00	0.38	0.00	0.50	52.83	0.01	0.00	1.34	0.00		0.00	0.57	43.24	98.96
SD14	ID = 2108 SD14 hbl6-ap	0.07	0.01	0.04	0.65	0.19	0.52	52.96	0.00	0.02	1.17	0.00		0.03	0.40	43.39	99.45
SD14	ID = 2133 SD14 hbl8-ap	0.34	0.11	0.17	0.24	0.00	0.50	52.59	0.20	0.00	1.60	0.29		0.00	0.83	43.38	100.25
SD14	ID = 2139 SD14 mhbl3-ap	0.38	0.00	0.04	0.47	0.00	0.58	53.20	0.00	0.01	1.40	0.25		0.12	0.50	43.62	100.57
SD5	ID = 2199 SD5 hbl1-ap	0.14	0.04	0.00	0.70	0.00	0.33	52.67	0.13	0.00	1.46	0.09		0.13	0.54	43.03	99.26
SD5	ID = 2204 SD5 cpx1-ap-c	0.28	0.00	0.08	0.25	0.00	0.15	53.24	0.00	0.00	1.51	0.00		0.16	0.69	42.97	99.33
SD5	ID = 2205 SD5 cpx1-ap-r	0.30	0.00	0.06	0.23	0.00	0.18	52.93	0.09	0.04	1.55	0.00		0.00	0.49	43.53	99.40
SD5	ID = 2225 SD5 ap1-c	0.00	0.00	0.00	0.14	0.00	0.00	53.39	0.10	0.03	1.08	0.00		0.00	0.58	43.70	99.02
SD5	ID = 2226 SD5 ap1-r	0.11	0.01	0.10	1.16	0.02	0.25	52.65	0.09	0.08	1.21	0.00		0.00	0.49	43.10	99.27
SD5	ID = 2240 SD5 cpx3-ap	0.30	0.01	0.06	0.11	0.23	0.28	52.94	0.01	0.00	1.87	0.00		0.02	0.77	42.89	99.49
SD5	ID = 2243 SD5 cpx3-ox1-ap1	0.15	0.14	0.08	2.52	0.00	0.20	51.08	0.22	0.00	1.81	0.00		0.00	0.73	41.99	98.92
SD5	ID = 2244 SD5 cpx3-ox1-ap2	0.32	0.10	0.00	1.89	0.17	0.21	51.58	0.52	0.02	2.42	0.00		0.00	0.00	41.74	98.97
SD5	ID = 2254 SD5 ox3-ap	0.32	0.13	0.03	2.99	0.00	0.24	51.89	0.07	0.00	1.31	0.00		0.00	0.78	42.61	100.37
SD5	ID = 2264 SD5 ap2-c	0.15	0.06	0.00	0.74	0.15	0.25	53.24	0.09	0.01	0.93	0.08		0.00	0.76	43.34	99.80
SD11	ID = 3094 SD11 cpx6-ap	0.09	0.01	0.00	0.75	0.05	0.30	53.00	0.08	0.07	0.92	0.00	0.01	0.00	0.31	43.77	99.37
SD11	ID = 3105 SD11 cpx8-ap	0.49	0.01	0.00	0.48	0.02	0.38	53.47	0.00	0.00	1.37	0.00	0.00	0.00	1.00	43.50	100.73
SD1	ID = 3134 SD1 cpx4-ap	0.35	0.00	0.14	0.55	0.14	0.17	52.28	0.00	0.00	1.39	0.14	0.00	0.00	0.59	43.27	99.04
SD1	ID = 3157 SD1 ap1	0.13	0.00	0.00	0.46	0.00	0.28	53.12	0.17	0.00	1.21	0.00	0.03	0.00	0.74	43.66	99.81
SD13	ID = 3183 SD13 cpx1-ap	0.37	0.00	0.04	0.44	0.12	0.22	52.71	0.08	0.03	1.51	0.00	0.07	0.00	0.68	43.36	99.63
SD13	ID = 3188 SD13 cpx1-ap2	0.91	0.07	0.14	0.70	0.11	0.45	52.47	0.00	0.14	1.73	0.12	0.04	0.00	0.68	42.81	100.38
SD13	ID = 3189 SD13 ap1	0.38	0.00	0.06	1.52	0.03	0.24	52.45	0.00	0.05	1.60	0.11	0.00	0.07	1.23	42.57	100.31
SD13	ID = 3205 SD13 ox1-ap	0.33	0.04	0.00	2.25	0.12	0.33	52.29	0.20	0.00	1.53	0.06	0.04	0.20	1.39	42.96	101.73
SD13	ID = 3220 SD13 ox3-ap	0.16	0.16	0.16	3.88	0.24	0.32	50.54	0.14	0.01	2.00	0.08	0.00	0.00	0.88	41.31	99.89
SD13	ID = 3224 SD13 hbl6-ap	0.65	0.00	0.01	0.20	0.07	0.72	51.67	0.38	0.04	2.98	0.04	0.12	0.00	1.66	42.53	101.07
SD13	ID = 3249 SD13 cpx9-ap	0.30	0.00	0.00	0.28	0.02	0.11	52.53	0.11	0.00	1.45	0.05	0.00	0.10	0.60	43.50	99.05
SD13	ID = 3312 SD13 ap1-c	0.30	0.00	0.01	0.91	0.19	0.13	51.70	0.00	0.00	2.32	0.00	0.00	0.20	0.63	42.47	98.86
SD13	ID = 3313 SD13 ap1-r	0.30	0.00	0.06	2.76	0.15	0.15	50.34	0.00	0.06	2.23	0.00	0.00	0.00	0.75	41.92	98.72

Sample	Description of Analysis	SiO_2	TiO_2	Al_2O_3	FeO	MnO	MgO	CaO	Na_2O	K_2O	Cl	NiO	V_2O_3	Cr_2O_3	SO_3	P_2O_5	Total
SD13	ID = 3319 SD13 ap2-c	0.15	0.00	0.02	0.73	0.00	0.06	52.34	0.00	0.04	1.69	0.00	0.11	0.01	0.71	43.25	99.11
SD13	ID = 3320 SD13 ap2-r	0.36	0.00	0.10	1.50	0.16	0.21	51.92	0.08	0.06	1.94	0.11	0.00	0.07	0.76	42.12	99.39
SD13	ID = 3329 SD13 ox2-ap	0.19	0.17	0.11	2.04	0.21	0.24	52.14	0.06	0.01	1.43	0.00	0.03	0.06	0.69	42.96	100.34
SD13	ID = 3330 SD13 ap3-c	0.37	0.01	0.06	1.12	0.19	0.13	52.38	0.00	0.01	1.68	0.00	0.00	0.09	0.93	42.74	99.71
SD13	ID = 3331 SD13 ap3-r	0.20	0.00	0.03	0.62	0.21	0.12	52.71	0.00	0.08	1.71	0.00	0.07	0.07	0.67	43.09	99.58
SD13	ID = 3341 SD13 cpx4-ap1	0.24	0.00	0.10	0.23	0.13	0.00	52.84	0.24	0.00	1.81	0.00	0.09	0.00	0.86	43.03	99.57
SD13	ID = 3348 SD13 cpx4-ox2-ap	0.15	0.00	0.04	1.45	0.12	0.09	52.43	0.20	0.03	1.69	0.05	0.00	0.18	0.85	42.98	100.26
SD4	ID = 3399 SD4 ox4-ap1-c	0.13	0.00	0.00	0.94	0.26	0.25	52.47	0.21	0.04	1.64	0.00	0.05	0.01	0.84	42.90	99.74
SD4	ID = 3400 SD4 ox4-ap1-r	0.31	0.00	0.10	1.24	0.00	0.27	52.27	0.12	0.02	1.65	0.02	0.00	0.00	0.65	43.05	99.70
SD4	ID = 3415 SD4 cpx4-ap1	0.65	0.00	0.00	0.06	0.08	0.20	51.81	0.12	0.02	2.90	0.19	0.00	0.04	1.38	41.75	99.20
SD28	ID = 2272 SD28 cpx1-ap	0.49	0.04	0.01	0.35	0.00	0.00	52.13	0.27	0.01	1.34	0.00		0.10	0.00	42.44	97.18
SD28	ID = 2281 SD28 ox1-ap	0.04	0.06	0.06	1.67	0.20	0.21	52.83	0.00	0.00	2.35	0.16		0.00	0.40	43.43	101.41
SD28	ID = 2284 SD28 ox2-ap	0.36	0.14	0.10	2.13	0.00	0.00	52.69	0.21	0.02	2.00	0.00		0.00	0.00	42.46	100.11
SD28	ID = 2293 SD28 hbl2-ap	0.30	0.00	0.05	0.60	0.00	0.00	52.71	0.00	0.00	1.68	0.00		0.00	0.00	43.09	98.43
SD28	ID = 2296 SD28 ap1	0.07	0.00	0.00	0.26	0.00	0.00	53.72	0.00	0.10	1.86	0.00		0.00	0.09	44.01	100.11
SD23a	ID = 2478 SD23a bi1-ap	0.66	0.03	0.08	0.82	0.00	0.00	52.65	0.01	0.23	1.74	0.00		0.02	0.79	42.62	99.65
SD23a	ID = 2505 SD23a bi2-ap1	0.21	0.03	0.01	0.73	0.19	0.24	52.12	0.27	0.09	1.76	0.00		0.00	0.00	42.82	98.47
SD9D	ID = 8098 SD9D cpx6-ap-c(=incl.1)	0.00	0.00	0.00	0.48	0.00	0.21	52.69	0.00	0.17	1.46	0.00	0.11	0.06	0.00	41.99	97.17
SD9D	ID = 8099 SD9D cpx6-ap-r(=incl.1)	0.00	0.10	0.00	0.23	0.00	0.15	52.28	0.00	0.21	1.51	0.04	0.00	0.01	0.05	41.57	96.15
E02-117	ID = 8390 E02-117 cpx2-ap	0.13	0.00	0.00	0.47	0.06	0.14	52.81	0.00	0.11	0.53	0.00	0.12	0.03	0.78	41.00	96.18
E02-117	ID = 8401 E02-117 ap1-c	0.00	0.09	0.00	0.08	0.03	0.18	53.28	0.20	0.12	0.46	0.00	0.11	0.00	0.39	41.53	96.47
E02-117	ID = 8402 E02-117 ap1-r	0.00	0.00	0.00	0.20	0.07	0.26	53.37	0.07	0.18	0.49	0.32	0.03	0.02	0.13	42.18	97.32

[all data in wt.%]

Sample	Description of Analysis	SiO_2	TiO_2	Al_2O_3	FeO	MnO	MgO	CaO	Na_2O	K_2O	Cl	NiO	V_2O_3	Cr_2O_3	SO_3	P_2O_5	Total
SD28	ID = 2297 SD28 bi1-c	36.87	5.62	14.13	10.72	0.08	17.25	0.04	0.35	9.13	0.15	0.20		0.00	0.06	0.05	94.65
SD28	ID = 2299 SD28 bi1-r	36.83	5.49	14.06	10.16	0.17	17.64	0.13	0.35	9.14	0.16	0.00		0.07	0.13	0.00	94.33
SD28	ID = 2313 SD28 bi2-c	36.67	5.66	14.12	11.46	0.23	16.84	0.00	0.00	8.89	0.12	0.00		0.00	0.15	0.00	94.14
SD28	ID = 2314 SD28 bi2-r	37.45	5.90	14.25	10.07	0.11	17.89	0.00	0.38	9.30	0.13	0.23		0.01	0.07	0.06	95.85
SD28	ID = 2317 SD28 bi3-c	36.55	5.70	14.36	11.13	0.04	17.32	0.02	0.00	9.05	0.12	0.04		0.00	0.03	0.04	94.40
SD28	ID = 2318 SD28 bi3-r	37.04	5.65	14.27	10.10	0.14	17.46	0.05	0.37	9.11	0.07	0.00		0.08	0.00	0.00	94.34
SD23a	ID = 2477 SD23a bi1-c	37.21	5.83	14.17	13.58	0.23	14.73	0.00	0.00	8.86	0.20	0.10		0.00	0.02	0.00	94.93
SD23a	ID = 2479 SD23a bi1-r	36.83	6.23	14.30	13.83	0.16	15.03	0.07	0.00	8.77	0.16	0.00		0.00	0.10	0.14	95.62
SD23a	ID = 2483 SD23a mbi1-c	37.28	6.03	14.12	14.06	0.22	15.12	0.12	0.00	8.83	0.18	0.00		0.02	0.10	0.02	96.10
SD23a	ID = 2484 SD23a mbi1-r	37.34	6.25	14.65	14.45	0.21	15.10	0.00	0.00	8.99	0.20	0.00		0.00	0.09	0.04	97.32
SD23a	ID = 2504 SD23a bi2-c	37.01	5.84	14.40	14.06	0.16	15.05	0.03	0.00	8.59	0.17	0.03		0.05	0.17	0.00	95.56
SD23a	ID = 2507 SD23a bi2-r	36.34	5.69	14.28	13.64	0.10	14.64	0.16	0.00	8.60	0.13	0.07		0.02	0.02	0.00	93.69
SD1	ID = 3127 SD1 cpx4-bi1	37.90	5.25	14.19	7.95	0.10	19.19	0.32	0.29	8.94	0.13	0.07	0.00	0.00	0.14	0.00	94.47
SD13	ID = 3240 SD13 bi1-c	37.05	5.40	13.88	13.54	0.08	15.19	0.03	0.63	8.79	0.15	0.00	0.00	0.11	0.00	0.00	94.86
SD13	ID = 3241 SD13 bi1-r	36.39	5.57	14.19	14.97	0.17	14.52	0.16	0.65	8.92	0.22	0.12	0.00	0.00	0.11	0.00	96.01
SD4	ID = 3423 SD4 bi1-c	35.92	5.79	14.05	13.90	0.13	14.48	0.05	0.59	8.76	0.12	0.00	0.00	0.14	0.00	0.01	93.73
SD4	ID = 3424 SD4 bi1-r	36.46	5.54	13.86	15.32	0.20	14.09	0.00	0.40	9.08	0.23	0.00	0.15	0.01	0.08	0.00	95.27

[all data in wt.%]

Sample	Description of Analysis	SiO_2	TiO_2	Al_2O_3	FeO	MnO	MgO	CaO	Na_2O	K_2O	Cl	NiO	V_2O_3	Cr_2O_3	SO_3	P_2O_5	Total
SD14	ID = 2066 SD14 cpx1-c	51.63	0.47	1.93	7.98	0.71	14.33	22.24	0.35	0.06	0.11	0.00		0.00	0.04	0.00	99.85
SD14	ID = 2077 SD14 cpx2-c	52.27	0.31	1.30	7.30	0.52	14.51	21.88	0.12	0.05	0.00	0.00		0.11	0.00	0.00	98.37
SD14	ID = 2084 SD14 cpx3-c	52.31	0.18	1.77	7.33	0.38	15.38	21.73	0.40	0.07	0.08	0.05		0.20	0.02	0.00	99.90
SD14	ID = 2087 SD14 cpx3-c1	52.35	0.38	2.71	5.03	0.06	16.22	22.81	0.23	0.00	0.05	0.10		0.18	0.00	0.01	100.13
SD14	ID = 2088 SD14 cpx4-c	52.15	0.49	2.08	4.70	0.04	16.37	22.78	0.00	0.00	0.05	0.27		0.57	0.00	0.00	99.50
SD14	ID = 2111 SD14 cpx5-c	51.53	0.22	1.87	7.54	0.42	14.39	21.94	0.00	0.07	0.12	0.00		0.18	0.00	0.00	98.28
SD15	ID = 8119 SD15 cpx15-c	50.86	0.41	2.10	7.63	0.57	14.30	21.41	0.36	0.00	0.02	0.16	0.06	0.11	0.00	0.10	98.09
SD5	ID = 2200 SD5 cpx1-c	50.04	0.66	4.28	7.14	0.25	14.16	22.12	0.21	0.06	0.00	0.09		0.17	0.00	0.00	99.18
SD5	ID = 2229 SD5 cpx2-c	53.07	0.23	1.04	7.09	0.78	15.30	22.10	0.10	0.06	0.00	0.00		0.00	0.00	0.00	99.77
SD5	ID = 2236 SD5 cpx3-c	52.60	0.26	1.24	7.08	0.63	14.75	21.93	0.38	0.05	0.00	0.11		0.13	0.00	0.00	99.16
SD5	ID = 2246 SD5 cpx4-c	51.83	0.54	2.01	6.58	0.45	14.52	22.16	0.27	0.01	0.00	0.00		0.40	0.00	0.00	98.77
SD5	ID = 2265 SD5 cpx5-c	52.31	0.31	2.06	7.35	0.45	15.22	22.09	0.25	0.02	0.04	0.05		0.15	0.00	0.00	100.30
SD1	ID = 3114 SD1 cpx1-c	52.80	0.31	1.86	7.31	0.45	15.08	21.79	0.50	0.06	0.06	0.00	0.00	0.24	0.04	0.00	100.53
SD1	ID = 3119 SD1 cpx2-c	52.88	0.27	1.44	7.08	0.72	15.28	21.63	0.24	0.04	0.06	0.00	0.04	0.08	0.01	0.00	99.78
SD1	ID = 3123 SD1 cpx3-c	52.09	0.33	1.68	7.95	0.51	14.34	21.56	0.64	0.05	0.06	0.15	0.09	0.23	0.00	0.09	99.78
SD1	ID = 3125 SD1 cpx4-c	51.94	0.42	2.50	6.54	0.27	16.11	21.74	0.24	0.06	0.08	0.00	0.13	0.13	0.01	0.00	100.17
SD1	ID = 3139 SD1 cpx5-c	51.41	0.28	2.31	8.38	0.39	13.69	22.35	0.44	0.00	0.06	0.00	0.00	0.16	0.08	0.10	99.66
SD1	ID = 3153 SD1 cpx6-c	52.66	0.20	0.98	7.87	0.83	14.11	22.19	0.38	0.07	0.06	0.00	0.03	0.29	0.05	0.13	99.86
SD1	ID = 3159 SD1 cpx7-c	52.23	0.23	1.35	7.38	0.51	15.32	21.33	0.29	0.00	0.02	0.07	0.01	0.11	0.06	0.00	98.92
SD1	ID = 3171 SD1 cpx8-c	52.87	0.45	1.29	7.62	0.44	15.65	21.25	0.64	0.06	0.06	0.03	0.00	0.09	0.00	0.00	100.46
SD13	ID = 3202 SD13 cpx1-c	51.66	0.44	2.36	7.46	0.51	14.83	21.44	0.49	0.00	0.03	0.00	0.12	0.33	0.00	0.18	99.85
SD13	ID = 3213 SD13 cpx2-c	51.54	0.37	2.34	7.60	0.24	14.72	22.10	0.30	0.02	0.08	0.09	0.09	0.21	0.16	0.00	99.86
SD13	ID = 3217 SD13 cpx3-c	51.22	0.49	2.98	7.68	0.28	14.38	21.21	0.52	0.02	0.02	0.00	0.00	0.14	0.00	0.01	98.96
SD13	ID = 3233 SD13 cpx4-c	52.47	0.23	1.49	7.37	0.65	15.02	21.94	0.38	0.00	0.06	0.00	0.08	0.07	0.00	0.12	99.88
SD13	ID = 3238 SD13 cpx8-c	51.78	0.29	1.87	8.54	0.60	14.27	21.16	0.62	0.04	0.04	0.00	0.00	0.08	0.05	0.15	99.49
SD13	ID = 3246 SD13 cpx9-c	52.24	0.25	1.08	6.50	0.52	15.00	22.32	0.31	0.00	0.08	0.00	0.23	0.32	0.02	0.34	99.23
SD13	ID = 3252 SD13 cpx10-c	52.47	0.28	1.63	6.83	0.59	14.93	21.88	0.31	0.04	0.08	0.00	0.08	0.16	0.00	0.06	99.35
SD13	ID = 3259 SD13 cpx11-c	50.18	0.43	1.56	7.33	0.64	14.40	20.71	0.36	0.05	0.05	0.16	0.04	0.04	0.00	0.00	95.96
SD13	ID = 3316 SD13 cpx2-c	51.98	0.36	1.69	6.83	0.48	14.60	22.09	0.58	0.10	0.02	0.01	0.08	0.23	0.00	0.00	99.05
SD13	ID = 3337 SD13 cpx3-c	52.75	0.26	1.33	7.05	0.51	15.17	21.68	0.37	0.01	0.07	0.04	0.00	0.17	0.00	0.02	99.43
SD13	ID = 3339 SD13 cpx3-c2	52.73	0.19	0.96	6.65	0.68	15.33	21.70	0.45	0.00	0.13	0.00	0.00	0.19	0.06	0.10	99.17
SD13	ID = 3340 SD13 cpx4-c	52.38	0.29	1.37	6.91	0.54	14.81	21.91	0.29	0.03	0.00	0.00	0.12	0.09	0.00	0.00	98.74
SD4	ID = 3390 SD4 cpx1-c	52.37	0.35	1.49	6.71	0.54	15.58	21.39	0.19	0.06	0.03	0.00	0.00	0.17	0.00	0.00	98.88

Sample	Description of Analysis	SiO_2	TiO_2	Al_2O_3	FeO	MnO	MgO	CaO	Na_2O	K_2O	Cl	NiO	V_2O_3	Cr_2O_3	SO_3	P_2O_5	Total
SD4	ID = 3393 SD4 cpx2-c	52.57	0.27	0.89	6.74	0.68	15.72	21.13	0.31	0.03	0.05	0.08	0.01	0.19	0.01	0.00	98.68
SD4	ID = 3403 SD4 cpx3-c	52.03	0.48	2.21	7.47	0.48	14.81	21.90	0.43	0.08	0.04	0.00	0.06	0.27	0.07	0.00	100.33
SD4	ID = 3413 SD4 cpx4-c	51.38	0.44	2.09	8.34	0.61	13.90	21.12	0.54	0.05	0.00	0.13	0.09	0.28	0.00	0.00	98.97
SD4	ID = 3431 SD4 cpx5-c	51.96	0.38	1.86	8.05	0.52	14.22	21.97	0.38	0.04	0.05	0.00	0.00	0.26	0.00	0.00	99.69
SD5	ID = 2196 SD5 hbl1-cpx	49.65	1.03	3.76	8.15	0.62	13.48	21.51	0.00	0.00	0.05	0.00		0.29	0.13	0.00	98.67
SD1	ID = 3168 SD1 ox5-cpx-c	52.68	0.28	1.20	7.05	0.58	15.00	21.90	0.45	0.00	0.04	0.00	0.12	0.10	0.03	0.00	99.45
SD14	ID = 2067 SD14 cpx1-r	51.10	0.59	2.76	7.90	0.61	14.74	21.44	0.03	0.06	0.10	0.00		0.24	0.00	0.00	99.57
SD14	ID = 2079 SD14 cpx2-r	51.38	0.45	2.24	7.29	0.41	14.54	22.02	0.01	0.06	0.08	0.00		0.15	0.09	0.00	98.72
SD14	ID = 2085 SD14 cpx3-r1	50.89	0.54	3.58	6.01	0.00	15.12	23.13	0.22	0.02	0.01	0.16		0.14	0.00	0.00	99.82
SD14	ID = 2086 SD14 cpx3-r2	49.40	0.86	4.81	8.67	0.31	13.16	21.99	0.36	0.01	0.01	0.00		0.15	0.04	0.00	99.77
SD14	ID = 2089 SD14 cpx4-r1	52.24	0.39	1.94	7.73	0.51	14.72	21.52	0.28	0.04	0.05	0.00		0.00	0.00	0.00	99.42
SD14	ID = 2091 SD14 cpx4-r2	51.44	0.30	2.25	8.67	0.57	13.76	21.29	0.25	0.07	0.04	0.04		0.04	0.06	0.09	98.87
SD14	ID = 2092 SD14 cpx4-r3	52.12	0.37	2.02	7.35	0.51	14.97	21.87	0.00	0.04	0.05	0.21		0.03	0.13	0.00	99.67
SD14	ID = 2114 SD14 cpx5-r1	51.60	0.45	2.48	7.61	0.16	14.60	21.98	0.19	0.07	0.04	0.11		0.04	0.12	0.00	99.45
SD14	ID = 2115 SD14 cpx5-r2	51.92	0.27	1.53	6.97	0.31	15.13	21.71	0.28	0.00	0.07	0.00		0.13	0.00	0.00	98.32
SD14	ID = 2116 SD14 cpx5-r3	50.16	0.60	3.48	7.93	0.41	14.15	21.71	0.39	0.01	0.04	0.11		0.04	0.06	0.07	99.16
SD15	ID = 8120 SD15 cpx15-r	51.10	0.33	1.44	7.37	0.55	14.72	21.46	0.44	0.09	0.00	0.00	0.09	0.14	0.06	0.00	97.79
SD5	ID = 2203 SD5 cpx1-r1	52.45	0.45	1.76	7.13	0.65	15.12	21.93	0.28	0.00	0.00	0.00		0.12	0.07	0.06	100.02
SD5	ID = 2206 SD5 cpx1-r2	51.45	0.44	2.39	7.34	0.42	14.46	21.85	0.16	0.00	0.06	0.00		0.25	0.11	0.03	98.96
SD5	ID = 2232 SD5 cpx2-r1	53.18	0.22	1.18	7.27	0.56	15.16	21.88	0.14	0.01	0.01	0.05		0.30	0.22	0.00	100.18
SD5	ID = 2234 SD5 cpx2-r2	52.62	0.38	1.88	7.19	0.56	14.94	21.72	0.00	0.06	0.05	0.12		0.11	0.02	0.00	99.65
SD5	ID = 2239 SD5 cpx3-r1	52.04	0.49	2.05	7.41	0.50	14.46	22.06	0.09	0.06	0.00	0.00		0.00	0.00	0.07	99.23
SD5	ID = 2248 SD5 cpx4-r1	51.92	0.38	2.26	8.70	0.61	14.20	20.72	0.00	0.08	0.07	0.00		0.19	0.06	0.00	99.19
SD5	ID = 2267 SD5 cpx5-r	51.96	0.52	2.20	7.31	0.36	14.96	21.71	0.17	0.04	0.00	0.00		0.02	0.00	0.00	99.25
SD1	ID = 3118 SD1 cpx1-r1	52.05	0.41	2.15	7.00	0.43	15.13	21.62	0.35	0.04	0.04	0.05	0.10	0.20	0.01	0.00	99.59
SD1	ID = 3120 SD1 cpx2-r	49.46	0.70	4.70	8.32	0.29	13.26	22.09	0.45	0.09	0.07	0.00	0.00	0.09	0.00	0.02	99.55
SD1	ID = 3124 SD1 cpx3-r	51.33	0.61	2.56	8.28	0.75	14.88	20.50	0.33	0.13	0.00	0.00	0.08	0.09	0.00	0.00	99.55
SD1	ID = 3140 SD1 cpx5-opx?	51.54	0.40	3.89	7.33	0.55	14.07	20.40	0.84	0.07	0.05	0.00	0.04	0.32	0.21	0.24	99.97
SD1	ID = 3142 SD1 cpx5-r	51.92	0.53	2.00	8.69	0.83	15.64	18.85	0.46	0.06	0.05	0.00	0.12	0.16	0.01	0.00	99.33
SD1	ID = 3143 SD1 mcpx1	51.08	0.60	2.13	8.15	0.59	15.29	19.74	0.45	0.08	0.06	0.00	0.15	0.10	0.06	0.11	98.60
SD1	ID = 3155 SD1 cpx6-r	53.81	0.30	1.27	8.79	0.77	16.19	19.52	0.41	0.00	0.01	0.00	0.06	0.06	0.00	0.00	101.19
SD1	ID = 3163 SD1 cpx7-r	50.70	0.60	2.84	8.51	0.57	14.55	20.64	0.42	0.03	0.04	0.03	0.09	0.07	0.05	0.13	99.29
SD1	ID = 3174 SD1 cpx8-r	51.43	0.39	1.56	6.88	0.61	15.19	20.83	0.40	0.09	0.37	0.00	0.00	0.09	0.14	0.02	98.03

Sample	Description of Analysis	SiO_2	TiO_2	Al_2O_3	FeO	MnO	MgO	CaO	Na_2O	K_2O	Cl	NiO	V_2O_3	Cr_2O_3	SO_3	P_2O_5	Total
SD13	ID = 3184 SD13 cpx1-r1	52.12	0.39	1.94	7.27	0.49	14.90	21.90	0.59	0.07	0.04	0.00	0.00	0.23	0.00	0.06	100.00
SD13	ID = 3185 SD13 cpx1-r2	51.52	0.64	2.32	7.56	0.57	14.20	21.91	0.51	0.00	0.00	0.00	0.06	0.12	0.00	0.00	99.41
SD13	ID = 3203 SD13 cpx1-r	52.35	0.28	1.47	6.78	0.47	15.30	22.02	0.60	0.18	0.06	0.00	0.08	0.22	0.00	0.00	99.81
SD13	ID = 3214 SD13 cpx2-r	50.81	0.65	3.27	8.46	0.27	13.91	21.30	0.32	0.18	0.08	0.00	0.07	0.23	0.00	0.00	99.56
SD13	ID = 3218 SD13 cpx3-r	51.44	0.68	3.51	8.24	0.56	13.88	21.10	0.62	0.09	0.07	0.10	0.00	0.00	0.01	0.00	100.30
SD13	ID = 3235 SD13 cpx4-r	52.00	0.43	2.02	8.30	0.63	14.27	21.33	0.63	0.01	0.04	0.15	0.00	0.02	0.00	0.01	99.84
SD13	ID = 3239 SD13 cpx8-r	49.81	0.86	3.77	9.17	0.49	13.74	20.43	0.45	0.12	0.04	0.00	0.08	0.10	0.04	0.00	99.12
SD13	ID = 3251 SD13 cpx9-r	51.45	0.68	2.47	7.88	0.49	14.50	21.58	0.38	0.12	0.01	0.01	0.10	0.33	0.00	0.00	100.00
SD13	ID = 3254 SD13 cpx10-r	51.45	0.41	2.34	7.32	0.43	14.84	21.31	0.27	0.00	0.07	0.00	0.08	0.12	0.06	0.00	98.70
SD13	ID = 3262 SD13 cpx11-r	52.50	0.32	1.54	7.06	0.62	15.31	21.45	0.37	0.05	0.23	0.00	0.06	0.29	0.10	0.03	99.92
SD13	ID = 3318 SD13 cpx2-r	52.26	0.35	1.42	6.36	0.56	14.67	22.26	0.23	0.06	0.02	0.00	0.00	0.35	0.12	0.08	98.74
SD13	ID = 3338 SD13 cpx3-r	51.48	0.57	2.30	7.64	0.62	14.64	21.43	0.46	0.06	0.05	0.03	0.03	0.21	0.04	0.00	99.56
SD13	ID = 3344 SD13 cpx4-r	50.92	0.42	2.44	8.72	0.43	13.54	21.40	0.46	0.05	0.09	0.00	0.00	0.31	0.00	0.02	98.80
SD4	ID = 3391 SD4 cpx1-r1	52.59	0.24	1.54	6.94	0.60	15.36	21.64	0.34	0.00	0.02	0.00	0.13	0.21	0.18	0.06	99.85
SD4	ID = 3392 SD4 cpx1-r2	48.72	0.78	5.42	7.91	0.09	13.67	21.94	0.24	0.06	0.05	0.00	0.20	0.00	0.00	0.02	99.10
SD4	ID = 3394 SD4 cpx2-r	49.64	0.68	3.49	8.38	0.62	13.80	20.92	0.38	0.06	0.02	0.00	0.01	0.24	0.00	0.00	98.24
SD4	ID = 3395 SD4 cpx2-r2	51.65	0.47	1.96	8.83	0.75	15.38	19.02	0.28	0.01	0.02	0.00	0.04	0.25	0.00	0.09	98.75
SD4	ID = 3404 SD4 cpx3-r	51.37	0.44	2.16	8.11	0.68	14.08	21.01	0.53	0.13	0.06	0.23	0.19	0.17	0.00	0.00	99.16
SD4	ID = 3418 SD4 cpx4-r1	51.59	0.37	2.21	8.40	0.54	14.22	21.40	0.60	0.03	0.03	0.00	0.09	0.27	0.07	0.00	99.82
SD4	ID = 3419 SD4 cpx4-r2	51.56	0.39	2.19	8.27	0.56	14.07	20.91	0.69	0.05	0.00	0.02	0.11	0.14	0.10	0.00	99.06
SD4	ID = 3437 SD4 cpx5-r1	50.94	0.40	2.04	8.16	0.50	13.64	22.29	0.56	0.02	0.01	0.00	0.08	0.22	0.09	0.10	99.05
SD4	ID = 3438 SD4 cpx5-r2	50.74	0.57	2.98	8.13	0.39	14.32	21.46	0.41	0.08	0.00	0.00	0.11	0.22	0.00	0.02	99.43
SD20	ID = 8092 SD20 cpx2-c	51.08	0.63	2.92	8.50	0.55	13.56	21.47	0.66	0.06	0.04	0.00	0.05	0.01	0.00	0.00	99.53
SD20	ID = 8096 SD20 cpx4-c	49.51	0.45	2.04	8.59	0.68	13.15	21.18	0.40	0.02	0.00	0.00	0.00	0.15	0.18	0.00	96.35
SD20	ID = 8112 SD20 cpx5-c	53.61	0.22	1.24	3.24	0.03	17.41	22.87	0.14	0.07	0.00	0.00	0.12	0.36	0.00	0.00	99.31
SD20	ID = 8097 SD20 cpx4-r	50.45	0.20	1.46	6.53	0.59	14.60	21.51	0.34	0.05	0.00	0.00	0.11	0.16	0.00	0.00	96.00
SD20	ID = 8093 SD20 cpx2-r	51.15	0.39	1.57	6.34	0.52	15.15	21.56	0.00	0.07	0.05	0.00	0.00	0.13	0.00	0.00	96.93
SD20	ID = 8113 SD20 cpx5-r	53.28	0.40	1.44	6.78	0.76	15.53	21.82	0.61	0.16	0.00	0.00	0.00	0.18	0.11	0.08	101.15
SD28	ID = 2271 SD28 cpx1-c	52.48	0.28	1.61	7.11	0.54	14.82	22.30	0.25	0.00	0.07	0.13		0.04	0.07	0.00	99.70
SD28	ID = 2274 SD28 cpx2-c	51.93	0.48	2.02	8.05	0.42	15.38	20.31	0.10	0.02	0.00	0.00		0.09	0.00	0.00	98.80
SD28	ID = 2286 SD28 cpx3-c	52.89	0.17	1.20	7.11	0.64	14.82	22.38	0.38	0.04	0.00	0.00		0.16	0.00	0.00	99.79
SD28	ID = 2288 SD28 cpx4-c	52.08	0.27	1.54	7.35	0.57	14.93	21.62	0.27	0.05	0.00	0.00		0.21	0.20	0.00	99.09
SD28	ID = 2302 SD28 cpx5-c	52.20	0.47	1.53	6.81	0.50	14.96	22.07	0.18	0.00	0.05	0.21		0.15	0.00	0.12	99.25

Sample	Description of Analysis	SiO_2	TiO_2	Al_2O_3	FeO	MnO	MgO	CaO	Na_2O	K_2O	Cl	NiO	V_2O_3	Cr_2O_3	SO_3	P_2O_5	Total
SD28	ID = 2306 SD28 cpx6-c	52.51	0.30	1.53	7.08	0.50	14.40	22.28	0.00	0.04	0.01	0.04		0.13	0.00	0.00	98.82
SD23a	ID = 2464 SD23a cpx1-c	51.84	0.48	1.92	8.47	0.61	14.30	21.71	0.38	0.03	0.00	0.01		0.19	0.07	0.00	100.01
SD23a	ID = 2469 SD23a cpx2-c	52.13	0.25	1.53	6.53	0.64	15.10	22.05	0.04	0.04	0.10	0.00		0.03	0.00	0.00	98.44
SD23a	ID = 2470 SD23a cpx3-c	52.61	0.36	1.74	6.84	0.48	15.25	21.72	0.28	0.07	0.04	0.00		0.14	0.02	0.02	99.57
SD23a	ID = 2485 SD23a cpx4-c	52.08	0.42	1.70	7.18	0.51	14.81	21.85	0.23	0.00	0.11	0.00		0.06	0.02	0.00	98.97
SD23a	ID = 2490 SD23a cpx5-c	51.91	0.47	1.85	7.67	0.65	14.84	21.72	0.27	0.06	0.04	0.00		0.01	0.12	0.00	99.61
SD23a	ID = 2498 SD23a cpx6-c	50.25	0.66	3.44	8.34	0.53	14.61	20.62	0.28	0.04	0.00	0.00		0.07	0.08	0.00	98.92
SD23a	ID = 2508 SD23a cpx7-c	52.04	0.43	1.74	8.21	0.50	14.30	22.72	0.33	0.03	0.00	0.00		0.00	0.00	0.08	100.38
SD23a	ID = 2524 SD23a cpx7-c	52.33	0.21	1.29	7.58	0.63	14.09	22.23	0.22	0.04	0.02	0.16		0.16	0.11	0.02	99.09
SD23a	ID = 2534 SD23a hbl8-cc	52.23	0.37	1.89	8.74	0.55	14.45	21.28	0.00	0.00	0.02	0.04		0.06	0.00	0.13	99.76
SD28	ID = 2273 SD28 cpx1-r	51.02	0.53	2.51	7.47	0.50	14.40	21.92	0.17	0.00	0.04	0.00		0.00	0.00	0.02	98.58
SD28	ID = 2279 SD28 cpx2-r	51.91	0.50	2.00	6.96	0.51	14.55	22.33	0.33	0.00	0.05	0.00		0.31	0.02	0.10	99.57
SD28	ID = 2287 SD28 cpx3-r	51.49	0.60	2.34	7.09	0.48	14.71	21.93	0.36	0.05	0.00	0.05		0.10	0.00	0.00	99.20
SD28	ID = 2291 SD28 cpx4-r	51.12	0.61	2.40	7.55	0.34	14.30	22.33	0.18	0.07	0.00	0.16		0.34	0.08	0.00	99.48
SD28	ID = 2303 SD28 cpx5-r	51.35	0.77	2.80	7.69	0.61	14.48	21.92	0.36	0.04	0.00	0.00		0.07	0.00	0.01	100.10
SD28	ID = 2307 SD28 cpx6-r	51.65	0.47	1.92	7.44	0.65	13.94	22.54	0.00	0.04	0.07	0.00		0.07	0.00	0.00	98.79
SD23a	ID = 2465 SD23a cpx1-r	51.98	0.49	1.96	8.17	0.71	14.26	21.93	0.17	0.08	0.00	0.00		0.09	0.00	0.00	99.84
SD23a	ID = 2468 SD23a cpx2-r	51.92	0.46	2.24	8.55	0.46	14.12	21.75	0.00	0.00	0.00	0.13		0.08	0.19	0.07	99.97
SD23a	ID = 2471 SD23a cpx3-r	51.59	0.46	2.36	7.63	0.57	14.73	21.40	0.24	0.08	0.09	0.14		0.10	0.00	0.00	99.39
SD23a	ID = 2486 SD23a cpx4-r	51.66	0.38	2.37	7.62	0.48	14.76	21.51	0.27	0.02	0.07	0.00		0.16	0.05	0.01	99.36
SD23a	ID = 2488 SD23a cpx5-r1	52.32	0.34	1.90	7.84	0.45	14.90	21.05	0.26	0.06	0.00	0.00		0.11	0.02	0.07	99.32
SD23a	ID = 2494 SD23a cpx5-r2	51.59	0.52	2.44	8.85	0.69	14.10	21.57	0.33	0.00	0.01	0.00		0.01	0.04	0.00	100.15
SD23a	ID = 2500 SD23a cpx6-r	52.92	0.22	1.16	6.74	0.52	15.35	21.45	0.20	0.00	0.06	0.00		0.21	0.09	0.00	98.92
SD23a	ID = 2509 SD23a cpx7-r	52.15	0.49	2.01	8.13	0.72	14.72	20.89	0.26	0.05	0.00	0.00		0.18	0.06	0.12	99.78
SD23a	ID = 2527 SD23a cpx7-r	52.27	0.47	1.99	7.50	0.53	14.61	21.89	0.29	0.07	0.07	0.14		0.14	0.00	0.04	100.01
SD23a	ID = 2536 SD23a hbl8-r	51.97	0.45	1.98	6.87	0.35	15.25	21.62	0.35	0.05	0.05	0.26		0.00	0.00	0.01	99.21
SD23a	ID = 2535 SD23a hbl8-ccc	52.67	0.49	1.73	8.17	0.71	14.79	21.71	0.11	0.02	0.00	0.00		0.04	0.00	0.00	100.44
SD23a	ID = 2518 SD23a mcpx2	52.23	0.38	2.44	6.28	0.00	17.05	20.48	0.14	0.03	0.05	0.00		0.17	0.07	0.05	99.37
SD32b	ID = 2380 SD32b cpx1-c	52.60	0.34	2.54	4.59	0.00	16.52	22.47	0.11	0.06	0.00	0.00		0.58	0.00	0.00	99.81
SD32b	ID = 2382 SD32b cpx2-c	51.92	0.37	2.52	4.35	0.00	16.32	22.79	0.00	0.03	0.00	0.00		0.75	0.00	0.00	99.05
SD32	ID = 8123 SD32 cpx11-c	52.21	0.43	1.74	7.73	0.72	15.34	21.02	0.52	0.06	0.00	0.00	0.00	0.13	0.04	0.00	99.94
SD32	ID = 8128 SD32 cpx12-c	51.20	0.43	2.03	8.78	0.73	14.17	20.54	0.79	0.08	0.00	0.00	0.00	0.12	0.09	0.01	98.97
SD32b	ID = 2384 SD32b cpx3-c	51.64	0.41	2.11	7.82	0.47	14.89	21.02	0.22	0.04	0.00	0.00		0.03	0.00	0.02	98.67

Sample	Description of Analysis	SiO_2	TiO_2	Al_2O_3	FeO	MnO	MgO	CaO	Na_2O	K_2O	Cl	NiO	V_2O_3	Cr_2O_3	SO_3	P_2O_5	Total
SD32b	ID = 2381 SD32b cpx1-r	51.77	0.31	1.81	7.36	0.44	14.71	21.59	0.31	0.04	0.08	0.00		0.11	0.00	0.09	98.62
SD32b	ID = 2383 SD32b cpx2-r	51.29	0.48	2.40	8.40	0.54	13.48	21.93	0.33	0.06	0.04	0.00		0.14	0.00	0.00	99.09
SD32b	ID = 2387 SD32b cpx3-r1	53.58	0.13	1.54	4.34	0.03	17.08	22.56	0.11	0.01	0.00	0.00		0.40	0.00	0.04	99.82
SD32	ID = 8124 SD32 cpx11-r	51.78	0.36	1.90	6.88	0.45	15.32	21.46	0.54	0.06	0.00	0.09	0.00	0.17	0.05	0.00	99.06
SD32	ID = 8129 SD32 cpx12-r	49.98	0.52	3.01	8.12	0.39	13.47	21.70	0.29	0.00	0.00	0.00	0.00	0.24	0.00	0.00	97.72
SD32b	ID = 2389 SD32b cpx3-r2	50.80	0.48	3.25	8.07	0.40	13.90	21.70	0.31	0.06	0.00	0.07		0.33	0.00	0.03	99.40
SD9c	ID = 3470 SD9c cpx1-c	50.60	0.98	4.37	5.63	0.06	15.55	21.88	0.33	0.07	0.06	0.00	0.08	0.62	0.07	0.00	100.30
SD9c	ID = 3472 SD9c cpx2-c	52.90	0.20	1.61	6.92	0.55	15.20	22.23	0.55	0.02	0.00	0.00	0.03	0.22	0.00	0.09	100.52
SD9c	ID = 3478 SD9c cpx3-c	53.15	0.43	1.50	7.01	0.65	15.08	22.10	0.16	0.05	0.05	0.00	0.06	0.12	0.00	0.06	100.42
SD9c	ID = 3484 SD9c cpx4-c	52.08	0.36	1.79	7.28	0.50	14.68	22.21	0.36	0.00	0.00	0.00	0.07	0.24	0.01	0.00	99.58
SD9c	ID = 3488 SD9c cpx5-c	52.79	0.21	1.48	8.47	0.93	14.46	21.07	0.61	0.03	0.00	0.00	0.00	0.20	0.00	0.00	100.25
SD9c	ID = 3471 SD9c cpx1-r	48.64	1.07	5.49	7.90	0.05	14.21	21.15	0.31	0.04	0.00	0.00	0.16	0.18	0.11	0.02	99.33
SD9c	ID = 3473 SD9c cpx2-r	52.37	0.55	2.05	7.26	0.46	14.93	22.48	0.42	0.04	0.03	0.00	0.00	0.24	0.00	0.00	100.83
SD9c	ID = 3479 SD9c cpx3-r	52.54	0.39	1.88	7.21	0.48	14.92	22.71	0.55	0.01	0.00	0.06	0.07	0.19	0.00	0.00	101.01
SD9c	ID = 3487 SD9c cpx4-r	51.40	0.69	2.57	7.53	0.52	14.40	21.78	0.50	0.04	0.00	0.05	0.05	0.32	0.00	0.06	99.91
SD9c	ID = 3489 SD9c cpx5-r	52.68	0.49	1.75	6.97	0.67	15.25	21.96	0.42	0.03	0.02	0.07	0.10	0.21	0.00	0.05	100.67
SD9c	ID = 3490 SD9c mcpx1-c	53.11	0.30	1.94	6.52	0.37	17.11	20.80	0.21	0.00	0.00	0.04	0.00	0.12	0.03	0.08	100.63
SD9c	ID = 3491 SD9c mcpx1-r	49.00	1.15	5.63	7.68	0.16	14.11	21.75	0.57	0.09	0.00	0.15	0.02	0.13	0.04	0.00	100.48
SD9D	ID = 8103 SD9D cpx6-c	51.59	0.50	2.09	7.09	0.54	14.63	21.62	0.41	0.03	0.00	0.00	0.10	0.14	0.04	0.13	98.91
SD9D	ID = 8102 SD9D cpx6-r	52.51	0.30	1.54	7.35	0.58	16.00	20.38	0.13	0.05	0.00	0.00	0.03	0.09	0.05	0.00	99.01
SD9D	ID = 8085 SD9D cpx9 r	49.88	0.57	2.59	7.41	0.37	14.14	21.70	0.47	0.08	0.05	0.05	0.00	0.10	0.12	0.00	97.53
T04-56	ID = 3492 T04-56 cpx1-c	52.74	0.20	1.58	6.79	0.36	15.70	21.60	0.33	0.09	0.03	0.00	0.00	0.08	0.05	0.00	99.55
T04-56	ID = 3501 T04-56 cpx2-c	51.70	0.46	2.43	8.10	0.61	13.64	21.80	0.24	0.00	0.00	0.00	0.12	0.26	0.00	0.00	99.36
T04-56	ID = 3508 T04-56 cpx3-c	52.54	0.46	1.75	7.36	0.46	15.36	21.69	0.42	0.00	0.02	0.05	0.08	0.17	0.00	0.06	100.42
T04-56	ID = 3512 T04-56 cpx4-c	50.88	0.51	3.54	8.39	0.28	15.42	20.37	0.48	0.05	0.00	0.00	0.09	0.27	0.00	0.00	100.28
T04-56	ID = 3516 T04-56 cpx5-c	51.29	0.46	2.36	7.86	0.48	14.47	22.01	0.32	0.00	0.00	0.00	0.00	0.12	0.00	0.00	99.37
T04-56	ID = 3526 T04-56 cpx6-c	52.59	0.53	2.01	8.69	0.58	16.26	19.77	0.25	0.00	0.02	0.00	0.04	0.07	0.00	0.00	100.81
T04-56	ID = 3499 T04-56 cpx1-r	51.94	0.67	2.52	7.89	0.42	15.22	20.47	0.26	0.03	0.04	0.00	0.05	0.21	0.00	0.01	99.73
T04-56	ID = 3503 T04-56 cpx2-r	52.45	0.39	1.98	7.84	0.63	14.39	21.95	0.48	0.12	0.03	0.22	0.22	0.00	0.13	0.00	100.83
T04-56	ID = 3509 T04-56 cpx3-r	52.17	0.53	2.20	6.98	0.39	15.47	21.68	0.28	0.03	0.00	0.06	0.00	0.18	0.00	0.00	99.97
T04-56	ID = 3515 T04-56 cpx4-r	51.46	0.64	3.28	8.18	0.05	14.48	22.00	0.17	0.08	0.02	0.00	0.06	0.22	0.02	0.00	100.66
T04-56	ID = 3519 T04-56 cpx5-r	52.06	0.58	2.26	8.39	0.34	15.53	20.58	0.35	0.03	0.07	0.00	0.10	0.09	0.15	0.02	100.55
SD11	ID = 2049 SD11 cpx1-c	52.40	0.50	1.75	7.39	0.57	15.97	20.98	0.23	0.00	0.00	0.00		0.04	0.00	0.00	99.83

Sample	Description of Analysis	SiO_2	TiO_2	Al_2O_3	FeO	MnO	MgO	CaO	Na_2O	K_2O	Cl	NiO	V_2O_3	Cr_2O_3	SO_3	P_2O_5	Total
SD11	ID = 2053 SD11 cpx2-c	52.34	0.55	2.43	7.60	0.54	16.12	20.73	0.31	0.03	0.00	0.05		0.04	0.10	0.00	100.84
SD11	ID = 2058 SD11 cpx3-c	53.02	0.45	1.60	7.70	0.48	16.26	20.66	0.25	0.04	0.00	0.00		0.24	0.00	0.00	100.70
SD11	ID = 2061 SD11 cpx4-c	50.19	0.82	4.19	8.34	0.28	14.35	21.16	0.33	0.02	0.00	0.12		0.02	0.00	0.00	99.82
SD11	ID = 2063 SD11 cpx5-c	51.62	0.62	2.31	7.60	0.34	15.58	20.57	0.11	0.04	0.00	0.00		0.11	0.00	0.00	98.90
SD11	ID = 3080 SD11 cpx-c	50.65	0.87	3.98	8.27	0.33	15.18	20.05	0.54	0.10	0.03	0.00	0.11	0.15	0.19	0.00	100.46
SD11	ID = 3081 SD11 cpx-c	53.89	0.25	1.26	4.45	0.29	17.99	21.23	0.25	0.00	0.00	0.00	0.00	1.05	0.00	0.00	100.67
SD11	ID = 3091 SD11 cpx6-c	52.34	0.53	2.14	8.43	0.46	15.83	20.31	0.47	0.09	0.00	0.03	0.04	0.06	0.15	0.00	100.89
SD11	ID = 3100 SD11 cpx7-c	53.36	0.27	1.56	5.29	0.13	17.62	21.62	0.31	0.00	0.06	0.06	0.13	0.36	0.06	0.00	100.84
SD11	ID = 3102 SD11 cpx8-c	50.05	0.69	3.93	8.07	0.24	14.18	22.07	0.15	0.05	0.02	0.00	0.00	0.11	0.13	0.00	99.69
SD11	ID = 3107 SD11 cpx9-c	53.62	0.33	1.20	4.31	0.03	17.63	21.86	0.08	0.10	0.08	0.00	0.00	0.63	0.04	0.01	99.93
SD11	ID = 3109 SD11 cpx10-c	47.88	1.33	6.57	8.36	0.27	12.85	22.24	0.32	0.04	0.00	0.00	0.07	0.14	0.00	0.00	100.06
SD11	ID = 2052 SD11 mcpx1-c	52.29	0.52	2.40	7.29	0.45	15.69	20.80	0.34	0.05	0.01	0.01		0.25	0.13	0.00	100.23
SD11	ID = 2050 SD11 cpx1-r	50.68	0.92	3.16	7.53	0.27	15.21	20.71	0.00	0.04	0.06	0.00		0.18	0.00	0.09	98.85
SD11	ID = 2054 SD11 cpx2-r	52.24	0.42	2.14	6.93	0.11	16.17	21.43	0.07	0.02	0.00	0.00		0.00	0.00	0.00	99.53
SD11	ID = 2059 SD11 cpx3-r	50.13	0.73	3.64	7.97	0.31	14.77	20.86	0.00	0.07	0.06	0.14		0.17	0.00	0.06	98.91
SD11	ID = 2062 SD11 cpx4-r	49.78	1.08	4.24	7.87	0.35	14.03	21.71	0.00	0.00	0.04	0.00		0.27	0.04	0.00	99.41
SD11	ID = 2064 SD11 cpx5-r	52.35	0.58	2.03	7.66	0.31	16.26	20.83	0.15	0.04	0.00	0.17		0.08	0.19	0.00	100.65
SD11	ID = 3067 SD11 cpx-r	51.13	0.75	3.41	7.38	0.33	15.22	20.89	0.34	0.02	0.10	0.00	0.00	0.19	0.21	0.00	99.97
SD11	ID = 3082 SD11 cpx-r1	48.48	1.02	5.46	8.18	0.12	13.90	21.87	0.22	0.06	0.00	0.08	0.04	0.19	0.01	0.00	99.64
SD11	ID = 3083 SD11 cpx-r2	52.11	0.44	2.70	4.58	0.09	16.50	21.98	0.37	0.02	0.00	0.03	0.07	1.41	0.09	0.00	100.41
SD11	ID = 3093 SD11 cpx6-r	51.40	0.69	2.92	7.33	0.40	15.42	20.58	0.23	0.08	0.04	0.00	0.07	0.26	0.00	0.07	99.51
SD11	ID = 3101 SD11 cpx7-r	50.16	1.27	4.50	9.00	0.33	14.19	19.37	0.56	0.27	0.07	0.00	0.00	0.23	0.01	0.02	99.99
SD11	ID = 3106 SD11 cpx8-r	51.45	0.68	2.84	7.26	0.49	15.66	21.17	0.60	0.13	0.09	0.11	0.00	0.03	0.13	0.00	100.65
SD11	ID = 3108 SD11 cpx9-r	53.03	0.94	7.80	8.42	0.38	12.57	16.82	1.66	0.47	0.01	0.00	0.01	0.12	0.02	0.09	102.36
SD11	ID = 3111 SD11 cpx11-r	51.09	0.72	3.31	7.49	0.36	15.22	20.70	0.28	0.00	0.00	0.06	0.00	0.30	0.00	0.00	99.54
E02-117	ID = 8382 E02-117 cpx1-c	50.12	0.62	3.21	8.19	0.49	13.39	22.38	0.38	0.01	0.06	0.00	0.09	0.08	0.02	0.00	99.04
E02-117	ID = 8385 E02-117 cpx2-c	47.93	1.19	5.19	8.65	0.32	12.71	22.15	0.53	0.02	0.05	0.00	0.00	0.12	0.05	0.00	98.91
E02-117	ID = 8392 E02-117 cpx3-c	52.29	0.41	1.29	7.76	0.91	13.50	22.39	0.51	0.08	0.01	0.00	0.15	0.12	0.00	0.00	99.42
E02-117	ID = 8400 E02-117 cpx4-c	48.71	0.88	4.42	8.54	0.32	12.84	21.80	0.53	0.00	0.01	0.00	0.10	0.17	0.06	0.00	98.38
E02-117	ID = 8380 E02-117 cpx1-r1	49.97	0.64	3.95	7.73	0.44	13.22	21.99	0.41	0.06	0.04	0.00	0.00	0.09	0.08	0.00	98.62
E02-117	ID = 8381 E02-117 cpx1-r2	49.60	0.73	3.54	8.05	0.41	12.92	21.98	0.55	0.01	0.00	0.05	0.01	0.13	0.00	0.02	98.00
E02-117	ID = 8393 E02-117 cpx3-r	51.71	0.33	1.18	8.42	0.80	13.20	22.54	0.60	0.04	0.07	0.00	0.11	0.30	0.07	0.00	99.37
E02-117	ID = 8395 E02-117 cpx4-r	51.45	0.53	2.11	7.40	0.45	14.29	22.20	0.29	0.12	0.06	0.00	0.01	0.11	0.11	0.00	99.13

Sample	Description of Analysis	SiO_2	TiO_2	Al_2O_3	FeO	MnO	MgO	CaO	Na_2O	K_2O	Cl	NiO	V_2O_3	Cr_2O_3	SO_3	P_2O_5	Total
E03-77	ID = 072 cpx-gm1 centre	52.27	0.62	2.27	6.99	0.39	15.90	21.16	0.39	0.06	0.07	0.12		0.03	0.00	0.14	100.41
E03-77	ID = 073 cpx-gm2 centre	49.74	0.91	4.02	8.15	0.45	13.83	21.23	0.60	0.04	0.04	0.06		0.07	0.00	0.00	99.14
E03-77	ID = 075 cpx-gm3 centre	51.27	0.70	2.75	7.37	0.39	15.53	20.69	0.33	0.10	0.00	0.00		0.11	0.00	0.00	99.24
E03-77	ID = 078 cpx-gm4 centre	51.96	0.96	1.26	11.47	0.91	15.44	17.46	0.59	0.07	0.01	0.00		0.12	0.00	0.00	100.25
E03-77	ID = 082 cpx-gm5 centre	51.64	0.74	1.27	9.32	0.71	16.00	18.38	0.13	0.10	0.00	0.00		0.02	0.02	0.43	98.76
E03-77	ID = 087 cpx-gm6 centre	51.32	0.76	2.48	9.66	0.70	15.19	18.33	0.26	0.16	0.00	0.00		0.01	0.00	0.00	98.87
E03-77	ID = 090 cpx-gm7 centre	52.52	0.63	1.90	7.06	0.47	16.23	20.19	0.19	0.04	0.07	0.04		0.01	0.04	0.13	99.52
E03-77	ID = 093 cpx-gm8 centre	51.55	0.69	2.28	7.56	0.44	15.98	20.70	0.43	0.01	0.01	0.00		0.00	0.00	0.00	99.65
E03-77	ID = 097 cpx-gm9 centre	49.64	1.04	2.01	9.17	0.54	14.07	20.28	0.46	0.03	0.00	0.00		0.15	0.02	0.48	97.89
E03-77	ID = 098 cpx-gm10 centre	51.45	0.79	3.33	7.16	0.33	14.82	21.45	0.52	0.01	0.00	0.00		0.13	0.00	0.00	99.99

[all data in wt.%]

Sample	Description of Analysis	SiO_2	TiO_2	Al_2O_3	FeO	MnO	MgO	CaO	Na_2O	K_2O	Cl	NiO	V_2O_3	Cr_2O_3	SO_3	P_2O_5	Total
SD14	ID = 2068 SD14 cpx1ox-c	0.15	6.79	2.47	82.52	0.51	1.87	0.14	0.00	0.02	0.01	0.03		0.12	0.00	0.00	94.63
SD14	ID = 2069 SD14 cpx1ox-r	0.15	6.72	2.62	83.40	0.75	1.90	0.33	0.10	0.00	0.04	0.00		0.23	0.00	0.00	96.24
SD14	ID = 2090 SD14 cpx4-ox1	0.17	6.08	2.44	81.95	0.75	1.89	0.36	0.00	0.08	0.07	0.00		0.01	0.00	0.00	93.80
SD14	ID = 2113 SD14 cpx5-ox1	0.30	6.56	3.24	82.52	0.67	2.30	0.03	0.11	0.00	0.00	0.03		0.18	0.15	0.00	96.09
SD5	ID = 2207 SD5 cpx1-ox	0.16	6.46	2.92	83.27	0.73	2.63	0.07	0.00	0.03	0.00	0.00		0.09	0.07	0.00	96.43
SD5	ID = 2235 SD5 cpx2-ox	0.10	6.58	3.04	82.83	0.55	2.17	0.09	0.12	0.02	0.00	0.02		0.21	0.01	0.06	95.80
SD5	ID = 2242 SD5 cpx3-ox1	0.07	6.66	3.20	82.54	0.75	2.25	0.11	0.08	0.00	0.06	0.00		0.06	0.07	0.13	95.98
SD1	ID = 3129 SD1 cpx4-ox1-c	0.11	15.86	1.43	72.59	0.56	2.45	0.39	0.00	0.00	0.02	0.00	0.46	0.00	0.00	0.10	93.98
SD1	ID = 3130 SD1 cpx4-ox1-r	0.41	5.07	2.32	82.20	0.86	2.31	0.57	0.13	0.00	0.04	0.30	0.41	0.07	0.08	0.05	94.82
SD1	ID = 3132 SD1 cpx4-ox2-c	0.23	6.84	2.91	83.36	0.77	2.24	0.06	0.21	0.02	0.02	0.00	0.52	0.00	0.06	0.00	97.25
SD1	ID = 3133 SD1 cpx4-ox2-r	0.18	6.71	2.80	81.91	0.71	2.22	0.06	0.07	0.09	0.10	0.00	0.54	0.00	0.05	0.00	95.44
SD1	ID = 3161 SD1 cpx7-ox1-c	0.05	6.98	2.60	82.10	0.64	2.16	0.03	0.12	0.00	0.08	0.21	0.36	0.00	0.20	0.00	95.54
SD1	ID = 3172 SD1 cpx8-ox-c	0.14	4.99	2.20	84.29	0.80	2.25	0.08	0.07	0.01	0.03	0.15	0.47	0.02	0.06	0.00	95.55
SD1	ID = 3173 SD1 cpx8-ox-r	0.12	4.90	2.20	83.50	0.60	2.51	0.32	0.11	0.00	0.12	0.09	0.54	0.00	0.00	0.13	95.14
SD13	ID = 3247 SD13 cpx9-ox1-c	0.16	5.12	2.26	83.88	0.89	2.15	0.24	0.05	0.03	0.10	0.00	0.40	0.00	0.00	0.04	95.33
SD13	ID = 3248 SD13 cpx9-ox1-r	0.16	5.17	2.44	82.47	0.74	2.29	0.28	0.15	0.06	0.00	0.09	0.30	0.07	0.01	0.00	94.24
SD13	ID = 3345 SD13 cpx4-ox	0.13	6.43	2.41	81.25	1.03	1.97	0.19	0.01	0.03	0.21	0.12	0.40	0.00	0.00	0.00	94.18
SD13	ID = 3346 SD13 cpx4-ox2-c	0.17	6.76	2.36	82.89	0.49	1.48	0.10	0.00	0.06	0.01	0.12	0.52	0.07	0.00	0.00	95.03
SD13	ID = 3347 SD13 cpx4-ox2-r	0.19	7.01	2.39	81.63	0.60	1.57	0.09	0.17	0.00	0.00	0.00	0.46	0.00	0.00	0.07	94.18
SD4	ID = 3416 SD4 cpx4-ox1-c	0.14	6.35	2.66	81.05	0.85	2.87	0.12	0.00	0.00	0.03	0.06	0.38	0.06	0.00	0.14	94.71
SD4	ID = 3417 SD4 cpx4-ox1-r	0.00	6.13	2.56	80.83	0.54	2.81	0.21	0.08	0.01	0.03	0.00	0.42	0.06	0.06	0.04	93.78
SD4	ID = 3434 SD4 cpx5-ox1	0.21	3.93	2.37	79.65	1.38	4.33	0.52	0.19	0.00	0.06	0.05	0.11	0.04	0.08	0.03	92.95
SD14	ID = 2083 SD14 hbl3-ox1	0.24	8.71	9.08	68.34	0.59	8.22	0.23	0.00	0.02	0.05	0.00		0.04	0.06	0.00	95.58
SD14	ID = 2126 SD14 hbl8-ox1	0.05	9.89	3.70	74.32	0.33	4.94	0.20	0.00	0.00	0.06	0.00		0.19	0.00	0.00	93.68
SD5	ID = 2210 SD5 hbl2-ox	0.19	9.39	6.29	68.80	0.59	9.38	0.27	0.00	0.04	0.10	0.00		0.13	0.07	0.00	95.25
SD5	ID = 2228 SD5 mhbl1-ox	0.07	6.58	4.54	78.36	0.59	4.86	0.21	0.00	0.00	0.05	0.00		0.06	0.00	0.00	95.32
SD13	ID = 3310 SD13 hbl5-ox-c	0.02	7.76	3.63	78.08	0.66	3.19	0.14	0.00	0.03	0.03	0.00	0.48	0.07	0.00	0.05	94.14
SD13	ID = 3311 SD13 hbl5-ox-r	0.11	7.69	3.81	77.86	0.63	3.23	0.27	0.00	0.00	0.04	0.14	0.43	0.00	0.07	0.00	94.28
SD4	ID = 3428 SD4 hbl6-ox1	0.19	2.18	9.59	67.92	0.84	10.94	0.16	0.00	0.05	0.03	0.06	0.00	0.05	0.00	0.00	92.01
SD13	ID = 3198 SD13 hbl1-opx?-ox	0.23	8.72	7.59	68.35	0.62	9.66	0.14	0.00	0.02	0.10	0.00	0.26	0.09	0.01	0.00	95.80
SD14	ID = 2070 SD14 ox1gm-c	0.28	7.40	1.98	82.97	0.50	1.61	0.00	0.09	0.00	0.06	0.00		0.14	0.00	0.03	95.06
SD14	ID = 2071 SD14 ox1gm-r	0.16	7.43	2.00	82.51	0.44	1.61	0.04	0.00	0.05	0.00	0.22		0.19	0.00	0.00	94.65
SD14	ID = 2072 SD14 ox2	0.14	6.70	2.82	83.19	0.70	1.92	0.13	0.00	0.03	0.04	0.14		0.00	0.06	0.12	95.99

Sample	Description of Analysis	SiO_2	TiO_2	Al_2O_3	FeO	MnO	MgO	CaO	Na_2O	K_2O	Cl	NiO	V_2O_3	Cr_2O_3	SO_3	P_2O_5	Total
SD14	ID = 2074 SD14 ox3	0.16	6.70	2.84	82.94	0.69	1.91	0.06	0.00	0.00	0.07	0.00		0.05	0.00	0.00	95.42
SD14	ID = 2117 SD14 ox4-c	0.03	7.18	2.68	83.22	0.76	1.73	0.03	0.01	0.01	0.00	0.00		0.03	0.00	0.00	95.68
SD14	ID = 2118 SD14 ox4-r	0.21	6.30	2.80	83.75	0.71	1.76	0.04	0.00	0.06	0.01	0.02		0.12	0.00	0.03	95.81
SD14	ID = 2119 SD14 ox5	0.20	6.16	2.81	83.76	0.73	1.79	0.00	0.05	0.06	0.00	0.00		0.15	0.00	0.00	95.71
SD14	ID = 2140 SD14 mox1	0.16	8.57	1.50	82.92	0.59	1.52	0.06	0.00	0.17	0.00	0.05		0.02	0.01	0.07	95.64
SD5	ID = 2213 SD5 ox1	0.20	6.94	2.88	83.36	0.55	1.86	0.05	0.00	0.04	0.08	0.26		0.08	0.10	0.00	96.40
SD5	ID = 2214 SD5 ox1-r	0.10	6.49	2.85	81.90	0.65	1.93	0.01	0.40	0.00	0.00	0.11		0.00	0.04	0.00	94.48
SD5	ID = 2215 SD5 ox2	0.15	7.04	2.34	84.44	0.49	1.56	0.05	0.00	0.00	0.00	0.00		0.00	0.00	0.07	96.14
SD5	ID = 2216 SD5 mox1	0.12	8.81	1.44	81.71	0.53	1.59	0.08	0.00	0.10	0.00	0.00		0.04	0.10	0.00	94.52
SD5	ID = 2253 SD5 ox3-c	0.08	6.86	2.83	83.84	0.82	2.02	0.04	0.00	0.05	0.05	0.00		0.27	0.00	0.00	96.86
SD5	ID = 2255 SD5 ox3-r	0.28	6.87	2.80	82.92	0.63	1.96	0.06	0.00	0.00	0.08	0.00		0.20	0.09	0.18	96.07
SD5	ID = 2256 SD5 ox3-c1	0.20	6.64	3.06	82.52	0.48	1.99	0.03	0.00	0.00	0.04	0.14		0.00	0.00	0.15	95.25
SD5	ID = 2257 SD5 ox4-c	0.18	6.71	2.83	83.45	0.62	1.91	0.00	0.00	0.00	0.01	0.15		0.00	0.00	0.00	95.86
SD5	ID = 2258 SD5 ox4-r	0.21	6.19	2.86	83.53	0.59	1.77	0.06	0.00	0.04	0.00	0.00		0.06	0.11	0.00	95.42
SD5	ID = 2259 SD5 ox5-c	0.12	6.90	2.92	82.64	0.65	2.04	0.08	0.10	0.06	0.00	0.31		0.00	0.00	0.00	95.82
SD5	ID = 2260 SD5 ox5-r	0.29	6.66	3.05	82.39	0.55	2.00	0.06	0.00	0.02	0.00	0.12		0.08	0.00	0.08	95.30
SD5	ID = 2261 SD5 ox6-c	0.19	6.82	2.39	83.98	0.62	1.73	0.00	0.06	0.00	0.09	0.13		0.00	0.00	0.00	96.01
SD1	ID = 3112 SD1 ox1-c	0.22	7.07	2.77	82.31	0.72	2.19	0.00	0.00	0.00	0.06	0.18	0.38	0.06	0.04	0.00	96.00
SD1	ID = 3113 SD1 ox1-r	0.16	7.04	2.40	81.66	0.70	1.93	0.05	0.01	0.02	0.02	0.05	0.43	0.02	0.12	0.12	94.73
SD1	ID = 3144 SD1 ox2-c	0.33	11.09	1.32	79.13	0.71	1.44	0.09	0.16	0.05	0.11	0.10	0.52	0.00	0.01	0.10	95.17
SD1	ID = 3145 SD1 ox3-c	0.15	7.18	2.55	83.62	0.68	1.90	0.04	0.18	0.00	0.02	0.00	0.41	0.01	0.00	0.07	96.82
SD1	ID = 3146 SD1 ox3-r	0.06	7.19	2.14	82.10	0.71	1.71	0.10	0.00	0.01	0.00	0.18	0.54	0.11	0.00	0.00	94.86
SD1	ID = 3156 SD1 ox4-c	0.10	7.08	2.76	81.13	0.72	2.05	0.00	0.00	0.06	0.09	0.00	0.45	0.00	0.12	0.00	94.56
SD1	ID = 3158 SD1 ox4-r	0.15	6.97	2.49	82.03	0.76	2.16	0.05	0.07	0.09	0.11	0.03	0.51	0.00	0.05	0.13	95.60
SD1	ID = 3167 SD1 ox5-c	0.18	7.14	2.45	81.68	0.80	1.92	0.06	0.00	0.00	0.08	0.03	0.59	0.00	0.09	0.00	95.03
SD1	ID = 3169 SD1 ox5-cpx-r	0.31	6.90	2.57	82.16	0.77	1.85	0.03	0.01	0.01	0.04	0.00	0.43	0.00	0.00	0.00	95.08
SD13	ID = 3190 SD13 inox1	0.00	8.10	1.29	82.14	0.51	1.75	0.09	0.01	0.02	0.00	0.18	0.45	0.00	0.00	0.01	94.56
SD13	ID = 3204 SD13 ox1-c	0.09	6.78	2.60	82.94	0.62	1.89	0.10	0.15	0.01	0.05	0.16	0.35	0.16	0.00	0.04	95.95
SD13	ID = 3206 SD13 ox1-r	0.01	6.66	2.58	82.09	0.60	2.01	0.00	0.09	0.04	0.04	0.02	0.44	0.00	0.13	0.00	94.72
SD13	ID = 3207 SD13 ox2-c	0.12	6.90	2.53	83.05	0.68	1.95	0.00	0.20	0.06	0.05	0.15	0.37	0.21	0.00	0.00	96.28
SD13	ID = 3208 SD13 ox2-r	0.19	6.73	2.65	81.94	0.65	2.00	0.68	0.01	0.03	0.07	0.04	0.33	0.00	0.11	0.45	95.89
SD13	ID = 3219 SD13 ox3-c	0.07	6.75	2.71	82.91	0.85	2.03	0.00	0.00	0.02	0.06	0.00	0.38	0.00	0.10	0.00	95.89
SD13	ID = 3221 SD13 ox3-r	0.15	6.63	2.74	82.56	0.64	2.04	0.12	0.00	0.00	0.09	0.04	0.37	0.05	0.00	0.05	95.48

Sample	Description of Analysis	SiO_2	TiO_2	Al_2O_3	FeO	MnO	MgO	CaO	Na_2O	K_2O	Cl	NiO	V_2O_3	Cr_2O_3	SO_3	P_2O_5	Total
SD13	ID = 3231 SD13 ox4-c	0.04	6.59	2.54	82.91	0.56	2.00	0.05	0.00	0.00	0.09	0.00	0.45	0.02	0.12	0.00	95.37
SD13	ID = 3232 SD13 ox4-r	0.14	6.50	2.62	82.54	0.70	1.99	0.10	0.00	0.00	0.00	0.01	0.54	0.00	0.02	0.00	95.16
SD13	ID = 3257 SD13 ox5-c	0.04	7.08	2.71	81.71	0.72	2.13	0.00	0.00	0.00	0.09	0.00	0.45	0.00	0.00	0.00	94.93
SD13	ID = 3258 SD13 ox5-r	0.16	6.87	2.76	80.64	0.86	2.08	0.16	0.11	0.00	0.09	0.13	0.36	0.00	0.00	0.05	94.28
SD13	ID = 3314 SD13 ox1-c	0.13	8.68	1.53	81.11	0.79	1.89	0.05	0.18	0.00	0.00	0.28	0.53	0.05	0.00	0.03	95.25
SD13	ID = 3315 SD13 ox1-r	0.10	8.44	1.50	81.22	0.73	1.62	0.08	0.11	0.04	0.04	0.00	0.57	0.14	0.00	0.00	94.59
SD13	ID = 3327 SD13 ox2-c	0.05	8.70	1.14	82.53	0.53	1.46	0.00	0.13	0.00	0.03	0.00	0.49	0.02	0.00	0.00	95.08
SD13	ID = 3328 SD13 ox2-r	0.47	8.02	1.34	81.70	0.58	1.41	0.19	0.14	0.03	0.07	0.00	0.46	0.08	0.00	0.09	94.58
SD4	ID = 3368 SD4 ox1-c	0.09	6.73	2.59	82.70	0.62	1.71	0.00	0.07	0.05	0.04	0.00	0.45	0.00	0.00	0.00	95.05
SD4	ID = 3369 SD4 ox1-r	0.14	6.51	2.66	80.99	0.66	1.90	0.08	0.11	0.10	0.01	0.11	0.42	0.15	0.02	0.00	93.86
SD4	ID = 3370 SD4 ox2-c	0.01	6.87	2.23	82.58	0.55	1.70	0.07	0.12	0.04	0.03	0.30	0.31	0.05	0.00	0.00	94.86
SD4	ID = 3371 SD4 ox2-r	0.28	6.61	2.20	82.51	0.53	1.71	0.10	0.15	0.03	0.02	0.17	0.36	0.00	0.01	0.08	94.76
SD4	ID = 3373 SD4 ox-c	0.18	6.66	2.95	82.10	0.68	2.03	0.00	0.00	0.00	0.00	0.15	0.39	0.01	0.00	0.17	95.32
SD4	ID = 3397 SD4 ox4-c	0.09	6.55	2.93	81.24	0.70	2.07	0.00	0.01	0.00	0.05	0.01	0.42	0.00	0.07	0.09	94.23
SD4	ID = 3398 SD4 ox4-c2	0.17	6.54	2.99	81.25	0.48	1.95	0.03	0.23	0.04	0.00	0.00	0.40	0.05	0.00	0.11	94.24
SD4	ID = 3401 SD4 ox4-r1	1.16	6.52	3.41	80.68	0.56	1.95	0.18	0.23	0.05	0.05	0.00	0.43	0.25	0.05	0.16	95.68
SD4	ID = 3402 SD4 ox4-r2	0.18	6.62	2.86	81.75	0.59	2.03	0.04	0.00	0.05	0.05	0.00	0.48	0.00	0.00	0.00	94.65
SD20	ID = 8109 SD20 cpx5 incl.4-ox	0.26	5.99	3.72	75.73	0.58	3.36	0.19	0.00	0.00	0.05	0.11	0.54	1.92	0.08	0.02	92.55
SD21b	ID = 1815 SD21b hbl-ox1-c	0.22	6.05	3.20	81.41	0.71	2.72	0.22	0.20	0.03	0.00	0.00		0.08	0.00	0.03	94.87
SD21b	ID = 1816 SD21b hbl-ox2-c	0.18	6.43	2.98	82.06	0.69	2.26	0.18	0.00	0.02	0.01	0.15		0.09	0.00	0.00	95.05
SD21b	ID = 1817 SD21b hbl-ox3-c	0.20	5.95	3.08	82.36	0.68	1.83	0.38	0.00	0.05	0.00	-0.15		0.04	0.00	0.00	94.42
SD21b	ID = 1818 SD21b hbl-ox4-c	0.24	5.66	3.40	82.42	0.47	2.11	0.23	0.18	0.00	0.00	0.13		0.19	0.00	0.00	95.03
SD21b	ID = 1819 SD21b ox1-c	0.17	6.45	3.51	81.67	0.67	2.25	0.07	0.11	0.00	0.01	0.16		0.11	0.00	0.01	95.19
SD21b	ID = 1820 SD21b ox1-r	0.08	6.21	3.72	81.62	0.60	2.78	0.04	0.28	0.04	0.00	0.32		0.02	0.00	0.00	95.71
SD21b	ID = 1821 SD21b ox2-c	0.25	6.32	3.78	82.82	0.57	2.51	0.01	0.15	0.01	0.00	0.00		0.08	0.19	0.26	96.95
SD21b	ID = 1822 SD21b ox3-c	0.15	6.42	3.45	82.04	0.47	2.59	0.00	0.19	0.00	0.00	0.09		0.09	0.00	0.06	95.55
SD21b	ID = 1823 SD21b ox3-r	0.50	5.69	3.73	81.62	0.63	2.86	0.03	0.01	0.00	0.00	0.00		0.06	0.00	0.00	95.13
SD23a	ID = 2491 SD23a cpx5-ox1	0.14	6.51	3.27	82.52	0.39	2.44	0.03	0.08	0.00	0.00	0.22		0.03	0.12	0.00	95.75
SD23a	ID = 2492 SD23a cpx5-ox2	0.06	6.29	3.61	82.18	0.52	2.69	0.04	0.11	0.00	0.01	0.00		0.25	0.01	0.00	95.77
SD23a	ID = 2493 SD23a cpx5-ox3	0.05	7.82	3.08	81.61	0.72	2.35	0.05	0.10	0.13	0.02	0.00		0.12	0.03	0.00	96.08
SD23a	ID = 2496 SD23a cpx5-ox4	0.09	6.53	3.74	80.89	0.49	2.61	0.24	0.01	0.04	0.07	0.13		0.00	0.11	0.37	95.32
SD23a	ID = 2499 SD23a cpx6-ox	0.18	6.26	3.67	81.12	0.60	2.37	0.20	0.00	0.00	0.00	0.00		0.16	0.11	0.00	94.67
SD23a	ID = 2526 SD23a cpx7-ox	0.13	6.75	2.63	83.17	0.71	1.68	0.06	0.05	0.00	0.04	0.00		0.20	0.00	0.00	95.42

Sample	Description of Analysis	SiO_2	TiO_2	Al_2O_3	FeO	MnO	MgO	CaO	Na_2O	K_2O	Cl	NiO	V_2O_3	Cr_2O_3	SO_3	P_2O_5	Total
SD23a	ID = 2467 SD23a ox1	0.11	5.93	4.17	82.11	0.29	2.70	0.03	0.00	0.05	0.04	0.17		0.20	0.12	0.13	96.05
SD23a	ID = 2506 SD23a ox2	0.00	6.59	2.81	81.22	0.83	2.19	0.04	0.01	0.04	0.04	0.03		0.14	0.00	0.00	93.94
SD23a	ID = 2519 SD23a ox3	0.17	6.44	4.01	80.38	0.51	2.88	0.00	0.00	0.07	0.00	0.13		0.00	0.00	0.14	94.73
SD25a	ID = 10513 SD25a_ox1	0.04	5.79	3.04	82.29	0.63	2.86	0.01	0.00	0.07	0.11	0.00		0.04	0.00	0.00	94.88
SD32b	ID = 2404 SD32b hbl4-ox-il	0.20	29.60	0.65	62.94	0.52	1.57	0.24	0.00	0.00	0.03	0.00		0.00	0.00	0.05	95.80
SD32b	ID = 2405 SD32b hbl4-ox-il-r	0.18	29.70	0.47	63.33	0.37	1.62	0.23	0.06	0.00	0.00	0.00		0.03	0.15	0.23	96.37
SD32b	ID = 2406 SD32b hbl4-ox2	0.13	6.19	3.34	80.62	0.60	2.94	0.72	0.36	0.04	0.11	0.13		0.02	0.10	0.93	96.23
SD32b	ID = 2399 SD32b ox1	0.07	6.37	3.37	81.23	0.52	2.88	0.02	0.15	0.00	0.00	0.00		0.28	0.00	0.00	94.89
SD32b	ID = 2400 SD32b ox2	0.22	5.94	3.49	81.05	0.80	3.12	0.03	0.00	0.03	0.00	0.00		0.07	0.06	0.00	94.81
SD28	ID = 2275 SD28 cpx2-ox	0.26	4.76	3.55	83.24	0.51	2.07	0.49	0.01	0.03	0.04	0.00		0.10	0.00	0.00	95.06
SD28	ID = 2289 SD28 cpx4-ox	0.04	6.24	2.43	83.27	0.81	2.10	0.21	0.06	0.01	0.04	0.00		0.09	0.02	0.00	95.32
SD9c	ID = 3485 SD9c cpx4-ox-c	0.14	7.11	2.53	82.73	0.66	2.15	0.14	0.08	0.00	0.00	0.15	0.45	0.10	0.00	0.00	96.24
SD9c	ID = 3486 SD9c cpx4-ox-r	0.17	6.64	2.58	81.98	0.72	2.19	0.30	0.06	0.00	0.05	0.00	0.44	0.11	0.00	0.00	95.24
SD28	ID = 2280 SD28 ox1-c	0.01	7.24	1.72	84.48	0.61	1.66	0.02	0.00	0.03	0.00	0.35		0.07	0.00	0.00	96.19
SD28	ID = 2282 SD28 ox1-r	0.10	6.60	1.57	85.27	0.46	1.51	0.17	0.00	0.08	0.00	0.00		0.02	0.00	0.00	95.78
SD28	ID = 2283 SD28 ox2-c	0.16	6.62	1.76	85.09	0.56	1.59	0.00	0.01	0.05	0.06	0.02		0.04	0.00	0.00	95.96
SD28	ID = 2285 SD28 ox2-r	0.05	6.48	1.75	85.12	0.53	1.69	0.00	0.00	0.00	0.00	0.10		0.19	0.01	0.00	95.92
SD28	ID = 2300 SD28 ox3-c	0.12	6.80	1.86	84.22	0.69	1.58	0.05	0.07	0.02	0.00	0.39		0.00	0.00	0.00	95.80
SD28	ID = 2301 SD28 ox3-r	0.09	6.72	2.02	84.68	0.69	1.73	0.13	0.00	0.02	0.00	0.34		0.01	0.00	0.00	96.43
SD28	ID = 2309 SD28 ox4-c	0.12	6.17	1.53	85.16	0.64	1.59	0.09	0.00	0.00	0.00	0.00		0.13	0.00	0.00	95.43
SD28	ID = 2312 SD28 ox4-r	0.13	6.31	1.58	84.86	0.65	1.61	0.11	0.01	0.00	0.04	0.00		0.12	0.07	0.00	95.49
SD9c	ID = 3474 SD9c ox1-c	0.18	6.72	1.96	84.04	0.70	1.94	0.14	0.11	0.00	0.00	0.00	0.62	0.05	0.00	0.00	96.46
SD9c	ID = 3475 SD9c ox1-r	0.16	6.63	2.03	84.25	0.70	1.78	0.06	0.00	0.06	0.08	0.00	0.45	0.00	0.00	0.00	96.20
SD9c	ID = 3476 SD9c ox2-c	0.11	6.51	2.17	83.47	0.63	1.83	0.06	0.23	0.00	0.00	0.04	0.59	0.11	0.00	0.00	95.75
SD9c	ID = 3477 SD9c ox2-r	0.07	5.41	2.26	85.47	0.59	1.76	0.05	0.00	0.01	0.00	0.29	0.39	0.00	0.00	0.00	96.30
SD9c	ID = 3480 SD9c ox3-c	0.01	7.17	2.18	83.96	0.72	1.90	0.00	0.00	0.04	0.07	0.00	0.52	0.00	0.00	0.00	96.57
SD9c	ID = 3481 SD9c ox3-r	0.04	6.62	2.38	82.63	0.62	1.97	0.07	0.00	0.04	0.00	0.00	0.55	0.09	0.00	0.00	95.01
SD9c	ID = 3482 SD9c ox4-c	0.20	6.90	1.98	83.43	0.62	2.08	0.00	0.06	0.00	0.00	0.01	0.44	0.00	0.00	0.00	95.72
SD9c	ID = 3483 SD9c ox4-r	0.15	6.99	2.00	83.21	0.63	1.98	0.03	0.00	0.01	0.04	0.12	0.51	0.09	0.00	0.04	95.80
T04-56	ID = 3494 T04-56 cpx1-ox1	0.28	7.55	4.83	77.65	0.62	3.41	0.35	0.32	0.00	0.00	0.00	0.42	0.09	0.08	0.00	95.60
T04-56	ID = 3495 T04-56 cpx1-ox2-c	0.10	9.65	3.71	79.22	0.54	3.33	0.04	0.08	0.00	0.04	0.00	0.40	0.15	0.00	0.08	97.34
T04-56	ID = 3496 T04-56 cpx1-ox2-r	0.09	9.26	3.54	78.46	0.73	3.38	0.09	0.00	0.05	0.00	0.09	0.63	0.00	0.01	0.00	96.33
T04-56	ID = 3513 T04-56 cpx4-ox-c	0.04	6.62	5.58	79.56	0.21	3.45	0.02	0.05	0.00	0.02	0.00	0.77	0.15	0.00	0.00	96.47

Sample	Description of Analysis	SiO_2	TiO_2	Al_2O_3	FeO	MnO	MgO	CaO	Na_2O	K_2O	Cl	NiO	V_2O_3	Cr_2O_3	SO_3	P_2O_5	Total
T04-56	ID = 3514 T04-56 cpx4-ox-r	0.73	6.44	5.80	77.76	0.34	3.69	0.41	0.00	0.00	0.01	0.00	0.59	0.00	0.04	0.00	95.81
T04-56	ID = 3517 T04-56 cpx5-ox-c	0.09	9.63	3.65	77.71	0.49	3.55	0.18	0.00	0.05	0.05	0.00	0.46	0.08	0.00	0.00	95.94
T04-56	ID = 3518 T04-56 cpx5-ox-r	0.15	9.25	3.67	77.25	0.60	3.48	0.39	0.13	0.05	0.06	0.17	0.41	0.00	0.01	0.04	95.66
T04-56	ID = 3527 T04-56 cpx6-ox1	0.11	9.29	4.00	78.19	0.55	3.84	0.09	0.15	0.00	0.03	0.09	0.46	0.07	0.02	0.01	96.90
T04-56	ID = 3506 T04-56 ox1-c	0.14	6.33	5.59	79.51	0.50	3.70	0.00	0.12	0.00	0.08	0.12	0.62	0.05	0.01	0.00	96.77
T04-56	ID = 3507 T04-56 ox1-r	0.13	6.47	5.41	79.25	0.48	3.64	0.05	0.07	0.03	0.03	0.06	0.43	0.00	0.09	0.00	96.14
T04-56	ID = 3537 T04-56 ox2-c	0.23	9.39	3.53	78.77	0.61	3.34	0.05	0.00	0.00	0.03	0.07	0.42	0.06	0.00	0.00	96.50
T04-56	ID = 3538 T04-56 ox2-r	0.19	9.29	3.49	78.72	0.57	3.52	0.09	0.00	0.00	0.02	0.03	0.62	0.14	0.11	0.00	96.79
T04-56	ID = 3539 T04-56 ox3-c	0.04	9.38	3.37	79.42	0.70	3.19	0.00	0.00	0.05	0.07	0.14	0.44	0.00	0.00	0.00	96.80
T04-56	ID = 3540 T04-56 ox3-r	0.36	9.43	3.51	78.20	0.74	3.25	0.11	0.00	0.06	0.08	0.07	0.60	0.21	0.00	0.00	96.62
SD11	ID = 2055 SD11 cpx2ox	0.24	8.80	3.64	79.15	0.58	3.14	0.34	0.00	0.00	0.01	0.00		0.15	0.04	0.10	96.19
SD11	ID = 2051 SD11 ox1	0.11	8.98	4.04	79.56	0.35	2.97	0.05	0.00	0.00	0.00	0.00		0.06	0.00	0.00	96.12
SD11	ID = 3104 SD11 cpx8-ox1	0.23	8.64	4.16	78.66	0.64	3.25	0.26	0.00	0.00	0.01	0.00	0.33	0.00	0.00	0.07	96.27
SD11	ID = 3110 SD11 cpx11-ox1	0.06	9.74	1.40	75.40	0.32	3.16	0.43	0.00	0.00	0.02	0.02	0.18	0.11	0.00	0.01	90.86
SD11	ID = 3097 SD11 mol2-ox	1.61	12.40	1.24	78.16	0.57	1.17	0.32	0.10	0.18	0.01	0.00	0.58	0.00	0.12	0.12	96.60
SD11	ID = 3085 SD11 ox1-c	0.08	9.13	3.11	80.47	0.78	1.77	0.03	0.18	0.00	0.07	0.15	0.47	0.20	0.00	0.08	96.53
SD11	ID = 3086 SD11 ox1-r	0.13	9.15	3.42	80.21	0.73	2.06	0.09	0.15	0.00	0.08	0.11	0.48	0.00	0.00	0.00	96.60
SD11	ID = 3087 SD11 ox2-c	0.24	9.49	3.44	80.47	0.69	2.70	0.00	0.11	0.02	0.00	0.00	0.48	0.06	0.00	0.00	97.70
SD11	ID = 3088 SD11 ox2-r	0.05	9.14	3.50	79.86	0.57	2.77	0.06	0.28	0.05	0.03	0.19	0.30	0.00	0.00	0.02	96.82
SD11	ID = 3089 SD11 ox3-c	0.27	9.04	3.61	79.86	0.50	2.78	0.07	0.00	0.00	0.02	0.00	0.53	0.00	0.07	0.00	96.75
SD11	ID = 3090 SD11 ox3-r	0.40	8.87	3.96	76.75	0.50	2.93	0.12	0.00	0.02	0.02	0.06	0.45	0.01	0.00	0.11	94.21
SD11	ID = 3084 SD11 opx-ox	0.15	8.10	2.93	80.67	0.70	2.71	0.14	0.09	0.00	0.00	0.13	0.44	0.09	0.00	0.00	96.15
E02-117	ID = 8349 E02-117 hbl1-ox1	0.08	6.99	4.03	78.53	0.84	2.77	0.20	0.00	0.04	0.01	0.00	0.63	0.03	0.00	0.00	94.15
E02-117	ID = 8350 E02-117 hbl1-ox2-c	0.10	7.38	4.43	79.04	0.56	2.58	0.00	0.00	0.00	0.02	0.07	0.33	0.00	0.00	0.00	94.51
E02-117	ID = 8351 E02-117 hbl1-ox2-r	0.13	7.10	4.41	77.91	0.47	2.91	0.08	0.00	0.05	0.04	0.21	0.43	0.00	0.00	0.04	93.78
E02-117	ID = 8361 E02-117 hbl2-ox-c	0.08	6.53	1.41	82.89	1.05	1.16	0.08	0.05	0.00	0.04	0.22	0.56	0.00	0.00	0.00	94.07
E02-117	ID = 8362 E02-117 hbl2-ox-r	0.30	6.61	1.53	81.69	1.15	1.18	0.11	0.16	0.00	0.06	0.15	0.26	0.03	0.04	0.01	93.28
E02-117	ID = 8407 E02-117 hbl5-ox	0.16	7.41	4.31	79.29	0.53	2.75	0.08	0.22	0.00	0.00	0.15	0.25	0.00	0.00	0.06	95.21
E02-117	ID = 8383 E02-117 cpx1-ox	0.22	7.27	3.38	78.98	0.91	2.34	0.30	0.15	0.00	0.00	0.03	0.35	0.00	0.00	0.00	93.93
E02-117	ID = 8387 E02-117 cpx2-ox1	0.30	6.64	4.20	79.11	0.71	2.65	0.36	0.00	0.06	0.00	0.06	0.49	0.00	0.00	0.00	94.58
E02-117	ID = 8388 E02-117 cpx2-ox2-c	0.08	7.15	4.30	78.62	0.64	2.62	0.13	0.00	0.07	0.03	0.00	0.38	0.00	0.00	0.00	94.02
E02-117	ID = 8389 E02-117 cpx2-ox2-r	0.08	7.20	4.42	78.69	0.55	2.71	0.21	0.23	0.00	0.03	0.03	0.35	0.00	0.02	0.00	94.52
E02-117	ID = 8397 E02-117 cpx4-ox1	0.07	7.01	2.94	79.86	0.99	2.22	0.16	0.21	0.09	0.00	0.00	0.42	0.00	0.00	0.00	93.97

Sample	Description of Analysis	SiO_2	TiO_2	Al_2O_3	FeO	MnO	MgO	CaO	Na_2O	K_2O	Cl	NiO	V_2O_3	Cr_2O_3	SO_3	P_2O_5	Total
E02-117	ID = 8399 E02-117 cpx4-ox2	0.23	7.01	3.39	79.33	0.63	2.09	0.31	0.01	0.02	0.01	0.04	0.47	0.00	0.01	0.00	93.55
E02-117	ID = 8357 E02-117 ox1-c1	0.16	6.92	3.49	79.35	0.67	2.22	0.00	0.01	0.02	0.00	0.09	0.33	0.31	0.01	0.01	93.59
E02-117	ID = 8358 E02-117 ox1-c2	0.06	6.95	3.66	80.15	0.63	2.45	0.02	0.00	0.04	0.04	0.00	0.56	0.23	0.03	0.00	94.82
E02-117	ID = 8359 E02-117 ox1-r	0.11	6.93	3.54	79.28	0.82	2.18	0.00	0.06	0.00	0.03	0.06	0.50	0.25	0.00	0.00	93.76

[all data in wt.%]

Sample	Description of Analysis	SiO_2	TiO_2	Al_2O_3	FeO	MnO	MgO	CaO	Na_2O	K_2O	Cl	NiO	V_2O_3	Cr_2O_3	SO_3	P_2O_5	Original Totals
SD1	ID = 3115 SD1 cpx1-glass1	69.11	0.57	13.00	2.48	0.07	1.56	3.10	3.55	6.21	0.26	0.00	0.00	0.09	0.01	0.00	97.90
SD1	ID = 3116 SD1 cpx1-glass2	69.50	0.51	14.75	1.82	0.14	0.66	1.53	3.96	6.55	0.35	0.00	0.00	0.01	0.07	0.15	97.55
SD1	ID = 3117 SD1 cpx1-glass3	68.47	0.55	14.86	1.77	0.07	0.91	2.73	4.65	5.16	0.15	0.00	0.00	0.00	0.24	0.43	98.42
SD1	ID = 3154 SD1 cpx6-glass	71.21	0.43	15.06	1.15	0.21	0.18	1.22	4.59	5.42	0.37	0.00	0.00	0.07	0.00	0.08	95.29
SD1	ID = 3170 SD1 cpx8-glass1	69.92	0.40	15.14	1.07	0.09	0.72	2.03	4.98	5.03	0.22	0.00	0.05	0.12	0.11	0.12	95.47
SD1	ID = 3174 SD1 cpx8-glass2	70.81	1.11	14.19	1.72	0.02	0.31	1.83	4.56	4.87	0.17	0.09	0.01	0.00	0.19	0.12	97.95
SD4	ID = 3412 SD4 cpx4-glass1	71.35	0.44	14.93	1.57	0.09	0.12	1.24	4.61	5.27	0.25	0.00	0.00	0.01	0.00	0.12	95.26
SD4	ID = 3414 SD4 cpx4-glass2	71.63	0.23	14.82	1.69	0.00	0.03	1.29	4.46	5.36	0.25	0.00	0.00	0.10	0.00	0.14	94.36
SD4	ID = 3432 SD4 cpx5-glass1	67.36	0.33	14.83	2.85	0.20	1.28	2.43	4.14	5.95	0.48	0.00	0.00	0.00	0.00	0.15	97.93
SD4	ID = 3436 SD4 cpx5-glass3	68.29	0.51	16.33	2.10	0.14	0.33	1.20	4.09	6.64	0.30	0.00	0.00	0.06	0.00	0.00	96.64
SD5	ID = 2237 SD5 cpx3-glass	68.85	0.37	16.10	1.27	0.10	0.56	1.36	4.05	7.07	0.16	0.00		0.00	0.01	0.08	97.67
SD5	ID = 2245 SD5 cpx4-glass1	66.30	0.58	16.85	2.06	0.00	1.88	1.66	4.93	5.19	0.36	0.00		0.04	0.15	0.00	98.22
SD13	ID = 3229 SD13 cpx3-glass1	66.98	0.50	12.68	2.85	0.09	3.03	5.16	3.86	4.11	0.28	0.09	0.00	0.00	0.06	0.31	97.49
SD13	ID = 3230 SD13 cpx3-glass2	64.49	0.48	14.60	3.02	0.08	2.01	4.19	4.65	5.68	0.30	0.00	0.00	0.12	0.40	0.00	98.52
SD13	ID = 3234 SD13 cpx4-glass1	70.55	0.37	14.62	1.66	0.14	0.54	1.50	4.52	5.16	0.19	0.27	0.01	0.16	0.14	0.15	97.40
SD13	ID = 3253 SD13 cpx10-glass	68.21	0.32	16.73	1.23	0.19	0.00	1.40	5.47	6.18	0.24	0.00	0.00	0.02	0.00	0.00	98.88
SD13	ID = 3261 SD13 cpx11-glass	67.89	0.17	14.19	1.69	0.16	0.46	3.53	4.14	5.15	0.45	0.00	0.00	0.00	0.00	2.17	95.63
SD15	ID = 8115 SD15 cpx15 incl.1	70.00	0.26	15.14	1.88	0.10	0.50	1.80	4.69	5.09	0.22	0.00	0.00	0.03	0.05	0.24	93.54
SD15	ID = 8116 SD15 cpx15 incl.2	70.40	0.29	15.26	1.85	0.09	0.17	1.72	4.53	5.17	0.30	0.00	0.04	0.03	0.01	0.14	93.54
SD15	ID = 8117 SD15 cpx15 incl.3a	69.89	0.26	15.90	1.25	0.10	0.58	1.86	4.75	5.12	0.03	0.00	0.09	0.02	0.13	0.01	95.53
SD15	ID = 8118 SD15 cpx15 incl.3b	69.85	0.30	15.96	1.16	0.09	0.46	1.75	4.77	5.14	0.04	0.06	0.15	0.09	0.16	0.00	95.36
SD1	ID = 3136 SD1 hbl2-glass1	60.45	0.89	18.09	3.69	0.14	0.61	0.49	8.96	6.27	0.28	0.00	0.00	0.00	0.05	0.08	97.85
SD1	ID = 3137 SD1 hbl2-glass2	59.66	1.10	17.81	3.62	0.09	1.03	0.84	9.02	6.22	0.24	0.00	0.04	0.08	0.20	0.04	97.03
SD1	ID = 3165 SD1 hbl6-glass1	65.74	0.60	16.64	2.06	0.12	1.50	2.91	4.95	4.77	0.34	0.00	0.00	0.07	0.00	0.29	95.84
SD4	ID = 3388 SD4 hbl2-glass1	64.57	0.49	18.93	0.87	0.09	0.14	1.39	5.70	7.66	0.00	0.00	0.00	0.04	0.11	0.00	97.56
SD4	ID = 3410 SD4 hbl4-glass2	63.47	0.21	19.20	0.94	0.14	0.56	2.55	5.72	6.87	0.02	0.15	0.01	0.00	0.00	0.16	98.82
SD4	ID = 3426 SD4 hbl6-glass1	66.30	0.74	17.82	1.46	0.09	0.66	2.24	5.50	4.20	0.36	0.00	0.00	0.00	0.19	0.44	96.48
SD13	ID = 3196 SD13 hbl1-glass1	62.97	0.75	17.64	2.54	0.02	1.61	1.93	5.52	6.59	0.23	0.00	0.00	0.00	0.06	0.14	97.75
SD13	ID = 3222 SD13 hbl6-glass	58.79	1.05	14.14	2.39	0.06	1.58	6.92	4.29	5.24	0.50	0.06	0.08	0.06	0.13	4.71	97.17
SD20	ID = 8086 SD20 cpx2 incl.1a	69.61	0.42	15.41	2.13	0.11	0.53	1.62	3.93	5.66	0.36	0.00	0.00	0.02	0.20	0.00	92.87
SD20	ID = 8087 SD20 cpx2 incl.1b	68.83	0.50	15.56	2.40	0.14	0.34	1.68	4.18	5.67	0.32	0.17	0.00	0.03	0.06	0.12	94.42
SD20	ID = 8088 SD20 cpx2 incl.2	68.13	0.46	15.42	2.78	0.19	0.47	1.78	4.49	5.59	0.38	0.00	0.00	0.05	0.16	0.09	97.15

Sample	Description of Analysis	SiO_2	TiO_2	Al_2O_3	FeO	MnO	MgO	CaO	Na_2O	K_2O	Cl	NiO	V_2O_3	Cr_2O_3	SO_3	P_2O_5	Original Totals
SD20	ID = 8089 SD20 cpx2 incl.3	67.13	0.63	16.87	2.45	0.13	0.33	2.28	4.38	4.87	0.44	0.00	0.00	0.04	0.26	0.17	92.95
SD20	ID = 8091 SD20 cpx2 incl.3b	67.23	0.67	17.03	2.49	0.14	0.39	2.34	3.96	4.93	0.38	0.00	0.00	0.13	0.10	0.21	92.61
SD20	ID = 8094 SD20 cpx4-incl.1	66.02	0.59	17.14	2.92	0.00	0.68	2.39	4.59	4.96	0.29	0.07	0.00	0.00	0.19	0.15	93.48
SD20	ID = 8095 SD20 cpx4-incl.4	66.91	0.59	16.95	1.85	0.13	0.23	2.15	4.70	5.79	0.33	0.11	0.00	0.00	0.25	0.00	90.85
SD20	ID = 8104 SD20 cpx5 incl.1a	66.67	0.46	16.74	2.68	0.00	0.89	2.31	4.36	5.09	0.38	0.14	0.00	0.00	0.28	0.00	95.22
SD20	ID = 8106 SD20 cpx5 incl.1c	66.99	0.47	16.41	2.61	0.26	0.69	2.27	4.41	5.09	0.38	0.00	0.01	0.00	0.24	0.18	95.99
SD20	ID = 8105 SD20 cpx5 incl.1b	64.76	0.47	19.01	1.99	0.09	0.46	4.61	4.23	3.70	0.24	0.00	0.00	0.01	0.27	0.16	95.70
SD20	ID = 8107 SD20 cpx5 incl.2	68.47	0.55	16.67	1.61	0.10	0.25	1.92	4.82	4.83	0.37	0.00	0.00	0.05	0.15	0.21	97.52
SD20	ID = 8114 SD20 cpx5 glass1	65.95	0.53	16.88	2.75	0.05	0.85	2.97	4.80	4.66	0.27	0.00	0.00	0.00	0.13	0.15	99.68
SD20	ID = 8108 SD20 cpx5 incl.3	66.40	0.53	16.92	2.89	0.00	0.82	2.98	4.09	4.79	0.30	0.07	0.04	0.03	0.04	0.10	97.88
SD23a	ID = 2489 SD23a cpx5-glass1	71.46	0.29	16.09	0.72	0.00	0.04	2.08	3.95	4.87	0.31	0.00		0.00	0.06	0.12	92.84
SD23a	ID = 2531 SD23a cpx8-glass1	68.68	0.62	17.40	1.85	0.02	0.00	1.03	2.49	7.15	0.41	0.00		0.00	0.22	0.12	94.70
SD23a	ID = 2532 SD23a cpx8-glass2	66.95	0.64	16.88	1.98	0.00	0.00	0.89	1.84	9.98	0.26	0.17		0.00	0.26	0.15	96.36
SD25	ID = 16 SD25-cpx1back-unknownglass	64.63	0.99	15.06	4.76	0.11	3.21	0.91	4.59	5.28	0.24	0.06	0.00	0.06	0.09	0.00	98.92
SD25	ID = 16 SD25-cpx1back-unknownglass	64.64	0.99	15.06	4.76	0.11	3.21	0.91	4.58	5.29	0.24	0.06	0.00	0.06	0.09	0.00	99.29
SD25	ID = 167 SD25-cpx1back-incl1	69.09	0.48	14.85	2.57	0.12	0.45	2.39	4.54	4.98	0.30	0.03	0.00	0.00	0.00	0.18	97.75
SD25	ID = 168 SD25-cpx1back-incl3	69.53	0.44	15.25	1.82	0.07	0.48	1.75	5.09	5.19	0.29	0.07	0.00	0.00	0.04	0.00	97.92
SD25	ID = 169 SD25-cpx1back-ukagain	66.87	0.64	15.18	3.73	0.05	1.95	1.07	5.10	4.97	0.19	0.07	0.00	0.06	0.00	0.11	98.81
SD25	ID = 170 SD25-cpx4back-incl1	69.38	0.50	15.79	1.76	0.04	0.27	1.71	5.08	5.14	0.19	0.09	0.00	0.01	0.02	0.00	95.31
SD25	ID = 171 SD25-cpx4back-incl3	70.25	0.43	16.65	1.02	0.07	0.81	1.81	3.29	4.77	0.34	0.13	0.00	0.00	0.12	0.31	93.88
SD25	ID = 172 SD25-cpx4back-uk1	69.01	0.49	15.61	2.14	0.13	0.67	1.61	4.35	5.30	0.36	0.00	0.00	0.02	0.14	0.18	98.93
SD25	ID = 173 SD25-cpx4back-incl3again	69.51	0.46	16.16	0.75	0.12	0.63	1.77	5.14	5.06	0.33	0.00	0.00	0.00	0.00	0.07	94.20
SD25	ID = 174 SD25-cpx3front-incl3	70.00	0.44	15.16	1.66	0.18	0.68	1.31	4.63	5.59	0.26	0.00	0.00	0.00	0.00	0.10	97.02
SD25	ID = 175 SD25-cpx3front-incl5	70.84	0.16	17.04	1.72	0.00	0.15	0.41	4.82	4.47	0.25	0.00	0.00	0.00	0.05	0.08	95.13
SD25	ID = 176 SD25-cpx3front-incl5again	68.67	0.21	16.32	1.25	0.11	0.06	0.65	7.38	4.70	0.26	0.00	0.00	0.12	0.14	0.11	96.98
SD25	ID = 178 SD25-cpx3front-gm	66.08	0.58	16.44	2.96	0.22	0.83	2.67	4.93	4.84	0.20	0.07	0.00	0.08	0.03	0.07	100.36
SD24	ID = 182 SD24-cpx3back incl2	69.37	0.66	15.24	2.32	0.12	0.38	1.19	4.67	5.60	0.38	0.01	0.00	0.00	0.06	0.00	92.97
SD24	ID = 183 SD24-cpx3back incl3	71.50	0.52	15.29	1.80	0.15	0.39	1.34	3.18	5.30	0.31	0.00	0.00	0.04	0.18	0.00	92.81
SD24	ID = 184 SD24-cpx3back incl3again	70.34	0.64	15.15	1.46	0.00	0.46	1.62	4.40	5.43	0.30	0.00	0.00	0.05	0.15	0.00	93.76
SD24	ID = 185 SD24-cpx3back incl1	70.35	0.60	15.08	1.84	0.12	0.37	1.20	4.65	5.60	0.13	0.05	0.00	0.01	0.00	0.00	93.70
SD24	ID = 186 SD24-cpx3back uk1	69.10	0.71	15.61	1.87	0.12	0.67	1.49	4.63	5.49	0.31	0.00	0.00	0.00	0.01	0.00	93.23
SD24	ID = 187 SD24-cpx2back incl1	69.67	0.51	15.44	1.76	0.20	0.38	1.33	4.60	5.79	0.26	0.00	0.00	0.00	0.00	0.08	92.77

Sample	Description of Analysis	SiO_2	TiO_2	Al_2O_3	FeO	MnO	MgO	CaO	Na_2O	K_2O	Cl	NiO	V_2O_3	Cr_2O_3	SO_3	P_2O_5	Original Totals
SD24	ID = 188 SD24-cpx2back incl2	69.93	0.47	15.30	1.82	0.33	0.26	1.35	4.29	5.86	0.33	0.00	0.00	0.01	0.04	0.01	92.28
SD24	ID = 189 SD24-cpx2back incl3	69.14	0.43	15.88	1.98	0.07	0.43	1.79	4.59	5.27	0.28	0.00	0.00	0.00	0.04	0.10	91.49
SD28	ID = 2278 SD28 cpx2-glass2	73.44	0.11	14.17	0.90	0.00	0.00	1.35	3.70	6.16	0.12	0.00		0.01	0.04	0.00	97.20
SD28	ID = 2290 SD28 cpx4-glass	72.04	0.07	14.95	0.81	0.06	0.00	1.20	3.50	7.05	0.16	0.00		0.04	0.12	0.00	
SD23a	ID = 2474 SD23a hbl1-glass	66.24	0.61	16.98	3.16	0.10	0.74	2.90	3.50	5.03	0.36	0.03		0.00	0.13	0.21	98.44
SD23a	ID = 2516 SD23a mhbl4-glass	63.83	0.41	17.27	2.93	0.15	0.58	4.23	4.22	5.28	0.37	0.14		0.00	0.35	0.21	98.99
SD32b	ID = 2402 SD32b hbl4-gl1	65.29	0.48	16.41	2.92	0.05	0.83	3.06	4.40	5.55	0.33	0.03		0.00	0.28	0.38	97.37
SD32	ID = 8121 SD32 cpx11 incl.1	67.08	0.46	16.62	1.91	0.00	0.17	1.21	5.85	6.14	0.30	0.00	0.03	0.00	0.16	0.07	95.83
SD32	ID = 8122 SD32 cpx11 incl.2	65.20	0.63	16.74	2.82	0.06	0.63	2.41	5.16	5.50	0.32	0.00	0.00	0.11	0.17	0.22	97.79
SD32	ID = 8125 SD32 cpx12 incl.1	70.94	0.40	15.74	0.80	0.09	0.00	1.79	5.04	4.84	0.30	0.00	0.00	0.00	0.05	0.00	92.57
SD32	ID = 8126 SD32 cpx12 incl.2	70.25	0.59	14.99	1.21	0.00	0.47	1.99	4.69	4.99	0.40	0.18	0.00	0.04	0.19	0.00	94.15
SD32	ID = 8127 SD32 cpx12 glass1	65.81	0.62	16.50	3.11	0.07	0.86	2.86	4.76	5.04	0.28	0.00	0.00	0.00	0.08	0.00	96.23
SD9D	ID = 8081 SD9D cpx9 glass1	65.83	0.60	16.72	2.66	0.28	0.96	2.60	4.85	4.95	0.26	0.07	0.00	0.05	0.12	0.04	96.55
SD9D	ID = 8082 SD9D cpx9 glass2	65.71	0.57	16.69	2.85	0.10	1.07	2.57	4.88	5.05	0.23	0.00	0.00	0.06	0.07	0.14	96.82
SD9D	ID = 8084 SD9D cpx9 glass4	66.02	0.53	16.63	2.90	0.09	0.93	2.73	4.77	4.93	0.24	0.00	0.00	0.09	0.05	0.07	96.57
SD9D	ID = 8100 SD9D cpx6-glass1	65.92	0.60	16.55	2.84	0.12	0.85	2.79	4.79	4.91	0.25	0.06	0.00	0.00	0.11	0.21	97.12
SD9D	ID = 8101 SD9D cpx6-glass2	64.44	0.60	17.84	2.67	0.05	0.79	3.40	4.91	4.49	0.26	0.07	0.03	0.00	0.15	0.29	97.02
T04-56	ID = 3497 T04-56 cpx1-glass2	65.93	0.60	16.46	3.27	0.11	0.72	2.19	5.08	5.06	0.26	0.00	0.06	0.08	0.01	0.15	98.54
T04-56	ID = 3498 T04-56 cpx1-glass3	68.20	0.57	17.31	1.14	0.10	0.18	1.81	5.66	4.30	0.33	0.00	0.01	0.00	0.15	0.25	95.84
T04-56	ID = 3502 T04-56 cpx2-glass1	66.75	0.70	17.12	1.81	0.16	0.19	1.88	5.58	4.90	0.46	0.00	0.00	0.01	0.19	0.27	96.23
T04-56	ID = 3504 T04-56 cpx2-glass2	63.97	0.58	15.92	3.99	0.24	1.39	3.30	4.79	4.92	0.31	0.00	0.00	0.00	0.23	0.36	99.21
SD11	ID = 3068 SD11 cpx-glass1	61.76	0.84	18.13	2.86	0.04	0.00	0.22	8.77	6.70	0.33	0.00	0.00	0.12	0.14	0.07	97.86
SD11	ID = 3092 SD11 cpx6-glass1	65.81	0.41	15.48	2.49	0.14	1.47	1.91	6.15	5.53	0.19	0.00	0.01	0.13	0.21	0.05	97.34
SD11	ID = 3103 SD11 cpx8-glass1	64.10	0.74	17.43	2.05	0.20	1.01	2.79	5.38	5.19	0.38	0.16	0.00	0.00	0.24	0.32	97.38
E02-117	ID = 8384 E02-117 cpx2-glass1	54.92	1.05	17.60	8.05	0.21	1.65	6.66	5.09	3.76	0.29	0.00	0.00	0.03	0.26	0.43	97.89
E02-117	ID = 8386 E02-117 cpx2-glass2	54.81	0.96	15.84	7.20	0.25	3.51	9.58	3.91	3.52	0.23	0.00	0.00	0.06	0.00	0.13	97.10
E02-117	ID = 8391 E02-117 cpx3-glass1	66.52	0.33	13.24	2.62	0.18	2.28	5.19	4.94	4.39	0.19	0.00	0.02	0.05	0.06	0.00	97.04
E02-117	ID = 8398 E02-117 cpx4-glass1	61.28	0.74	17.13	4.36	0.25	1.10	4.83	5.64	3.90	0.23	0.00	0.09	0.00	0.44	0.00	96.07
MI-5	ID = 9010 MI-5 cpx1-gl1	70.22	0.48	15.85	0.33	0.00	0.18	2.05	4.21	6.37	0.10	0.00	0.00	0.00	0.05	0.15	97.73
MI-5	ID = 9011 MI-5 cpx1-gl2	68.42	0.36	15.64	1.14	0.12	0.98	2.67	2.85	7.22	0.31	0.00	0.00	0.06	0.00	0.23	99.06
MI-5	ID = 9012 MI-5 cpx2-gl1	65.14	0.62	15.85	1.54	0.13	2.03	3.47	3.70	7.10	0.14	0.00	0.00	0.00	0.02	0.26	99.48
MI-5	ID = 9013 MI-5 cpx3-gl1	68.01	0.42	16.26	1.85	0.05	0.01	1.14	3.78	6.98	0.31	0.00	0.00	0.07	0.71	0.41	98.15

Sample	Description of Analysis	SiO_2	TiO_2	Al_2O_3	FeO	MnO	MgO	CaO	Na_2O	K_2O	Cl	NiO	V_2O_3	Cr_2O_3	SO_3	P_2O_5	Original Totals
MI-5	ID = 9014 MI-5 cpx3-gl2	68.39	0.37	17.01	0.66	0.00	0.00	1.45	3.76	7.67	0.32	0.00	0.02	0.09	0.07	0.18	98.90
MI-5	ID = 9015 MI-5 cpx4-gl1	66.58	0.50	16.14	0.92	0.05	0.87	2.39	4.70	6.50	0.33	0.00	0.03	0.09	0.08	0.82	98.96
MI-5	ID = 9016 MI-5 cpx5-gl1	65.27	0.20	18.67	0.51	0.13	0.02	1.05	5.30	8.80	0.00	0.00	0.01	0.04	0.00	0.00	100.32
MI-5	ID = 9017 MI-5 cpx6-gl1	68.89	0.35	17.49	0.31	0.06	0.17	1.13	5.86	5.29	0.15	0.00	0.00	0.11	0.04	0.14	98.28
MI-5	ID = 9018 MI-5 cpx6-gl1b	69.54	0.24	17.30	0.51	0.05	0.02	1.05	5.68	5.42	0.15	0.00	0.00	0.04	0.00	0.00	97.82
MI-5	ID = 9019 MI-5 cpx7-gl1	66.57	0.47	17.86	0.90	0.03	0.04	1.23	4.05	7.95	0.47	0.00	0.00	0.00	0.06	0.36	99.60
MI-5	ID = 9020 MI-5 cpx8-gl1	65.15	0.14	18.65	0.63	0.00	0.08	0.89	5.02	9.14	0.00	0.14	0.00	0.06	0.00	0.11	100.69
MI-5	ID = 9021 MI-5 cpx9-gl1	62.61	0.73	14.04	6.81	0.11	2.50	4.23	3.93	4.75	0.04	0.07	0.00	0.01	0.00	0.16	99.98
MI-5	ID = 9022 MI-5 cpx10-gl1	64.18	0.72	15.20	1.84	0.10	3.03	4.79	3.27	6.46	0.09	0.00	0.00	0.10	0.01	0.20	98.89
MI-5	ID = 9023 MI-5 cpx11-gl1	67.36	0.43	16.23	1.99	0.02	0.34	1.38	3.83	6.84	0.22	0.26	0.01	0.03	0.78	0.27	98.81
MI-5	ID = 9024 MI-5 cpx11-gl2	68.36	0.38	17.13	0.54	0.08	0.11	1.14	3.80	7.73	0.27	0.00	0.10	0.00	0.21	0.14	99.21
MI-5	ID = 9025 MI-5 cpx11-gl2b	67.87	0.44	16.93	0.99	0.09	0.00	1.43	3.31	7.66	0.35	0.02	0.00	0.00	0.51	0.40	97.69
MI-5	ID = 9026 MI-5 cpx13-gl1	68.02	0.25	16.55	0.72	0.13	0.63	1.77	4.33	7.43	0.16	0.00	0.00	0.00	0.01	0.00	98.69
MI-5	ID = 179 MI-5-cpx6back-uk1	71.00	0.34	16.32	0.56	0.09	0.00	0.90	5.60	4.93	0.20	0.00	0.00	0.00	0.00	0.06	93.83
MI-5	ID = 180 MI-5-cpx7back-incl1	70.07	0.38	16.67	0.68	0.00	0.22	0.93	5.37	5.35	0.16	0.01	0.00	0.01	0.00	0.16	97.25
MI-5	ID = 181 MI-5-cpx7back-uk1	70.08	0.35	16.35	0.79	0.12	0.00	0.75	5.50	5.56	0.29	0.06	0.00	0.00	0.04	0.10	96.23
T04-62	ID = 9027 T04-62 cpx1-gl1	63.55	0.70	17.61	2.58	0.16	0.57	1.76	5.80	6.60	0.33	0.00	0.00	0.08	0.07	0.20	100.05
T04-62	ID = 9028 T04-62 cpx1-gl2	62.02	0.70	15.77	3.60	0.02	2.01	3.43	5.53	5.73	0.41	0.16	0.10	0.07	0.04	0.41	99.99
T04-62	ID = 9029 T04-62 cpx1-gl3	60.75	1.28	17.51	2.72	0.15	1.28	2.53	6.78	6.39	0.22	0.00	0.13	0.00	0.14	0.12	100.25
T04-62	ID = 9030 T04-62 cpx2-gl1	67.76	0.58	16.73	0.76	0.02	0.21	1.64	5.59	5.40	0.23	0.07	0.00	0.01	0.18	0.81	97.98
T04-62	ID = 9031 T04-62 cpx3-gl1	64.66	1.02	16.99	2.89	0.22	0.35	0.95	5.72	6.43	0.39	0.00	0.05	0.00	0.14	0.19	99.35
T04-62	ID = 9032 T04-62 cpx4-gl1	61.64	0.79	16.70	3.19	0.13	1.35	2.00	7.26	6.33	0.15	0.08	0.00	0.00	0.13	0.25	99.16
T04-62	ID = 9033 T04-62 cpx4-gl2	64.04	0.77	17.72	2.42	0.01	0.79	1.56	5.97	6.23	0.16	0.00	0.00	0.00	0.00	0.32	99.83
T04-62	ID = 9034 T04-62 cpx5-gl1	60.93	0.65	15.57	4.60	0.21	4.46	2.10	5.46	5.49	0.24	0.00	0.00	0.06	0.02	0.23	100.96
T04-62	ID = 9035 T04-62 gm-gl1	64.79	0.56	18.37	1.79	0.05	0.34	3.50	5.34	4.81	0.17	0.00	0.00	0.07	0.06	0.14	98.72
T04-62	ID = 9036 T04-62 cpx6-gl1	65.89	0.85	15.24	2.94	0.15	0.39	1.11	5.07	6.96	0.63	0.00	0.09	0.00	0.00	0.66	99.72
T04-62	ID = 9037 T04-62 cpx7-gl1	67.24	0.81	15.49	2.46	0.17	0.28	0.44	5.36	6.55	0.74	0.14	0.00	0.00	0.00	0.30	99.01
T04-62	ID = 9038 T04-62 cpx8-gl1	64.53	0.60	17.98	2.38	0.07	0.24	1.50	6.02	5.46	0.42	0.10	0.00	0.09	0.21	0.38	99.10
T04-62	ID = 9039 T04-62 cpx9-gl1	59.71	1.04	16.94	3.59	0.18	0.93	2.04	8.79	6.25	0.33	0.00	0.01	0.05	0.11	0.04	98.12
T04-62	ID = 9040 T04-62 cpx10-gl1	67.42	1.08	17.21	1.26	0.09	0.34	1.45	5.47	5.13	0.14	0.00	0.14	0.00	0.02	0.24	98.76
T04-62	ID = 9041 T04-62 cpx11-gl1	65.08	1.57	16.39	3.88	0.15	0.40	1.65	5.30	4.81	0.29	0.00	0.00	0.00	0.18	0.28	99.21
T04-62	ID = 9042 T04-62 cpx12-gl1	67.85	0.37	17.20	0.93	0.16	0.24	1.86	5.40	5.12	0.31	0.00	0.03	0.00	0.10	0.42	99.64

Sample	Description of Analysis	SiO_2	TiO_2	Al_2O_3	FeO	MnO	MgO	CaO	Na_2O	K_2O	Cl	NiO	V_2O_3	Cr_2O_3	SO_3	P_2O_5	Original Totals
T04-62	ID = 9043 T04-62 cpx12-gl2	68.31	0.56	17.27	0.80	0.18	0.07	1.68	5.53	4.70	0.30	0.00	0.00	0.08	0.19	0.34	97.07
T04-62	ID = 9044 T04-62 cpx12-gl3	67.73	0.77	16.92	1.29	0.00	0.22	1.68	5.40	5.02	0.19	0.05	0.14	0.05	0.20	0.34	99.47
T04-62	ID = 9045 T04-62 cpx12-gl4	65.75	1.25	17.37	1.93	0.17	0.23	1.82	5.44	5.20	0.31	0.01	0.14	0.00	0.07	0.29	98.85
T04-62	ID = 9046 T04-62 cpx13-gl1	61.05	0.55	15.04	0.77	0.11	0.30	6.64	4.90	4.72	0.43	0.00	0.00	0.16	0.12	5.20	97.99
T04-62	ID = 9046 T04-62 cpx13-gl1	61.05	0.55	15.04	0.77	0.11	0.30	6.64	4.90	4.72	0.43	0.00	0.00	0.16	0.12	5.20	97.99
T04-57	ID = 9047 T04-57 cpx1-gl1	62.13	0.75	14.91	4.23	0.09	3.76	2.39	5.45	5.66	0.28	0.02	0.00	0.04	0.15	0.14	100.11
T04-57	ID = 9048 T04-57 cpx2-gl1	67.13	0.63	16.71	0.97	0.06	0.64	1.97	5.74	5.24	0.37	0.00	0.04	0.01	0.18	0.31	98.18
T04-57	ID = 9049 T04-57 cpx3-gl1	63.55	0.61	17.78	2.05	0.00	0.71	1.53	7.63	5.50	0.30	0.00	0.11	0.06	0.07	0.10	98.04
T04-57	ID = 9050 T04-57 cpx3-gl1b	64.55	0.76	18.20	1.92	0.01	0.09	0.30	7.65	5.70	0.34	0.00	0.09	0.14	0.02	0.21	98.40
T04-57	ID = 9051 T04-57 cpx3-gl2	67.58	0.59	16.68	0.87	0.08	0.81	2.66	5.34	4.71	0.35	0.00	0.00	0.00	0.24	0.08	97.36
T04-57	ID = 9052 T04-57 cpx4-gl1	63.61	0.80	17.90	2.43	0.15	0.00	0.72	6.61	7.08	0.33	0.00	0.02	0.02	0.00	0.33	99.23
T04-57	ID = 9053 T04-57 cpx4-gl2	62.74	0.84	16.29	3.09	0.18	1.67	3.36	4.94	5.87	0.47	0.12	0.05	0.16	0.00	0.22	99.51
T04-57	ID = 9054 T04-57 cpx4-gl3	68.23	0.56	16.41	0.82	0.00	0.63	2.63	5.58	4.53	0.35	0.03	0.00	0.05	0.08	0.10	97.20
T04-57	ID = 9055 T04-57 cpx4-gl4	63.37	0.80	17.97	2.75	0.15	0.09	0.78	6.31	6.90	0.44	0.00	0.03	0.02	0.04	0.36	100.19
T04-57	ID = 9056 T04-57 cpx4-gl5	61.95	0.67	17.62	3.07	0.06	0.14	0.76	8.67	6.28	0.36	0.01	0.00	0.12	0.08	0.21	99.13
T04-57	ID = 9057 T04-57 cpx4-gl6	63.48	0.61	17.29	3.07	0.11	0.78	2.00	5.40	6.20	0.62	0.00	0.00	0.06	0.14	0.24	98.71
T04-57	ID = 9058 T04-57 cpx5-gl1	66.93	0.48	18.08	0.69	0.09	0.16	1.45	5.25	6.24	0.30	0.00	0.06	0.00	0.06	0.20	99.02
T04-57	ID = 9059 T04-57 cpx6-gl1	62.72	0.62	18.67	2.04	0.13	0.00	0.54	8.80	5.73	0.35	0.00	0.00	0.00	0.04	0.35	98.37
T04-57	ID = 9060 T04-57 cpx6-gl2	67.03	0.44	17.95	0.68	0.01	0.04	1.69	5.08	6.20	0.32	0.11	0.06	0.00	0.07	0.32	97.70
T04-57	ID = 9061 T04-57 cpx6-gl3	66.22	0.34	18.16	0.86	0.16	0.09	1.67	5.75	5.78	0.38	0.00	0.06	0.04	0.22	0.26	98.66
T04-57	ID = 9062 T04-57 cpx7-gl1	60.82	1.04	17.21	4.01	0.11	0.00	0.60	9.37	6.16	0.33	0.00	0.00	0.01	0.00	0.33	98.96
T04-57	ID = 9063 T04-57 cpx7-gl2	61.14	1.00	17.42	3.17	0.21	0.25	0.76	9.15	6.06	0.36	0.00	0.05	0.04	0.06	0.32	99.44
T04-57	ID = 9064 T04-57 cpx7-gl2b	61.18	0.80	17.32	3.12	0.00	0.07	0.68	10.02	5.64	0.39	0.00	0.04	0.05	0.33	0.34	99.46
T04-57	ID = 9065 T04-57 cpx8-gl1	65.24	0.66	18.18	2.15	0.00	0.34	0.86	5.22	6.55	0.39	0.00	0.00	0.04	0.00	0.35	99.38
T04-57	ID = 9066 T04-57 cpx8-gl2	65.12	0.71	17.92	2.37	0.02	0.33	0.66	5.37	6.55	0.53	0.00	0.07	0.09	0.00	0.25	98.98
T04-57	ID = 9067 T04-57 cpx9-gl1	65.76	0.66	17.59	2.49	0.16	0.18	1.69	4.45	6.31	0.43	0.09	0.00	0.00	0.18	0.00	98.40
E03-77	ID = 9068 E03-77 cpx1-gl1	69.37	0.11	17.05	0.55	0.06	0.18	1.67	5.22	5.05	0.31	0.05	0.09	0.01	0.08	0.18	98.51
E03-77	ID = 9069 E03-77 cpx2-gl1	69.54	0.48	16.60	0.42	0.00	0.15	1.11	5.09	5.81	0.35	0.18	0.05	0.00	0.05	0.16	98.20
E03-77	ID = 9070 E03-77 cpx3-gl1	62.49	1.00	18.67	1.67	0.09	0.25	0.19	7.88	6.81	0.30	0.06	0.15	0.00	0.16	0.28	99.75
E03-77	ID = 9071 E03-77 cpx4-gl1	64.53	0.79	19.64	1.35	0.00	0.00	1.26	7.76	4.64	0.00	0.00	0.00	0.00	0.04	0.00	99.24
E03-77	ID = 9072 E03-77 cpx5-gl1	70.09	0.36	16.49	0.74	0.00	0.26	1.57	4.91	4.97	0.32	0.00	0.09	0.02	0.12	0.07	98.38
E03-77	ID = 9073 E03-77 cpx6-gl1	67.30	0.44	16.71	2.34	0.12	0.17	0.70	6.55	5.36	0.24	0.00	0.00	0.00	0.00	0.06	98.61

Sample	Description of Analysis	SiO_2	TiO_2	Al_2O_3	FeO	MnO	MgO	CaO	Na_2O	K_2O	Cl	NiO	V_2O_3	Cr_2O_3	SO_3	P_2O_5	Original Totals
E03-77	ID = 9073 E03-77 cpx5-gl2	67.30	0.44	16.71	2.34	0.12	0.17	0.70	6.55	5.36	0.24	0.00	0.00	0.00	0.00	0.06	98.61
E03-77	ID = 9074 E03-77 cpx6-gl1	65.56	0.79	18.18	0.86	0.03	0.25	0.70	7.10	5.88	0.23	0.00	0.00	0.01	0.12	0.28	99.56
E03-77	ID = 9075 E03-77 cpx6-gl2	65.89	0.66	17.97	0.81	0.00	0.09	0.55	7.19	5.90	0.30	0.00	0.04	0.05	0.18	0.35	99.26
E03-77	ID = 9076 E03-77 cpx6-gl3	65.95	0.73	18.08	0.94	0.00	0.11	0.45	7.29	5.89	0.31	0.00	0.02	0.04	0.08	0.11	98.12
E03-77	ID = 9077 E03-77 cpx6-gl4	70.07	0.45	16.65	0.38	0.09	0.04	1.06	5.55	5.14	0.15	0.00	0.00	0.04	0.20	0.17	98.35
E03-77	ID = 9078 E03-77 cpx7-gl1	64.22	0.76	18.95	1.38	0.16	0.20	0.73	6.65	6.24	0.33	0.11	0.00	0.00	0.00	0.26	98.88
E03-77	ID = 9079 E03-77 cpx8-gl1	64.62	0.86	17.91	1.48	0.03	0.60	1.72	5.04	6.93	0.36	0.11	0.00	0.00	0.05	0.30	100.06
E03-77	ID = 9080 E03-77 cpx9-gl1	66.73	0.58	16.40	1.17	0.09	0.93	2.26	4.90	6.48	0.27	0.02	0.00	0.00	0.07	0.09	98.78

[all data in wt.%]

Sample	Description of Analysis	SiO_2	TiO_2	Al_2O_3	FeO	MnO	MgO	CaO	Na_2O	K_2O	Cl	NiO	Cr_2O_3	SO_3	P_2O_5	Original Total
SR29	ID = 6696 SR29 H glass1a	66.47	0.54	16.39	2.77	0.16	0.86	2.86	4.33	5.08	0.18	0.00	0.00	0.16	0.18	99.51
SR29	ID = 6697 SR29 H glass1b	68.15	0.57	16.30	2.29	0.11	0.00	2.26	4.62	5.42	0.22	0.00	0.00	0.00	0.07	97.50
SR29	ID = 6698 SR29 H glass2a	66.32	0.63	16.64	2.94	0.13	0.92	2.54	4.48	4.97	0.28	0.00	0.10	0.00	0.04	97.34
SR29	ID = 6699 SR29 H glass3a	68.52	0.49	16.05	2.29	0.01	0.00	2.05	4.42	5.83	0.22	0.00	0.00	0.00	0.11	97.94
SR29	ID = 6700 SR29 H glass3b	68.29	0.53	15.98	2.41	0.04	0.00	1.94	4.58	5.73	0.28	0.00	0.00	0.08	0.13	96.86
SR29	ID = 6701 SR29 H glass4a	66.46	0.42	16.75	2.24	0.12	0.95	3.01	4.58	4.99	0.17	0.00	0.03	0.00	0.27	98.50
SR29	ID = 6702 SR29 H glass4b	67.56	0.43	16.67	2.09	0.04	0.67	2.44	4.44	5.31	0.25	0.00	0.00	0.00	0.08	94.30
SR29	ID = 6703 SR29 H glass5a	67.57	0.46	16.83	2.19	0.00	0.56	2.48	4.41	5.19	0.23	0.01	0.00	0.07	0.00	97.55
SR29	ID = 6704 SR29 H glass5b	67.57	0.53	16.52	2.08	0.14	0.63	2.46	4.57	5.22	0.20	0.00	0.00	0.00	0.09	95.18
SR29	ID = 6705 SR29 H glass6a	66.17	0.41	17.79	1.87	0.07	0.74	3.33	4.80	4.62	0.10	0.01	0.00	0.00	0.08	98.25
SR29	ID = 6975 SR29 H2 glass1a	66.45	0.35	17.77	1.79	0.12	0.00	3.23	4.74	5.05	0.21	0.16	0.04	0.06	0.01	98.72
SR29	ID = 6976 SR29 H2 glass1b	66.15	0.54	17.45	2.53	0.07	0.61	3.13	4.61	4.70	0.11	0.00	0.06	0.00	0.04	97.92
SR29	ID = 6977 SR29 H2 glass1c	66.65	0.39	17.03	2.06	0.09	0.69	2.96	4.39	5.25	0.24	0.00	0.05	0.00	0.20	98.61
SR29	ID = 6978 SR29 H2 glass2a	68.92	0.41	16.58	1.52	0.09	0.00	2.11	4.55	5.38	0.04	0.14	0.01	0.14	0.10	98.14
SR29	ID = 6979 SR29 H2 glass2b	66.61	0.48	18.03	1.31	0.11	0.24	3.63	5.01	4.17	0.00	0.01	0.09	0.07	0.22	98.51
SR29	ID = 6980 SR29 H2 glass2c	66.47	0.37	17.55	1.75	0.00	0.77	3.55	4.78	4.48	0.05	0.00	0.03	0.09	0.10	98.73
SR29	ID = 6982 SR29 H2 glass3b	68.63	0.45	16.93	1.24	0.00	0.09	2.25	4.72	5.49	0.11	0.00	0.00	0.06	0.01	95.92
SR29	ID = 6983 SR29 H2 glass3c	69.17	0.49	16.37	1.35	0.00	0.00	2.06	4.77	5.44	0.12	0.11	0.00	0.10	0.00	97.43
SR29	ID = 6984 SR29 H2 glass4a	66.87	0.42	16.75	2.32	0.13	0.66	2.80	4.65	5.02	0.11	0.08	0.02	0.02	0.15	99.03
SR29	ID = 6985 SR29 H2 glass4b	67.14	0.52	17.37	2.03	0.06	0.00	2.94	4.70	4.98	0.12	0.00	0.00	0.10	0.04	97.75
SR29	ID = 6986 SR29 H2 glass5a	65.28	0.43	18.08	2.04	0.06	0.80	4.03	4.87	4.27	0.13	0.00	0.00	0.00	0.00	99.15
SR29	ID = 6987 SR29 H2 glass5b	67.33	0.58	15.86	2.76	0.07	1.06	2.36	4.36	5.14	0.19	0.09	0.00	0.05	0.14	98.33
SR29	ID = 6989 SR29 H2 glass6a	66.85	0.49	15.88	2.99	0.00	1.24	2.35	4.29	5.53	0.30	0.00	0.00	0.00	0.08	98.62
SR29	ID = 6990 SR29 H2 glass6b	66.89	0.45	16.88	2.33	0.08	0.66	2.48	4.58	5.29	0.18	0.00	0.04	0.00	0.13	97.34
SR40	ID = 6649 SR40 H glass1a	68.52	0.46	16.48	1.81	0.01	0.00	2.68	4.77	4.99	0.07	0.00	0.00	0.08	0.11	97.06
SR40	ID = 6650 SR40 H glass2a	69.15	0.39	16.18	1.66	0.09	0.00	2.10	4.59	5.43	0.13	0.05	0.00	0.12	0.10	98.20
SR40	ID = 6651 SR40 H glass2b	68.91	0.49	14.97	2.17	0.08	0.89	2.24	4.35	5.23	0.14	0.05	0.00	0.20	0.28	99.41
SR40	ID = 6652 SR40 H glass3a	68.45	0.55	16.72	1.70	0.01	0.00	2.57	4.64	4.93	0.14	0.07	0.00	0.12	0.09	97.77
SR40	ID = 6653 SR40 H glass3b	68.73	0.46	16.82	1.71	0.04	0.00	2.72	4.68	4.61	0.13	0.00	0.01	0.07	0.01	97.02
SR40	ID = 6654 SR40 H glass4a	67.79	0.42	16.10	2.11	0.10	0.66	2.83	4.64	4.96	0.17	0.15	0.00	0.07	0.00	98.71
SR40	ID = 6655 SR40 H glass4b	68.81	0.54	15.85	2.17	0.10	0.56	2.11	4.22	5.41	0.14	0.00	0.00	0.08	0.00	98.11
SR40	ID = 6657 SR40 H glass5b	67.36	0.37	17.65	1.14	0.02	0.22	3.19	4.93	4.46	0.11	0.22	0.04	0.20	0.08	98.03
SR40	ID = 6658 SR40 H glass6a	70.11	0.47	14.71	2.07	0.12	0.56	1.50	4.16	5.78	0.20	0.07	0.03	0.16	0.06	98.76

Sample	Description of Analysis	SiO_2	TiO_2	Al_2O_3	FeO	MnO	MgO	CaO	Na_2O	K_2O	Cl	NiO	Cr_2O_3	SO_3	P_2O_5	Original Total
SR40	ID = 6659 SR40 H glass6b	68.32	0.34	17.10	1.44	0.00	0.24	3.00	4.64	4.71	0.13	0.06	0.00	0.00	0.00	97.58
SR40	ID = 6660 SR40 H glass7a	67.49	0.36	17.60	1.62	0.08	0.00	2.97	5.13	4.49	0.07	0.06	0.01	0.11	0.00	98.19
SR40	ID = 6661 SR40 H glass7b	69.47	0.52	15.52	1.96	0.06	0.52	1.87	4.34	5.47	0.21	0.00	0.00	0.04	0.00	97.36
SR40	ID = 6662 SR40 H glass8a	69.43	0.43	15.75	1.52	0.00	0.00	2.11	4.48	5.60	0.22	0.13	0.01	0.00	0.32	97.18
SR40	ID = 6663 SR40 H glass8b	66.67	0.52	16.72	1.97	0.00	0.94	3.70	4.79	4.41	0.14	0.00	0.00	0.00	0.13	98.78
SR40	ID = 6664 SR40 H glass9a	66.91	0.44	16.99	2.02	0.14	0.64	3.23	4.70	4.61	0.13	0.06	0.03	0.01	0.06	99.27
SR40	ID = 6665 SR40 H glass9b	70.41	0.44	14.92	1.92	0.15	0.00	1.56	4.18	6.19	0.13	0.00	0.06	0.01	0.02	97.56
SR40	ID = 6666 SR40 H glass10a	69.71	0.44	15.99	1.57	0.00	0.00	2.26	4.43	5.25	0.29	0.06	0.00	0.00	0.00	98.11
SR40	ID = 6667 SR40 H glass10b	68.56	0.47	16.91	1.23	0.21	0.00	2.42	4.66	5.30	0.16	0.00	0.00	0.02	0.05	98.18
SR40	ID = 6668 SR40 L glass1a	68.89	0.48	16.38	1.51	0.00	0.00	2.49	4.61	5.37	0.12	0.00	0.06	0.00	0.06	97.12
SR40	ID = 6669 SR40 L glass1b	67.14	0.40	17.50	1.34	0.05	0.62	3.41	4.77	4.56	0.13	0.03	0.00	0.05	0.00	98.66
SR40	ID = 6959 SR40 H2 glass1b	67.24	0.39	17.65	1.61	0.16	0.00	3.42	4.78	4.48	0.17	0.00	0.00	0.10	0.00	98.25
SR40	ID = 6962 SR40 H2 glass3a	70.95	0.53	15.10	1.63	0.08	0.00	1.33	4.11	5.98	0.23	0.00	0.00	0.00	0.05	97.48
SR40	ID = 6963 SR40 H2 glass3b	69.83	0.40	15.80	1.54	0.08	0.00	1.98	4.51	5.56	0.16	0.00	0.08	0.02	0.04	97.20
SR40	ID = 6964 SR40 H2 glass4a	69.92	0.63	15.99	1.72	0.01	0.23	1.81	4.33	5.07	0.19	0.00	0.00	0.01	0.09	98.43
SR40	ID = 6965 SR40 H2 glass4b	70.17	0.48	14.62	1.95	0.17	0.61	1.57	3.94	5.96	0.19	0.00	0.03	0.11	0.20	98.39
SR40	ID = 6966 SR40 H2 glass5a	69.24	0.33	15.54	2.19	0.05	0.56	1.84	4.27	5.55	0.26	0.02	0.00	0.13	0.02	97.81
SR40	ID = 6968 SR40 H2 glass5c	68.88	0.62	16.08	1.92	0.00	0.00	2.22	4.58	5.34	0.19	0.10	0.00	0.00	0.05	97.74
SR40	ID = 6971 SR40 H2 glass6a	69.00	0.43	15.78	1.60	0.03	0.57	2.26	4.65	5.29	0.09	0.18	0.01	0.05	0.05	98.49
SR40	ID = 6972 SR40 H2 glass6b	68.19	0.49	17.08	1.27	0.00	0.00	2.71	4.86	5.15	0.11	0.00	0.00	0.07	0.05	97.26
SR40	ID = 6973 SR40 H2 glass6c	70.91	0.48	14.25	1.90	0.16	0.00	1.84	3.92	5.95	0.18	0.02	0.00	0.00	0.38	97.77
SR41	ID = 6671 SR41 H glass1b	69.30	0.33	15.93	1.78	0.06	0.00	2.28	4.51	5.36	0.24	0.11	0.07	0.00	0.02	97.31
SR41	ID = 6673 SR41 H glass3a	69.92	0.54	15.70	1.68	0.00	0.00	1.83	4.49	5.62	0.17	0.00	0.00	0.00	0.05	98.23
SR41	ID = 6674 SR41 H glass3b neu	70.89	0.47	14.87	1.76	0.03	0.00	1.72	4.01	5.80	0.22	0.00	0.00	0.13	0.09	98.06
SR41	ID = 6675 SR41 H glass3c neu	69.22	0.40	15.15	2.17	0.00	0.57	2.01	4.42	5.74	0.15	0.00	0.00	0.04	0.13	98.38
SR41	ID = 6676 SR41 H glass4a	67.82	0.38	17.30	1.47	0.08	0.00	2.80	4.84	5.05	0.14	0.00	0.03	0.00	0.08	98.14
SR41	ID = 6677 SR41 H glass4b	67.18	0.69	16.01	2.61	0.00	0.68	2.91	4.49	4.90	0.18	0.18	0.00	0.00	0.17	99.24
SR41	ID = 6678 SR41 H glass5a	67.47	0.42	17.88	1.21	0.00	0.24	3.29	4.57	4.73	0.11	0.07	0.00	0.00	0.00	98.17
SR41	ID = 6679 SR41 H glass5b	69.26	0.52	15.93	1.95	0.00	0.00	1.94	4.56	5.57	0.15	0.00	0.01	0.08	0.02	97.33
SR41	ID = 6680 SR41 H glass6a	70.33	0.51	14.43	1.88	0.14	0.71	1.70	4.07	5.70	0.20	0.02	0.01	0.10	0.19	97.15
SR41	ID = 6681 SR41 H glass6b	65.18	0.95	13.99	4.44	0.15	2.77	3.19	3.72	5.11	0.14	0.00	0.00	0.06	0.30	98.29
SR41	ID = 6682 SR41 H glass6c	68.99	0.47	14.95	2.09	0.13	0.58	1.90	4.18	5.66	0.25	0.17	0.00	0.19	0.45	93.82
SR41	ID = 6683 SR41 H glass7a	68.37	0.73	15.53	2.72	0.16	0.00	1.46	4.78	5.84	0.16	0.06	0.00	0.00	0.17	98.02

Sample	Description of Analysis	SiO_2	TiO_2	Al_2O_3	FeO	MnO	MgO	CaO	Na_2O	K_2O	Cl	NiO	Cr_2O_3	SO_3	P_2O_5	Original Total
SR41	ID = 6684 SR41 H glass7b	68.94	0.91	14.92	2.99	0.13	0.00	1.10	4.76	5.90	0.10	0.00	0.00	0.00	0.25	97.57
SR41	ID = 6991 SR41 H2 glass1a	68.97	0.31	16.85	1.34	0.00	0.00	2.37	4.72	5.23	0.13	0.07	0.00	0.00	0.00	97.08
SR41	ID = 6992 SR41 H2 glass1b	70.79	0.33	14.89	1.68	0.10	0.00	1.50	4.08	6.24	0.14	0.00	0.00	0.07	0.18	98.07
SR41	ID = 6993 SR41 H2 glass1c	69.12	0.40	16.51	1.33	0.13	0.00	2.45	4.59	5.27	0.14	0.06	0.00	0.00	0.01	98.08
SR41	ID = 6994 SR41 H2 glass2a	67.46	0.33	17.80	1.51	0.00	0.21	3.17	4.62	4.71	0.13	0.05	0.00	0.00	0.00	98.43
SR41	ID = 6995 SR41 H2 glass2b	70.38	0.51	15.05	1.63	0.16	0.23	1.49	4.19	6.03	0.17	0.00	0.04	0.00	0.11	98.25
SR41	ID = 6996 SR41 H2 glass2c	68.77	0.33	16.86	1.35	0.00	0.17	2.56	4.62	5.15	0.18	0.00	0.00	0.00	0.00	98.19
SR41	ID = 6998 SR41 H2 glass3b	67.50	0.45	16.96	1.80	0.04	0.66	2.96	4.50	4.93	0.14	0.00	0.00	0.01	0.05	98.01
SR41	ID = 6999 SR41 H2 glass3c	69.45	0.52	15.17	2.07	0.01	0.61	1.81	4.18	5.89	0.19	0.08	0.00	0.00	0.00	97.59
SR41	ID = 7000 SR41 H2 glass4a	70.45	0.62	14.96	1.82	0.05	0.00	1.70	4.27	5.70	0.18	0.00	0.00	0.10	0.13	97.67
SR41	ID = 7001 SR41 H2 glass4b	66.95	0.37	17.09	2.56	0.01	0.64	3.08	4.62	4.37	0.15	0.00	0.02	0.13	0.00	97.86
SR41	ID = 7003 SR41 H2 glass5a	66.55	0.30	18.09	1.43	0.01	0.00	3.82	4.73	4.47	0.13	0.02	0.00	0.12	0.33	97.93
SR41	ID = 7004 SR41 H2 glass5b	68.85	0.39	16.40	1.66	0.00	0.22	2.23	4.42	5.49	0.19	0.05	0.04	0.01	0.04	98.46
SR41	ID = 7005 SR41 H2 glass5c	68.59	0.35	16.54	1.67	0.00	0.00	2.69	4.49	5.29	0.20	0.03	0.00	0.00	0.15	98.24
SR41	ID = 7006 SR41 H2 glass6a	68.80	0.40	16.68	1.36	0.13	0.00	2.03	4.97	5.60	0.00	0.00	0.00	0.02	0.00	97.46
SR41	ID = 7007 SR41 H2 glass6b	69.14	0.77	14.79	2.91	0.14	0.61	1.60	4.22	5.65	0.01	0.01	0.00	0.02	0.13	97.38
SR42	ID = 6685 SR42 H glass1a	69.22	0.44	15.23	1.97	0.14	0.64	2.14	4.20	5.76	0.15	0.07	0.03	0.02	0.00	98.65
SR42	ID = 6686 SR42 H glass1b	69.02	0.44	15.36	2.08	0.15	0.68	2.05	4.05	5.74	0.18	0.09	0.00	0.00	0.15	97.55
SR42	ID = 6687 SR42 H glass2a	68.34	0.47	16.92	1.75	0.00	0.00	2.55	4.71	4.92	0.13	0.00	0.02	0.11	0.07	97.23
SR42	ID = 6688 SR42 H glass2b	70.42	0.45	15.35	1.86	0.01	0.00	1.78	4.14	5.70	0.11	0.00	0.00	0.12	0.04	96.80
SR42	ID = 6689 SR42 H glass3a	69.86	0.42	15.78	1.48	0.07	0.22	1.82	4.33	5.59	0.25	0.00	0.03	0.04	0.08	94.38
SR42	ID = 6691 SR42 H glass4a	69.14	0.36	15.52	2.05	0.01	0.61	2.13	4.39	5.52	0.24	0.02	0.00	0.00	0.00	98.38
SR42	ID = 6692 SR42 H glass4b	68.53	0.44	16.40	1.71	0.08	0.00	2.73	4.45	5.23	0.14	0.00	0.15	0.07	0.06	97.20
SR42	ID = 6694 SR42 H glass5b	68.75	0.37	15.80	1.55	0.18	0.59	2.64	4.54	5.07	0.08	0.16	0.00	0.00	0.26	98.53
SR42	ID = 7008 SR42 H2 glass1a	68.44	0.43	16.67	1.88	0.12	0.00	2.65	4.64	4.90	0.13	0.00	0.10	0.00	0.02	97.16
SR42	ID = 7009 SR42 H2 glass1b	69.12	0.56	16.01	1.80	0.05	0.00	2.24	4.45	5.49	0.14	0.00	0.00	0.00	0.13	97.81
SR42	ID = 7010 SR42 H2 glass1c	69.40	0.51	15.90	1.73	0.05	0.00	1.95	4.25	5.79	0.15	0.17	0.00	0.00	0.10	98.39
SR42	ID = 7011 SR42 H2 glass2a	66.52	0.48	17.24	1.95	0.04	0.85	3.44	4.85	4.39	0.02	0.00	0.00	0.09	0.12	99.58
SR42	ID = 7012 SR42 H2 glass2b	67.50	0.42	17.62	1.63	0.00	0.00	3.42	4.69	4.30	0.08	0.07	0.00	0.12	0.13	97.36
SR42	ID = 7014 SR42 H2 glass3b	68.34	0.49	15.92	1.98	0.14	0.63	2.22	4.49	5.48	0.16	0.01	0.00	0.13	0.01	98.61
SR42	ID = 7016 SR42 H2 glass3d	69.19	0.54	15.63	1.86	0.05	0.23	1.71	4.38	5.97	0.24	0.00	0.00	0.00	0.19	98.45
SR42	ID = 7020 SR42 H2 glass5c	67.20	0.42	17.28	1.84	0.01	0.57	3.36	4.75	4.32	0.10	0.00	0.00	0.00	0.15	97.96
SR42	ID = 7023 SR42 H2 glass6c	68.15	0.35	16.55	1.53	0.04	0.00	2.96	4.91	4.78	0.16	0.07	0.20	0.12	0.17	99.11

Sample	Description of Analysis	SiO_2	TiO_2	Al_2O_3	FeO	MnO	MgO	CaO	Na_2O	K_2O	Cl	NiO	Cr_2O_3	SO_3	P_2O_5	Original Total
SR42	ID = 7024 SR42 H2 glass6d	68.86	0.30	16.36	1.55	0.10	0.00	2.39	4.62	5.24	0.14	0.08	0.00	0.13	0.22	98.88
SR42	ID = 7025 SR42 H2 glass6e	66.99	0.39	17.42	1.88	0.00	0.18	3.43	4.89	4.54	0.09	0.01	0.07	0.05	0.04	98.79
SR42	ID = 7028 SR42 H2 glass6h	68.24	0.40	16.89	1.35	0.05	0.28	2.41	4.94	5.15	0.12	0.00	0.00	0.00	0.19	98.07
SR42	ID = 7030 SR42 H2 glass6j	69.13	0.31	16.25	1.69	0.00	0.00	2.20	4.65	5.32	0.20	0.03	0.00	0.05	0.16	97.35
Ma23	ID = 7031 Ma23 H2 glass1a	69.42	0.56	15.26	1.78	0.06	0.79	1.29	4.81	5.84	0.06	0.00	0.00	0.01	0.12	98.62
Ma23	ID = 7032 Ma23 H2 glass1b	72.05	0.51	13.50	1.94	0.06	0.49	0.68	4.17	6.50	0.02	0.00	0.00	0.00	0.08	98.46
Ma23	ID = 7033 Ma23 H2 glass1c	67.97	0.60	16.91	1.56	0.04	0.61	2.23	4.71	5.23	0.07	0.00	0.00	0.00	0.07	96.87
Ma23	ID = 7034 Ma23 H2 glass1d	66.15	1.06	13.26	3.66	0.26	2.94	2.73	3.72	5.61	0.06	0.06	0.01	0.07	0.40	95.55
Ma23	ID = 7035 Ma23 H2 glass2a	66.06	0.57	17.15	2.19	0.11	0.79	2.76	5.08	4.81	0.19	0.00	0.11	0.00	0.17	98.23
Ma23	ID = 7036 Ma23 H2 glass2b	67.84	0.66	15.75	2.25	0.06	0.75	1.90	4.60	5.63	0.24	0.00	0.07	0.12	0.13	98.57
Ma23	ID = 7037 Ma23 H2 glass2c	67.19	0.49	16.81	2.14	0.04	0.78	2.41	4.73	5.17	0.16	0.04	0.00	0.00	0.04	98.04
Ma23	ID = 7038 Ma23 H2 glass3a	67.98	0.41	16.34	1.72	0.03	0.57	2.33	4.63	5.47	0.08	0.00	0.06	0.12	0.26	98.56
Ma23	ID = 7039 Ma23 H2 glass3b	70.12	0.49	15.60	1.43	0.00	0.00	1.96	4.24	5.81	0.09	0.00	0.00	0.00	0.26	97.78
Ma23	ID = 7040 Ma23 H2 glass3c	67.66	0.33	17.49	1.29	0.00	0.00	2.82	4.73	5.28	0.06	0.05	0.00	0.12	0.17	96.96
Ma23	ID = 7042 Ma23 H2 glass4b	69.13	0.44	16.35	1.46	0.00	0.00	2.25	4.64	5.41	0.00	0.07	0.03	0.08	0.12	98.45
Ma23	ID = 7043 Ma23 H2 glass5a	66.65	0.63	16.01	2.78	0.09	1.14	2.52	4.62	5.18	0.15	0.00	0.00	0.14	0.07	98.75
Ma23	ID = 7044 Ma23 H2 glass5b	66.24	0.64	17.12	2.41	0.03	0.61	2.92	4.73	4.96	0.22	0.00	0.00	0.06	0.06	98.72
Ma23	ID = 7045 Ma23 H2 glass6a	67.42	0.54	16.45	2.24	0.01	0.54	2.01	4.43	5.99	0.16	0.00	0.00	0.10	0.09	97.59
Ma23	ID = 7046 Ma23 H2 glass6b	66.35	0.50	16.70	2.54	0.18	0.72	2.72	4.74	5.00	0.17	0.10	0.00	0.00	0.26	98.72
Ma23	ID = 7047 Ma23 H2 glass6c	65.95	0.30	16.98	2.48	0.01	0.65	2.94	4.81	5.10	0.12	0.03	0.07	0.09	0.46	98.54
Ma30	ID = 6707 Ma30 H glass1a	66.75	0.51	18.21	1.37	0.11	0.00	3.09	5.10	4.52	0.08	0.03	0.00	0.04	0.19	97.21
Ma30	ID = 6709 Ma30 H glass2a	68.44	0.40	16.91	1.16	0.00	0.10	2.15	4.87	5.54	0.08	0.16	0.08	0.05	0.04	99.03
Ma30	ID = 6710 Ma30 H glass2b	70.47	0.38	15.32	1.53	0.13	0.00	1.22	4.50	6.07	0.17	0.00	0.01	0.03	0.16	99.15
Ma30	ID = 6712 Ma30 H glass3a	67.95	0.46	17.15	1.23	0.00	0.24	2.34	4.82	5.56	0.09	0.17	0.00	0.00	0.00	98.43
Ma30	ID = 6713 Ma30 H glass3b	71.33	0.50	14.51	1.94	0.06	0.00	1.05	4.01	6.27	0.22	0.00	0.00	0.05	0.07	97.52
Ma30	ID = 6714 Ma30 H glass3c	68.79	0.45	16.20	1.57	0.00	0.57	1.82	4.87	5.50	0.12	0.00	0.01	0.10	0.00	99.02
Ma30	ID = 6716 Ma30 H glass4b	68.73	0.47	16.43	1.60	0.00	0.00	2.28	4.67	5.34	0.22	0.00	0.00	0.16	0.09	97.80
Ma30	ID = 6717 Ma30 H glass5a	69.67	0.46	15.94	1.46	0.09	0.00	1.55	4.64	5.78	0.27	0.05	0.09	0.00	0.00	98.25
Ma30	ID = 6718 Ma30 H glass5b	68.45	0.66	16.59	1.58	0.00	0.00	2.06	4.63	5.56	0.20	0.00	0.00	0.01	0.26	99.15
Ma30	ID = 7049 Ma30 H2 glass1b	68.48	0.50	16.66	1.65	0.00	0.00	2.02	4.78	5.57	0.07	0.08	0.00	0.00	0.18	99.34
Ma30	ID = 7050 Ma30 H2 glass1c	68.05	0.41	17.15	1.10	0.00	0.17	2.03	5.15	5.72	0.03	0.00	0.00	0.04	0.14	98.20
Ma30	ID = 7051 Ma30 H2 glass2a	70.92	0.60	14.74	1.44	0.11	0.00	0.98	4.17	6.69	0.21	0.12	0.00	0.01	0.00	98.15
Ma30	ID = 7052 Ma30 H2 glass2b	69.75	0.51	14.68	1.95	0.01	0.49	1.62	4.01	6.28	0.21	0.00	0.00	0.01	0.47	97.91

Sample	Description of Analysis	SiO_2	TiO_2	Al_2O_3	FeO	MnO	MgO	CaO	Na_2O	K_2O	Cl	NiO	Cr_2O_3	SO_3	P_2O_5	Original Total
Ma30	ID = 7054 Ma30 H2 glass3a	67.54	0.19	17.91	1.28	0.00	0.06	2.84	5.18	4.89	0.11	0.00	0.00	0.00	0.00	97.62
Ma30	ID = 7055 Ma30 H2 glass3b	70.07	0.56	15.42	1.92	0.00	0.00	1.48	4.56	5.93	0.07	0.00	0.00	0.00	0.00	98.52
Ma30	ID = 7056 Ma30 H2 glass3c	70.37	0.31	15.22	1.47	0.00	0.20	1.60	4.66	5.97	0.13	0.02	0.04	0.01	0.00	96.83
Ma30	ID = 7057 Ma30 H2 glass4a	67.84	0.45	17.22	1.51	0.05	0.00	2.15	5.05	5.51	0.14	0.00	0.00	0.00	0.08	99.25
Ma30	ID = 7058 Ma30 H2 glass4b	67.38	0.45	17.31	1.73	0.01	0.00	2.78	4.85	5.10	0.16	0.00	0.00	0.04	0.18	98.09
Ma30	ID = 7059 Ma30 H2 glass5a	67.96	0.55	17.05	1.52	0.00	0.00	2.38	4.99	5.14	0.14	0.00	0.00	0.08	0.18	98.70
Ma30	ID = 7060 Ma30 H2 glass5b	69.93	0.51	15.36	1.68	0.00	0.00	1.36	4.48	6.20	0.22	0.00	0.00	0.07	0.19	97.49
Ma30	ID = 7061 Ma30 H2 glass5c	70.39	0.64	15.16	1.62	0.02	0.15	1.32	4.24	6.24	0.22	0.00	0.00	0.00	0.00	98.57
E03-35	ID = 9097 E03-35L_glass1a	74.56	0.35	13.03	2.08	0.12	0.19	1.37	4.49	3.41	0.22	0.13	0.00	0.00	0.04	93.84
E03-35	ID = 9098 E03-35L_glass1b	74.82	0.12	13.37	2.14	0.00	0.16	1.34	4.37	3.44	0.21	0.01	0.00	0.00	0.02	92.46
E03-35	ID = 9099 E03-35H_glass2a	67.27	0.52	16.74	1.99	0.06	0.72	2.56	4.71	5.03	0.16	0.11	0.00	0.00	0.13	98.74
E03-35	ID = 9100 E03-35H_glass2b	68.06	0.51	15.62	2.46	0.02	1.01	2.12	4.28	5.37	0.21	0.00	0.06	0.04	0.23	98.37
E03-35	ID = 9113 E03-35L_glass4a	76.08	0.14	12.86	1.39	0.16	0.21	1.15	4.09	3.62	0.25	0.00	0.03	0.00	0.02	92.50
E03-35	ID = 9114 E03-35L_glass5a	74.92	0.26	13.35	2.23	0.09	0.11	1.39	3.90	3.47	0.17	0.00	0.00	0.11	0.00	92.78
E03-36	ID = 7078 E03-36 H glass1a	69.87	0.43	15.95	1.91	0.13	0.00	1.95	4.37	5.31	0.00	0.04	0.00	0.00	0.05	98.20
E03-36	ID = 7079 E03-36 H glass1b	69.28	0.44	16.28	1.78	0.09	0.00	2.01	4.48	5.52	0.08	0.00	0.00	0.00	0.04	98.02
E03-36	ID = 7080 E03-36 H glass2a	67.12	0.41	17.26	2.02	0.00	0.00	3.34	4.74	4.63	0.15	0.00	0.01	0.15	0.16	98.25
E03-36	ID = 7082 E03-36 H glass2c	68.90	0.44	16.40	1.82	0.01	0.00	2.29	4.61	5.21	0.17	0.00	0.00	0.00	0.15	97.98
E03-36	ID = 7083 E03-36 H glass3a	69.59	0.57	15.19	2.14	0.01	0.58	1.52	4.11	5.63	0.23	0.00	0.14	0.01	0.28	98.71
E03-36	ID = 7084 E03-36 H glass3b	68.45	0.41	16.99	1.69	0.15	0.00	2.50	4.82	4.82	0.10	0.02	0.00	0.00	0.05	99.01
E03-36	ID = 7085 E03-36 H glass3c	68.40	0.39	16.86	1.75	0.11	0.00	2.35	4.68	5.10	0.13	0.12	0.00	0.01	0.09	98.64
E03-36	ID = 7086 E03-36 H glass4a	67.15	0.50	17.16	2.02	0.02	0.56	3.12	4.42	4.65	0.15	0.09	0.00	0.00	0.14	99.22
E03-36	ID = 7087 E03-36 H glass4b	67.54	0.46	17.02	1.88	0.00	0.00	3.13	4.62	4.88	0.23	0.00	0.00	0.00	0.25	98.56
E03-36	ID = 7088 E03-36 H glass5a	68.64	0.43	16.83	1.31	0.08	0.24	2.21	4.65	5.49	0.10	0.00	0.00	0.00	0.01	98.99
E03-36	ID = 7090 E03-36 H glass5c	68.65	0.33	17.06	1.23	0.05	0.00	2.99	4.91	4.64	0.05	0.00	0.00	0.09	0.00	96.19
E03-37	ID = 7062 E03-37 H glass1a	67.15	0.37	17.77	1.48	0.12	0.00	3.08	5.10	4.63	0.15	0.00	0.00	0.02	0.12	98.76
E03-37	ID = 7062 E03-37 H glass1a	67.15	0.37	17.77	1.48	0.12	0.00	3.08	5.10	4.63	0.15	0.00	0.00	0.02	0.12	98.76
E03-37	ID = 7063 E03-37 H glass1b	68.49	0.47	15.65	2.29	0.00	0.56	1.74	4.64	5.73	0.26	0.08	0.00	0.09	0.00	98.82
E03-37	ID = 7064 E03-37 H glass1c	68.42	0.44	16.79	1.51	0.00	0.00	2.35	4.79	5.43	0.14	0.00	0.00	0.11	0.01	97.79
E03-37	ID = 7065 E03-37 H glass2a	63.70	0.79	16.43	4.34	0.19	1.49	3.30	4.45	4.70	0.19	0.00	0.00	0.01	0.40	98.85
E03-37	ID = 7066 E03-37 H glass2b	63.58	0.79	16.78	3.86	0.13	1.52	3.40	4.63	4.87	0.16	0.00	0.00	0.00	0.26	99.10
E03-37	ID = 7067 E03-37 H glass3a	66.45	0.46	18.25	1.43	0.00	0.00	2.80	5.42	4.97	0.04	0.00	0.00	0.00	0.18	98.47
E03-37	ID = 7070 E03-37 H glass4a	68.05	0.32	17.31	1.26	0.00	0.22	2.39	4.95	5.23	0.13	0.08	0.00	0.00	0.05	98.65

Sample	Description of Analysis	SiO_2	TiO_2	Al_2O_3	FeO	MnO	MgO	CaO	Na_2O	K_2O	Cl	NiO	Cr_2O_3	SO_3	P_2O_5	Original Total
E03-37	ID = 7071 E03-37 H glass4b	69.14	0.54	15.75	2.05	0.00	0.00	1.74	4.44	6.01	0.16	0.03	0.00	0.01	0.12	98.07
E03-37	ID = 7072 E03-37 H glass4c	67.72	0.36	16.87	2.03	0.00	0.00	2.61	4.92	5.21	0.15	0.00	0.00	0.07	0.05	98.08
E03-37	ID = 7074 E03-37 H glass5b	66.09	0.91	17.12	2.63	0.06	0.00	2.97	5.03	4.79	0.15	0.03	0.00	0.06	0.15	98.47
E03-37	ID = 7076 E03-37 H glass6a	68.80	0.46	16.40	1.33	0.05	0.17	1.76	4.88	5.91	0.06	0.00	0.00	0.12	0.05	99.14
E03-37	ID = 7077 E03-37 H glass6b	68.50	0.54	16.42	1.87	0.00	0.00	1.95	4.89	5.58	0.08	0.00	0.00	0.08	0.09	98.03
E02-23	ID = 9022 E02-23H_glass1a	68.52	0.66	15.56	2.54	0.05	0.65	1.59	4.55	5.43	0.19	0.22	0.00	0.04	0.02	97.65
E02-23	ID = 9023 E02-23H_glass1b	67.70	0.62	15.73	2.72	0.01	0.81	1.64	4.65	5.54	0.29	0.00	0.00	0.06	0.23	97.95
E02-23	ID = 9024 E02-23H_glass2a	68.23	0.42	17.00	1.47	0.00	0.00	2.18	4.93	5.43	0.05	0.00	0.00	0.12	0.15	97.74
E02-23	ID = 9025 E02-23H_glass2b	67.72	0.52	16.12	2.05	0.00	1.08	2.05	4.74	5.59	0.10	0.00	0.00	0.04	0.00	98.25
E02-23	ID = 9026 E02-23H_glass3a	69.33	0.69	14.95	2.37	0.05	0.55	1.14	4.27	6.15	0.21	0.00	0.01	0.00	0.26	98.19
E02-23	ID = 9027 E02-23H_glass3b	67.87	0.54	16.98	2.15	0.00	0.00	2.18	4.81	5.29	0.15	0.00	0.00	0.00	0.02	97.74
E02-23	ID = 9028 E02-23H_glass4a	67.83	0.37	17.17	1.59	0.00	0.14	2.25	5.06	5.21	0.07	0.00	0.00	0.18	0.11	98.05
E02-23	ID = 9029 E02-23H_glass4b	70.04	0.50	15.08	1.76	0.00	0.19	1.61	4.78	5.75	0.22	0.00	0.00	0.01	0.06	95.82
E02-23	ID = 9031 E02-23H_glass5b	67.64	0.54	15.73	2.47	0.30	0.96	1.93	4.57	5.44	0.20	0.00	0.04	0.06	0.11	98.90
E02-23	ID = 9033 E02-23H_glass6a	67.73	0.68	15.69	2.46	0.14	0.54	1.68	4.63	5.84	0.24	0.00	0.00	0.00	0.37	98.82
E02-23	ID = 9034 E02-23H_glass6b	66.65	0.44	17.25	1.79	0.05	0.61	2.49	5.19	5.20	0.17	0.00	0.00	0.00	0.15	98.99
E02-24	ID = 9008 E02-24H_glass1a	67.13	0.34	17.36	1.67	0.00	0.59	2.72	5.07	4.81	0.10	0.15	0.06	0.00	0.00	98.46
E02-24	ID = 9009 E02-24H_glass1b	69.21	0.45	16.05	1.68	0.04	0.00	1.63	4.74	5.82	0.13	0.06	0.00	0.05	0.14	98.16
E02-24	ID = 9010 E02-24H_glass2a	70.19	0.43	15.29	1.75	0.13	0.24	1.49	4.20	5.82	0.23	0.00	0.02	0.02	0.18	98.24
E02-24	ID = 9011 E02-24H_glass2b	69.55	0.44	15.86	1.99	0.13	0.00	1.82	4.44	5.52	0.21	0.00	0.00	0.02	0.02	98.22
E02-24	ID = 9012 E02-24H_glass3a	67.76	0.44	17.48	1.32	0.13	0.23	2.52	5.07	4.84	0.05	0.04	0.00	0.12	0.00	98.83
E02-24	ID = 9014 E02-24H_glass4a	67.89	0.40	17.15	1.50	0.00	0.56	2.50	4.74	5.03	0.16	0.00	0.00	0.02	0.04	98.02
E02-24	ID = 9015 E02-24H_glass4b	66.04	0.37	17.14	2.20	0.15	1.36	2.97	4.82	4.54	0.16	0.07	0.00	0.00	0.16	98.94
E02-24	ID = 9016 E02-24H_glass5a	69.06	0.51	16.37	1.69	0.03	0.00	1.95	4.55	5.52	0.16	0.08	0.00	0.03	0.04	97.80
E02-24	ID = 9017 E02-24H_glass5b	69.96	0.56	14.47	2.26	0.04	0.69	1.12	4.03	6.10	0.18	0.00	0.00	0.15	0.42	97.97
E02-24	ID = 9018 E02-24H_glass5c	68.12	0.51	14.53	2.56	0.18	1.32	2.86	4.04	5.51	0.12	0.00	0.00	0.09	0.16	98.78
E02-24	ID = 9019 E02-24H_glass6a	67.96	0.47	16.42	1.78	0.00	0.71	2.26	4.66	5.36	0.00	0.07	0.00	0.16	0.15	98.54
E02-24	ID = 9020 E02-24H_glass6b	70.66	0.58	14.68	1.82	0.08	0.66	1.47	4.05	5.85	0.09	0.00	0.00	0.00	0.05	98.43
E02-24	ID = 9021 E02-24H_glass6c	67.98	0.46	16.82	1.64	0.03	0.53	2.71	4.68	4.97	0.04	0.10	0.03	0.00	0.00	97.57
E02-25	ID = 8995 E02-25H_glass1a	67.38	0.51	17.91	1.39	0.07	0.00	3.30	4.37	4.77	0.10	0.05	0.00	0.04	0.10	98.48
E02-25	ID = 8996 E02-25H_glass1b	66.66	0.50	16.84	2.05	0.08	1.03	3.11	4.25	5.02	0.09	0.00	0.00	0.02	0.36	98.40
E02-25	ID = 8997 E02-25H_glass2a	70.46	0.66	15.01	1.70	0.05	0.25	1.23	4.74	5.50	0.16	0.00	0.05	0.00	0.19	97.65
E02-25	ID = 8998 E02-25H_glass2b	69.71	0.58	15.57	1.90	0.03	0.00	2.10	4.47	5.30	0.18	0.00	0.00	0.06	0.11	97.07

Sample	Description of Analysis	SiO_2	TiO_2	Al_2O_3	FeO	MnO	MgO	CaO	Na_2O	K_2O	Cl	NiO	Cr_2O_3	SO_3	P_2O_5	Original Total
E02-25	ID = 9000 E02-25H_glass3b	66.98	0.44	17.83	1.46	0.00	0.27	2.82	4.77	5.11	0.05	0.00	0.00	0.04	0.23	98.62
E02-25	ID = 9001 E02-25H_glass4a	65.49	0.56	16.80	2.83	0.00	1.01	3.21	4.71	4.68	0.24	0.04	0.15	0.00	0.27	99.12
E02-25	ID = 9002 E02-25H_glass5a	68.89	0.42	16.77	1.20	0.00	0.20	2.18	4.61	5.58	0.05	0.00	0.00	0.00	0.10	98.39
E02-25	ID = 9003 E02-25H_glass5b	70.82	0.39	15.17	1.31	0.12	0.17	1.51	4.09	6.25	0.04	0.06	0.00	0.07	0.00	97.79
E02-25	ID = 9004 E02-25H_glass5c	68.24	0.44	17.30	1.22	0.00	0.00	2.72	4.86	5.06	0.04	0.00	0.00	0.07	0.05	98.12
E02-25	ID = 9005 E02-25H_glass6a	67.03	0.37	17.06	2.30	0.00	0.93	3.07	4.31	4.63	0.14	0.06	0.02	0.02	0.07	98.20
E02-28	ID = 8979 E02-28H_glass1b	66.73	0.65	17.01	2.22	0.00	0.57	2.46	4.79	5.26	0.19	0.02	0.00	0.00	0.09	98.33
E02-28	ID = 8980 E02-28H_glass1c	67.36	0.49	15.75	2.86	0.09	1.14	2.04	4.40	5.54	0.16	0.12	0.00	0.00	0.04	97.99
E02-28	ID = 8981 E02-28H_glass2a	67.45	0.51	15.37	3.07	0.08	0.99	1.98	4.66	5.57	0.10	0.00	0.04	0.04	0.13	99.32
E02-28	ID = 8982 E02-28H_glass2b	67.79	0.54	15.31	2.65	0.14	0.81	1.53	4.84	5.77	0.23	0.05	0.00	0.16	0.18	98.63
E02-28	ID = 8984 E02-28H_glass3b	67.71	0.55	16.23	2.42	0.03	0.90	1.90	4.48	5.36	0.22	0.00	0.00	0.06	0.15	97.18
E02-28	ID = 8985 E02-28H_glass4a	63.90	0.84	16.92	3.20	0.09	1.25	2.58	4.93	5.30	0.26	0.18	0.10	0.05	0.40	98.57
E02-28	ID = 8986 E02-28H_glass4b	64.15	0.83	17.21	3.33	0.00	1.35	3.06	5.05	4.53	0.25	0.03	0.00	0.13	0.08	99.14
E02-28	ID = 8989 E02-28H_glass5b	67.59	0.64	16.22	2.06	0.03	0.73	2.38	4.67	5.28	0.14	0.12	0.00	0.00	0.14	98.55
E02-28	ID = 8990 E02-28H_glass5c	66.89	0.52	16.50	2.22	0.10	0.97	2.31	4.64	5.38	0.11	0.00	0.01	0.06	0.28	98.25
E02-28	ID = 8991 E02-28H_glass6a	64.45	0.84	17.98	2.24	0.04	0.00	2.93	5.40	5.51	0.00	0.05	0.00	0.00	0.56	98.36
E02-28	ID = 8992 E02-28H_glass6b	65.84	0.89	17.47	2.23	0.07	0.00	2.36	5.32	5.56	0.05	0.01	0.00	0.00	0.18	97.70
E02-28	ID = 8993 E02-28H_glass7a	69.57	0.34	16.64	1.56	0.00	0.18	2.01	4.55	4.83	0.27	0.00	0.00	0.04	0.01	97.89
E02-28	ID = 8994 E02-28H_glass7b	66.81	0.30	18.56	0.98	0.00	0.15	2.00	5.42	5.61	0.06	0.00	0.02	0.00	0.07	96.80
E02-40	ID = 9048 E02-40H_glass1a	67.32	0.37	17.83	1.17	0.00	0.00	2.62	5.21	5.19	0.02	0.00	0.00	0.05	0.21	96.31
E02-40	ID = 9050 E02-40H_glass2a	66.17	0.56	17.21	3.14	0.00	0.87	2.17	4.62	5.03	0.04	0.06	0.00	0.12	0.00	94.98
E02-40	ID = 9051 E02-40H_glass2b	66.73	0.46	16.07	2.36	0.16	1.23	2.65	4.50	5.31	0.05	0.04	0.00	0.09	0.36	96.26
E02-40	ID = 9052 E02-40H_glass3a	68.80	0.69	16.52	1.31	0.00	0.27	1.91	4.77	5.62	0.01	0.00	0.00	0.10	0.00	97.81
E02-40	ID = 9053 E02-40H_glass3b	67.61	0.67	17.50	1.50	0.08	0.00	2.23	5.24	5.11	0.00	0.00	0.00	0.00	0.06	97.72
E02-40	ID = 9055 E02-40H_glass4b	65.09	0.56	18.59	1.93	0.04	0.68	3.55	4.80	4.36	0.05	0.04	0.05	0.00	0.25	96.25
E02-40	ID = 9056 E02-40H_glass5a	62.86	0.61	17.01	4.29	0.06	2.13	4.00	4.57	3.88	0.21	0.04	0.00	0.00	0.33	98.98
E02-41	ID = 9036 E02-41H_glass1b	63.20	0.81	17.44	3.78	0.00	1.28	3.76	4.97	4.04	0.25	0.05	0.07	0.00	0.34	94.34
E02-41	ID = 9037 E02-41H_glass1c	63.77	0.85	16.72	3.98	0.16	1.30	3.56	4.94	4.01	0.21	0.09	0.04	0.00	0.37	97.83
E02-41	ID = 9038 E02-41H_glass2a	73.59	0.63	13.34	1.43	0.08	0.00	0.64	3.39	6.74	0.16	0.00	0.00	0.01	0.00	95.88
E02-41	ID = 9039 E02-41H_glass2b	68.44	0.53	17.23	1.07	0.00	0.06	1.44	5.16	5.61	0.05	0.08	0.03	0.20	0.10	96.82
E02-41	ID = 9040 E02-41H_glass2c	69.67	0.39	16.69	1.03	0.01	0.00	1.51	4.80	5.73	0.06	0.00	0.00	0.01	0.10	95.53
E02-41	ID = 9041 E02-41H_glass3a	62.36	0.60	19.00	2.86	0.09	0.97	4.86	4.84	3.93	0.11	0.06	0.02	0.00	0.30	98.44
E02-41	ID = 9042 E02-41H_glass3b	63.12	0.60	18.81	2.97	0.09	0.78	4.28	4.98	3.83	0.21	0.05	0.06	0.04	0.18	93.95

Sample	Description of Analysis	SiO_2	TiO_2	Al_2O_3	FeO	MnO	MgO	CaO	Na_2O	K_2O	Cl	NiO	Cr_2O_3	SO_3	P_2O_5	Original Total
E02-41	ID = 9043 E02-41H_glass4a	63.33	0.88	16.83	4.14	0.18	1.69	3.69	4.88	3.82	0.14	0.00	0.00	0.00	0.42	98.48
E02-41	ID = 9044 E02-41H_glass5a	62.47	0.88	17.25	4.45	0.13	1.80	3.91	4.71	3.86	0.22	0.00	0.00	0.01	0.29	98.87
E02-41	ID = 9046 E02-41H_glass6a	67.90	0.33	17.98	0.65	0.09	0.00	2.30	5.09	5.53	0.11	0.00	0.00	0.00	0.00	96.21
E02-41	ID = 9047 E02-41H_glass6b	66.02	0.61	18.55	1.66	0.00	0.00	2.69	5.24	5.15	0.02	0.00	0.00	0.06	0.00	96.19
E02-4	ID = 9089 E02-4H_glass1a	67.53	0.35	17.45	1.52	0.11	0.22	2.80	4.75	4.99	0.00	0.07	0.05	0.01	0.14	98.03
E02-4	ID = 9090 E02-4H_glass1b	67.82	0.52	16.51	1.85	0.00	0.59	2.20	4.91	5.30	0.04	0.04	0.07	0.05	0.09	97.99
E02-4	ID = 9093 E02-4H_glass3b	67.99	0.65	15.34	2.60	0.00	1.29	2.06	4.10	5.73	0.09	0.03	0.00	0.01	0.11	97.46
E02-4	ID = 9092 E02-4H_glass3a	67.52	0.76	15.22	2.80	0.11	1.63	2.30	3.98	5.52	0.00	0.00	0.00	0.00	0.14	98.07
E02-4	ID = 9094 E02-4H_glass4a	68.29	0.52	16.31	1.99	0.01	0.00	2.48	4.78	5.40	0.05	0.02	0.00	0.09	0.06	97.37
E02-4	ID = 9095 E02-4H_glass5a	67.01	0.38	17.53	2.18	0.02	0.00	2.73	4.88	5.00	0.03	0.00	0.00	0.05	0.19	97.46
E02-4	ID = 9096 E02-4H_glass5b	69.10	0.50	16.73	1.24	0.00	0.00	2.35	4.52	5.37	0.03	0.04	0.00	0.10	0.00	97.25
E02-5	ID = 9077 E02-5H_glass1a	68.81	0.49	15.88	1.87	0.10	0.59	2.35	4.31	5.35	0.20	0.05	0.00	0.00	0.00	98.75
E02-5	ID = 9078 E02-5H_glass1b	69.12	0.40	16.42	1.49	0.11	0.00	2.44	4.48	5.32	0.16	0.03	0.00	0.01	0.02	98.07
E02-5	ID = 9079 E02-5H_glass2a	68.08	0.37	17.07	1.50	0.00	0.53	2.67	4.53	4.97	0.03	0.09	0.00	0.00	0.16	98.32
E02-5	ID = 9081 E02-5H_glass3a	69.14	0.47	15.57	1.75	0.07	0.79	1.89	4.30	5.53	0.13	0.07	0.00	0.00	0.29	98.80
E02-5	ID = 9082 E02-5H_glass3b	68.67	0.55	16.65	1.49	0.04	0.00	2.70	4.54	5.07	0.14	0.05	0.01	0.00	0.08	97.45
E02-5	ID = 9084 E02-5H_glass4b	71.28	0.55	14.64	1.51	0.15	0.00	1.47	3.89	6.01	0.27	0.06	0.00	0.15	0.01	97.46
E02-5	ID = 9085 E02-5H_glass5a	73.26	0.30	14.42	0.70	0.00	0.08	0.63	4.02	6.45	0.00	0.00	0.14	0.00	0.00	96.63
E02-5	ID = 9086 E02-5H_glass5b	73.00	0.25	14.67	0.53	0.00	0.14	0.89	4.23	5.93	0.05	0.19	0.00	0.12	0.00	97.91
E02-5	ID = 9088 E02-5H_glass6b	69.71	0.53	15.72	1.91	0.00	0.00	1.81	4.46	5.41	0.06	0.18	0.00	0.15	0.06	97.97
E02-6	ID = 9069 E02-6H_glass1a	67.97	0.63	16.02	2.31	0.11	0.52	2.12	4.37	5.62	0.11	0.00	0.00	0.00	0.22	98.87
E02-6	ID = 9070 E02-6H_glass1b	69.44	0.43	16.23	1.33	0.02	0.12	1.99	4.80	5.39	0.12	0.00	0.00	0.00	0.13	97.12
E02-6	ID = 9071 E02-6H_glass2a	70.86	0.50	15.10	1.53	0.04	0.00	1.18	4.44	6.11	0.19	0.00	0.00	0.05	0.00	97.63
E02-6	ID = 9072 E02-6H_glass2b	69.93	0.47	15.51	1.79	0.01	0.18	1.55	4.55	5.77	0.20	0.00	0.01	0.01	0.01	97.97
E02-6	ID = 9073 E02-6H_glass3a	69.06	0.53	15.17	1.83	0.09	0.00	1.93	4.41	6.03	0.19	0.03	0.00	0.13	0.58	98.27
E02-6	ID = 9074 E02-6H_glass3b	69.54	0.53	15.81	1.38	0.13	0.00	1.56	4.55	5.96	0.14	0.00	0.00	0.17	0.22	97.61
E02-6	ID = 9075 E02-6H_glass4a	69.35	0.70	15.45	2.29	0.09	0.00	1.50	4.17	6.11	0.18	0.00	0.00	0.00	0.15	97.36
E02-7	ID = 9060 E02-7H_glass1b	68.32	0.51	15.93	1.84	0.10	0.89	1.80	4.74	5.40	0.15	0.13	0.07	0.10	0.01	97.77
E02-7	ID = 9061 E02-7H_glass2a	70.10	0.65	15.22	1.78	0.00	0.00	1.80	4.56	5.37	0.16	0.00	0.00	0.13	0.24	97.44
E02-7	ID = 9062 E02-7H_glass2b	67.81	0.52	16.70	1.92	0.00	0.62	2.65	4.95	4.48	0.15	0.00	0.00	0.00	0.20	98.77
E02-7	ID = 9063 E02-7H_glass3a	68.09	0.57	16.99	1.74	0.01	0.00	2.22	4.73	5.42	0.17	0.00	0.04	0.00	0.02	98.67
E02-7	ID = 9064 E02-7H_glass3b	67.81	0.51	17.20	1.60	0.00	0.00	2.65	4.51	5.38	0.13	0.00	0.00	0.20	0.00	98.36
E02-7	ID = 9066 E02-7H_glass4b	68.81	0.39	16.52	1.26	0.05	0.23	2.14	4.60	5.64	0.06	0.16	0.00	0.00	0.13	98.50

Sample	Description of Analysis	SiO_2	TiO_2	Al_2O_3	FeO	MnO	MgO	CaO	Na_2O	K_2O	Cl	NiO	Cr_2O_3	SO_3	P_2O_5	Original Total
E02-7	ID = 9068 E02-7H_glass5b	68.05	0.49	15.30	2.48	0.02	0.93	2.83	4.23	5.27	0.05	0.00	0.00	0.07	0.28	98.06
E02-7	ID = 7106 E02-7 H glass1a	67.23	0.36	17.74	1.51	0.05	0.00	2.69	5.43	4.91	0.03	0.00	0.00	0.04	0.00	98.81
E02-7	ID = 7107 E02-7 H glass1b	67.75	0.44	17.44	1.40	0.00	0.00	2.39	5.31	5.20	0.06	0.00	0.00	0.00	0.01	98.32
E02-7	ID = 7108 E02-7 H glass2a	67.90	0.38	17.37	1.29	0.03	0.15	2.92	5.01	4.66	0.13	0.00	0.01	0.08	0.06	97.83
E02-7	ID = 7109 E02-7 H glass2b	66.52	0.56	16.76	3.10	0.10	0.56	2.32	4.83	5.08	0.11	0.00	0.00	0.00	0.06	98.51
E02-7	ID = 7110 E02-7 H glass3a	67.56	0.48	17.82	1.22	0.00	0.00	2.66	5.00	5.19	0.06	0.00	0.00	0.00	0.02	97.49
E02-7	ID = 7112 E02-7 H glass4b	65.23	0.76	17.69	1.82	0.00	0.69	2.82	5.33	5.39	0.00	0.08	0.00	0.01	0.17	98.79
E02-7	ID = 7113 E02-7 H glass4c	65.78	0.79	17.26	1.86	0.01	0.00	2.54	5.30	5.97	0.05	0.09	0.00	0.05	0.29	98.93
E02-7	ID = 7114 E02-7 H glass5a	71.94	0.58	13.84	1.76	0.11	0.50	1.18	3.88	5.69	0.11	0.13	0.00	0.00	0.27	98.38
E02-7	ID = 7115 E02-7 H glass5b	73.52	0.56	12.71	2.18	0.00	0.91	0.77	3.26	5.78	0.08	0.00	0.00	0.00	0.22	96.22
E02-7	ID = 7118 E02-7 H glass7b	69.58	0.47	15.99	1.29	0.00	0.14	1.88	4.76	5.71	0.02	0.00	0.00	0.00	0.15	98.98
E02-7	ID = 7119 E02-7 H glass8a	68.76	0.39	16.62	1.41	0.00	0.00	2.40	4.98	4.95	0.14	0.03	0.15	0.00	0.17	98.82
E02-7	ID = 7120 E02-7 H glass8b	68.70	0.44	16.78	1.04	0.00	0.25	1.90	4.83	5.74	0.06	0.12	0.06	0.00	0.06	99.28
E02-7	ID = 7121 E02-7 H glass8c	67.97	0.57	16.95	1.27	0.09	0.16	2.41	4.86	5.34	0.13	0.06	0.00	0.07	0.13	98.77
E02-8	ID = 9102 E02-8H_glass1a	66.43	0.86	16.08	2.75	0.01	0.87	2.00	4.78	5.75	0.21	0.17	0.00	0.01	0.06	98.44
E02-8	ID = 9103 E02-8H_glass1b	65.57	0.83	15.39	2.84	0.21	1.22	2.25	4.50	6.07	0.17	0.00	0.00	0.00	0.94	97.98
E02-8	ID = 9104 E02-8H_glass2a	68.75	0.44	16.14	1.72	0.06	0.55	1.85	4.79	5.42	0.20	0.02	0.00	0.05	0.01	98.57
E02-8	ID = 9105 E02-8H_glass2b	71.28	0.51	14.80	1.72	0.00	0.00	1.23	4.30	5.84	0.28	0.00	0.03	0.00	0.00	98.08
E02-8	ID = 9106 E02-8H_glass3a	69.93	0.49	15.33	1.99	0.12	0.00	1.52	4.67	5.44	0.19	0.09	0.00	0.09	0.13	98.26
E02-8	ID = 9107 E02-8H_glass4a	67.14	0.46	16.11	2.32	0.14	1.11	2.67	4.72	4.98	0.24	0.00	0.00	0.01	0.09	99.08
E02-8	ID = 9109 E02-8H_glass5a	71.53	0.50	14.24	1.48	0.00	0.50	1.13	4.39	6.11	0.02	0.00	0.00	0.11	0.00	96.92
E02-8	ID = 9109 E02-8H_glass5b	70.56	0.38	14.18	2.00	0.00	1.05	1.15	4.55	5.87	0.05	0.13	0.00	0.04	0.05	95.98
E02-8	ID = 9110 E02-8H_glass6a	68.99	0.46	15.84	1.77	0.04	0.53	1.67	4.53	5.61	0.30	0.14	0.00	0.00	0.11	96.96
E02-8	ID = 9111 E02-8H_glass6b	69.37	0.47	15.50	2.00	0.16	0.26	1.52	4.59	5.57	0.23	0.00	0.00	0.08	0.25	97.41
E02-8	ID = 9112 E02-8H_glass7a	67.06	0.51	16.55	2.44	0.05	1.30	2.88	4.24	4.63	0.21	0.00	0.00	0.00	0.12	98.48
E02-72	ID = 9155 E02-72L_glass1a	68.73	0.30	17.06	0.92	0.00	0.22	2.29	4.91	5.13	0.17	0.18	0.00	0.08	0.00	98.17
E02-72	ID = 9156 E02-72L_glass1b	69.35	0.36	15.59	1.82	0.04	0.77	2.25	4.37	5.05	0.23	0.00	0.00	0.00	0.16	98.35
E02-72	ID = 9155 E02-72H_glass1a	69.16	0.58	15.59	2.10	0.00	0.65	1.78	4.36	5.50	0.17	0.00	0.00	0.09	0.01	97.80
E02-72	ID = 9156 E02-72H_glass1b	70.12	0.55	15.45	1.85	0.09	0.00	1.53	4.18	5.98	0.14	0.00	0.02	0.00	0.08	98.12
E02-72	ID = 9157 E02-72H_glass2a	68.52	0.48	16.07	2.04	0.18	0.00	2.28	4.66	5.14	0.26	0.00	0.09	0.00	0.28	97.88
E02-72	ID = 9158 E02-72H_glass2b	68.40	0.48	16.29	1.89	0.03	0.55	2.47	4.42	5.16	0.22	0.09	0.00	0.00	0.00	97.50
E02-72	ID = 9159 E02-72H_glass3a	71.81	0.57	14.33	1.69	0.06	0.00	0.83	3.82	6.49	0.22	0.02	0.00	0.16	0.00	95.90
E02-72	ID = 9160 E02-72H_glass3b	70.57	0.52	15.30	1.47	0.15	0.00	1.27	4.25	6.01	0.16	0.00	0.00	0.07	0.24	96.50

Sample	Description of Analysis	SiO_2	TiO_2	Al_2O_3	FeO	MnO	MgO	CaO	Na_2O	K_2O	Cl	NiO	Cr_2O_3	SO_3	P_2O_5	Original Total
E02-72	ID = 9161 E02-72H_glass4a	70.49	0.70	14.24	2.08	0.00	0.62	0.67	3.97	6.84	0.13	0.00	0.00	0.00	0.27	97.73
E02-72	ID = 9162 E02-72H_glass4b	69.28	0.62	15.74	1.78	0.06	0.54	1.58	4.66	5.64	0.07	0.00	0.00	0.02	0.00	97.76
E02-72	ID = 9163 E02-72H_glass5a	71.05	0.38	15.11	1.53	0.04	0.00	1.58	4.09	6.01	0.12	0.01	0.01	0.06	0.00	97.14
E02-72	ID = 9164 E02-72H_glass5b	69.15	0.53	16.39	1.45	0.00	0.00	2.37	4.47	5.35	0.07	0.12	0.00	0.00	0.10	98.38
E02-73	ID = 9140 E02-73H_glass1a	69.24	0.43	16.34	1.61	0.07	0.00	2.37	4.69	4.98	0.19	0.00	0.00	0.08	0.00	98.35
E02-73	ID = 9141 E02-73H_glass1b	70.43	0.42	15.09	1.95	0.06	0.00	1.58	4.31	5.81	0.12	0.00	0.01	0.13	0.07	96.83
E02-73	ID = 9143 E02-73H_glass2b	71.62	0.45	14.97	1.46	0.05	0.45	0.79	3.44	6.54	0.06	0.01	0.00	0.00	0.15	95.24
E02-73	ID = 9144 E02-73H_glass3a	67.50	0.71	16.72	1.51	0.08	0.73	2.44	4.95	5.06	0.02	0.00	0.00	0.00	0.28	97.82
E02-73	ID = 9145 E02-73H_glass3b	68.81	0.64	16.18	1.53	0.03	0.58	1.67	5.10	5.34	0.00	0.06	0.00	0.00	0.05	98.61
E02-73	ID = 9146 E02-73H_glass4a	69.23	0.63	15.30	2.24	0.07	0.00	1.77	4.50	5.72	0.21	0.00	0.00	0.00	0.32	97.72
E02-73	ID = 9147 E02-73H_glass5a	74.04	0.47	14.97	0.74	0.00	0.01	0.69	2.85	6.18	0.00	0.00	0.00	0.00	0.05	93.81
E02-73	ID = 9148 E02-73H_glass5b	71.30	0.50	16.15	0.80	0.07	0.00	0.99	3.96	5.84	0.02	0.02	0.00	0.07	0.27	94.81
E02-73	ID = 9149 E02-73H_glass6a	70.15	0.48	15.56	1.45	0.00	0.00	1.52	4.54	5.85	0.24	0.01	0.00	0.07	0.13	96.00
E02-73	ID = 9150 E02-73H_glass6b	69.54	0.56	15.07	1.97	0.18	0.62	1.69	4.30	5.83	0.12	0.01	0.01	0.09	0.00	97.64
E02-73	ID = 9151 E02-73H_glass7a	70.81	0.84	14.26	2.26	0.08	0.20	1.00	3.97	6.17	0.22	0.03	0.00	0.01	0.14	97.80
E02-73	ID = 9152 E02-73H_glass8a	73.61	0.67	13.18	1.96	0.00	0.00	0.87	2.99	6.19	0.21	0.07	0.00	0.01	0.22	97.92
E02-73	ID = 9153 E02-73H_glass8b	68.36	0.44	17.03	1.39	0.00	0.22	2.19	4.60	5.50	0.13	0.00	0.00	0.01	0.12	97.94
E02-73	ID = 9154 E02-73H_glass8c	69.13	0.39	15.91	1.69	0.00	0.24	1.65	4.51	5.88	0.11	0.05	0.05	0.00	0.40	98.27
E02-73	ID = 9197 E02-73L_glass1b	70.17	0.25	16.85	0.46	0.00	0.01	2.05	4.88	5.28	0.00	0.00	0.01	0.04	0.00	98.88
E02-74	ID = 9129 E02-74L_glass2a	68.01	0.57	16.65	1.93	0.03	0.00	2.09	4.98	5.28	0.23	0.08	0.00	0.00	0.14	98.40
E02-74	ID = 9130 E02-74L_glass2b	67.99	0.54	16.09	2.24	0.01	0.62	1.91	4.75	5.50	0.20	0.00	0.00	0.02	0.14	98.81
E02-74	ID = 9132 E02-74L_glass3b	66.58	0.60	16.36	2.21	0.14	0.88	2.74	4.90	4.69	0.23	0.00	0.00	0.06	0.60	99.20
E02-74	ID = 9131 E02-74L_glass3a	70.02	0.63	15.92	2.20	0.05	0.00	1.37	3.55	5.83	0.28	0.00	0.00	0.06	0.08	96.19
E02-74	ID = 9133 E02-74L_glass4a	69.06	0.58	14.87	2.40	0.07	1.45	1.03	4.25	5.87	0.06	0.15	0.00	0.11	0.08	97.85
E02-74	ID = 9134 E02-74L_glass5a	64.45	0.69	16.93	3.41	0.17	0.85	2.47	5.08	5.31	0.29	0.00	0.01	0.05	0.27	98.32
E02-74	ID = 9136 E02-74L_glass5c	64.14	1.02	16.70	3.33	0.00	1.42	2.86	5.00	5.07	0.31	0.07	0.00	0.00	0.08	97.66
E02-74	ID = 9137 E02-74L_glass6a	66.65	0.43	16.81	2.29	0.12	0.85	2.47	4.97	5.11	0.14	0.00	0.00	0.00	0.16	98.67
E02-74	ID = 9138 E02-74L_glass6b	66.70	0.63	17.25	2.43	0.01	0.00	2.84	4.88	4.76	0.19	0.00	0.00	0.12	0.18	98.01
E02-74	ID = 9138 E02-74L_glass6b	66.70	0.63	17.25	2.43	0.01	0.00	2.84	4.88	4.76	0.19	0.00	0.00	0.12	0.18	98.01
E02-74	ID = 9139 E02-74L_glass7a	67.33	0.87	15.98	2.62	0.05	0.00	1.76	4.80	6.09	0.30	0.00	0.00	0.00	0.20	97.58
E02-75	ID = 9115 E02-75H_glass1a	66.58	0.68	17.30	2.03	0.00	0.00	2.44	5.29	5.17	0.22	0.00	0.03	0.00	0.25	98.81
E02-75	ID = 9116 E02-75H_glass1b	66.73	0.79	16.46	2.35	0.16	0.93	2.16	5.01	5.23	0.11	0.00	0.00	0.07	0.01	98.37
E02-75	ID = 9117 E02-75H_glass2a	65.53	0.89	17.00	2.62	0.06	0.66	2.23	5.17	5.50	0.18	0.00	0.04	0.00	0.12	98.23

Sample	Description of Analysis	SiO_2	TiO_2	Al_2O_3	FeO	MnO	MgO	CaO	Na_2O	K_2O	Cl	NiO	Cr_2O_3	SO_3	P_2O_5	Original Total
E02-75	ID = 9118 E02-75H_glass3a	64.46	0.99	15.96	3.83	0.05	1.69	2.45	4.61	5.50	0.30	0.00	0.00	0.06	0.10	98.39
E02-75	ID = 9119 E02-75H_glass4a	66.08	0.88	16.97	2.48	0.08	0.00	2.10	5.11	5.98	0.16	0.01	0.00	0.00	0.14	98.15
E02-75	ID = 9120 E02-75H_glass4b	66.60	0.94	15.82	2.74	0.17	0.72	1.42	4.53	6.38	0.26	0.00	0.00	0.06	0.36	98.26
E02-75	ID = 9121 E02-75H_glass5a	67.00	0.77	16.38	2.42	0.13	0.68	1.60	4.71	5.83	0.21	0.13	0.00	0.00	0.13	99.53
E02-75	ID = 9122 E02-75H_glass5b	67.42	0.61	16.11	2.56	0.07	0.71	1.82	4.74	5.60	0.15	0.03	0.00	0.03	0.14	98.73
E02-75	ID = 9123 E02-75H_glass6a	67.45	0.65	16.10	2.09	0.00	0.76	1.89	4.72	6.09	0.15	0.02	0.06	0.02	0.00	97.96
E02-75	ID = 9124 E02-75H_glass6b	68.39	0.54	16.07	1.79	0.13	0.18	1.44	4.98	6.05	0.16	0.14	0.06	0.00	0.05	98.62
E02-75	ID = 9125 E02-75H_glass7a	66.55	0.71	16.72	2.39	0.09	0.00	2.21	5.10	5.54	0.25	0.26	0.00	0.00	0.17	98.67
E02-75	ID = 9126 E02-75H_glass7b	65.43	0.74	16.31	2.85	0.03	1.19	2.48	4.72	5.43	0.27	0.00	0.00	0.10	0.45	98.68
E02-76	ID = 9186 E02-76H_glass1a	64.89	0.91	16.25	3.23	0.05	1.23	2.68	5.43	4.94	0.20	0.00	0.00	0.00	0.18	97.61
E02-76	ID = 9187 E02-76H_glass1b	64.08	0.69	17.36	3.04	0.17	1.02	2.65	5.23	5.29	0.23	0.04	0.00	0.05	0.14	98.45
E02-76	ID = 9188 E02-76H_glass2a	67.02	0.61	17.22	2.05	0.08	0.59	2.40	5.15	4.44	0.14	0.00	0.00	0.09	0.20	98.38
E02-76	ID = 9190 E02-76H_glass3a	68.06	0.53	16.04	2.79	0.02	0.00	1.69	4.91	5.36	0.21	0.00	0.08	0.12	0.17	97.71
E02-76	ID = 9191 E02-76H_glass3b	67.40	0.60	15.96	3.01	0.21	0.82	2.17	4.57	5.10	0.16	0.00	0.00	0.00	0.00	98.15
E02-76	ID = 9192 E02-76H_glass4a	67.71	0.52	16.14	2.32	0.07	0.75	2.06	4.80	5.17	0.28	0.00	0.07	0.06	0.05	97.48
E02-76	ID = 9193 E02-76H_glass4b	67.71	0.65	16.70	2.22	0.00	0.59	2.25	4.79	4.82	0.25	0.00	0.00	0.00	0.00	98.04
E02-76	ID = 9194 E02-76H_glass5a	65.83	0.51	17.75	2.28	0.11	0.64	2.76	5.11	4.64	0.16	0.09	0.00	0.07	0.05	98.98
E02-76	ID = 9195 E02-76H_glass5b	67.44	0.64	17.18	2.13	0.07	0.00	2.26	4.79	5.23	0.05	0.09	0.00	0.00	0.12	98.35
E02-77	ID = 9175 E02-77H_glass1a	68.05	0.37	17.26	1.57	0.07	0.00	2.78	4.64	5.01	0.24	0.00	0.00	0.00	0.01	97.21
E02-77	ID = 9176 E02-77H_glass1b	70.08	0.46	14.91	1.68	0.12	0.23	1.22	4.31	6.50	0.24	0.00	0.08	0.00	0.16	98.18
E02-77	ID = 9177 E02-77H_glass2a	70.23	0.67	14.39	2.49	0.19	0.61	1.01	3.77	6.23	0.26	0.00	0.00	0.00	0.13	98.20
E02-77	ID = 9178 E02-77H_glass2b	70.49	0.67	14.88	2.04	0.03	0.00	1.06	4.33	6.26	0.11	0.00	0.00	0.00	0.13	97.45
E02-77	ID = 9179 E02-77H_glass3a	67.91	0.47	17.26	1.91	0.00	0.00	2.57	4.84	4.79	0.11	0.00	0.00	0.07	0.07	98.01
E02-77	ID = 9180 E02-77H_glass3b	66.04	0.60	17.40	2.38	0.05	0.57	2.96	4.88	4.75	0.16	0.07	0.00	0.00	0.14	98.61
E02-77	ID = 9181 E02-77H_glass3c	69.50	0.60	14.09	2.80	0.14	0.62	1.14	4.01	6.24	0.22	0.10	0.00	0.00	0.53	98.34
E02-77	ID = 9182 E02-77H_glass4a	69.65	0.37	15.79	1.37	0.00	0.53	1.97	4.56	5.57	0.18	0.00	0.00	0.01	0.00	96.11
E02-77	ID = 9183 E02-77H_glass4b	68.69	0.50	16.51	1.61	0.02	0.00	1.95	4.87	5.47	0.12	0.00	0.00	0.26	0.00	97.88
E02-77	ID = 9184 E02-77H_glass5a	69.66	0.56	16.17	1.69	0.00	0.00	1.99	4.52	5.15	0.08	0.18	0.00	0.00	0.00	96.62
E02-77	ID = 9185 E02-77H_glass5b	68.39	0.30	17.13	1.65	0.00	0.00	2.41	4.67	5.12	0.13	0.02	0.08	0.09	0.00	97.60
E02-77	ID = 9185 E02-77H_glass5b	68.39	0.30	17.13	1.65	0.00	0.00	2.41	4.67	5.12	0.13	0.02	0.08	0.09	0.00	97.60
E02-78	ID = 9165 E02-78H_glass1a	68.47	0.49	16.37	1.75	0.09	0.75	2.52	4.23	5.08	0.08	0.00	0.00	0.17	0.00	97.94
E02-78	ID = 9166 E02-78H_glass1b	67.18	0.43	17.00	2.33	0.07	0.58	3.16	4.53	4.46	0.13	0.14	0.00	0.00	0.00	98.71
E02-78	ID = 9168 E02-78H_glass2b	68.53	0.37	15.57	2.37	0.05	0.84	2.41	4.18	5.21	0.20	0.13	0.13	0.00	0.00	99.00

Sample	Description of Analysis	SiO_2	TiO_2	Al_2O_3	FeO	MnO	MgO	CaO	Na_2O	K_2O	Cl	NiO	Cr_2O_3	SO_3	P_2O_5	Original Total
E02-78	ID = 9169 E02-78H_glass3a	70.44	0.47	15.52	1.62	0.02	0.00	2.18	4.27	5.38	0.09	0.00	0.00	0.00	0.00	98.12
E02-78	ID = 9170 E02-78H_glass3b	69.38	0.38	16.00	1.50	0.00	0.00	2.25	4.55	5.53	0.15	0.00	0.11	0.01	0.13	97.80
E02-78	ID = 9171 E02-78H_glass4a	67.92	0.68	15.85	2.35	0.03	0.58	1.77	4.75	5.52	0.11	0.13	0.00	0.00	0.30	98.13
E02-78	ID = 9172 E02-78H_glass4b	67.98	0.35	16.74	2.00	0.06	0.00	2.11	5.16	5.29	0.14	0.00	0.00	0.10	0.07	97.93
E02-78	ID = 9173 E02-78H_glass5a	69.92	0.54	15.80	1.60	0.01	0.00	1.90	4.53	5.44	0.06	0.00	0.00	0.06	0.14	98.13
E02-78	ID = 9174 E02-78H_glass5b	69.88	0.37	15.63	2.12	0.14	0.00	1.84	4.28	5.62	0.10	0.00	0.00	0.03	0.00	96.83
SR13	ID = 9243 SR13_glass1a	66.84	0.38	17.70	1.43	0.05	0.56	3.51	4.85	4.41	0.11	0.06	0.00	0.00	0.10	98.92
SR13	ID = 9245 SR13_glass1c	68.16	0.33	17.56	1.23	0.02	0.00	3.01	4.87	4.60	0.09	0.01	0.00	0.12	0.00	97.17
SR13	ID = 9246 SR13_glass2a	67.05	0.37	17.78	1.54	0.00	0.00	3.29	5.00	4.52	0.12	0.20	0.08	0.04	0.00	97.81
SR13	ID = 9247 SR13_glass2b	68.55	0.38	17.33	1.19	0.00	0.00	2.67	4.58	5.13	0.17	0.00	0.00	0.00	0.00	97.46
SR13	ID = 9248 SR13_glass3a	69.78	0.59	15.45	2.02	0.08	0.00	1.64	4.55	5.55	0.24	0.00	0.00	0.11	0.00	97.14
SR13	ID = 9249 SR13_glass3b	69.80	0.66	15.18	2.09	0.04	0.24	1.53	4.59	5.51	0.12	0.10	0.00	0.13	0.00	97.22
SR13	ID = 9250 SR13_glass4a	69.82	0.42	16.30	1.07	0.19	0.21	2.15	4.41	5.25	0.05	0.07	0.00	0.06	0.00	98.29
SR13	ID = 9251 SR13_glass4b	71.13	0.27	15.61	1.20	0.04	0.00	1.92	4.23	5.48	0.04	0.02	0.00	0.00	0.05	97.31
SR13	ID = 9252 SR13_glass5a	70.49	0.56	15.39	1.57	0.05	0.00	1.90	4.38	5.51	0.15	0.00	0.00	0.00	0.00	98.38
SR13	ID = 9253 SR13_glass5b	71.95	0.54	14.45	1.67	0.00	0.00	1.30	3.79	6.05	0.18	0.00	0.00	0.05	0.02	97.73
SR13	ID = 9254 SR13_glass6a	69.82	0.31	15.92	1.53	0.11	0.00	2.23	4.30	5.58	0.15	0.00	0.04	0.01	0.00	97.91
SR13	ID = 10580_SR13_glass1a	68.21	0.41	17.15	0.99	0.09	0.15	2.41	5.07	4.97	0.08	0.03	0.09	0.23	0.11	97.20
SR13	ID = 10581_SR13_glass1b	70.26	0.36	16.17	1.21	0.00	0.10	2.19	4.57	5.02	0.09	0.02	0.00	0.00	0.00	95.90
SR13	ID = 10582_SR13_glass2a	69.90	0.39	15.58	1.51	0.07	0.16	1.37	4.36	6.41	0.14	0.00	0.00	0.00	0.10	97.24
SR13	ID = 10583_SR13_glass3a	68.44	0.37	17.19	1.44	0.04	0.23	2.24	4.79	5.08	0.12	0.00	0.06	0.00	0.00	97.56
SR13	ID = 10585_SR13_glass4a	68.78	0.35	17.02	1.42	0.03	0.00	3.01	4.52	4.64	0.12	0.02	0.00	0.07	0.02	97.30
SR13	ID = 10587_SR13_glass5a	68.44	0.49	16.68	1.43	0.13	0.15	2.41	4.90	5.03	0.14	0.00	0.00	0.17	0.01	97.77
SR13	ID = 10589_SR13_glass6a	68.91	0.42	16.49	1.41	0.04	0.14	2.24	4.79	5.27	0.17	0.00	0.00	0.04	0.06	97.27
SR13	ID = 10590_SR13_glass6b	68.32	0.53	15.91	1.74	0.16	0.65	1.99	4.71	5.61	0.20	0.00	0.00	0.08	0.09	97.87
SR13	ID = 9255 SR13_glass6b	70.34	0.62	15.46	1.55	0.00	0.00	1.50	4.46	5.99	0.07	0.00	0.00	0.00	0.00	97.82
Py7	ID = 8954 Py7H_glass1a	69.60	0.66	15.51	2.04	0.02	0.00	1.32	5.00	5.50	0.11	0.00	0.09	0.14	0.00	97.54
Py7	ID = 8955 Py7H_glass1b	70.87	0.64	14.51	2.29	0.16	0.10	0.80	4.38	5.87	0.19	0.05	0.00	0.09	0.05	96.71
Py7	ID = 9436 Py7_glass1a	67.10	0.50	16.35	2.71	0.02	0.71	2.57	4.41	5.25	0.16	0.01	0.00	0.00	0.21	98.88
Py7	ID = 9438 Py7_glass1c	67.54	0.58	16.04	2.72	0.04	0.98	2.08	4.58	5.17	0.08	0.00	0.07	0.00	0.10	95.54
Py7	ID = 8956 Py7H_glass2a	66.63	0.65	16.59	2.71	0.20	0.68	2.50	4.40	5.17	0.26	0.09	0.00	0.01	0.10	98.61
Py7	ID = 8957 Py7H_glass3a	68.83	0.46	16.94	1.58	0.08	0.00	2.71	4.54	4.56	0.00	0.15	0.00	0.00	0.14	98.03
Py7	ID = 8958 Py7H_glass3b	68.41	0.52	16.88	1.31	0.03	0.16	2.36	4.58	5.55	0.05	0.00	0.00	0.15	0.00	98.70

Sample	Description of Analysis	SiO_2	TiO_2	Al_2O_3	FeO	MnO	MgO	CaO	Na_2O	K_2O	Cl	NiO	Cr_2O_3	SO_3	P_2O_5	Original Total
Py7	ID = 8959 Py7H_glass4a	66.59	0.56	16.45	2.73	0.08	1.00	2.57	4.27	5.27	0.27	0.00	0.00	0.00	0.20	99.58
Py7	ID = 8960 Py7H_glass4b	67.12	0.50	16.65	2.17	0.00	0.56	2.31	4.87	5.17	0.23	0.12	0.00	0.00	0.30	97.96
Py7	ID = 8961 Py7H_glass5a	67.32	0.47	17.27	2.00	0.10	0.00	2.85	4.75	4.87	0.15	0.17	0.00	0.00	0.04	97.74
Py7	ID = 8962 Py7H_glass5b	67.06	0.60	16.72	2.53	0.06	0.73	2.95	4.61	4.54	0.04	0.00	0.00	0.00	0.15	98.49
Py7	ID = 8963 Py7L_glass6a	66.84	0.55	16.41	2.22	0.20	0.88	2.64	4.42	5.22	0.25	0.00	0.05	0.00	0.32	98.14
Py7	ID = 8964 Py7L_glass6b	67.02	0.51	16.41	2.55	0.07	0.82	2.28	4.44	5.40	0.25	0.00	0.00	0.10	0.14	98.54
Py7	ID = 8965 Py7L_glass7a	66.87	0.64	16.53	2.53	0.12	0.74	2.47	4.43	5.23	0.24	0.00	0.08	0.04	0.07	98.67
Py9	ID = 9453 Py9_glass1a	71.95	0.65	14.63	1.01	0.00	0.01	0.62	4.17	6.80	0.01	0.03	0.00	0.07	0.05	96.94
Py9	ID = 9454 Py9_glass1b	71.02	0.49	15.38	0.93	0.06	0.00	0.86	4.85	6.27	0.00	0.00	0.00	0.02	0.11	97.87
Py9	ID = 9455 Py9_glass2a	69.74	0.70	14.65	2.36	0.00	0.23	0.93	4.34	6.36	0.26	0.00	0.00	0.07	0.36	97.10
Py9	ID = 9456 Py9_glass2b	70.39	0.69	14.47	2.28	0.13	0.00	0.98	4.30	6.25	0.17	0.19	0.04	0.00	0.09	97.91
Py9	ID = 9457 Py9_glass3a	70.37	0.68	14.52	2.29	0.02	0.00	1.43	4.24	6.01	0.20	0.00	0.00	0.06	0.19	96.14
Py9	ID = 9457 Py9_glass3a	70.37	0.68	14.52	2.29	0.02	0.00	1.43	4.24	6.01	0.20	0.00	0.00	0.06	0.19	96.14
Py9	ID = 9458 Py9_glass3b	70.73	0.60	14.51	2.13	0.17	0.00	0.95	4.29	6.06	0.20	0.07	0.00	0.09	0.19	97.77
Py9	ID = 9459 Py9_glass4a	69.18	0.56	16.51	1.36	0.00	0.60	2.18	4.72	4.78	0.08	0.03	0.00	0.00	0.00	98.07
Py9	ID = 9460 Py9_glass4b	69.15	0.48	16.72	1.20	0.00	0.12	2.22	4.91	4.88	0.08	0.18	0.06	0.00	0.00	96.10
Py9	ID = 9461 Py9_glass5a	68.43	0.57	16.63	2.16	0.06	0.00	2.36	4.31	5.13	0.11	0.14	0.00	0.10	0.00	98.31
Py9	ID = 9462 Py9_glass5b	67.65	0.47	17.53	1.49	0.00	0.27	2.19	4.96	5.43	0.01	0.00	0.00	0.00	0.00	98.00
Py9	ID = 9463 Py9_glass6a	70.38	0.65	14.30	2.61	0.11	0.19	1.03	4.48	5.84	0.27	0.00	0.00	0.12	0.01	96.75
Py9	ID = 9464 Py9_glass6b	70.10	0.59	14.21	2.96	0.02	0.50	0.84	4.26	6.14	0.23	0.07	0.00	0.05	0.01	97.17
Py9	ID = 9465 Py9_glass6c	68.99	0.64	15.94	2.02	0.06	0.00	1.68	4.85	5.44	0.24	0.00	0.00	0.01	0.13	97.16
Py9	ID = 9466 Py9_glass7a	71.17	0.61	14.53	1.85	0.09	0.13	0.69	3.92	6.59	0.17	0.16	0.00	0.07	0.00	97.24
Py9	ID = 9467 Py9_glass7b	72.32	0.72	13.48	2.27	0.08	0.00	0.64	3.63	6.44	0.23	0.00	0.00	0.14	0.04	97.30
Py9	ID = 8932 Py9H_glass2a	69.27	0.37	16.16	1.50	0.06	0.00	2.11	4.82	5.40	0.17	0.00	0.00	0.12	0.01	97.62
Py9	ID = 8933 Py9H_glass2b	67.63	0.48	16.92	1.73	0.05	0.56	2.77	4.71	4.86	0.16	0.00	0.00	0.05	0.07	98.21
Py9	ID = 8934 Py9H_glass3a	68.46	0.39	17.01	1.31	0.03	0.17	2.54	4.71	5.17	0.13	0.00	0.02	0.00	0.06	97.74
Py9	ID = 8935 Py9H_glass3b	69.23	0.49	16.71	1.08	0.00	0.00	2.42	4.69	5.20	0.08	0.00	0.00	0.10	0.00	95.59
Py9	ID = 8936 Py9H_glass4a	68.79	0.56	16.13	1.80	0.05	0.00	1.56	4.78	6.11	0.05	0.00	0.00	0.00	0.17	98.10
Py9	ID = 8937 Py9H_glass4b	68.43	0.55	15.64	2.06	0.14	0.57	1.66	4.24	6.26	0.16	0.00	0.00	0.28	0.02	97.15
Py9	ID = 8938 Py9H_glass5a	68.05	0.63	16.58	1.77	0.04	0.00	2.15	4.84	5.54	0.14	0.07	0.00	0.05	0.12	98.13
Py9	ID = 8939 Py9H_glass5b	70.00	0.50	14.94	1.94	0.04	0.56	1.14	4.27	6.31	0.20	0.00	0.00	0.00	0.09	96.22
Py13	ID = 9278 Py13_glass1a	70.59	0.67	14.08	1.89	0.00	0.24	0.89	4.43	6.63	0.11	0.00	0.01	0.00	0.45	96.51
Py13	ID = 9279 Py13_glass1b	66.84	0.71	15.52	2.44	0.13	1.59	0.70	4.45	6.97	0.23	0.00	0.00	0.12	0.31	96.91

Sample	Description of Analysis	SiO_2	TiO_2	Al_2O_3	FeO	MnO	MgO	CaO	Na_2O	K_2O	Cl	NiO	Cr_2O_3	SO_3	P_2O_5	Original Total
Py13	ID = 9280 Py13_glass2a	67.82	0.31	17.33	1.69	0.02	0.22	3.40	4.42	4.49	0.16	0.00	0.06	0.00	0.06	98.59
Py13	ID = 9281 Py13_glass2b	70.68	0.46	15.28	1.59	0.00	0.00	2.02	4.18	5.48	0.17	0.00	0.06	0.07	0.00	97.40
Py13	ID = 9282 Py13_glass3a	67.06	0.38	17.18	1.61	0.02	0.64	3.35	4.84	4.54	0.11	0.27	0.00	0.00	0.00	98.57
Py13	ID = 9283 Py13_glass3b	69.39	0.33	15.90	1.56	0.13	0.00	1.89	4.45	5.84	0.17	0.13	0.00	0.08	0.12	98.11
Py13	ID = 9284 Py13_glass4a	68.68	0.41	16.64	1.85	0.00	0.00	2.60	4.46	5.15	0.12	0.00	0.00	0.08	0.00	97.00
Py13	ID = 9285 Py13_glass4b	68.60	0.42	16.28	1.74	0.10	0.54	2.35	4.49	5.20	0.13	0.05	0.00	0.00	0.10	97.94
Py13	ID = 9286 Py13_glass5a	67.34	0.43	17.61	1.48	0.06	0.28	3.08	4.70	4.72	0.10	0.19	0.00	0.01	0.00	98.08
Py13	ID = 9287 Py13_glass5b	68.23	0.54	16.01	2.04	0.09	0.55	2.03	4.49	5.79	0.14	0.00	0.00	0.10	0.00	98.64
Py16	ID = 9268 Py16_glass1a	67.45	0.40	17.13	2.14	0.06	0.00	2.92	4.74	4.86	0.11	0.00	0.00	0.05	0.13	98.01
Py16	ID = 9269 Py16_glass1b	68.69	0.55	15.61	2.01	0.18	0.52	2.19	4.34	5.63	0.21	0.00	0.00	0.00	0.07	97.91
Py16	ID = 9270 Py16_glass2a	68.46	0.44	16.71	1.86	0.00	0.00	2.30	4.72	5.12	0.09	0.18	0.05	0.05	0.01	96.99
Py16	ID = 9271 Py16_glass2b	66.21	0.94	14.56	4.76	0.13	1.67	2.09	4.03	5.33	0.13	0.00	0.04	0.00	0.10	97.99
Py16	ID = 9272 Py16_glass3a	67.61	0.19	17.38	1.52	0.14	0.28	2.96	4.63	4.88	0.11	0.04	0.02	0.12	0.11	98.09
Py16	ID = 9273 Py16_glass3b	69.41	0.36	16.46	1.57	0.00	0.00	2.41	4.50	5.11	0.11	0.00	0.00	0.00	0.07	97.51
Py16	ID = 9274 Py16_glass4a	67.96	0.45	17.28	1.62	0.11	0.12	2.73	4.66	4.80	0.10	0.00	0.00	0.08	0.08	97.97
Py16	ID = 9275 Py16_glass4b	67.55	0.55	16.69	1.95	0.13	0.80	2.71	4.54	4.80	0.11	0.00	0.00	0.00	0.15	98.25
Py16	ID = 9276 Py16_glass5a	67.79	0.34	17.48	1.57	0.00	0.19	3.06	4.86	4.49	0.18	0.00	0.01	0.03	0.00	98.03
Py16	ID = 9277 Py16_glass5b	68.71	0.53	14.04	3.03	0.19	1.34	2.05	3.97	5.61	0.25	0.07	0.05	0.00	0.17	98.10
Py19	ID = 8915 Py19H_glass1a	69.25	0.33	16.36	1.42	0.00	0.00	2.36	4.85	5.17	0.10	0.00	0.14	0.00	0.01	97.77
Py19	ID = 8916 Py19H_glass1b	68.49	0.58	15.61	2.26	0.04	0.66	2.29	4.48	5.32	0.13	0.05	0.06	0.00	0.04	98.76
Py19	ID = 8917 Py19H_glass2a	69.50	0.46	16.30	1.57	0.03	0.00	2.17	4.44	5.32	0.21	0.00	0.00	0.00	0.00	97.23
Py19	ID = 8918 Py19H_glass2b	68.37	0.53	17.08	1.75	0.00	0.00	2.92	4.17	4.87	0.21	0.02	0.00	0.07	0.00	96.88
Py19	ID = 8919 Py19H_glass3a	69.58	0.43	14.97	2.19	0.08	0.64	1.93	4.30	5.73	0.06	0.00	0.00	0.05	0.04	97.61
Py19	ID = 8921 Py19H_glass4a	69.08	0.46	16.42	1.24	0.00	0.26	2.33	4.47	5.44	0.11	0.00	0.01	0.02	0.16	97.69
Py19	ID = 8922 Py19H_glass4b	68.94	0.43	16.33	1.20	0.00	0.23	1.67	4.80	6.03	0.12	0.10	0.00	0.04	0.11	94.49
Py19	ID = 8923 Py19H_glass5a	69.05	0.43	16.67	1.35	0.06	0.00	2.64	4.53	5.03	0.06	0.05	0.00	0.13	0.00	97.84
Py19	ID = 8925 Py19H_glass6b	70.17	0.33	15.84	1.25	0.03	0.17	1.95	4.12	5.79	0.12	0.00	0.00	0.00	0.23	98.12
Py19	ID = 8926 Py19H_glass7a	68.93	0.65	15.44	1.92	0.15	0.66	1.48	4.28	6.06	0.14	0.00	0.00	0.11	0.18	98.69
Py19	ID = 8927 Py19H_glass7b	67.18	0.42	16.79	1.96	0.11	0.84	2.84	4.95	4.75	0.15	0.00	0.00	0.00	0.01	98.34
Py19	ID = 8928 Py19L_glass8a	71.75	0.26	14.97	1.31	0.02	0.14	1.66	4.62	5.27	0.00	0.00	0.00	0.00	0.00	97.03
Py19	ID = 8929 Py19L_glass8b	69.02	0.17	17.19	0.95	0.00	0.18	1.52	5.59	5.27	0.00	0.04	0.00	0.06	0.00	98.81
Py20	ID = 8899 Py20L_glass1a	64.87	0.74	16.77	3.39	0.13	1.10	2.93	4.97	4.33	0.24	0.00	0.06	0.11	0.36	97.48
Py20	ID = 8900 Py20H_glass2a	70.13	0.48	15.51	1.51	0.02	0.00	1.52	4.29	6.04	0.19	0.05	0.00	0.00	0.26	97.28

Sample	Description of Analysis	SiO_2	TiO_2	Al_2O_3	FeO	MnO	MgO	CaO	Na_2O	K_2O	Cl	NiO	Cr_2O_3	SO_3	P_2O_5	Original Total
Py20	ID = 8901 Py20H_glass2b	67.03	0.45	18.04	1.45	0.00	0.27	3.11	4.88	4.48	0.15	0.06	0.00	0.07	0.00	97.93
Py20	ID = 8904 Py20H_glass4a	67.91	0.54	16.92	2.09	0.14	0.00	2.67	4.81	4.74	0.04	0.07	0.00	0.05	0.01	97.87
Py20	ID = 8905 Py20H_glass4b	71.99	0.52	14.25	1.58	0.06	0.00	1.29	3.87	6.26	0.02	0.06	0.00	0.00	0.07	97.30
Py20	ID = 8906 Py20H_glass4c	69.42	0.37	16.43	1.52	0.00	0.26	2.15	4.53	5.10	0.03	0.00	0.07	0.10	0.02	97.99
Py20	ID = 8907 Py20H_glass5a	75.90	0.67	12.03	2.76	0.11	0.00	0.00	2.90	5.45	0.04	0.12	0.01	0.00	0.00	95.16
Py20	ID = 8908 Py20H_glass5b	76.16	0.44	11.94	1.75	0.03	0.18	0.00	2.98	6.06	0.01	0.24	0.00	0.18	0.02	94.73
Py20	ID = 8909 Py20H_glass6a	68.78	0.61	16.09	2.02	0.12	0.00	1.80	4.62	5.69	0.11	0.11	0.00	0.00	0.05	98.68
Py20	ID = 8911 Py20H_glass7a	67.54	0.53	16.74	1.81	0.21	0.71	3.30	4.24	4.74	0.12	0.00	0.00	0.05	0.01	97.68
Py20	ID = 8912 Py20H_glass7b	66.86	0.47	17.26	1.87	0.06	0.00	3.86	4.67	4.70	0.11	0.00	0.00	0.00	0.15	97.94
Py20	ID = 8913 Py20H_glass8a	70.25	0.59	15.31	1.86	0.04	0.00	2.01	4.09	5.60	0.19	0.00	0.00	0.00	0.07	96.67
Py20	ID = 8914 Py20H_glass9a	67.48	0.36	17.94	1.23	0.06	0.22	3.31	4.86	4.39	0.15	0.00	0.00	0.00	0.00	97.83
Py20	ID = 9256 Py20_glass1a	70.63	0.49	15.63	1.37	0.00	0.00	1.70	4.28	5.71	0.00	0.00	0.07	0.00	0.11	96.42
Py20	ID = 9257 Py20_glass1b	70.34	0.59	14.49	2.34	0.11	0.68	1.37	3.79	6.05	0.00	0.06	0.00	0.05	0.10	96.81
Py20	ID = 9258 Py20_glass2a	68.52	0.45	16.67	1.91	0.00	0.00	2.65	4.43	4.90	0.10	0.22	0.00	0.04	0.11	97.59
Py20	ID = 9259 Py20_glass2b	67.75	0.44	17.18	1.85	0.06	0.00	3.12	4.49	4.78	0.15	0.00	0.00	0.00	0.17	97.39
Py20	ID = 9260 Py20_glass2c	68.04	0.40	17.26	1.62	0.04	0.00	2.97	4.61	4.92	0.14	0.00	0.00	0.00	0.00	97.59
Py20	ID = 9261 Py20_glass3a	69.60	0.43	15.81	1.65	0.04	0.00	1.90	4.61	5.69	0.16	0.05	0.00	0.00	0.06	97.23
Py20	ID = 9262 Py20_glass3b	68.81	0.51	15.37	2.22	0.00	0.71	2.07	4.38	5.72	0.19	0.00	0.00	0.00	0.02	97.87
Py20	ID = 9263 Py20_glass4a	71.98	0.50	14.61	1.42	0.04	0.17	1.14	4.29	5.60	0.09	0.00	0.03	0.00	0.11	97.83
Py20	ID = 9264 Py20_glass4b	70.09	0.34	16.07	1.15	0.00	0.09	1.95	4.81	5.17	0.09	0.12	0.00	0.00	0.10	97.84
Py20	ID = 9265 Py20_glass5a	69.41	0.44	16.16	1.58	0.14	0.00	2.13	4.25	5.68	0.00	0.04	0.00	0.00	0.17	97.96
Py20	ID = 9266 Py20_glass5b	74.33	0.53	13.61	0.82	0.04	0.11	0.62	2.96	6.98	0.00	0.00	0.00	0.00	0.00	96.83
Py20	ID = 9267 Py20_glass5c	68.24	0.66	16.06	2.80	0.08	0.00	2.49	4.40	5.04	0.06	0.05	0.10	0.01	0.00	97.77
WW3	ID = 9288 WW3_glass1a	73.83	0.43	13.22	1.30	0.02	0.49	0.46	3.99	6.07	0.14	0.00	0.00	0.00	0.05	95.99
WW3	ID = 9289 WW3_glass1b	70.92	0.56	15.44	1.38	0.00	0.00	1.60	4.99	5.07	0.04	0.00	0.00	0.00	0.00	97.65
WW3	ID = 9290 WW3_glass1c	74.13	0.53	13.52	1.11	0.03	0.05	0.63	3.83	6.00	0.09	0.00	0.00	0.00	0.06	95.46
WW3	ID = 9291 WW3_glass2a	72.24	0.56	13.83	1.53	0.00	0.50	0.71	4.14	6.09	0.10	0.07	0.00	0.06	0.16	97.92
WW3	ID = 9294 WW3_glass3b	73.61	0.54	13.79	1.09	0.00	0.14	1.10	4.45	5.01	0.11	0.00	0.09	0.00	0.07	98.30
WW3	ID = 9294 WW3_glass3b	73.61	0.54	13.79	1.09	0.00	0.14	1.10	4.45	5.01	0.11	0.00	0.09	0.00	0.07	98.30
WW3	ID = 9296 WW3_glass4a	73.23	0.42	14.24	1.07	0.00	0.17	0.59	3.80	6.38	0.09	0.00	0.00	0.00	0.00	95.15
WW3	ID = 9297 WW3_glass4b	75.31	0.56	12.67	1.27	0.00	0.11	0.75	3.63	5.63	0.06	0.00	0.00	0.00	0.00	93.90
WW3	ID = 9298 WW3_glass4c	73.32	0.36	14.23	0.83	0.00	0.08	0.58	4.11	6.23	0.07	0.00	0.00	0.00	0.17	96.25
WW3	ID = 9299 WW3_glass5a	72.32	0.61	14.42	1.47	0.08	0.00	1.24	4.22	5.38	0.09	0.00	0.00	0.07	0.10	97.43

Sample	Description of Analysis	SiO_2	TiO_2	Al_2O_3	FeO	MnO	MgO	CaO	Na_2O	K_2O	Cl	NiO	Cr_2O_3	SO_3	P_2O_5	Original Total
WW3	ID = 9300 WW3_glass5b	71.22	0.72	14.10	2.61	0.07	0.00	0.91	4.53	5.48	0.07	0.03	0.00	0.04	0.22	99.21
WW6	ID = 9301 WW6_glass1a	70.75	0.60	15.06	1.66	0.13	0.00	2.02	4.11	5.31	0.20	0.00	0.00	0.16	0.00	94.84
WW6	ID = 9302 WW6_glass1b	66.68	0.45	17.92	1.77	0.11	0.00	2.84	5.01	4.90	0.09	0.10	0.00	0.11	0.00	96.08
WW6	ID = 9303 WW6_glass2a	68.92	0.46	16.63	1.37	0.06	0.00	2.35	4.69	5.39	0.12	0.00	0.00	0.00	0.00	97.40
WW6	ID = 9304 WW6_glass2b	67.38	0.35	17.81	1.38	0.09	0.28	3.08	4.87	4.61	0.07	0.07	0.00	0.00	0.02	97.43
WW6	ID = 9305 WW6_glass3a	67.10	0.46	17.65	1.32	0.00	0.25	2.85	5.10	4.86	0.19	0.03	0.06	0.13	0.00	98.74
WW6	ID = 9306 WW6_glass3b	69.43	0.61	15.15	1.92	0.19	0.64	2.03	4.23	5.54	0.13	0.04	0.00	0.02	0.06	97.60
WW6	ID = 9307 WW6_glass4a	74.43	0.72	14.03	0.74	0.00	0.16	1.01	3.50	5.23	0.08	0.00	0.00	0.00	0.10	96.34
WW6	ID = 9308 WW6_glass4b	70.93	0.52	16.14	1.08	0.00	0.03	1.64	4.77	4.59	0.09	0.00	0.00	0.11	0.09	96.86
WW6	ID = 9309 WW6_glass4c	72.68	0.43	15.14	0.94	0.05	0.18	1.32	4.13	5.05	0.03	0.06	0.00	0.00	0.00	96.00
WW6	ID = 9310 WW6_glass5a	67.11	0.37	17.62	1.97	0.11	0.00	3.03	4.85	4.61	0.15	0.04	0.07	0.00	0.07	98.12
WW20	ID = 9313 WW20_glass1a	68.33	0.49	16.28	1.63	0.03	0.20	2.21	4.86	5.52	0.18	0.00	0.00	0.06	0.19	97.89
WW20	ID = 9315 WW20_glass1c	69.70	0.53	14.98	1.87	0.21	0.74	1.42	4.19	6.23	0.10	0.00	0.00	0.00	0.02	98.50
WW20	ID = 9317 WW20_glass2b	71.36	0.65	14.69	1.71	0.00	0.00	0.88	4.42	6.08	0.07	0.00	0.00	0.13	0.00	96.87
WW20	ID = 9319 WW20_glass3a	68.00	0.41	17.14	1.23	0.00	0.24	2.29	5.02	5.41	0.10	0.08	0.00	0.00	0.08	97.82
WW20	ID = 9320 WW20_glass3b	66.85	0.54	16.84	1.96	0.10	0.90	3.18	4.65	4.88	0.07	0.00	0.00	0.04	0.00	98.24
WW20	ID = 9321 WW20_glass4a	67.30	0.63	17.78	1.36	0.02	0.20	3.15	4.68	4.67	0.14	0.00	0.00	0.00	0.06	97.59
WW20	ID = 9322 WW20_glass4b	66.25	0.59	15.44	2.33	0.12	1.04	3.45	4.13	5.13	0.23	0.00	0.00	0.12	1.17	98.67
WW20	ID = 9323 WW20_glass5a	69.03	0.50	16.15	1.70	0.14	0.00	1.51	4.85	5.82	0.15	0.00	0.00	0.10	0.04	97.55
WW20	ID = 9324 WW20_glass5b	67.74	0.52	17.25	1.51	0.05	0.00	2.48	4.92	5.18	0.14	0.18	0.00	0.00	0.01	97.69
WW20	ID = 9325 WW20_glass6a	67.30	0.52	16.93	1.68	0.08	0.58	2.45	4.93	5.31	0.12	0.00	0.00	0.00	0.09	97.90
WW20	ID = 9326 WW20_glass6b	68.58	0.36	16.74	1.68	0.00	0.00	1.83	4.79	5.67	0.16	0.00	0.00	0.00	0.19	97.95
WW20	ID = 9327 WW20_glass7a	67.89	0.38	17.33	1.06	0.00	0.24	2.90	4.87	5.22	0.06	0.00	0.00	0.00	0.05	98.12
WW20	ID = 9328 WW20_glass7b	68.29	0.37	16.67	1.65	0.13	0.00	2.74	4.58	5.36	0.09	0.08	0.00	0.01	0.02	97.72
Ma40	ID = 9439 Ma40_glass1a	67.53	0.49	17.53	1.42	0.00	0.26	2.87	4.68	5.02	0.01	0.08	0.00	0.00	0.11	98.57
Ma40	ID = 9440 Ma40_glass1b	68.57	0.34	16.96	1.44	0.01	0.00	2.65	4.55	5.19	0.06	0.08	0.00	0.14	0.01	96.76
Ma40	ID = 9441 Ma40_glass2a	67.70	0.47	16.78	1.62	0.06	0.68	2.73	4.58	5.36	0.01	0.00	0.00	0.00	0.01	98.42
Ma40	ID = 9442 Ma40_glass2b	68.64	0.32	17.07	0.90	0.00	0.14	2.95	4.78	4.75	0.06	0.14	0.00	0.07	0.17	97.85
Ma40	ID = 9444 Ma40_glass3b	66.58	0.55	16.08	3.50	0.12	0.80	1.93	4.50	5.53	0.20	0.00	0.00	0.06	0.14	97.82
Ma40	ID = 9446 Ma40_glass4a	66.69	0.53	16.37	2.55	0.05	1.10	2.60	4.69	5.03	0.16	0.02	0.00	0.04	0.16	98.06
Ma40	ID = 9447 Ma40_glass4b	67.21	0.56	16.40	2.27	0.06	0.74	2.23	4.82	5.22	0.25	0.11	0.00	0.00	0.13	98.31
Ma40	ID = 9449 Ma40_glass5b	70.65	0.60	14.75	1.68	0.08	0.51	1.35	3.91	6.24	0.06	0.06	0.00	0.00	0.09	97.63
Ma40	ID = 9450 Ma40_glass5c	69.80	0.36	16.18	0.96	0.01	0.14	1.94	4.79	5.64	0.00	0.00	0.00	0.00	0.19	97.04

Sample	Description of Analysis	SiO_2	TiO_2	Al_2O_3	FeO	MnO	MgO	CaO	Na_2O	K_2O	Cl	NiO	Cr_2O_3	SO_3	P_2O_5	Original Total
Ma40	ID = 9451 Ma40_glass6a	67.94	0.65	15.43	2.66	0.10	0.74	1.88	4.29	5.72	0.31	0.14	0.00	0.00	0.14	97.63
Ma40	ID = 9452 Ma40_glass6b	67.22	0.48	17.53	2.01	0.07	0.00	2.77	4.80	4.76	0.16	0.04	0.00	0.14	0.00	97.83
WW34	ID = 9470 WW34_glass1b	69.64	0.41	16.13	1.12	0.10	0.11	1.79	4.41	5.93	0.09	0.00	0.00	0.08	0.19	98.49
WW34	ID = 9471 WW34_glass1c	69.70	0.42	15.65	1.58	0.04	0.00	2.43	4.14	5.45	0.10	0.14	0.00	0.08	0.27	97.85
WW34	ID = 9472 WW34_glass2a	67.45	0.43	17.70	1.31	0.00	0.23	3.05	4.81	4.74	0.07	0.00	0.00	0.02	0.17	99.52
WW34	ID = 9473 WW34_glass2b	68.93	0.42	16.77	1.24	0.00	0.17	2.17	4.54	5.44	0.11	0.00	0.04	0.08	0.08	98.16
WW34	ID = 9475 WW34_glass3b	69.21	0.46	16.63	1.28	0.17	0.00	2.62	4.48	4.95	0.09	0.10	0.00	0.00	0.00	97.89
WW34	ID = 9476 WW34_glass3c	69.84	0.39	15.93	1.46	0.17	0.00	2.20	4.33	5.52	0.11	0.00	0.00	0.05	0.00	97.83
WW34	ID = 9477 WW34_glass4a	69.74	0.43	16.28	1.29	0.11	0.00	1.89	4.54	5.50	0.11	0.00	0.00	0.04	0.05	97.04
WW34	ID = 9478 WW34_glass4b	69.73	0.34	16.23	1.57	0.00	0.21	2.18	4.08	5.24	0.21	0.04	0.00	0.03	0.13	98.04
WW34	ID = 9479 WW34_glass5a	67.17	0.55	16.87	2.17	0.16	0.00	2.28	4.89	5.39	0.12	0.06	0.00	0.13	0.21	98.31
WW34	ID = 9481 WW34_glass5c	67.60	0.63	16.38	2.18	0.00	0.56	1.95	4.79	5.67	0.17	0.01	0.02	0.00	0.04	98.14
WW27	ID = 9498 WW27_glass1b	70.44	0.60	14.76	1.93	0.14	0.00	1.46	3.90	6.20	0.20	0.09	0.07	0.00	0.21	98.67
WW27	ID = 9499 WW27_glass2a	70.09	0.34	15.76	1.60	0.12	0.00	2.08	4.20	5.44	0.16	0.05	0.00	0.06	0.10	98.17
WW27	ID = 9500 WW27_glass2b	70.39	0.40	14.88	1.78	0.00	0.57	1.66	3.92	6.07	0.11	0.12	0.00	0.00	0.09	98.10
WW27	ID = 9501 WW27_glass3a	70.48	0.50	15.57	1.62	0.00	0.00	1.62	4.29	5.57	0.25	0.01	0.00	0.01	0.09	97.77
WW27	ID = 9502 WW27_glass3b	69.59	0.30	15.56	1.97	0.16	0.57	1.78	4.04	5.58	0.28	0.10	0.00	0.00	0.06	98.63
WW27	ID = 9503 WW27_glass4a	69.42	0.55	16.29	1.36	0.12	0.08	1.77	5.07	5.21	0.09	0.00	0.00	0.02	0.00	98.20
WW27	ID = 9504 WW27_glass5a	71.36	0.29	14.83	1.72	0.08	0.00	1.81	3.83	5.84	0.20	0.01	0.00	0.02	0.00	97.70
WW27	ID = 9505 WW27_glass5b	69.73	0.43	16.41	1.24	0.06	0.00	2.06	4.45	5.43	0.07	0.00	0.00	0.02	0.08	97.43
WW27	ID = 9506 WW27_glass6a	71.08	0.57	14.92	1.35	0.03	0.00	1.50	3.89	6.09	0.18	0.00	0.00	0.17	0.20	98.35
WW8	ID = 9508 WW8_glass1a	73.46	0.47	14.20	1.01	0.00	0.12	1.22	4.16	5.16	0.08	0.00	0.00	0.02	0.10	98.43
WW8	ID = 9510 WW8_glass2a	73.21	0.45	13.68	1.40	0.02	0.19	0.75	4.14	5.76	0.20	0.00	0.09	0.02	0.09	98.81
WW8	ID = 9545 WW8_glass3	72.84	0.41	14.26	1.51	0.04	0.00	0.98	4.14	5.44	0.23	0.12	0.00	0.02	0.00	96.83
WW4	ID = 9512 WW4_glass1a	72.58	0.73	13.73	1.53	0.07	0.55	0.70	4.07	5.95	0.02	0.00	0.00	0.00	0.08	97.63
WW4	ID = 9513 WW4_glass1b	72.82	0.45	14.33	1.42	0.00	0.00	1.20	4.22	5.36	0.07	0.13	0.00	0.01	0.00	95.90
WW4	ID = 9514 WW4_glass2b	73.49	0.20	14.63	0.90	0.04	0.05	1.93	4.07	4.62	0.05	0.00	0.00	0.01	0.00	97.76
WW4	ID = 9515 WW4_glass2b	74.29	0.40	12.91	1.30	0.28	0.00	0.96	4.03	5.42	0.08	0.06	0.00	0.16	0.11	97.38
WW4	ID = 9516 WW4_glass3a	74.04	0.49	14.03	1.29	0.07	0.00	0.69	3.62	5.52	0.16	0.00	0.00	0.09	0.00	96.04
WW4	ID = 9517 WW4_glass3b	73.79	0.58	14.55	1.45	0.16	0.00	0.83	3.48	4.80	0.18	0.11	0.00	0.02	0.05	96.06
WW4	ID = 9518 WW4_glass4a	72.69	0.63	13.22	2.01	0.06	0.00	0.63	4.26	6.30	0.16	0.00	0.00	0.00	0.04	95.67
WW4	ID = 9520 WW4_glass4c	71.15	0.54	14.47	1.95	0.00	0.25	0.94	4.63	5.76	0.13	0.00	0.07	0.01	0.09	97.43
WW4	ID = 9521 WW4_glass5a	71.60	0.43	14.47	1.72	0.03	0.50	0.85	4.33	5.89	0.08	0.03	0.00	0.02	0.06	98.65

Sample	Description of Analysis	SiO_2	TiO_2	Al_2O_3	FeO	MnO	MgO	CaO	Na_2O	K_2O	Cl	NiO	Cr_2O_3	SO_3	P_2O_5	Original Total
WW4	ID = 9522 WW4_glass5b	71.49	0.64	14.51	1.45	0.00	0.25	1.04	4.65	5.46	0.09	0.07	0.00	0.17	0.18	99.39
Py30	ID = 9523 Py30_glass1a	67.25	0.58	15.48	3.17	0.09	0.87	2.35	4.22	5.60	0.22	0.10	0.00	0.00	0.06	98.53
Py30	ID = 9524 Py30_glass1b	68.54	0.44	16.31	2.23	0.02	0.00	2.17	4.42	5.59	0.22	0.00	0.00	0.00	0.07	97.37
Py30	ID = 9525 Py30_glass2	68.61	0.63	16.53	1.43	0.00	0.00	1.79	5.03	5.52	0.17	0.16	0.00	0.06	0.05	97.80
Py30	ID = 9526 Py30_glass3a	67.37	0.54	16.30	2.43	0.03	0.57	2.51	4.78	5.05	0.23	0.05	0.00	0.05	0.09	98.60
Py30	ID = 9527 Py30_glass3b	67.83	0.44	16.84	2.30	0.00	0.00	2.65	4.64	4.98	0.24	0.00	0.00	0.08	0.00	97.64
Py30	ID = 9528 Py30_glass4a	68.70	0.55	15.96	2.15	0.00	0.00	1.97	4.16	6.06	0.29	0.05	0.01	0.10	0.00	96.69
Py30	ID = 9529 Py30_glass4b	68.43	0.59	16.39	2.08	0.00	0.00	2.44	4.40	5.41	0.24	0.00	0.00	0.02	0.00	97.06
Py30	ID = 9531 Py30_glass5a	67.47	0.76	15.75	2.75	0.13	0.84	1.78	4.55	5.56	0.20	0.00	0.01	0.12	0.08	99.30
Py30	ID = 9532 Py30_glass5b	68.02	0.60	15.93	2.51	0.02	0.55	1.62	4.62	5.70	0.19	0.08	0.00	0.00	0.16	98.76
P12	ID = 9533 P12_glass1a	70.73	0.51	15.49	1.51	0.02	0.00	1.66	4.24	5.66	0.17	0.00	0.00	0.00	0.00	97.81
P12	ID = 9534 P12_glass1b	68.40	0.33	16.88	1.36	0.02	0.19	2.52	4.55	5.25	0.19	0.00	0.00	0.11	0.18	99.15
P12	ID = 9535 P12_glass1c	70.50	0.42	15.21	1.46	0.04	0.55	1.64	4.20	5.63	0.21	0.00	0.00	0.04	0.11	98.78
P12	ID = 9536 P12_glass2a	69.44	0.33	16.29	1.45	0.00	0.00	2.25	4.47	5.55	0.14	0.00	0.07	0.00	0.02	98.26
P12	ID = 9537 P12_glass2b	68.36	0.28	17.02	1.53	0.04	0.00	2.77	4.68	4.92	0.15	0.00	0.00	0.14	0.10	98.69
P12	ID = 9538 P12_glass2c	69.44	0.44	16.14	1.54	0.03	0.23	2.33	4.24	5.45	0.16	0.00	0.00	0.01	0.00	98.22
P12	ID = 9539 P12_glass3a	68.56	0.41	16.28	1.95	0.00	0.54	2.34	4.64	4.95	0.11	0.05	0.00	0.00	0.16	99.49
P12	ID = 9540 P12_glass4a	69.33	0.32	16.06	1.64	0.00	0.00	2.07	4.58	5.66	0.15	0.09	0.00	0.00	0.09	99.04
P12	ID = 9541 P12_glass4b	67.87	0.43	16.28	1.77	0.12	0.60	2.44	4.62	5.22	0.19	0.10	0.00	0.16	0.19	99.49
P12	ID = 9542 P12_glass5a	70.93	0.39	15.08	1.80	0.00	0.00	1.46	4.16	6.04	0.09	0.01	0.03	0.00	0.01	97.47
P12	ID = 9544 P12_glass5c	71.35	0.44	14.90	1.34	0.12	0.00	1.23	4.05	6.31	0.06	0.00	0.00	0.15	0.04	98.44
SR9	ID = 10533_Sr9_gl1a	70.85	0.67	15.26	2.11	0.28	0.52	1.44	3.28	5.26	0.22	0.00	0.05	0.04	0.00	95.06
SR9	ID = 10534_Sr9_gl1b	69.74	0.59	15.39	2.21	0.20	0.00	1.59	4.56	5.13	0.24	0.19	0.00	0.11	0.05	96.86
SR9	ID = 10537_Sr9_gl3a	70.86	0.59	15.52	2.06	0.19	0.54	1.49	3.02	5.39	0.28	0.01	0.05	0.00	0.00	95.23
SR9	ID = 10538_Sr9_gl3b	70.11	0.63	15.25	2.11	0.18	0.00	1.47	4.77	5.04	0.28	0.00	0.00	0.15	0.00	97.03
SR9	ID = 10539_Sr9_gl3c	69.21	0.50	15.39	2.17	0.12	0.61	1.65	4.90	5.03	0.33	0.00	0.00	0.01	0.08	97.17
SR9	ID = 10540_Sr9_gl4a	67.80	0.40	16.73	1.33	0.07	0.00	2.92	5.17	4.70	0.13	0.16	0.13	0.00	0.46	96.38
SR9	ID = 10541_Sr9_gl4b	67.90	0.49	17.35	1.47	0.00	0.00	2.85	4.90	4.68	0.16	0.00	0.00	0.00	0.21	96.17
SR9	ID = 10543_Sr9_gl5b	67.55	0.23	17.94	0.52	0.05	0.00	0.94	5.44	7.24	0.03	0.00	0.06	0.01	0.00	96.94
SR9	ID = 10545_Sr9_gl6b	68.83	0.69	15.47	2.08	0.21	0.52	1.60	4.89	5.07	0.23	0.01	0.00	0.07	0.33	96.13
WW19	ID = 10546_WW19_gl1a	74.84	0.46	13.03	1.23	0.12	0.12	0.55	3.74	5.70	0.16	0.00	0.00	0.02	0.04	94.64
WW19	ID = 10547_WW19_gl1b	75.63	0.47	12.65	1.19	0.19	0.00	0.42	3.56	5.72	0.16	0.01	0.00	0.00	0.00	94.34
WW19	ID = 10549_WW19_glass2b	68.56	0.87	14.33	3.23	0.10	0.78	0.70	4.52	6.45	0.14	0.00	0.00	0.01	0.31	97.56

Sample	Description of Analysis	SiO_2	TiO_2	Al_2O_3	FeO	MnO	MgO	CaO	Na_2O	K_2O	Cl	NiO	Cr_2O_3	SO_3	P_2O_5	Original Total
WW19	ID = 10551_WW19_glass3b	67.56	0.74	15.31	3.03	0.12	0.56	1.59	5.06	5.62	0.02	0.10	0.02	0.02	0.24	98.47
WW19	ID = 10552_WW19_glass4a	66.98	0.91	15.34	3.47	0.13	0.77	1.61	4.67	5.69	0.20	0.06	0.01	0.00	0.15	97.13
WW19	ID = 10553_WW19_glass4b	66.79	0.80	16.06	2.78	0.07	0.54	1.77	4.95	5.51	0.18	0.16	0.00	0.07	0.30	97.32
SR3	ID = 10555_SR3_glass2a	66.94	0.45	16.62	2.81	0.08	0.68	2.28	5.05	4.55	0.27	0.08	0.00	0.08	0.11	97.63
SR3	ID = 10557_SR3_glass3a	68.84	0.40	16.14	2.03	0.12	0.00	1.92	4.29	5.87	0.26	0.01	0.00	0.00	0.11	96.43
SR3	ID = 10558_SR3_glass3b	69.16	0.37	16.09	2.05	0.05	0.00	1.85	4.25	5.83	0.29	0.00	0.00	0.00	0.06	96.47
SR3	ID = 10559_SR3_glass3c	67.82	0.58	16.37	2.35	0.08	0.00	2.15	4.42	5.88	0.27	0.00	0.00	0.02	0.07	96.85
SR3	ID = 10561_SR3_glass4b	66.74	0.46	16.79	2.38	0.26	0.59	2.51	4.69	5.23	0.18	0.00	0.00	0.05	0.11	98.28
SR3	ID = 10563_SR3_glass5b	68.47	0.62	16.33	2.11	0.00	0.00	1.55	4.80	5.95	0.10	0.00	0.00	0.07	0.00	97.31
SR3	ID = 10564_SR3_glass5c	68.04	0.53	16.40	1.99	0.10	0.00	1.79	5.10	5.64	0.13	0.05	0.00	0.06	0.16	97.10
SR3	ID = 10566_SR3_glass6b	67.19	0.43	17.13	2.48	0.05	0.00	2.79	4.40	5.13	0.27	0.11	0.00	0.00	0.00	97.41
SR3	ID = 10567_SR3_glass6c	66.98	0.27	17.49	2.14	0.00	0.53	2.97	4.26	4.88	0.15	0.00	0.00	0.13	0.20	97.23
SR12	ID = 10569_SR12_glass1b	70.95	0.45	15.36	1.32	0.05	0.00	1.72	4.49	5.54	0.03	0.00	0.00	0.01	0.08	96.31
SR12	ID = 10570_SR12_glass2a	69.29	0.48	15.81	1.68	0.03	0.56	1.98	4.40	5.42	0.23	0.00	0.00	0.05	0.06	96.81
SR12	ID = 10571_SR12_glass2b	69.07	0.35	16.26	1.63	0.05	0.00	2.13	4.64	5.46	0.18	0.00	0.00	0.00	0.23	96.74
SR12	ID = 10573_SR12_glass3b	69.92	0.50	15.06	2.15	0.10	0.00	1.35	4.26	6.32	0.21	0.12	0.00	0.00	0.00	96.45
SR12	ID = 10574_SR12_glass4a	68.21	0.51	15.80	2.10	0.11	0.53	1.84	4.40	5.89	0.36	0.04	0.00	0.09	0.10	97.59
SR12	ID = 10575_SR12_glass4b	69.00	0.43	15.51	2.04	0.11	0.00	1.82	4.57	5.80	0.34	0.04	0.00	0.17	0.15	97.20
SR12	ID = 10576_SR12_glass5a	71.47	0.54	14.74	1.38	0.00	0.14	1.23	3.97	6.22	0.21	0.00	0.00	0.08	0.01	96.12
SR12	ID = 10577_SR12_glass5b	70.03	0.43	15.75	1.25	0.00	0.18	1.77	4.43	5.75	0.14	0.07	0.04	0.08	0.07	97.14
SR12	ID = 10578_SR12_glass6a	70.40	0.38	15.32	1.54	0.17	0.15	1.37	4.11	6.08	0.22	0.07	0.00	0.09	0.09	97.33
SR12	ID = 10579_SR12_glass6b	71.71	0.39	14.41	1.63	0.00	0.17	1.08	3.84	6.41	0.25	0.08	0.00	0.02	0.00	97.31
SR11	ID = 10591_SR11_glass1a	70.18	0.43	14.41	1.93	0.19	0.86	1.93	3.97	5.50	0.17	0.05	0.00	0.14	0.23	98.43
SR11	ID = 10592_SR11_glass1b	70.48	0.41	15.46	1.48	0.14	0.00	1.70	4.42	5.56	0.15	0.00	0.00	0.02	0.17	97.60
SR11	ID = 10593_SR11_glass2a	70.66	0.48	15.14	1.85	0.00	0.00	1.68	4.17	5.68	0.13	0.01	0.00	0.13	0.05	96.94
SR11	ID = 10594_SR11_glass2b	67.14	0.41	17.65	1.50	0.12	0.15	3.18	4.96	4.50	0.13	0.12	0.00	0.06	0.07	98.61
SR11	ID = 10595_SR11_glass3a	66.95	0.71	15.93	2.52	0.03	0.68	2.01	5.35	5.04	0.23	0.07	0.04	0.01	0.42	97.15
SR11	ID = 10596_SR11_glass4a	69.37	0.50	15.11	1.85	0.07	0.72	0.93	4.41	6.79	0.15	0.10	0.00	0.00	0.00	97.51
SR11	ID = 10597_SR11_glass4b	70.89	0.44	14.93	1.55	0.00	0.00	0.72	4.41	6.69	0.21	0.14	0.03	0.00	0.00	95.66
SR11	ID = 10598_SR11_glass5	69.36	0.51	16.06	1.76	0.13	0.00	2.19	4.42	5.10	0.26	0.00	0.00	0.00	0.21	96.97
SR11	ID = 10599_SR11_glass6a	70.47	0.45	15.38	1.27	0.02	0.16	1.59	4.33	5.95	0.20	0.00	0.00	0.01	0.16	97.00
SR11	ID = 10600_SR11_glass6b	71.49	0.58	14.50	1.79	0.08	0.00	1.15	3.95	6.15	0.23	0.01	0.07	0.00	0.00	97.67
Py31	ID = 10601_Py31_glass1a	68.55	0.37	16.65	1.65	0.00	0.00	2.26	4.57	5.54	0.20	0.00	0.00	0.01	0.21	96.36

Sample	Description of Analysis	SiO_2	TiO_2	Al_2O_3	FeO	MnO	MgO	CaO	Na_2O	K_2O	Cl	NiO	Cr_2O_3	SO_3	P_2O_5	Original Total
Py31	ID = 10602_Py31_glass1b	67.54	0.62	15.60	2.52	0.10	0.66	1.88	4.65	5.62	0.28	0.00	0.00	0.27	0.28	97.01
Py31	ID = 10603_Py31_glass2a	68.00	0.69	16.32	1.88	0.00	0.00	1.42	5.31	6.06	0.16	0.08	0.00	0.04	0.04	96.68
Py31	ID = 10604_Py31_glass2b	67.37	0.78	16.92	1.72	0.13	0.00	2.00	5.24	5.65	0.12	0.00	0.00	0.00	0.08	96.71
Py31	ID = 10606_Py31_glass3b	71.79	0.84	13.99	1.80	0.08	0.20	0.83	4.07	6.08	0.16	0.00	0.00	0.04	0.11	97.34
Py31	ID = 10607_Py31_glass4a	69.09	0.37	16.73	1.30	0.00	0.01	2.58	4.65	5.07	0.05	0.01	0.00	0.00	0.12	96.76
Py31	ID = 10608_Py31_glass4b	67.68	0.38	17.37	1.52	0.06	0.28	2.91	5.05	4.64	0.06	0.00	0.04	0.01	0.00	96.85
Py31	ID = 10610_Py31_glass5b	69.83	0.47	15.36	1.71	0.00	0.15	1.65	4.59	5.93	0.21	0.00	0.07	0.01	0.00	96.86
SD21	ID = 8228 SD21 glass4b	65.47	0.66	17.25	2.86	0.00	1.04	3.17	4.74	4.46	0.18	0.00	0.00	0.00	0.17	95.34
SD21	ID = 8230 SD21 glass5a	65.05	0.47	17.60	2.85	0.11	0.79	3.63	4.72	4.27	0.26	0.00	0.09	0.00	0.15	97.22
SD20	ID = 8232 SD20 glass1a	65.60	0.62	16.95	3.08	0.00	1.04	3.03	4.60	4.76	0.24	0.02	0.04	0.01	0.00	96.70
SD20	ID = 8233 SD20 glass2a	65.21	0.59	16.86	3.19	0.12	1.17	3.20	4.61	4.56	0.26	0.00	0.03	0.04	0.17	96.05
SD20	ID = 8233 SD20 glass2a	63.07	0.42	18.88	2.59	0.16	0.82	5.04	4.40	3.97	0.27	0.00	0.00	0.23	0.15	97.64
SD20	ID = 8236 SD20 glass5a	64.36	0.57	16.95	3.34	0.09	1.01	3.60	4.84	4.73	0.25	0.14	0.03	0.09	0.00	96.15
SD20	ID = 8237 SD20 glass6a	65.63	0.41	16.55	2.98	0.14	1.01	2.80	4.87	4.91	0.40	0.00	0.03	0.22	0.04	97.01
SD20	ID = 8238 SD20 glass7a	65.26	0.43	16.77	2.96	0.16	1.06	3.21	4.58	4.80	0.27	0.00	0.04	0.17	0.29	97.38
SD20	ID = 8239 SD20 glass8a	65.80	0.56	16.62	2.71	0.12	1.04	2.73	4.94	4.92	0.25	0.00	0.09	0.06	0.15	97.79
SD20	ID = 8240 SD20 glass9a	65.30	0.62	16.90	3.00	0.09	0.95	3.42	4.56	4.61	0.22	0.15	0.02	0.10	0.06	98.31
SD23	ID = 2466 SD23a glass1	68.19	0.34	15.73	2.54	0.07	0.63	2.30	4.44	5.26	0.34	0.03	0.00	0.12	0.01	98.19
SD23	ID = 2482 SD23a glass2	66.82	0.41	16.43	3.06	0.00	0.78	2.82	4.09	4.89	0.28	0.00	0.00	0.14	0.28	97.75
SD25	ID = 10493 SD25a_gl1	66.13	0.50	16.91	2.89	0.06	1.12	2.99	4.18	4.71	0.28	0.00	0.00	0.00	0.23	96.22
SD25	ID = 10494 SD25a_gl2	66.20	0.47	16.62	2.94	0.06	0.86	2.75	4.77	4.86	0.27	0.08	0.11	0.00	0.00	96.62
SD25	ID = 10496 SD25a_gl2	67.60	0.47	16.61	2.59	0.00	0.83	2.51	3.89	5.10	0.27	0.00	0.00	0.07	0.06	95.72
SD25	ID = 10497 SD25a_gl3	66.22	0.48	16.69	2.94	0.03	1.27	3.12	4.18	4.56	0.16	0.20	0.06	0.00	0.09	96.69
SD25	ID = 10498 SD25a_gl4	66.39	0.62	16.59	2.71	0.10	0.90	2.52	4.79	4.85	0.32	0.00	0.00	0.00	0.21	96.85
SD25	ID = 10500 SD25a_gl5	66.74	0.49	16.74	2.88	0.16	0.91	2.61	3.90	4.93	0.33	0.06	0.00	0.04	0.20	95.86
SD25	ID = 10501 SD25a_gl6	66.72	0.57	16.49	2.46	0.25	0.95	2.58	4.68	4.90	0.15	0.01	0.03	0.02	0.18	97.69
SD25	ID = 10502 SD25a_gl7	66.72	0.67	16.23	2.64	0.11	0.85	2.28	4.81	5.16	0.23	0.00	0.00	0.07	0.24	97.47
SD25	ID = 10505 SD25a_gl8	66.55	0.57	16.51	2.67	0.05	0.90	2.49	4.59	5.09	0.26	0.10	0.07	0.00	0.14	96.71
SD25	ID = 10506 SD25a_gl9	66.84	0.60	16.88	2.69	0.00	0.85	2.65	4.07	5.07	0.33	0.00	0.00	0.02	0.00	96.32
SD25	ID = 10515 SD25a_gl10	67.02	0.44	16.35	2.68	0.20	0.91	2.27	4.71	5.10	0.24	0.00	0.00	0.08	0.00	97.41
SD25	ID = 10516 SD25a_gl11	67.16	0.52	16.47	2.60	0.00	0.72	2.24	4.60	5.11	0.24	0.00	0.09	0.17	0.09	96.92
SD25	ID = 10517 SD25a_gl12	66.19	0.54	16.93	2.44	0.04	0.97	2.48	5.12	4.87	0.20	0.15	0.00	0.01	0.05	97.73
SD25	ID = 10518 SD25a_gl13	66.26	0.60	16.68	2.67	0.07	0.82	2.51	4.75	5.04	0.27	0.08	0.11	0.00	0.14	96.72

Sample	Description of Analysis	SiO_2	TiO_2	Al_2O_3	FeO	MnO	MgO	CaO	Na_2O	K_2O	Cl	NiO	Cr_2O_3	SO_3	P_2O_5	Original Total
SD25	ID = 10523 SD25a_gl14	67.03	0.57	16.52	2.71	0.03	0.76	2.18	4.78	4.96	0.24	0.00	0.00	0.14	0.07	98.47
SD25	ID = 10525 SD25a_gl15	66.55	0.59	16.91	2.22	0.15	0.99	2.57	4.89	4.90	0.21	0.00	0.00	0.00	0.02	96.06
SD32b	ID = 2393 SD32b glass2	67.27	0.49	16.69	2.93	0.04	0.95	2.79	3.72	4.91	0.21					96.74
SD32b	ID = 2409 SD32b glass4	66.80	0.44	16.64	3.06	0.04	0.72	2.64	4.30	5.01	0.36					98.40
SD32a	ID = SD32a_glass1_w	65.69	0.68	16.86	2.86	0.14	0.91	3.17	4.87	4.60	0.23					96.26
SD32a	ID = 10462 SD32a_glass1_b	66.31	0.60	16.81	2.99	0.15	1.06	2.65	4.04	5.07	0.31					97.00
SD32a	ID = 10463 SD32a_glass2_b	66.08	0.61	16.56	2.72	0.25	0.99	2.79	4.88	4.91	0.21					95.81
SD32a	ID = 10464 SD32a_glass3_b	65.74	0.55	16.52	3.32	0.17	1.04	2.83	4.57	4.97	0.28					96.71
SD32a	ID = 10469 SD32a_glass1_lb	66.70	0.51	16.84	2.75	0.01	1.05	2.61	4.35	4.95	0.23					95.67
SD32a	ID = 10470 SD32a_glass2_lb	65.89	0.57	16.66	2.79	0.30	0.96	2.92	4.89	4.79	0.23					96.29
SD32a	ID = 10471 SD32a_glass3_lb	67.64	0.59	16.80	2.79	0.05	0.85	2.95	3.61	4.50	0.23					95.64
SD32a	ID = 10472 SD32a_glass4_lb	67.13	0.56	16.57	2.50	0.17	0.72	2.50	4.45	5.14	0.27					96.39
SD32a	ID = 10474 SD32a_glass5_lb	65.58	0.54	17.06	3.48	0.25	1.14	3.46	3.44	4.81	0.25					94.90
SD31a	ID = 10773_SD31a_glass3	65.47	0.52	16.82	3.34	0.14	1.09	3.12	4.60	4.66	0.24					97.25
SD31a	ID = 10774_SD31a_glass4	64.83	0.58	16.90	3.52	0.32	1.13	3.27	4.68	4.50	0.27					96.92
SD31a	ID = 10776_SD31a_glass6	65.17	0.68	16.46	3.62	0.23	1.17	2.96	4.72	4.73	0.27					97.51
SD31a	ID = 10777_SD31a_glass7	65.11	0.60	17.10	3.33	0.14	1.02	3.27	4.50	4.72	0.21					97.29
SD31a	ID = 10779_SD31a_glass9	65.65	0.58	16.76	3.30	0.21	0.98	2.89	4.58	4.76	0.29					97.94
T04-66	ID = 203 T04-66 glass1	66.69	0.65	16.54	2.48	0.12	0.88	2.28	4.88	5.24	0.10	0.13	0.00	0.00	0.01	99.29
T04-66	ID = 204 T04-66 glass2	67.54	0.70	15.94	2.40	0.02	0.67	1.89	4.80	5.70	0.12	0.00	0.00	0.00	0.22	97.80
T04-66	ID = 205 T04-66 glass3	67.25	0.44	16.54	2.22	0.12	0.64	2.36	4.93	5.19	0.18	0.04	0.04	0.00	0.05	98.47
T04-66	ID = 206 T04-66 glass4	67.75	0.44	15.82	2.54	0.05	0.68	1.81	4.64	5.66	0.15	0.17	0.00	0.09	0.19	98.89
T04-66	ID = 207 T04-66 glass5	66.17	0.60	16.55	2.66	0.19	1.18	2.97	4.66	4.79	0.15	0.00	0.00	0.01	0.06	97.67
T04-66	ID = 208 T04-66 glass6	67.22	0.58	16.00	2.51	0.17	0.62	2.07	4.91	5.52	0.17	0.00	0.06	0.00	0.17	98.20
T04-66	ID = 209 T04-66 glass7	69.26	0.64	15.53	2.37	0.00	0.30	1.51	4.05	5.91	0.15	0.16	0.00	0.10	0.01	97.23
T04-66	ID = 210 T04-66 glass7again	67.17	0.59	16.25	2.46	0.00	0.92	2.51	4.91	5.02	0.11	0.06	0.00	0.00	0.00	97.18
T04-66	ID = 211 T04-66 glass8	67.34	0.61	15.62	2.56	0.22	0.89	1.92	4.77	5.69	0.22	0.00	0.00	0.00	0.14	98.05
T04-66	ID = 212 T04-66 glass9	67.85	0.63	15.92	2.42	0.09	0.60	1.87	4.92	5.46	0.16	0.00	0.00	0.00	0.08	98.65
T04-66	ID = 213 T04-66 glass10	68.65	0.63	15.17	2.66	0.16	0.70	1.70	4.06	5.94	0.15	0.00	0.00	0.00	0.19	97.13
T04-66	ID = 214 T04-66 glass10again	67.60	0.58	16.07	2.61	0.10	0.85	1.89	4.66	5.44	0.11	0.00	0.00	0.01	0.06	98.31
T04-66	ID = 215 T04-66 glass11	66.96	0.64	16.07	2.66	0.11	0.82	2.16	4.76	5.40	0.13	0.14	0.07	0.00	0.07	98.33
T04-66	ID = 216 T04-66 glass12	67.79	0.54	15.41	2.86	0.11	1.13	1.91	4.53	5.59	0.13	0.00	0.00	0.00	0.00	97.67
SD33	ID = 217 SD33 glass1	67.20	0.55	16.31	2.40	0.15	0.62	2.27	4.89	5.34	0.14	0.00	0.00	0.00	0.11	97.68

Sample	Description of Analysis	SiO_2	TiO_2	Al_2O_3	FeO	MnO	MgO	CaO	Na_2O	K_2O	Cl	NiO	Cr_2O_3	SO_3	P_2O_5	Original Total
SD33	ID = 218 SD33 glass2	66.64	0.55	16.57	2.65	0.10	0.90	2.27	4.83	5.22	0.16	0.04	0.07	0.00	0.00	98.20
SD33	ID = 219 SD33 glass3	66.74	0.58	16.64	2.31	0.23	0.58	2.55	4.95	5.13	0.20	0.00	0.00	0.00	0.08	98.27
SD33	ID = 220 SD33 glass4	66.92	0.64	16.38	2.67	0.06	0.79	2.43	4.52	5.38	0.19	0.00	0.00	0.00	0.01	98.45
SD33	ID = 221 SD33 glass5	65.84	0.55	16.99	2.45	0.19	0.69	2.88	5.22	5.00	0.19	0.00	0.00	0.00	0.00	99.13
SD33	ID = 222 SD33 glass6	66.39	0.46	15.69	3.26	0.14	1.09	2.37	5.10	5.14	0.18	0.00	0.00	0.07	0.10	99.16
SD33	ID = 223 SD33 glass7	67.21	0.46	16.01	2.60	0.04	0.75	1.90	4.86	5.65	0.31	0.08	0.06	0.00	0.07	98.44
SD33	ID = 224 SD33 glass8	67.17	0.63	15.84	2.71	0.07	0.88	1.89	4.52	5.68	0.26	0.14	0.03	0.04	0.13	97.47
SD33	ID = 225 SD33 glass9	66.65	0.58	16.75	2.37	0.12	0.76	2.34	4.95	5.11	0.18	0.17	0.01	0.00	0.00	98.63
SD33	ID = 226 SD33 glass10	66.10	0.71	16.25	2.93	0.05	0.84	2.56	4.80	5.32	0.24	0.08	0.04	0.00	0.07	98.42
SD27	ID = 227 SD27 glass1	65.46	0.61	17.21	2.86	0.16	0.74	3.23	4.73	4.64	0.22	0.00	0.08	0.00	0.07	95.78
SD27	ID = 228 SD27 glass2	65.04	0.59	16.86	3.36	0.14	1.14	3.24	4.63	4.78	0.17	0.00	0.03	0.00	0.00	98.08
SD27	ID = 229 SD27 glass3	65.24	0.61	16.60	3.33	0.06	1.06	3.08	4.30	5.15	0.15	0.07	0.15	0.06	0.13	98.57
SD27	ID = 230 SD27 glass4	64.91	0.62	17.04	3.16	0.07	0.89	3.45	4.66	4.61	0.28	0.13	0.02	0.08	0.08	98.03
SD27	ID = 231 SD27 glass5	65.33	0.66	16.93	3.10	0.26	0.83	2.94	4.71	5.07	0.16	0.00	0.00	0.00	0.02	97.69
SD27	ID = 232 SD27 glass6	65.80	0.66	16.91	2.81	0.14	0.63	3.25	4.51	4.93	0.17	0.09	0.00	0.01	0.08	97.35
SD27	ID = 233 SD27 glass7	65.05	0.50	16.86	3.47	0.10	1.06	3.34	4.54	4.84	0.23	0.00	0.00	0.00	0.00	97.49
SD27	ID = 234 SD27 glass8	65.15	0.64	16.78	3.36	0.14	0.95	3.27	4.70	4.74	0.24	0.00	0.00	0.00	0.02	97.71
SD27	ID = 235 SD27 glass9	65.38	0.70	16.69	3.05	0.07	0.83	3.09	4.79	4.85	0.17	0.12	0.00	0.02	0.23	98.37
SD27	ID = 236 SD27 glass10	65.46	0.69	16.95	2.96	0.10	0.82	3.23	4.85	4.72	0.21	0.00	0.00	0.02	0.00	97.77
T04-146	ID = 3441 T04-146 glass1	66.72	0.25	18.13	1.35	0.10	0.35	2.95	5.10	4.82	0.04	0.00	0.02	0.08	0.07	98.24
T04-146	ID = 3445 T04-146 glass5a	67.71	0.48	16.65	2.14	0.06	0.39	2.20	4.81	5.14	0.25	0.05	0.00	0.00	0.12	97.31
T04-146	ID = 3446 T04-146 glass5b	66.30	0.52	17.42	2.43	0.13	0.48	2.85	5.05	4.55	0.26	0.00	0.00	0.00	0.00	99.29
T04-115	ID = 8241 T04-115 glass1a	66.45	0.59	16.57	2.60	0.16	0.81	2.54	4.94	4.97	0.25	0.00	0.00	0.00	0.11	97.13
T04-115	ID = 8242 T04-115 glass2a	64.93	0.66	16.56	3.31	0.25	1.28	3.04	4.94	4.64	0.25	0.01	0.00	0.01	0.11	99.07
T04-115	ID = 8243 T04-115 glass3a	66.03	0.51	16.75	2.57	0.13	0.63	2.74	4.95	5.05	0.34	0.00	0.07	0.22	0.01	97.21
T04-115	ID = 8244 T04-115 glass4a	66.77	0.50	16.43	2.68	0.13	0.84	2.36	4.86	5.05	0.26	0.00	0.03	0.06	0.01	95.41
T04-115	ID = 8245 T04-115 glass4b	66.17	0.68	16.49	2.81	0.11	0.85	2.42	4.79	5.07	0.34	0.00	0.01	0.10	0.15	96.03
T04-122	ID = 8332 T04-122 glass1b	64.60	0.75	16.97	3.07	0.17	1.05	3.48	4.72	4.49	0.20	0.07	0.06	0.09	0.27	98.67
T04-122	ID = 8334 T04-122 glass2a	65.20	0.41	16.88	3.00	0.17	1.02	3.06	4.92	4.84	0.26	0.01	0.02	0.02	0.19	93.14
T04-122	ID = 8335 T04-122 glass3a	65.09	0.62	16.83	3.20	0.18	1.02	2.90	4.72	4.77	0.32	0.00	0.01	0.17	0.18	95.20
T04-122	ID = 8337 T04-122 glass4b	67.60	0.28	17.30	1.17	0.04	0.46	2.97	4.93	4.95	0.01	0.00	0.03	0.11	0.16	97.83
T04-122	ID = 8341 T04-122 glass6a	68.89	0.32	15.76	2.02	0.00	0.51	1.83	4.67	5.47	0.19	0.09	0.09	0.09	0.07	98.23
T04-122	ID = 8342 T04-122 glass6b	68.59	0.42	15.98	2.17	0.10	0.47	1.97	4.54	5.39	0.32	0.05	0.01	0.00	0.00	98.15

Sample	Description of Analysis	SiO_2	TiO_2	Al_2O_3	FeO	MnO	MgO	CaO	Na_2O	K_2O	Cl	NiO	Cr_2O_3	SO_3	P_2O_5	Original Total
T04-122	ID = 8343 T04-122 glass7a	66.72	0.48	16.74	2.63	0.12	0.86	2.57	4.70	4.87	0.20	0.01	0.01	0.00	0.07	97.60
T04-82	ID = 8344 T04-82 glass1a	66.42	0.53	16.98	2.31	0.07	0.77	2.67	4.96	4.89	0.15	0.09	0.00	0.15	0.01	98.24
T04-82	ID = 8345 T04-82 glass1b	67.23	0.46	16.40	2.29	0.00	0.65	2.38	4.76	5.22	0.29	0.00	0.05	0.09	0.18	97.93
T04-82	ID = 8346 T04-82 glass1c	67.35	0.42	16.39	2.11	0.05	0.62	2.33	4.91	5.49	0.22	0.00	0.00	0.00	0.11	97.43
T04-82	ID = 8347 T04-82 glass2a	67.14	0.51	16.93	1.86	0.13	0.49	3.01	5.00	4.51	0.14	0.02	0.00	0.12	0.13	98.24
T04-173	ID = 3358 T04-173 glass1a	71.36	0.48	15.01	0.95	0.09	0.17	0.88	4.32	6.39	0.05	0.00	0.13	0.00	0.16	96.66
T04-173	ID = 3359 T04-173 glass1b	71.81	0.42	14.95	1.03	0.20	0.07	1.30	4.27	5.86	0.00	0.01	0.08	0.00	0.00	96.15
T04-173	ID = 3360 T04-173 glass2a	71.15	0.59	14.76	1.92	0.00	0.01	1.26	4.42	5.41	0.13	0.00	0.06	0.12	0.15	97.24
T04-173	ID = 3361 T04-173 glass2b	72.37	0.79	13.65	1.96	0.00	0.16	0.76	4.07	5.92	0.17	0.04	0.00	0.00	0.11	97.96
T04-173	ID = 3362 T04-173 glass3a	72.14	0.55	14.06	1.32	0.00	0.29	0.72	3.78	6.51	0.00	0.08	0.09	0.22	0.24	96.91
T04-173	ID = 3363 T04-173 glass3b	71.48	0.31	15.11	1.22	0.05	0.11	1.39	4.28	5.90	0.04	0.00	0.08	0.00	0.02	97.28
T04-173	ID = 3364 T04-173 glass4a	69.89	0.42	16.09	1.18	0.09	0.22	1.66	4.48	5.91	0.05	0.00	0.00	0.00	0.00	96.99
T04-173	ID = 3365 T04-173 glass4b	69.18	0.28	16.80	0.88	0.01	0.07	2.63	4.69	5.11	0.06	0.00	0.08	0.09	0.10	97.22
T04-173	ID = 3366 T04-173 glass5a	69.09	0.70	14.77	2.46	0.03	0.66	1.29	4.31	6.15	0.26	0.07	0.01	0.00	0.20	99.10
T04-173	ID = 3367 T04-173 glass5b	67.11	0.62	16.66	1.92	0.04	0.41	2.00	5.13	5.42	0.27	0.00	0.22	0.00	0.19	98.55
T04-98	ID = 3463 T04-98 glass2	67.07	0.58	16.95	3.23	0.14	1.15	2.68	2.70	4.56	0.66	0.00	0.04	0.08	0.16	92.96
T04-98	ID = 3466 T04-98 glass4	63.98	0.63	16.96	4.75	0.11	1.52	3.91	3.21	4.14	0.23	0.00	0.16	0.02	0.37	97.11
T04-98	ID = 3467 T04-98 glass5	66.24	0.68	16.76	3.60	0.21	1.09	2.89	3.17	4.83	0.29	0.00	0.11	0.00	0.12	97.92
T04-98	ID = 3462 T04-98 glass1a	64.72	0.40	15.49	3.24	0.17	1.98	4.54	4.56	4.53	0.23	0.01	0.05	0.01	0.06	97.77
T04-98	ID = 3464 T04-98 glass3a	64.80	0.67	17.51	2.07	0.00	0.75	2.69	5.56	5.19	0.16	0.09	0.14	0.02	0.35	98.99
T04-98	ID = 3465 T04-98 glass3b	65.59	0.78	16.73	2.51	0.04	0.85	1.94	5.31	5.86	0.19	0.00	0.00	0.00	0.20	99.38
T04-98	ID = 3468 T04-98 glass5b	65.18	0.71	16.67	3.22	0.16	1.00	3.09	4.81	4.84	0.24	0.00	0.02	0.00	0.07	99.24
T04-98	ID = 3469 T04-98 glass5c	64.98	0.51	17.07	3.20	0.06	0.99	3.11	4.69	4.69	0.33	0.02	0.06	0.03	0.25	95.94
E03-78	ID = 2608 E03-78 glass1a	65.69	0.63	16.31	3.84	0.09	1.15	2.56	4.70	4.55	0.27	0.00	0.00	0.00	0.21	98.62
E03-78	ID = 2608 E03-78 glass1a	65.38	0.72	16.45	3.71	0.27	1.04	2.49	4.47	4.63	0.29	0.00	0.00	0.04	0.49	98.62
E03-78	ID = 2610 E03-78 glass2a	64.28	0.52	17.86	2.73	0.23	0.68	3.49	5.28	4.20	0.21	0.00	0.06	0.00	0.46	99.52
T04-56	ID = 3350 T04-56 glass1b	61.07	0.82	17.66	5.16	0.10	1.62	4.51	5.17	3.31	0.12	0.00	0.00	0.12	0.32	98.65
T04-56	ID = 3355 T04-56 glass3b	61.76	0.74	16.93	5.12	0.13	1.85	5.17	4.77	2.82	0.27	0.00	0.21	0.00	0.21	98.45
T04-56	ID = 3357 T04-56 glass4b	60.89	0.85	17.32	4.67	0.17	2.04	5.12	2.53	5.58	0.27	0.01	0.16	0.08	0.30	97.98
T04-56	ID = 3500 T04-56 glass1	61.78	0.74	17.55	4.39	0.10	1.70	4.67	4.69	3.48	0.12	0.05	0.17	0.00	0.55	99.70
T04-56	ID = 3505 T04-56 glass2	61.29	0.67	17.94	4.42	0.15	1.58	5.11	4.68	3.67	0.18	0.00	0.00	0.05	0.26	99.47
T04-56	ID = 3510 T04-56 glass3	62.08	0.83	16.78	4.96	0.20	1.84	4.03	4.67	4.06	0.19	0.00	0.02	0.00	0.33	99.01
T04-56	ID = 3511 T04-56 glass4	61.97	0.98	16.70	4.89	0.17	1.81	3.97	4.77	4.03	0.16	0.00	0.08	0.04	0.44	98.61

Sample	Description of Analysis	SiO_2	TiO_2	Al_2O_3	FeO	MnO	MgO	CaO	Na_2O	K_2O	Cl	NiO	Cr_2O_3	SO_3	P_2O_5	Original Total
T04-56	ID = 3532 T04-56 glass6	62.01	0.81	17.10	4.63	0.00	1.81	4.42	4.53	4.04	0.20	0.11	0.03	0.01	0.30	99.21
T04-56	ID = 3533 T04-56 glass7	61.65	0.87	17.09	4.62	0.32	1.79	4.46	4.66	3.90	0.14	0.00	0.07	0.10	0.34	98.26
T04-56	ID = 3534 T04-56 glass8	62.32	0.72	16.94	4.84	0.03	1.68	4.03	4.62	4.13	0.21	0.00	0.13	0.12	0.23	98.61
T04-56	ID = 3535 T04-56 glass9	62.05	0.77	17.34	4.55	0.07	1.73	4.53	4.65	3.77	0.21	0.00	0.00	0.13	0.19	98.86
T04-56	ID = 3536 T04-56 glass10	61.68	0.82	17.58	4.74	0.03	1.73	4.69	4.59	3.67	0.23	0.00	0.03	0.02	0.18	98.83
T04-56	ID = 3349 T04-56 glass1a	61.58	0.75	17.48	4.62	0.26	1.80	4.84	4.84	3.29	0.09	0.13	0.00	0.00	0.31	98.74
T04-56	ID = 3351 T04-56 glass1c	61.49	0.78	17.40	4.42	0.16	1.72	4.86	5.03	3.39	0.15	0.00	0.11	0.07	0.42	99.06
T04-56	ID = 3352 T04-56 glass2a	60.94	0.77	17.67	4.38	0.23	1.59	5.58	5.31	2.57	0.13	0.11	0.11	0.21	0.40	99.00
T04-56	ID = 3353 T04-56 glass2b	61.50	0.82	17.11	4.66	0.23	2.12	4.93	5.63	2.35	0.20	0.00	0.10	0.06	0.28	98.47
T04-56	ID = 3356 T04-56 glass4a	60.45	0.87	17.47	4.65	0.05	1.73	4.96	3.26	5.46	0.22	0.00	0.27	0.26	0.36	97.30
T04-53	ID = 8063 T04-53 glass1a	65.60	0.72	17.74	1.83	0.19	0.21	2.29	5.58	5.25	0.14	0.00	0.00	0.00	0.44	99.44
T04-53	ID = 8064 T04-53 glass1b	65.83	0.80	16.34	2.55	0.11	0.45	2.09	4.97	6.14	0.21	0.00	0.00	0.00	0.51	99.28
T04-53	ID = 3296 T04_53 glass1a	64.15	0.75	18.51	1.83	0.01	0.39	3.14	5.91	4.95	0.18	0.00	0.13	0.00	0.05	98.45
T04-53	ID = 3297 T04_53 glass1b	66.04	0.69	17.31	1.61	0.10	0.43	2.38	5.22	5.68	0.10	0.00	0.05	0.06	0.32	97.15
T04-53	ID = 8065 T04-53 glass2a	65.04	0.79	16.62	2.72	0.16	0.94	2.54	5.06	5.55	0.26	0.00	0.04	0.00	0.27	99.14
T04-53	ID = 8066 T04-53 glass2b	66.15	0.78	17.35	1.76	0.10	0.22	2.11	5.56	5.73	0.16	0.00	0.02	0.06	0.00	97.26
T04-53	ID = 8067 T04-53 glass3a	65.00	0.48	18.54	1.96	0.03	0.20	3.11	5.42	4.92	0.15	0.00	0.11	0.01	0.07	97.65
T04-53	ID = 8069 T04-53 glass4a	64.51	0.78	17.98	2.08	0.05	0.78	2.58	5.70	5.01	0.15	0.05	0.15	0.01	0.16	98.73
T04-53	ID = 8071 T04-53 glass5a	64.81	0.72	17.91	1.93	0.06	0.35	2.87	5.64	5.19	0.05	0.00	0.03	0.02	0.43	98.06
T04-53	ID = 8072 T04-53 glass5b	65.10	0.62	17.73	2.13	0.03	0.50	2.68	5.47	5.35	0.11	0.00	0.04	0.01	0.24	98.76

[all data in wt.%]

Sample	Description of Analysis	SiO_2	TiO_2	Al_2O_3	FeO	MnO	MgO	CaO	Na_2O	K_2O	Cl	NiO	V_2O_3	Cr_2O_3	SO_3	P_2O_5	Total
SD11	ID = 2057 SD11 ol1-r	38.37	0.01	0.17	27.64	0.86	34.09	0.17	0.00	0.00	0.00	0.00		0.00	0.05	0.08	101.44
SD11	ID = 3095 SD11 mol1	36.96	0.03	0.00	29.56	1.03	31.63	0.50	0.00	0.06	0.04	0.00	0.01	0.00	0.00	0.48	100.31
SD11	ID = 3096 SD11 mol2	36.59	0.04	0.01	30.58	0.87	30.82	0.20	0.20	0.04	0.00	0.05	0.04	0.07	0.00	0.49	100.00
SD11	ID = 3098 SD11 ol2-c	38.78	0.00	0.00	23.27	0.83	37.53	0.10	0.00	0.07	0.06	0.00	0.00	0.00	0.00	0.00	100.64
SD11	ID = 3099 SD11 ol2-r	38.15	0.07	0.00	25.16	1.02	35.02	0.13	0.00	0.00	0.04	0.00	0.11	0.00	0.01	0.16	99.87
MI-5	ID = 070 opx-gm1 centre	38.11	0.01	0.20	28.18	1.09	33.42	0.19	0.00	0.01	0.02	0.00		0.01	0.01	0.00	101.25
MI-5	ID = 070 opx-gm2 centre	38.15	0.00	0.00	27.92	1.08	33.85	0.14	0.15	0.00	0.00	0.00		0.03	0.00	0.00	101.32
E03-77	ID = 076 opx-gm4 core	38.21	0.08	0.00	27.85	1.34	33.54	0.05	0.26	0.06	0.00	0.00		0.00	0.00	0.00	101.39
E03-77	ID = 080 opx-gm5 core	37.76	0.00	0.00	28.49	0.90	32.53	0.18	0.00	0.00	0.00	0.00		0.00	0.00	0.11	99.97
E03-77	ID = 099 opx-gm16 centre	37.51	0.08	0.00	27.82	1.04	32.50	0.15	0.01	0.10	0.00	0.00		0.00	0.05	0.00	99.26
T04-62	ID = 101 T04-62 opx-gm1 centre	37.73	0.15	0.00	27.33	1.24	33.08	0.24	0.00	0.03	0.00	0.00		0.01	0.05	0.09	99.95
T04-62	ID = 101 T04-62 opx-gm1 centre	37.73	0.15	0.00	27.33	1.24	33.08	0.24	0.00	0.03	0.00	0.00		0.01	0.05	0.09	99.95
T04-62	ID = 102 T04-62 opx-gm2 centre	36.99	0.00	0.12	27.89	1.17	32.55	0.24	0.17	0.09	0.01	0.00		0.00	0.00	0.20	99.43
T04-62	ID = 103 T04-62 opx-gm3 centre	36.93	0.00	0.00	32.13	1.29	29.03	0.25	0.17	0.11	0.06	0.07		0.03	0.14	0.16	100.37
T04-62	ID = 104 T04-62 opx-gm4 centre	37.55	0.03	0.00	28.25	1.29	32.42	0.61	0.00	0.03	0.07	0.02		0.00	0.00	0.18	100.45
T04-62	ID = 105 T04-62 opx-gm5 core	37.85	0.05	0.08	27.58	0.99	33.63	0.32	0.01	0.08	0.00	0.00		0.00	0.00	0.00	100.59
T04-62	ID = 106 T04-62 opx-gm5 rim	37.99	0.10	0.17	27.88	1.13	32.22	0.29	0.00	0.16	0.01	0.00		0.09	0.00	0.00	100.04
T04-62	ID = 107 T04-62 opx-gm6 centre	37.33	0.11	0.00	28.97	1.29	31.89	0.49	0.15	0.02	0.02	0.00		0.00	0.00	0.15	100.42
T04-62	ID = 108 T04-62 opx-gm7 centre	37.21	0.00	0.11	28.39	1.19	32.10	0.34	0.00	0.07	0.00	0.00		0.00	0.01	0.13	99.55
T04-62	ID = 109 T04-62 opx-gm8 centre	37.01	0.00	0.00	29.22	1.12	31.18	0.23	0.32	0.08	0.03	0.00		0.00	0.08	0.19	99.46
T04-62	ID = 110 T04-62 opx-gm9 centre	34.24	1.36	0.07	31.51	1.14	30.32	1.31	0.15	0.01	0.03	0.06		0.03	0.00	0.65	100.88
T04-62	ID = 111 T04-62 opx-gm10 centre	36.87	0.04	0.00	29.59	1.42	30.70	0.44	0.14	0.12	0.04	0.00		0.00	0.13	0.14	99.63

[all data in wt.%]

Sample	Description of Analysis	SiO_2	TiO_2	Al_2O_3	FeO	MnO	MgO	CaO	Na_2O	K_2O	Cl	NiO	V_2O_3	Cr_2O_3	SO_3	P_2O_5	Total
SD13	ID = 3197 SD13 hbl1-opx?	54.33	0.74	2.85	9.23	0.42	30.23	2.09	0.17	0.10	0.03	0.08	0.00	0.15	0.00	0.00	100.42
T04-56	ID = 3528 T04-56 cpx6-r	54.58	0.15	1.08	15.41	0.87	26.84	1.35	0.00	0.05	0.00	0.00	0.03	0.16	0.00	0.00	100.52
SD11	ID = 2056 SD11 ol1-c	53.55	0.23	0.15	20.52	1.25	22.55	1.66	0.00	0.00	0.08	0.05		0.00	0.00	0.00	100.04
E03-77	ID = 074 opx-gm3 centre	53.62	0.37	1.72	15.97	0.92	25.40	1.50	0.00	0.01	0.00	0.00		0.00	0.08	0.00	99.59
E03-77	ID = 077 opx-gm4 rim	53.27	0.33	2.17	15.80	0.81	25.56	1.34	0.41	0.00	0.05	0.00		0.00	0.07	0.00	99.81
E03-77	ID = 081 opx-gm5 rim	53.56	0.32	0.55	18.54	1.17	22.79	2.68	0.19	0.12	0.05	0.01		0.00	0.01	0.00	99.99
E03-77	ID = 083 opx-gm6 centre	50.98	1.03	0.67	18.26	1.10	22.03	5.17	0.21	0.00	0.01	0.23		0.03	0.00	0.01	99.73
E03-77	ID = 084 opx-gm7 centre	50.34	0.39	0.89	18.01	1.06	23.68	2.50	0.26	0.12	0.04	0.04		0.06	0.09	0.11	97.59
E03-77	ID = 085 opx-gm7.2 centre	53.73	0.33	0.70	17.81	1.12	23.45	2.67	0.18	0.07	0.05	0.07		0.00	0.04	0.00	100.22
E03-77	ID = 086 opx-gm8 centre	53.15	0.37	0.68	18.06	1.20	22.35	3.38	0.00	0.08	0.00	0.00		0.09	0.04	0.07	99.47
E03-77	ID = 088 opx-gm9 centre	53.60	0.39	0.65	17.53	1.14	21.75	4.83	0.36	0.09	0.03	0.00		0.03	0.02	0.00	100.42
E03-77	ID = 089 opx-gm10 centre	49.98	0.29	1.42	18.03	1.23	20.33	5.44	0.11	0.28	0.07	0.06		0.00	0.08	1.54	98.86
E03-77	ID = 091 opx-gm11 centre	52.55	0.50	0.89	15.31	1.01	20.91	7.35	0.00	0.14	0.04	0.00		0.01	0.00	0.40	99.11
E03-77	ID = 092 opx-gm12 centre	54.15	0.25	0.71	18.38	1.26	22.06	3.66	0.36	0.16	0.02	0.00		0.00	0.00	0.05	101.06
E03-77	ID = 094 opx-gm13 centre	53.75	0.28	0.44	17.76	1.07	23.20	2.39	0.00	0.14	0.00	0.00		0.00	0.00	0.00	99.03
E03-77	ID = 095 opx-gm14 centre	53.79	0.45	0.80	16.07	1.10	24.99	1.97	0.00	0.02	0.03	0.00		0.00	0.00	0.00	99.22
E03-77	ID = 096 opx-gm15 centre	53.51	0.38	0.45	18.47	1.32	22.69	2.71	0.00	0.05	0.03	0.00		0.06	0.00	0.10	99.77
E03-77	ID = 100 opx-gm17 centre	53.52	0.36	0.41	17.39	1.26	23.11	3.01	0.57	0.06	0.01	0.00		0.01	0.00	0.00	99.71

[all data in wt.%]

Sample	Description of Analysis	SiO_2	TiO_2	Al_2O_3	FeO	MnO	MgO	CaO	Na_2O	K_2O	Cl	NiO	V_2O_3	Cr_2O_3	SO_3	P_2O_5	Total
SD1	ID = 3126 SD1 cpx4-plg1	56.09	0.04	26.89	0.48	0.00	0.17	10.00	5.64	0.60	0.00	0.00	0.03	0.05	0.05	0.00	100.05
SD1	ID = 3128 SD1 cpx4-plg2	51.88	0.05	29.36	0.70	0.07	0.10	13.06	4.12	0.30	0.00	0.07	0.04	0.09	0.00	0.00	99.83
SD1	ID = 3131 SD1 cpx4-plg3	54.00	0.02	28.33	0.56	0.10	0.14	11.31	4.92	0.61	0.02	0.00	0.03	0.24	0.04	0.07	100.41
SD1	ID = 3141 SD1 cpx5-plg1	56.46	0.17	25.05	0.81	0.00	0.39	9.01	5.76	0.81	0.02	0.00	0.05	0.19	0.00	0.00	98.71
SD1	ID = 3160 SD1 cpx7-plg	56.64	0.01	26.62	0.68	0.00	0.10	9.49	5.92	0.48	0.00	0.05	0.00	0.18	0.00	0.00	100.17
SD4	ID = 3396 SD4 cpx2-plg	55.89	0.06	25.17	0.83	0.01	0.59	9.76	5.72	0.73	0.03	0.00	0.00	0.08	0.02	0.09	98.98
SD4	ID = 3405 SD4 cpx3-plg	53.41	0.00	27.69	0.62	0.15	0.00	11.04	4.82	0.55	0.05	0.00	0.00	0.05	0.00	0.00	98.38
SD5	ID = 2201 SD5 cpx1-plg1	55.31	0.07	26.76	0.60	0.00	0.01	9.98	5.38	0.50	0.02	0.00		0.00	0.07	0.00	98.70
SD5	ID = 2202 SD5 cpx1-plg2	53.65	0.00	27.99	0.67	0.00	0.01	11.70	4.89	0.38	0.00	0.00		0.00	0.01	0.00	99.30
SD5	ID = 2230 SD5 cpx2-plg1	53.59	0.06	28.09	0.36	0.02	0.00	11.58	4.55	0.41	0.09	0.14		0.00	0.00	0.00	98.89
SD5	ID = 2231 SD5 cpx2-plg2	57.44	0.12	25.73	0.48	0.00	0.01	8.66	6.11	0.63	0.00	0.00		0.00	0.00	0.00	99.18
SD5	ID = 2238 SD5 cpx3-plg1	56.15	0.01	26.55	0.50	0.05	0.09	9.29	5.59	0.82	0.06	0.07		0.00	0.05	0.00	99.23
SD5	ID = 2241 SD5 cpx3-plg2	56.30	0.04	26.42	0.52	0.00	0.09	9.77	5.47	0.91	0.00	0.00		0.04	0.00	0.00	99.56
SD13	ID = 3179 SD13 cpx1-plg1-c	49.96	0.12	30.80	0.70	0.11	0.01	14.51	2.91	0.30	0.00	0.00	0.04	0.12	0.06	0.00	99.65
SD13	ID = 3180 SD13 cpx1-plg1-r	49.17	0.01	31.44	0.67	0.02	0.12	15.07	2.70	0.26	0.01	0.09	0.08	0.10	0.14	0.00	99.89
SD13	ID = 3181 SD13 cpx1-plg2-c	52.83	0.00	28.75	0.54	0.00	0.10	12.04	4.37	0.39	0.05	0.00	0.02	0.09	0.00	0.00	99.19
SD13	ID = 3182 SD13 cpx1-plg2-r	53.21	0.04	28.45	0.61	0.01	0.00	11.36	4.71	0.39	0.03	0.00	0.00	0.15	0.00	0.00	98.97
SD13	ID = 3236 SD13 cpx4-plg	56.69	0.12	26.12	0.64	0.04	0.25	9.08	6.15	0.63	0.00	0.00	0.05	0.01	0.08	0.00	99.88
SD13	ID = 3250 SD13 cpx9-plg	52.81	0.02	28.34	0.63	0.15	0.00	11.63	4.36	0.41	0.11	0.00	0.00	0.00	0.00	0.00	98.47
SD13	ID = 3260 SD13 cpx11-plg-c	57.98	0.03	25.11	0.48	0.04	0.00	7.80	6.48	0.92	0.00	0.00	0.00	0.00	0.00	0.00	98.85
SD13	ID = 3332 SD13 cpx3-plg1	53.52	0.14	28.17	0.76	0.12	0.00	11.23	4.35	1.17	0.09	0.17	0.00	0.04	0.01	0.00	99.77
SD13	ID = 3333 SD13 cpx3-plg2	52.96	0.05	28.09	0.54	0.10	0.03	11.54	4.27	0.82	0.00	0.00	0.00	0.01	0.05	0.06	98.52
SD13	ID = 3342 SD13 cpx4-plg-c	53.39	0.01	28.13	0.38	0.00	0.00	11.33	4.75	0.45	0.04	0.00	0.07	0.10	0.00	0.01	98.66
SD13	ID = 3343 SD13 cpx4-plg-r	55.70	0.00	25.73	0.43	0.06	0.01	8.87	5.76	0.65	0.04	0.00	0.05	0.15	0.06	0.16	97.67
SD4	ID = 3421 SD4 hbl5-plg1	52.85	0.00	28.08	0.62	0.00	0.00	11.59	4.19	0.98	0.00	0.08	0.00	0.06	0.00	0.00	98.45
SD5	ID = 2211 SD5 hbl2-plg	54.46	0.25	27.44	0.59	0.00	0.15	10.51	4.53	1.32	0.06	0.02		0.03	0.00	0.06	99.42
SD5	ID = 2221 SD5 hbl4-plg1	51.46	0.04	29.76	0.46	0.03	0.15	13.17	3.93	0.34	0.00	0.04		0.06	0.02	0.04	99.50
SD5	ID = 2222 SD5 hbl4-plg2	55.09	0.00	27.58	0.59	0.00	0.18	10.45	5.27	0.55	0.00	0.12		0.10	0.02	0.00	99.95
SD5	ID = 2250 SD5 hbl5-plg1	51.68	0.06	29.25	0.58	0.04	0.15	12.85	3.72	0.56	0.05	0.07		0.00	0.18	0.00	99.19
SD5	ID = 2251 SD5 hbl5-plg2	55.33	0.08	27.35	0.70	0.04	0.13	10.07	5.07	1.10	0.01	0.08		0.00	0.00	0.06	100.02
SD14	ID = 2102 SD14 hbl5-plg1	54.44	0.08	27.71	0.54	0.00	0.09	10.56	5.06	0.56	0.00	0.00		0.00	0.02	0.00	99.06
SD14	ID = 2103 SD14 hbl5-plg2	54.91	0.06	27.34	0.60	0.00	0.03	10.31	5.31	0.54	0.06	0.23		0.01	0.11	0.00	99.51
SD14	ID = 2104 SD14 hbl6-plg1	50.07	0.00	30.52	0.80	0.00	0.00	14.10	3.23	0.27	0.00	0.00		0.00	0.00	0.00	98.99

Sample	Description of Analysis	SiO_2	TiO_2	Al_2O_3	FeO	MnO	MgO	CaO	Na_2O	K_2O	Cl	NiO	V_2O_3	Cr_2O_3	SO_3	P_2O_5	Total
SD14	ID = 2105 SD14 hbl6-plg2	49.16	0.07	31.39	0.87	0.00	0.00	15.20	2.57	0.26	0.00	0.00		0.08	0.00	0.00	99.60
SD14	ID = 2123 SD14 hbl8-plg1	56.04	0.09	26.68	0.48	0.00	0.10	9.52	5.79	0.86	0.00	0.10		0.00	0.00	0.01	99.67
SD14	ID = 2124 SD14 hbl8-plg2	45.88	0.00	33.46	0.78	0.06	0.01	17.60	1.36	0.17	0.00	0.00		0.00	0.12	0.00	99.44
SD14	ID = 2125 SD14 hbl8-plg3	46.12	0.08	33.33	0.82	0.00	0.05	17.29	1.64	0.25	0.05	0.06		0.00	0.06	0.00	99.75
SD14	ID = 2127 SD14 hbl8-plg4	51.64	0.00	29.85	0.57	0.03	0.01	13.12	3.67	0.33	0.04	0.00		0.03	0.10	0.00	99.39
SD14	ID = 2128 SD14 hbl8-plg5	50.20	0.11	30.20	0.50	0.00	0.00	14.05	3.18	0.37	0.00	0.00		0.13	0.09	0.00	98.83
SD13	ID = 3237 SD13 hbl8-plg	56.18	0.13	26.81	0.45	0.03	0.00	9.50	5.87	0.60	0.06	0.00	0.00	0.04	0.12	0.00	99.80
SD13	ID = 3307 SD13 hbl5-plg1	54.06	0.09	27.60	0.61	0.00	0.00	10.87	4.66	0.69	0.00	0.00	0.00	0.11	0.01	0.12	98.82
SD13	ID = 3321 SD13 hbl6-plg1	51.55	0.05	29.40	0.87	0.00	0.13	12.66	3.72	0.69	0.03	0.00	0.00	0.06	0.00	0.06	99.22
SD13	ID = 3324 SD13 hbl7-plg	55.81	0.01	26.64	0.76	0.11	0.00	9.57	5.51	0.91	0.01	0.00	0.00	0.17	0.05	0.00	99.55
SD13	ID = 3186 SD13 plg1-c	55.16	0.00	27.09	0.41	0.00	0.20	10.10	5.48	0.54	0.07	0.00	0.00	0.03	0.00	0.00	99.08
SD13	ID = 3187 SD13 plg1-r	52.47	0.00	28.37	0.67	0.00	0.06	11.72	4.48	0.40	0.20	0.07	0.00	0.10	0.02	0.00	98.57
SD20	ID = 8090 SD20 cpx2 incl.3-plg	51.99	0.00	27.99	0.73	0.06	0.10	11.56	4.53	0.41	0.04	0.01	0.06	0.01	0.06	0.00	97.55
SD20	ID = 8110 SD20 cpx5 plg-c	52.92	0.01	28.26	0.63	0.00	0.06	12.01	4.29	0.36	0.00	0.00	0.01	0.00	0.00	0.00	98.55
SD20	ID = 8111 SD20 cpx5 plg-r	54.02	0.02	27.35	0.67	0.00	0.00	10.81	4.95	0.58	0.00	0.00	0.00	0.11	0.00	0.00	98.51
SD28	ID = 2276 SD28 cpx2-plg1	55.28	0.02	27.27	0.58	0.09	0.08	10.38	5.67	0.48	0.02	0.00		0.00	0.01	0.00	99.88
SD28	ID = 2308 SD28 cpx6-plg	54.66	0.00	27.41	0.39	0.00	0.00	10.88	5.22	0.42	0.02	0.00		0.00	0.02	0.00	99.02
SD23a	ID = 2495 SD23a cpx5-plg1	52.51	0.01	28.49	0.89	0.00	0.06	11.72	4.47	0.38	0.05	0.07		0.00	0.00	0.00	98.65
SD23a	ID = 2525 SD23a cpx7-plg	51.19	0.05	29.54	0.90	0.03	0.00	13.16	3.87	0.34	0.00	0.00		0.13	0.00	0.00	99.21
SD23a	ID = 2533 SD23a cpx8-plg	55.73	0.03	26.30	0.59	0.07	0.18	9.37	5.59	0.63	0.04	0.11		0.15	0.00	0.16	98.95
SD28	ID = 2269 SD28 hbl1-plg1	58.74	0.03	24.79	0.43	0.00	0.01	7.59	6.68	0.97	0.01	0.00		0.00	0.10	0.06	99.41
SD28	ID = 2298 SD28 bi1-plg1	58.29	0.15	25.25	0.82	0.00	0.03	8.01	6.87	0.72	0.02	0.06		0.00	0.19	0.00	100.41
SD25a	ID = 10495 SD25a_plg1m	53.41	0.10	27.24	0.58	0.00	0.19	10.57	5.19	0.46	0.04	0.03		0.00	0.00	0.00	97.81
SD25a	ID = 10503 SD25a_plg2p	54.88	0.02	26.56	0.39	0.00	0.09	9.68	5.63	0.56	0.00	0.09		0.07	0.00	0.00	97.97
SD25a	ID = 10504 SD25a_plg2p_rim	54.46	0.06	27.58	0.43	0.00	0.14	10.48	5.08	0.50	0.00	0.00		0.00	0.01	0.00	98.74
SD25a	ID = 10508 SD25a_plg3m	49.77	0.01	29.93	0.68	0.09	0.11	13.79	3.45	0.33	0.05	0.04		0.08	0.12	0.00	98.45
SD25a	ID = 10509 SD25a_plg4m	54.51	0.16	26.58	0.75	0.03	0.16	10.12	4.66	1.03	0.05	0.01		0.07	0.10	0.00	98.23
SD25a	ID = 10510 SD25a_plg5p	52.57	0.00	27.95	0.28	0.00	0.06	11.14	4.75	0.39	0.00	0.00		0.00	0.09	0.00	97.23
SD25a	ID = 10511 SD25a_plg5p_rim2	53.61	0.14	27.92	0.67	0.00	0.18	11.04	5.08	0.43	0.00	0.01		0.00	0.05	0.00	99.13
SD25a	ID = 10512 SD25a_plg5p_centre	55.52	0.14	26.36	0.36	0.00	0.00	9.25	5.96	0.55	0.03	0.00		0.00	0.01	0.00	98.18
SD25a	ID = 10514 SD25a_plg6m	53.56	0.11	27.42	0.56	0.00	0.03	10.56	4.99	0.47	0.02	0.00		0.00	0.17	0.00	97.89
SD25a	ID = 10524 SD25a_plg7m	50.89	0.00	29.29	0.69	0.00	0.08	12.69	3.88	0.39	0.04	0.25		0.19	0.23	0.00	98.62
SD25a	ID = 10526 SD25a_plg8p	52.28	0.15	28.13	0.51	0.00	0.00	11.83	4.51	0.42	0.00	0.05		0.06	0.12	0.00	98.06

Sample	Description of Analysis	SiO_2	TiO_2	Al_2O_3	FeO	MnO	MgO	CaO	Na_2O	K_2O	Cl	NiO	V_2O_3	Cr_2O_3	SO_3	P_2O_5	Total
SD25a	ID = 10527 SD25a_plg8p_c	50.48	0.01	29.78	0.41	0.00	0.10	12.93	3.64	0.29	0.00	0.05		0.10	0.04	0.00	97.83
SD25a	ID = 10529 SD25a_plg9m	52.72	0.01	28.15	0.61	0.00	0.09	11.40	4.52	0.42	0.07	0.08		0.16	0.02	0.00	98.25
SD25a	ID = 10530 SD25a_plg10m	51.75	0.08	28.58	0.84	0.00	0.14	11.82	4.31	0.32	0.03	0.04		0.03	0.00	0.00	97.94
SD25a	ID = 10532 SD25a_plg11m	50.51	0.06	29.64	0.76	0.06	0.04	13.31	3.64	0.37	0.00	0.11		0.00	0.00	0.00	98.50
SD32b	ID = 2388 SD32b plg1	50.63	0.06	29.90	0.76	0.00	0.08	13.71	3.57	0.33	0.00	0.03		0.25	0.00	0.00	99.32
SD32a	ID = SD32a_glass2_w	52.69	0.01	28.09	0.61	0.01	0.13	11.72	4.32	0.40	0.01	0.00		0.00	0.00	0.00	97.99
SD32a	ID = SD32a_plg1_w	51.85	0.06	27.54	0.86	0.00	0.16	12.49	2.92	1.07	0.05	0.00		0.01	0.00	0.00	97.01
SD32a	ID = SD32a_plg1b_w	53.10	0.08	28.17	0.58	0.00	0.16	11.20	4.71	0.41	0.02	0.00		0.00	0.00	0.00	98.43
SD32a	ID = SD32a_plg2_w	55.22	0.16	26.14	0.94	0.00	0.20	9.63	4.83	1.01	0.04	0.02		0.05	0.12	0.00	98.36
SD32a	ID = 10460 SD32a_plg3_w	56.70	0.19	23.78	1.11	0.06	0.00	8.32	4.94	1.54	0.05	0.00		0.00	0.02	0.12	96.83
SD32a	ID = 10473 SD32a_amph2_w	56.32	0.01	26.88	0.45	0.00	0.10	9.42	5.86	0.54	0.00	0.09		0.13	0.12	0.00	99.92
E02-117	ID = 8364 E02-117 hbl2-plg1-c	50.62	0.08	29.90	0.59	0.08	0.00	13.00	3.88	0.29	0.07	0.00	0.00	0.07	0.01	0.00	98.59
E02-117	ID = 8365 E02-117 hbl2-plg1-r	57.99	0.12	25.13	0.47	0.00	0.17	7.64	6.81	0.56	0.00	0.00	0.00	0.05	0.06	0.00	99.00
E02-117	ID = 8366 E02-117 hbl2-plg2-c	52.79	0.12	28.72	0.19	0.00	0.09	11.77	4.66	0.32	0.04	0.00	0.00	0.09	0.00	0.00	98.79
E02-117	ID = 8367 E02-117 hbl2-plg2-r	52.26	0.01	28.86	0.66	0.00	0.00	11.98	4.78	0.37	0.00	0.00	0.01	0.14	0.12	0.00	99.19
E02-117	ID = 8370 E02-117 hbl3-plg1-c	47.45	0.00	32.47	0.60	0.00	0.00	16.49	2.15	0.18	0.00	0.10	0.00	0.05	0.16	0.00	99.65
E02-117	ID = 8371 E02-117 hbl3-plg1-r	48.98	0.05	30.86	0.70	0.03	0.00	14.57	3.07	0.17	0.00	0.06	0.00	0.05	0.14	0.00	98.68
E02-117	ID = 8373 E02-117 hbl3-plg2-r	47.40	0.11	32.19	0.72	0.00	0.00	16.67	2.10	0.15	0.00	0.00	0.00	0.12	0.00	0.00	99.46
E02-117	ID = 8376 E02-117 hbl4-plg-r	46.88	0.03	31.98	0.60	0.00	0.00	16.25	2.20	0.18	0.00	0.00	0.00	0.06	0.00	0.00	98.18
E02-117	ID = 8377 E02-117 hbl4-plg-c	46.19	0.11	32.84	0.66	0.03	0.00	16.93	1.80	0.18	0.02	0.00	0.00	0.10	0.04	0.00	98.90
E02-117	ID = 8379 E02-117 cpx1-plg	49.85	0.15	30.32	0.74	0.00	0.00	13.93	3.39	0.23	0.02	0.00	0.04	0.07	0.00	0.00	98.74
E02-117	ID = 8396 E02-117 cpx4-plg1	48.78	0.00	30.76	0.60	0.14	0.00	14.52	2.97	0.22	0.00	0.00	0.00	0.10	0.00	0.00	98.09
E02-117	ID = 8403 E02-117 hbl5-plg-c	46.42	0.01	32.54	0.44	0.00	0.07	16.82	1.82	0.15	0.00	0.13	0.00	0.03	0.00	0.00	98.43
E02-117	ID = 8404 E02-117 hbl5-plg2	47.31	0.00	32.21	0.61	0.00	0.00	16.38	1.97	0.18	0.00	0.00	0.00	0.07	0.08	0.00	98.81
SD21b	ID = 1789 SD21b mplg1-c	51.59	0.08	28.82	0.55	0.00	0.00	12.32	4.00	0.42	0.02	0.00		0.09	0.01	0.00	97.90
SD21b	ID = 1790 SD21b mplg1-r	52.90	0.10	28.58	0.36	0.01	0.04	12.14	4.26	0.56	0.02	0.02		0.05	0.05	0.00	99.09
SD21b	ID = 1791 SD21b mplg1-cnew	55.00	0.00	26.46	0.41	0.01	0.00	9.94	5.43	0.64	0.02	0.00		0.03	0.00	0.01	97.95
SD21b	ID = 1792 SD21b mplg2-c	50.64	0.02	29.62	0.51	0.00	0.00	13.13	3.83	0.37	0.00	0.00		0.01	0.00	0.00	98.13
SD21b	ID = 1793 SD21b mplg2-r	52.57	0.05	28.20	0.46	0.00	0.00	11.43	4.63	0.47	0.04	0.00		0.00	0.05	0.00	97.90
SD21b	ID = 1794 SD21b mplg3-c	50.55	0.02	29.96	0.49	0.00	0.00	13.45	3.63	0.28	0.01	0.00		0.08	0.02	0.00	98.49
SD21b	ID = 1795 SD21b mplg4-c	55.76	0.14	26.38	0.62	0.01	0.01	9.84	5.46	0.78	0.04	0.00		0.06	0.00	0.00	99.10
SD21b	ID = 1798 SD21b mplg7-c	54.37	0.09	27.29	0.57	0.03	0.05	10.68	5.03	0.49	0.02	0.00		0.05	0.05	0.00	98.72
SD21b	ID = 1799 SD21b mplg7-r	53.69	0.15	27.99	0.45	0.00	0.10	11.39	4.96	0.44	0.00	0.00		0.09	0.00	0.00	99.26

Sample	Description of Analysis	SiO_2	TiO_2	Al_2O_3	FeO	MnO	MgO	CaO	Na_2O	K_2O	Cl	NiO	V_2O_3	Cr_2O_3	SO_3	P_2O_5	Total
SD21b	ID = 1800 SD21b mplg8-c	56.02	0.10	26.15	0.29	0.02	0.04	9.00	6.10	0.69	0.02	0.00		0.03	0.00	0.00	98.46
SD21b	ID = 1801 SD21b mplg8-r	54.00	0.07	27.27	0.69	0.02	0.05	10.52	5.37	0.55	0.00	0.00		0.01	0.01	0.00	98.56
SD21b	ID = 1802 SD21b mplg9-c	53.40	0.00	28.36	0.49	0.09	0.00	11.87	4.64	0.38	0.00	0.00		0.02	0.00	0.00	99.25
SD21b	ID = 1803 SD21b mplg9-r	56.09	0.17	27.20	0.52	0.01	0.01	10.15	5.47	0.55	0.00	0.06		0.00	0.06	0.00	100.29
SD21b	ID = 1809 SD21b mplg9-cnew	53.16	0.12	28.18	0.52	0.06	0.00	11.58	4.53	0.40	0.02	0.00		0.05	0.00	0.00	98.62
SD21b	ID = 1811 SD21b mplg10-c	52.94	0.02	27.99	0.71	0.00	0.04	11.70	4.69	0.42	0.03	0.00		0.04	0.03	0.01	98.62
SD21b	ID = 1812 SD21b mplg10-r	53.08	0.00	28.50	0.65	0.00	0.05	11.77	4.37	0.43	0.00	0.05		0.00	0.00	0.00	98.90
SD21b	ID = 1813 SD21b mplg11-c	48.16	0.00	31.68	0.62	0.02	0.05	15.57	2.50	0.24	0.00	0.00		0.13	0.02	0.00	98.99
SD21b	ID = 1814 SD21b mplg11-r?	46.41	0.00	32.97	0.61	0.00	0.06	17.12	1.61	0.11	0.04	0.16		0.03	0.00	0.00	99.12
SD32b	ID = 1824 SD32b mplg1-c	52.13	0.00	28.90	0.61	0.06	0.13	12.09	4.52	0.36	0.00	0.00		0.19	0.01	0.00	99.00
SD32b	ID = 1825 SD32b mplg1-r	57.86	0.13	26.76	0.83	0.02	0.26	10.14	5.32	0.74	0.00	0.00		0.00	0.06	0.00	102.12
SD32b	ID = 1826 SD32b mplg2-c	54.34	0.11	28.03	0.56	0.00	0.00	10.81	5.05	0.48	0.01	0.05		0.03	0.09	0.02	99.58
SD32b	ID = 1827 SD32b mplg2-r	52.85	0.14	28.34	0.46	0.03	0.07	11.83	4.55	0.49	0.01	0.00		0.00	0.00	0.00	98.77
SD32b	ID = 1828 SD32b mplg3-c	51.24	0.19	29.71	0.57	0.16	0.00	13.16	3.64	0.29	0.00	0.00		0.15	0.00	0.00	99.11
SD32b	ID = 1829 SD32b mplg3-r	54.02	0.09	28.06	0.51	0.07	0.22	11.40	4.65	0.48	0.01	0.10		0.07	0.06	0.00	99.74
SD32b	ID = 1830 SD32b mplg4-c	51.84	0.06	29.15	0.77	0.01	0.00	12.81	4.08	0.36	0.00	0.09		0.12	0.00	0.00	99.29
SD32b	ID = 1831 SD32b mplg4-r1?	56.36	0.16	26.96	1.23	0.00	0.28	11.32	3.88	1.20	0.02	0.00		0.13	0.00	0.00	101.54
SD32b	ID = 1832 SD32b mplg4-r2	51.10	0.03	29.73	0.70	0.00	0.02	13.33	3.89	0.26	0.00	0.11		0.06	0.08	0.00	99.31
SD32b	ID = 1833 SD32b mplg5	53.69	0.00	28.51	0.52	0.17	0.05	11.71	4.72	0.43	0.00	0.06		0.07	0.00	0.00	99.93
SD32b	ID = 1834 SD32b mplg6-c	49.46	0.01	30.90	0.53	0.15	0.04	14.67	3.04	0.24	0.00	0.00		0.08	0.00	0.00	99.12
SD32b	ID = 1835 SD32b mplg6-r	53.42	0.16	28.63	0.50	0.00	0.04	11.65	4.66	0.50	0.00	0.26		0.00	0.06	0.00	99.88
SD32b	ID = 1836 SD32b mplg7-c	52.91	0.12	28.43	0.47	0.02	0.04	11.97	4.42	0.41	0.04	0.02		0.04	0.15	0.00	99.04
SD32b	ID = 1837 SD32b mplg7-r	55.10	0.06	27.18	0.65	0.00	0.19	10.62	5.02	0.56	0.05	0.00		0.16	0.00	0.00	99.59
SD32b	ID = 1838 SD32b mplg8-c	54.70	0.02	28.17	0.31	0.00	0.08	11.11	4.84	0.44	0.00	0.00		0.02	0.00	0.00	99.69
SD32b	ID = 1839 SD32b mplg8-r	54.42	0.18	28.03	0.36	0.04	0.00	11.10	4.94	0.49	0.01	0.00		0.02	0.02	0.00	99.61
SD32b	ID = 1840 SD32b mplg9-c	54.28	0.07	27.53	0.57	0.00	0.00	10.67	4.88	0.53	0.04	0.00		0.05	0.01	0.00	98.63
SD32b	ID = 1841 SD32b mplg9-r	54.63	0.00	27.87	0.56	0.23	0.04	11.13	5.16	0.63	0.03	0.00		0.12	0.02	0.00	100.42

[all data in wt.%]

Sample	Notes	Eruption Episode	SiO_2	TiO_2	Al_2O_3	FeO	MnO	MgO	CaO	Na_2O	K_2O	P_2O_5	H_2O	LOI	Total
SD1	lava dome	Pyramid	57.08	0.752	17.77	6.90	0.15	2.82	7.25	3.89	2.87	0.28		0.05	99.81
SD2	lava dome	Pyramid	56.97	0.751	17.74	6.87	0.15	2.86	7.22	3.85	2.89	0.28		0.24	99.82
SD6	lava dome	Pyramid	57.41	0.751	17.57	6.99	0.15	2.86	6.92	3.87	2.94	0.24		0.18	99.86
SD10	lava dome	Pyramid	57.03	0.752	17.75	6.95	0.15	2.88	7.27	3.86	2.91	0.28		0.05	99.87
SD14	lava dome	Pyramid	57.14	0.752	17.79	6.88	0.15	2.88	7.23	3.88	2.91	0.28		0.05	99.94
SD15	lava dome	Pyramid	57.14	0.751	17.69	6.93	0.15	2.91	7.28	3.89	2.89	0.28		0.05	99.95
SD4	lava dome	Pyramid	56.91	0.769	17.78	6.93	0.15	2.89	7.24	3.91	2.86	0.28	0.00	-0.01	99.72
SD5	lava dome	Pyramid	56.94	0.788	17.68	7.06	0.15	2.95	7.23	3.90	2.85	0.25	0.00	0.01	99.81
SD7	lava dome	Pyramid	56.39	0.789	17.67	7.13	0.15	3.02	7.45	3.87	2.76	0.28	0.01	0.04	99.57
SD13	lava dome	Pyramid	57.51	0.744	17.41	6.59	0.14	2.90	7.07	3.91	2.97	0.28	0.03	0.25	99.82
TO5-39	on top of lava dome	Pyramid	57.77	0.728	17.15	6.44	0.14	2.83	6.84	3.63	2.94	0.24	0.24	0.72	99.68
TO4-168	RAD	Pyramid	57.22	0.753	17.31	6.76	0.15	3.17	7.34	3.73	2.83	0.27	0.21	0.14	99.90
DS6	BAF	Tahurangi	58.36	0.691	17.31	6.15	0.14	2.71	6.74	3.95	3.12	0.24		0.28	99.69
P7	BAF	Tahurangi	58.06	0.736	17.12	6.56	0.15	2.87	6.83	3.40	2.93	0.25	0.38	0.93	100.22
TO4-171	BAF	Tahurangi	57.16	0.743	17.23	6.75	0.14	3.09	7.27	3.79	2.87	0.27	0.13	0.19	99.63
TO4-158	BAF	Tahurangi	57.09	0.736	17.28	6.69	0.15	3.04	7.23	3.88	2.88	0.27	0.08	0.26	99.58
TO4-158	BAF	Tahurangi	57.07	0.741	17.29	6.72	0.15	3.19	7.23	3.79	2.90	0.27	0.21	0.32	99.89
TO4-170	BAF	Tahurangi	58.41	0.714	17.19	6.39	0.14	2.83	6.90	3.82	3.03	0.24	0.11	0.06	99.81
TO4-177	BAF	Tahurangi	57.09	0.743	17.38	6.77	0.15	3.11	7.34	3.80	2.85	0.27	0.20	0.16	99.88
TO4-178	BAF	Tahurangi	57.70	0.765	17.40	6.65	0.15	2.83	7.00	3.93	3.04	0.28	0.21	-0.15	99.80
SD20	pumice	Burrell	55.56	0.770	17.19	7.31	0.15	3.45	7.54	3.52	2.71	0.27	0.12	1.12	99.70
SD24	pumice	Burrell	55.80	0.753	17.05	7.01	0.15	3.44	7.59	3.70	2.74	0.27	0.09	0.78	99.36
SD35	pumice	Burrell	55.58	0.761	17.20	7.09	0.15	3.49	7.68	3.69	2.69	0.27	0.12	1.04	99.75
TO4-19	pumice	Burrell	55.93	0.754	17.20	7.18	0.15	3.45	7.62	3.54	2.67	0.26	0.18	0.85	99.80
TO4-22	pumice	Burrell	56.00	0.768	17.19	7.17	0.15	3.35	7.64	3.59	2.71	0.27	0.16	0.84	99.84
TO4-65	pumice	Burrell	55.80	0.757	17.04	7.15	0.15	3.47	7.71	3.59	2.71	0.27	0.30	0.85	99.78
TO4-96	pumice	Burrell	55.52	0.770	17.17	7.25	0.15	3.61	8.01	3.80	2.64	0.27	0.19	0.55	99.93
P10	BAF	Burrell	55.71	0.780	17.17	7.21	0.15	3.62	8.00	3.59	2.63	0.26	0.22	0.47	99.81
SD9b	black dense	Burrell	55.86	0.767	17.15	7.14	0.15	3.61	7.91	3.72	2.68	0.26	0.00	0.26	99.52
SD27	black dense	Burrell	55.95	0.757	17.20	7.09	0.15	3.51	7.80	3.72	2.70	0.27	0.06	0.37	99.57
SD29	black vesicular	Burrell	55.75	0.752	17.11	7.14	0.15	3.62	7.88	3.72	2.66	0.26	0.11	0.48	99.62
SD33	black dense	Burrell	55.90	0.757	17.21	7.09	0.15	3.57	7.89	3.70	2.67	0.27	0.00	0.42	99.63

Sample	Notes	Eruption Episode	SiO_2	TiO_2	Al_2O_3	FeO	MnO	MgO	CaO	Na_2O	K_2O	P_2O_5	H_2O	LOI	Total
TO4-3	black dense	Burrell	57.06	0.784	17.35	6.78	0.15	3.01	7.24	3.97	2.98	0.31	0.05	-0.07	99.62
SD9a	grey bread	Burrell	56.44	0.772	17.24	6.92	0.15	3.17	7.49	3.86	2.82	0.28	0.00	-0.08	99.07
SD9c	sugary grey	Burrell	57.65	0.760	17.29	6.54	0.14	2.91	6.99	3.99	3.07	0.28	0.00	-0.02	99.62
SD28	grey bread	Burrell	57.21	0.772	17.40	6.65	0.14	2.96	7.11	3.97	3.02	0.29	0.02	-0.05	99.49
TO4-1	grey dense	Burrell	57.58	0.749	17.35	6.62	0.15	2.88	7.03	3.98	3.02	0.28	0.10	-0.03	99.70
TO4-21	grey dense	Burrell	56.83	0.756	17.32	6.98	0.16	3.20	7.12	3.94	2.89	0.28	0.13	0.11	99.71
TO4-24	grey bread	Burrell	59.51	0.669	17.17	5.97	0.14	2.54	6.33	3.98	3.25	0.24	0.04	-0.08	99.75
SD34	dark grey dense	Burrell	57.05	0.792	17.34	6.75	0.15	3.01	7.20	3.99	3.02	0.31	0.00	-0.03	99.58
SD39	dark grey dense	Burrell	57.63	0.766	17.28	6.58	0.15	2.89	6.95	3.98	3.09	0.28	0.00	-0.02	99.60
TO4-167	BAF	Burrell	57.65	0.751	17.22	6.52	0.15	2.80	6.92	3.86	3.04	0.28	0.13	0.46	99.78
P1	BAF	Burrell	56.59	0.740	17.22	6.69	0.15	3.19	7.34	3.81	2.94	0.27		0.34	99.27
NZ1	BAF	Burrell	57.58	0.763	17.33	6.65	0.14	2.90	7.06	3.84	2.99	0.28	0.16	0.14	99.84
P6	BAF	Burrell	57.31	0.718	17.14	6.47	0.14	2.87	6.96	3.73	2.91	0.24	0.29	0.74	99.51
TO4-174	BAF	Puniho	57.51	0.727	17.12	6.51	0.14	2.90	6.93	3.51	2.95	0.26	0.21	0.97	99.72
TO4-166	BAF	Waiweranui	57.86	0.754	17.35	6.57	0.14	2.80	6.96	3.89	3.04	0.28	0.11	0.14	99.91
NZ2	BAF	Waiweranui	56.33	0.781	17.59	6.49	0.14	2.48	6.58	4.01	2.86	0.29		0.24	97.79
DS22	BAF	Waiweranui	58.99	0.672	17.07	5.96	0.14	2.63	6.56	3.87	3.12	0.23	0.13	0.25	99.63
TO4-160	BAF	Waiweranui	58.48	0.713	17.24	6.29	0.14	2.70	6.78	3.86	3.06	0.24	0.13	0.17	99.80
NZ4	BAF	Waiweranui	58.19	0.660	16.83	5.66	0.13	2.55	6.21	3.95	3.19	0.23		0.34	97.94
TO4-163	BAF	Newall	58.18	0.722	17.18	6.41	0.14	2.78	6.84	3.80	3.03	0.24	0.16	0.35	99.81
TO4-162	BAF	Newall	57.54	0.726	17.33	6.47	0.14	2.85	6.88	3.59	2.94	0.25	0.43	0.83	99.98
NZ3	BAF	Newall	59.11	0.683	17.07	5.99	0.14	2.66	6.54	3.73	3.14	0.23	0.15	0.18	99.63
PY19	surge	Newall	58.36	0.701	17.09	6.20	0.14	2.71	6.72	3.82	3.03	0.24	0.15	0.42	99.58
TO5-34	BAF	Newall	58.10	0.709	17.25	6.28	0.14	2.74	6.86	3.72	2.96	0.24	0.19	0.75	99.94
E02-26	BAF	Newall	55.74	0.869	17.37	7.53	0.16	3.28	7.62	3.80	2.71	0.30		0.26	99.63
TO4-165	BAF	Te Popo	59.14	0.673	17.21	5.90	0.13	2.62	6.56	3.90	3.14	0.23	0.13	0.10	99.73
TO4-152	BAF	Te Popo	59.06	0.671	17.07	5.89	0.13	2.56	6.46	3.88	3.15	0.23	0.14	0.44	99.67
TO4-172	BAF	Maero	58.24	0.723	17.21	6.37	0.14	2.83	6.91	3.84	3.02	0.24	0.19	0.09	99.80
TO4-180	BAF	Maero	57.82	0.707	17.21	6.31	0.14	2.79	6.82	3.60	2.98	0.25	0.22	0.92	99.76
SR21	BAF	Maero	58.99	0.681	17.06	5.94	0.14	2.60	6.48	3.89	3.17	0.23	0.15	0.36	99.68
SD12	coulée	Maero	57.01	0.780	17.68	6.75	0.15	2.69	7.09	3.96	3.04	0.30		0.33	99.78
T04-202	block	Maero	57.45	0.771	17.72	6.65	0.15	2.62	7.07	4.02	3.00	0.30	0.03	-0.05	99.71

Sample	Notes	Eruption Episode	SiO_2	TiO_2	Al_2O_3	FeO	MnO	MgO	CaO	Na_2O	K_2O	P_2O_5	H_2O	LOI	Total
DS24a	BAF	pre-Maero	55.63	0.862	18.40	7.56	0.17	2.58	8.10	3.68	2.21	0.31	0.19	0.33	100.02
TO4-52	scoria-and-ash flow	pre-Burrell	54.12	0.962	17.52	8.36	0.17	3.57	8.27	3.74	2.43	0.33	0.05	0.07	99.61
TO4-56	scoria-and-ash flow	pre-Maero	55.02	0.878	17.48	7.98	0.17	3.32	7.65	3.77	2.40	0.28	0.12	0.32	99.39
Main cone lava flows															
TO4-57	lava flow	pre-Burrell	54.06	0.961	17.57	8.34	0.17	3.53	8.27	3.80	2.44	0.33	0.10	0.00	99.57
TO4-58	lava flow	pre-Burrell	54.53	0.944	17.47	8.26	0.17	3.52	8.21	3.83	2.47	0.32	0.02	-0.02	99.73
TO4-59	lava flow	pre-Burrell	54.15	0.972	17.63	8.38	0.17	3.56	8.29	3.82	2.44	0.33	0.13	-0.01	99.86
TO4-61	lava flow	pre-Burrell	54.38	0.970	17.57	8.41	0.17	3.64	8.37	3.82	2.45	0.33	0.06	-0.04	100.13
TO4-62	lava flow	pre-Burrell	53.78	0.980	17.46	8.63	0.17	3.75	8.52	3.79	2.37	0.33	0.14	-0.01	99.91
TO4-63	lava flow	pre-Burrell	53.87	0.967	17.52	8.52	0.17	3.68	8.48	3.80	2.40	0.33	0.11	0.07	99.91
TO4-199	lava flow	pre-Maero	54.19	0.955	17.48	8.90	0.17	3.95	8.67	3.66	2.17	0.27	0.05	-0.24	100.23
TO4-200	lava flow	pre-Maero	53.76	0.939	17.31	8.77	0.17	3.85	8.54	3.60	2.15	0.27	0.08	-0.24	99.19
MI5	lava flow	Maero	54.24	0.972	17.70	8.44	0.16	3.54	8.42	3.87	2.44	0.33	0.06	-0.20	99.97
E03-77	lava flow	Maero	54.45	0.926	17.43	8.40	0.17	3.68	8.36	3.83	2.52	0.34	0.05	-0.11	100.05
SD11	lava flow	Maero	54.19	0.930	17.51	8.36	0.17	3.79	8.42	3.69	2.55	0.35		0.05	100.01
Fanthams Peak lava flows (collected by Rosenthal, 2005)															
AR4	lava flow	pre-Kaupokonui	52.53	1.001	18.08	9.28	0.17	3.63	9.02	3.60	2.03	0.29	0.03	-0.17	99.49
AR19	lava flow	pre-Kaupokonui	51.79	1.010	18.34	9.61	0.19	3.72	9.75	3.43	1.79	0.29	0.04	-0.09	99.89
AR23	lava flow	pre-Kaupokonui	52.42	1.001	18.18	9.32	0.17	3.64	9.17	3.60	2.01	0.30	0.05	-0.18	99.70
AR25	lava flow	pre-Kaupokonui	51.13	1.031	18.27	9.81	0.19	3.92	10.01	3.34	1.70	0.29	0.06	-0.15	99.61
AR36	lava flow	pre-Kaupokonui	51.98	1.000	18.43	9.49	0.19	3.62	9.63	3.49	1.82	0.29	0.06	-0.07	99.93
AR37	lava flow	pre-Kaupokonui	52.25	0.999	18.14	9.29	0.17	3.59	9.10	3.54	2.03	0.29	0.08	0.06	99.53
AR39	lava flow	pre-Kaupokonui	52.50	1.000	18.17	9.24	0.17	3.60	9.13	3.61	2.03	0.29	0.10	-0.09	99.74
AR47	lava flow	pre-Kaupokonui	52.99	0.992	18.07	9.21	0.17	3.63	9.07	3.62	2.05	0.29	0.00	-0.24	99.86
AR49	lava flow	pre-Kaupokonui	52.84	0.989	18.13	9.09	0.17	3.54	8.92	3.65	2.07	0.29	0.11	-0.01	99.78

[all data in wt.%]

Sample	Notes	Eruption Episode	As	Ba	Ce	Cr	Cu	Ga	La	Nb	Ni	Pb	Rb	Sc	Sr	Th	U	V	Y	Zn	Zr	Co
SD1	lava dome	Pyramid	4	1007	19.0	7.0	53	20	18	7	7.0	15.0	78	15	627	<1	<1	160	20.0	63.0	139	
SD2	lava dome	Pyramid	1	1019	36.0	11.0	73	22	20	7	10.0	21.0	76	17	617	<1	<1	163	20.0	70.0	143	
SD6	lava dome	Pyramid	5	990	24.0	8.0	44	20	17	7	11.0	18.0	78	14	602	<1	<1	172	19.0	68.0	143	
SD10	lava dome	Pyramid	3	984	28.0	<1	67	20	16	7	11.0	19.0	78	18	624	<1	<1	153	20.0	68.0	143	
SD14	lava dome	Pyramid	4	1007	29.0	4.0	55	21	24	7	10.0	15.0	77	15	617	<1	<1	164	20.0	63.0	142	
SD15	lava dome	Pyramid	3	982	29.0	4.0	66	19	25	7	10.0	19.0	77	17	615	<1	<1	160	20.0	70.0	142	
SD4	lava dome	Pyramid		789		9.1	109	20		6	6.3	13.0	74	17	603			187	22.9	81.4	144	
SD5	lava dome	Pyramid		785		12.0	55	19		6	5.1	15.0	74	15	600			195	23.5	82.0	143	
SD7	lava dome	Pyramid		762		7.9	77	20		6	6.4	13.0	72	13	613			198	23.4	78.1	140	
SD13	lava dome	Pyramid		755		28.3	110	22		7	8.1	15.0	78	14	591			184	23.1	78.1	150	
TO5-39	on top of lava dome	Pyramid		1055	41.3	29.1	46.5	19.5	20.5	5.4	8.2	17.1	83	10.9	545	10	2.5	176	21.2	62.5	154	
TO4-168	RAD	Pyramid		1096	42.0	35.4	36.4	19.7	17.5	5	9.9	18.0	87	14.4	559	9	4.2	155	20.3	58.4	157	
DS6	BAF	Tahurangi	5	1026	25.0	20.0	55	20	18	7	11.0	16.0	84	15	561	<1	<1	157	18.0	62.0	150	
P7	BAF	Tahurangi		1024	39.1	35.0	50.8	19.5	21.2	5.1	9.0	17.5	83	11.8	551	8.8	3.3	184	21.1	64.9	153	
TO4-171	BAF	Tahurangi		1052	41.0	42.5	64.5	19.9	15.6	5.1	8.9	15.4	78	12.8	577	7.7	2.6	169	22.0	62.4	150	
TO4-158	BAF	Tahurangi		1094	36.3	29.0	63.2	20.4	19.6	5.3	10.2	16.3	75	12.3	585	7.2	1.9	176	22.7	66.4	152	
TO4-158	BAF	Tahurangi		1078	44.1	37.1	62.8	19.7	20.7	5.6	12.8	18.1	79	9.7	586	7.7	1.8	175	21.5	65.3	151	
TO4-170	BAF	Tahurangi		1048	35.6	37.2	49.6	19.8	17.1	5	9.7	16.6	85	12.2	548	9.5	3.3	167	20.8	60.4	154	
TO4-177	BAF	Tahurangi		1099	40.3	40.1	56.6	19.6	21	5.1	10.1	17.8	79	10.4	592	8.6	3.3	170	21.4	63.3	151	
TO4-178	BAF	Tahurangi		1170	39.2	21.0	78.2	20.1	21.5	5.1	8.4	15.9	82	11.7	610	7.8	3.8	179	22.9	58.8	158	
SD20	pumice	Burrell		701	*41.5*	42.5	76	19	*21*	6	11.9	13.8	70	19	584	*14*		201	21.7	80.0	134	
SD24	pumice	Burrell		705	*32.7*	51.5	110	20	*19*	6	17.8	15.9	70	20	569	*12*		194	21.8	78.3	135	
SD35	pumice	Burrell		706	*38.5*	44.5	81	21	*20*	6	8.9	12.8	68	19	569	*9*		197	21.7	78.1	133	
TO4-19	pumice	Burrell		977	40.7	45.2	51.2	19	21.7	5	11.6	15.7	72	15.6	566	6.8	2.1	199	21.3	72.6	139	
TO4-22	pumice	Burrell		990	38.9	48.9	26.1	19.4	19.6	4.9	10.1	15.8	72	13	574	7.1	2.8	202	21.6	72.2	142	
TO4-65	pumice	Burrell		965	37.7	47.0	111.3	19.1	20.2	4.9	12.6	16.7	71	22.5	558	7.3	2.8	206	21.6	75.3	139	
TO4-96	pumice	Burrell		944	38.0	54.3	77.1	19.4	15.7	4.5	13.5	16.1	69	16.2	573	8.7	4	214	22.2	75.0	138	
P10	BAF	Burrell		961	40.4	56.2	42.6	19.5	22.4	4.3	13.7	15.9	70	18.7	574	7.2	4.2	202	21.9	72.3	138	
SD9b	black dense	Burrell		720		47.7	68	19		6	11.0	12.0	69	19	576			201	22.2	78.7	132	
SD27	black dense	Burrell		736	*39*	46.8	104	19	*19*	5	11.0	13.9	71	18	577	*12*		195	21.9	77.7	133	
SD29	black vesicular	Burrell		996	37.3	45.6	73.9	20.0	17.7	5.2	11.7	15.3	66	19.2	572	6.3	0.0	197	22.1	71.6	138	
SD33	black dense	Burrell		703	*21*	48.8	93	22	*15*	5	12.9	14.9	69	17	578	*13*		196	21.9	78.7	132	

Sample	Notes	Eruption Episode	As	Ba	Ce	Cr	Cu	Ga	La	Nb	Ni	Pb	Rb	Sc	Sr	Th	U	V	Y	Zn	Zr	Co
TO4-3	black dense	Burrell		1143	44.6	24.7	41.7	20.6	18.9	5.3	8.2	16.9	75	11.5	637	9.3	2.4	186	23.7	62.3	157	
SD9a	grey bread	Burrell		777		29.4	47	21		7	7.7	12.0	70	17	602			192	22.6	77.8	140	
SD9c	sugary grey	Burrell		797		22.9	62	23		7	8.1	15.0	78	17	597			183	23.3	78.3	153	
SD28	grey bread	Burrell		811		21.9	34	21		7	9.6	12.0	77	17	610			187	23.4	78.8	150	
TO4-1	grey dense	Burrell		1128	45.0	22.4	44.0	20.6	20.5	5.6	7.2	16.1	77	10.8	608	9.3	1.8	184	23.6	65.8	156	
TO4-21	grey dense	Burrell		1181	38.0	22.5	34.3	21.0	18.9	5.3	9.1	17.5	76	9.5	619	8.5	2.2	179	22.1	62.4	149	
TO4-24	grey bread	Burrell		1173	37.2	24.2	31.1	20.0	17.2	5.6	7.9	20.3	87	11.7	550	9.2	2.4	151	20.7	56.0	166	
SD34	dark grey dense	Burrell		784		23.9	56	22		7	4.1	15.0	76	17	627			196	23.1	81.0	152	
SD39	dark grey dense	Burrell		830		24.9	89	20		6	6.0	15.0	81	14	597			183	23.7	78.2	154	
TO4-167	BAF	Burrell		1111	44.8	31.4	70.4	20	19.7	5.2	7.7	17.2	84	12.7	589	8.7	2.3	176	22.1	65.6	160	
P1	BAF	Burrell	4	970	43.0	36.0	57	20	25	7	14.0	18.0	74	15	582	<1	<1	186	21.0	76.0	142	
NZ1	BAF	Burrell		1103	39.9	36.8	79.2	19.7	20.9	5.3	7.6	17.3	81	10.1	596	8.6	1.7	188	22.3	64.2	157	
P6	BAF	Burrell		1049	37.9	33.8	44.8	19.8	20.6	5.3	9.3	16.1	81	16.4	554	8.3	2.8	184	21.0	65.6	152	
TO4-174	BAF	Puniho		1032	39.6	33.9	50.7	19.8	20.4	5	9.8	17.7	81	13.1	548	8.7	3	182	21.0	64.3	152	
TO4-166	BAF	Waiweranui		1143	40.0	27.3	68.7	20.1	20.7	5.1	7.7	14.3	83	10.7	594	8.5	3.2	163	21.7	60.1	158	
NZ2	BAF	Waiweranui		908	28.2	9.0	46.8	17.2		8.0	/	9.7	76		618	6.6		169	26.5	78.7	172	11.5
DS22	BAF	Waiweranui		1077	35.1	45.2	49.4	19.6	19.6	5.5	10.2	17.9	89	10.8	536	10	2.6	163	21.0	64.5	162	
TO4-160	BAF	Waiweranui		1061	37.0	36.4	61.8	20	22.1	5.2	11.9	17.8	78	14.8	581	8.2	4.4	182	22.1	65.8	151	
NZ4	BAF	Waiweranui		973	41.4	29.1	16.6	15.5		7.7	4.7	15.9	96		494	8.6		143	22.5	70.5	175	10.0
TO4-163	BAF	Newall		1060	38.4	34.9	42	19.5	18.5	4.9	8.2	16.2	85	15.2	550	9	2.6	175	21.4	61.6	155	
TO4-162	BAF	Newall		1064	39.7	39.8	55	19.6	19.4	5.1	9.5	17.4	80	11.9	549	9.6	2.8	178	20.2	63.7	154	
NZ3	BAF	Newall		1093	34.5	38.1	46.9	20.2	18.9	5.4	9.9	18.2	90	15	536	10.6	2.3	162	20.8	62.1	163	
PY19	surge	Newall		1048	39.6	35.6	45.9	19.2	19.6	5.1	8.8	16.4	86	11.6	538	8.6	2.9	170	20.9	63.3	157	
TO5-34	BAF	Newall		1165	43.2	54.2	41.3	19.7	21.8	4.8	7.9	18.3	85	10	571	8.8	3.4	164	21.0	59.2	155	
E02-26	BAF	Newall	2	916	38.0	18.0	100	20	25	7	9.0	14.0	67	17	655	<1	<1	201	21.0	74.0	130	
TO4-165	BAF	Te Popo		1085	33.2	36.3	38.1	19.3	19.4	5.3	8.4	17.2	89	12	541	9.1	3	154	20.7	57.8	161	
TO4-152	BAF	Te Popo		1108	40.9	42.8	46.2	18.9	20.9	5.1	8.5	15.7	90	13.6	531	9.1	2.5	150	21.4	60.1	163	
TO4-172	BAF	Maero		1061	40.0	38.2	48.9	19.5	19.9	5.1	10.2	16.9	84	13	556	8.9	3.5	170	21.5	61.0	155	
TO4-180	BAF	Maero		1088	40.6	26.3	48.9	19.2	21.5	5	9.0	17.3	84	10.9	549	9.8	3.6	167	20.7	61.2	154	
SR21	BAF	Maero		1069	41.3	32.5	51.4	19	21.1	5.2	9.2	18.4	89	10.1	534	9.1	3.6	164	20.6	62.5	163	
SD12	coulée	Maero	2	1051	27.0	7.0	72	21	27	7	9.0	16.0	80	16	653	<1	<1	173	20.0	66.0	147	
T04-202	block	Maero		1229	43.1	7.5	85.2	21.7	18.7	5.5	6.2	15.0	78	7.3	654	8.0	0.0	162	23.4	52.2	152	

Sample	Notes	Eruption Episode	As	Ba	Ce	Cr	Cu	Ga	La	Nb	Ni	Pb	Rb	Sc	Sr	Th	U	V	Y	Zn	Zr	Co
DS24a	BAF	pre-Maero		828	41.0	34.4	28.7	20.9	16.2	4.7	4.2	15.1	59	12.4	640	6.4	2.8	191	26.1	78.6	137	
TO4-52	scoria-and-ash flow	pre-Burrell		995	36.9	15.1	106.5	21.1	18.9	4.9	7.2	12.7	59	15.8	721	6.4	2.4	228	25.3	67.7	129	
TO4-56	scoria-and-ash flow	pre-Maero		861	36.0	14.5	106.9	20.5	17.3	5.1	7.7	15.3	57	16.6	588	5.3	0.0	231	23.5	81.6	129	
Main cone lava flows																						
TO4-57	lava flow	pre-Burrell		989	33.5	14.2	119.3	21.4	14.9	5.2	7.3	15.3	59	15.5	723	6.7	0.0	232	25.3	66.7	130	
TO4-58	lava flow	pre-Burrell		985	40.5	19.0	113.0	21.1	18.4	5.0	7.2	13.1	60	16.5	695	6.7	0.0	239	24.9	73.4	131	
TO4-59	lava flow	pre-Burrell		991	36.3	15.4	116.2	21.1	17.6	5.2	8.5	14.7	59	19.0	713	5.2	0.0	246	25.1	74.9	128	
TO4-61	lava flow	pre-Burrell		993	37.1	17.5	108.4	21.9	14.4	5.5	6.4	14.0	61	15.8	736	5.9	1.8	230	25.7	66.9	129	
TO4-62	lava flow	pre-Burrell		978	35.1	19.0	128.3	21.5	17.5	4.7	7.5	13.3	56	16.4	702	5.0	1.8	259	25.3	75.6	126	
TO4-63	lava flow	pre-Burrell		1008	40.6	18.1	132.0	22.0	17.1	5.1	7.8	14.9	58	17.5	722	6.2	3.6	230	25.1	65.8	127	
TO4-199	lava flow	pre-Maero		885	43.7	16.0	113.0	21.4	11.8	4.4	8.3	12.6	49	18.0	636	4.8	0.0	246	24.6	70.2	114	
TO4-200	lava flow	pre-Maero		913	36.8	17.6	184.4	20.8	14.8	4.3	8.3	12.4	50	15.1	636	5.4	2.1	245	24.5	65.5	115	
MI5	lava flow	Maero		1014	43.2	13.2	202.4	20.7	17.0	5.1	6.3	18.9	56	17.7	716	5.5	2.4	254	24.5	81.4	126	
E03-77	lava flow	Maero		1033	37.9	19.1	81.4	21.3	18.1	4.7	8.3	16.4	63	14.0	710	5.6	2.5	231	25.6	63.6	139	
SD11	lava flow	Maero	1	934	26.0	18.0	123	19.0	15.0	8.0	13.0	13.0	63	16.0	708	<1	<1	239	23.0	75.0	127	
Fanthams Peak lava flows (collected by Rosenthal, 2005)																						
AR4	lava flow	pre-Kaupokonui		867	34.9	13.3	100	20.6	17.5	3.5	6.1	11.8	47	16.0	643	5	1.2	271	23.9	74.4	106	
AR19	lava flow	pre-Kaupokonui		750	31.5	22.8	84.3	20.8	15.1	3.3	5.4	11.3	39	16.7	660	4.3	2.6	256	25.1	77.6	91	
AR23	lava flow	pre-Kaupokonui		851	38.0	17.1	92.7	20.8	15.4	4.1	7.5	10.1	48	21.0	653	5.7	2.0	267	24.1	74.4	106	
AR25	lava flow	pre-Kaupokonui		764	32.5	21.8	60.5	21.0	14.1	3.3	8.5	11.0	37	22.3	654	2.9	1.9	287	24.9	77.2	89	
AR36	lava flow	pre-Kaupokonui		770	34.0	13.8	85.2	20.6	13.1	3.6	6.9	9.5	40	17.3	662	3.3	2.1	265	26.0	82.8	94	
AR37	lava flow	pre-Kaupokonui		859	37.0	14.3	101.4	20.5	16.8	3.8	7.6	11.8	48	15.6	657	4.4	2.4	262	24.7	76.5	107	
AR39	lava flow	pre-Kaupokonui		859	34.5	13.8	94.7	20.6	16.1	3.9	6.3	12.4	48	16.6	655	5.4	2.4	268	24.0	76.8	106	
AR47	lava flow	pre-Kaupokonui		889	33.9	14.2	80.1	21.1	17.4	4	5.7	12.4	48	13.8	653	5.3	2.2	254	24.2	73.3	108	
AR49	lava flow	pre-Kaupokonui		896	31.1	13.8	115.3	21.0	18.9	3.9	6.8	12.0	49	15.8	654	5.4	3.0	251	24.2	76.6	111	

[all data in ppm]

Sample	Sc	Ti	V	Cr	Ni	Rb	Sr	Y	Zr	Nb	Cs	Ba	La	Ce	Pr	Nd	Sm	Eu	Gd	Dy	Er	Yb	Lu	Hf	Ta	Pb	Th	U
SD4	16.9	4952	189	13.7	6.04	76.1	573	17.5	132	5.11	4.48	943	18.6	37.2	4.34	18.0	3.77	1.11	3.57	3.20	1.81	1.89	0.29	3.48	0.59	11.9	7.65	2.27
SD6	16.9	5006	197	11.3	6.60	87.2	556	17.4	148	5.89	5.14	1033	17.6	35.3	4.14	16.5	3.72	1.11	3.33	3.20	1.85	1.94	0.33	3.95	0.66	16.1	8.90	2.51
SD7	18.6	4951	196	9.77	6.89	52.7	544	18.0	110	4.51	3.05	822	16.7	33.7	4.06	17.3	3.92	1.08	3.54	3.30	1.93	1.85	0.29	2.97	0.55	8.2	6.33	1.48
T05-39	16.2	4564	177	27.7	149	79.1	547	16.4	136	5.24	4.92	931	18.8	37.6	4.37	17.7	3.63	1.04	3.26	3.00	1.69	1.76	0.28	3.62	0.38	14.5	8.26	1.98
SD13	16.7	4915	203	28.8	8.73	78.2	560	17.4	130	5.32	4.39	973	19.0	38.8	4.47	18.5	3.95	1.15	3.37	3.18	1.79	1.82	0.29	3.54	0.65	11.4	7.78	2.16
SD12	13.7	5216	205	9.06	3.95	86.3	625	15.9	118	5.08	4.49	971	18.4	39.4	4.53	18.8	3.90	1.11	3.36	2.89	1.68	1.72	0.26	3.22	0.58	20.7	7.08	2.23
SD35	19.6	5177	207	45.1	13.2	62.0	532	16.4	112	4.48	3.50	838	16.6	34.3	4.11	17.0	3.77	1.07	3.29	3.11	1.74	1.79	0.26	3.08	1.18	8.0	6.83	1.72
T04-22	18.8	4951	207	37.1	10.6	64.8	562	17.2	124	4.93	3.86	887	18.0	35.7	4.19	17.9	3.78	1.08	3.45	3.28	1.82	1.82	0.28	3.37	0.42	8.2	7.65	1.90
T04-96	20.8	5028	212	49.8	14.2	67.4	564	17.2	118	4.71	3.72	891	17.2	35.8	4.17	17.4	3.69	1.14	3.51	3.21	1.79	1.88	0.29	3.21	0.39	13.9	7.23	1.87
SD20	19.8	5509	214	47.0	18.2	55.4	540	16.3	115	4.64	3.23	871	18.4	38.4	4.42	17.9	3.74	1.07	3.39	3.03	1.67	1.71	0.27	3.11	1.06	12.4	6.77	1.67
P10	21.3	5387	219	56.1	23.0	59.2	538	16.8	112	4.66	3.44	838	16.4	34.6	4.10	17.1	3.67	1.08	3.31	3.11	1.68	1.77	0.27	3.02	0.38	14.1	6.56	1.89
T04-65	20.2	4904	213	42.4	11.0	67.6	524	17.3	120	4.76	4.05	856	17.2	34.8	4.11	17.4	3.73	1.06	3.41	3.10	1.77	1.85	0.29	3.23	0.38	12.5	7.02	2.01
T04-19	20.3	4867	192	38.4	11.9	68.0	565	17.0	119	4.54	3.84	890	17.4	35.0	4.12	17.2	3.70	1.13	3.47	3.22	1.80	1.90	0.28	3.29	0.36	10.2	7.48	1.94
SD24	19.9	5013	198	50.6	12.1	65.1	529	16.6	114	4.45	3.24	825	16.6	33.3	4.05	17.1	3.77	1.07	3.28	3.02	1.69	1.76	0.28	3.06	0.98	10.4	6.68	2.05
SD9a	20.2	5104	216	32.7	10.3	67.6	545	18.6	132	5.11	1.81	890	18.8	38.7	4.59	19.6	4.19	1.15	3.95	3.47	1.96	2.02	0.30	3.54	0.53	9.7	7.39	2.16
SD29	19.6	5101	209	50.1	12.7	60.5	543	16.9	114	4.37	3.43	856	16.9	34.6	4.10	17.4	3.77	1.09	3.50	3.17	1.79	1.80	0.28	3.16	0.33	14.3	7.10	1.78
T04-166	16.8	5300	193	28.3	11.3	64.0	583	17.5	131	5.15	3.62	966	19.9	39.9	4.70	19.5	4.10	1.17	3.81	3.28	1.85	1.87	0.28	3.55	0.38	11.8	8.18	1.82
P6	18.0	4766	180	32.3	25.8	67.9	518	16.8	126	5.14	3.84	911	17.9	36.7	4.24	17.8	3.71	1.08	3.32	3.09	1.75	1.85	0.28	3.33	0.46	13.0	7.93	1.87
T04-158	16.0	4991	175	28.5	10.3	95.2	567	17.0	147	6.01	5.33	1098	19.9	40.2	4.54	18.5	3.83	1.12	3.44	3.03	1.74	1.88	0.29	3.77	0.45	13.8	9.06	2.58
T04-163	15.9	4217	161	27.3	9.09	81.9	523	15.5	129	5.11	4.67	952	17.3	36.0	4.06	16.3	3.30	1.04	2.96	2.81	1.63	1.67	0.26	3.45	0.40	13.2	8.03	2.09
T04-180	16.4	4094	166	32.0	8.44	85.2	537	15.7	130	5.20	5.86	940	18.4	36.8	4.19	17.3	3.62	1.05	3.28	2.90	1.59	1.64	0.26	3.51	0.36	11.4	8.67	2.58
P7	15.7	4797	193	27.8	7.66	85.4	544	16.5	139	5.60	4.90	975	19.4	38.6	4.37	17.9	3.73	1.05	3.26	3.04	1.72	1.79	0.28	3.67	0.47	11.3	8.56	2.25
T04-178	19.5	5313	216	39.5	11.2	62.5	533	17.6	125	5.37	2.52	897	18.5	39.1	4.52	18.8	4.05	1.14	3.57	3.34	1.81	1.85	0.28	3.40	0.37	10.7	7.51	1.96
DS22	16.6	4506	176	33.4	9.06	75.4	497	16.1	133	5.37	4.35	944	18.1	36.8	4.14	17.0	3.50	0.98	3.16	2.99	1.65	1.72	0.26	3.55	0.64	14.6	8.19	2.14
T04-172	17.9	4872	185	30.0	9.74	66.0	504	16.6	124	5.10	3.85	886	17.6	36.0	4.18	17.2	3.59	1.05	3.42	3.03	1.69	1.76	0.27	3.30	0.37	12.4	7.32	1.88
T04-167	15.8	4712	190	22.9	7.96	74.5	571	16.6	132	5.53	4.38	996	18.9	39.8	4.51	18.2	3.77	1.12	3.52	3.06	1.69	1.83	0.27	3.49	0.35	14.3	8.08	2.16
SR21	16.1	4419	162	33.4	10.6	71.0	506	16.9	139	5.49	4.15	961	19.2	37.7	4.36	17.7	3.77	1.05	3.34	3.01	1.72	1.79	0.29	3.71	0.45	14.1	8.68	2.01
T04-152	17.1	4169	162	36.0	10.5	64.1	470	16.1	124	4.94	4.08	860	17.6	35.0	4.14	17.0	3.58	0.98	3.21	2.93	1.69	1.73	0.25	3.39	0.37	13.0	7.79	1.81
T04-174	18.0	4756	195	35.8	10.7	72.6	510	16.0	127	5.48	4.13	918	17.7	36.7	4.26	17.3	3.74	1.25	3.26	2.94	1.63	1.71	0.27	3.38	0.41	13.4	7.66	1.96
T04-168	20.9	5277	226	44.9	13.9	55.6	476	18.1	109	4.77	3.18	815	16.0	34.8	4.18	18.3	3.99	1.11	3.60	3.40	1.87	1.93	0.29	3.08	0.42	13.8	6.37	1.68
T04-162	15.9	4301	160	23.2	7.91	80.1	560	18.0	140	5.67	4.57	979	18.8	37.1	4.38	18.4	4.02	1.34	3.55	3.35	1.87	2.01	0.30	3.89	0.43	10.7	9.04	2.22
T04-158	17.9	5632	216	34.1	14.1	68.9	547	17.5	127	5.18	3.92	935	18.3	37.6	4.40	18.6	3.92	1.14	3.51	3.33	1.82	1.86	0.30	3.38	0.38	14.1	7.56	2.00
T04-165	13.3	4749	141	29.4	9.89	119	568	16.6	175	6.77	6.00	1191	21.3	42.1	4.66	18.4	3.65	1.03	3.12	2.83	1.69	1.92	0.30	4.62	0.55	16.1	11.3	3.26

Sample	Sc	Ti	V	Cr	Ni	Rb	Sr	Y	Zr	Nb	Cs	Ba	La	Ce	Pr	Nd	Sm	Eu	Gd	Dy	Er	Yb	Lu	Hf	Ta	Pb	Th	U
Py19	15.8	5072	189	36.9	12.5	89.2	527	15.9	133	5.41	5.11	997	19.1	39.4	4.31	18.1	3.59	1.05	3.16	2.85	1.64	1.73	0.28	3.39	0.47	10.7	8.46	2.75
T05-34	19.5	5385	206	50.3	11.7	51.7	502	15.7	109	4.30	3.00	770	16.4	33.1	3.92	16.6	3.43	1.00	3.13	2.85	1.65	1.69	0.26	3.00	0.30	14.1	6.55	1.51
NZ1	16.4	5334	192	24.3	9.14	79.4	582	17.0	138	5.54	4.86	979	19.7	40.7	4.78	19.5	4.02	1.14	3.52	3.11	1.71	1.80	0.29	3.59	0.43	10.5	8.35	2.20
P1	18.8	5077	201	43.1	12.2	62.4	543	17.3	128	5.30	3.69	927	18.1	37.4	4.35	18.0	3.84	1.08	3.46	3.17	1.76	1.81	0.29	3.49	0.98	13.3	7.62	1.76
DS6	16.6	5055	205	34.4	12.0	64.3	508	16.5	132	5.33	3.85	927	18.3	36.5	4.24	17.3	3.68	1.00	3.20	3.03	1.74	1.79	0.27	3.56	0.66	13.7	8.10	1.77
T04-177	18.4	4885	208	25.8	9.11	66.0	532	16.9	117	4.55	3.63	886	17.2	34.6	4.14	17.5	3.79	1.12	3.44	3.17	1.77	1.79	0.28	3.15	0.32	10.2	6.85	1.91
T04-171	16.8	4533	162	25.7	8.89	101	580	18.9	175	6.80	5.87	1108	21.5	43.8	4.90	19.9	4.12	1.11	3.58	3.30	1.95	1.98	0.32	4.46	0.50	9.5	10.8	2.58
NZ3	14.7	4109	150	25.8	7.61	96.7	524	16.4	143	5.71	5.42	993	19.5	39.5	4.46	18.2	3.63	1.04	3.18	2.97	1.66	1.90	0.28	3.83	0.45	13.5	9.02	2.59
T04-170	15.9	5069	188	26.0	8.17	95.7	559	17.1	145	5.71	5.48	1039	20.2	40.9	4.60	18.9	3.79	1.08	3.47	3.01	1.74	1.84	0.29	3.83	0.41	11.9	8.86	2.58
T04-200	21.0	5000	202	12.7	13.9	38.0	559	15.2	68	2.91	0.94	604	11.6	24.8	3.14	13.8	3.24	1.01	3.11	2.79	1.56	1.60	0.24	1.97	0.21	9.0	3.58	1.01
MI-5	20.8	6299	242	9.31	6.40	50.3	635	18.8	103	4.61	1.07	822	16.3	35.2	4.40	19.5	4.50	1.28	4.11	3.64	1.93	1.93	0.28	2.96	0.31	16.0	5.34	1.37
E03-77	23.3	6977	315	19.4	10.7	45.3	619	19.1	99	4.08	2.22	732	15.8	33.6	4.28	19.4	4.60	1.36	4.18	3.70	1.98	1.95	0.27	2.82	0.27	11.8	4.97	1.29
T04-61	21.5	5522	200	11.1	6.10	58.0	674	20.6	118	4.93	3.04	893	18.6	38.3	4.80	20.9	4.81	1.39	4.50	4.07	2.21	2.16	0.31	3.35	0.34	11.8	6.43	1.51
T04-57	20.2	8596	356	12.0	6.81	69.9	696	20.9	132	5.88	3.65	1007	20.1	42.6	5.18	22.8	4.80	1.42	4.63	4.02	2.12	2.15	0.31	3.64	0.40	13.6	6.87	1.84
T04-56	19.4	5912	218	13.2	7.07	56.5	557	18.0	108	4.80	3.13	771	15.6	33.0	4.03	17.6	3.79	1.12	3.64	3.34	1.80	1.83	0.29	3.11	0.37	10.0	5.61	1.55
DS24a	14.7	6242	201	6.25	4.17	51.7	610	20.0	114	4.52	2.89	717	15.7	35.0	4.45	19.6	4.25	1.23	3.89	3.74	2.05	2.10	0.33	3.10	0.36	11.2	5.20	1.26
E02-26	19.2	6323	230	24.4	8.66	60.2	621	18.7	118	4.91	2.90	865	18.6	38.6	4.63	19.9	4.26	1.24	3.87	3.51	1.96	1.93	0.28	3.21	0.74	10.9	6.20	1.65

[all data in ppm]